



HAL
open science

Synthesis and optical properties of graphene nanostructures

Daniel Medina Lopez

► **To cite this version:**

Daniel Medina Lopez. Synthesis and optical properties of graphene nanostructures. Organic chemistry. Université Paris-Saclay, 2023. English. NNT : 2023UPASF060 . tel-04925287

HAL Id: tel-04925287

<https://theses.hal.science/tel-04925287v1>

Submitted on 2 Feb 2025

HAL is a multi-disciplinary open access archive for the deposit and dissemination of scientific research documents, whether they are published or not. The documents may come from teaching and research institutions in France or abroad, or from public or private research centers.

L'archive ouverte pluridisciplinaire **HAL**, est destinée au dépôt et à la diffusion de documents scientifiques de niveau recherche, publiés ou non, émanant des établissements d'enseignement et de recherche français ou étrangers, des laboratoires publics ou privés.

Synthesis and optical properties of graphene nanostructures

Synthèse et propriétés optiques de nanostructures de graphène

Thèse de doctorat de l'université Paris-Saclay

École doctorale n°571 : sciences chimiques : molécules, matériaux,
instrumentation et biosystèmes (2MIB)

Spécialité de doctorat : Chimie

Graduate School : Chimie. Référent : Faculté des sciences d'Orsay

Thèse préparée dans l'unité de recherche **NIMBE** (Université Paris-Saclay, CEA, CNRS), sous la direction de **Stéphane CAMPIDELLI**, Directeur de recherche CEA

Thèse soutenue à Paris-Saclay, le 13 octobre 2023, par

Daniel MEDINA LOPEZ

Composition du Jury

Membres du jury avec voix délibérative

Anna PROUST Professeure, Sorbonne Université	Présidente
Pierre-Antoine BOUIT Chargé de recherche, HDR, Université de Rennes	Rapporteur & Examineur
Claire KAMMERER Maîtresse de conférences, HDR, Université Toulouse III	Rapporteur & Examinatrice
David KREHER Professeur, Université de Versailles Saint- Quentin-en-Yvelines	Examineur
Valérie MARVAUD Directrice de recherche, Sorbonne Université	Examinatrice

Titre : Synthèse et propriétés optiques de nanostructures de graphène

Mots clés : synthèse bottom-up, graphène, nanoparticules, nanomeshes, nanographene, photoluminescence

Résumé : Au cours des dernières années, le graphène a suscité une attention considérable en raison de ses excellentes propriétés mécaniques, thermiques et électriques. Cependant, l'absence de gap électronique dans le graphène constitue une barrière pour des applications en optique et optoélectronique. Pour surmonter cette limitation, l'ouverture d'une bande interdite impliquant la nanostructuration du graphène a été développée au fil des années. Ce travail de thèse se concentre sur la synthèse « bottom-up » et les études optiques de deux matériaux graphéniques : les nanoparticules de graphène et les nanomeshes de graphène.

Les nanoparticules de graphène ont tendance à s'agréger par des interactions π - π , ce qui limite l'étude de leurs propriétés optiques intrinsèques. Grâce à l'approche « bottom-up » il est possible de contrôler la taille, la forme et les bords des structures avec une précision atomique, permettant de concevoir des architectures spécifiques pour limiter le processus d'agrégation.

La première partie de cette thèse est consacrée à la synthèse d'une famille de nanoparticules de graphène de forme allongée, qui, grâce à l'intégration de groupes fonctionnels volumineux dans leur structure, sont hautement solubles dans des solvants organiques. Cette solubilité améliore leur processabilité et a permis une description précise des propriétés photophysiques de ces nanoparticules en combinant des données expérimentales et théoriques.

La deuxième partie explore deux méthodes pour augmenter la solubilité des nanoparticules. Soit en élargissant la stratégie employée dans la famille allongée, soit en brisant le caractère purement bidimensionnel des nanoparticules de graphène par la synthèse des structures hélicoïdales.

La dernière section est consacrée à la synthèse de différents précurseurs organiques et à leur dépôt sur des surfaces métalliques afin de les assembler en nanomeshes de graphène.

Title : Synthesis and optical properties of graphene nanostructures

Keywords : Bottom-up synthesis, graphene, nanoparticles, nanomeshes, nanographene, photoluminescence

Abstract : In recent years, graphene has captured significant attention due to its excellent mechanical, thermal, and electrical properties. However, the absence of a bandgap in graphene constitutes a barrier for applications in optics and optoelectronics. To overcome this limitation, bandgap engineering involving the nanostructuration of graphene has been developed over the years. This thesis work focus on the bottom-up synthesis and optical studies of two nanostructured graphenic objects: graphene quantum dots (GQDs) and graphene nanomeshes (GNMs).

The tendency of nanographene materials to aggregate via π -stacking interactions constitutes a limitation in the study of their intrinsic optical properties. Thanks to the bottom-up approach, it is possible to control the structure's size, shape, and edges with atomic precision, enabling the design of specific architectures to limit the aggregation process.

The first part of this thesis is dedicated to the synthesis of a family of rod-shaped graphene nanoparticles that exhibit a high solubility thanks to the integration of bulky functional groups into their structure. Thanks to this enhanced solubility and processability, an accurate description of the photophysical properties of these GQDs, combining experimental and theoretical data, was possible.

The second part explores on further increasing the solubility of GQDs by expanding the strategy employed in the rod-shaped family and by breaking the purely two-dimensional character of GQDs through twisted or helical structures.

The last section is dedicated to the synthesis of different organic precursors and their deposition on metallic surfaces for their assembly into GNMs.

RESUME EN FRANÇAIS

SYNTHESE ET PROPRIETES OPTIQUES DE NANOSTRUCTURES DE GRAPHENE

Depuis la découverte du graphène en 2004, plusieurs propriétés intéressantes telles qu'une haute conductivité, une grande résistance mécanique et une transparence optique ont été mises en évidence. Cependant, l'absence de gap énergétique limite les applications du graphène en optique et optoélectronique. Pour ouvrir une bande interdite dans le graphène, il est possible de nano-structurer le matériau. En réduisant les deux dimensions du graphène à une taille nanométrique, on obtient des nanoparticules de graphène. En réduisant une seule de ses dimensions, on forme des nanorubans de graphène. Finalement, il est possible de créer un réseau de trous réguliers de taille nanométrique dans un feuillet de graphène pour obtenir des nanomeshes de graphène. Pendant ce travail de thèse nous nous sommes principalement intéressés à deux structures graphéniques : les nanoparticules et les nanomeshes de graphène.

Ces nanomatériaux peuvent être synthétisés *via* une approche descendante ou ascendante. C'est la deuxième qui a été pertinente dans ce travail de thèse car elle permet une synthèse à l'atome près. Il est donc possible de créer des matériaux avec une taille, une forme et des groupements fonctionnels bien définis. Avec des structures contrôlées et homogènes, il est possible de s'intéresser aux propriétés optiques intrinsèques des nanoparticules. Les études sur les propriétés optiques intrinsèques des nanoparticules de graphène sont rares. La première raison repose sur le fait que la majorité des nanoparticules étudiées ont été synthétisées par des méthodes descendantes et, du fait de leur méthode de synthèse, ces particules ne sont pas toutes identiques et elles contiennent des multiples défauts et inhomogénéités qui régissent leurs propriétés optiques. Avec le développement croissant par la synthèse organique de grands hydrocarbures aromatiques polycycliques (PAHs), de nouveaux défis ont émergé concernant notamment la faible solubilité de ces molécules. Tout d'abord, les études optiques se sont limitées à l'observation de petits PAHs, comme l'hexabenzocoronène. En raison des interactions π - π importantes, les nanoparticules de graphène les plus grands n'ont été étudiés que par spectroscopie d'absorption, donnant lieu à des spectres présentant des transitions larges et difficiles à analyser. En réponse à ce problème, des substituants ont été ajoutés le long des bords des nanoparticules (par exemple, des chaînes alkyles, des groupements *tert*-butyle, des atomes de chlore ou des groupes alcoxy). Bien que ces substituants aient aidé à améliorer légèrement la solubilité des PAH, pour la plupart, ils continuent à s'agréger, limitant ainsi l'étude de leur propriétés. Cette faible solubilité impacte également la possibilité de purification. Cependant, avoir des échantillons purs de nanoparticules de graphène pour les études optiques est très important car la présence d'impuretés peut conduire à une mauvaise interprétation du comportement optique.

Dans la première partie de cette thèse, nous nous sommes concentrés sur l'amélioration de la solubilité des nanoparticules de graphène. Dans un premier temps, nous avons synthétisé une famille de nanoparticules de graphène de forme allongée et de symétrie C_{2h} portant des groupes *tert*-butyle le long de leur axe principal. Cette famille est composée de quatre membres : $C_{78}tBu_6$, $C_{96}tBu_8$, $C_{114}tBu_{10}$ et $C_{132}tBu_{12}$ d'une taille allant de 1,99 nm à 3,11 nm (**Figure R.1**). La stratégie de synthèse de cette famille repose sur la formation d'un dendrimère polyphénylène à partir d'une réaction de Diels-Alder entre un cœur portant des groupements alcynes et une cyclopentadienone. Ce dendrimère est ensuite soumis à une cyclodéshydrogénation, ou réaction de Scholl, pour créer les nouvelles liaisons carbone-carbone et obtenir un domaine graphénique.

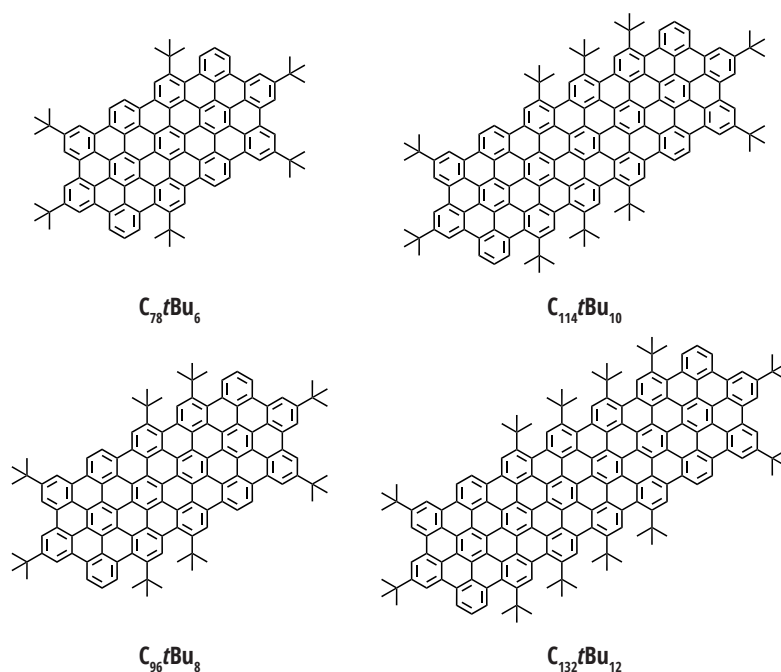


Figure R.1 | Structures des nanoparticules allongées partiellement *tert*-butylées.

Avec cette famille, nous avons constaté que le positionnement des groupements fonctionnels joue un rôle crucial pour supprimer les interactions π - π . Les premières observations optiques ont suggéré que les plus grandes nanoparticules sont hautement solubles et individualisées en solution malgré leur grande taille. Étonnamment, le plus petit membre, la nanoparticule **$C_{78}tBu_6$** , a montré un comportement qui pourrait être expliqué par l'agrégation en solution. L'inverse est généralement vrai : à fur et à mesure que la taille augmente, les interactions π - π deviennent plus importantes, et donc l'agrégation augmente. Pour mieux comprendre ce processus, des calculs sur deux nanoparticules de cette famille allongée, la **$C_{96}tBu_8$** et la **$C_{78}tBu_6$** , ont été effectués en collaboration avec des théoriciens de l'Université de Mons en Belgique et l'Université de Varsovie en Pologne. Ces calculs ont mis à jour deux raisons pour lesquelles l'agrégation dans **$C_{96}tBu_8$** est supprimée, qui sont liées à la présence de groupes *tert*-butyles adjacents le long de l'axe principal de la nanoparticule : l'encombrement stérique des groupement fonctionnels et l'existence de conformères stables et instables. En effet, le positionnement des groupements *tert*-butyles engendre la présence de conformères, six dans le cas de **$C_{96}tBu_8$** . Lors du processus d'agrégation, les calculs ont montré la présence d'une barrière énergétique générée par l'encombrement stérique des *tert*-butyles. Néanmoins, cette barrière peut être surmontée si les groupes fonctionnels sont préalablement disposés dans des configurations spécifiques. Dans le cas de **$C_{96}tBu_8$** , les conformères avec des configurations permettant le début d'agrégation sont très énergétiques et n'existent pratiquement pas en solution, ce qui confère une grande solubilité à la nanoparticule. Dans le cas de **$C_{78}tBu_6$** , ses deux conformères existent et ils sont tous deux présents solution, ce qui constitue un point d'entrée au processus d'agrégation.

La grande solubilité de la famille des nanoparticules allongées a permis une purification efficace des nanoparticules par des techniques standard en chimie organique : précipitations, chromatographie sur colonne de silice et chromatographie d'exclusion stérique. Il a été possible d'obtenir des échantillons de nanoparticules de grande pureté. De plus, grâce à leur solubilité accrue, leur structure a pu être confirmée par spectrométrie de masse et par résonance magnétique nucléaire (RMN). Ces échantillons purs et solubles ont permis d'effectuer des expériences optiques plus poussées en collaboration avec des physiciens au laboratoire LUMIN à l'ENS Paris-Saclay. La nanoparticule **$C_{96}tBu_8$** a été prise comme exemple pour décrire les propriétés optiques de la famille allongée. Cette nanoparticule présente un spectre d'absorption bien défini avec des bandes

d'absorption fines permettant d'apprécier le couplage vibronique. En combinaison avec des descriptions théoriques, il a été possible d'attribuer les pics observés dans les spectres d'absorption et d'émission aux transitions électroniques et à leurs vibrations associées. Ces attributions ont été confirmées par des expériences d'anisotropie de fluorescence, où il a été possible d'observer la variation de l'orientation du dipôle des transitions d'absorption par rapport au dipôle d'émission. Enfin, des expériences à l'échelle de la molécule unique ont été réalisées pour la nanoparticule **C₉₆tBu₈**. Un excellent accord a été trouvé entre les propriétés optiques en solution et celles observées pour une seule molécule, confirmant que **C₉₆tBu₈** est hautement individualisée en solution.

Avec cette famille de nanoparticules de graphène allongées, il a été possible d'ajuster l'absorption et l'émission de plus de 150 nm en fonction de la taille (**Figure R.2**). Une émission jusqu'au proche infrarouge a été observée pour le plus grand membre de la famille. D'ailleurs, l'augmentation de la taille a eu une influence sur la distribution des charges des transitions électroniques, générant des différences entre les intensités des différentes transitions électroniques dans les spectres d'absorption. Enfin, cette famille de nanoparticules allongées possède des rendements quantiques très élevés, jusqu'à 94% pour **C₉₆tBu₈**. C'est l'un des plus hauts rendements décrits pour des nanoparticules de graphène. Tous ces comportements intéressants de la famille allongée des nanoparticules nous ont encouragés à intégrer **C₇₈tBu₆** et **C₉₆tBu₈** dans des diodes électroluminescentes organiques en tant que matériaux émissifs. Bien que les performances des dispositifs ne soient pas encore optimales, cela a servi de preuve de concept pour les applications potentielles de ces nanoparticules.

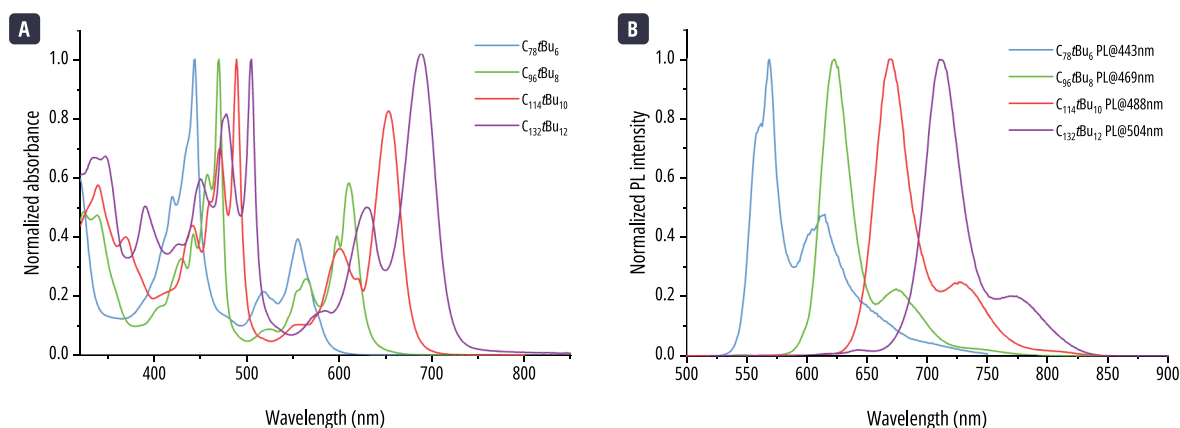


Figure R.2 | (a) Spectres d'absorption des nanoparticules allongées partiellement *tert*-butylées. (b) Spectres d'émission.

Pour augmenter davantage la solubilité des nanoparticules, nous avons procédé à l'ajout des groupements *tert*-butyles supplémentaires le long de l'axe des nanoparticules. Ceci a généré une famille de nanoparticules entièrement *tert*-butylées, composée de quatre membres (**Figure R.3**) : **C₆₀tBu₈**, **C₇₈tBu₁₀**, **C₉₆tBu₁₂**, et **C₁₁₄tBu₁₄**. En outre, un cinquième membre, la **C₁₃₂tBu₁₆**, est en cours de synthèse. Les groupes fonctionnels supplémentaires ont été très efficaces pour supprimer l'agrégation des plus petits membres de la famille : **C₆₀tBu₈** et **C₇₈tBu₁₀**. Les premières mesures optiques ont révélé de nouveaux comportements pour ces membres par rapport à la famille précédente. D'ailleurs, les groupements *tert*-butyles supplémentaires ont eu un effet bathochrome de l'absorption et l'émission et ont engendré un effet moins prononcé dans la distribution de charges en fonction de la taille, par rapport à la famille partiellement *tert*-butylée (**Figure R.4**).

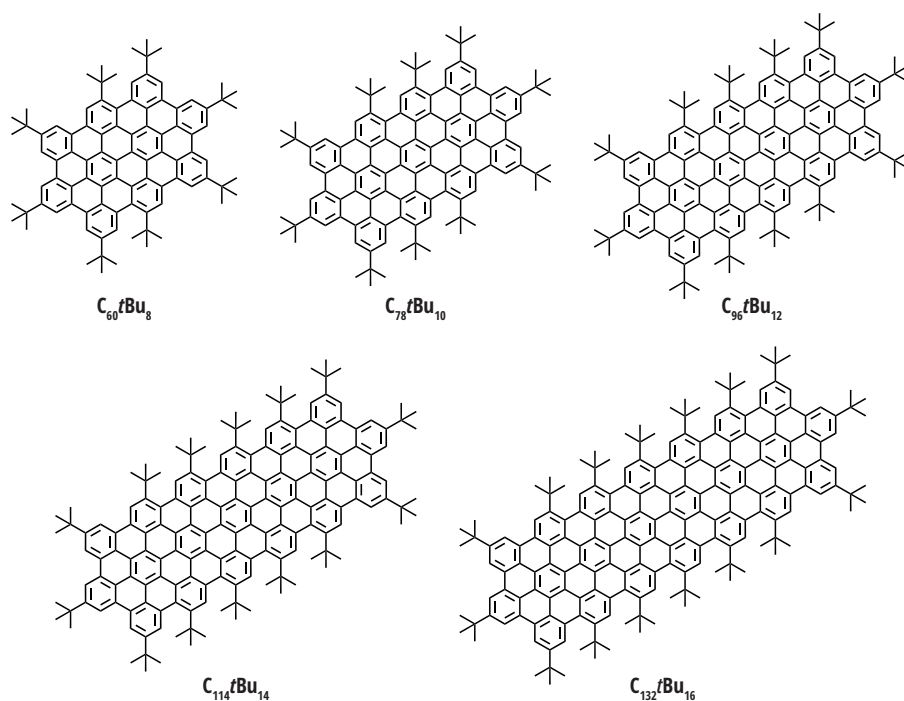


Figure R.3 | Structures des nanoparticules allongées complètement *tert*-butylées.

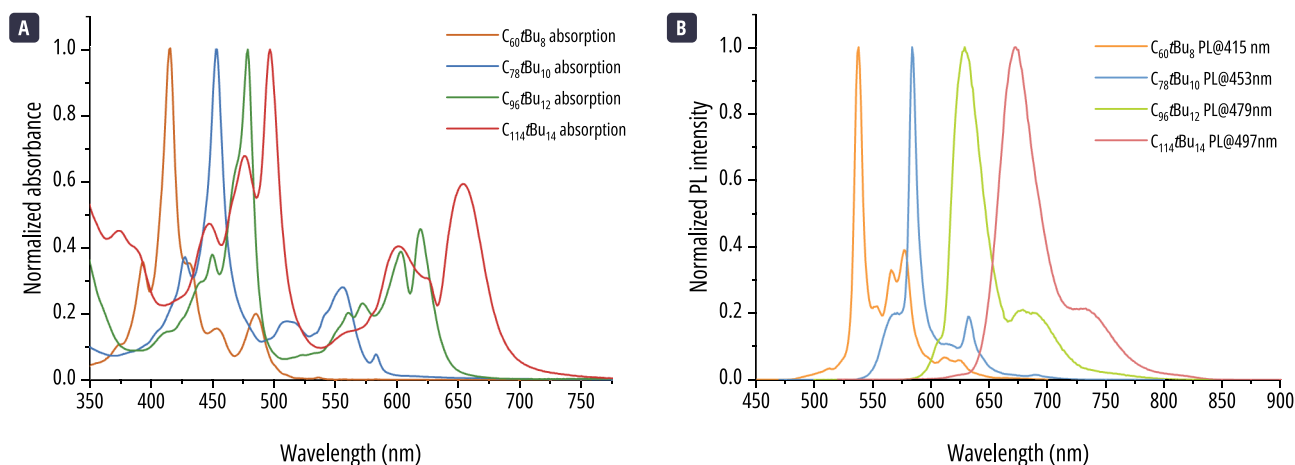


Figure R.4 | (a) Spectres d'absorption des nanoparticules allongées complètement *tert*-butylées. (b) Spectres d'émission des nanoparticules.

Une stratégie alternative pour augmenter la solubilité des nanoparticules de graphène consiste à briser leur caractère bidimensionnel pour diminuer les interactions π - π . Cette approche a été testée lors de cette thèse avec la synthèse d'hélicènes (Figure R.5). Trois triple-[6]hélicènes ont été ciblés en introduisant un encombrement stérique dans leur structure pour prévenir la planarisation : $(C_{30}tBu_4)_3-T[6]H$, $(C_{36})_3-T[6]H$, et $(C_{36}tBu_5)_3-T[6]H$. Il a été observé que lorsque seuls des groupes *tert*-butyles sont utilisés pour ajouter un encombrement stérique, comme c'est le cas pour $(C_{30}tBu_4)_3-T[6]H$, ces groupes sont enlevés lors de l'oxydation de Scholl et une nanoparticule plane est obtenue. L'oxydation du dendrimère hautement encombré **44**, a démontré l'importance de la caractérisation des structures obtenues par d'autres méthodes que la spectrométrie de masse. Or, cette dernière est la méthode de choix d'analyse des hydrocarbures aromatiques polycycliques de grande taille du fait de leur faible solubilité. L'analyse est particulièrement importante car le mécanisme d'oxydation de Scholl n'est pas encore totalement compris, et des réarrangements imprévus peuvent avoir lieu. Le spectre de masse lors de l'étape de cyclodéshydrogénation du dendrimère **44** a donné la valeur m/z et les distributions isotopiques attendues pour $(C_{36}tBu_5)_3-T[6]H$. Cependant, l'analyse par RMN a montré une distribution de pics inattendue. C'est grâce à la mesure de la structure par diffraction de rayons-X sur un

monocristal que nous avons pu identifier que l'hélicène cible n'a pas été formé. À sa place, la nanoparticule bis-spiro **47** a été obtenue, cette structure possède deux carbones au centre de la molécule où l'hybridation sp^2 a été brisée. Cette nanoparticule bis-spiro possède des bonnes propriétés chiroptiques qui ont été analysées par dichroïsme circulaire et par spectroscopie de luminescence de circulairement polarisée. Finalement, une nanoparticule possédant deux domaines graphéniques attachés de façon covalente, $(C_{72}tBu_8)_2$, a pu être synthétisée et caractérisée par RMN. Dans cette thèse nous présentons ses études optiques préliminaires.

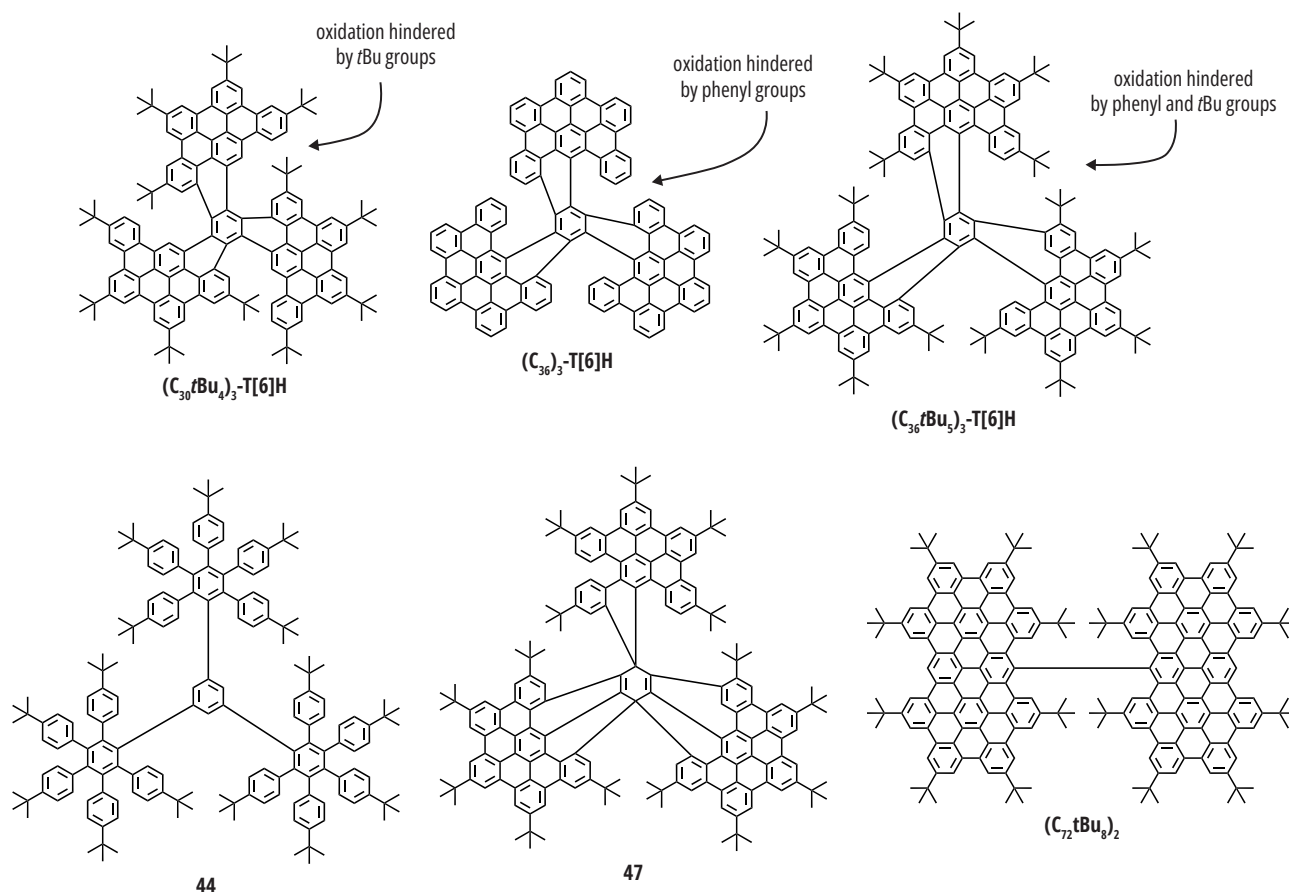


Figure R.5 | Structure des différentes nanoparticules de graphène hélicoïdales.

La dernière partie de ce travail de thèse a été consacrée à la synthèse de différents précurseurs de nanomeshes de graphène et à leur dépôt sur une surface métallique pour leur assemblage (voir **Figure R.6** pour les structures). L'objectif principal est la synthèse du **GNM-1**, qui garde une structure graphénique partout dans sa structure. Pour cela un précurseur de forme hexagonale **67** avec des groupes halogènes pour guider le couplage à la surface a été synthétisé. Nos premières tentatives de dépôt sur surface de ce précurseur se sont confrontées à une faible adsorption à la surface du fait de sa nature tridimensionnelle. Pour améliorer son adsorption, le précurseur a été cyclodéshydrogéné pour obtenir un dérivé de l'hexabenzocoronène **72**. Ce composé a montré une meilleure adsorption à la surface et a donné de très beaux assemblages supramoléculaires. Cependant, il n'a pas donné le réseau bidimensionnel attendu à cause d'une mauvaise accessibilité aux sites de couplage par l'encombrement stérique des atomes d'hydrogène adjacents. Une stratégie alternative pour la formation de nanomeshes de graphène a également été introduite : la synthèse en surface de nanorubans de graphène suivie de leur fusion latérale. Néanmoins, l'obtention de grands nanorubans de graphène avec nos deux précurseurs en forme de trapèze (**73** et **74**) s'est avérée compliquée. Lors du recuit, seulement des structures désordonnées ont été obtenues.

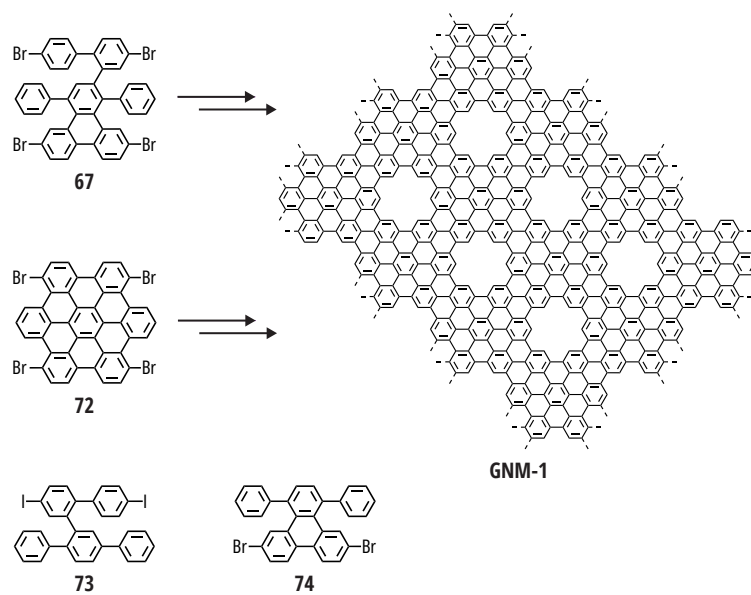


Figure R.6 | Structures des différents précurseurs testés pour l'obtention d'une nanomaille de graphène. Structure de la nanomaille de graphène ciblée **GNM-1**.

REMERCIEMENTS

Je souhaite remercier spécialement mon directeur de thèse, Stéphane Campidelli, pour toute la confiance qu'il m'a accordée pendant ces années. Merci pour toutes ces discussions et pour ta vive passion pour la chimie.

Je voudrais remercier les membres du jury : Dr. Anna Proust, Dr. Claire Kammerer, Dr. David Kreher, Dr. Pierre-Antoine Bouit et Dr. Valérie Marvaud. Merci pour tous vos regards sur ce travail.

Je remercie tous nos collaborateurs sans qui ce travail de thèse ne serait pas ce qu'il est aujourd'hui : Jean-Sébastien L., Loïc R., Thomas L., Christine E., Hugo L-F., David B., Nicolas R., Silvio O., Fabien L., Bruno J., Gaspard H., Sylvain C., Grégory P., Lilian E., Sylvain L., Yannick D., et Van Bihn V. Merci pour votre aide, vos conseils et vos explications.

Je remercie toute l'équipe du LICSEN et du NIMBE. Merci à Vincent pour son soutien et sa bonne humeur. Je remercie les stagiaires, thésards, post-docs et permanents que j'ai côtoyés au fil de ces années pour leur bienveillance et jovialité, ils ont grandement contribué à mon épanouissement au laboratoire. Je souhaite tout particulièrement remercier Nathan, Raphaël, Yuemin, Cynthia, Kevin, Lina et Ndrina. Merci également aux stagiaires que j'ai pu encadrer pendant ma thèse : Liliana, Félicien et Cynthia.

Je remercie mes amis qui m'ont accompagné toutes ces années : Lucie, Lina, Clara, Pierre, Milan, Raquel, Montse, Emilio, Alexis, Juliette, Lauralie, Alexandre, Pauline, Adrien, Estelle et Linh. Merci pour les bons moments partagés ensemble et qui m'ont permis d'équilibrer ce travail.

Un énorme merci à Guillaume. Merci d'avoir été là. Merci pour ton soutien constant et tes conseils.

Finalmente quiero agradecer a mi toda mi familia por todo su aliento. A mis papas, Margarita y Humberto, por todo su apoyo a lo largo de todos estos años, que hoy culminan con este trabajo. Hoy termino esta meta con ustedes, sepan que este logro también es suyo. A mis hermanos, Pamela y Rogelio, por nuestra complicidad y por su presencia a lo largo de esta aventura.

Para Victoria y Ma. Alberta.

TABLE OF CONTENTS

RESUME EN FRANÇAIS	I
REMERCIEMENTS.....	VII
TABLE OF CONTENTS	XI
LIST OF ABBREVIATIONS	XIII
CHAPTER 1 INTRODUCTION	1
1.1 Graphene	3
1.1.1 Properties and applications.....	4
1.1.2 Opening a band gap in graphene	5
1.2 Nanographene synthesis	7
1.2.1 Graphene quantum dots	8
1.2.2 Graphene nanoribbons	15
1.2.3 Graphene nanomeshes	17
1.3 Optical properties of QDs	22
1.3.1 Generalities.....	22
1.3.2 Optical Studies of QDs.....	25
1.4 Scope of this work	29
CHAPTER 2 SOLUBLE ROD-SHAPED GRAPHENE QUANTUM DOTS	31
2.1 Introduction	34
2.1.1 Scholl reaction.....	34
2.1.2 Preceding work.....	36
2.2 A change in functional groups	37
2.2.1 Synthesis and studies of the triangular C ₉₆ QD	37
2.2.2 Synthesis of a first rod-shaped C ₉₆ QD	40
2.3 Synthesis and optical studies of C ₉₆ tBu ₈	42
2.3.1 Synthesis	43
2.3.2 Characterization	47
2.3.3 Optical properties.....	54
2.4 Varying the rod-size	66
2.4.1 Synthesis	66
2.4.2 Characterizations.....	69
2.4.3 Optical studies.....	75
2.5 Towards the first applications	80
2.6 Conclusion.....	82

CHAPTER 3	TOWARDS MORE SOLUBLE QDs	85
3.1	Fully <i>tert</i> -butylated rod-shape QDs	87
3.1.1	Synthesis	88
3.1.2	Characterizations	92
3.1.3	Optical properties	96
3.2	Twisted nanographenes	102
3.2.1	C ₉₆ based triple [6]helicenes	103
3.2.2	GQD propeller	113
3.3	Conclusion	121
CHAPTER 4	GRAPHENE NANOMESHES	123
4.1	Generalities	125
4.1.1	Reaction Mechanisms	125
4.1.2	Scanning probe microscopies	126
4.1.3	Experimental parameters	127
4.1.4	Preceding work and current objective	129
4.2	A GQD strategy for a GNM precursor	131
4.2.1	First approaches to the synthesis of a tetra-halogenated precursor	131
4.2.2	An alternative approach to the synthesis of a polyphenylene precursor	134
4.2.3	A GQD as a GNM precursor	137
4.3	A GNR strategy to obtain GNM	143
4.3.1	General strategy	144
4.3.2	An iodinated GNR precursor	146
4.3.3	A brominated GNR precursor	147
4.3.4	Revising the synthesis of a GNR	149
4.4	Conclusion	150
CHAPTER 5	CONCLUSION	153
CHAPTER 6	EXPERIMENTAL SECTION	161
6.1	Techniques	163
6.2	Solvents and reagents	164
6.3	Protocols	164
REFERENCES		193
APPENDIX 1		209
APPENDIX 2		216

LIST OF ABBREVIATIONS

Abbreviation	Definition
AAO	Anodic aluminum oxide
AFM	Atomic force microscopy
ARPES	Angular resolved photoemission spectroscopy
B ₂ Pin ₂	Bispinacolato diboron
BCP	Bathocuproine
C-C	Carbon-carbon
CD	Circular dichroism
CEA	Commissariat à l'énergie atomique
CHP	Hexaiodo-cyclohexa- <i>m</i> -phenylene
CNT	Carbon nanotube
COF	Covalent organic framework
COSY	Correlated spectroscopy
CP	Cyclopentadienone
CPL	Circularly polarized luminescence
CTPA	Carbonyl-bridged triphenylamines
CV	Cyclic voltammetry
CVD	Chemical vapor deposition
DCM	Dichloromethane
DCTB	Trans-2-[3-(4- <i>tert</i> -butylphenyl)-2-methyl-2-propenylidene]malononitrile
DDQ	2,3-dichloro-5,6-dicyano-1,4-benzoquinone
DFT	Density function theory
DMSO	Dimethyl sulfoxide
DP-DBBA	Diphenyl-10,10'-dibromo-9,9'-bianthracene
dppf	1,1'-Ferrocenediyl-bis(diphenylphosphine)
EC	Electrochemical
EL	Electroluminescence
ENS	École normale supérieure
EQE	External quantum efficiency
Et ₃ N	Triethylamine
EtOH	Ethanol
eV	Electron volt
FCC	Face-centered cubic
GDQ	Graphene quantum dot
GNM	Graphene nanomesh
GNR	Graphene nanoribbon
GO	Graphene oxide
GRM	Graphene related materials
GS	Graphene sheets
h-BN	Hexagonal boron nitride

HBC	Hexa- <i>peri</i> -benzocoronene
HMBC	Heteronuclear multiple bond correlation
HOMO	Highest occupied molecular orbital
HPLC	High performance liquid chromatography
HRMS	High resolution mass spectroscopy
HSE	Heyd–Scuseria–Ernzerhof
HSQC	Heteronuclear single quantum coherence
<i>i</i> -prOBpin	Iso-(propoxy)boronpinacol
IC	Internal crossing
IM2NP	Institut Matériaux Microélectronique Nanoscience de Provence
ISC	Intersystem crossing
ITO	Indium tin oxide
LED	Light-emitting diode
LPICM	Laboratoire de Physique des Interfaces et des Couches Minces
LUMIN	Lumière, Matière et Interfaces
LUMO	Lowest unoccupied molecular orbital
M_A	Absorption transition moment
MALDI	Matrix assisted laser desorption ionization
M_E	Emission transition moment
MeNO ₂	Nitromethane
MeOH	Methanol
MOF	Metal-organic framework
MS	Mass spectrometry
MSA	Methanesulfonic acid
<i>n</i> -BuLi	<i>n</i> -butyllithium
NBS	<i>N</i> -bromosuccinimide
nc-AFM	Non-contact atomic force microscopy
NIR	Near-infrared
NMR	Nuclear magnetic resonance
NOESY	Nuclear overhauser effect spectroscopy
o-DCB	Ortho-dichlorobenzene, 1,2-dichlorobenzene
OAc	Acetate
OLED	Organic light-emitting diode
OTf	Triflate
OXD-7	1,3-bis[2-(4- <i>tert</i> -butylphenyl)-1,3,4-oxadiazol-5-yl]benzene
PAH	Polycyclic aromatic hydrocarbon
PEDOT:PSS	Poly(3,4-ethylenedioxythiophene) polystyrene sulfonate
Ph	Phenyl
PIFA	[Bis(trifluoroacetoxy)ido]-benzene
PL	Photoluminescence
PLE	Photoluminescence excitation
PS	Polystyrene

PTFE	Polytetrafluoroethylene
PVK	Polyvinylcarbazole
r.t.	Room temperature
rGO	Reduced graphene oxide
SCE	Saturated calomel electrode
SEC	Size exclusion chromatography
SEM	Scanning electron microscopy
SMS	Single-molecule spectroscopy
Sphos	2-dicyclohexylphosphino-2',6'-dimethoxybiphenyl
STM	Scanning tunneling microscopy
TADF	Thermally activated delayed fluorescence
TBPB	1,3,5-tris(4-bromophenyl)benzene
TCB	1,2,4-trichlorobenzene
TCNQ	Tetracyanoquinone
TD	Time dependent
TD-DFT	Time dependent density function theory
TEB	1,3,5-tris-(4-ethynylphenyl)benzene
TEM	Transmission electron microscopy
THF	Tetrahydrofuran
TLC	Thin layer chromatography
TmPyPB	1,3,5-Tris(3-pyridyl-3-phenyl)benzene
TMS	Trimethylsilane
TMSA	Trimethylsilylacetylene
TOCSY	Total correlation spectroscopy
ToF	Time of flight
Tol	Toluene
TRPL	Time-resolved photoluminescence
UHV	Ultra high vacuum
UV	Ultraviolet
XRD	X-ray diffraction
ZPL	Zero-photon line

Chapter 1 INTRODUCTION

CONTENTS

1.1	Graphene	3
1.1.1	Properties and Applications	4
1.1.2	Opening a Band Gap in Graphene	5
1.2	Nanographene synthesis	7
1.2.1	Graphene quantum dots	8
1.2.2	Graphene nanoribbons	15
1.2.3	Graphene nanomeshes	17
1.3	Optical properties of GQDs	22
1.3.1	Generalities	22
1.3.2	Optical Studies of GQDs	25
1.4	Scope of this work	29

1.1 GRAPHENE

In graphene (**Figure 1.1a**), the $2s$, $2p_x$ and $2p_y$ orbitals of a free carbon atom are averaged, or hybridized, to give three sp^2 orbitals, leaving the $2p_z$ orbital unchanged (**Figure 1.1b-c**). The three hybridized orbitals lying in the same plane form σ -bonds with neighboring carbon atoms. These bonds form a 120° angle between each other and are responsible for the mechanical properties in graphene. The remaining $2p_z$ orbitals, perpendicular to the sigma plane, overlap with adjacent orbitals creating a π -bond where electrons can be delocalized (**Figure 1.1d**). These delocalized orbitals are responsible for the intriguing electronic properties in graphene. Two π systems can interact in a non-covalent fashion which is responsible of the spontaneous stacking of graphene layers. When multiple graphene layers stack following an ABA arrangement, we obtain graphite, a natural carbon allotrope.

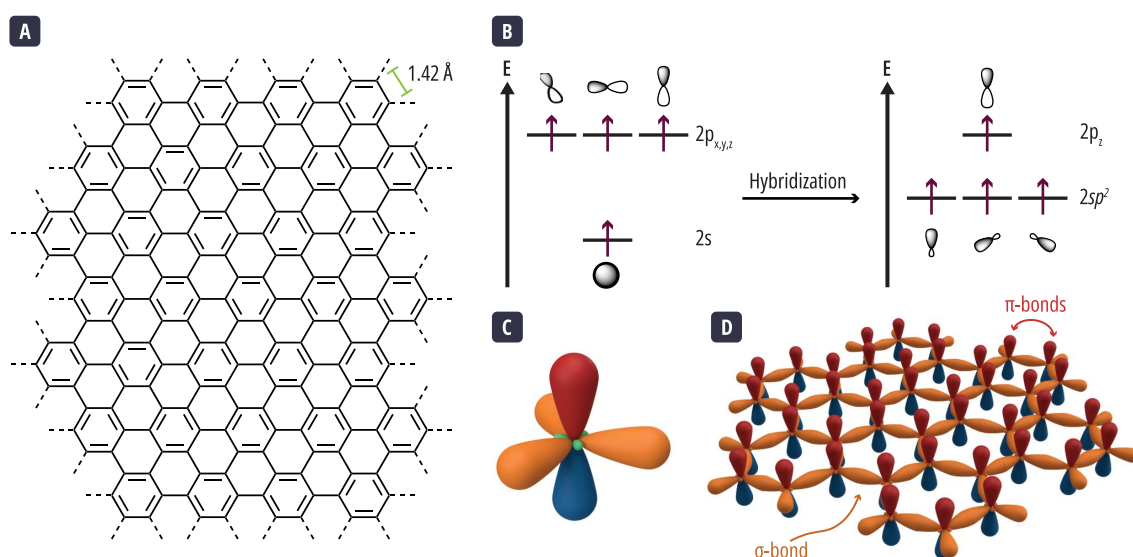


Figure 1.1 | (a) Schematic representation of graphene. (b) Representation of atomic orbitals energy levels before and after sp^2 hybridization in a free carbon atom. (c) Model of sp^2 hybridized atomic orbitals. (d) Model of atomic orbitals in graphene forming, in-plane, σ -bonds, and, out-of-plane, π -bonds.

In 1947, P. R. Wallace, a Canadian physicist at McGill University, published a theoretical study describing graphite's electrical conductivity. As a mathematical simplification, he established that no conductivity happened between carbon layers, thus viewing graphite as a monolayer, he reported the first description of graphene.¹ Over the years, many theoretical studies of the electronic and magnetic properties of a monolayer of graphite followed.^{2,3} Nevertheless, its synthesis remained challenging for over half a century. The first isolation and characterization of graphene was reported in 2004 by A. K. Geim and N. S. Novoselov, who mechanically exfoliated graphite and were able to measure its quantum Hall effect.^{4,5} Their work opened the door for multiple physical studies of graphene and other two-dimensional materials. In 2010, Geim and Novoselov were awarded the Physics Nobel for their work on graphene and its implications in two-dimensional materials research.⁶

1.1.1 PROPERTIES AND APPLICATIONS

To better understand the electronic properties of graphene, we can apply a tight binding model and consider only π -bands, neglecting the sigma-bands (**Figure 1.2**).⁷ When observing the electronic structure of graphene, firstly, we notice that at the center of the hexagonal Brillouin zone, the valence π^* -band and conduction π -band have their maximum and minimum energy, respectively. The π -band is here completely bonding, and the π^* -band antibonding. At the K and K' points, the π -band and π^* -band degenerate in the shape of Dirac cones. As we move away from the K and K' points, the energy increases linearly at π^* and decreases linearly at π . This linear relationship results in electrons propagating through graphene as being of zero mass and traveling at relativistic speeds.⁸

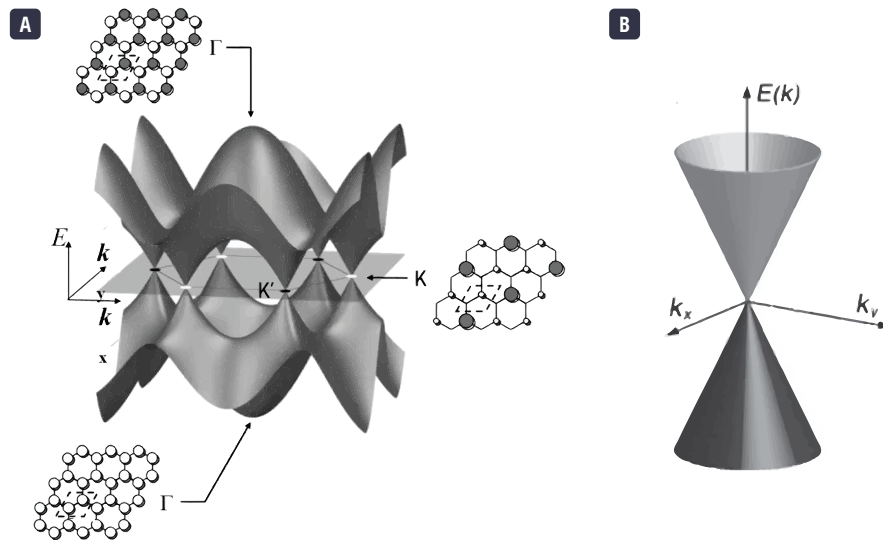


Figure 1.2 | Electronic band structure of graphene. (a) π and π^* band structure of graphene with atomic orbitals representations in Γ and K points.⁷ (b) Closer view of a Dirac cone in the K point.

Graphene is quasi-transparent, absorbing only 2.3% of visible and infrared light,⁹ which makes graphene an exciting candidate for transparent conducting electrodes.^{10,11} Early thermal conductivity measurements in suspended graphene showed a considerable value of $3\,000\text{ W}\cdot\text{m}^{-1}\cdot\text{K}^{-1}$.¹² This property has led to applications as thermal sensors and heat management.^{13–16} Graphene's tensile strength, the maximum stress a material can withstand before rupture, is 130 GPa, and its Young module of 1 TPa.¹⁷ These values correspond to a hundred times those of structural steel.¹⁸ It has also been observed that graphene is good at distributing impact energy.¹⁹ These interesting mechanical properties have encouraged researchers and the industry to consider graphene as a potential material for applications in the military, automobile, aerospace, and sports industries.^{20–22}

Electron mobility in graphene has been measured to be $200\,000\text{ cm}^2\cdot\text{V}^{-1}\cdot\text{s}^{-1}$ on suspended graphene. Still, when in contact with an interface such as silicon dioxide, this value drops to $15\,000\text{ cm}^2\cdot\text{V}^{-1}\cdot\text{s}^{-1}$ but remains in the high-end values of electron mobilities.^{4,23} Our modern society is utterly reliant on electronics. With increasing demand and a growing necessity for smaller and more performant electronic components, graphene is an interesting candidate to tackle these problems. Graphene may be incorporated into analogic and digital components. J. Kedzierski *et al.* reported in 2008 the synthesis of graphene transistors, which exhibited mobilities up to $5\,000\text{ cm}^2\cdot\text{V}^{-1}\cdot\text{s}^{-1}$ and $I_{\text{on}}/I_{\text{off}}$ ratios up to seven.²⁴ Although the observed electron mobility is very high compared to silicon devices, the $I_{\text{on}}/I_{\text{off}}$ ratios are minimal and hinder its applications in digital electronics. This low ratio is an intrinsic consequence of the absence of bandgap resulting in an inability to turn off the conduction. Therefore, great interest has been given to engineering an energy gap in graphene.

1.1.2 OPENING A BAND GAP IN GRAPHENE

As discussed before, opening a bandgap in graphene would enable new applications, notably in electronics and optoelectronics; thus, in the following paragraphs, we will shed some light on some strategies that can be taken to modify graphene's band structure. It is important to comment that, in principle, graphene is defined by its properties previously described (*i.e.*, the presence of Dirac cones, absence of a bandgap, and composed exclusively of carbon atoms). When we modify its properties by functionalizing graphene or opening a bandgap, we talk about graphenic materials or graphene related materials (GRM).

We can divide the here described methods for opening a bandgap in graphene into two groups. The first one consists of ways that do not modify the intrinsic structure of graphene. The change in band structure comes instead from graphene's interaction with its environment, such as in bilayer graphene or heterostructures. The second group consists of strategies that change the configuration of graphene by introducing new chemical elements or limiting the size of graphene to nanometric dimensions.

Interactions with its environment can modify the band structure of graphene. Otha *et al.* reported that a 320 meV bandgap could be observed in bilayer graphene when a disparity of the layers was induced by changing the carrier concentrations with the deposition of potassium atoms on the top layer (**Figure 1.3a**).²⁵ Another way of creating a gap in graphene without changing its underlining structure can relate to how it is synthesized and its interaction with a substrate. For example, Zhou *et al.* observed, using angular resolved photoemission spectroscopy (ARPES), that samples prepared by epitaxial growth on silicon carbide (SiC) had a different spectrum to the one expected for free-standing graphene, which was explained by the presence of a bandgap.²⁶ In a similar mindset, a gap can be engineered by integrating graphene in a Van der Waals heterostructure of two-dimensional materials. For instance, Wang *et al.* reported a 160 meV gap in an epitaxially synthesized graphene/hexagonal boron nitride (h-BN) heterostructure.²⁷ The band gap opening is caused by the mismatch of the lattice between the two structures that generates a Moiré superlattice potential. It is worth noting that heterostructures of two-dimensional materials are a trending topic among researchers because they allow for a synergy of properties between two different two-dimensional materials and the appearance of new properties not present in the isolated materials.

A commonly used method for bandgap engineering is chemical doping, which involves introducing new chemical elements in the structure of graphene. However, it is important to keep in mind that creating new covalent bonds with a carbon in graphene will break its sp^2 character and disturb the π -bands of the material. One strategy for chemical doping involves exposing graphene, who has a reactive surface with available p_z orbitals, with an external element or molecule. Hydrogenation is an example of this type of functionalization; upon exposing graphene to hydrogen plasma, Elias *et al.* observed that the material behaved as an insulator, and upon annealing, the sample partially recovered the properties of pristine graphene.²⁸ Instead of hydrogen, fluorine can be reacted with graphene via exposure to xenon difluoride (XeF_2) to obtain fluorographene, which also exhibits an insulating behavior (**Figure 1.3b**).^{29,30} Similarly to hydrogenated graphene, fluorination in graphene is reported to be reversible.³¹ A final example of this approach is graphene oxide (GO), a regularly studied material analogous to graphene and obtained by treating graphite with various oxidants (**Figure 1.3c**).³² Oxygen is incorporated into the graphene sheet as epoxy bridges, hydroxy, or carboxy groups. GO can be reduced to obtain reduced graphene oxide (rGO) with a diminished oxygen content, restoring some properties of graphene.³³ The bandgap can be tuned depending on the rate of oxygen incorporated in GO or rGO.³⁴⁻³⁶

Another doping possibility is substituting one carbon atom in the graphene lattice with another element. Carbon can be replaced with similar atoms, such as boron or nitrogen. Usachov *et al.* reported a nitrogen-doped graphene exhibiting a bandgap of 0.2 eV, detected by ARPES (**Figure 1.3d**).³⁷ Later, Chan *et al.* reported the synthesis of graphene doped with boron and nitrogen domains exhibiting bandgaps up to 0.6 eV for low B-N concentrations.³⁸ Other examples of substitutional doping can be found with phosphorous,³⁹ silicon,^{40,41} iron,⁴² manganese,⁴³ and other transition elements.⁴⁴ However, altering the chemical structure of graphene, either by functionalizing (as described in the last paragraph) or by substituting a carbon atom in its structure, can harm the unique electrical properties of pristine graphene.⁴⁵ For example, in rGO, the electron mobility drops to the order of tens of $\text{cm}^2 \cdot \text{V}^{-1} \cdot \text{s}^{-1}$.⁴⁶

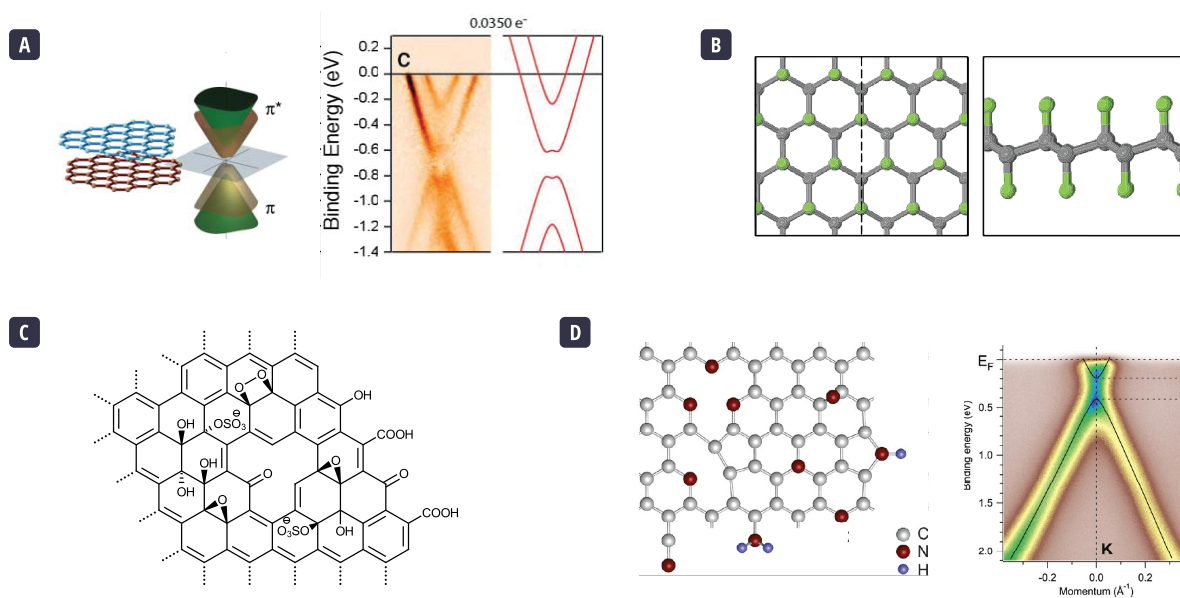


Figure 1.3 | Examples of approaches to open a bandgap in graphene. **(a)** Left, Representation of an asymmetric graphene bilayer by doping the top layer. Right, the energy -momentum dispersion relation measured and calculated for potassium absorption on a graphene layer.⁴⁷ **(b)** Top (left) and lateral (right) view of fluorographene. Gray balls represent carbon atoms and green balls fluorine atoms.⁴⁸ **(c)** A structure of graphene oxide. **(d)** Right, a structure of graphene doped with nitrogen atoms. Left, ARPES measurement for the nitrogen-doped graphene.³⁷

Finally, to create a bandgap in graphene it is possible through the nanostructuring of the material. Quantum confinement limits the distribution of charge carriers in space, creating a gap that increases in energy as size diminishes. Graphene has two dimensions that can be reduced to take advantage of this quantum effect. Upon reduction of one of its dimensions, we obtain graphene nanoribbons (GNRs - **Figure 1.4b**). When limiting both dimensions of graphene, we get graphene quantum dots (GQDs - **Figure 1.4a**), also named graphene nanoparticles. In both cases, we do not change the intrinsic structure of graphene; nevertheless, edges can no longer be neglected and will directly impact the electronic properties of graphene. Another way to use this quantum confinement is by creating a superlattice of nanopores that act as quantum wells.⁴⁹ These superstructures are known as graphene nanomeshes (GNM - **Figure 1.4c**).

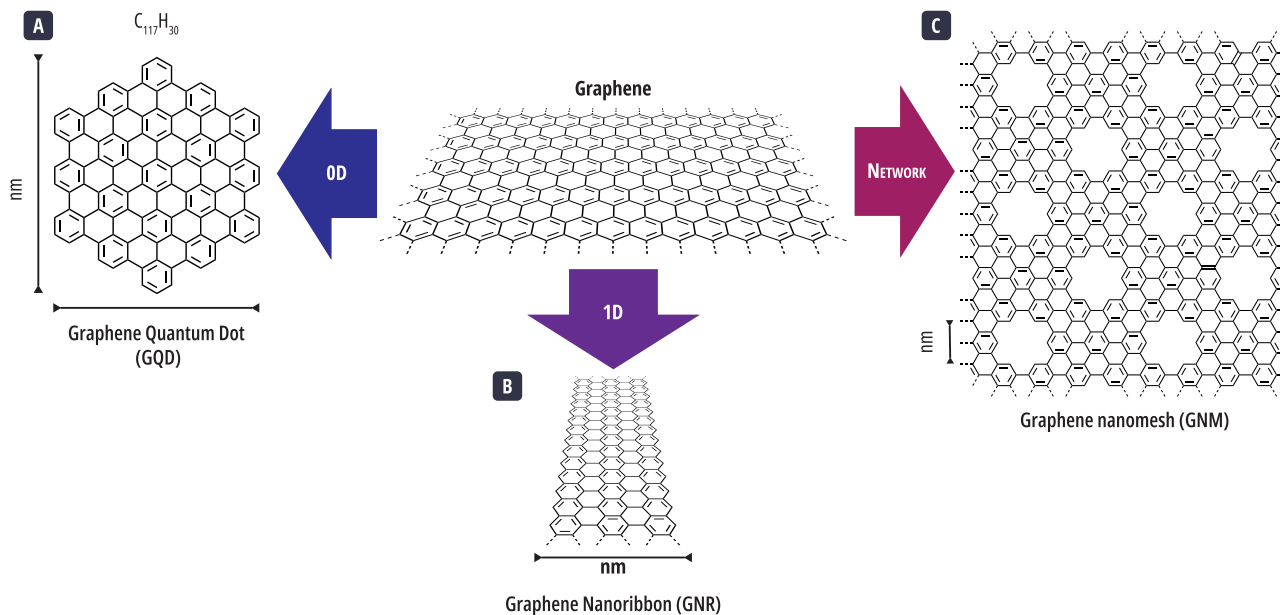


Figure 1.4 | Nanostructuring to open a bandgap in graphene. **(a)** Reducing both dimensions of graphene to obtain GQDs. **(b)** The reduction of only one dimension gives GNRs. **(c)** A network of nanoholes can be structured in bidimensional graphene to form GNMs.

In this section, we reviewed different methods of engineering an energy gap in the electronic structure of graphene. For clarity purposes, they were presented separately, but it is worth noting that they can also be combined. As an example, we can cite a nitrogen-doped GQD.⁵⁰ The scope of this thesis work is the investigation of the optical properties of graphene nanostructures, particularly graphene quantum dots and graphene nanomeshes. The following section discusses how these graphene nanostructures can be synthesized.

1.2 NANOGRAFENE SYNTHESIS

Material synthesis can be divided into two large groups: top-down and bottom-up. A top-down strategy consists in taking a bulk material which is then shaped, via physical or chemical methods, into the desired structure (**Figure 1.5a**). In opposition, we have the bottom-up strategy, which consists of assembling sub-units to obtain the target structure (**Figure 1.5b**). The first synthesis of graphene was achieved by mechanical exfoliation, a top-down technique. Using tape, Geim and Novoselov repeatedly peeled a highly oriented pyrolytic graphite and then carefully transferred it into a silicon oxide substrate where they could observe domains of graphene monolayers.⁴ Later, large-area graphene films were also obtained by Li *et al.* through chemical vapor deposition (CVD), a bottom up approach, of methane on a copper surface.⁵¹ Many examples of nanographene synthesis were developed in the years following the first graphene publication, motivated by the challenge of bandgap engineering in graphene. This section discusses strategies for top-down and bottom-up synthesis of GQDs and GNMs.

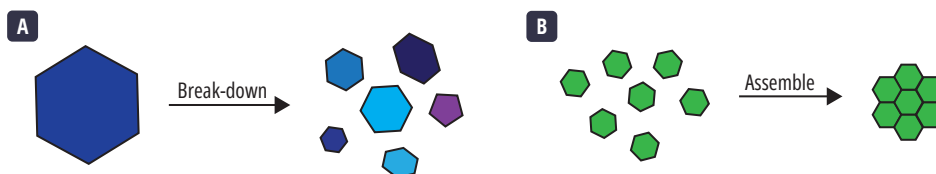


Figure 1.5 | Schematic illustration of top-down and bottom-up approaches. **(a)** Top-down approach: breaking down of the bulk material. **(b)** Bottom-up approach: assembly of sub-units.

1.2.1 GRAPHENE QUANTUM DOTS

TOP-DOWN APPROACH

One of the most common routes for synthesizing GQDs is the oxidative cutting of carbon-based precursors, such as graphite, coal, or amorphous carbon (**Figure 1.6a**). In general, the synthesis these GQDs starts with the formation of graphene oxide: graphite is exposed to potassium permanganate (KMnO_4), sodium nitrate (NaNO_3), and sulfuric acid (H_2SO_4). This method for the synthesis of GO, was first described by Hummers in the middle of the XXth century.⁵² Shen *et al.* further oxidized GO with nitric acid (HNO_3) to cleave it into smaller sheets. The treated GO was passivated with polyethylene glycol, and then reduced with hydrazine to obtain the GQDs.⁵³ The obtained nanoparticles had a dispersity between 5 and 19 nm with a 13 nm average diameter. A similar pathway was proposed by Pan *et al.*, using a solvothermal approach the authors deoxidized GO to obtain graphene sheets (GS).⁵⁴ These GS were re-exposed to H_2SO_4 and HNO_3 under sonication, acids were removed, and the sheets dispersed in a basic solution and heated. The obtained GQDs ranged in size from 5-13 nm with an average size of 9 nm.

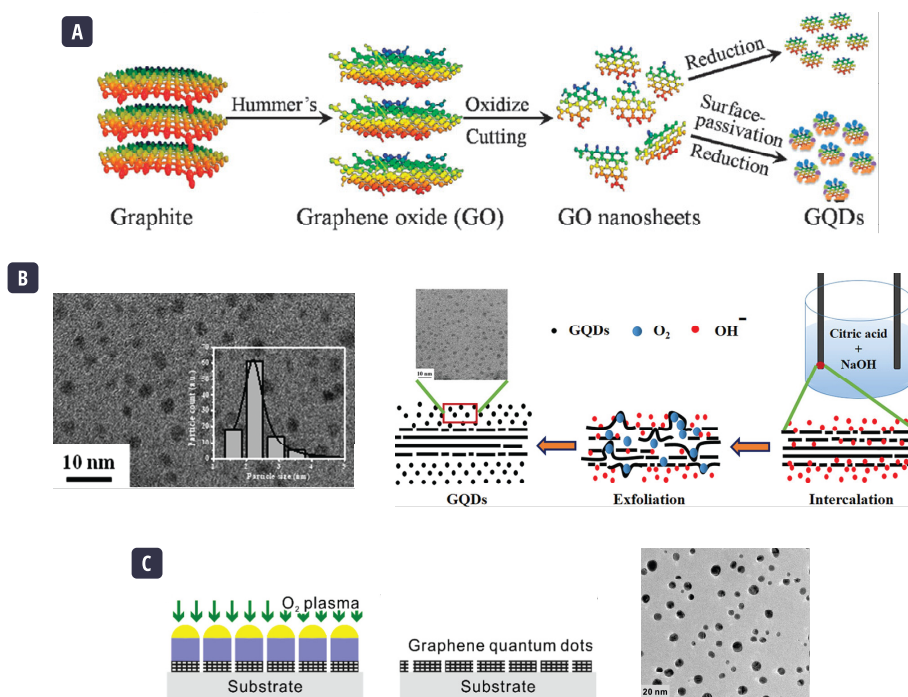


Figure 1.6 | Top-down synthesis of GQDs. **(a)** Schematic representation of the synthesis of GQD through oxidative cutting followed by reduction.⁵⁵ **(b)** Schematic representation of the electrochemical method to get GQDs proposed by Ahirwar *et al.* A transmission electron microscope (TEM) image of the obtained nanoparticles is also given.⁵⁶ **(c)** Schematic representation of the strategy proposed by Kang *et al.* for on surface synthesis of GQDs and a TEM image of the obtained nanoparticles.⁵⁷

Ahirwar *et al.* synthesized GQDs using an electrochemical method.⁵⁶ They heated graphite rods to create defects in the surface, where, mounted as electrodes in an electrochemical setup, exfoliation occurred at the defect sites yielding oxidized GQDs (**Figure 1.6b**). The nanoparticles' oxidation ratio was found to depend on the electrolyte composition in citric acid and sodium hydroxide. Using this electrochemical method, the authors obtained GQDs with average sizes of 2.2-3.4 nm with distributions of 1.5-4.5 nm. Kang *et al.* proposed a method involving etching a graphene layer previously protected by a SiO_2 layer serving as a substrate for the growth of gold nanoparticles.⁵⁷ These nanoparticles act as masks for the graphene below, and after etching and subsequent removal of the gold and SiO_2 layer, GQDs were obtained (**Figure 1.6c**). Etching was done using oxygen plasma which created some oxygen impurities and vacancies. Subsequent annealing of the nanoparticles helped to diminish these defects. The

observed GQDs had an average size of 12-27 nm and a distribution of 5.9 nm. Alternative methods such as solvothermal, hydrothermal, ultrasounds, chemical exfoliation, and micro-wave exfoliation, among others, have been described over the years.^{58,59}

BOTTOM-UP APPROACH

Bottom-up graphene quantum dots synthesis methods consist of taking subunits of the final material, usually small organic molecules, and assembling them. The assembly can be done with various methods like epitaxial growth, solvothermal methods, template methods, pyrolysis, or organic chemical synthesis.⁵⁹ It is the latter that is of utmost importance for the purposes of this thesis. From a bottom perspective, we notice graphene as an infinite array of benzene subunits. Between these two extrema, benzene, and graphene, there is a plethora of finite structures (**Figure 1.7a**). For the smaller part of this spectrum, molecules have been known under the name of polycyclic aromatic hydrocarbons (PAHs) since the beginning of the XXth century. These molecules occur naturally in coal, petroleum, and as side products of the combustion of organic materials.⁶⁰ When the polycyclic aromatic hydrocarbons reach a nanometric size, they can be assimilated to graphene quantum dots.[†] Using an organic chemistry approach, it is possible to tailor the structure of the GQD: its size, shape, and edges (**Figure 1.7b**). For instance, due to the hexagonal lattice of graphene, there are two types of possible edges in GQDs: armchair or zigzag. Also, on these edges, it is conceivable to add functional groups. All these parameters that define the structure of the GQD will impact its properties and, more earnestly, for the scope of this work, on its optical properties.

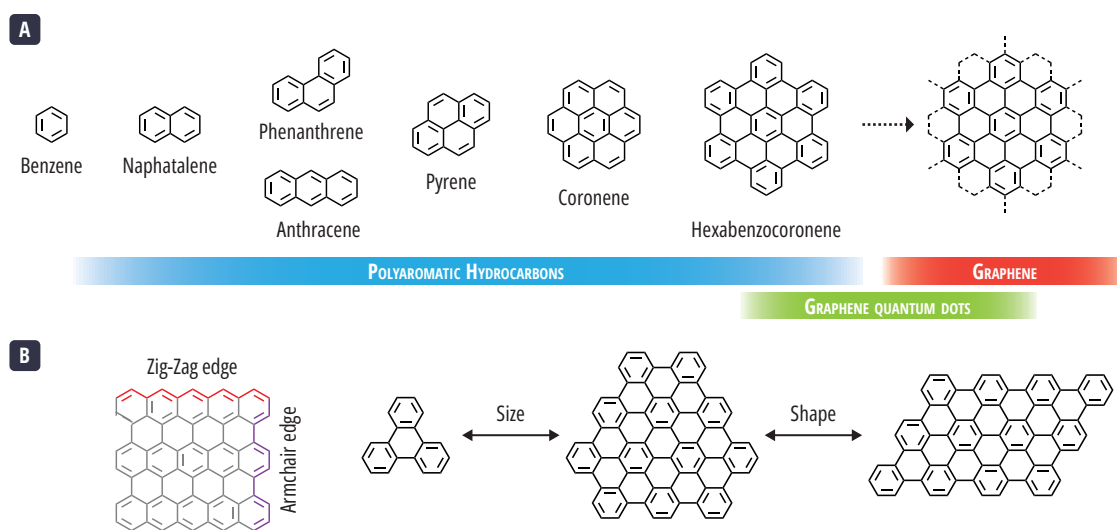
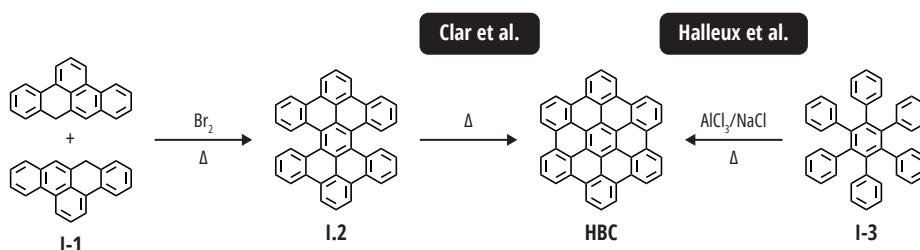


Figure 1.7 | Organic chemistry for the synthesis of GQDs. **(a)** Illustration of some molecular entities in the spectrum between benzene and graphene. **(b)** Organic chemistry can synthesize specific edges, sizes, and shapes of GQDs.

R. Scholl and E. Clar were pioneers in the synthesis of small PAHs during the first half of the XXth century.⁶¹⁻⁶⁵ When referring to large polycyclic aromatics that can be assimilated to GQDs, hexa-*peri*-benzocoronene (HBC), also known as "super-benzene", is a prototype model that contains 42 sp^2 hybridized carbon atoms. Clar *et al.*⁶⁶ and Halleux *et al.*⁶⁷ were the first to describe the synthesis of HBC in 1958 (**Scheme 1.1**). They each proposed a different synthetic route. Clar *et al.* proposed a

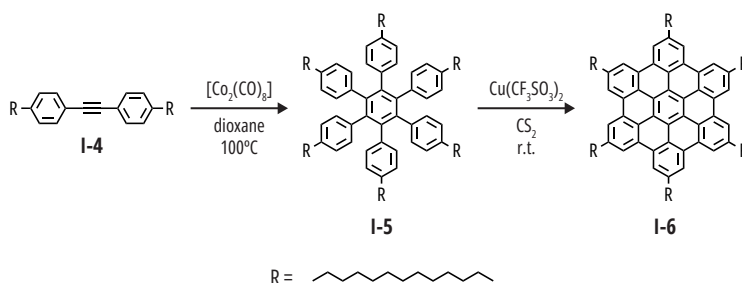
[†] It is important to state that from now on the term polycyclic aromatic hydrocarbons will be indistinguishably used to refer to graphene quantum dots or graphene nanoparticles synthesized through an organic chemistry approach. Even though PAH are in principle molecules, because of their size, they can also be assimilated to quantum dots. A distinction will be made when talking about polycyclic aromatics smaller than 1 nm by referring to them as small PAHs.

strategy consisting of the bromination of 2:3-7:8-dibenzo-*peri*-naphthene **I-1** and subsequent heating to 153°C to obtain tetrabenzoperopyrene **I-2**. Further heating of **I-2** gave HBC. Instead, Halleux *et al.* proceeded to the cyclodehydrogenation of hexaphenylbenzene **I-3** in a melt blend of AlCl₃ and NaCl.



Scheme 1.1 | First synthetic pathways to HBC. From left to the middle, the steps proposed by Clar *et al.* for the synthesis of HBC. From right to middle, the strategy proposed by Halleux *et al.*

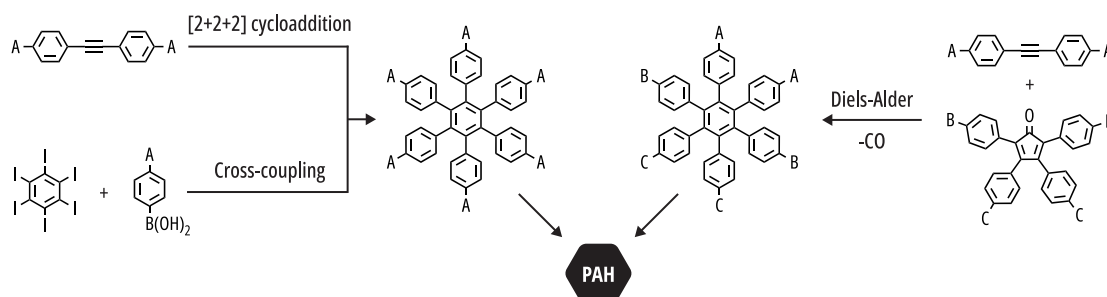
These first examples of the synthesis of HBC were complicated, involving heating to high temperatures and low reaction yields. Thus, for almost 30 years, no further interest was given to the synthesis of larger PAHs. By the end of the XXth century, with the advances in organic chemistry, a new concern was brought to the synthesis of these large PAHs. Stabel *et al.* described the synthesis of an alkyl chain substituted HBC in milder and simpler conditions.⁶⁸ The authors took a similar approach to the one proposed by Halleux *et al.*: the synthesis of a polyphenylene dendrimer followed by a Scholl oxidation to create the new carbon-carbon (C-C) bonds and achieve the graphitization of the molecule (**Scheme 1.2**). The polyphenylene precursor **I-5** was synthesized by [2+2+2] cycloaddition of a substituted diphenyl acetylene **I-4** catalyzed by Co₂(CO)₈. Then **I-5** was cyclodehydrogenated with Cu(OTf)₂. The synthesis was later optimized by using a milder oxidant, iron(III) chloride.⁶⁹



Scheme 1.2 | Alkyl-substituted HBC synthesis. Cyclotrimerization of an alkyl-substituted biphenyl acetylene to synthesize a polyphenylene dendrimer followed by Scholl cyclodehydrogenation.

In this approach, the polyphenylene dendrimer is a crucial intermediate in the overall synthesis of large polycyclic aromatics because its structure will account for the final shape, size, and placement of functional groups. We can find various examples of oligopolyphenylenes synthesized throughout the past century.^{70–72} Later, thanks to the progress made in the synthesis of large PAHs by K. Müllen and his collaborators, these polyphenylenes were graphitized. Three main synthetic approaches can be taken to obtain polyphenylene dendrimers: cyclotrimerization, Diels-Alder reaction, and cross-couplings (**Scheme 1.3**). Metal-catalyzed [2+2+2] cycloadditions, or cyclotrimerization, of ethynyl functions can be achieved using cobalt or rhodium catalysts.⁷³ The advantage of this reaction is that using only one precursor, it is possible to achieve the polyphenylene. The downside is that, to prevent the formation of isomers, the precursors should be symmetric, thus, giving only sixfold-symmetrically substituted molecules. Diels-Alder reaction, a [4+2] cycloaddition, consists in reacting a diene with a dienophile to create a new cycle.⁷⁴ In our case of interest, this can be achieved by reacting a substituted cyclopentadienone with a substituted alkyne to form a substituted six-member aromatic ring through the extrusion of carbon monoxide. This strategy allows for lower symmetry

dendrimers, but two precursors must be prepared. Finally, cross-coupling, such as the Suzuki-Miyaura reaction, can be used to create phenyl-phenyl bonds.⁷⁵ This strategy allows for a more precise construction of the polyphenylene but present the disadvantage to create only one carbon-carbon bond at a time, leading to lower yields and extra steps.



Scheme 1.3 | Strategies for polyphenylene dendrimer synthesis. Three different pathways for the synthesis of polyphenylene dendrimers which can be then used to obtain PAHs: cyclotrimerization, cross-coupling, and Diels-Alder reaction.

Following the approach to synthesize a polyphenylene through a Diels-Alder reaction, and with the milder conditions developed by K. Müllen and his collaborators in the 90s, the library of large PAH grew bigger. Different sizes and symmetries were achieved (**Figure 1.8**).^{76–80} The biggest two-dimensional structure reported to this date is a hexagonal PAH containing 222 sp^2 carbon atoms **I-7**, synthesized by Simpson *et al.*⁸¹ As the structures become bigger, the π -stacking effect is more important, increasing the difficulty of their synthesis and characterization. To address this problem, different functional groups, including alkyl-, alkylphenyl-, alkylester-chains, arylamine, or *tert*-butyl, among others, were designed into the surface of the PAH to try to counteract this problem. For example, we have a triangular-shaped 168 sp^2 carbon atoms quantum dot substituted with trialkyl phenyl groups **I-8** synthesized by Yan *et al.*⁸² The research team observed an increase in the solubility compared to previous unsubstituted examples. The procedure for synthesizing large polycyclic aromatic hydrocarbons from a polyphenylene dendrimer followed by Scholl oxidation is quite versatile, yet it has limitations. The first one is that the number of steps increases as the structure complexifies. Secondly, the oxidation conditions can be harsh, generating undesired side products or destroying the functional groups in the process.⁸³ We can find reports of cleavage of alkyloxy and alkylthio substituents when using $FeCl_3$ as an oxidant.⁸⁴ Over the years, protocols using milder oxidants, like 2,3-dichloro-5,6-dicyano-1,4-benzoquinone (DDQ) or [bis(trifluoroacetoxy)ido]-benzene (PIFA), have been perfected, generating less undesired products and compatible with a broader spectrum of functional groups.^{85,86} Finally, the Scholl oxidation permits the formation of only armchair structures.

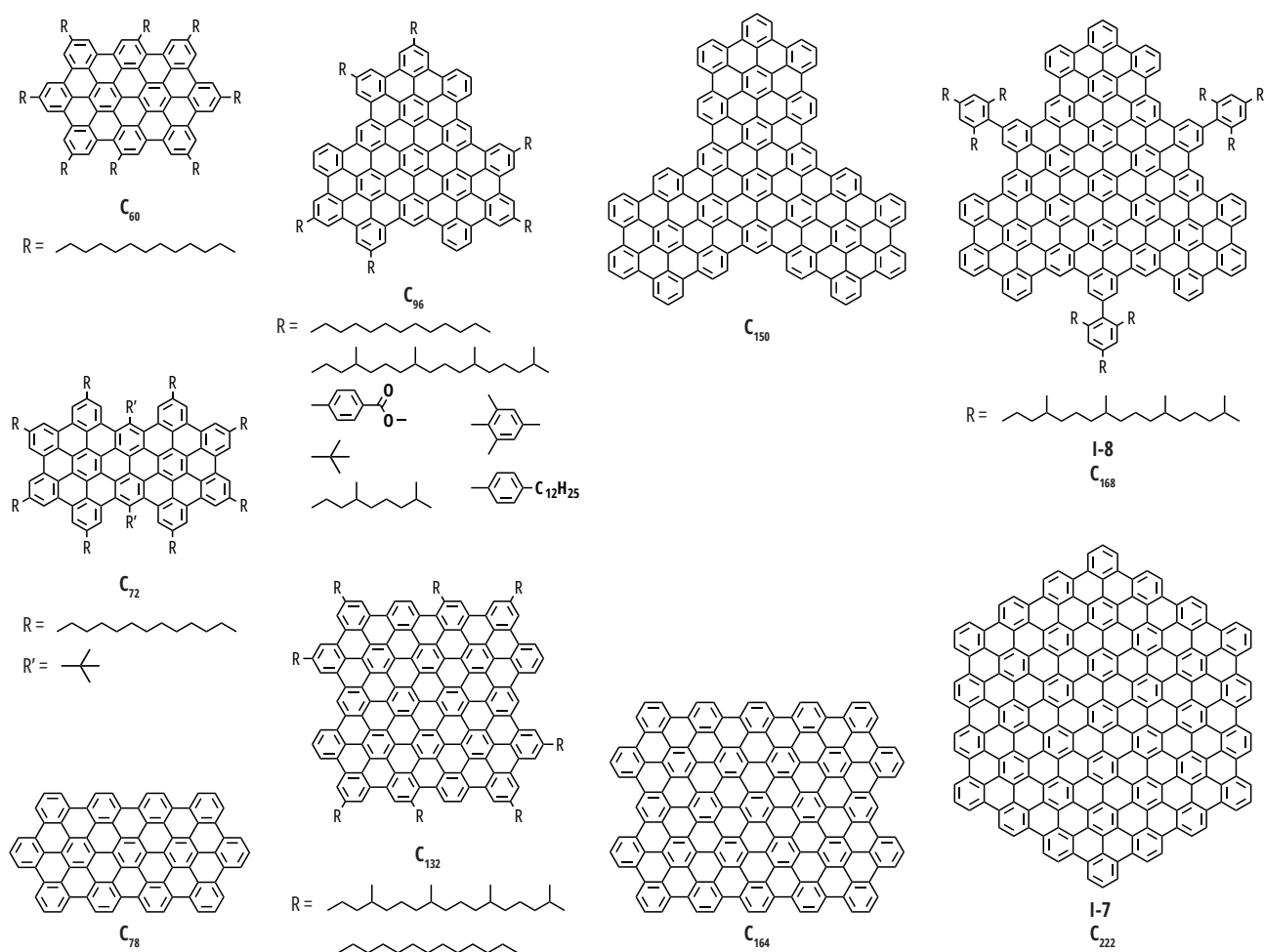


Figure 1.8 | Different sizes and symmetries of large PAHs synthesized through the years, containing 60,^{77,79} 72,⁸⁷ 78,^{79,88} 96,^{69,89,90} 132,⁹¹ 150,⁹² 164,⁸⁰ 168⁸², and 222⁸¹ sp^2 carbon atoms with different shapes and substituents.

At the middle of the XXth century, E. Clar studied the aromaticity of polycyclic aromatic hydrocarbons and postulated the π -sextet rule.⁹³ In PAHs, the electrons are delocalized, which leads to the existence of multiple resonance structures. In their Kekulé representation we get an alternation of single and double bonds. A Clar sextet is identified when a benzene-like ring, containing six π -electrons (or three double bonds), is present in the Kekulé structure. Clar sextets are typically represented by a circle inside the hexagonal ring. The notation is depicted in **Figure 1.9** for phenanthrene and triphenylene. For a molecule with multiple resonance structures, the most stable configuration is the one that contains the greatest number of Clar sextets.⁹⁴ A PAH composed exclusively of π -sextets is referred to as being “fully benzenoid”. These are the most stable PAHs and have the largest band gaps. All the structures discussed so far have been fully benzenoid, and they all have armchair edges. The addition of a zigzag edge will give a structure that it is no longer composed exclusively of Clar sextets, the most stable representation will also have double bonds, as in the phenanthrene example. These types of PAHs are less stable and exhibit different reactivities and properties. We will now focus more attention on these structures.

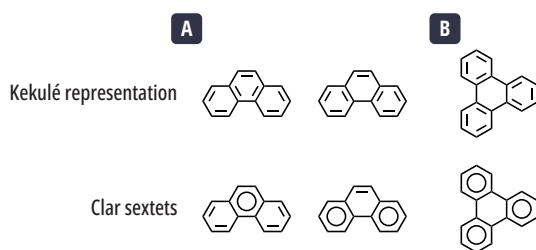
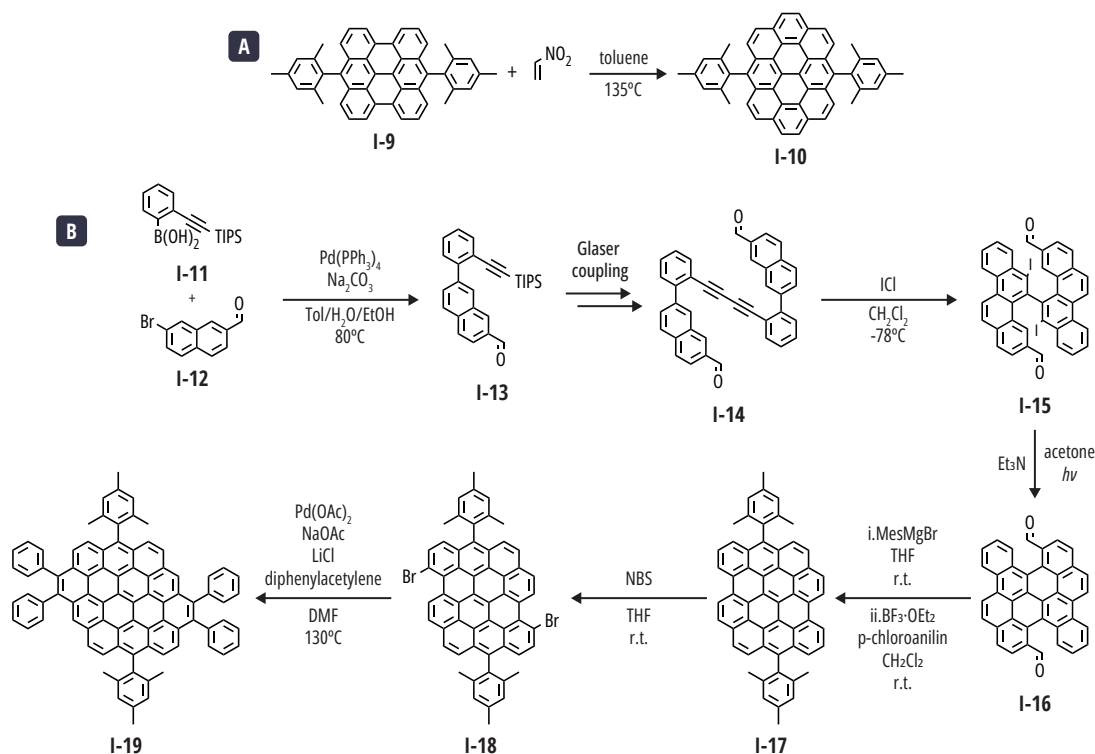


Figure 1.9 | Kekulé and Clar representations of (a) two resonant structures of phenanthrene and (b) triphenylene.

Zigzag-edged nanoparticles display different physical and chemical properties than their armchair counterparts. For instance, they exhibit increased chemical reactivity, smaller optical gaps, and open-shell characters.^{95,96} To create zigzag edges in a molecular chemistry fashion, one must extend an existing π system. This π -extension can be achieved through a Diels-Alder reaction, acetylene cyclization, cyclotrimerizations, ring-closing olefin metathesis, cross couplings, or intra Friedel-Crafts reactions, among others.^{64,97–104} For instance, Fort *et al.*, reacted nitroethylene to the bay region of 7,14-dimesitylbisanthene **I-9** through a Diels-Alder reaction to get the corresponding ovalene **I-10** (Scheme 1.4a).¹⁰⁵ Chen *et al.* reported the synthesis of a nanographene containing 42 sp^2 carbon atoms and zigzag edges, whose synthetic pathway is a good illustration of different strategies for π -extension (Scheme 1.4b).¹⁰⁶ They started with the synthesis of bi(naphthylphenyl)diyne **I-14** through a Suzuki coupling between **I-11** and **I-12**, to incorporate the first zigzag edge, followed by a Glaser-coupling. **I-14** underwent an acetylene cyclization with iodine monochloride to yield the iodinated bichrysene **I-15**. Photochemical cyclo-deiodo-dehydrogenation of **I-15** gave intermediate **I-16** which, through nucleophilic attack on the aldehyde group with a Grignard agent, and subsequent intra Friedel-Crafts and oxidation, gave compound **I-17**. Upon bromination of **I-17** and a Pd-catalyzed benzannulation, the circumpyrene **I-19** was formed.



Scheme 1.4 | π -expansion strategies for zigzag edged nanographenes. (a) Synthesis of an ovalene through Diels-Alder π -extension.¹⁰⁵

(b) Synthesis of a circumpyrene using different reactions for the π -expansion of the aromatic system to get zigzag edges.¹⁰⁶

The synthesis of nanographene through an organic chemistry process faces the challenge of the low solubility of the intermediates or final compounds. This can have consequences in their processability and characterization. The most common employed method of characterization is mass spectrometry.¹⁰⁷ This technique has limitations, the first one being that it is not a quantitative method, and the second that it does not allow to distinguish between different constitutional isomers. We already saw how it is possible to incorporate different functional groups into the GDQ to increase its solubility. An alternative technique for diminishing π interactions between large PAHs is adding a tri-dimensional character to the structure. This can be attained by inducing nonplanarity in the structure by creating sterically congested structures through the incorporation of functional groups in hindering positions or through the integration of five-, seven- or eight-member rings into the structure.^{108–111}

As part of this PhD thesis, we targeted the synthesis of two twisted nanographenes structures: propellers and helicenes. Concerning nanographene propellers, in 2004, Simpson *et al.* reported the synthesis of a tri-hexabenzocoronene propeller with three distinct graphenic domains, held together at a central phenyl.¹¹² Each sp^2 domain oriented themselves in different directions for steric reasons, thus giving a three-dimensional character to the overall structure (**Figure 1.10a**).

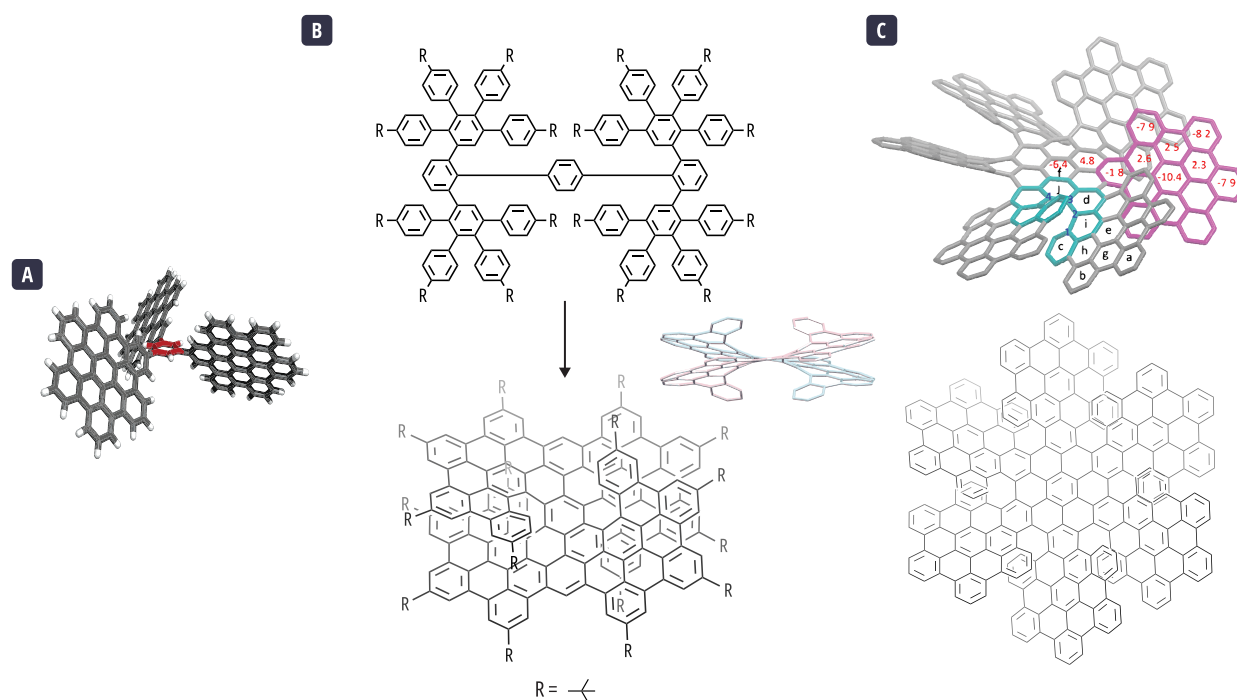


Figure 1.10 | Examples of three-dimensional nanographenes. **(a)** Calculated structure of a propeller-type GQD with 3 distinct HBC subunits held together by a benzene ring.¹¹² **(b)** Synthetic scheme of a double [9]helicene and its single-crystal structure.¹¹³ **(c)** Single-crystal structure and schematic representation of a helicoidal 258 carbons GQD with six [7]-fused rings helicene.¹¹⁴

Using a parallel approach to the synthesis of planar GQDs, a congested polyphenylene dendrimer can be enforced to take a three-dimensional conformation during the oxidation step. It is possible to introduce into their structures *ortho*-fused phenyl rings, named helicenes since they adopt a helical configuration.¹¹⁵ The library of so synthesized nanographenes, also called π -extended helicenes, has been enlarged in the past few years.^{111,116,117} For example, Tan *et al.* reported the synthesis of a twisted GQD containing two helicenes, each composed of nine *ortho*-annulated benzene rings (**Figure 1.10b**).¹¹³ Zhu *et al.*, were able to synthesize a twisted nanographene with 258 conjugated carbon atoms (**Figure 1.10c**).¹¹⁴ This structure is, so far, the biggest polycyclic aromatic hydrocarbon synthesized in an organic chemistry fashion. It is essential to keep in mind that breaking the planar structure may have an impact on the electronic properties of graphene but in the case of helical structures also adds a new optical property: chirality.^{118,119} We will further discuss helicenes and their chiral properties in Chapter 3.

1.2.2 GRAPHENE NANORIBBONS

The synthesis of graphene nanoribbons has been extensively developed in the past years, notably by K. Müllen and A. Narita. The synthesis of these graphenic structures was not the primary objective of this thesis, hence, a shorter introduction will be provided.

TOP-DOWN APPROACH

The top-down approaches to the synthesis of graphene nanoribbons consist mainly on the cutting graphene through lithography techniques, mechanical techniques, or by unzipping carbon nanotubes (CNTs).¹²⁰ In 2007, Han *et al.* reported the synthesis of a GNR through electron-beam lithography of graphene flakes.¹²¹ The year after, Li *et al.* exfoliated and sonicated expandable graphite to obtain GNR that were then characterized through atomic force microscopy (AFM).¹²² They observed nanoribbons with widths from 10 nm to 50 nm. In the same research group, Jiao *et al.* reported the unzipping of multi-walled carbon nanotubes embedded in a poly(methyl methacrylate) through argon plasma etching to obtain GNRs.¹²³ The obtained nanoribbons had smooth edges with widths distributions between 10 nm and 20 nm.

BOTTOM-UP APPROACH

The first synthesis of aromatic, carbon-based ribbon structures was reported by Stille *et al.* in the 1970s.¹²⁴ Though they contained hexagonal and pentagonal aromatic rings, they can be viewed as the first examples of GNR-like structures. In the following years, some examples of benzene-narrow nanoribbons were reported.^{125,126} Later at the beginning of the XXIst century, the approach of synthesizing a polyphenylene precursor followed by its Scholl oxidation to create the new carbon-carbon bonds, primarily developed for the synthesis of large PAHs, was also extended to the synthesis of GNRs. The first examples following this approach, allowed to achieve wider nanoribbons but suffered of numerous defects due to possible isomerizations during the oxidation step.^{127,128} It was in 2008 that Yang *et al.* reported the first synthesis of a graphene nanoribbon structurally defined through a Suzuki-Miyaura polymerization (**Figure 1.11a**).¹²⁹ Their structure contained an armchair edge with nine rows of carbon atoms ($N = 9$) but its length was limited to ≈ 12 nm. Different GNRs synthesized in liquid-phase have been reported after this first example of structurally defined nanoribbon.^{130,131} They were achieved through Suzuki-Miyaura polymerization,^{132–134} Yamamoto polymerization,^{135–138} Diels-Alder polymerization,^{139–141} or crystal topochemical polymerization.¹⁴² To illustrate this we give the following examples. In 2012, Schwab *et al.* reported the synthesis of a laterally extended GNR through a Yamamoto polymerization (**Figure 1.11b**).¹³⁵ The obtained nanoribbons exhibited a number average molecular weight of $44\,000\text{ g}\cdot\text{mol}^{-1}$ with a very narrow distribution. In 2014, Narita *et al.* reported the synthesis of cove-type nanoribbon synthesized through a Diels-Alder polymerization (**Figure 1.11c**). The obtained GNRs had longitudinal extensions over 600 nm.

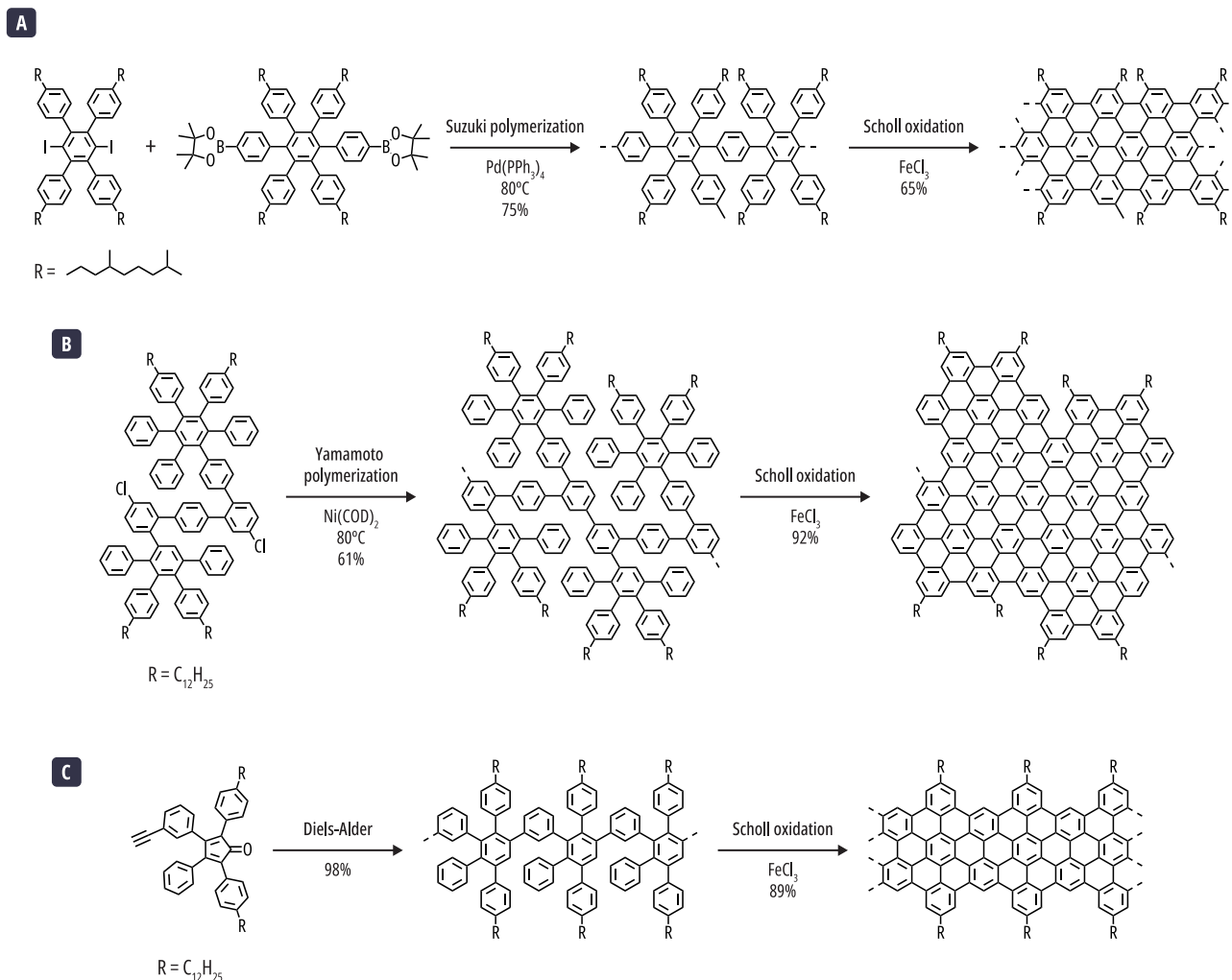
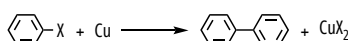


Figure 1.11 | Solution mediated synthesis of GNRs. **(a)** First structurally defined GNR. The nanoribbon was obtained through a Suzuki polymerization followed by Scholl oxidation.¹²⁹ **(b)** Synthesis of a GNR through Yamamoto polymerization in solution.¹³⁵ **(c)** Synthesis of a cove-type GNR through Diels-Alder polymerization.¹⁴⁰

The previously cited examples were all synthesized through liquid-phase chemistry. Another popular route for the synthesis of structurally defined graphene nanoribbons is on-surface chemistry. On-surface chemistry consist in adsorbing a molecular precursor on a surface, more commonly a metallic surface but other surfaces like ionic crystals or bulk insulators can be employed.^{143–145} In the case of the metallic surfaces, the surface atoms act as a heterogeneous catalyst, and allow chemical reactions, such as Ullmann coupling, to take place.^{146,147} Different parameters like the surface, the precursor design, the temperature, and the environment play an important role on the reactivity of the adsorbed precursors.¹⁴⁸ On-surface reactions are commonly characterized by scanning probe microscopy techniques such as scanning tunneling microscope (STM) and non-contact atomic force microscopy (nc AFM) with functionalized probes. A more detail presentation of these techniques will be given in Chapter 4; however, they allow a characterization molecule by molecule. The first coupling reactions on a metallic surface were reported by the end of the last century.^{149,150} However, the field started to rapidly develop by the end of the 2000's after the work of Grill *et al.*, who reported the first covalent molecular network synthesized on-surface from porphyrin building blocks.¹⁵¹ As we will see in the following examples, and in the nanomeshes section, Ullmann coupling is a choice reaction for the on-surface formation of carbon-carbon (C-C) bonds. In this coupling, two precursors containing halogen atoms are linked together by the presence of a metallic atom (**Scheme 1.5**).¹⁵²



Scheme 1.5 | Copper promoted Ullmann coupling of biphenyl. X = I, Br.

The first on-surface synthesis of a graphene nanoribbon was reported by Cai *et al.*¹⁵³ They deposited a 10-10'-dibromo-9,9'-bianthracene on an Au(111) and Ag(111) surface. After heating the surface in two steps to achieve Ullmann coupling and cyclodehydrogenation, they observed by STM the presence of straight N = 7 armchair GNRs (**Figure 1.12a-b**). In the same report they described the synthesis of a chevron-type graphene nanoribbon with lengths of approximately 20 nm (**Figure 1.12c-d**). After this seminal work, numerous structures have been synthesized over the years, varying in widths, shape, edges and dopants.^{153–155} For example, in 2016, Ruffieux *et al.* reported the synthesis of a graphene nanoribbon with zigzag edge topology on an Au(111) surface (**Figure 1.12e-f**). The designed precursor had additional methyl groups that would undergo oxidative ring closure to form a new six-member ring on the surface and create the zigzag edge. The observed GNR had lengths of approximately 50 nm.

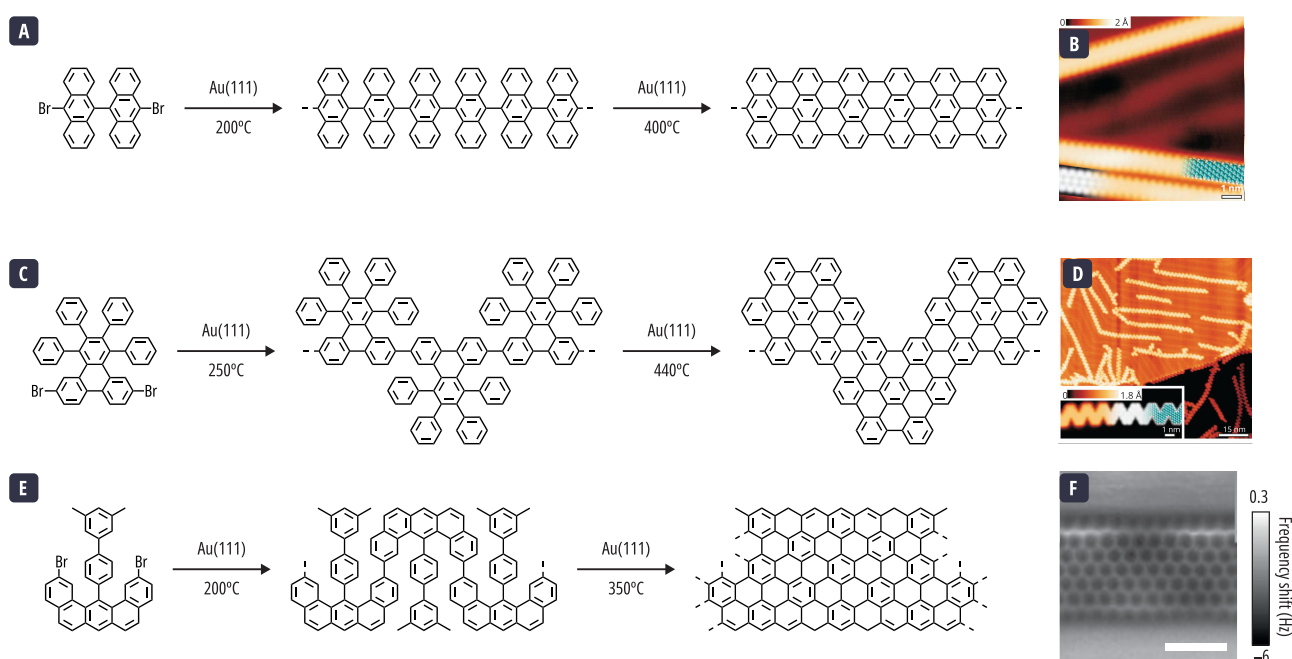


Figure 1.12 | On-surface synthesis of GNRs. **(a)** Scheme of the reaction on a gold surface of 10-10'-dibromo-9,9'-bianthracene to obtain a GNR. **(b)** STM image of the obtained nanoribbon with a partially overlaid molecular model. **(c)** Scheme of the reaction on a gold surface of 6,11-dibromo-1,2,3,4-tetraphenyltriphenylene to give chevron-type GNR. **(d)** STM image of the nanoribbons with a partially overlaid model. (a-d)¹⁵³ **(e)** Scheme of the reaction to obtain a N = 6 zigzag graphene nanoribbon on a gold surface. **(f)** nc-AFM image of the nanoribbon taken with a CO-functionalized tip. (e-f)¹⁵⁶

1.2.3 GRAPHENE NANOMESHES

TOP-DOWN APPROACH

The general top-down strategy for synthesizing graphene nanomeshes involves taking monolayer or bilayer graphene to carve a pattern of nanometric-sized pores. The modeling of nanometric holes in the graphene sheet can be achieved via physical or chemical etching. Bai *et al.* used for the first time the designation "graphene nanomesh" for a well-organized nanoporous graphene layer synthesized using block copolymer nanolithography.¹⁵⁷ The authors transferred a graphene layer on a substrate, followed by the deposition of a protective silicon oxide and a polymer layer. This serves as a template for fluoride-based reactive ions to partially degrade the coating and form the nanopores. Subsequent exposure to an oxygen plasma craved

the holes in graphene, and after cleaning the oxide layer, the GNM was revealed (**Figure 1.13a-b**). Different neck widths and hole periodicities, ranging in the tenths of nanometers, were obtained using this method. In an analogous method, Zeng *et al.* used anodic aluminum oxide (AAO) as an etch mask over reduced GO for creating GNMs via oxygen plasma etching (**Figure 1.13c-d**).¹⁵⁸ Akhavan proposed a different approach using local photodegradation of a graphene oxide sheet in contact with a vertically positioned ZnO nanorod to produce GNM (**Figure 1.13e-f**).¹⁵⁹ Using this method, the obtained pores ranged around 200 nm.

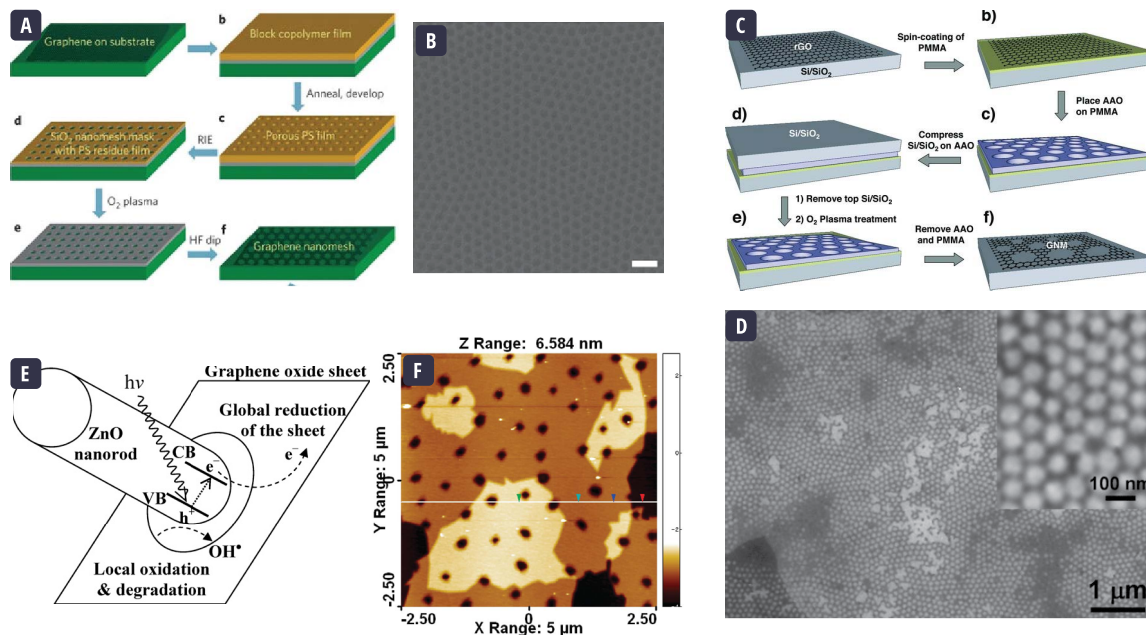


Figure 1.13 | Top-down strategies for the synthesis of GNM. **(a)** Schematic fabrication process of a graphene nanomesh using a SiO_x mask and plasma etching. **(b)** SEM image of the GNM structure obtained after etching and removal of the oxide mask. Scale bar, 100 nm. (a-b)¹⁵⁷. **(c)** Schematic fabrication process of a GNM using an AAO mask and plasma etching. **(d)** SEM image of a large area GNM after removal of AAO. (c-d)¹⁵⁸. **(e)** Schematic illustration of the mechanism of the formation of GNM using ZnO nanorods as photocatalysts. **(f)** AFM image of a GNM obtained using ZnO nanorods. (e-f)¹⁵⁹.

BOTTOM-UP APPROACH

The bottom-up graphene nanomesh can be synthesized via the templated growth of carbon-based precursors. The template can come from external materials or it can be designed into the precursor's architecture. As we will see later in this section, the latter uses molecular chemistry's reactivity principles to design the precursor's shape, size, and chemical functions. Let us first be interested in external templating for GNM synthesis. A nanomesh can be achieved by epitaxial growth on a copper surface containing patterned aluminum oxide dots acting as a growth barrier, as was reported by Safron *et al.* (**Figure 1.14a-b**).¹⁶⁰ The nanopatterned oxide layer was achieved by electron beam and bloc copolymer lithography, which, after CVD growth, was chemically removed along with the copper substrate yielding GNM with pores of an average size of 14 nm and neck width of 24 nm (**Figure 1.14c**). In a similar approach, Jung *et al.* used a gold nanonetwork as a growth template for CVD, obtaining GNMs with an average neck width of 23 nm (**Figure 1.14d-e**).¹⁶¹

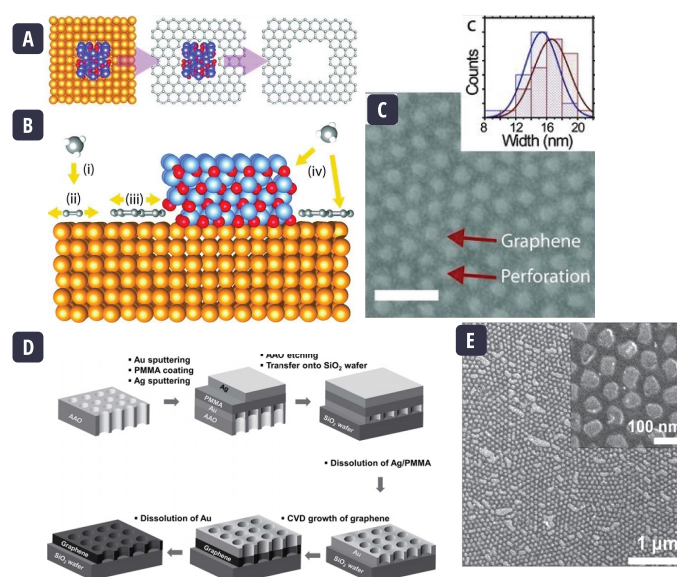


Figure 1.14 | Bottom-up synthesis of GNM via CVD growth. **(a)** Deposition of Al_2O_3 on a copper surface, graphene grows around the oxide island to achieve the nanohole after removal of the island. **(b)** Steps of CVD growth: methane gas decomposes into carbon (i), diffuses (ii), nucleates (iii), and grows (iv) on the copper surface. **(c)** SEM image with an insert of the neck width distribution of the grown nanomesh. Scale bar, 100 nm. (a-c)¹⁶⁰ **(d)** Schematic illustration of the fabrication steps of a gold nanonetwork and GNM growth. **(e)** FE-SEM image of the obtained graphene nanomesh and magnification image. (d,e)¹⁶¹

From a molecular point of view, we can compare graphene nanomeshes to a popular porous structure: metal-organic frameworks (MOFs), a macromolecular architecture made of organic linkers and metal atoms. If, instead of linking the organic monomers through coordination bonds, they are covalently connected between them, we obtain covalent organic frameworks (COFs). When aryl-aryl bonds link together these COFs, and we limit their structure to only two dimensions, we achieve GNM. In this case, the synthesis is guided by the information contained within the precursors in the character of functional groups. These chemical functions can react in solution, on an interface, or in a solid state.^{162,163} For the purposes intended in this thesis work, we will further be interested in on-surface synthesis. As previously discussed, in the past years, surface-assisted graphene nanoribbons synthesis has attracted a lot of attention because of the precise control allowed by the technique. Recently, this has also extended to the synthesis of two-dimensional carbon materials, as we will discuss shortly.

In this perspective, Bieri *et al.* deposited an hexaiodo-cyclohexa-*m*-phenylene (CHP) on an Ag(111) surface and, after annealing at 532°C, obtained two-dimensional polyphenylene networks (**Figure 1.15a**).¹⁶⁴ They performed the analysis using scanning tunneling microscopy (STM) and observed perfect agreement with the expected structure, exhibiting an interpore distance of 7.4 Å and continuous domains of up to 10x10 nm (**Figure 1.15b-c**). Gutzler *et al.* reported further analysis of the surface's role in forming 2D nanoporous networks.¹⁶⁵ They deposited 1,3,5-tris(4-bromophenyl)benzene (TBPB) in graphite(001), Cu(111), and Ag(110) surfaces. The graphite surface only yielded a supramolecular assembly of TBPB molecules, which desorbed at larger temperatures. Similarly, for the Ag(110) surface, a supramolecular arrangement and little initiation of polymerization were observed at temperatures of 110°C. Upon annealing the Cu(111) surface at 300°C, disordered polymerization was observed with not only the expected hexagonal macrocyclization but also pentagonal and heptagonal (**Figure 1.15d-e**). This work showed the necessity of the metallic surface in carrying out the C-C coupling. Later, Blunt *et al.*, deposited 1,3,5-tris(4-bromophenyl)benzene (TBPB) on an Ag(111) in an attempt to obtain the same hexagonal network as Gutzler *et al.* with a different precursor, and also observed disordered macrocyclizations (**Figure 1.15f-g**).¹⁶⁶ Nevertheless, larger continuous domains of porous networks were obtained. One of the most impressive examples of GNM synthesis used a three-step approach. First, the

formation of a graphene nanoribbon, followed by its cyclodehydrogenation and finally their cross-dehydrogenative coupling (**Figure 1.15h**).¹⁶⁷ For this, Vilas-Varela *et al.*, deposited diphenyl–10,10'-dibromo-9,9'-bianthracene (DP-DBBA) on Au(111) and heated up the surface to 200°C coupling the monomers into a GNR. Further annealing at 400°C triggered the intramolecular cyclodehydrogenation, and cross-coupling is achieved at 450°C (**Figure 1.15i**). A highly ordered GNM with continuous domains up to 50x70nm was reported (**Figure 1.15j-k**).

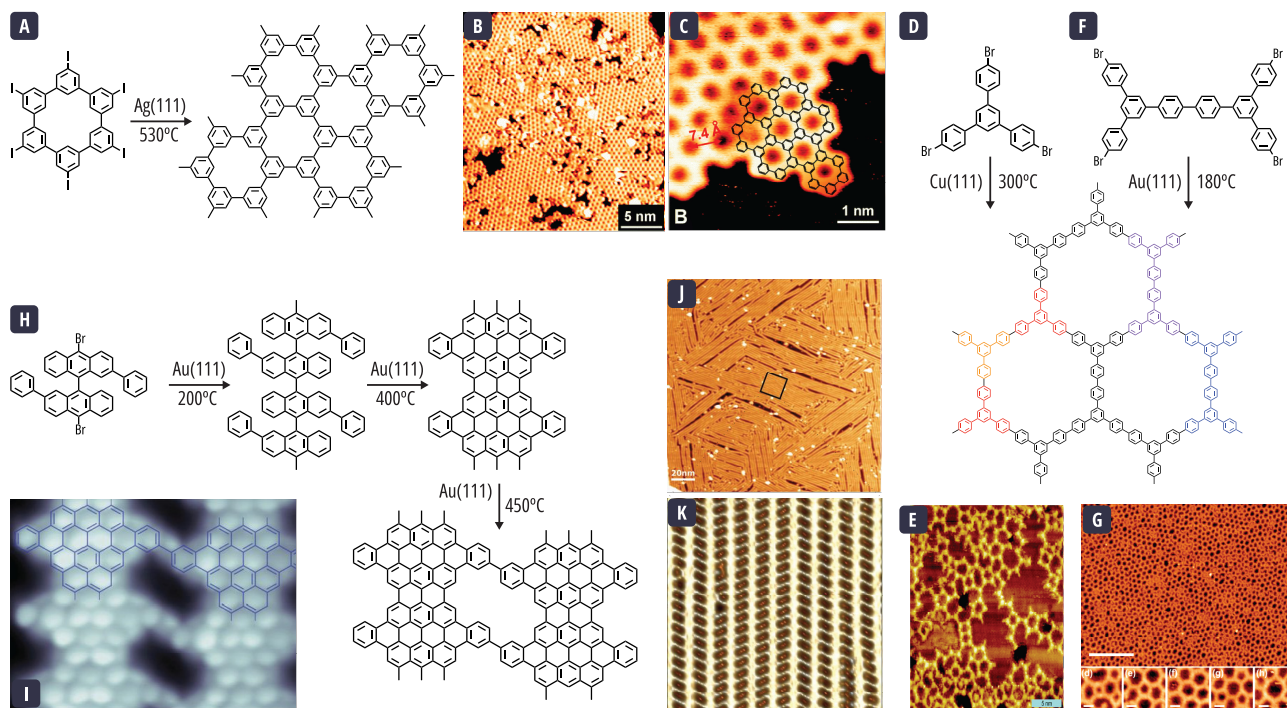


Figure 1.15 | On-surface synthesis of graphene nanomeshes. **(a)** Scheme of the reaction on a silver surface of CHP to give a polyphenylene network. **(b)** STM image of polyphenylene network after polymerization on a silver surface at 530°C, and **(c)** a magnification of an edge with the overlaid chemical structure. (a-c)¹⁶⁴. **(d)** Scheme of the reaction on a copper surface of TBPB and the expected hexagonal porous network. **(e)** STM image of the protopolymer obtained after annealing of TBPB on a copper surface at 300°C. (d-e)¹⁶⁵. **(f)** Scheme of the reaction on a gold surface of TBPB, an alternative precursor to obtaining the porous hexagonal network as in (d). **(g)** STM image of the obtained polyphenylene network after annealing on a gold surface at 180°C. Scale bar, 1.9 nm. Inserts showing different macrocyclizations observed. Scale bars, 14 Å. (f-g)¹⁶⁵. **(h)** Reaction pathway of DP-DBBA undergoing Ullmann coupling, intracyclodehydrogenation, and cross-coupling at three different temperatures on a gold surface to give nanoporous graphene. **(i)** Constant height mode nc AFM CO-functionalized tip image of a GNM obtained from annealing DP-DBBA at different temperatures on a gold surface. **(j)** STM image of a gold surface covered by DP-DBBA GNR and fused domains of GNM. **(k)** Laplacian-filtered topographic close-up image of the black rectangle in (j). (h-k)¹⁶⁷.

Covalent organic frameworks containing heteroatoms are also of interest.^{168,169} Recently, Steiner *et al.*, reported the formation of 2D-COF from carbonyl-bridged triphenylamines (CTPA) substituted with iodine and bromine atoms.¹⁷⁰ They achieved a doped nanoporous network through hierarchical reactivity. First, they formed, on an Au(111) surface, CTPAs macrocycles at a first temperature by activating the C-I bonds. Secondly, they reticulated the macrocycles into a 2D network by heating at a farther temperature to activate the C-Br bonds (**Figure 1.16a-c**). Another synthesis strategy for doped GNM is to couple halogen-substituted porphyrins on-surface. For example, Lafferentz *et al.* also followed a hierarchical approach to obtaining porphyrin-containing covalent organic frameworks (**Figure 1.16d**).¹⁷¹ Though Ullmann coupling is a widespread choice for on-surface C-C coupling because of the absence of secondary reactions, other reactions have been employed to obtain 2D-COF such as cyclotrimerization of alkyne or acetyl functions.¹⁷² For instance, Liu *et al.* obtained a polyphenylene network by a [2+2+2]

cyclization reaction of 1,3,5-tris-(4-ethynylphenyl)benzene (TEB) on an Au(111) surface at 160°C (**Figure 1.16e**).¹⁷³ Through this strategy they were able to observe regular domains of polyphenylene network (**Figure 1.16f**). There are other reactions that can be applied for on surface C-C, such as Bergman cyclization, Glaser coupling, boronic acid condensation, and dehydrogenative coupling, that have been, up to this date, primarily used for the synthesis of graphene nanoribbons.¹⁶³

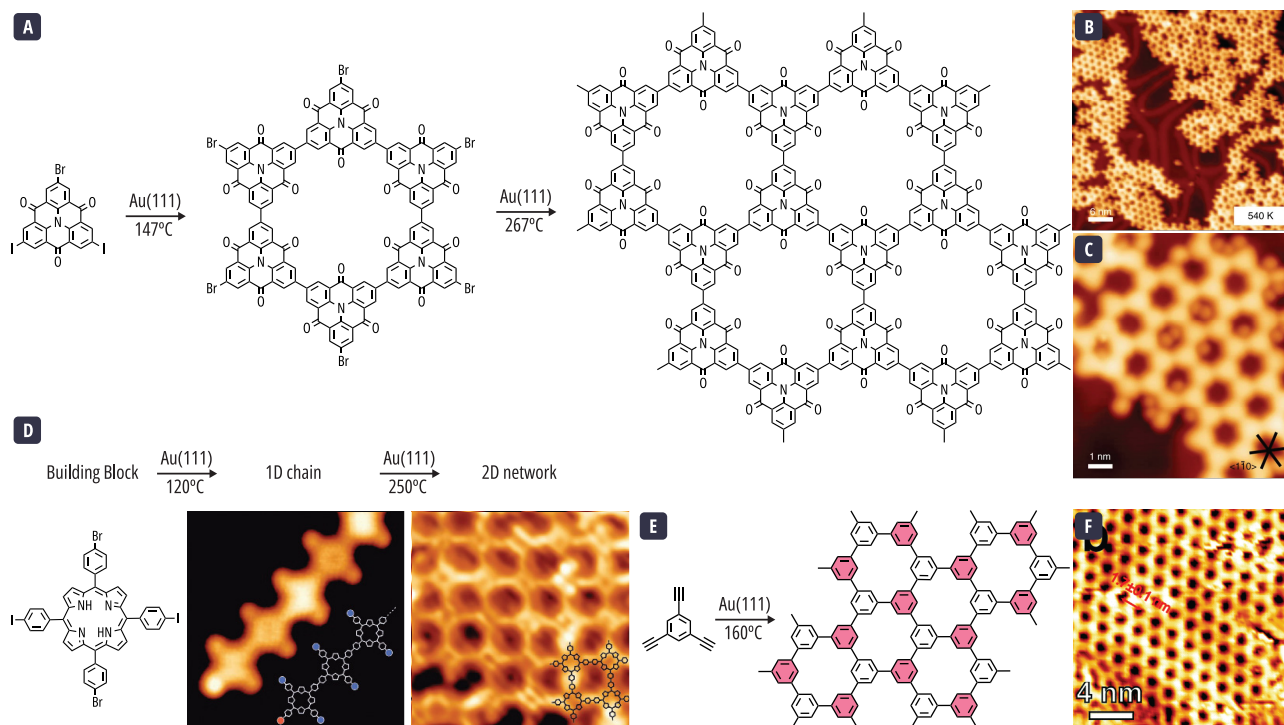


Figure 1.16 | Doped GNM and alternative reactions to Ullmann coupling. **(a)** Scheme of the reaction of the hierarchical formation of an N-O-doped GNM on a gold surface. First, the formation of brominated macrocycles at 147°C followed by the formation of the two-dimensional network at 267°C. **(b,c)** STM image of the covalent porous network formed after annealing at 267°C of CTPA precursor on a gold surface. **(a-c)**¹⁷⁰. **(d)** Summary of the synthesis of a porphyrin-based 2D nanoporous network on a gold surface. Left, chemical representation of the porphyrin building block. Middle, STM image of the 1D chain formed after heating to 120°C. Right, STM image with the overlaid structure of the reticulated 2D network after annealing at 250°C. ¹⁷¹ **(e)** Scheme of the trimerization reaction of TEB molecules on a gold surface at 160°C to yield a 2D-COF. Highlighted the phenyl ring formed in the trimerization of three alkyne functions. **(f)** STM image of a regular domain of COF obtained by trimerization of alkyne functions in TEB on a gold surface. **(f-g)**¹⁷³.

As illustrated in the previously cited examples, the neck of the GNMs synthesized is a simple carbon-carbon bond (**Figure 1.17a**). So far, there are no reports of synthesized nanoporous graphene with a neck containing two or more C-C bonds keeping the hexagonal structure of graphene (**Figure 1.17b**). Overcoming this challenge is one objective of this thesis work. Recently, Multu *et al.* described the on-surface synthesis of a GNM containing a neck with two C-C bonds.¹⁷⁴ They deposited methylated 6,11-dibromo-1,2,3,4-tetraphenyltriphenylene on an Au(111) surface and thermally activated Ullmann coupling at 220°C to form graphene nanoribbons which were then heated at 430°C to achieve cyclodehydrogenation and cross-dehydrogenative coupling. A five-member ring is formed in the annealing step because of the presence of a methyl group, and upon cross-coupling, a rubicene neck is formed (**Figure 1.17d-c**). Though rubicenes exhibit interesting properties, the graphene hexagonal network is broken.

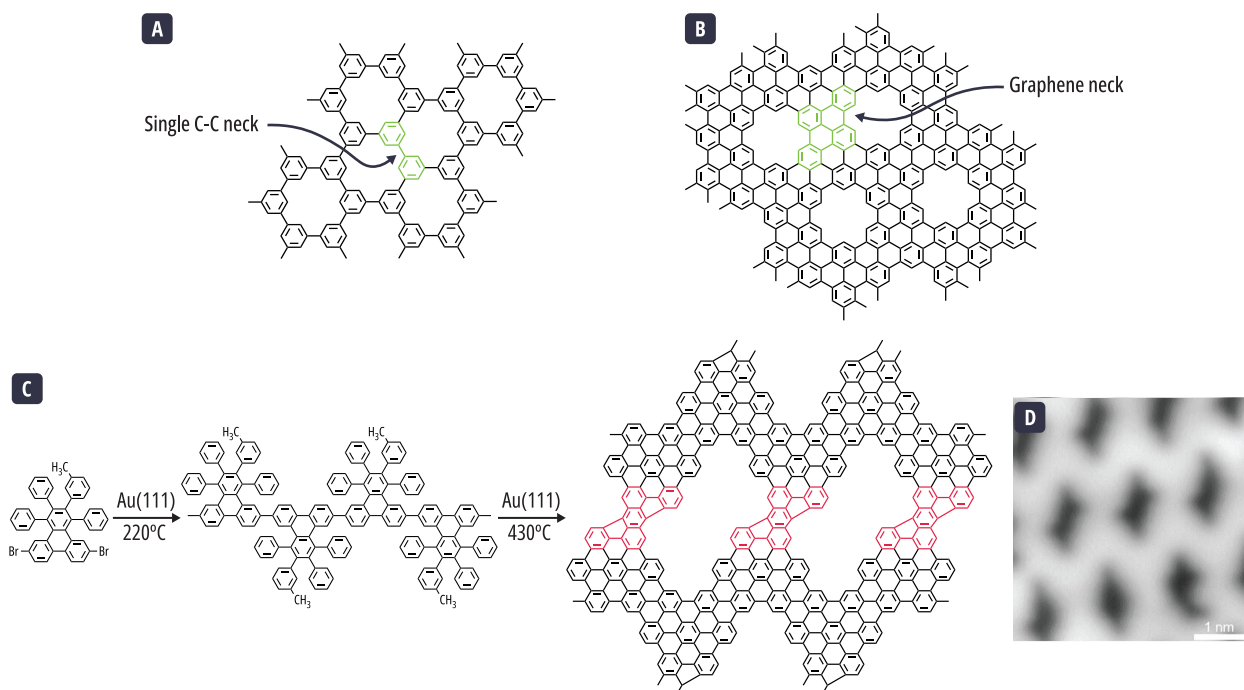


Figure 1.17 | Graphene neck in the nanomesh structure. **(a)** Structure of a 2D nanoporous network with single C-C bond neck. **(b)** Structure of a GNM with a graphene-like neck. **(c)** Reaction scheme for the synthesis on a gold surface of a GNM with a rubicene neck highlighted in red. First, the formation of a 1D zigzag chain followed by subsequent intramolecular dehydrogenation and inter-cross-coupling. **(d)** Topographic STM image of the rubicene necked GNM. (c-d)¹⁷⁴

1.3 OPTICAL PROPERTIES OF GQDs

As we saw in the previous sections, it is possible to open a bandgap in graphene by quantum confinement. The nanometric-sized graphene structures can be synthesized in a bottom-up fashion using an organic chemistry methodology. In this way, it is possible to obtain atomically precise architectures for which is now possible to study the true intrinsic optical properties of graphene quantum dots. The study of optical properties is achieved through the study of the absorption and emission features of the nano-object coupled with theoretical studies. Having a better understanding of the effect that size, symmetry, and functional groups have on the optical behavior of nanographene is of significant interest to facilitate its applications and be able to tailor the desired properties. This section will discuss important photophysical definitions and some examples of the optical studies performed so far for GQDs.

1.3.1 GENERALITIES

When considering light as an electromagnetic wave, it is composed of an oscillating electric field and a magnetic field perpendicular to each other with a given frequency (wavelength) (**Figure 1.18a**). In natural light, these fields have no preferential orientation and so the light is said to be unpolarized. However, when there is a preferential orientation of their electromagnetic fields, light is said to be polarized. Light can be linearly, circularly, or elliptically polarized. Linearly polarized light has its electric fields oscillating in a single direction. Circularly polarized light results from the combination of two distinct electromagnetic waves with the same amplitude propagating perpendicular to each other but with a phase offset of $\pi/2$ or $3\pi/2$. This makes the electric field vector to rotate in a circular pattern as the waves propagate (**Figure 1.18b**). If the two waves have different amplitudes or phases, the resulting light is called elliptically polarized.

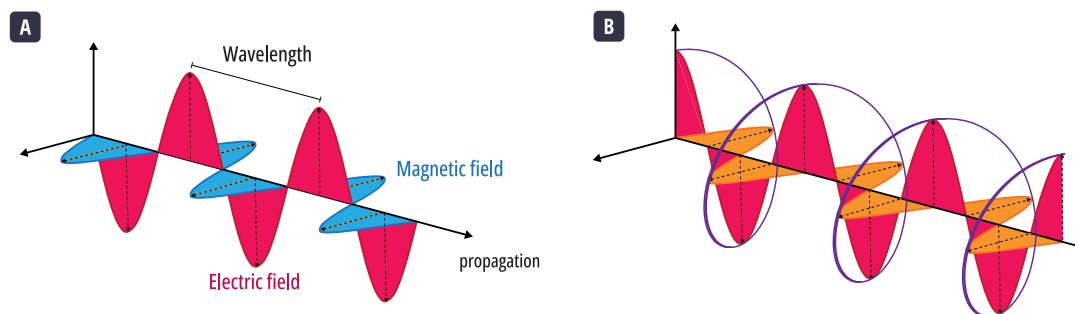


Figure 1.18 | (a) Wave composition of light, an electric (red) and magnetic (blue) field perpendicular to each other. (b) Combination of two electric fields (red and orange) with identical amplitude but offset by $3\pi/4$ whose sum (purple) creates a left-handed circular polarization.

Upon interaction with light, a molecule can absorb its energy and undergo an internal modification. In the ultraviolet (UV), visible, and near-infrared (NIR) regions of the electromagnetic spectrum, the energy corresponds to the displacement of an electron from an occupied orbital to an unoccupied orbital; this is called an electronic transition. For a given transition to happen, it must respect symmetry and spin multiplicity selection rules. The spin selection rule states that for a transition to be allowed, spin multiplicity must not change between the initial and final state ($\Delta S=0$). The ability of a transition to happen is associated with its *absorption coefficient* (ϵ) and is related to the concentration (c), light path (l), and the ratio between incident to transmitted light (I_0/I) at a specific wavelength by Beer-Lambert's law (**Equation 1.1**). In practice, forbidden transitions can happen because of additional interactions that might not be considered theoretically, but will have lower absorption coefficients than allowed transitions.

$$A(\lambda) = \log\left(\frac{I_0}{I}\right) = \epsilon(\lambda)lc$$

Equation 1.1 | Beer-Lambert's law.

After the absorption of light, a very fast process, a molecule goes to an excited state. It will return to its ground state through radiative decay, with the emission of a photon, or through non-radiative decay, by thermal relaxation and environmental interactions. Depending on spin multiplicity, the excited states can be divided into singlet S_n ($s=0$) or triplet T_n ($s=1$) states. A non-radiative transition between two states with same spin multiplicity, i.e. $S_n \rightarrow S_{n-1}$, is called internal crossing (IC). As stated in Kasha's rule, the IC to a high vibrational level will be followed by an immediate vibrational relaxation to the lowest level in the new excited state. The IC conversion between excited states is faster than between the first excited state and the ground state because of a higher energy difference; therefore, there can be competition with other processes. One of these processes is the emission of a photon in the $S_1 \rightarrow S_0$ relaxation, called fluorescence. The non-radiative passage from a singlet to a triplet state $S_n \rightarrow T_n$ is called intersystem crossing (ISC). This transition, in principle forbidden, is possible thanks to the spin-orbit coupling with a more pronounced effect for molecules containing or interacting with heavy atoms. The radiative transition from the triplet to the ground singlet state $T_1 \rightarrow S_0$ is known as phosphorescence. Because of the spin selection rule, phosphorescence is going to happen at a much slower rate than fluorescence. The timescale of fluorescence lies between 10^{-10} - 10^{-7} s, and for phosphorescence between 10^{-6} - 10 s. All these processes can be summarized using a Jablonski diagram (**Figure 1.19**).

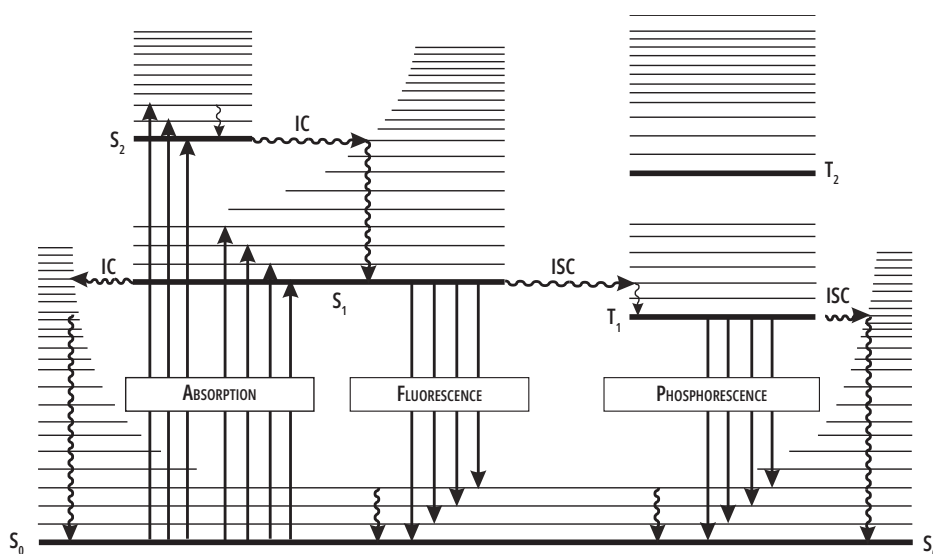


Figure 1.19 | Jablonski diagram. Thick lines represent electronic states and thin lines vibrational states.¹⁷⁵

In some cases, as for small polycyclic aromatic hydrocarbons, it is possible to see also the vibrational structure in the electronic spectra of the molecules. As seen in the Jablonski diagram (**Figure 1.19**), upon absorption of a photon, the transition from the ground state to a vibrational level v_n of an excited state can take place. Conversely, the emission happens from v_0 of S_1 to the vibrational levels v_n of the ground state. The transition from v_0 in S_1 to v_0 in S_0 is labeled as 0-0 and is commonly known as zero-photon line (ZPL). The spacing between vibrational levels and the Franck-Condon factors, that determine the intensity of the vibronic bands, are virtually similar between S_1 and S_0 . Because of this, the emission gives the impression of being the mirror image of the absorption at the lowest energies (**Figure 1.20a**). The energy difference between the maximum of the absorption band lowest in energy and the maximum of the first emission band corresponds to the Stokes shift (**Figure 1.20b**). It is possible to lose the vibronic structure because of the broadening of the absorption bands. The effect can come from the existence of a large set of vibrational levels generating a quasi-continuum in the electronic states; this is homogeneous broadening. Another reason is heterogeneous broadening, a consequence of the molecule's interaction with its environment or the presence of additional chromophores whose spectrum overlaps.

When we are interested in fluorescence molecules, there are two crucial pieces of information about the radiative process. The first one is the lifetime of the excited state τ_s . It can be measured by recording the fluorescence intensity over time after an excitation pulse. The intensity decreases exponentially. The second important piece of information is the *quantum yield* Φ_F , which is the ratio of emitted photons over absorbed photons. Other essential behaviors of the emitters are photobleaching and blinking. Photobleaching occurs when the molecule loses its emissive properties after prolonged exposure to light. This can result from chemical damage done to the emitter during the excited lifetime. Blinking is the intermittent emission over extensive periods of time. This results from temporarily forming a "dark" non-emissive state with a relatively long lifetime. This can be, for example, a molecule that stays trapped in a triplet state after ISC limiting its capacity of emitting or reabsorbing a photon until it returns to the ground state. In contrast to photobleaching, once the molecule returns to the ground state, it can reabsorb and decay by a fluorescent path again.

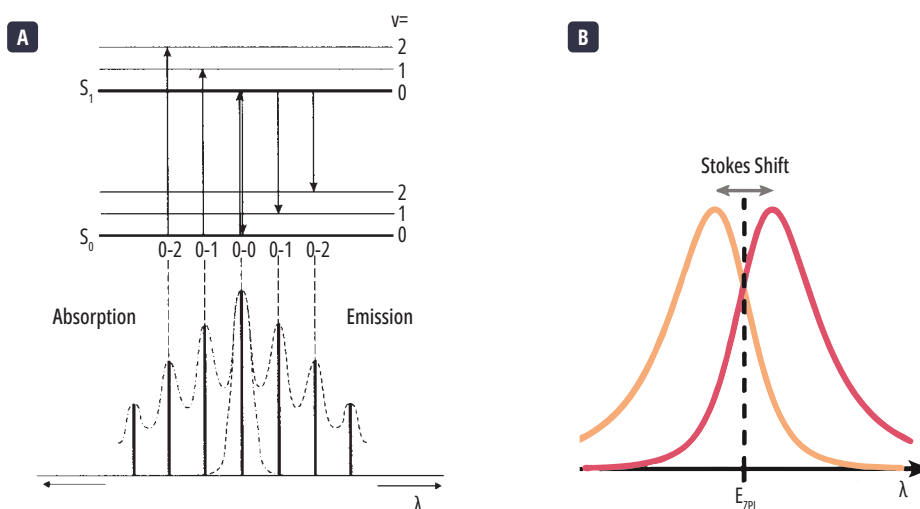


Figure 1.20 | (a) Mirror absorption and emission and associated transitions.¹⁷⁵ (b) Stokes shift between an absorption (orange) and emission (red).¹⁷⁶

1.3.2 OPTICAL STUDIES OF GQDs

First optical studies on top-down synthesized GQDs showed that their optical properties were mainly governed by defects states.^{177–179} During these first studies, the challenge relied in the distinction between the intrinsic emission and the emission originated by defects in the GQD. The intrinsic emission is caused by the sp^2 carbon, while the defect emission can be caused by the presence of undesired functional groups at the edges as well as missing or by unhybridized sp^2 carbon atoms in the core of the quantum dot. Considering this issue, this is where a synthetic organic chemistry approach comes in handy. With tailored and homogeneous architectures, it is possible to study and better understand the intrinsic optical properties of GQDs. However, advanced optical studies of the intrinsic properties of graphene quantum dots are scarce. As we will see in the following examples, their solubility and derived issues, continue to handicap the optical studies. In the synthesis section, we already described how to tackle this problem with structure design.

So far, among large PAHs seen as GQDs, the photophysics of hexabenzocoronene and its derivatives is the most extensively described. Because of its small size and relatively easy synthesis, an extensive library of compounds has been developed over the years.⁷⁶ The use of different functional groups has improved its solubility in various organic solvents and even in aqueous media with surfactants.^{180,181} Recently, Haines *et al.* focused on how the nanographene's substituent groups and symmetry affect the HBC's electronic properties (**Figure 1.21a-b**).¹⁸² First, they observed that when the symmetry of HBC was broken with the presence of the electron-withdrawing group, previously forbidden transitions were observed. Moreover, as the electron-withdrawing effect increased, the authors observed attenuation of the main band and a red-shifted absorption and emission spectra, and the appearance of phosphorescence at low temperatures (**Figure 1.21c**). The strong electron withdrawing group, NO_2 , significantly impacted the electronic properties of HBC, triggering a redistribution of charge density with high influence of the solvent (**Figure 1.21d**).

Initial photophysical studies of larger "organic" GQDs were limited to absorption spectroscopy (**Figure 1.21e**).¹⁸³ The recorded absorption spectra become broader as the size of the nanoparticle increases and their solubility decreases, even in the presence of solubilizing functional groups. Later, Tan *et al.* described the synthesis of a series of chloro-functionalized GQDs ranging from 42 to 222 sp^2 carbon atoms (**Figure 1.21f**).¹⁸⁴ The absorption of the GQDs extended from the ultraviolet to near-infrared (**Figure 1.21g**). They observed that the absorption bands were shaper and better resolved than those of homologue

nanoparticles functionalized with alkyl chains. This suggested that the chlorinated nanoparticles exhibited less aggregation in solution. Additionally, they also reported a bathochromic shift in the absorption spectra, compared to their hydrogenated counterparts, due to the electron-withdrawing effects of the chlorine atoms.

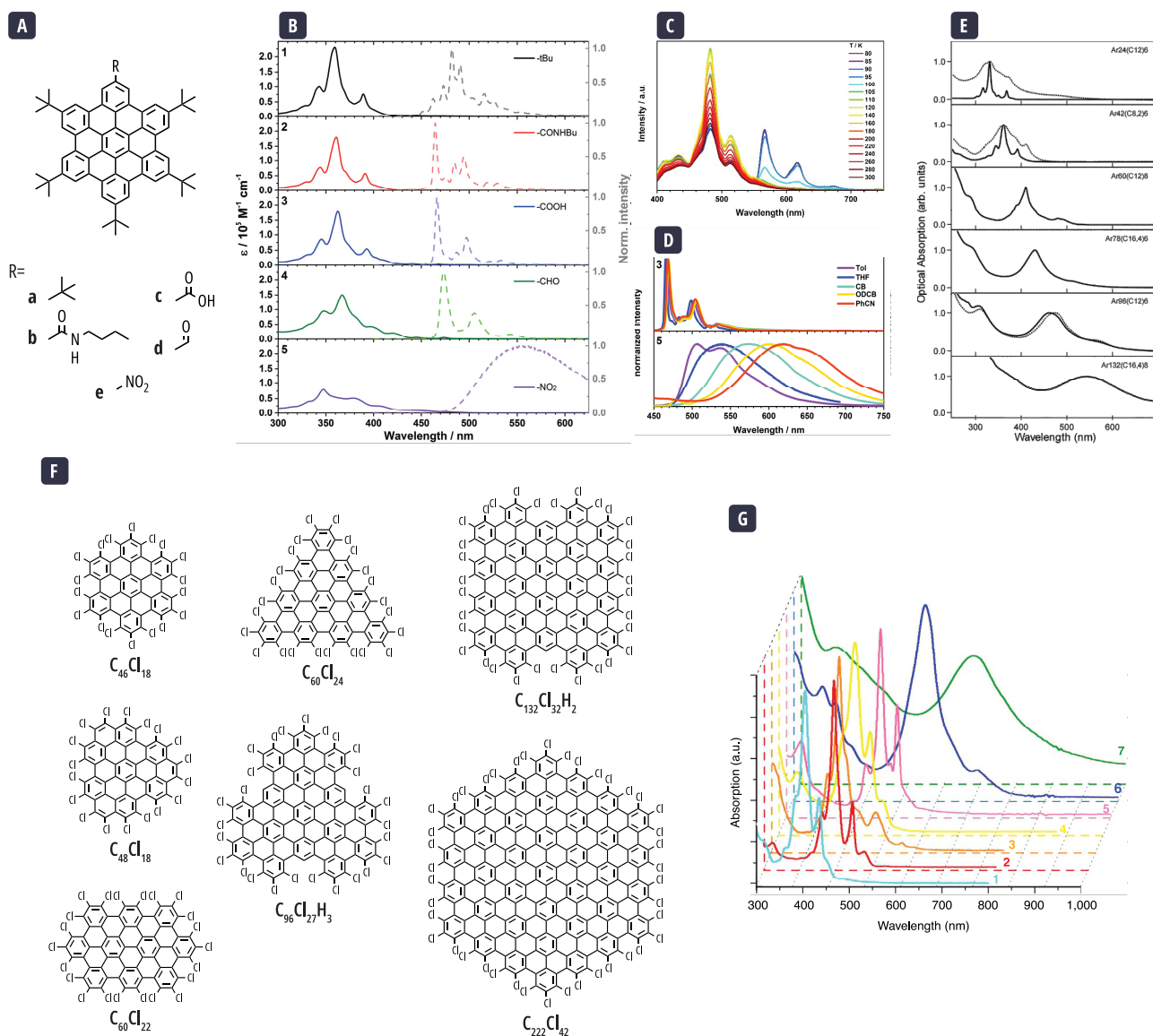


Figure 1.21 | Optical studies of HBC derivatives and larger GQDs in solution. **(a)** Chemical structure of HBC derivatives with an increasing electron-withdrawing group. **(b)** Absorption (plain) and emission (dotted) spectra of 5a-e from top to bottom, respectively. **(c)** PL spectra of 5a at different temperatures in MeTHF. At low temperatures, the new PL bands were attributed to phosphorescence. **(d)** PL emission of 5c (top) and 5e (bottom) in different solvents upon excitation at 350 nm. 5e exhibits high solvatochromism. (a-d)¹⁸². **(e)** Absorption spectra of large PAHs with an increasing number of conjugated carbon atoms from top to bottom.¹⁸³ **(f)** Structures of large PAHs with chlorinated edges. **(g)** Absorption spectra of the chlorinated PAHs in toluene. (f-g)¹⁸⁴

Besides aggregation, solubility raises another issue when it limits the purification process of the GQDs. If impurities are present in the sample, and they have a strong interaction with light, they can interfere with the interpretation of optical data and make it difficult to assign the intrinsic optical properties to the GQDs. For instance, the first studies conducted on a C₁₃₂ GQD with side alkyl chains, whose structure is given in **Figure 1.22a**, described that a small singlet-triplet energy splitting led to a significant increase in intersystem crossing, giving rise to fluorescence and phosphorescence (**Figure 1.22b**).¹⁸⁵ Further investigations on the same molecule suggested that the observed optical properties came rather from impurities and not from the intrinsic

emission of the GQD.¹⁸⁶ The peak previously attributed to fluorescence emission would rather come from existing impurities in the sample, and the emission peak assigned to phosphorescence resulted rather from fluorescent emission of the GQD (**Figure 1.22b**).

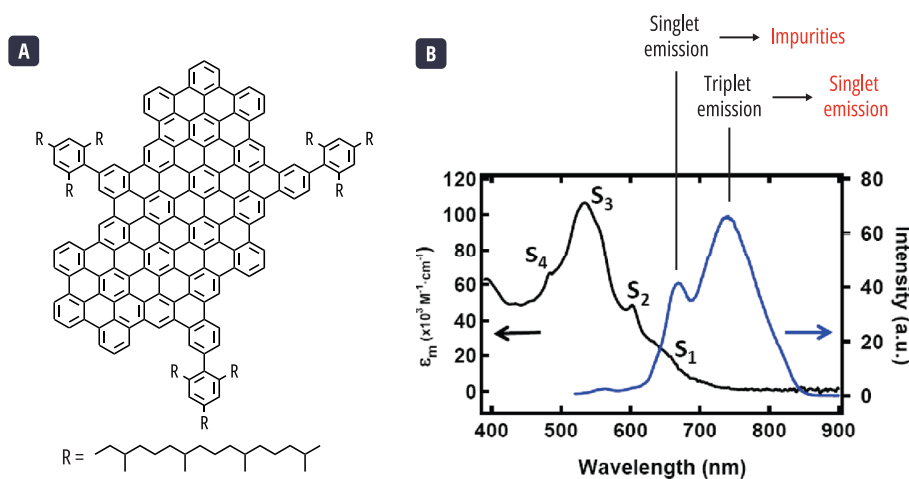


Figure 1.22 | (a) Structure of the C_{132} functionalized with trialkyl phenyl group.⁸² (b) Absorption (black) and emission spectra (blue) of the C_{132} GQD. On top the first attributions of the origin of the emission. In red the second attribution after further studies.¹⁸⁵

A notorious comprehensive photophysical examination by Zhao *et al.*, explored single molecule experiments of a triangular (T) alkyl-substituted 96 sp^2 carbon atom GQD, **(T) $C_{96}(C_{12}H_{25})_6$** (**Figure 1.23a**).¹⁸⁷ They reported single-emitter studies to address the intrinsic emission of the GQD. PAH materials had previously been tested as single photons source for over thirty years. Initially, these experiments were conducted by physicists on small and easy accessible molecules such as pentacene, terrylene, dibenzoanthracene, dibenzoterrylene.^{188–190}

In this study, the large PAH emitter was embedded in a polystyrene matrix for which a photoluminescence map was recorded. At optimized emitter concentrations, the observed bright spots had sizes corresponding to the diffraction limit. A typical photoluminescence (PL) spectrum of a spot is given in **Figure 1.23b**. This spectrum is composed of three peaks attributed to the zero-phonon line and its vibronic replicas. The time-resolved photoluminescence (TRPL) experiments on the whole emission spectrum, showed a monoexponential decay indicating that a single transition was in play in the emission of the GQD (**Figure 1.23c**). At the main emission peak, the time trace of the PL intensity of a spot under continuous irradiation of light showed a good stability without any blinking. The bleaching of the spot takes place with a single jump from a constant intensity to zero (**Figure 1.23d**). This discrete single jump was an indication of the observation of a single object.

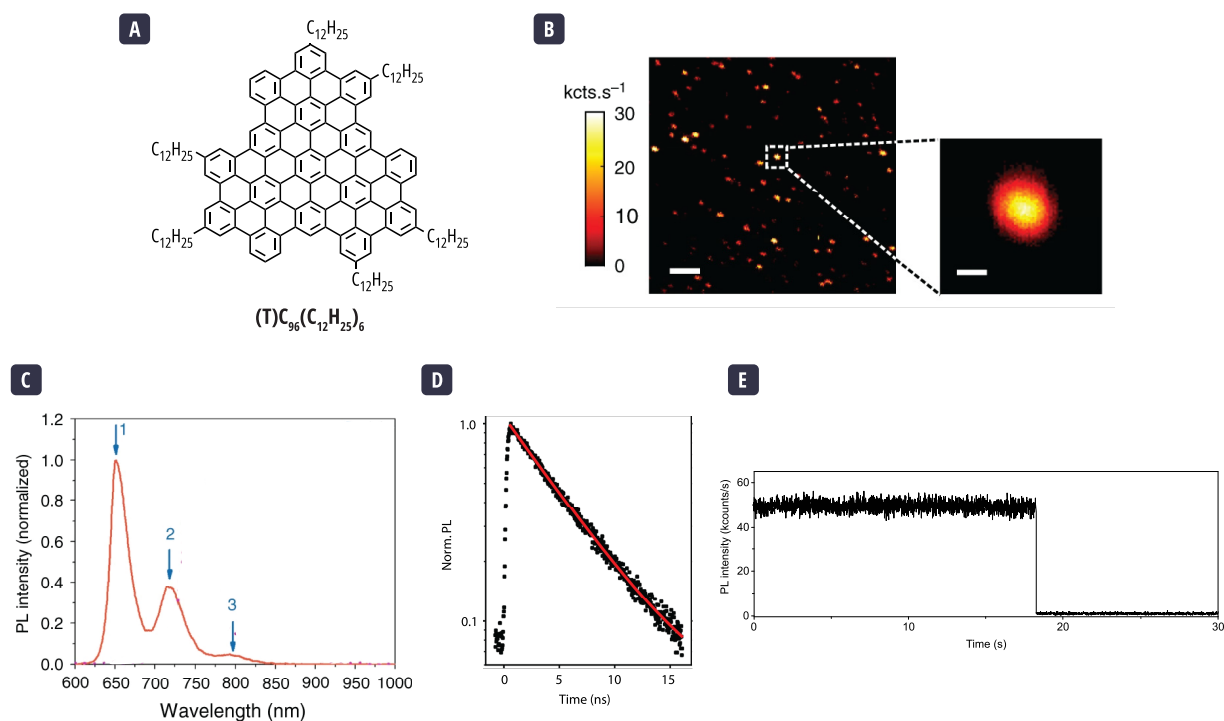


Figure 1.23 | (a) Structure of the $(T)C_{96}(C_{12}H_{25})_6$ (b) PL map of GQD in a polystyrene matrix (scale bar, 3 μ m) and (b) amplification of the bright spot in the white box (scale bar, 200 nm). (c) PL spectrum of a $(T)C_{96}(C_{12}H_{25})_6$ spot. (d) TRPL of $(T)C_{96}(C_{12}H_{25})_6$ on the whole spectrum. (e) Time trace of the PL of $(T)C_{96}(C_{12}H_{25})_6$ around the time of bleaching.¹⁸⁷

Having a single emitter allowed the authors to explore single photon emission. This was achieved by using a Hanbury Brown-Twiss setup to record the second-order correlation function $g^{(2)}(t)$ of different bright spots. This setup is shown in **Figure 1.24a**. The emitted light from the sample passes through a beam splitter that leads to two detectors. When a photon passes through a beam splitter, it can be either transmitted or reflected. For a single photon the probability that both detectors detect a signal at the same time drops to zero. This is reflected by the second-order correlation function, which drops to zero at very short times for a single photon-emitter. This phenomenon is called photon antibunching and it can have important applications for quantum cryptography.^{191,192} This was observed for $(T)C_{96}(C_{12}H_{25})_6$ (**Figure 1.24b**). In this study, the authors also showed that $(T)C_{96}(C_{12}H_{25})_6$ has good photostability, shows no blinking, has a brightness comparable to the brightest quantum emitters, and behaves as a single photon emitter at room temperature.

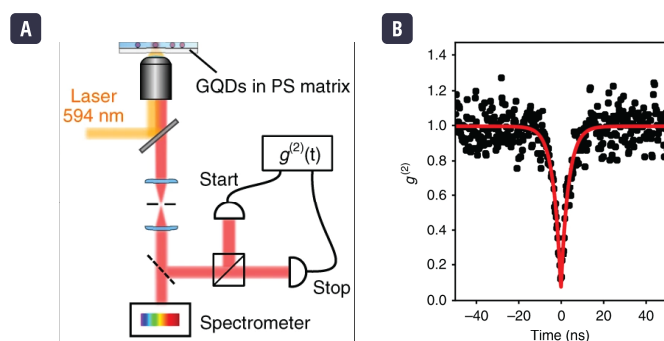


Figure 1.24 | (a) Setup of the used micro-luminescence setup. To the right the beam splitter and the two detectors for a Hanbury Brown-Twiss experiment. (b) Second-order correlation function recorder for a $C_{96}-C_{12}$ spot with the superimposed fit. A weak value of $g^{(2)}(0)$ indicates a strong antibunching and single-photon emission.¹⁸⁷

Because of the π -stacking interactions, unfunctionalized PAHs are difficult to individualize. As we discussed in this section, optical studies of poorly solubilized graphene nanoparticle give broaden absorption spectra. Furthermore, low solubility

can impact the processability of the GQD and its purity, however, the presence of impurities can hide the intrinsic optical properties of the target nanoparticle. This is where the collaboration between chemists and physicists has a particular importance, to develop new chromophores that are pure and easy to manipulate (*i.e.* soluble and easy to individualize in solution) and exhibiting stable emission and tuneable wavelength.

1.4 SCOPE OF THIS WORK

To facilitate applications of graphene for optical and optoelectronic applications, it is necessary to open a bandgap, which can be achieved through nanostructuring. Throughout this PhD thesis, we focus on two nanostructured graphenic materials: graphene quantum dots and graphene nanomeshes. We will describe their synthesis and the study of their intrinsic optical properties. Understanding the relationship between the structure (size, symmetry, and substituents) of a GQD and its optical properties will facilitate its application by helping with the reverse engineer a requested property.

The first part is dedicated to the synthesis of a rod-shaped family of GQDs functionalized with *tert*-butyl groups to help with their solubility. This family is composed of four members containing 78 to 132 sp^2 carbon atoms in their structure. We will discuss how the positioning of this bulky groups is important not only for their reactivity but also for their enhanced solubility. This easily processable GQDs family allowed to conduct thorough optical studies in collaboration with the Lumière, Matière et Interfaces (LUMIN) laboratory at ENS Paris-Saclay. A special focus will be made for the $C_{96}tBu_8$ GQDs (**Figure 1.25**), before comparing it to the other members of the GQD family. The interpretation of the optical behavior of the GQDs was backed-up by quantum-chemical calculations performed by collaborators at Mons University in Belgium and Warsaw University in Poland. Finally, we will present the preliminary studies of a first application of these nanoparticles as an emissive material.

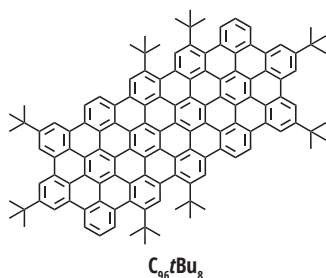


Figure 1.25 | Structure of the $C_{96}tBu_8$ GQD.

The second part is oriented towards our efforts to further increase the solubility of GQDs. First, by expanding the strategy used in the first part of the PhD thesis. In this mindset, a new family of rod-shaped graphene nanoparticles with additional *tert*-butyl functional groups was synthesized, and their preliminary optical studies are presented in this part. The second strategy to improve the solubility of GQDs consisted in synthesizing twisted nanographenes, specifically of two types: π -extended helicenes and nanographene propellers. The synthesis of helicenes adds a new optical property to the GQDs: chirality. The exploration of the chiroptical property in an helicene-like GQD will be presented in this chapter.

In the last part, the synthesis of new organic precursors that could lead to graphene nanomeshes will be presented. These precursors were designed to assemble into a GNM with a neck containing two or more C-C bonds keeping the hexagonal structure of graphene GNM with a graphenic necks (**Figure 1.26**). The on-surface deposition and assembly into GNMs was done by collaborators at the Institut Matériaux Microélectronique Nanoscience de Provence (IM2NP) in Aix-Marseille University.

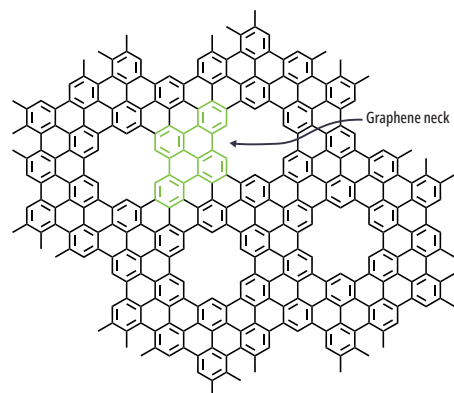


Figure 1.26 | Structure of the target **GNM-1** with a graphene-like neck.

Chapter 2 SOLUBLE ROD-SHAPED GRAPHENE QUANTUM DOTS

CONTENTS

2.1	Introduction	34
2.1.1	Scholl reaction	34
2.1.2	Preceding work	36
2.2	A change in functional groups	37
2.2.1	Synthesis and studies of the triangular C ₉₆ GQD	37
2.2.2	Synthesis of a first rod-shaped C ₉₆ GQD	40
2.3	Synthesis and optical studies of C ₉₆ tBu ₈	42
2.3.1	Synthesis	43
2.3.2	Characterization	47
2.3.3	Optical properties	54
2.4	Varying the rod-size	66
2.4.1	Synthesis	66
2.4.2	Characterizations	69
2.4.3	Optical studies	75
2.5	Towards the first applications	80
2.6	Conclusion	82

CHAPTER 2 SOLUBLE ROD-SHAPED GRAPHENE QUANTUM DOTS

The main objective of this thesis is to synthesize well-defined graphene quantum dots to better understand their intrinsic optical properties. To carefully control and tune the structure of the quantum dots, we synthesize them through a bottom-up organic chemistry approach. In this chapter, we will present the synthesis of a family of highly soluble graphene quantum dots with an elongated rod shape. This enhanced solubility originates from the presence of closely positioned bulky *tert*-butyl groups along the long axis of the nanoparticles. The family of rod-shaped GQDs comprises four members that only differ in size but keep the same C_{2v} symmetry: **C₇₈tBu₆**, **C₉₆tBu₈**, **C₁₁₄tBu₁₀**, and **C₁₃₂tBu₁₂** (Figure 2.1). For simplicity, these nanoparticles are referred to by the number of sp^2 carbon atoms present in their structure, followed by the nature of their substituents. The sizes of the nanoparticles range between 1.99 nm and 3.11 nm.

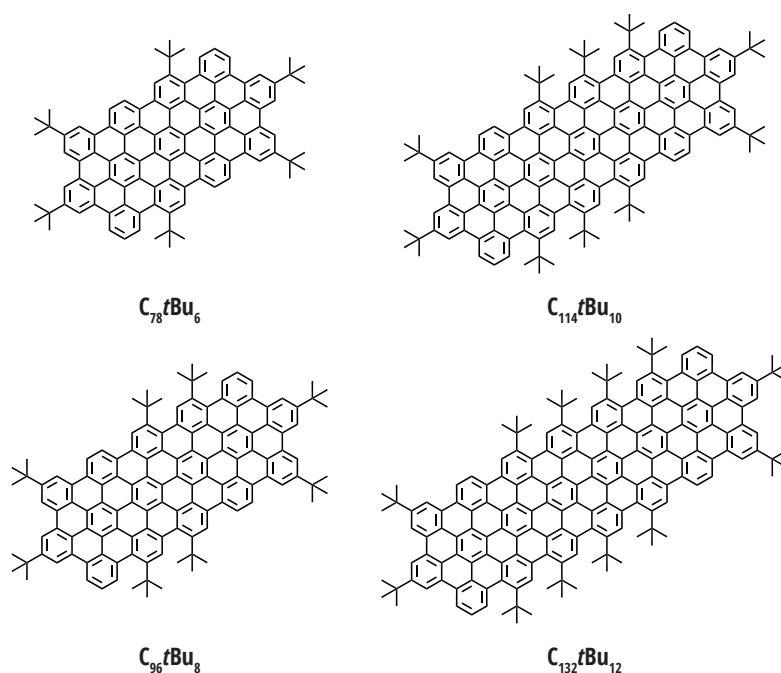


Figure 2.1 | Structures of the four members of the rod-shaped family.

We will begin this chapter with some generalities on an essential chemical reaction employed when synthesizing large PAHs: the Scholl oxidation. We will then discuss the steps that led us to the synthesis of this family of GQDs. We will make a special focus on the synthesis, characterizations, optical experiments, and theoretical calculations of **C₉₆tBu₈**. Next, we will shed some light on the synthesis and characterizations of the other members of this rod-shaped family. We will conclude by presenting a first concrete application for two members of the family.

2.1 INTRODUCTION

2.1.1 SCHOLL REACTION

The general strategy employed for the synthesis of the GQDs, consists in the synthesis of a polyphenylene dendrimer through a [4+2] cycloaddition of a cyclopentadienone with a phenyl alkyne core. This polyphenylene dendrimer is then cyclodehydrogenated through the Scholl reaction. This is a crucial step since it ensures the formation of long delocalized sp^2 domains. We will discuss further the reaction mechanism of this critical reaction in our approach to synthesizing GQDs.

The Scholl oxidation, also known as cyclodehydrogenation, is an intramolecular reaction that results in the formation of carbon-carbon (C-C) bonds between two aryl units in the presence of an oxidant under acidic conditions. Essentially, the new C-C bond generally forms a new cycle while eliminating two hydrogen atoms. This process was initially described by R. Scholl in 1910 when he reported the formation of a C-C bond in a dianthraquinone using aluminum(III) chloride at 140°C for a period of 45 minutes.¹⁹³ Over time, various reaction conditions involving different combinations of oxidants/acid have been developed, including $\text{AlCl}_3/\text{CuCl}_2$, $\text{AlCl}_3/\text{Cu}(\text{OTf})_2$, FeCl_3 , MoCl_5 , PIFA/BF_3 , and $\text{DDQ}/\text{CF}_3\text{SO}_3\text{H}$, among others.^{85,194–198}

Even though the Scholl reaction has been extensively developed over recent decades for the synthesis of large polycyclic aromatic hydrocarbons due to its efficiency in forming multiple C-C bonds in a single step, the reaction mechanism remains elusive. Two of the most widely accepted proposed mechanisms include the formation of an arenium cation intermediate or the formation of a radical-cation intermediate. Both mechanisms are illustrated in **Figure 2.2**.

The first mechanism initiates with the protonation, or the formation of a sigma-complex with a Lewis acid, to generate the arenium cation. This is followed by the formation of the C-C bond through the attack of the adjacent phenyl on the electrophilic site. Subsequently, after a deprotonation step, the dihydro intermediate undergoes aromatization via an oxidation and the release of two hydrogen atoms.⁸⁶ The second mechanism, involving the radical-cation intermediate, begins with the monoelectronic oxidation of an aromatic ring. Through the reaction with a neighbouring phenyl, a radical-cation intermediate is formed along with a C-C bond. A subsequent single electron oxidation leads to the formation of an arenium cation. Ultimately, after a deprotonation step, the aromaticity is restored.^{199,200}

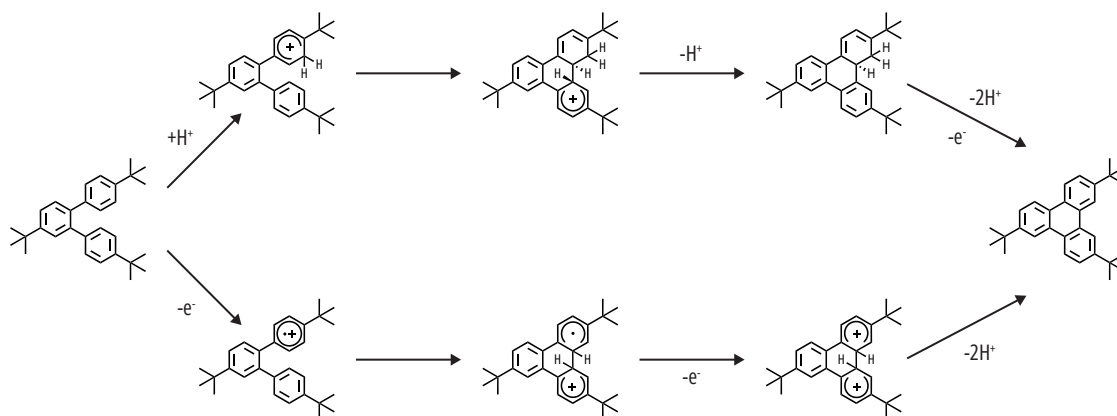


Figure 2.2 | Proposed Scholl reaction mechanisms. On top, the arenium-cation mechanism. Below the radical-cation mechanism.

The poor understanding of the reactional mechanism makes it difficult to predict the outcome of a Scholl oxidation. Additionally, the regioselectivity of the reaction cannot always be predicted.^{83,201} For every new precursor subjected to this reaction, the nature of the oxidant, the acid, the number of oxidant equivalents, and the reaction time needed to successfully

achieve complete cyclodehydrogenation can vary drastically. It is important to carefully test and determine these parameters for a successful Scholl reaction. For instance, if the reaction times or oxidant equivalents are not sufficient, not all C-C bonds are going to be formed. Inversely, if too much oxidant or reaction times are used the molecule can undergo degradations.

The Scholl reactions conducted in this thesis work were performed using iron(III) chloride or 2,3-dichloro-5,6-dicyano-1,4-benzoquinone (DDQ) as oxidants. Let's first be interested in the general conditions and considerations employed when working with iron(III) chloride. The reaction takes place in a dichloromethane/nitromethane solvent system. Dichloromethane effectively solubilizes the polyphenylene dendrimer precursors, while nitromethane ensures the solubility of the iron salt. The use of a metallic chloride salt generates hydrogen chloride as a byproduct, which can react with the nanoparticles and precursors to form chloro-substituted species. To enable the continuous removal of hydrogen chloride during the reaction, an argon flow setup is used. This helps to evacuate hydrogen chloride as it forms in the gaseous state. Besides, anhydrous solvents are employed to prevent the capture of hydrogen chloride.

The setup employed in the Scholl oxidations with iron(III) chloride is illustrated in **Figure 2.3**. First, high quality argon passes through a drying tube, then arrives to a first chamber containing dry non-stabilized dichloromethane. This step allows for the saturation of the gas with the solvent and prevents rapid evaporation in the main reaction chamber. Subsequently, the argon continues to a reaction chamber that contains the dendrimer solubilized in dichloromethane. A dropping funnel containing a reservoir of the solvent is added to the setup in case there is significant evaporation during the reaction. Finally, the setup is open to allow the evacuation of the gases. Through this opening iron(III) chloride is slowly added to start the reaction.

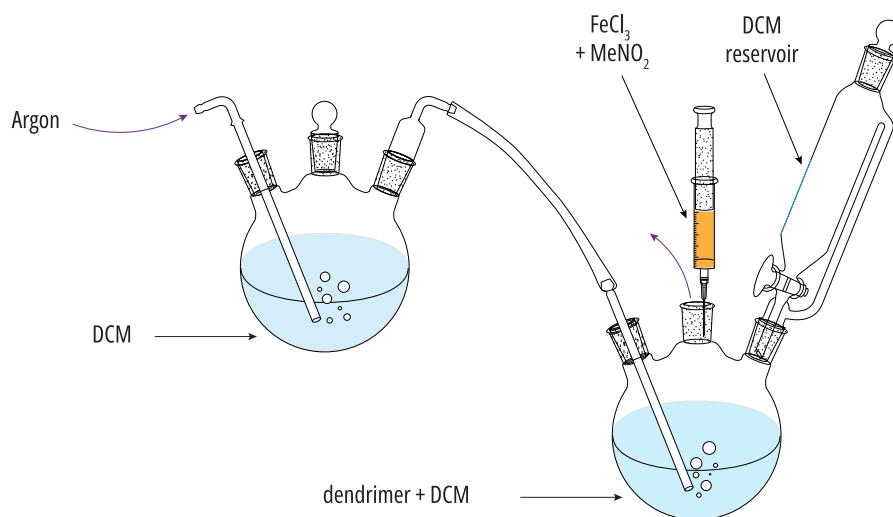


Figure 2.3 | Setup for the oxidation with iron(III) chloride.

The oxidation with 2,3-dichloro-5,6-dicyano-1,4-benzoquinone (DDQ) is more straightforward. It is performed in dry dichloromethane at 0°C under argon. These precautions are taken to prevent the decomposition of DDQ. To achieve the C-C bond formation it is necessary to add an acid to the mixture. We mostly employ methanesulfonic acid and trifluoromethanesulfonic acid. The use of strong acids increases the reactivity of DDQ towards the Scholl reaction but can also be responsible for some degradations.⁸⁵ The reaction works better if the acid is slowly added to a mixture of dendrimer and DDQ.

2.1.2 PRECEDING WORK

Before the work carried out during this thesis, our research laboratory, in collaboration with Prof. Jean-Sebastien Lauret's research team at ENS Paris-Saclay, were interested in the optical study of a triangular-shaped (T) GQD containing 96 sp^2 carbon atoms and six dodecyl alkyl chains as substituents, $(T)C_{96}(C_{12}H_{25})_6$ and the fully chlorinated derivative $(T)C_{96}Cl_{27}$.¹⁸⁷ Although these chemical structures were already described in the literature, they remained interesting because, so far, no advanced optical studies of large bottom-up synthesized GQDs existed. The synthesis of these quantum dots were first described by Tomovic *et al.* and Tan *et al.*, respectively.^{89,184}

As introduced in the general introduction, in these first single-molecule optical studies of $(T)C_{96}(C_{12}H_{25})_6$, it was shown that the nanoparticle has good photostability, shows no blinking, has a brightness comparable to the brightest quantum emitters, and behaves as a single photon emitter at room temperature.¹⁸⁷ These first interesting results were an encouragement to continue to explore the optical behavior of the triangular C_{96} nanoparticle with alkyl chains. During the beginning of my PhD work, I carried out the resynthesis of $(T)C_{96}(C_{12}H_{25})_6$ for additional optical studies. The results gave the emergence of two publications, which are described in the following paragraphs.

The first publication focused on the effect of vibration and aggregation on the optical properties of $(T)C_{96}(C_{12}H_{25})_6$.²⁰² This study combined experimental observations and advanced theoretical calculations combining electron-vibronic coupling. The DFT/DFT calculations indicated that transitions to S_1 and S_2 were forbidden due to the C_3 symmetry of the GQD. However, the S_2 transition is partially allowed when the symmetry is broken by out-of-plane distortions.

To further investigate the effects of aggregation, calculations of a dimer were conducted who showed a blue shift in the optical transition and a decrease in radiative decay. In the PL spectrum in solution, the two emission bands at higher wavelengths are associated with the monomer and were confirmed by single molecule studies that exclude all contributions of external objects. A band at shorter wavelengths is present, which may be attributed to the emission of byproducts of the Scholl reaction. However, photoluminescence experiments over time showed that the ratio of intensities in the PL changes with an iso-emissive point, suggesting a population conversion (**Figure 2.4**). The aggregates are less emissive, and calculations showed a blue shift in their optical transitions. It is possible that at these wavelengths, the contribution of small aggregates is being observed.

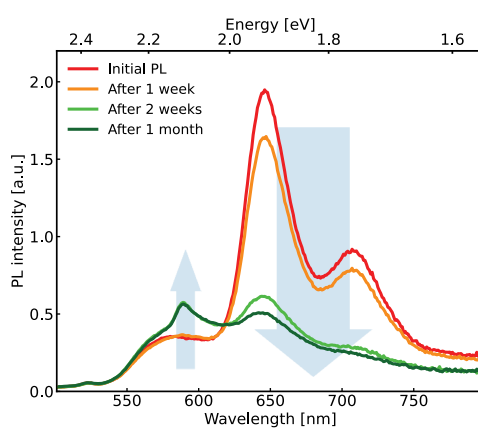


Figure 2.4 | Evolution over time of the photoluminescence of $(T)C_{96}(C_{12}H_{25})_6$ in 1,2,4-trichlorobenzene.²⁰²

In a second publication, for a deeper understanding of the photophysics, $(T)C_{96}(C_{12}H_{25})_6$ was examined at cryogenic temperatures.²⁰³ Low temperatures lead to a significant narrowing of the emission, resulting in high-resolution details. The

vibronic coupling to the 0-0 zero phonon line can be clearly distinguished (**Figure 2.5**). For instance, the lines at 1362 cm^{-1} and 1676 cm^{-1} are characteristic of the C=C stretching in polycyclic aromatic hydrocarbons (PAHs). The vibrations at lower energies are vibrations delocalized in the entire structure of the molecule and are dependent on its size and symmetry. These constitute the vibronic fingerprint of the GQD.

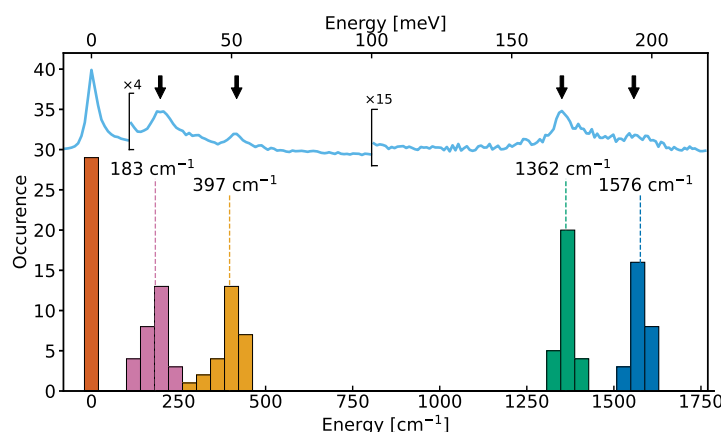


Figure 2.5 | Photoluminescence spectrum of $(\text{T})\text{C}_{96}(\text{C}_{12}\text{H}_{25})_6$ at 7K. On top, a typical spectrum of a single GQD. Below, histograms of the vibronic replicas for different single GQDs.²⁰³

In these further optical studies, combining experimental and theoretical descriptions, it was possible to appreciate the effect of symmetry. For instance, the C_3 symmetry of $(\text{T})\text{C}_{96}(\text{C}_{12}\text{H}_{25})_6$ is responsible for two states as dark. However, molecular vibrations can break the symmetry and brighten a dark state. At low temperatures, the nanoparticle exhibits a vibronic fingerprint. To further explore the effect of symmetry and size on the optical properties, we decided to synthesize C_{2h} rod-shaped nanoparticles.

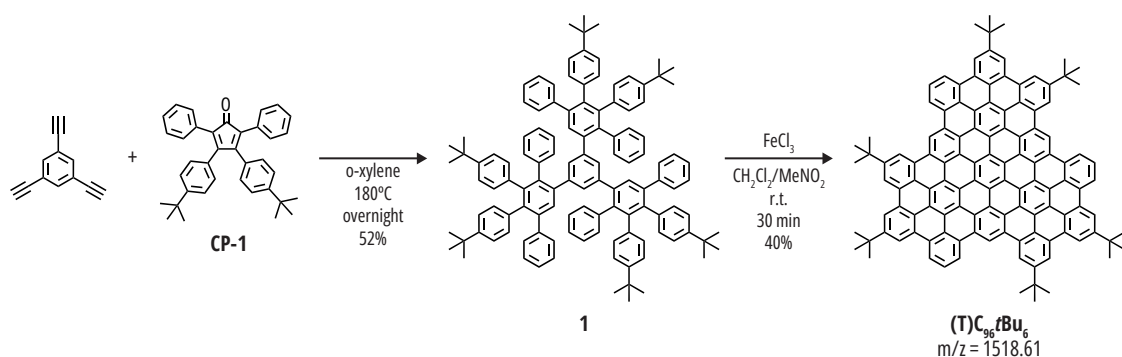
2.2 A CHANGE IN FUNCTIONAL GROUPS

Before discussing the synthesis, properties, and applications of the rod-shaped family, it would be beneficial to discuss the steps that led us to the design of the $\text{C}_{96}\text{tBu}_8$ structure. We were initially interested in altering the functional groups in the previously presented triangular $(\text{T})\text{C}_{96}(\text{C}_{12}\text{H}_{25})_6$ GQD. As a result, we synthesized the analogue *tert*-butylated precursor, $(\text{T})\text{C}_{96}\text{tBu}_6$. We then aimed to explore how a change in symmetry would impact the properties of a nanoparticle containing 96 sp^2 carbon atoms, while maintaining the *tert*-butyl group. Consequently, we aimed for the synthesis of a rod-shaped nanoparticle, $\text{C}_{96}\text{tBu}_4$. In this section, we will discuss the successes and challenges encountered in the synthesis of these two structures.

2.2.1 SYNTHESIS AND STUDIES OF THE TRIANGULAR C_{96} GQD

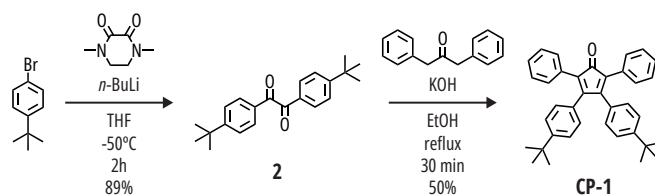
SYNTHESIS

The synthetic strategy of $(\text{T})\text{C}_{96}\text{tBu}_6$ was first described by Iyer *et al.*⁶⁹ The first step consists of the Diels-Alder reaction between the commercially available 1,3,5-triethynylbenzene and 3,4-bis(4-(*tert*-butyl)phenyl)-2,5-diphenylcyclopenta-2,4-dien-1-one **CP-1** to obtain the polyphenylene dendrimer **1**. The dendrimer is then oxidized with anhydrous iron(III) chloride to yield the cyclodehydrogenated nanoparticle $(\text{T})\text{C}_{96}\text{tBu}_6$ (**Scheme 2.1**).



Scheme 2.1 | Synthetic route to **(T)C₉₆tBu₆**.

The disubstituted *tert*-butyl cyclopentadienone **CP-1** was synthesized according to literature protocols as depicted in **Scheme 2.2**.^{69,204–206} The 1,2-bis(4-(*tert*-butyl)phenyl)ethane-1,2-dione **2** is obtained by the lithiation of the commercially available 1-bromo-4-*tert*-butylbenzene in the presence of *n*-butyllithium, followed by the addition to 1,4-diternethylpiperazine-2,3-dione. The disubstituted dione **2** is then reacted with the commercially available 1,3-diphenylacetone in a Knoevenagel condensation to yield **CP-1**.



Scheme 2.2 | Synthetic route to the cyclopentadienone **CP-1**.

As depicted in **Scheme 2.1**, the oxidation of the polyphenylene dendrimer into **(T)C₉₆tBu₆** was achieved using iron(III) chloride as oxidant. Complete fusion of the GQD was observed in thirty minutes in the presence of five equivalents of oxidant per C-C bond. We noticed that our reaction was completed more quickly than the three hours reported in the literature. Moreover, complete oxidation of **(T)C₉₆tBu₆** proceeds significantly faster than its alkyl chain analogue **(T)C₉₆(C₁₂H₂₅)₆**, which requires over seven hours. We attribute this enhanced reactivity to the electron-donating character of the *tert*-butyl substituents.²⁰⁰

Due to the low solubility of GQDs, the reaction completion is primarily characterized by MALDI-ToF mass spectrometry. The mass spectrum of the crude product is presented in **Figure 2.6a**. It is possible to notice peaks corresponding to the presence of incompletely oxidized and chlorinated side-products, along with the desired GQD. The strong nature of the oxidant employed in the Scholl reaction makes the presence of side products inevitable. Hence, it is imperative to perform a purification step to isolate the target GQD from the rest of the impurities.

(T)C₉₆tBu₆ is insoluble in common organic solvents, and our attempts to perform column chromatography or size exclusion chromatography did not result in any nanoparticle migration. Therefore, we proceeded with a washing step of the powder in an attempt to reduce the presence of the soluble impurities. For this, the powder obtained after the Scholl reaction was dispersed in a small amount of dichloromethane. The dispersion was sonicated for thirty minutes to give a dark orange solution which was allowed to rest for 48 hours. The solution was then ultracentrifuged for thirty minutes at 100 000 g. The pellet was recovered and analysed by MALDI-ToF (**Figure 2.6b-d**). We notice that this purification step efficiently removes a good number of impurities. Additionally, in the spectrum, two main peaks at $m/z = 1518$ and $m/z = 3038$ can be distinguished. The first peak can be attributed to the monomer and the latter to a dimeric species. We hypothesize that the dimeric species forms through

a slight offset rotation of two GQDs, to minimize the steric hindrance between the *tert*-butyl groups, around the axis perpendicular to the stacking plane (**Figure 2.6e**) A similar behaviour was described by Zhao *et al.* in an analogous mesityl-substituted C₉₆ triangular nanoparticle.⁹⁰

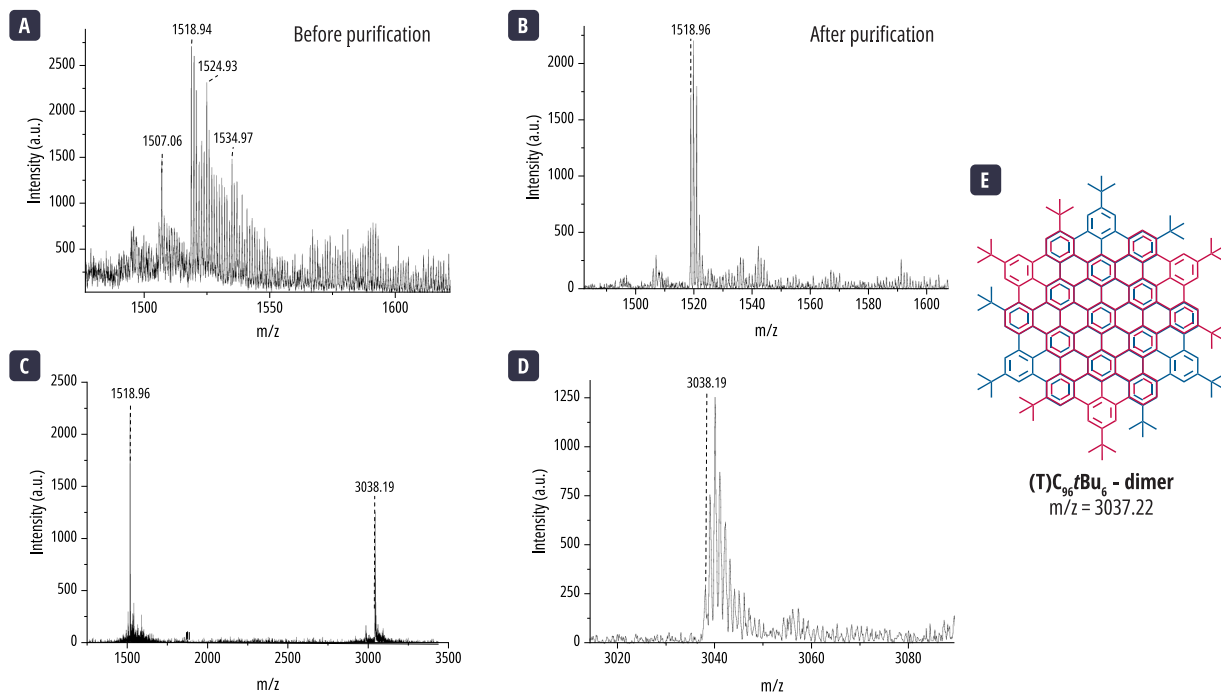


Figure 2.6 | Characterization of the oxidation step of (T)C₉₆tBu₆. **(a)** MALDI-ToF spectrum of the reaction crude of the Scholl oxidation in the presence of 5 equivalents of FeCl₃ for 30 minutes. **(b)** MALDI-ToF spectrum after a purification step. **(c)** Full spectrum after purification showing two main peaks. **(d)** Zoom in on the dimer region. **(e)** Proposed interactions between two (T)C₉₆tBu₆ nanoparticles.

The optical studies of (T)C₉₆tBu₆ were performed in 1,2,4-trichlorobenzene (TCB) and are presented in **Figure 2.7a**. This solvent was also used for the optical studies performed on (T)C₉₆(C₁₂H₂₅)₆. In the absorption spectrum, it is possible to distinguish a main peak at 473 nm and a small shoulder at 530 nm. The emission spectrum shows five distinguishable emission bands at 510, 564, 595, 645, and 700 nm. Taking the theoretical and optical studies performed on (T)C₉₆(C₁₂H₂₅)₆ as point of reference, the peaks at 645 and 700 nm can be attributed to the emission of the monomer. The emission bands at higher energies likely originate from emissive impurities or result from further aggregation of the nanoparticles. Compared to the alkyl chain substituted analogue, (T)C₉₆tBu₆ exhibits narrower absorption bands, while the emission spectrum in solution remains very similar for both nanoparticles. This can be appreciated in **Figure 2.7b**.

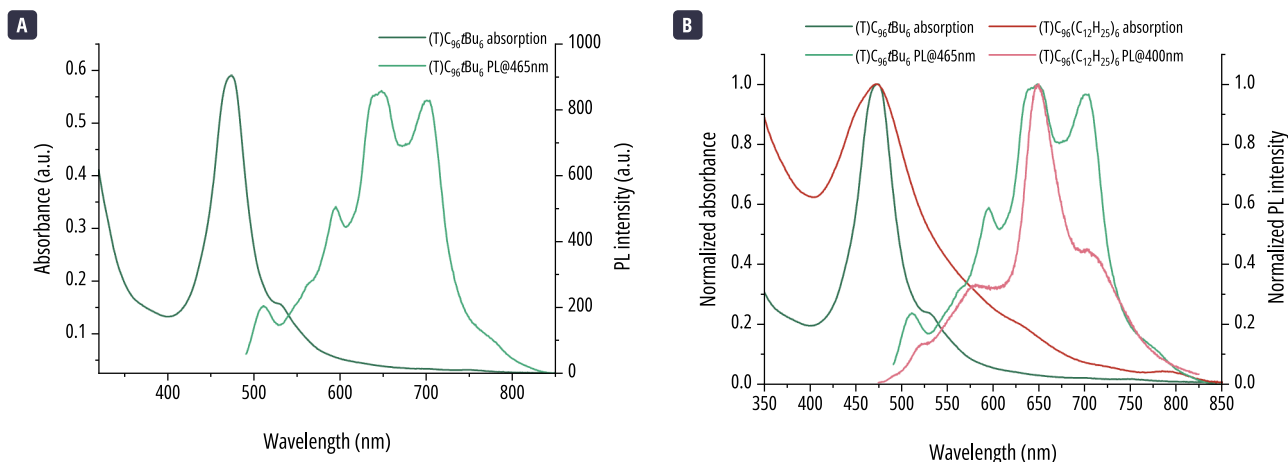
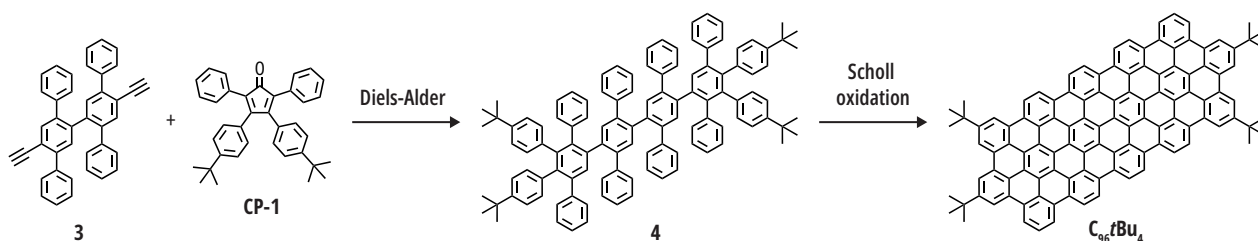


Figure 2.7 | (a) Absorption and emission spectra of (T) $C_{96}tBu_6$ in 1,2,4-trichlorobenzene. (b) Comparison of the absorption and the emission of (T) $C_{96}(C_{12}H_{25})_6$.

The synthesis and optical analysis of (T) $C_{96}tBu_6$ provided important insights to be considered for future GQD syntheses. Firstly, the introduction of *tert*-butyl groups increased the reactivity towards the Scholl reaction. Additionally, these bulky functional groups appear to partially decrease π -stacking interactions. As a result, we were able to obtain sharper and more resolved absorption lines than in the case of unsubstituted or alkyl chain substituted triangular GQDs. Finally, although the solubility of (T) $C_{96}tBu_6$ was not optimal for traditional organic chemistry purification techniques, we developed a purification protocol relying on the difference in solubility between the chlorinated and partially fused derivatives and the target GQD.

2.2.2 SYNTHESIS OF A FIRST ROD-SHAPED C_{96} GQD

To pursue our main goal, a better understanding of the structure and optical properties relationship, we next decided to synthesize a rod-shaped $C_{96}tBu_4$ GQD. This nanoparticle would also contain 96 sp^2 carbon atoms as the triangular GQD, but arranged in an elongated shape along a main axis. We would incorporate four *tert*-butyl functional groups at the extremities of the GQDs. Its synthesis consisted in taking a diterphenyl alkyne substituted core **3** and reacting it with the *tert*-butyl substituted tetraphenylcyclopentadienone **CP-1** to obtain the corresponding polyphenylene dendrimer **4**. Finally, the target GQD would be obtained after the Scholl oxidation and carbon-carbon bond formation on **4** (Scheme 2.3). The alkyne core will be responsible for giving the shape to the final quantum dot, while the cyclopentadienone incorporates the desired functional groups to the structure to increase the solubility.

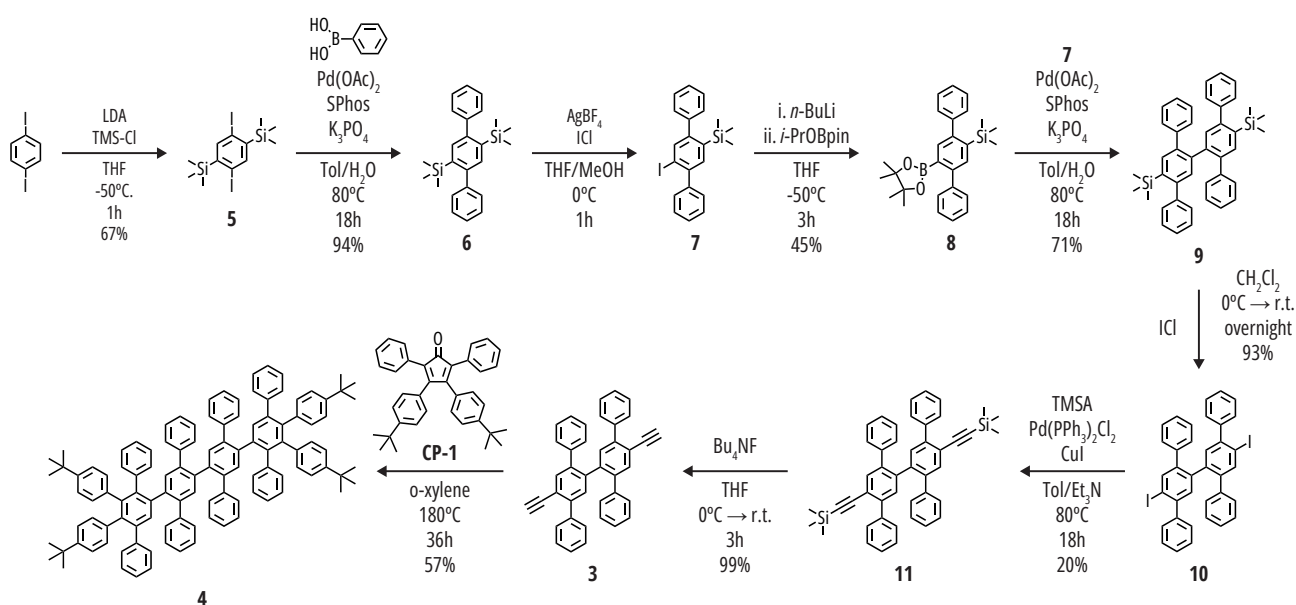


Scheme 2.3 | General view of the synthetic strategy to $C_{96}tBu_4$.

CORE AND DENDRIMER SYNTHESIS

An important step to acquire the desired nanoparticle is the synthesis of the corresponding polyphenylene dendrimer. As mentioned before, it is obtained after the Diels-Alder reaction between an alkyne core and a cyclopentadienone. The corresponding alkyne core **3** is not commercially available, as was the case for the triangular-shaped nanoparticles previously

presented, so we need to synthesize the molecule. The synthesis of **4** is based on previously defined syntheses designed in the PhD work of Dr. Julien Lavie for unsubstituted GQDs.^{80,207} The general procedure is summarized in **Scheme 2.4**. The terphenyl synthesis begins with the silylation of the commercially available 1,4-diiodobenzene to yield 1,4-diiodo-2,5-bis(trimethylsilyl)benzene **5**. Through a Suzuki-Miyaura coupling between compound **5** and phenylboronic acid, we obtain the bistrimethylsilyl-terphenyl **6**. To achieve an iododesilylation, compound **6** is reacted with iodine monochloride in the presence of a silver salt. This silver salt helps to precipitate residual halogen atoms and prevent further iodination, along with low equivalents of iodine monochloride, to ensure the formation of monoiodinated terphenyl derivative **7**.²⁰⁸ Subsequent lithiation and borylation with 2-Isopropoxy-4,4,5,5-tetramethyl-1,3,2-dioxaborolane (*i*-PrOBpin) of **7**, afforded the monosilyl terphenyl boronic ester **8**. The Suzuki-Miyaura coupling between compounds **7** and **8** afforded the bistrimethylsilyl-diterphenyl **9**. Iododesilylation of **9** was achieved with iodine monochloride to give the diiodo-diterphenyl derivative **10**. To form the diterphenyl-diethynyl-trimethylsilane **11**, compound **10** was reacted with trimethylsilylacetylene (TMSA) in Sonogashira conditions. Finally, the diterphenyl-alkyne core **3** was achieved upon removal of the trimethylsilyl group in compound **11** under the presence of tetrabutylammonium fluoride. With the diterphenyl-alkyne core and the tetraphenylcyclopentadienone we proceeded to the Diels-Alder reaction to obtain the polyphenylene dendrimer **4**. The structure of the dendrimer was confirmed by MALDI-ToF spectrometry and ¹H and ¹³C NMR spectroscopy.

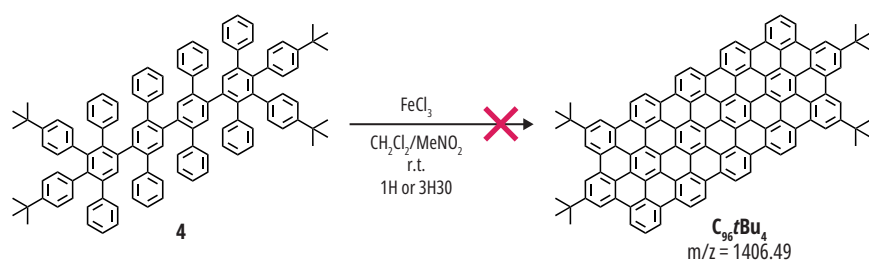


Scheme 2.4 | Synthetic route to dendrimer **4**.

SCHOLL OXIDATION

Once we have the polyphenylene dendrimer, we can then proceed to form **C₉₆tBu₄** under the conditions shown in **Scheme 2.5**. We used iron(II) chloride as oxidant, dissolved in nitromethane. For our first oxidation attempt, we used similar conditions as for **(T)C₉₆tBu₆**, 6.6 equivalent of oxidant per carbon-carbon bond created in this step for one hour at room temperature. After precipitation in an excess of methanol and filtration through a PTFE filter, a dark orange powder was recovered. This powder did not exhibit high solubility in common organic solvents, MALDI-ToF mass spectrometry analysis was performed using a TCNQ matrix. The mass spectrum exhibits a main peak at $m/z = 1414.81$. We can vaguely distinguish a peak around $m/z = 1406.49$, the expected exact mass for the target GQD **C₉₆tBu₄** (**Figure 2.8**). Because of the low solubility of the nanoparticle, we cannot confirm the structure of the species at the origin of the main peak. Nevertheless, the mass difference

with the target structure is of eight units likely to come from eight protons or four C-C bonds not formed. Following the principle of parsimony, we hypothesize that the unformed bonds are located at the molecule's centre, to preserve a symmetric entity, yielding a butterfly-like configuration. Besides, we can easily imagine a π -interaction between two phenyl rings from each "wing" of the butterfly structure due to the rotation of the middle C-C bond. This interaction may stabilize the structure and prevent further oxidation. To force the oxidation, we decided to increase the reaction time to 3 hours and a half, nonetheless these conditions did not yield the desired structure, again the main peaked remained $m/z = 1414.54$. This result seems to be aligned with the hypothesis that the species at the origin of this mass peak is stabilized and is less reactive, as in the proposed butterfly structure. To validate this hypothesis, further work involving this intermediate's purification and characterization via NMR or single crystal X-ray diffraction (XRD) is needed. However, the low solubility of the intermediate represents a significant challenge.



Scheme 2.5 | Scholl oxidation of dendrimer **4** into $C_{96}tBu_4$.

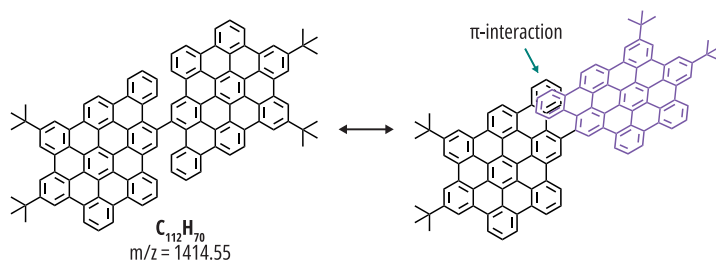
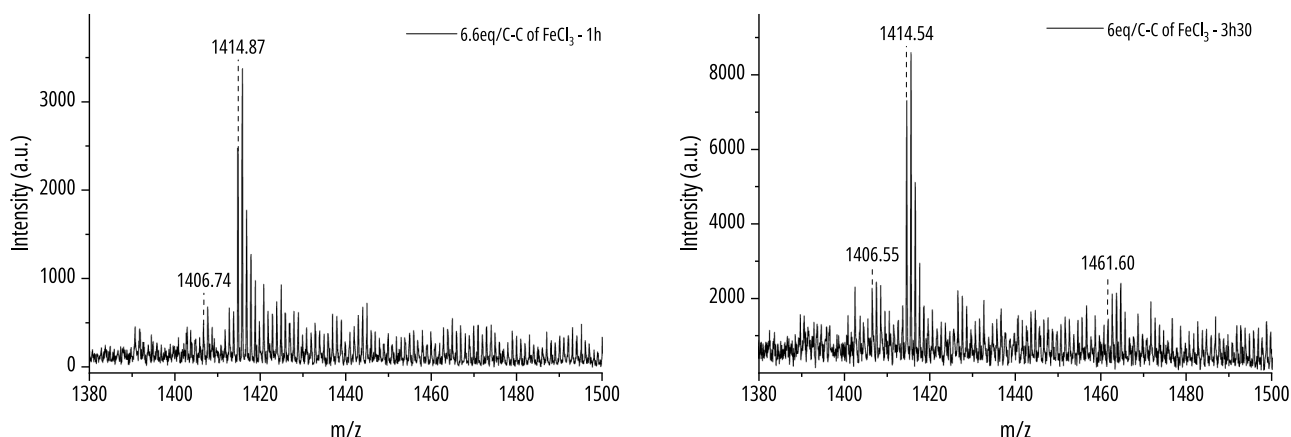
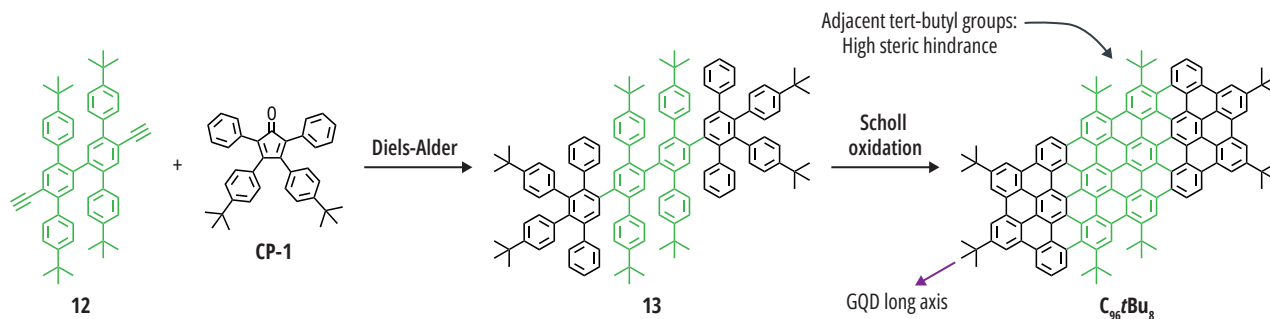


Figure 2.8 | MALDI-ToF mass spectra of reaction crude of the synthesis of $C_{96}tBu_4$. Left, with 6.6 eq of $FeCl_3$ during 1 h. Right, with 6.6 equivalents of $FeCl_3$ during 3h30. Below, proposed butterfly-like incomplete structure.

2.3 SYNTHESIS AND OPTICAL STUDIES OF $C_{96}tBu_8$

The initial synthesis of a *tert*-butyl substituted, elongated GQD was unsuccessful, possibly due to the formation of a stabilized butterfly-like intermediate. To prevent this, the approach was modified to add four *tert*-butyl groups along the GQD's long axis. This additional steric hindrance along the axis of the nanoparticle may diminish the π - π interaction between opposite central phenyls during the carbon-carbon bond formation and prevent the stabilization of the butterfly-like intermediate.

However, this adjustment also introduces an additional risk as the increased steric congestion at the middle of the GQD could obstruct the carbon-carbon bond formation between the adjacent phenyls. This issue was highlighted by Arslan *et al.*, who reported the synthesis a similarly hindered hexa-*peri*-benzocoronene derivate where complete fusion could not be observed.²⁰⁹ Nevertheless, the increased reactivity we had observed so far for *tert*-butyl substituted derivatives, encouraged us pursue the synthesis of the rod-shape **C₉₆tBu₈** through an analogous synthetic pathway to **C₉₆tBu₄**, presented in **Scheme 2.6**.



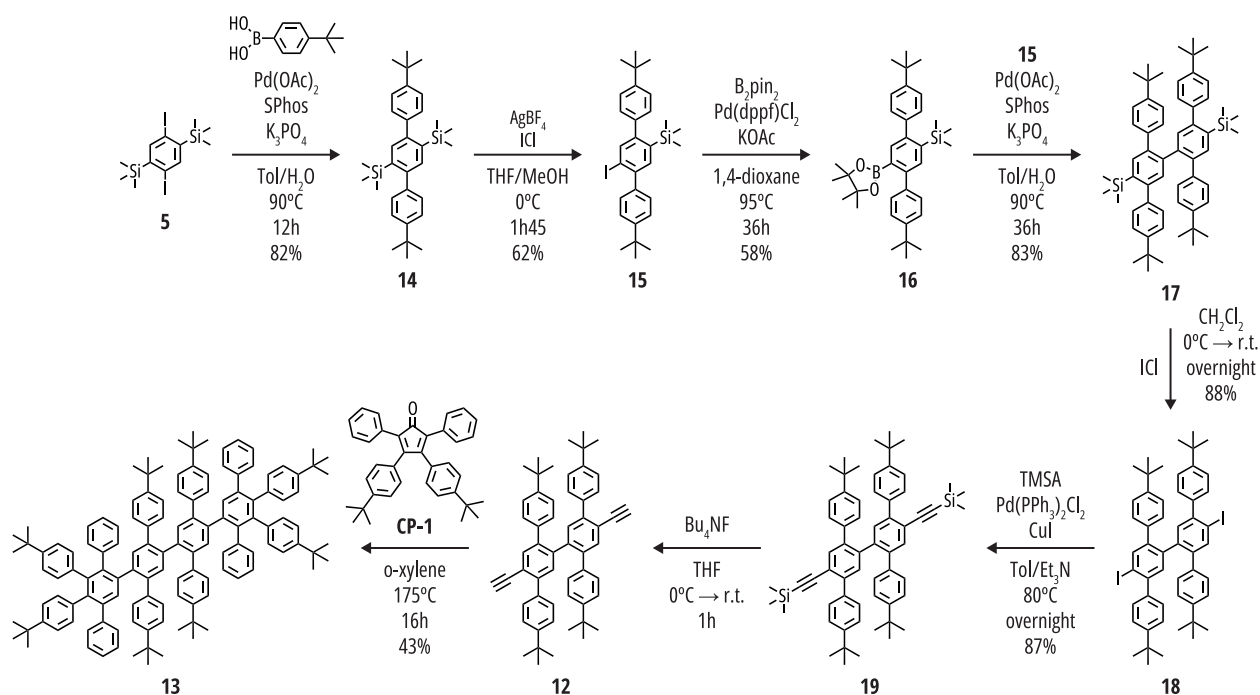
Scheme 2.6 | General synthetic strategy to **C₉₆tBu₈**.

2.3.1 SYNTHESIS

DENDRIMER SYNTHESIS

The synthesis of octa-*tert*-butyl substituted dendrimer **13** follows an analogous approach as the dendrimer **4**. The complete reaction scheme is given in **Scheme 2.7**. The substituents along the molecule's axis are introduced through the diterphenyl alkyne core **12**. The process starts with compound **5** and 4-*tert*-butylphenylboronic acid reacting through a Suzuki-Miyaura coupling to produce the di-*tert*-butyl terphenyl bistrimethylsilane **14**. Compound **14** undergoes iododesilylation using 0.9 equivalents of iodine monochloride and a silver salt to afford the monoiodinated derivate **15**. The borylation of **15** is achieved through palladium catalysed Miyaura conditions, resulting in the monoborylated compound **16**. The lithiation and addition conditions employed for the synthesis of the un-*tert*-butylated terphenyl analogue, resulted in low yields and a significant amount of the hydrogenated derivate. Better yields were achieved through Miyaura borylation conditions. However, these yields remain heavily dependent on the conditions employed. For instance, low reaction times do not allow for total conversion of the monoiodinated precursor. Inversely, high reaction times promote the ester hydrolysis and the protodeboration reaction. To avoid these parasitic reactions, we remove as many water traces as possible. To maintain a dry environment, reactant powders are stored and weighed in a glove box, dried under gentle heating overnight, and the reaction is carried out in a sealed Schlenk reactor.

The Suzuki-Miyaura coupling of the iodinated precursor **15** and the borylated terphenyl **16** in the presence of palladium(II) acetate affords the diterphenyl bistrimethylsilane **17**. Iododesilylation of **17** using iodine monochloride gives the diiodo-diterphenyl derivate **18**. The trimethylsilane protected alkyne functions are added to compound **18** through a Sonogashira coupling with trimethylsilylacetylene, resulting in derivate **19**. The *tert*-butyl substituted diterphenyl alkyne core **12** was achieved upon removal of the trimethylsilane group under the presence of tetrabutylammonium fluoride. Finally, the polyphenylene dendrimer **13** is obtained through the Diels-Alder reaction of core **12** and the *tert*-butyl substituted tetraphenylcyclopentadienone **CP-1**.



Scheme 2.7 | Synthetic route to dendrimer **13**.

MALDI-ToF spectrometry, ^1H , and ^{13}C NMR spectroscopy confirm the dendrimer structure. In the ^1H NMR spectra we can distinguish characteristic signals of the target structure (**Figure 2.9**). First, we can discern four signals in the aliphatic region, integrating each for eighteen protons, each attributed to two symmetrically equivalent *tert*-butyl groups. We can also distinguish three singlets corresponding to central protons in the dendrimer at high chemical shifts. The remaining aromatic signals are superimposed in the 6.45-7.50 ppm region.

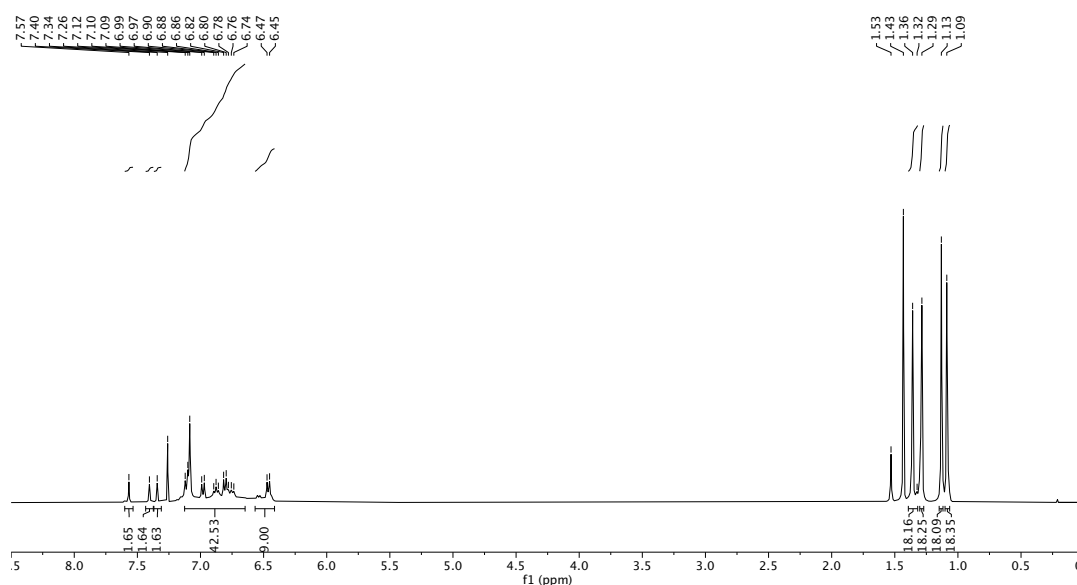
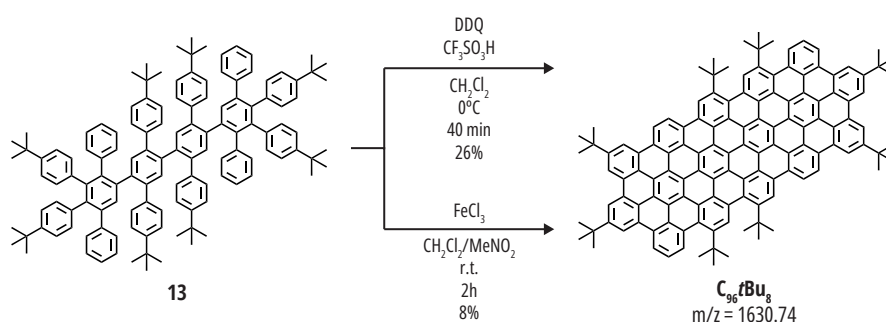


Figure 2.9 | ^1H NMR spectrum of dendrimer **13** (400Mz, CDCl_3 , 298K).

SCHOLL OXIDATION

The octa-*tert*-butyl substituted elongated dendrimer **13** was subjected to the carbon-carbon bond formation process to produce the desired rod-shaped GQD $\text{C}_{96}\text{tBu}_8$. The reaction summary is given in **Scheme 2.8**. The Scholl oxidation was first conducted using iron(III) chloride as oxidant. The advancement of the reaction was monitored by MALDI-ToF mass spectrometry.

Complete fusion of the nanoparticle was observed after two hours using 9 equivalents of oxidant per C-C bond formed at room temperature. The GQDs formation was confirmed by MALDI-ToF mass spectrometry, which is given in **Figure 2.10a**. The mass spectrum shows the presence of the fully cyclodehydrogenated product M^+ along with some impurities. Although we could not identify all the additional peaks, we could distinguish a monochlorinated (M^+-Cl) and a hydroxylated (M^+-OH) byproducts. Despite the presence of side products, obtaining the desired nanoparticle was a major success considering the steric hindrance caused by the adjacent central *tert*-butyl groups. We attribute this to an increased reactivity of the dendrimer towards the Scholl oxidation, likely caused by the electron-donating character of the substituents. These functional groups also have a beneficial effect on the solubility of the GQD. As we will elaborate, these adjacent *tert*-butyl groups play an important role by adding steric hindrance around the structure and slightly twisting the nanoparticle. This greatly reduces the π - π interaction between GQDs, subsequently improving its solubility. Note that dendrimer **13** can also be converted into GQD **C₉₆tBu₈** using 2,3-dichloro-5,6-dicyano-1,4-benzoquinone (DDQ) in the presence of triflic acid (see next page).



Scheme 2.8 | Scholl oxidation of dendrimer **13** into GQD **C₉₆tBu₈**.

The enhanced solubility of the synthesized GQD permits greater processability and allows the use of traditional organic chemistry purification methods such as column chromatography or size exclusion chromatography, which were not possible with previous GQDs (**Figure 2.10b**). For optimal purification, we conduct an initial washing step. The crude oxidation reaction mixture is precipitated in an excess of methanol, yielding a dark green dispersion which is then filtered through teflon to produce a dark green powder. This precipitate is dissolved in a small amount of freshly distilled THF, sonicated for 2 minutes and left to settle overnight before performing an ultra-centrifugation step at 130 000 g for 30 minutes. The pellet is recovered and a size exclusion chromatography using Bio-beads S-X3 is performed to separate impurities from the desired product. These impurities have a shorter elution path and emerge in early fractions of the column. The desired product is recovered as a bright red solution and dried as a dark green powder with a reddish metallic appearance upon light exposure. Despite the extensive purification, the mass spectra still showed minor peaks of the hydroxylated side products. However, this impurity may more easily ionize due to heteroatoms and be only present in trace quantities. Comparison of mass spectra before and after purification demonstrates the effectiveness of the purification steps.

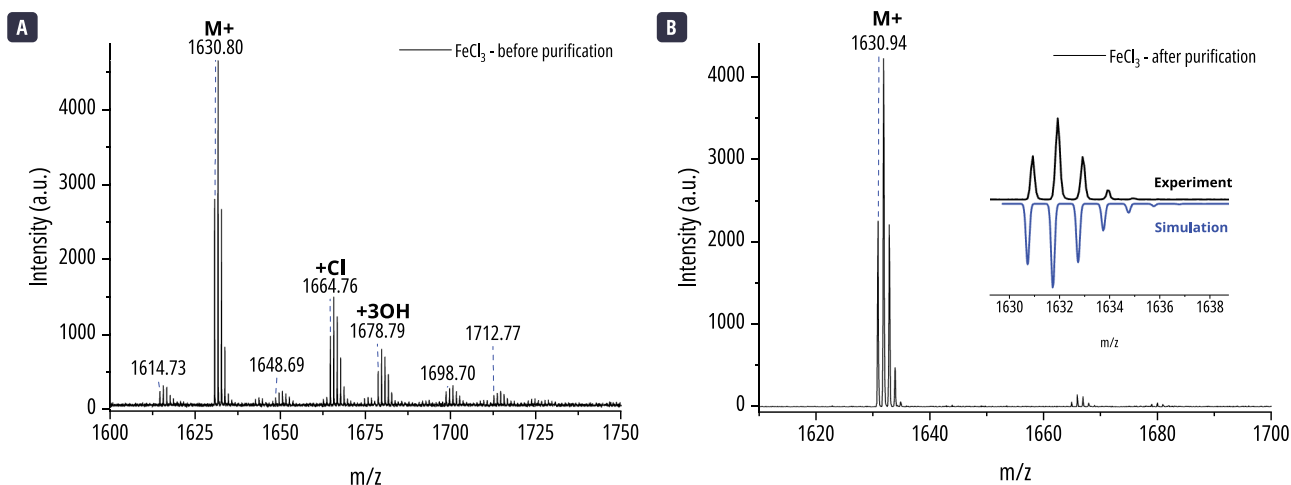


Figure 2.10 | MALDI-ToF mass spectra of the oxidation of **C₉₆tBu₈** with FeCl₃. **(a)** Before purification. We can distinguish multiple peaks corresponding to impurities. **(b)** After purification. A much cleaner mass spectrum is obtained but some peaks corresponding to impurities can still be distinguished. The insert compares the isotopic pattern of the M⁺ peak with a theoretical distribution.

Alternatively, the purification efficiency can be followed by fluorescence spectroscopy. We will later be interested to the detailed description of the optical properties of the GQD, for now, let's just focus on the differences on photoluminescence spectra before and after purification given in **Figure 2.11**. The difference is mainly noticeable at shorter wavelengths. The emission at these wavelengths has previously been associated to the emission of impurities and aggregates.²⁰² The disappearance of these emission bands can be used to control efficiency of the purification process.

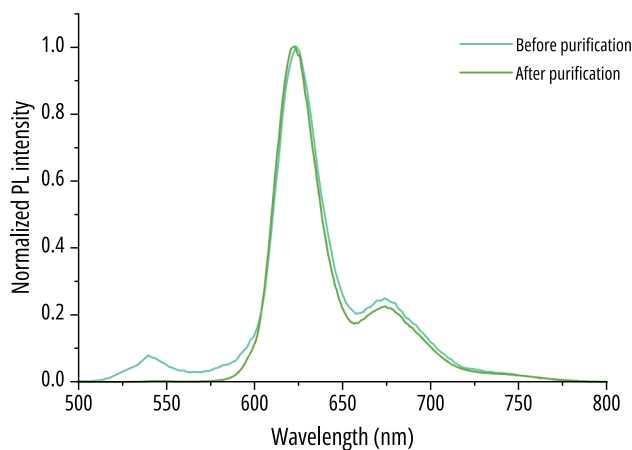


Figure 2.11 | Photoluminescence spectrum of **C₉₆tBu₆** before and after purification. Excitation wavelength @470 nm in TCB.

The overall reaction yield of the oxidation reaction was a low 8%, which was obtained after a thorough purification. Some product is lost during the washing step. Additionally, some nanoparticle is lost during the size exclusion chromatography, where some fractions had to be discarded due to overlapping elution of the product and certain impurities (note that the products discarded during the purification steps can be recycled). To increase the reaction yield and facilitate the purification step, milder oxidation conditions were explored. We opted for 2,3-dichloro-5,6-dicyano-1,4-benzoquinone (DDQ), a mild double-electron oxidant, in the presence of a small amount of trifluoromethanesulfonic acid (triflic acid).²¹⁰ To prevent oxidant degradation, the oxidation is carried out in dry dichloromethane at 0°C. In addition, only small amounts of triflic acid are used, which also limits the nanoparticle's decay. For optimal results, the acid is slowly added to a cooled-down solution of the polyphenylene dendrimer and DDQ. For **C₉₆tBu₈**, complete carbon-carbon bond formation was observed after one hour in a diluted dendrimer solution containing 2% v/v of triflic acid and 1.8 equivalents of DDQ per carbon-carbon bond.

A comparison of the mass spectra from the crude reaction mixture using FeCl_3 and DDQ reveals that the latter provides a cleaner reaction with fewer undesired side products, as shown in **Figure 2.12a**. This indicates that DDQ is a more suitable oxidant for this reaction. Furthermore, the purification process is facilitated when using the DDQ protocol. In fact, repeating the precipitation process twice is sufficient to yield a highly pure product, as evidenced by the MALDI-ToF mass spectrum in **Figure 2.12b**, and the fluorescence spectrum and NMR spectra, which we will discuss in the next sections. The cleaner protocol using DDQ, and more straightforward purification process, allowed us to increase the reaction yield of highly pure GQD up to 27%. It is important to highlight that a significant number of nanoparticles remained solubilized during the precipitation step, reducing the overall yield. These nanoparticles can be recovered from the supernatant through precipitation in methanol and a repurification as described above.

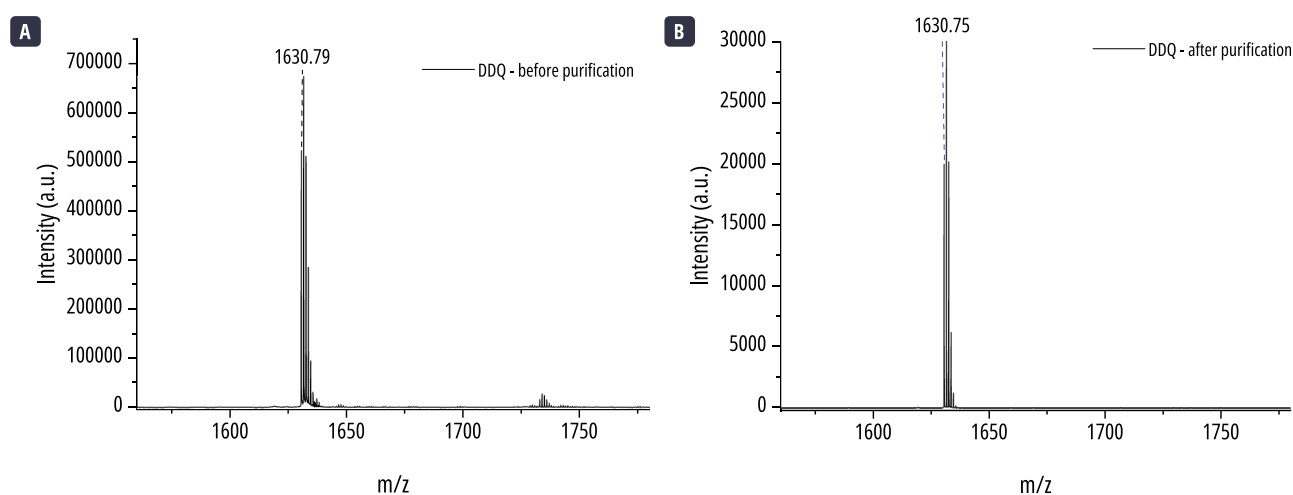


Figure 2.12 | MALDI-ToF mass spectra of the oxidation of $\text{C}_{96}\text{tBu}_8$ with DDQ. **(a)** Before purification. We can distinguish a few peaks corresponding to impurities. **(b)** After purification.

2.3.2 CHARACTERIZATION

The enhanced solubility of $\text{C}_{96}\text{tBu}_8$ allowed us to implement an efficient purification protocol and opened the door to in-depth chemical characterizations. In this section we will first present NMR studies performed on the GQD to verify its structure, followed by electrochemical characterization. Finally, we will shine some light on theoretical studies of the aggregation process of the nanoparticle, to better understand the origin of the nanoparticle's high solubility.

NUCLEAR MAGNETIC RESONANCE SPECTROSCOPY

Traditionally, due to the poor solubility of large polycyclic aromatic hydrocarbons, mass spectrometry is the primary technique employed to confirm the formation of the desired nanoparticle and to assess its purity. However, this technique is merely qualitative and cannot definitively verify a chemical structure. There are very few NMR characterizations of bottom-up synthesized graphene nanoparticles bigger than 78 sp^2 carbon atoms. In some cases, the structure could be confirmed by single-crystal XRD structure. Thanks to the high solubility of our $\text{C}_{96}\text{tBu}_8$, we could perform ^1H , ^1H - ^1H , and ^1H - ^{13}C NMR experiments, thereby unambiguously attributing the proton signals to the desired structure.

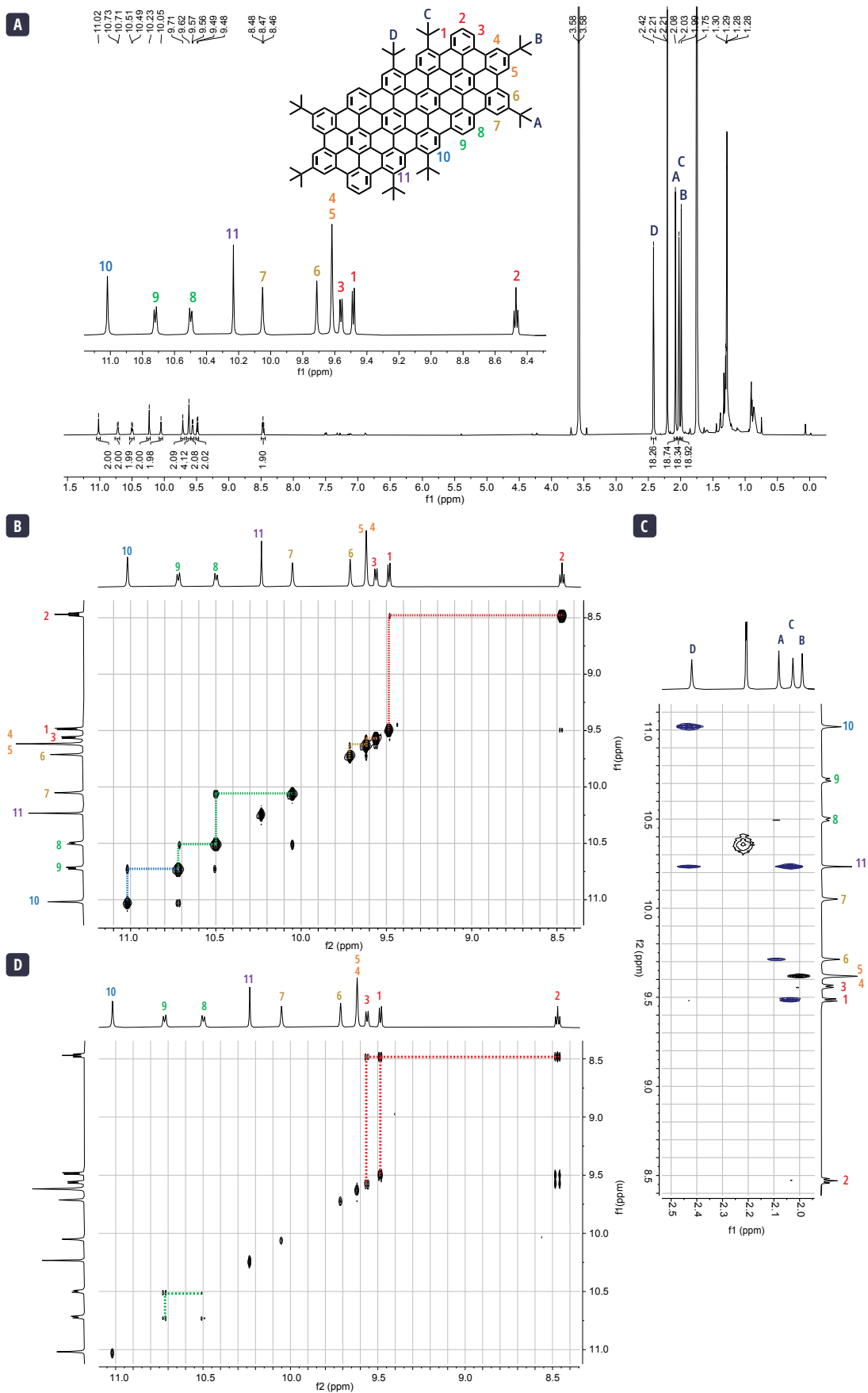


Figure 2.13 | NMR spectra of $C_{96}tBu_8$ (600 Mz, THF- d_8 + CS_2 , 298K). **(a)** 1H NMR spectrum and attribution of peaks to the $C_{96}tBu_8$ structure. **(b)** 1H - 1H NOESY spectrum in the aromatic region with dotted lines showing the correlation interactions between protons. **(c)** 1H - 1H NOESY spectrum in the aliphatic-aromatic region with dotted lines showing the correlation interactions between protons. **(d)** 1H - 1H COSY spectra with dotted lines showing the correlation interactions between protons.

The NMR experiments were performed in a 600 MHz Brücker spectrometer at concentrations of $5 \cdot 10^{-4}$, using a 2:3 ratio mixture of deuterated tetrahydrofuran (THF- d_8) and carbon disulfide as solvent. Carbon disulfide has very good solvating properties for large aromatic molecules. However, given its high toxicity and flammability, extreme caution was exercised. All experiments involving CS_2 were carried out in gas-tight NMR tubes. First, to prevent any release of vapours into the NMR room and prevent health hazards. Additionally, using air-tight tubes also prevents the evaporation of carbon disulfide due to its low boiling point and high volatility. Evaporation of the solvents could lead to the aggregation or precipitation of the nanoparticles between experiments.

In the 1H NMR spectrum of **C₉₆tBu₈**, we observe well-resolved aromatic signals between 8.4 and 11 ppm. We can distinguish five singlets, four doublets and one triplet within this region. The integral sum of these aromatic signals corresponds to the expected twenty-two protons. The triplet at 8.47 ppm can be easily attributed to the only proton, labelled as 2, having two other immediate proton neighbours. The cross-peaks of triplet 2 with doublets at 9.48 and 9.56 ppm in the 1H - 1H correlation spectroscopy (COSY) NMR spectrum, allowed us to identify the three-proton system with a coupling constant of 7.2 Hz. The two remaining doublets at 10.72 and 10.50 ppm correspond to protons 9 and 8, constituting the two-proton system with coupling constant of 8.3 Hz. The rest of the aromatic protons do not interact closely with other protons, resulting in singlet multiplicities. In the aliphatic region, we observe several peaks corresponding to the solvent trace, the *tert*-butyl protons, water, and some impurities. We could attribute all the aromatic and aliphatic signals through 1H - 1H Nuclear Overhauser Effect Spectroscopy (NOESY) NMR. The system's simplicity facilitated this process, where each proton only has two neighbours in space, either an aromatic proton or a *tert*-butyl proton. Complete attribution is given in **Figure 2.13a**.

Despite recording more than 133 120 scans, an exploitable ^{13}C NMR spectrum could not be obtained due to the low concentration of the sample and a high number of carbon atoms in the structure. Nonetheless, we performed two-dimensional heteronuclear 1H - ^{13}C NMR spectroscopy techniques, specifically Heteronuclear Single Quantum Coherence (HSQC) and Heteronuclear Multiple Bond Correlation (HMBC) NMR spectroscopies. These methods allowed us to observe the carbon atoms that could benefit from nuclear spin polarization transfer from the much more sensitive hydrogen atoms. In the HSQC NMR spectroscopy (**Figure 2.14a**), we observe the correlation between a proton and the directly linked carbon atom. In the corresponding spectrum, we detect the expected twelve cross-peaks from the aromatic protons and carbons in their respective aromatic regions. Furthermore, we observe the expected four cross-peaks from the *tert*-butyl protons and carbons in their respective aliphatic regions.

HMBC NMR spectroscopy lets us observe the correlation between a proton and a carbon separated by two or three bonds. In the corresponding spectrum (**Figure 2.14b**), the aliphatic protons give us essential information that confirms the structure of the target quantum dot. Each *tert*-butyl proton is correlated with an aliphatic quaternary carbon of the functional group. We observe these cross-peaks at the carbon's aliphatic region. Moreover, we observe a cross-peak of the *tert*-butyl proton with a carbon in the aromatic region, corresponding to the quaternary carbon bearing the functional group. The last proof of the GQD structure are the cross-peaks showing the correlation between the aromatic protons positioned in the same aromatic ring as a *tert*-butyl group and the corresponding quaternary aliphatic carbons of the functional group.

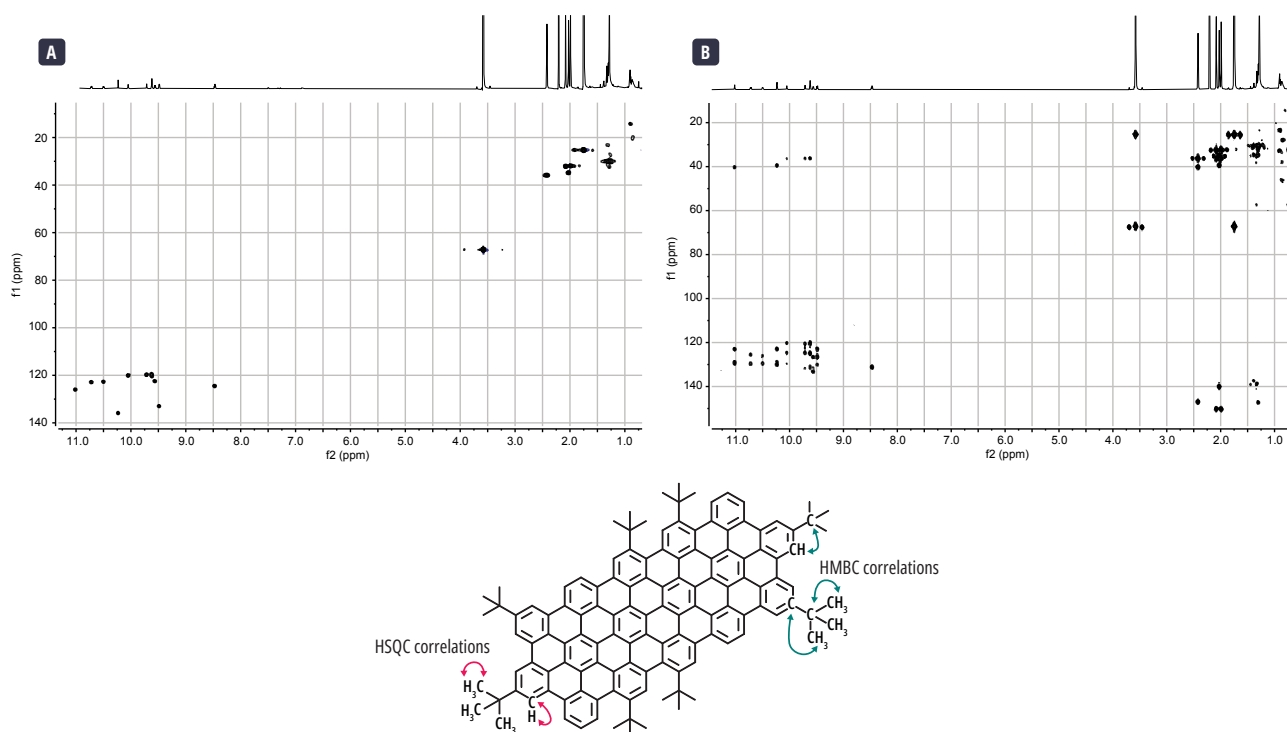


Figure 2.14 | NMR spectra of **C₉₆tBu₈** (600 Mz, THF-*d*₈+CS₂, 298K). **(a)** ¹H-¹³C HSQC spectra. **(b)** ¹H-¹³C HMBC spectra. Below, the main correlations observed in the HSQC NMR spectrum (pink) and in the HMBC NMR spectrum (cyan).

As a closing remark in the analysis of the NMR spectra of **C₉₆tBu₈**, it is important to address the traces of impurities observed in the ¹H NMR spectrum. Indeed, it is possible to distinguish some signals in the region between 6.5 and 7.5 ppm and some aliphatic peaks around 1.29 ppm that were not attributed to the GQD, water, or THF. No correlation between these signals and the ones attributed to **C₉₆tBu₈** was observed in the two-dimensional experiments. But correlations were detected between these impurities' peaks. HMBC spectroscopy showed that the peak at 1.29 ppm exhibits a similar behaviour as the *tert*-butyl groups in the GQD, suggesting that the impurities possess a *tert*-butyl group attached to an aromatic ring. In the ¹H NMR spectrum, we could distinguish some unexpected doublets and doublets of doublets multiplicities, significantly up-field in comparison to the aromatic signals of the target GQD. These observations suggest that, if there is more than one, these impurities come from largely unfused or broken dendrimer-like structures, where doublets of doublets multiplicities could be generated. An alternative explanation to the origin of these impurities might be that they were introduced from external sources during sample handling. The difference observed in the intensities for the impurity's signals between two NMR spectra from a same nanoparticle solution in two different tubes is a first indication that this could be the case. An additional indication is that no impurity signals could be observed for other GQDs structures where the same purification protocol was followed. Even though extreme precautions were taken to prevent any external contamination during sample handling and preparation, given the low concentration at which we perform the NMR experiments, any slight quantity of external impurity will be easily distinguishable. In any case, these signals do not interfere with our signal attribution to the **C₉₆tBu₈** structure. Such deep characterization of large, planar, and individualized GQDs had not yet been reported.

ELECTROCHEMICAL CHARACTERIZATION

The enhanced solubility also allowed us to perform cyclic voltammogram experiments (CV) to investigate the redox behaviour of **C₉₆tBu₈** (**Figure 2.15a**). The voltammogram was recorded under argon atmosphere at room temperature, using a supporting electrolyte of a 0.1 M solution of tetra-*n*-butylammonium hexafluorophosphate in anhydrous 1,2-dichlorobenzene (*o*-

DCB). The three-electrode setup consisted of a platinum working electrode, a platinum counter electrode, and Ag/Ag⁺ reference electrode (10 mM AgNO₃). Experiments were conducted at a scan rate of 100 mV/s in *o*-DCB, as the nanoparticles exhibit good solubility in this solvent. The voltammogram curves were recalibrated using the half-wave potential ($E_{Fc^+/Fc}$) for the ferrocenium/ferrocene couple as an external reference, measured under the same conditions before the GQD measurement.

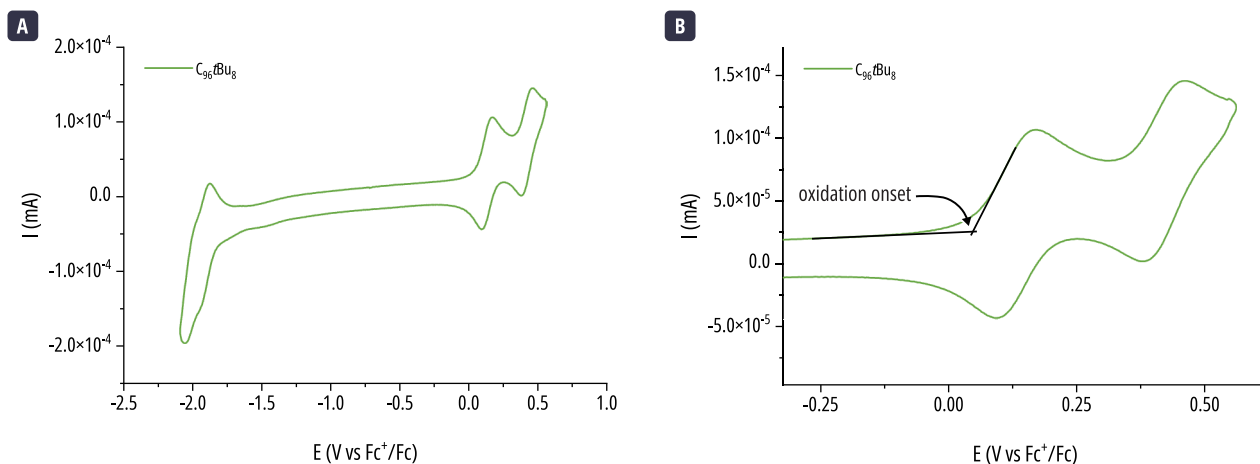


Figure 2.15 | (a) Cyclic voltammogram of **C₉₆tBu₈**. (b) Graphical determination of the oxidation onset of the first oxidation wave.

For the cyclic voltammetry curve of **C₉₆tBu₈**, we can distinguish at positive potentials two reversible oxidation waves with a half-potential of 0.132 and 0.421 V vs. Fc⁺/Fc for the first and second peak, respectively. In contrast, at negative potentials, an irreversible reduction wave is present.

The half wave potentials ($E_{1/2}$) were calculated from the experimental peak anodic potential ($E_{p,a}$) and peak cathodic potential ($E_{p,c}$) using **Equation 2.1**.

$$E_{1/2} = \frac{E_{p,a} + E_{p,c}}{2}$$

Equation 2.1

The CV can also be used to calculate the positioning of the HOMO and LUMO energy levels. To determine the experimental position of the electrochemical highest occupied molecular orbital (HOMO) energy level (E_{HOMO}^{EC}) of **C₉₆tBu₈**, we use the onset potential of the first oxidation wave. The numerical value was calculated using the empirical relation given in **Equation 2.2**.^{211,212}

$$E_{HOMO}^{EC} = -(E_{ox,onset} + 4.8) \text{ eV}$$

Equation 2.2

The positioning of the energy level of the Fc⁺/Fc couple is assumed to be -4.8 eV below vacuum level.²¹³ The oxidation onset potential ($E_{ox,onset}$) was estimated graphically by the intersection point between the tangent of the oxidation wave and the tangent to the baseline current in the voltammogram (**Figure 2.15b**). An approximate estimation of the lowest occupied molecular orbital (LUMO) level (E_{LUMO}^{EC}) was made by using the relationship in **Equation 2.2** with the reduction onset ($E_{red,onset}$) value instead of $E_{ox,onset}$. Finally, the electrochemical bandgap (E_{gap}^{EC}) was determined using **Equation 2.3**. All

these values are summarized in **Table 1**. It is important to note that the reduction wave is not clearly distinguishable and therefore the onset and LUMO values may not be accurate.

$$E_{gap}^{Ec} = E_{LUMO}^{Ec} - E_{HOMO}^{Ec}$$

Equation 2.3

Table 1 | Summary of the electrochemical values measured for **C₉₆tBu₈**. Potential values are reported vs. Fc⁺/Fc.

GQD	E _{1/2, ox1} (V)	E _{1/2, ox2} (V)	E _{ox, onset} (V)	E _{red, onset} (V)	E _{ec, HOMO} (eV)	E _{ec, LUMO} (eV)	E _{ec, gap} (eV)
C ₉₆ tBu ₈	0.132	0.421	0.045	-1.812	-4.85	-2.99	1.86

AGGREGATION OF THE C₉₆ GQD: A THEORETICAL DESCRIPTION

To better understand the aggregation process of **C₉₆tBu₈**, a theoretical study of the interaction between two nanoparticles was performed by Dr. Nicolas Rolland and Prof. David Beljonne from Mons University in Belgium and by Dr. Silvio Osella from Warsaw University in Poland.

Because of the presence of *tert*-butyl groups along the main axis of the nanoparticle, different conformers of **C₉₆tBu₈** can exist. These bulky groups can be positioned, with respect to the molecular plane, either up (U) or down (D). The combination of these configurations results in six possible conformers with varying degrees of distortion in the molecule's aromatic plane, induced by the positions of the functional groups, as can be seen in **Figure 2.16**. Among all these conformers, two are the most stable: UD-UD and UD-DU (see **Table 2**).

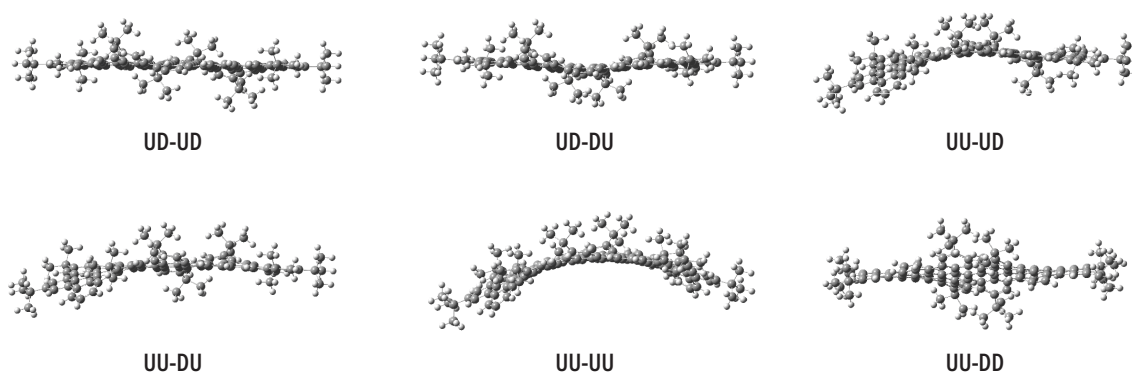


Figure 2.16 | Structures of the six possible conformers of **C₉₆tBu₈**, depending on the position of the central *tert*-butyl groups. U stand for an “up” position with respect to the molecular plane. D stands for a “down” position. The hyphen separates the side along which the *t*-Bu group is positioned with respect to the long axis of the molecule.

Table 2 | Theoretical values of relative energy and relative abundance of the six possible conformers of **C₉₆tBu₈**. The relative energies are reported considering the UD-DU as point of reference. Relative abundance was calculated at room temperature.

Conformer	UD-DU	UD-UD	UU-UD	UU-DU	UU-UU	UU-DD
ΔE _{conformers} (eV)	0.00	0.02	0.34	0.39	0.66	0.78
Abundance @298 K	0.6851	0.3149	1.28·10 ⁻⁶	1.99·10 ⁻⁷	4.03·10 ⁻¹²	3.82·10 ⁻¹⁴

To understand the aggregation, the potential of mean force curve was calculated considering the most stable conformers (**Figure 2.17**). These curves illustrate how the system energy changes as a function of the distance between two GQDs. The curves are obtained by initially pushing two nanoparticles towards each other from 20 Å to 2 Å. From the push curve (blue), three minima can be observed. The push curve had to be corrected to account for conformational dissipations during calculations due to finite sampling. The corrected push curve (black) was constructed by matching the push minima to the pull minima. Minimum 1 (min1) depicts two nanoparticles facing each other but separated by a solvent layer. Minimum 2 (min2), around 4 Å, corresponds to a dimer where the two nanoparticles have half of their *tert*-butyls up and half down. And minimum 3 (min3) is a dimer where both molecules are in the UU-UU configuration, and the *tert*-butyl groups point "outwards" of the aggregate.

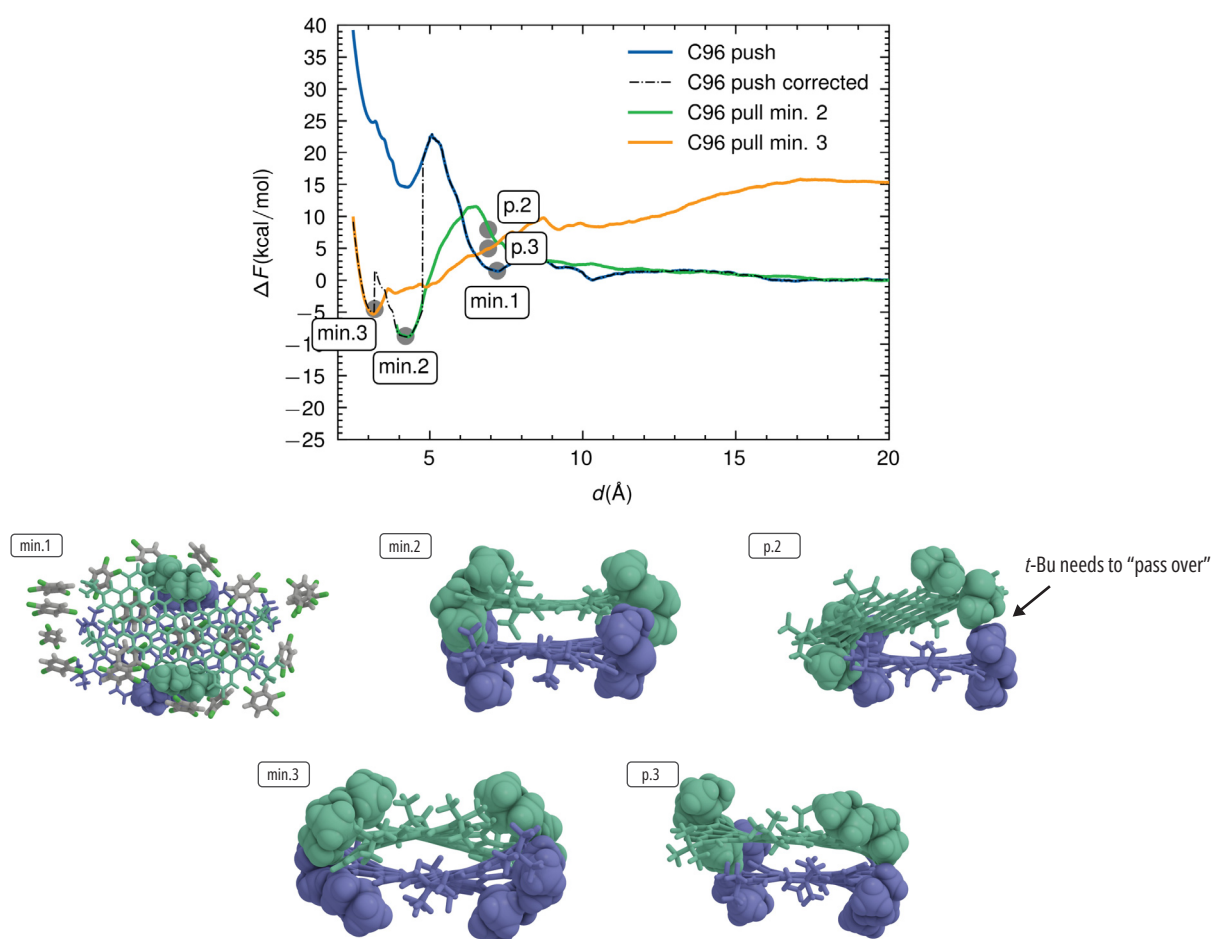


Figure 2.17 | Potential of mean force curve. Variation of the free energy as a function of distance between the center of mass of two GQDs. Five different illustrations of the dimer conformation at the different points along the curves. For clarity, only the central *tert*-butyl groups are represented as Van der Waals spheres.

To understand the dimer dissociation, and therefore also the association process, the GQDs are pulled apart from min2 or min3. When pulling from min2, there is an energy barrier that needs to be overcome. Looking at the conformation of a point after the barrier (p. 2), it is noticeable that one side of the GQD is still closely interacting and the other is farther apart. To go from min2 to p2, a *tert*-butyl group from the top molecule must "pass over" the group of the down molecule. In other words, they need to overcome the steric hindrance of the bulky *tert*-butyl groups before being in close interaction. We can draw an analogy to a container and its lid. To fully close the lid, one needs to apply some pressure to pass the edge of the lid over the edge of the container.

When pulling from min3, no energy barrier was observed, and molecules at point 3 (p3) are forming a dimer where one side of the molecule has their *tert*-butyl groups pointing outwards and on the other side, one group points inwards and the other outwards. This means that nanoparticles are in a UU-XX configuration, and that these conformers can spontaneously aggregate together. However, calculations showed that these conformers are less favoured and are almost non-existent in solution (refer to **Table 2**).

The calculations confirmed that the presence of more than one *tert*-butyl groups along the main axis of the nanoparticle contribute to its good solubility. Another important parameter is the non-existence of certain conformers in solution. Indeed, if the nanoparticle is in a conformation where each side of the molecule has a *tert*-butyl group is up and the other down, they need to overcome a steric barrier before being in close interaction. For the conformers where only one *tert*-butyl group points up, aggregation is possible, but significantly less likely to happen since they are less favoured.

2.3.3 OPTICAL PROPERTIES

We previously discussed the synthesis of **C₉₆tBu₈**, especially the interesting high solubility of the quantum dot conferred by the presence of adjacent *tert*-butyl groups along its main axis. This high solubility enabled us to obtain highly pure samples of **C₉₆tBu₈** and fully confirm its structure and purity by NMR spectroscopy. Now, we will turn our attention to its intriguing optical properties. The classical optical characterization by absorption, photoluminescence (PL) and photoluminescence excitation (PLE) spectroscopy were performed in our laboratory. The advanced optical experiments such as time-resolved photoluminescence (TR-PL), polarized-resolved photoluminescence, photoluminescence quantum yield determination and the insight for the physical interpretation of the data were performed at LUMIN laboratory in ENS Paris-Saclay by Dr. Thomas Liu, Hugo Levy-Falk, Dr. Loic Rondin, and Prof. Jean-Sebastian Lauret.

In-depth optical studies of the GQD were performed in spectrophotometric grade 1,2,4-trichlorobenzene (TCB). This solvent has been largely used by our research team and collaborators to study the optical properties of substituted graphene nanoparticles.

ABSORPTION, EMISSION, AND EXCITATION SPECTRA

The absorption spectrum of **C₉₆tBu₈** in TCB is presented in **Figure 2.18**. At first glance, we can clearly distinguish a well-resolved spectrum with sharp absorption bands. This level of resolution is indicative of a high degree of solubility of the GQD and a good suggestion of the presence of individualized nanoparticles in the solution. On the absorption spectrum, we can appreciate two sets of peak progressions around the two peaks at 470 nm and 610 nm. In total, we can discern ten absorption peaks located at 610 (**peak a**), 597 (**peak b**), 564 (**peak b**), 554 (**peak d**), 522 (**peak e**), 470 (**peak f**), 457 (**peak g**), 442 (**peak h**), 429 (**peak i**), and 405 (**peak j**) nm. **C₉₆tBu₈** has a high molar absorption coefficient (ϵ). At the main absorption peak, ϵ_{470} reaches a value of 458 181 M⁻¹.cm⁻¹.

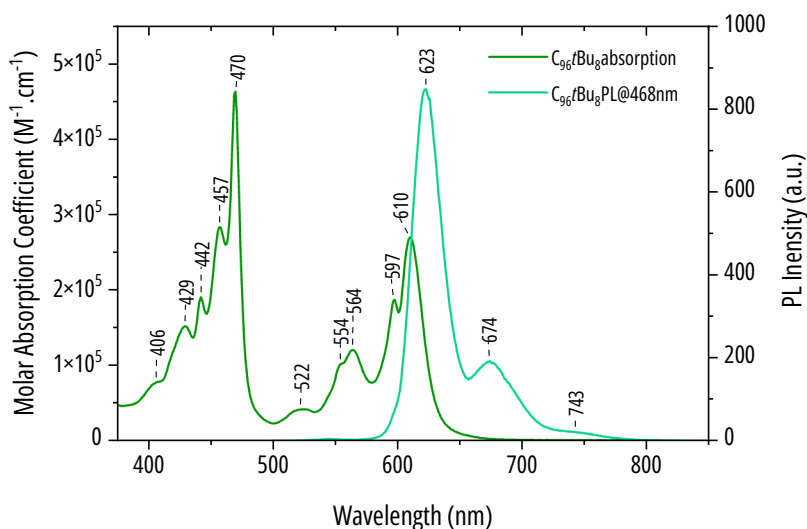


Figure 2.18 | Absorption (green) and emission (cyan) spectra of $C_{96}fBu_8$ in 1,2,4-trichlorobenzene. Photoluminescence spectrum is given for an excitation wavelength of 468 nm.

The emission spectrum of the nanoparticle exhibits three distinct emission bands (**Figure 2.18**). The Stokes shift between the absorption and emission is 13 nm. We can distinguish an emission with a mirror symmetry to the lowest energy absorption bands around 500 and 600 nm. The first emission peak is located at 623 nm. A second peak of smaller intensity is located at 674 nm, and a third broad small peak can be distinguished around 743 nm. The calculated fluorescence quantum yield using an integration sphere, is 94%. This value is among the highest values observed for GQDs.²¹⁴ Such a high value is accounted by the rigidity of the structure and the high individualization of the nanoparticles in solution. Such high luminescent properties can be distinguished to the naked eye. Three photos of a solution of $C_{96}fBu_8$ are given in **Figure 2.19**. When looked directly through natural light, the solution containing the GQD is translucent. When looked under natural light, it is no longer possible to see through the solution due to the emission of $C_{96}fBu_8$.

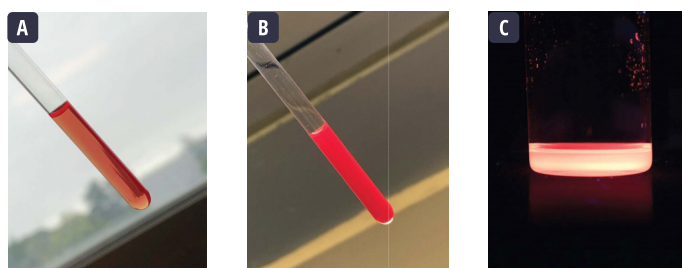


Figure 2.19 | (a) A solution of $C_{96}fBu_8$ in o-DCB looked directly through natural light. (b) Same solution in (a) looked under natural light. (c) A solution of $C_{96}fBu_8$ in TCB under a 366 nm UV light.

The photoluminescence excitation (PLE) spectrum of $C_{96}fBu_8$ was recorded for the two primary emission peaks at 623 nm and 678 nm, as shown in **Figure 2.20**. It is observable that the absorption and PLE spectra for both wavelengths overlay perfectly. We can discern all the absorption features, with the bands located at the same wavelength and a similar bandwidth. This correspondence is an indication that the absorbance and emission features are originated by the same emissive object. This observation is again consistent with the hypothesis that we are observing individualized nanoparticles in solution without any significant presence of aggregates. This is in strong contrast with the observations made for less soluble nanoparticles, such as $(T)C_{96}(C_{12}H_{25})_6$, where a neat difference between its absorption and PLE spectra is present.²⁰²

Time-resolved photoluminescence (TRPL) experiments on both emission peaks revealed similar dynamics. The observed decay could be accurately fitted to a monoexponential with a lifetime of 2.9 ns. This monoexponential behavior is an indication that a single electronic transition is taking place at the emission wavelength. Additionally, the correspondence of the decay dynamics between both emission peaks agrees that we have a single emitting entity in solution.

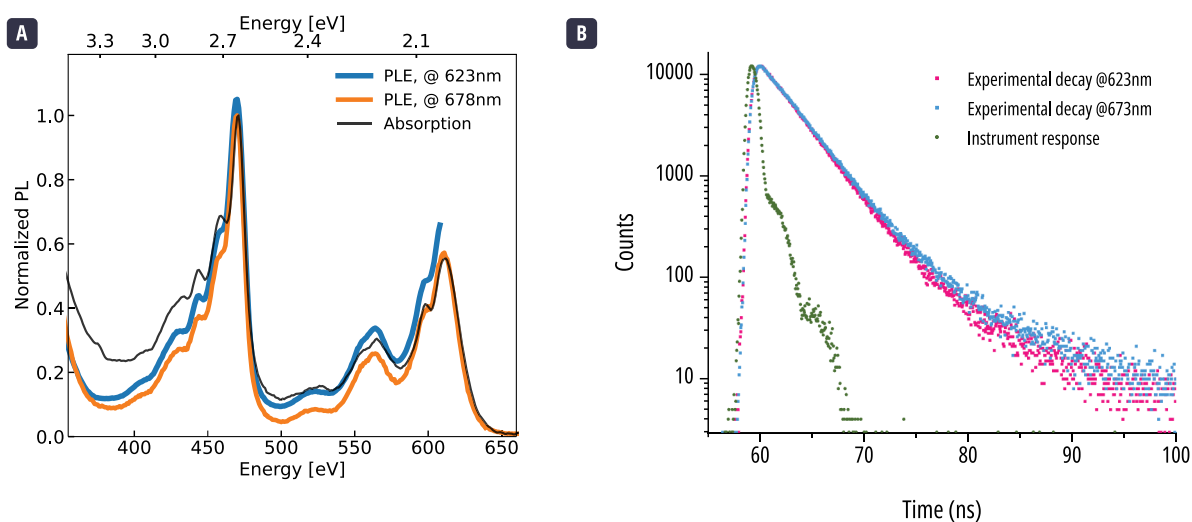


Figure 2.20 | Photoluminescence excitation and time resolved spectra for $C_{96}tBu_8$. **(a)** PLE spectra of $C_{96}tBu_8$ in TCB at two emission wavelengths. **(b)** Time resolved fluorescence spectra in TCB at the same two wavelengths.

We wanted to test the solubility of $C_{96}tBu_8$ in common organic solvents. For that, we dispersed the nanoparticle in three different common organic solvents: dichloromethane, tetrahydrofuran, and toluene (**Figure 2.21**). All three solvent yielded absorption and emission spectra similar to those obtained in 1,2,4-trichlorobenzene. In all cases, we observe a similar pattern of well-resolved absorption and emission bands. We can notice an hypsochromic shift as we increase the polarity of the solvent in comparison to TCB. Furthermore, PLE measurements on the emission bands reveal spectra that overlay perfectly with their respective absorption spectrum, just like in TCB. This suggest that $C_{96}tBu_8$ is highly soluble even in non-aromatic solvents.

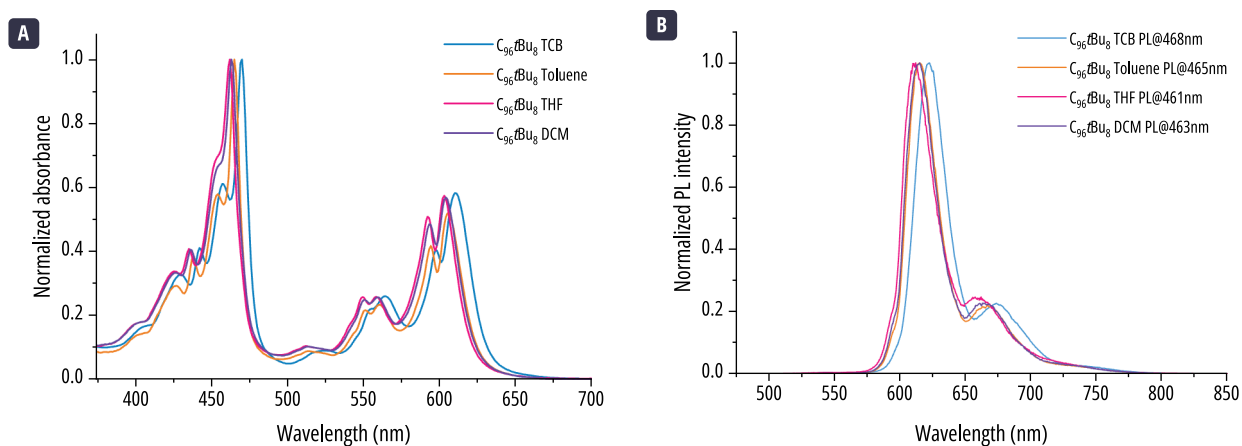


Figure 2.21 | **(a)** Absorption and **(b)** emission spectra of $C_{96}tBu_8$ in different organic solvents.

The sharp absorption and emission peaks provide rich information regarding the photo-physical properties of the GQD. Both the excitation and time-resolved experiments confirm that we are observing individualized objects in solution at concentrations needed to perform optical measurements in common organic solvents. As a result, the absorption and emission spectra are highly resolved. In the following paragraphs, we will provide theoretical insight of the nanoparticle to better understand the origin of these optical properties.

THEORETICAL INSIGHT

Having individualized nanoparticles in solution allows to bring forth a more detailed interpretation of the optical behaviour of the GQD. This understanding is possible thanks to the association of experimental observations and a theoretical description of the nanoparticle's optical properties. These theoretical calculations were performed by Dr. Silvio Osella from University of Warsaw in Poland, and Dr. Nicolas Rolland and Prof. David Beljonne from Mons University in Belgium.

Our colleagues provided us with the theoretical electronic transitions involved in the absorption spectrum of the nanoparticle. They performed their calculations with density function theory (DFT) using a HSE function and 6-31G(d,p) basis set in the gas phase. Initially they conducted a geometry optimization of the nanoparticle at its ground state. Then, using TD-DFT single point calculations, they identified four bright excited states for **C₉₆tBu₈**, reported in **Table 3**. We find a good agreement when comparing these values to the experimental observations. This is particularly evident for the first electronic transition to the S₁ state (see pink lines in **Figure 2.22a**). For this first transition at **peak a**, which involves the HOMO and LUMO orbitals, the theoretical calculations outputted a value of 615 nm and experimentally the first absorption band is located at 610nm, giving a difference of only 5 nanometres. We attributed **peak f** to the S₀→S₄ transition and **peak g** to the S₀→S₉ transition. The energy difference between the theoretical and experimental values were found to be 12 nm for state S₄ and 3 nm for S₉.

Table 3 | Values of the theoretical bright electronic transitions for **C₉₆tBu₈**. Transition to S₂ has a very low oscillator strength, therefore it is considered as a dark transition. However, its value is reported in this table as a point of reference. H and L stand for HOMO and LUMO, respectively.

State	ΔE (nm)	Oscillator strength (f)	Transition involved
S ₁	615	1.01	H → L
S ₂	572	0.01	H-1 → L
S ₄	482	0.62	H → L+1
S ₉	455	1.19	H-1 → L+1
S ₁₇	404	0.2	H-2 → L+2

In the absorption spectrum we distinguish more absorption bands than those attributed solely to electronic transition between ground and excited states. Given that the absorption spectrum originates from a single species in solution, as previously discussed, we attribute all these bands to the vibronic progressions of the transitions. To gain a deeper understanding of the vibrational effects in photophysics of **C₉₆tBu₈**, we reverted to theoretical calculations. The vibronic coupling was computed for the first transition. To do this, to an optimized geometry of the S₁ state, calculated using TD-DFT, was applied an undistorted displaced harmonic oscillator model in the Franck-Condon approximation. **Figure 2.22b** shows the comparison between the experimental and computed absorption and emission vibronic spectra for the S₀→S₁ transition. As we can notice there is an excellent agreement between both spectra. However, the accordance is more flagrant for the PL spectrum, where the thermal population of the vibrational modes account for the observed linewidth. In contrast, the experimental absorbance spectrum has sharper features.

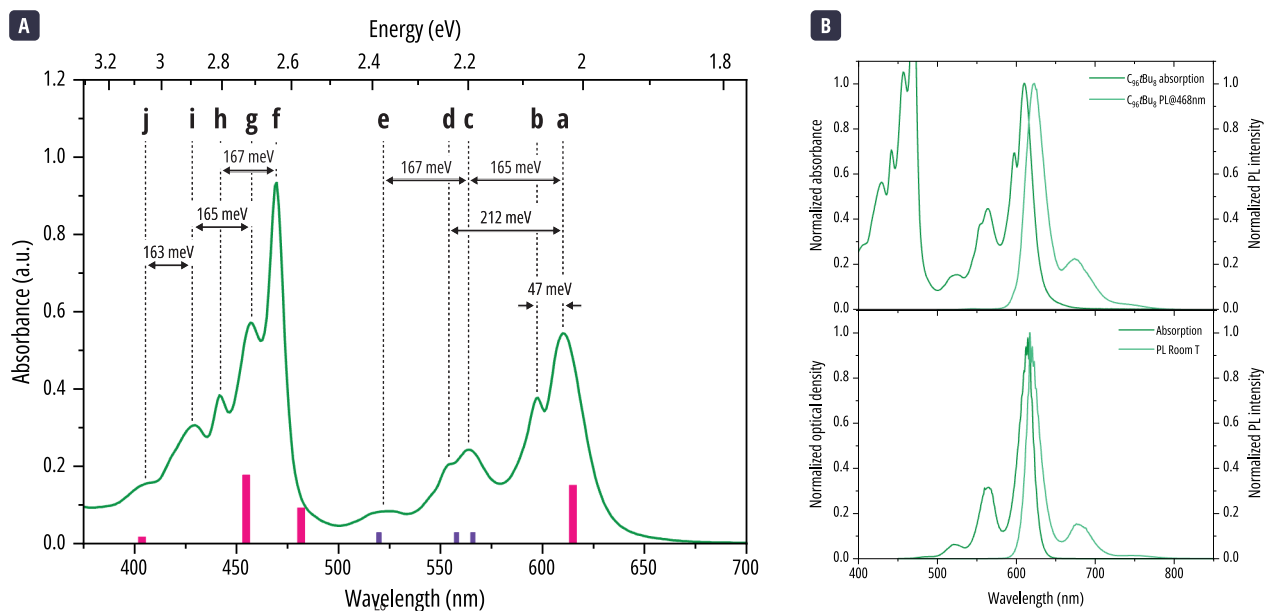


Figure 2.22 | Attribution of the absorption peaks of $C_{96}tBu_8$ in TCB. **(a)** Energy differences for the different peaks in the absorption spectrum of $C_{96}tBu_8$. Pink bars correspond to the theoretical transitions, with their relative intensities corresponding to their relative oscillator strength. Purple bars correspond to the theoretical values of the vibronic replicas associated to the $S_0 \rightarrow S_1$ electronic transition.

(b) On top, the experimental spectra for the normalized absorption and emission of the $S_0 \rightarrow S_1$ transition. Below, the calculated absorption and emission spectra for the $S_0 \rightarrow S_1$ transition and their vibronic replicas at room temperature.

To complete the description of the absorption spectrum, the energy differences between the different peaks were calculated (**Figure 2.22a**). For the $S_0 \rightarrow S_1$ electronic transition (**peak a**) we distinguish two important values of ~ 165 meV (**peak a-c**; **peak c-e**) and 212 meV (**peak a-d**). These values agree with the theoretical energies calculated for two vibrational modes of the stretching of the C=C bond in an aromatic core (**Figure 2.23**): 166 meV (1338.88 cm^{-1}) and 205 meV (1653.44 cm^{-1}). We reported similar values observed in the vibronic replicas in the emission of $(T)C_{96}(C_{12}H_{25})_6$.²⁰² **Peak c** corresponds to the 0-1 replica of the 1338.88 cm^{-1} vibrational mode, and **peak e** to the 0-2 replica. **Peak d** is attributed to the 0-1 coupling of the 1653.44 cm^{-1} vibrational mode. In the higher energy part of the spectrum, for **peak f** and **g**, their associated (0-1) vibronic replica to the 1338.88 cm^{-1} vibrational mode is assigned to **peak h** and **i**, respectively. It is possible that **Peak j** contains the 0-2 replica of the 1338.88 cm^{-1} vibrational mode or that it is originated by the transition to S_{17} , whose theoretical value also aligns with this peak.

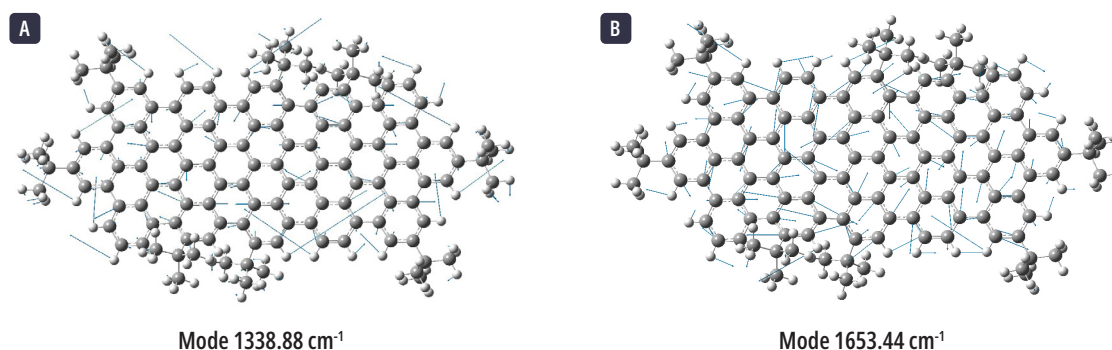


Figure 2.23 | Representation of the calculated vibrations modes coupled to the $S_0 \rightarrow S_1$ transition of $C_{96}tBu_8$. **(a)** Vibration with a frequency of 1338.88 cm^{-1} (166 meV). **(b)** Vibration with a frequency of 1653.44 cm^{-1} (205 meV).

As one can notice, **peak b** was not discussed previously since its attribution remains unclear. The energy difference between this peak and **peak a** is 47 meV. The theoretical calculations did not yield any vibrational mode with similar energy, leaving us to think that it originates from an external reason. The most intuitive hypothesis for the origin of this peak would be

the presence of aggregates in solution. However, as discussed earlier, the experimental observations indicate that the QD is highly individualized in solution. This was further confirmed by concentration experiments (**Figure 2.24**), for which no significant effects were observed. There is no change in the peaks position, the linewidth, or the peaks intensity ratio to suggest that concentration has any effect. Additionally, there is no evidence of the presence of aggregates in the NMR or MALDI-ToF spectra. Notably, the NOESY spectrum does not show any spatial correlation that would suggest the presence of a dimer. All the correlations are well accounted for the monomer.

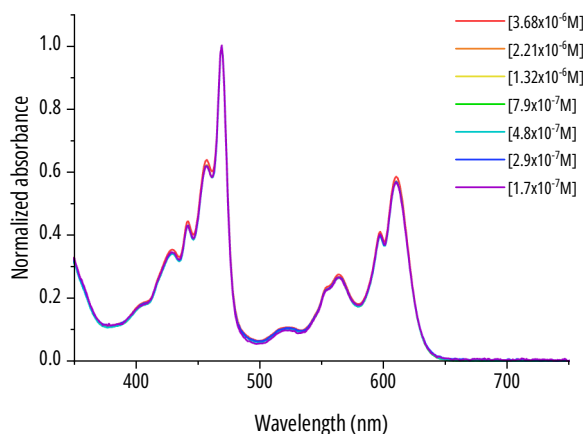


Figure 2.24 | Concentration dependent absorption spectra of $C_{96}fBu_8$ in TCB.

An alternative explanation to the origin of **peak b** could be the presence of stable conformers. The theoretical electronic transitions were computed for the six conformers and are given in **Table 4**. At most, the shift of the electronic transition's energies between the different conformers is 14 meV for the first transition. This value is still lower than the 47 meV observed experimentally but within the same order of magnitude. It is important to note that these conformers also exhibit an energy shift for the $S_0 \rightarrow S_9$ transition but no peak with an energy difference within the same order of magnitude was observed. However, it is possible that they remain hidden under adjacent peaks. As a final remark, theoretical calculations on the energy of these conformers showed that only UD-DU and UD-UD would exist in solution. The additional conformers have a high energy difference to UD-DU, and their relative abundance at 298 K would be very low (see **Table 2**). These two "stable" conformers have very close theoretical values for their electronic transitions. If **peak b** originates from these conformers, the difference between the theoretical and experimental observations may be explained by the environmental effects not considered in the calculations. This is a question that warrants further investigation.

Table 4 | Theoretical energy values of the first bright electronic transitions and their bandgap values for the six possible conformers of $C_{96}fBu_8$. All energy values are given in eV. For the electronic transitions, the oscillator strength (o.s.) is given in parenthesis.

Conformer	UD-DU	UD-UD	UU-UD	UU-DU	UU-UU	UU-DD
S_1 (eV) (o.s.)	2.015 (1.02)	2.017 (1.01)	2.016 (1.02)	2.022 (1.02)	2.013 (1.02)	2.031 (1.02)
S_2 (eV) (o.s.)	2.169 (0.01)	2.168 (0.01)	2.175 (0.01)	2.175 (0.01)	2.181 (0.01)	2.181 (0.01)
S_4 (eV) (o.s.)	2.571 (0.61)	2.571 (0.62)	2.570 (0.53)	2.571 (0.52)	2.572 (0.55)	2.574 (0.57)
S_9 (eV) (o.s.)	2.731 (1.12)	2.728 (1.19)	2.744 (1.01)	2.736 (1.08)	2.758 (1.04)	2.738 (1.04)
E_{gap} (eV)	1.92	1.92	1.93	1.92	1.91	1.92

Finally, this theoretical insight allowed us to know the orientation of the absorption transition moments within the molecule. To confirm the attribution of the electronic transitions in the absorption spectrum, it is possible to perform anisotropy experiments. The results are presented in the following paragraphs.

FLUORESCENCE ANISOTROPY EXPERIMENTS

In this sub-section we will discuss the fluorescence anisotropy experiments performed for **C₉₆tBu₈**. A quick introduction to the technique is going to be given, followed by the presentation of the results.

INTRODUCTION TO THE TECHNIQUE

Fluorescence anisotropy is a spectroscopic technique that takes advantage of linearly polarized light to gain detailed information about the properties of an emissive molecule. In this section we will only make a quick introduction to the principles behind fluorescence anisotropy. For a more comprehensive and detailed description of this process, the reader is encouraged to read dedicated works.^{175,215} It has been known that small polycyclic aromatic molecules have their electronic transitions polarized along different axis within the molecule.²¹⁶ The QDs of the rod-shape family, who are also polycyclic aromatic hydrocarbons, exhibit similar properties. To investigate the orientation of the electronic transitions, it is possible to perform fluorescence anisotropy experiments.

When a molecule is exposed to polarized light, the probability it absorbs the light depends on the orientation of the absorption transition moment (\vec{M}_A) relative to the direction of the polarized light. The absorption and emission (\vec{M}_E) transition moments are oriented in specific directions within the molecule. In a solution containing randomly oriented fluorophores that are immobile, the polarized light will predominantly excite those fluorophores whose absorption transition moment aligns parallel with the electric vector of the light. This results in a partial orientation of the excited molecules, a phenomenon referred to as photoselection (**Figure 2.25**). Consequently, the fluorophores will also emit light that is polarized, reflecting the orientation of their emission transition moments. To prevent the reorientation of the chromophores between the absorption and the emission, that would lead to a depolarization through rotational diffusion or energy transfers, the experiments need to be performed in a solid or viscous media.

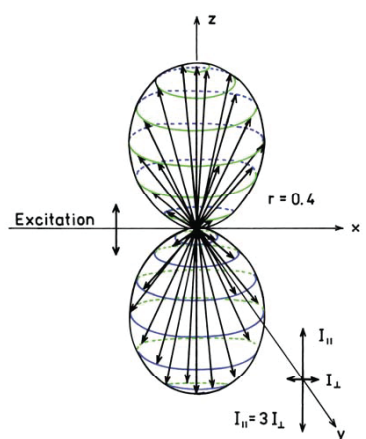


Figure 2.25 | Distribution of excited states for an incident light polarized perpendicular to the z-axis.²¹⁵

The anisotropy (r) is defined as the ratio of the excess of the emission intensity parallel to the incident polarized light divided by the total emission intensity, as given in the following relationship:

$$r = \frac{I_{\parallel} - I_{\perp}}{I_{\parallel} + 2I_{\perp}}$$

Equation 2.4

Where I_{\parallel} is the intensity of the emission polarized parallel to the incident light, and I_{\perp} the intensity of the emission polarized perpendicularly. For a homogeneous solution of randomly oriented molecules, this value is comprised between -0.2 and 0.4 because of the photoselection probability. Not all excited fluorophores will have their absorption transition moment parallel to the polarization of incident light (**Figure 2.25**). If we assume the absorption and emission transition moments are collinear, not all emitted light will have a polarization parallel to \vec{M}_A . This implies that the maximum anisotropy value will be 0.4. However, in reality, \vec{M}_A and \vec{M}_E are not necessarily collinear, so we also need to account for the angle (α) between these two vectors. If \vec{M}_A and \vec{M}_E are perpendicular to each other, the value of anisotropy reaches its minimum -0.2. With these considerations, the fundamental anisotropy (r_0) of a molecule, where no other depolarizing processes are considered, is defined as follows:

$$r_0 = \frac{2}{5} \left(\frac{3 \cos^2(\alpha) - 1}{2} \right)$$

Equation 2.5

To measure fluorescence anisotropy, the experimental setup in **Figure 2.26** is commonly used. Initially, the incident light passes through a monochromator (M) that selects a specific wavelength of light, which then passes through a first polarizer (P_1) to yield vertically polarized light that illuminates the sample. The light emitted from the sample consists of two components, one polarized parallel and the other perpendicularly to the plane of the incident light. To separate these two components, the emitted light then passes through a second polarizer (P_2) that can be positioned either vertically (V) or horizontally (H). After passing through another monochromator, the intensity of the polarized light is then detected and recorded.

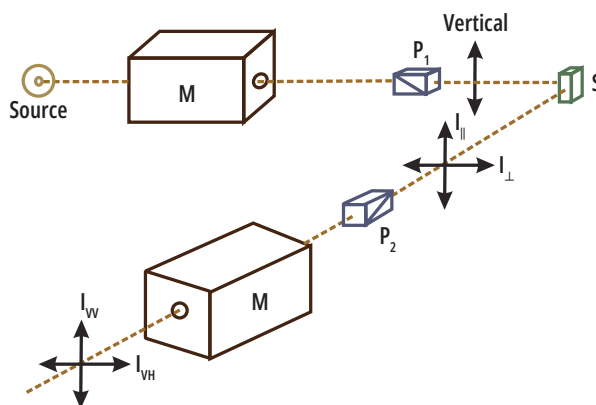


Figure 2.26 | Schematic drawing of a setup for measuring the steady-state anisotropy. M=monochromator, P=polarizer, S=sample.¹⁷⁵

The intensities are typically denoted with subscripts indicating the orientation of the polarizers P_1 (excitation) and P_2 (emission) respectively. For example, I_{VV} refers to the intensity measured when both P_1 and P_2 are vertically oriented, and I_{VH} refers to the intensity when P_1 is vertically oriented and P_2 is horizontally oriented. These intensities are used to calculate the fluorescence anisotropy with the following relation:

$$r = \frac{I_{VV} - GI_{VH}}{I_{VV} + 2GI_{VH}}$$

Equation 2.6

G is a correction factor that considers the difference of the instrument's sensitivity to vertically and horizontally polarized light. Factor G is measured by setting P_1 to a horizontal position and acquiring I_{HV} and I_{HH} . If the incident light is horizontally polarized, the measured intensity of the vertical and horizontal components both originate from perpendicular emission to the incident light and should be equal. Therefore, the ratio of their intensities reflects the instrument's sensitivity. Finally, to recover the anisotropy value, four intensity measurements are required at each excitation wavelength (λ_{exc}): I_{VV} , I_{VH} , I_{HV} , and I_{HH} .

EXPERIMENTAL RESULTS

The theoretical calculations showed that the transition moments for $C_{96}tBu_8$ are oriented along the longitudinal and transverse axis of the nanoparticle. For instance, the $S_0 \rightarrow S_1$ and $S_0 \rightarrow S_9$ transitions are aligned to the longitudinal axis of the nanoparticle. Inversely, the $S_0 \rightarrow S_4$ transition is positioned along the transverse axis. This can be appreciated in **Figure 2.27**. The $S_0 \rightarrow S_2$ transition is not shown in the figure since the calculated oscillator strength is very small (See **Table 3**), but calculations indicated that the transition is aligned along the transverse axis. These different alignments of the electronic transitions make possible to perform the anisotropy experiments on the QDs.

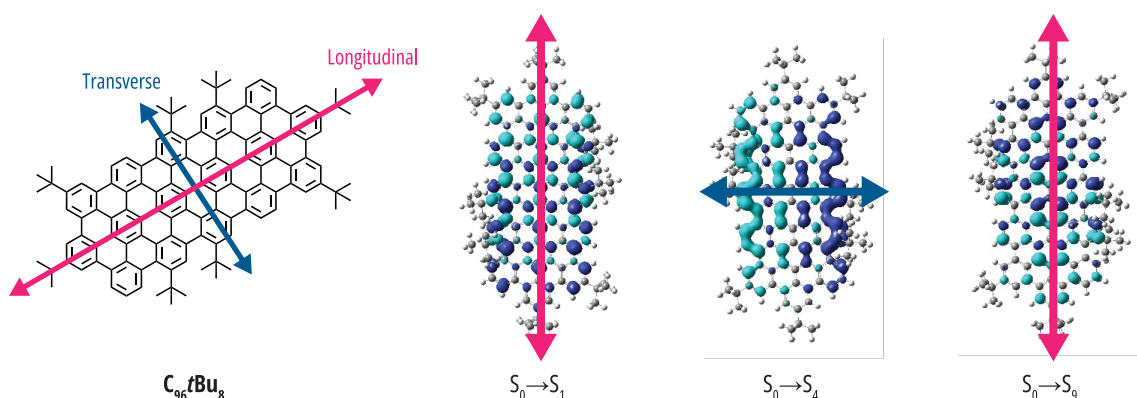


Figure 2.27 | Longitudinal and transverse electronic transitions of $C_{96}tBu_8$. Representations on the right show the calculated electron-hole distributions associated to the electronic transition.

The measurements were performed in a solution of castor oil and 1,2,4-trichlorobenzene (90/10). The viscosity of castor oil will allow to immobilize the nanoparticles in solution during the experimental time window. Measurements were performed at 629 nm, in the main peak of photoluminescence of $C_{96}tBu_8$ who do not overlap with the emission the castor oil, who also exhibits fluorescence (**Figure 2.28a**). **Figure 2.28b** shows the anisotropy curve and the PLE measured for $C_{96}tBu_8$ in the mixture of solvents. The PLE spectrum of $C_{96}tBu_8$ recorded in a solution of castor oil and TCB is the same as in only TCB, which indicates that at this wavelength we are primarily observing the nanoparticle.

Concerning the anisotropy curve, we notice that it is relatively flat above 500 nm and varies with the excitation wavelength below 500 nm. The oscillations observed in the anisotropy curve present maxima and minima that align nicely with the peaks in the PLE spectrum. This variation is to be understood as the change in the angle between the absorption (\vec{M}_A) and emission (\vec{M}_E) transition moments.

At values over 500 nm, where the observed transitions correspond to $S_1 \rightarrow S_0$, the maximum anisotropy is 0.37. This value, close to the theoretical maximum of 0.4, indicates that $\vec{M}_A(S_0 \rightarrow S_1)$ and $\vec{M}_E(S_1 \rightarrow S_0)$ are closely aligned (see **Equation 2.5**). The emission observed for the nanoparticle originates exclusively from the $S_1 \rightarrow S_0$ transition. Therefore, the variations below 500 nm correspond to the angle difference between the $\vec{M}_A(S_0 \rightarrow S_4)$ and $\vec{M}_E(S_1 \rightarrow S_0)$, and between $\vec{M}_A(S_0 \rightarrow S_9)$ and $\vec{M}_E(S_1 \rightarrow S_0)$.

Theoretical calculations indicate that $\vec{M}_A(S_0 \rightarrow S_4)$ is perpendicular to $\vec{M}_A(S_0 \rightarrow S_1)$, which explains the variation towards negative values around the peaks assigned to this transition. Analogously, for the peaks assigned to the $S_0 \rightarrow S_3$ transition, where \vec{M}_A lies parallel to $\vec{M}_A(S_0 \rightarrow S_1)$, the curve returns to positive anisotropy values.

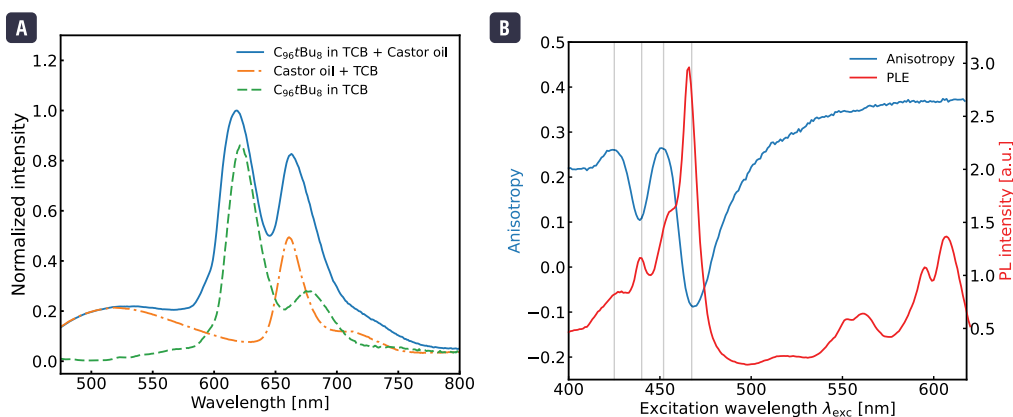


Figure 2.28 | Photoluminescence and anisotropy curve for measurements of **C₉₆fBu₈** in castor oil/TCB. **(a)** Comparison of the PL curve of the solvent system, and the fluorophore with and without the solvent system. We can observe that around 629 nm the castor oil exhibits very little luminescence. **(b)** Curves of the PLE and anisotropy measures of **C₉₆fBu₈** in castor oil/TCB.

The dependence of the anisotropy curve to the absorption transition moment can be better visualized in **Figure 2.29a**, where the parallel and orthogonal components in the PLE spectrum are separated.^{215,217} We see that the parallel component contains the peaks attributed to the $S_0 \rightarrow S_1$ and $S_0 \rightarrow S_3$ transitions and their respective vibronic peaks. The perpendicular component has only the peaks attributed to $S_0 \rightarrow S_4$ and its vibronic replica. The experimental data is in excellent agreement with the theoretical spectrum of the separated parallel and perpendicular components (**Figure 2.29b**). In this way, we can confirm the attribution of peaks for **C₉₆fBu₈**. We observe in the experimental perpendicular component spectrum that there is no PLE peak around 570 nm, the region where the theoretical $S_0 \rightarrow S_2$ transition occurs. This supports our assertion that **peak b** does not originate from this electronic transition. As previously discussed, this peak is associated with the $S_0 \rightarrow S_1$ electronic transition, and thus, it appears in the parallel PLE spectrum.

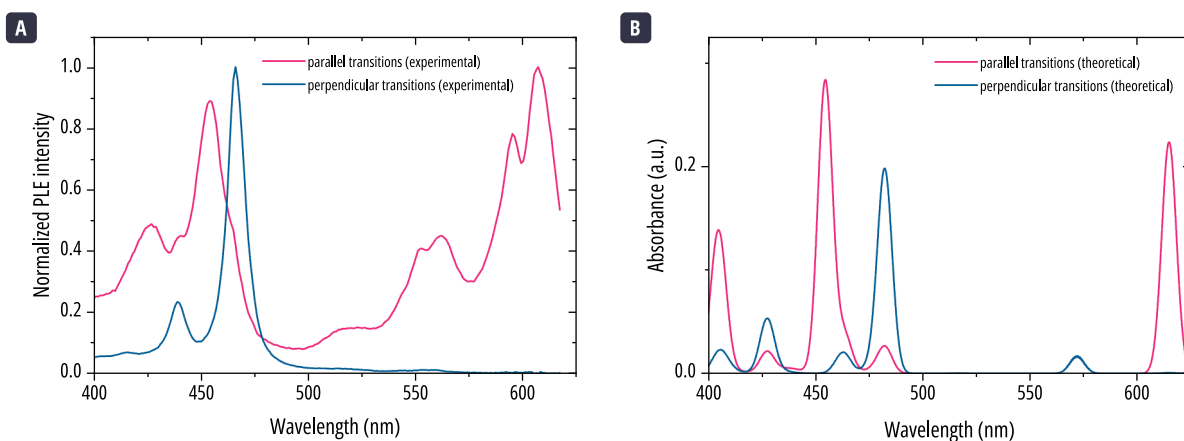


Figure 2.29 | Experimental and theoretical curves for the separated parallel and perpendicular components of **C₉₆fBu₈** PLE. **(a)** Experimental curve derived from the anisotropy and PLE measurements at 629 nm. **(b)** Theoretical curve showing the parallel and perpendicular electronic transitions along the main axis of the nanoparticle.

SINGLE-MOLECULE EXPERIMENTS

Single molecule spectroscopy (SMS) is a relatively young technique that allows to get more detailed information about a molecule than in solution, where the observed properties are the average of the ensemble.²¹⁸ Besides the single molecule experiments can give us interesting information about dynamic processes or quantum properties of the GQD. In the introduction, we already discussed how SMS allowed to determine that **(T)C₉₆(C₁₂H₂₅)₆** behaves as a single photon emitter at room temperature, has a high photostability, does not exhibit any blinking, and enabled the distinction of the intrinsic emission of the GQD and impurities in the sample.^{187,202,203} Using this technique, it is possible to observe and measure only the intrinsic optical properties of a single GQD without the influence of impurities or aggregates that would be otherwise averaged in solution experiments. **C₉₆tBu₈** already shows very interesting properties in solution, such as high individualization, high purity, and high quantum yields. All this makes the investigation at a single molecule level more exciting.

To perform single molecules experiments, **C₉₆tBu₈** was dispersed in TCB and mixed with a solution of polystyrene (PS) in TCB. The mixed solution is then deposited by spin coating on a glass substrate previously treated with plasma. The sample is then dried on a hotplate for 1 h at 90°C. A photoluminescence map of the sample is measured with a home-built micro-PL setup at ambient conditions. A schematic representation of the setup is presented in **Figure 2.30**. A light source passes through an objective to excite the sample. The emitted light then passes through dichroic mirror to separate the excitation and emission light, then through a confocal pinhole to reduce any contribution of neighboring out-of-focus emitters.

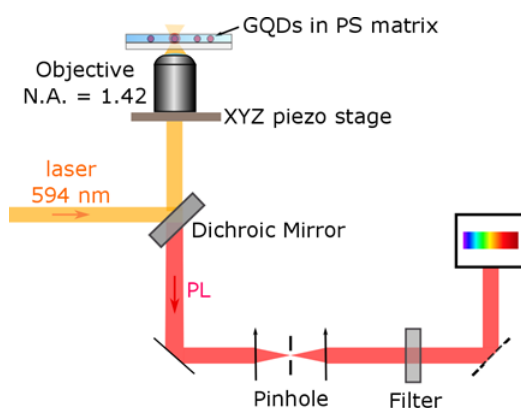


Figure 2.30 | Schematic representation of the setup used for single molecule experiments.

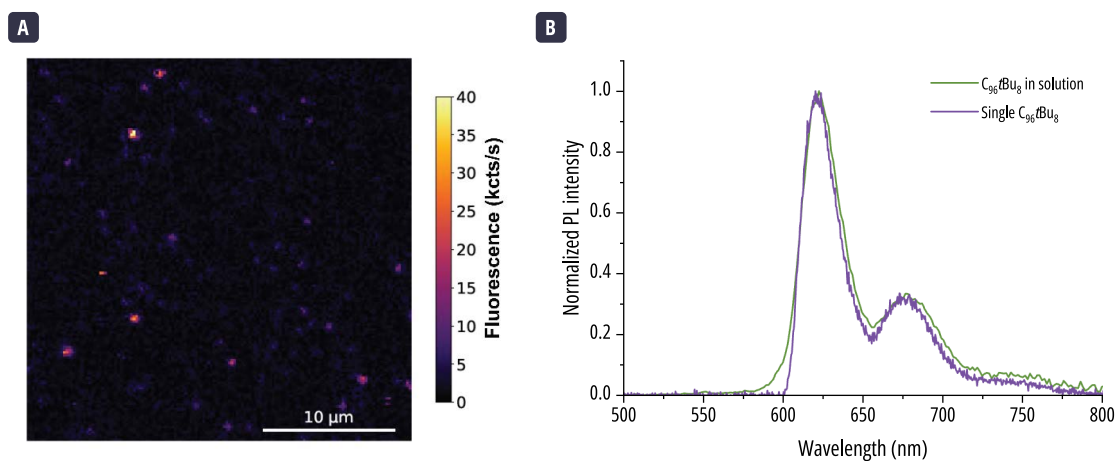


Figure 2.31 | Single molecule measurements for **C₉₆tBu₈**. **(a)** PL map of a sample of **C₉₆tBu₈** in a PS matrix. **(b)** Superimposition of the photoluminescence spectrum of a single **C₉₆tBu₈** and of a solution of **C₉₆tBu₈** in TCB.

A PL map of a sample is presented in **Figure 2.31a**. It is possible to notice luminescent spots in the PS matrix the size of a few hundred nanometer corresponding to the diffraction limit. The PL spectrum of one spot is recorded, and as can be distinguished in **Figure 2.31b**, the emission spectra of one spot fits very well to the one obtained in solution measurements. The deviation observed at shorter wavelengths can be explained using a cut-off filter in the micro-PL setup.

This accordance is an indication that we are observing the same objects in solution and in the polymer matrix. To confirm that we are indeed observing a single emitter, further characterizations were performed. First, the observation of the PL intensity over the continuous illumination of the chromophore can give an indication of the number of emitters in an observed spot. For instance, the PL intensity of a spot will experience a series of discrete jumps over time if more than one object is present. On the contrary, in the case of a single emitter, the intensity should experience a single jump to 0. The trace of the PL intensity for a typical spot **C₉₆tBu₈** in a PS matrix is given in **Figure 2.32**. It can be observed that a single drop in PL intensity takes place, confirming that a single emitter is present. Additionally, the PL intensity of **C₉₆tBu₈** remains constant without any blinking, showing a high photostability.

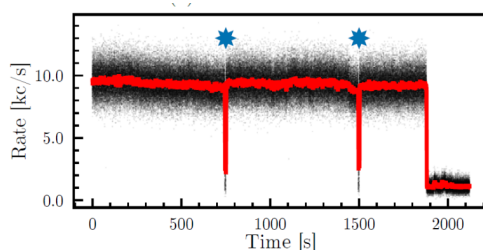


Figure 2.32 | Time trace of the photoluminescence of **C₉₆tBu₈**. Red line corresponds to the moving average. Blue stars indicate manual adjustments made to the setup.

The second order correlation function $g^{(2)}(t)$ of **C₉₆tBu₈** was measured adding a Hanbury Brown-Twiss setup to the initial micro-luminescence setup (**Figure 2.33a**). The emitted light passes through a 50:50 beam splitter before its detection. A first detector is used to give a start signal, and a second a stop signal. The second order correlation function for **C₉₆tBu₈** is given in **Figure 2.33b**. The fit gave a $g^{(2)}(0) = 0.17$. Values of $g^{(2)}(0)$ lower than 0.5 are associated to single photon emitters, since the probability of a single photon to be detected by the two detectors should be zero. The measured value confirms that the **C₉₆tBu₈** is a single photon emitter, and that the observed properties from the luminescent spots are originated from a single molecule.

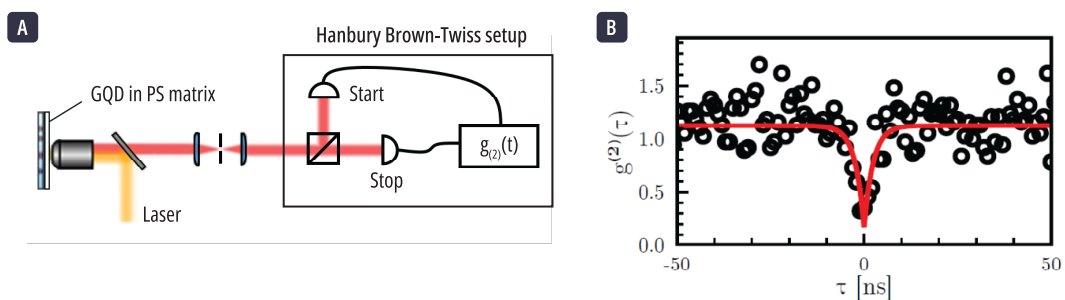


Figure 2.33 | (a) Hanbury Brown-Twiss setup. (b) Measured $g^{(2)}(0)$ for **C₉₆tBu₈**. The red lines correspond to the fit.

C₉₆tBu₈ behaves as a single photon emitter with high photostability. The excellent agreement between the photoluminescence from single molecule spectroscopy and from solution supports that the GQD is well individualized in solution. To gain more resolution, single molecule experiments at low temperature experiments are being performed. Additionally, to

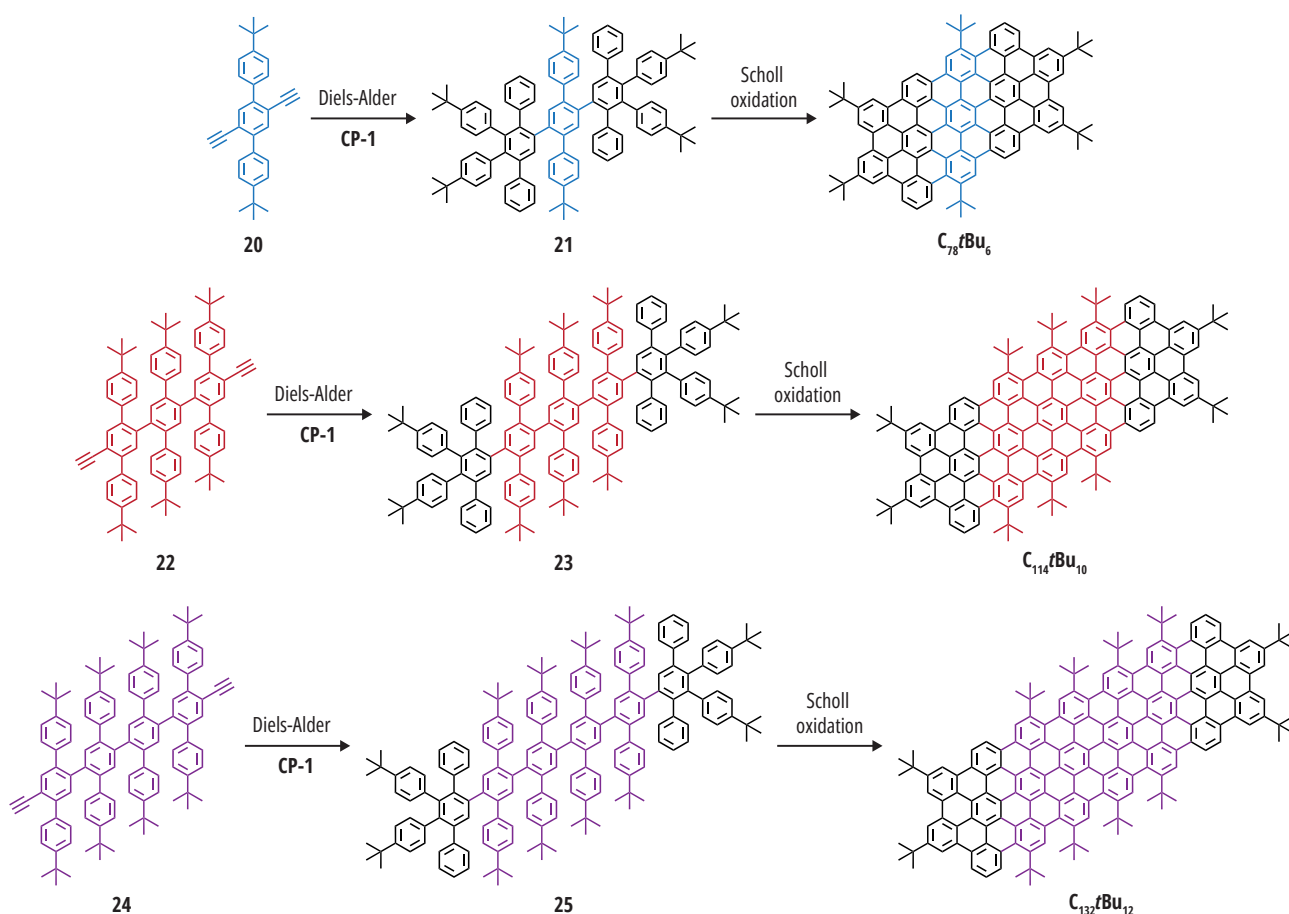
minimize the impact of the environment on the observed properties, single molecule depositions in a single crystal matrix are being tested.

2.4 VARYING THE ROD-SIZE

The high solubility of **C₉₆tBu₈** enabled us to perform unprecedented optical experiments. With the intention of exploring how a change in size of the aromatic core of the QD, while keeping the same C_{2h} symmetry, is going to affect their optical properties, we now turn our attention the synthesis, chemical and optical characterization of the other members of the rod-shaped family of QDs: **C₇₈tBu₆**, **C₁₁₄tBu₁₀**, and **C₁₃₂tBu₁₂**. Within this family, the size of the aromatic core of the nanoparticle ranges from 1.99 nm for the smaller member to 3.11 nm for the largest compound.

2.4.1 SYNTHESIS

The synthesis of **C₇₈tBu₆**, **C₁₁₄tBu₁₀**, and **C₁₃₂tBu₁₂** follows the same strategy as that for **C₉₆tBu₈**. Firstly, a terphenyl alkyne core is synthesized, which is then subjected to a Diels-Alder reaction with **CP-1** to yield the corresponding polyphenylene dendrimer. Then, this dendrimer is oxidized through a Scholl reaction to form the new C-C bonds. As illustrated in **Scheme 2.9**, it is possible to tune the size of the QD by changing the number of terphenyl rows in the alkyne core. Furthermore, since the alkyne core is responsible for introducing the *tert*-butyl groups along the main axis of the nanoparticle, increasing the size of the core will also increase the number of solubilizing groups in the final structure. We have previously discussed that these groups play a definitive role in the high solubility of **C₉₆tBu₈** and as will be discussed later, they also play a crucial role in the solubility properties of the other members of the rod-shaped family.



Scheme 2.9 | General synthetic strategy to the synthesis of **C₇₈tBu₆**, **C₁₁₄tBu₁₀**, and **C₁₃₂tBu₁₂**.

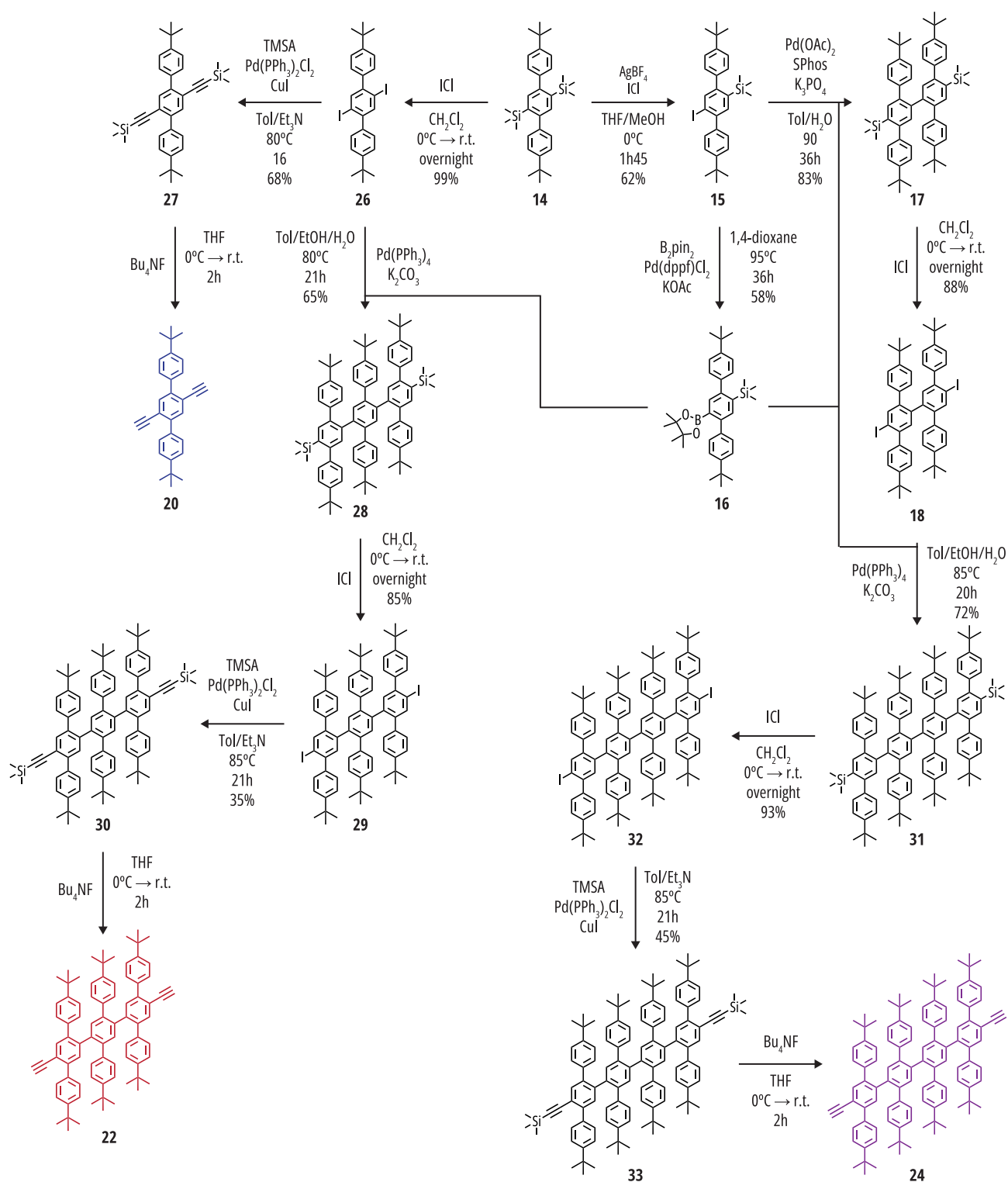
CORE SYNTHESIS

The general strategy for the synthesis of the different alkyne cores **20**, **22**, and **24** relies on the one employed for the alkyne core for **C₉₆tBu₈**. As one may observe, the size of the cores increases along with the size of the GQD. Consequently, the number of reaction steps needed to synthesize the alkyne core will also increase. The synthetic route to these cores is summarized in **Scheme 2.10**. It is important to highlight that although the number of steps increases with the size, some precursors used in the synthesis of one core are also employed in the synthesis of another core of the rod-shaped family. This shared methodology helps streamline the overall synthetic process.

The general strategy for the synthesis of the alkyne cores is as follows. First, a trimethylsilyl-disubstituted terphenyl is synthesized, their respective synthesis will be discussed shortly. Depending on the target size of the nanoparticle, this intermediate varies in number of terphenyl rows. Therefore, for **C₇₈tBu₆** it is a mono-terphenyl derivative **14**, for **C₁₁₄tBu₁₀** it is a tri-terphenyl derivative **28**, and for **C₁₃₂tBu₁₂** it is a tetra-terphenyl **31**. This trimethylsilyl-disubstituted terphenyl then undergoes iododesilylation in the presence of iodine monochloride to give the corresponding diiodo derivatives **26**, **29**, and **32**. Subsequently, a Sonogashira coupling with trimethylsilylacetylene produces the protected alkyne terphenyls derivatives **27**, **30**, and **33**. Finally, upon deprotection of the alkyne functions in the presence of tetrabutylammonium fluoride, the desired **20**, **22**, and **24** alkyne cores are obtained. The deprotection is performed prior to use and the alkyne cores are used without any further purification.

Let's now discuss the synthesis of the corresponding trimethylsilyl-disubstituted terphenyl derivatives **14**, **29**, and **31**. The synthesis of terphenyl **14** was already described in last section as an intermediate for the synthesis of **C₉₆tBu₈**. Now, it is also serves as an intermediate product in the synthesis of **C₇₈tBu₆**. The synthesis of the tri-terphenyl derivative **28** relies in the Suzuki-Miyaura coupling between the diiodo terphenyl **26** and the mono-borylated terphenyl **16**, in the presence of a palladium catalyser. This coupling works better with tetrakis(triphenylphosphine)palladium(0) than in the presence palladium(II) diacetate with 2-dicyclohexylphosphino-2',6'-dimethoxybiphenyl (SPhos) as ligand, as was the case for the di-terphenyl derivative **17**. This can be explained by the fact that using smaller ligands in the palladium complex intermediates reduces the steric hindrance, allowing the reaction to proceed more easily. Since we are now synthesizing rather large precursors, steric considerations become significant.

The tetra-terphenyl derivative **31** is achieved through the Suzuki-Miyaura coupling between the diiodo di-terphenyl derivative **18** and the mono-borylated terphenyl **16**. Again, the reaction only proceeded when tetrakis(triphenylphosphine)palladium(0) was used. Despite the considerable size of the product, the reaction proceeded with a good yield. It's noteworthy that for the synthesis of **31**, we use the diiodo-di-terphenyl that was employed in the synthesis of **C₉₆tBu₈**. We also observed that the pinacol boronic ester **16** plays a central role in the synthesis of the alkynes cores for **C₉₆tBu₈**, **C₁₁₄tBu₁₀**, and **C₁₃₂tBu₁₂**. We have previously discussed the limitations encountered in the synthesis of **16**; however, it's important to emphasize that the relatively low yields, coupled with the extreme sensitivity of the reaction to the presence of water, constitute a challenge for producing large quantities of the alkyne cores.

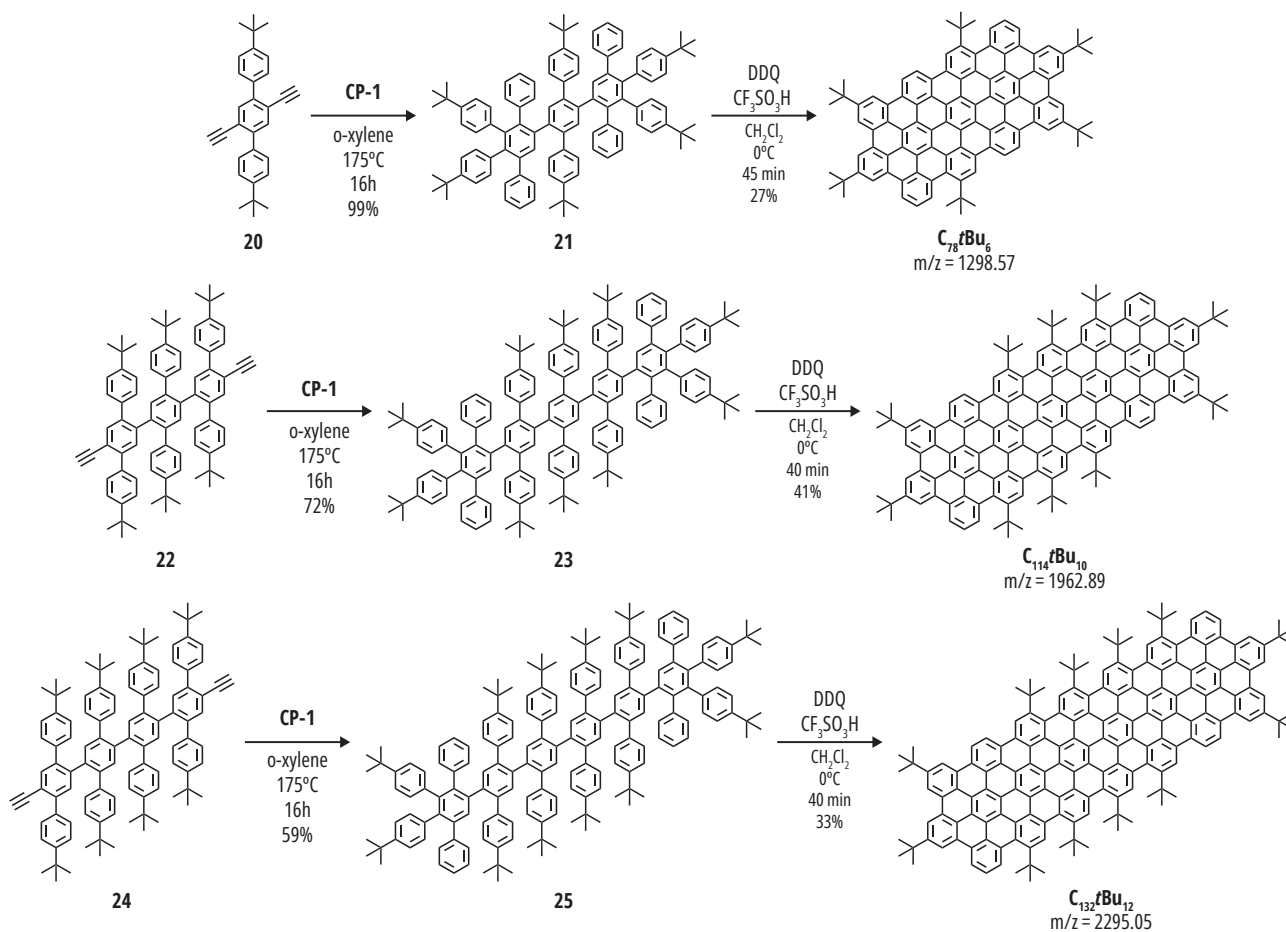


Scheme 2.10 | Synthetic route to alkyne cores **20**, **22**, and **24**.

DENDRIMER SYNTHESIS AND SCHOLL OXIDATION

To synthesize the polyphenylene dendrimers, the corresponding terphenyl alkyne core is reacted with *tert*-butyl substituted tetraphenylcyclopentadienone **CP-1** in Diels-Alder conditions (see **Scheme 2.11** for the details of the conditions employed). As for the synthesis of **C₉₆tBu₈**, the oxidation of the dendrimer into the corresponding nanoparticles **C₇₈tBu₆** and **C₁₁₄tBu₁₀**, was achieved using iron(III) chloride as oxidant as well as DDQ in the presence of trifluoromethane sulfonic acid.

Oxidation with DDQ yielded cleaner reactions, so here we only focus on these conditions. **C**₁₃₂**tBu**₁₂ was only oxidized in the presence of DDQ.



Scheme 2.11 | Dendrimer synthesis and Scholl oxidation route to obtain **C**₇₈**tBu**₆, **C**₁₁₄**tBu**₁₀, and **C**₁₃₂**tBu**₁₂.

The three GQDs exhibited high solubilities as **C**₉₆**tBu**₈, therefore purification was possible through a precipitation step followed by column chromatography or a size exclusion chromatography. If the oxidation is performed with DDQ, the purification step can be achieved by two steps of precipitation and ultracentrifugation, as was the case for **C**₉₆**tBu**₈. To assess the completion during the reaction and the quality of the purification MALDI-ToF spectrometry was used (see next section).

2.4.2 CHARACTERIZATIONS

CHEMICAL CHARACTERIZATION

MASS SPECTROMETRY

The MALDI-ToF spectra of **C**₇₈**tBu**₆, **C**₁₁₄**tBu**₁₀, and **C**₁₃₂**tBu**₁₂ after purification are presented in **Figure 2.34**. For all three nanoparticles the zoom in the monomer region shows the lack of additional peaks corresponding to byproducts. Besides, the theoretical isotopic pattern fully agrees with the experimental pattern. As can be observed, a peak corresponding to the dimer of **C**₇₈**tBu**₆ is present in the mass spectrum. This dimer peak was not observed for **C**₁₁₄**tBu**₁₀, and **C**₁₃₂**tBu**₁₂.

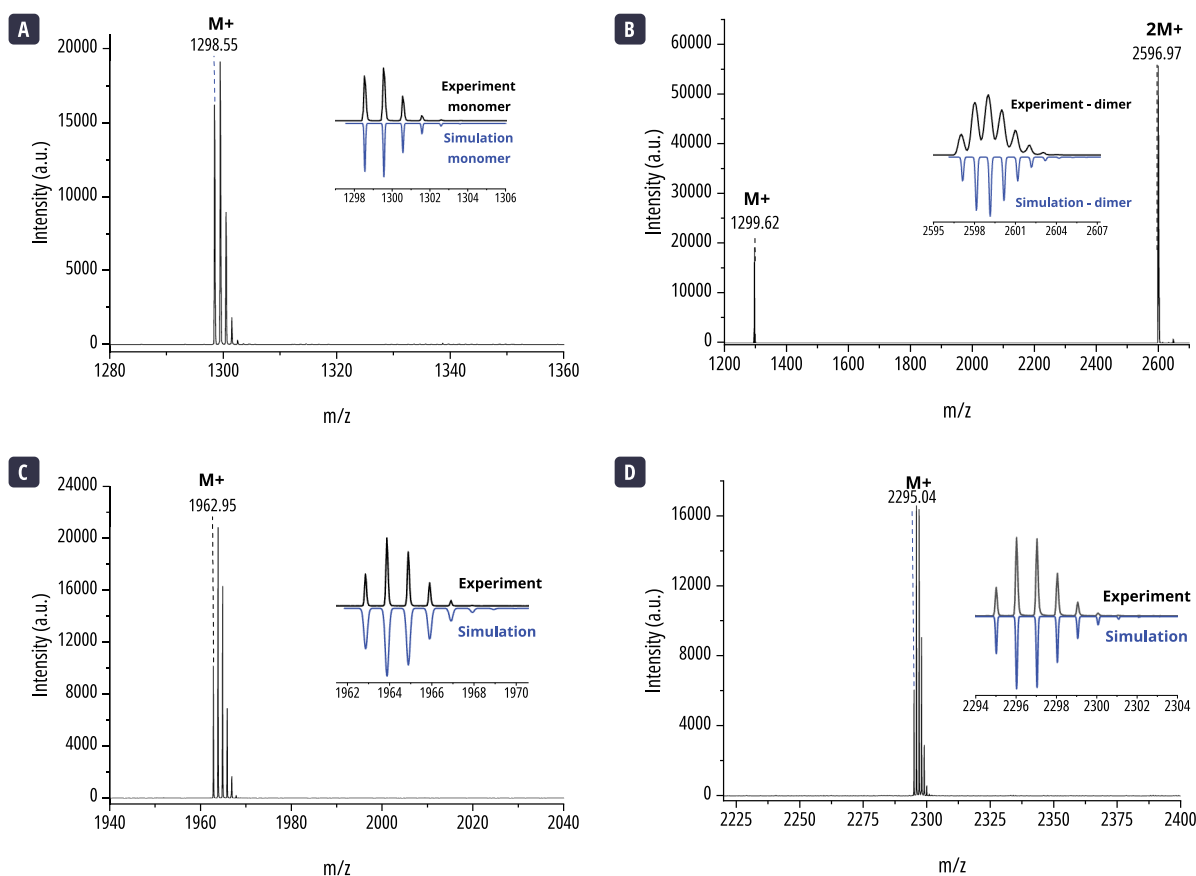


Figure 2.34 | MALDI-ToF spectra of $C_{78}tBu_6$, $C_{114}tBu_{10}$, and $C_{132}tBu_{12}$ after purification. **(a)** Zoom in on the monomer peak region of $C_{78}tBu_6$. The insert compares the isotopic pattern of the M^+ peak with a theoretical distribution. **(b)** Full mass spectrum of $C_{78}tBu_6$. The insert compares the isotopic pattern of the dimer peak with a theoretical distribution. **(c)** Zoom in the main peak region of $C_{114}tBu_{10}$. The insert compares the isotopic pattern of the M^+ peak with a theoretical distribution. **(d)** Zoom in the main peak region of $C_{132}tBu_{12}$. The insert compares the isotopic pattern of the M^+ peak with a theoretical distribution.

NMR SPECTROETRY

The structure of the GQDs was confirmed by NMR spectroscopy. Attribution was achieved through COSY and NOESY experiments. As for $C_{96}tBu_8$, HSQC and HMBC experiment confirmed the attribution and structure of the GQDs. Here only the 1H NMR are presented, the spectra from the 2D experiments are given in Appendix 1. The NMR spectra of $C_{114}tBu_{10}$, and $C_{132}tBu_{12}$ are very clean (**Figure 2.35**). Even though some solvent signals like benzene (7.28 ppm), dichloromethane (5.39 ppm), and water (2.21 ppm) are present, the downfield aromatic region shows only well resolved signals that were attributed to the nanoparticles. Along with $C_{96}tBu_8$, a trend in the distribution of the proton signals can be observed. For instance, the triplet corresponding to proton 2 is the most up-field signal of the nanoparticle. The singlet attributed to proton 10, in the same position within the three structures, gives the most down-field signal. Finally, the two *tert*-butyl groups at the exterior of the GQD give the most up-field signals for these groups.

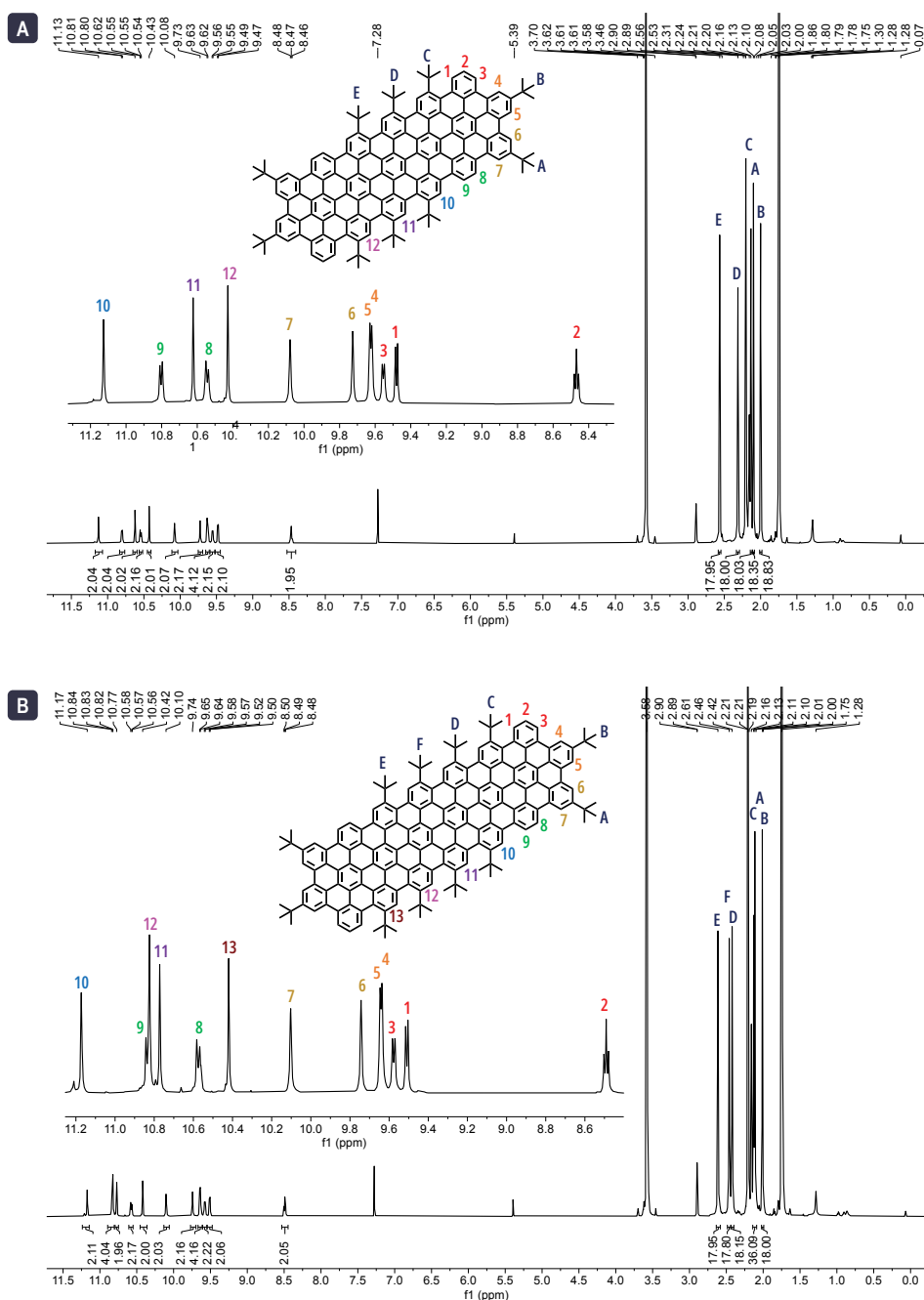


Figure 2.35 | ^1H NMR spectra (600Mz, $\text{THF-d}_8+\text{CS}_2$, 298K) of (a) $\text{C}_{114}\text{tBu}_{10}$ and (b) $\text{C}_{132}\text{tBu}_{12}$ with attributions to the structure.

In contrast, the attribution of peaks made to $\text{C}_{78}\text{tBu}_6$ does not follow the same logic as for the other members of the rod-shaped family (**Figure 2.36**). For example, the proton in position 2 does not give the most up-field signal as was the case for the other GQDs. The size of the nanoparticle, as the distribution of *tert*-butyl groups, seem to have an impact on the electronic distribution within the core. As additional comment on the NMR spectra of $\text{C}_{78}\text{tBu}_6$, let's address the presence of additional broad peaks on the aromatic region. Indeed, it is possible to distinguish well resolved signals, that in help with the complementary experiments were attributed to the monomer of the GQD. However, the aromatic region is marked by multiple broad peaks. In the NOESY spectrum, these broader peaks appear to interact with each other. Given that these broad peaks also overlap with the monomer peaks, the NOESY spectrum presents complex correlations. The assignment of the monomer peaks was based on COSY NMR experiments, where strong coupling between the hydrogens was observed.

The origin of these broad peaks could be attributed to impurities, partially fused derivatives, or the presence of aggregates. Among these possibilities, the presence of aggregates seems to be the most plausible explanation, as there were no traces of impurities or partially fused derivatives found in the mass spectrum. However, a peak corresponding to the GQD dimer, with higher intensity than the one of monomer, is present. It has also been described that π -stacking interactions can lead to a broadening of NMR signals.²¹⁹ To corroborate this hypothesis, it would be interesting to perform NMR experiments in the presence of different ratios of anti-solvents to observe if there is a change in the signals intensities that would suggest the passage from monomer to dimer or multimeric aggregates.

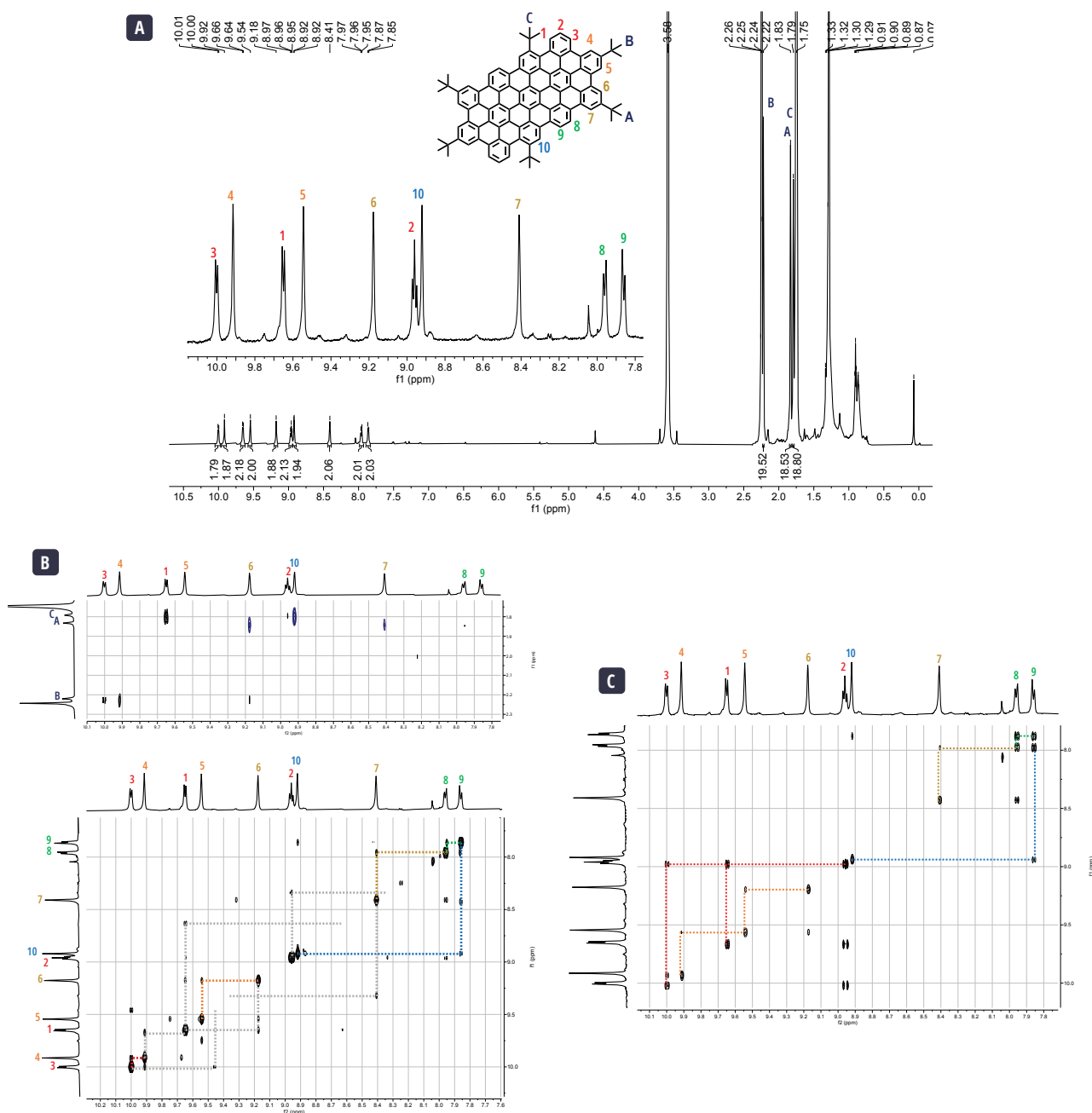


Figure 2.36 | NMR spectra of $C_{78}tBu_6$ (600Mz, THF- d_8 + CS_2 , 298K). (a) 1H spectrum and attribution of peaks to the $C_{78}tBu_6$ structure. (b) 1H - 1H NOESY spectra with dotted lines showing the correlation interactions between protons. Gray lines represent interactions attributed to the small broad peaks. (c) 1H - 1H COSY spectra with dotted lines showing the correlation interactions between protons.

ELECTROCHEMISTRY

The electrochemical properties of **C₇₈tBu₆**, **C₁₁₄tBu₁₀**, and **C₁₃₂tBu₁₂** were examined under the same conditions as detailed in **Section 2.3.2**. The cyclic voltammograms are presented in **Figure 2.37**. For the three nanoparticles, two reversible oxidation waves are visible. In the case of **C₇₈tBu₆**, no reduction wave is apparent, though a small bump at low potentials suggests an irreversible reduction. For **C₁₁₄tBu₁₀**, an irreversible reduction wave is observed. The intensity of the reduction seems to be larger than that of the oxidation, suggesting a multi-electronic process. For **C₁₃₂tBu₁₂**, a reversible reduction wave is present.

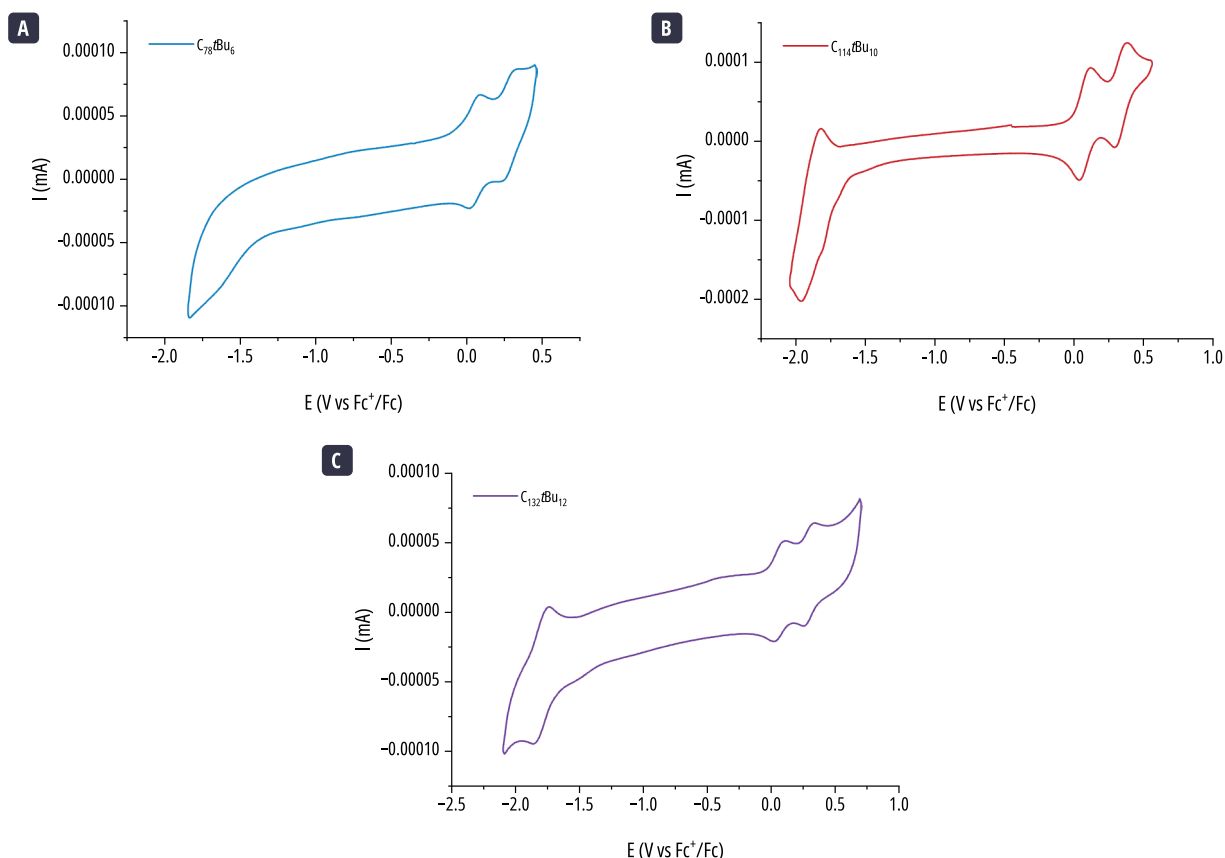


Figure 2.37 | Cyclic voltammograms of **C₇₈tBu₆**, **C₁₁₄tBu₁₀**, and **C₁₃₂tBu₁₂**.

Table 5 | Summary of the electrochemical values measured for **C₇₈tBu₆**, **C₉₆tBu₈**, **C₁₁₄tBu₁₀**, and **C₁₃₂tBu₁₂**. Potential values are reported vs. Fc⁺/Fc.

GQD	$E_{1/2, ox1}$ (V)	$E_{1/2, ox2}$ (V)	$E_{ox, onset}$ (V)	$E_{red, onset}$ (V)	$E_{ec, HOMO}$ (eV)	$E_{ec, LUMO}$ (eV)	$E_{ec, gap}$ (eV)
C₇₈tBu₆	0.055	0.2845	-0.064	-1.514	-4.74	-3.29	1.45
C₉₆tBu₈	0.132	0.421	0.045	-1.812	-4.85	-2.99	1.86
C₁₁₄tBu₁₀	0.078	0.335	-0.016	-1.619	-4.78	-3.13	1.65
C₁₃₂tBu₁₂	0.062	0.287	-0.031	-1.646	-4.77	-3.15	1.62

Following the same treatment as described in **Section 2.3.2**, we obtain the values reported in **Table 5**. We can discern a trend in the position of the first oxidation wave. **C₉₆tBu₈** has the highest half-wave potential and then in order of increasing size this potential diminishes. One would expect for **C₇₈tBu₆** to exhibit a higher value since it is the smaller member of the family and therefore should possess a larger band gap. Nonetheless, **C₇₈tBu₆** exhibits the lowest half wave potential for the first oxidation.

A similar trend is observed for the electrochemical band gap. We can attribute this strange behavior of the nanoparticle to the presence of aggregates on the sample that modify the electrochemical properties.

THEORETICAL STUDIES: THE SOLUBILITY OF THE C₇₈ GQD

C₇₈tBu₆ exhibits a different behavior as the other members of the rod-shaped family. In the mass spectra we observe a dimer peak, the ¹H NMR spectrum possess unattributed broad signals, the electrochemical behavior is different, and, as we will see later, the optical properties of this nanoparticle also differ from the rest of the family. All these observations suggest that C₇₈tBu₆ aggregates in solution. To better understand the aggregation process of the small member of the rod-shaped family, we turned again to theoretical descriptions. In C₇₈tBu₆, the central *tert*-butyl groups can be either up or down with respect to the molecule's aromatic plane. Two conformers U-U and U-D are possible (Table 6).

Table 6 | Theoretical values of relative energy and relative abundance of the two possible conformers of C₇₈tBu₆. The relative energies are reported considering the U-U as point of reference. Relative abundance was calculated at room temperature.

Conformer	U-U	U-D
$\Delta E_{\text{conformers}}$ (eV)	0.000	0.008
Abundance @298 K	0.5785	0.4215

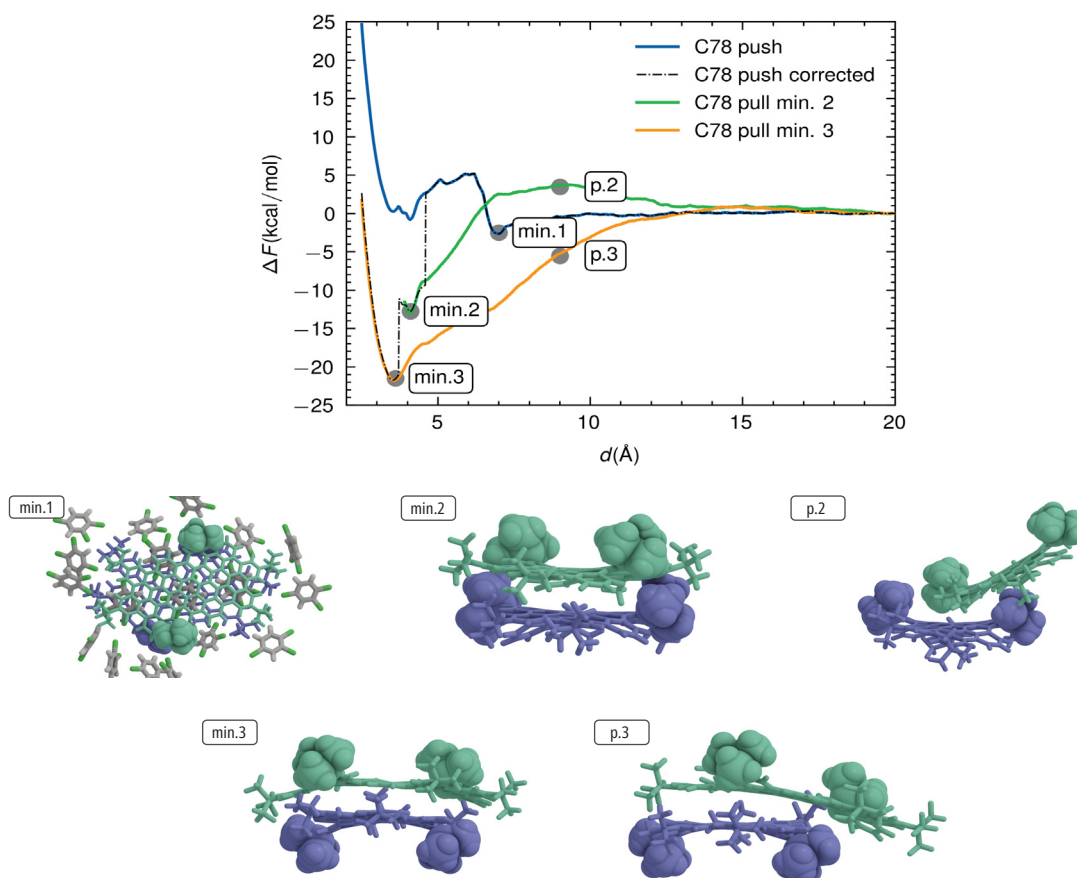


Figure 2.38 | Potential of mean force curve of C₇₈tBu₆. Variation of the free energy as a function of distance between the center of mass of two GQDs. Five different illustrations of the dimer conformations at the different points along the curves. For clarity, only the central *tert*-butyl groups are represented as Van der Waals spheres.

Push-pull experiments were carried out by Dr. Nicolas Rolland and Prof. David Beljonne. The potential of mean force for the distance between the centre of mass of two GQDs is presented in **Figure 2.38**. In the push curve, three minimums were identified. The first one (min1) corresponds to a scenario where two nanoparticles are separated by a solvent layer. A second minimum (min2) represents a dimer where two nanoparticles face each other at 4 Å. For this dimer, one molecule has its *tert*-butyl group facing inwards, while the other is facing outwards. A third minimum (min3) is observed for a dimer where both nanoparticles have their *tert*-butyl groups facing outwards. When performing the pull experiments from min2 or min3, no significant potential barrier is observed, suggesting that aggregation is favourable process.

With regards to **C₇₈tBu₆**, both conformers can exist in solution (see **Table 6**). Consequently, during the association process, two nanoparticles can interact such that at least on one side of the forming dimer their *tert*-butyl groups point outward. This constitutes an entry point to the formation of min3, for which no significant energy barrier was observed. The absence of more than one adjacent *tert*-butyl groups along the main axis allows the aggregation of nanoparticles.

2.4.3 OPTICAL STUDIES

Let's now turn our attention the optical behavior of these new members of the rod-shaped family of graphene quantum dots. So far, **C₇₈tBu₆** has demonstrated distinct behavior compared to the rest of the GQDs. The differences observed appear to originate from a lower solubility of the nanoparticle. For instance, the mass spectra displayed a peak that could be attributed to a dimer structure, and the NMR spectrum revealed broad peaks that could originate from aggregation. None of these observations were made for the larger members of the rod-shaped family, who despite their large size remain highly soluble. Additionally, theoretical studies indicated that **C₇₈tBu₆** has a propensity to aggregate due to the lack of adjacent *tert*-butyl groups. Consequently, the optical behavior of **C₇₈tBu₆** is impacted by its intrinsic lower solubility. Therefore, we will discuss its optical properties separately.

C₇₈tBu₆

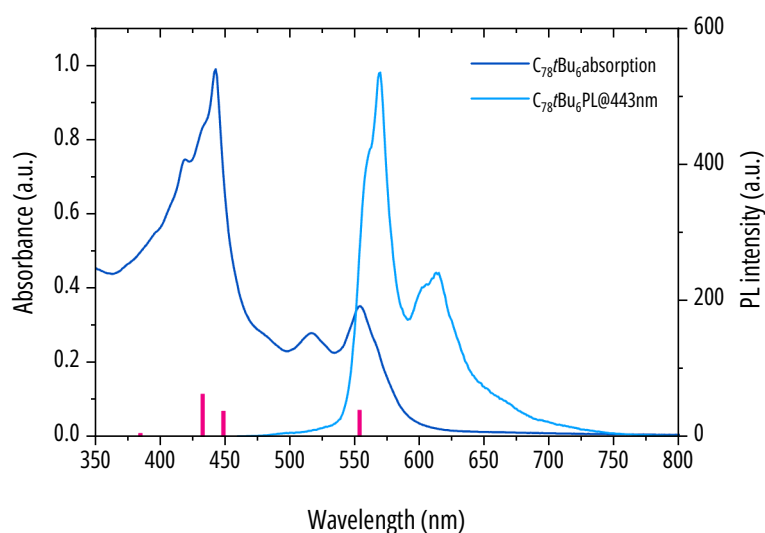


Figure 2.39 | Absorption and emission spectra of **C₇₈tBu₆** in TCB. Excitation at 443 nm. Pink lines show the theoretical electronic transitions for the **C₇₈tBu₆** monomer.

The absorption and emission spectra of $C_{78}tBu_6$ in 1,2,4-trichlorobenzene are presented in **Figure 2.39**. The absorption spectrum exhibits a maximum at 443 nm. We can identify two sets of band progressions: the first spanning from 474 nm to 555 nm, and the second from 375 nm to 443 nm. However, it appears to be a loss of resolution from the one observed for $C_{96}tBu_8$.

The photoluminescence spectrum exhibits a main emission peak at 570 nm. Adjacent to this maximum, a shoulder of a secondary peak can be distinguished at lower wavelengths. A separate set of two peaks is apparent at 614 nm. Above 625 nm, there is a broad tail. This emission contrasts with the one observed for $C_{96}tBu_8$, where three distinct bands were present. We can clearly observe an effect of aggregation on the optical properties: an absorption spectrum with broader peaks and an emission spectrum with multiple peaks. The quantum yield diminishes to lower values of 78%, nevertheless, the nanoparticle remains highly fluorescent.

To determine whether all the emission peaks originate from the same source, excitation experiments were conducted at the five wavelengths corresponding to the peaks in the emission spectrum (561 nm, 570 nm, 603 nm, 614 nm, and 662 nm). The photoluminescence excitation (PLE) spectra are displayed in **Figure 2.40a**. It is possible to distinguish three different types of PLE spectra. The first one is observed for the two peaks at shorter wavelengths, 561 nm and 570 nm. The PLE spectrum mirrors the absorption pattern of $C_{78}tBu_6$. At the longest wavelength, 662 nm, the PLE spectrum is extremely broad, obscuring all definition of the peaks around 400 nm, and the peaks at longer wavelengths appear to undergo a slight bathochromic shift. The pair of emission peaks at 603 nm and 614 nm exhibits an intermediate behavior. Regardless, the PLE spectra do not perfectly overlap with the absorption spectrum, implying that the absorption spectrum may be the result of multiple emissive sources.

To gain a better insight to the nature of the origin of the emission peaks, we performed time-resolved experiments. The spectra of the TR-PL experiments were measured at the same wavelengths that the PLE experiments is presented in **Figure 2.40b**. We can observe a matching behavior to the PLE. The first pair of peaks exhibit a similar decay, different from the one of the second pair of peaks. For the five peaks, the decay can be described by a double exponential. The fitting yielded two lifetime values, a short lifetime of ~4.5 ns and a longer lifetime of ~12-18 ns.

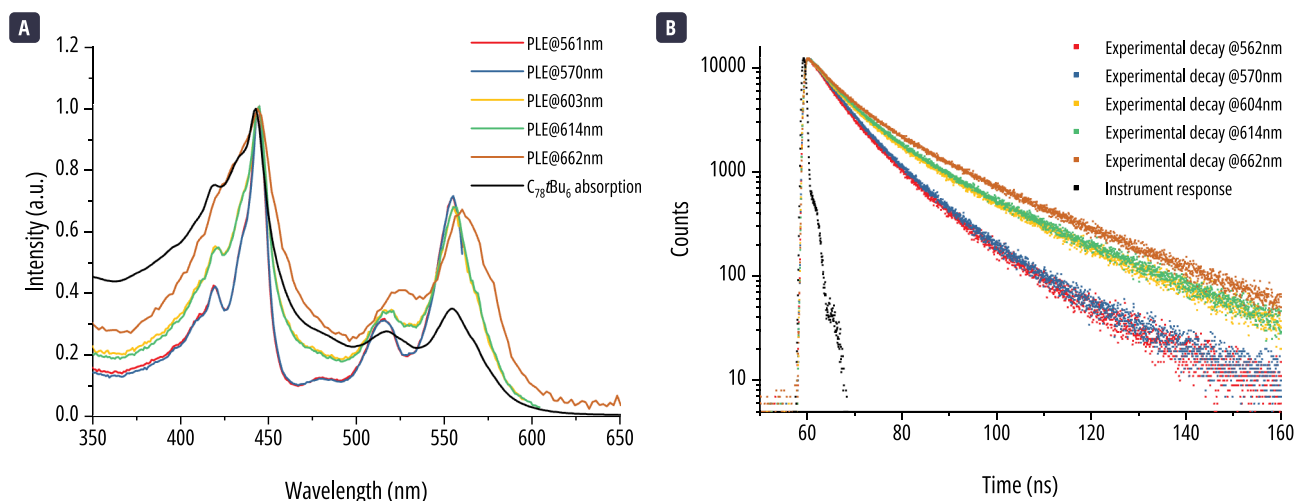


Figure 2.40 | Photoluminescence excitation and time resolved spectra for $C_{78}tBu_6$. **(a)** PLE spectra of $C_{78}tBu_6$ in TCB at five emission wavelengths. **(b)** Time-resolved fluorescence spectra in TCB at the same five wavelengths.

To confirm the presence of aggregates, experiments were conducted at varying concentrations. As can be seen in **Figure 2.41a**, when the concentration diminishes, the absorption spectrum gains in resolution. Furthermore, the solubility of this small

GQD seems to be significantly influenced by the choice of solvent (**Figure 2.41b-c**). The absorption and emission spectra in common organic solvents such as toluene, tetrahydrofuran, and dichloromethane vary greatly from those recorded in TCB. In these solvents, the resolution in the 375 nm – 450 nm region is significantly reduced, with only two distinguishable shoulders. The emission spectra also exhibit a notable contrast between these alternative solvents and TCB. The peaks at longer wavelengths become more prominent, and the resolution is lost in the PL spectrum.

The PLE spectra in these alternative solvents can give us some information on the absorption and emission of the aggregates. We will now exclusively focus on toluene since tetrahydrofuran and dichloromethane give similar results (**Figure 2.41d**). The PLE spectrum recorded for a wavelength at the beginning of the emission peak (555nm) gives a well-resolved spectrum, similar to the one observed in TCB at shorter wavelengths. The PLE at higher wavelengths gives a broad spectrum, alike to the absorption spectrum. Additionally, this broad spectrum resembles to the PLE spectrum obtained at the longer wavelength (662 nm) in TCB. The aggregates for this nanoparticle seem to have a red shift in the emission compared to the monomer.

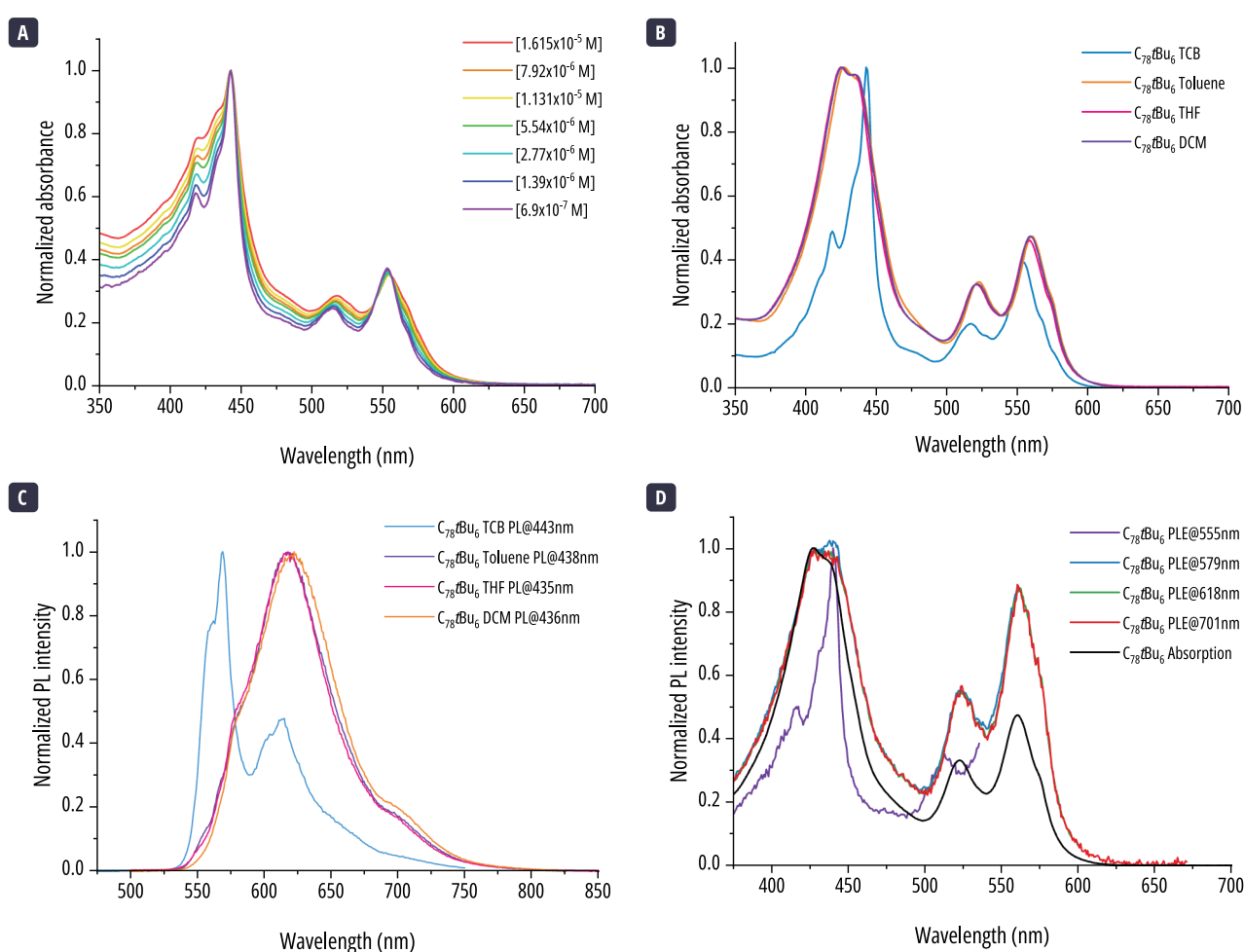


Figure 2.41 | (a) Absorption spectra of $C_{78}tBu_6$ in TCB at different concentrations. (b) Absorption spectra of $C_{78}tBu_6$ in TCB, toluene, THF and CH_2Cl_2 . (c) Emission spectra of $C_{78}tBu_6$ in TCB, toluene, THF and CH_2Cl_2 . (d) PLE spectra of $C_{78}tBu_6$ in toluene at four different emission wavelengths.

All these observations seem to agree that $C_{78}tBu_6$ aggregates in solution. In TCB, the monomers coexist with other species, such as dimers or higher aggregates. In other solvents, the aggregates seem to predominate in solution. These aggregates seem to experience a bathochromic shift in the absorption in the 500 nm – 600 nm region, and a red shifted emission in comparison to the monomer. As an additional remark, the NMR data indicates that the monomer is predominant in CS_2 even at

high concentrations ($\sim 10^{-4}$ M). However, overtime, a precipitate began to deposit on the bottom of the NMR tube. Optical experiments in CS_2 , where much lower concentrations are needed, could help determine the optical properties of the monomer. These experiments are yet to be done since sealed cuvettes are needed to work with CS_2 .

THE LARGE MEMBERS OF THE FAMILY: $C_{114}tBu_{10}$ AND $C_{132}tBu_{12}$

In contrast to $C_{78}tBu_6$, for $C_{114}tBu_{10}$, and $C_{132}tBu_{12}$ we recover a well-defined spectrum very similar to the one described for $C_{96}tBu_8$. Their corresponding absorption and emission spectra are given in **Figure 2.42** for $C_{114}tBu_{10}$, and **Figure 2.43** for $C_{132}tBu_{12}$. In the absorption spectrum we recover a similar progression to the one described for $C_{96}tBu_8$, where we distinguish the electronic transitions and their vibrational progressions. Their emission spectra exhibit two distinguishable peaks, and in the case of $C_{114}tBu_{10}$ we can discern a third peak. For both nanoparticles we still find a good agreement between the theoretical prediction and the experimental (see bars below the absorption spectrum). In both cases, the emission can be attributed to the 0-0 transition and their vibronic replicas for the C=C stretching. The fluorescence quantum yields were calculated using an integration sphere: it is 91% for $C_{114}tBu_{10}$ and 88% for $C_{132}tBu_{12}$. These are excellent values, considering the nanoparticles emit in the red region of the electromagnetic spectrum.

Despite the large size of these GQDs, the nanoparticles remain highly individualized in solution at the dilute concentrations needed for optics experiments. We recover similar features to the ones observed for $C_{96}tBu_8$: perfect matching between the absorption and excitation spectra for all emission peaks, no dependence of the absorption spectrum to concentration, high quantum yields, and monoexponential lifetimes. Their solubility remains very high in other organic solvents with similar line shapes and a slight solvatochromic effect with a blue shift with respect to TCB.

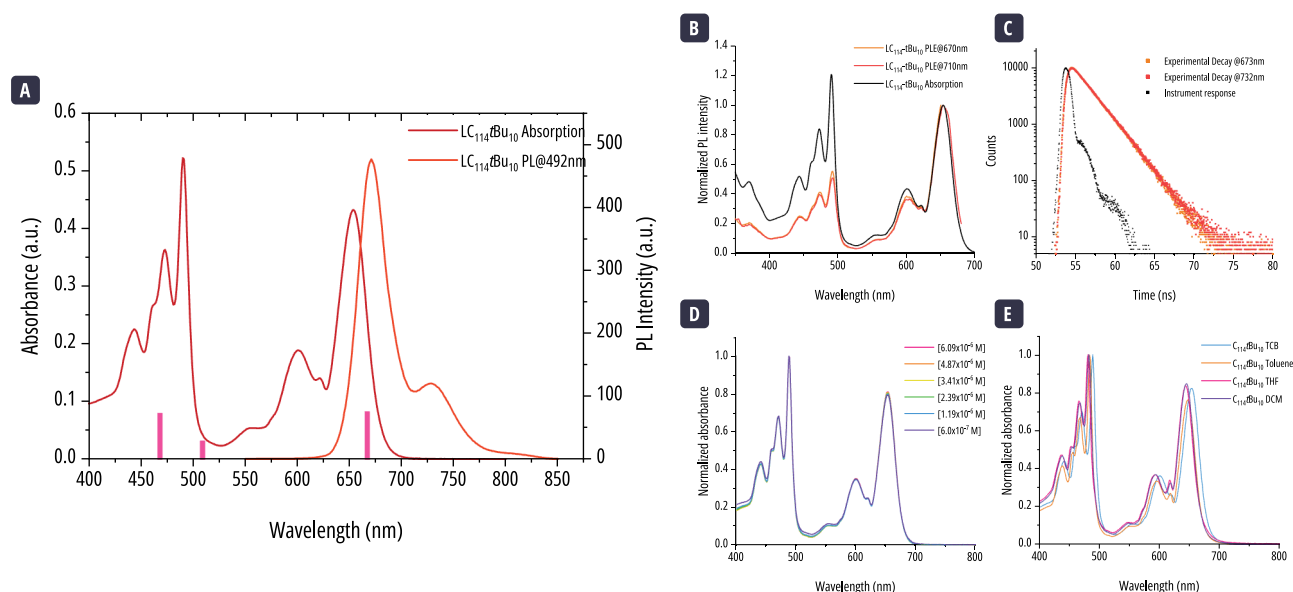


Figure 2.42 | Optical properties of $C_{114}tBu_{10}$. **(a)** Absorption and emission spectra in TCB. Pink bars represent the theoretical electronic transitions, their height is proportional to their oscillator strengths. **(b)** PLE spectra at the two main wavelengths of emission. **(c)** Time resolved fluoresce spectra at the same two wavelengths of excitation. **(d)** Concentration dependant absorption spectra. **(e)** Absorption spectra in TCB, toluene, tetrahydrofuran, dichloromethane.

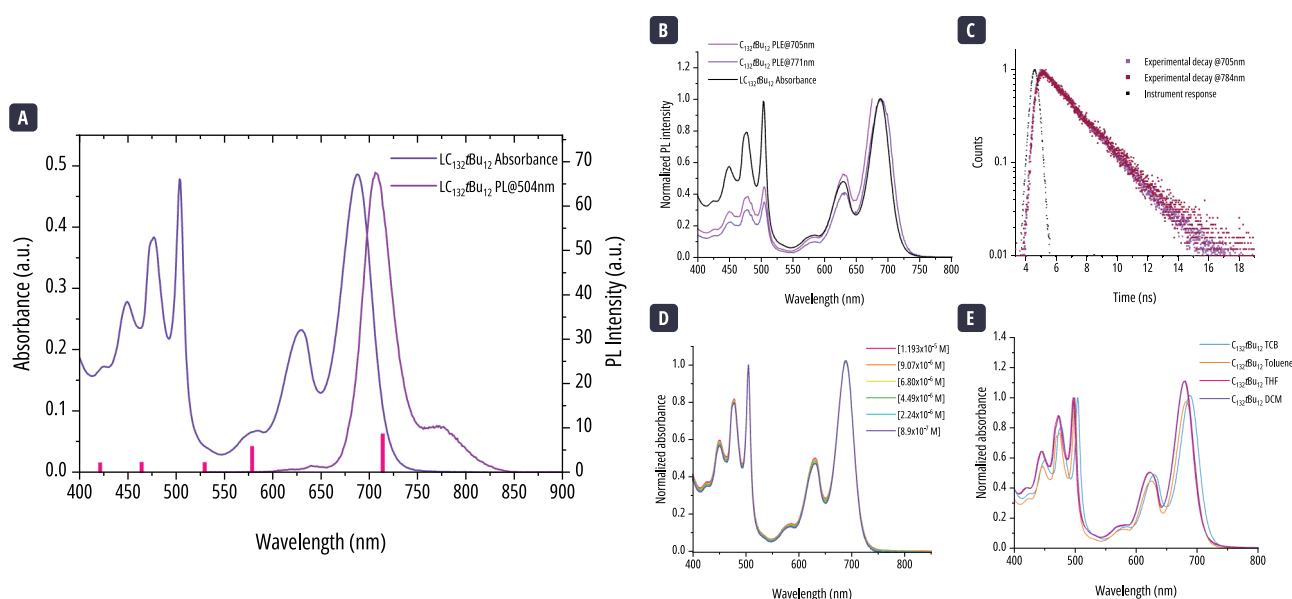


Figure 2.43 | Optical properties of $C_{132}tBu_{12}$. (a) Absorption and emission spectra in TCB. Pink bars represent the theoretical electronic transitions, their height is proportional to their oscillator strengths. (b) PLE spectra at the two main wavelengths of emission. (c) Time-resolved fluorescence spectra at the main emission peak. (d) Concentration-dependent absorption spectra. (e) Absorption spectra in TCB, toluene, tetrahydrofuran, dichloromethane.

COMPARISON OF ALL THE ROD-SHAPED FAMILY

If we compare the optical properties of the four members, it is possible to gain additional insight into their behavior as a family. The absorption and emission spectra of the four GQDs are given in **Figure 2.44**. As can be expected, the first observation is the red shift of the emission as the size of the GQD increases. The wavelength of the lowest transition is 558 nm for $C_{78}tBu_6$ and 668 nm for $C_{132}tBu_{12}$. We can tune the absorption and emission of the GQDs over a range of 110 nm by changing their size.

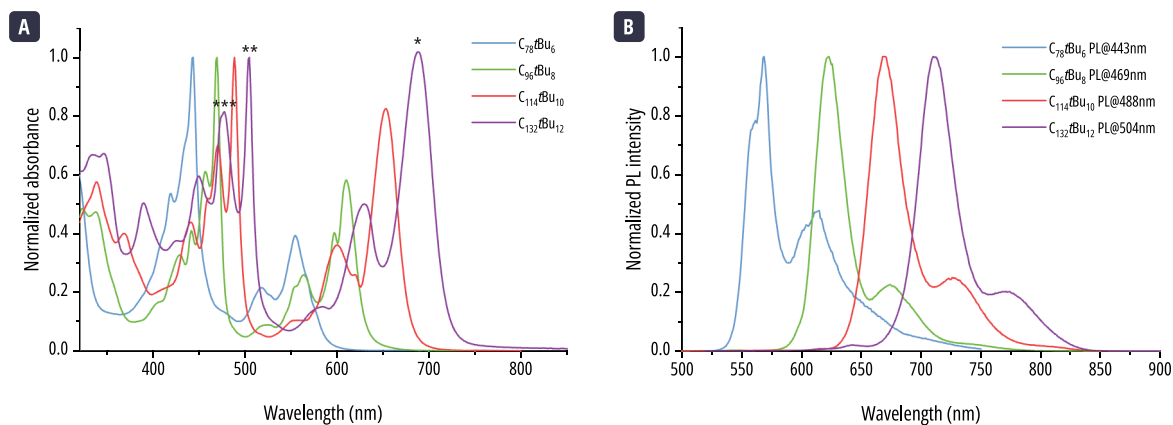


Figure 2.44 | Comparison of the (a) absorption and (b) emission of $C_{78}tBu_6$, $C_{96}tBu_8$, $C_{114}tBu_{10}$, and $C_{132}tBu_{12}$ in TCB. The asterisks (*) indicate the first, second, and third bright electronic transitions for $C_{132}tBu_{12}$.

If we examine the absorption spectrum in greater detail, we can observe that the intensity of the first electronic transition (marked with a “*” in the $C_{132}tBu_{12}$ absorption spectrum) increases relative to the intensity of the second bright electronic transition (marked with “**”). A similar trend can be observed between the third bright electronic transition (marked with “***”) and the second electronic transition. This is because, as with $C_{96}tBu_8$, the charge density of the first electronic transition is distributed along the longitudinal axis, the second transition along the transverse axis, and the third transition is again along the longitudinal axis of the nanoparticle. As the nanoparticle increases in size, also does the longitudinal axis, whereas

the transverse axis remains constant. Therefore, the intensity of the transitions along the longitudinal axis increases with size, while the intensity of the transverse transition remains constant.

2.5 TOWARDS THE FIRST APPLICATIONS

Light-emitting diodes (LEDs) are a device that emits light when a current flows through it. The basic architecture is an emissive material sandwiched between two electrodes. When the emissive material is an organic molecule, the device is more precisely named an organic light-emitting diode (OLED). This molecule requires a high luminescence quantum yield in the solid state, good carrier mobility, chemical stability, and color purity.²²⁰ GQDs synthesized in an organic chemistry fashion are promising candidates as emissive materials.

First advances in the integration of hydroxylated GQDs, synthesized via a solvothermal approach, into a photoluminescent device were recently reported by Yuan *et al.*²²¹ To date, there have been no reports of OLED devices fabricated with bottom-up synthesized graphene quantum dots with well-defined structures. The interesting results for the rod-shaped family of GQD described throughout this chapter encouraged us to test them as emissive materials. The most interesting properties to be exploited for this application are their high quantum yields and the possibility to tune the emission wavelength. Indeed, by altering the number of sp^2 carbon atoms in the GQD structure, we were able to adjust the emission wavelengths across a range of 200 nm. Moreover, all four members of the family showed high quantum yields, notably **C₉₆tBu₈**, which demonstrated a quantum yield in solution of 94%. On top of this, the GQDs also have high chemical stability, good photostability, and narrow emissions.

The efficiency of an OLED is characterized by its external quantum efficiency (EQE), that is, the number of emitted photons per injected charges. This quantum efficiency is related to the probability of charge recombination in the organic material, the fluorescence quantum yield, and the number of emitted photons that can escape the device. A combination of these parameters restricts the EQE of conventional fluorescent OLEDs to 5%.²²⁰

The OLED devices were fabricated and characterized by Dr. Fabien Lucas at Laboratoire de Physique des Interfaces et des Couches Minces (LPICM) in École Polytechnique using a conventional device architecture. In **Figure 2.45** a schematic representation of the device architecture is given. The structure is composed of an anode, a hole injection layer, an emissive layer, a hole blocking layer, an electron transport layer, and a cathode. Indium tin oxide (ITO) is used as the transparent anode. The hole injection layer contains poly(3,4-ethylenedioxythiophene) polystyrene sulfonate (PEDOT:PSS). The emissive layer is composed of polyvinylcarbazole (PVK) as a hole transporter, 1,3-bis[2-(4-*tert*-butylphenyl)-1,3,4-oxadiazol-5-yl]benzene (OXD-7) as an electron transporter, and the emissive GQD. The hole blocking layer is composed of bathocuproine (BCP). The electron transport layer is composed of 1,3,5-Tris(3-pyridyl-3-phenyl)benzene (TmPyPB). Finally, a Li/Al cathode is used. The anode, the hole injection layer, and the emissive layer were deposited by spin coating. The other layers were deposited under vacuum.

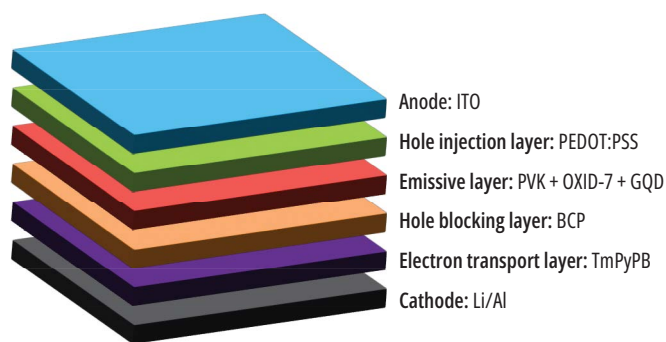


Figure 2.45 | Schematic representation of the OLED device architecture.

We chose to test only **C₇₈tBu₆** and **C₉₆tBu₈** as the emissive material, mainly due to synthetic considerations. Indeed, multiple milligrams of products were required for the tests, and these two GQDs could be more easily synthesized in larger quantities due to fewer reactional steps involved. The characterizations of the OLEDs are given in **Figure 2.46**.

The device built with **C₇₈tBu₆** revealed a discrepancy between the electroluminescence (EL) spectrum and the photoluminescence spectrum in a TCB solution. The EC was broadened, the peak resolution was lost, and the maximum emission was red shifted by 50 nm. This pattern mirrored our comparison of optical studies between TCB and toluene, dichloromethane, and THF, where we attributed the observed difference to the aggregation of the GQD. The OLED containing **C₇₈tBu₆** had a maximum quantum efficiency of 1.36%, which although low, is close to the 5% theoretical maximum for a fluorescent OLED. The required voltage (V_{on}) to produce brightness was 7.3 V. The maximum luminance was 9.16 cd.m⁻², and the current efficiency was 0.28 cd.A⁻¹. The OLED emitted red light.

Turning our attention to the OLED using **C₉₆tBu₈** as an emissive material, the EL and PL spectra showed better alignment. A red shift of 15 nm in the EL spectrum was noted. We were able to discern the vibronic coupling in the emission peaks. However, the EL spectrum was considerably broader than the PL spectrum in solution. This broadening might be a result of the new environment, although no evidence of this was observed during single-molecule studies of PL in a polymer matrix. The EQE of the OLED was 0.85%. The maximum luminance was 209.16 cd.m⁻², and the current efficiency was 0.11 cd.A⁻¹. The V_{on} voltage was notably higher, at 15 V. This OLED emitted deeper red light.

Although the performances are far from state-of-the-art, we achieved a proof-of-concept. Well-defined graphene quantum dot structures can be used to fabricate organic light-emitting diodes. The high V_{on} voltages indicate that the interfaces need to be saturated before injecting charges into the GQD. This could be improved by using other fabrication techniques such as evaporation of the emissive molecule instead of spin coating. However, the evaporation of large molecules can be challenging due to the high temperatures required, which may not be tolerated by an organic molecule. Further studies into the thermal stability of GQDs are necessary before proceeding with this approach. Alternatively, synthesizing smaller GQDs, which would more readily sublime, can be considered. To improve the external quantum efficiency, new architectures such as hyperfluorescent OLEDs could be envisioned.²²² A thermally activated delayed fluorescence (TADF) can be employed to recover the triplet excitons, which constitute 75% of the excitons lost in fluorescent OLEDs and transfer them to the emissive material.

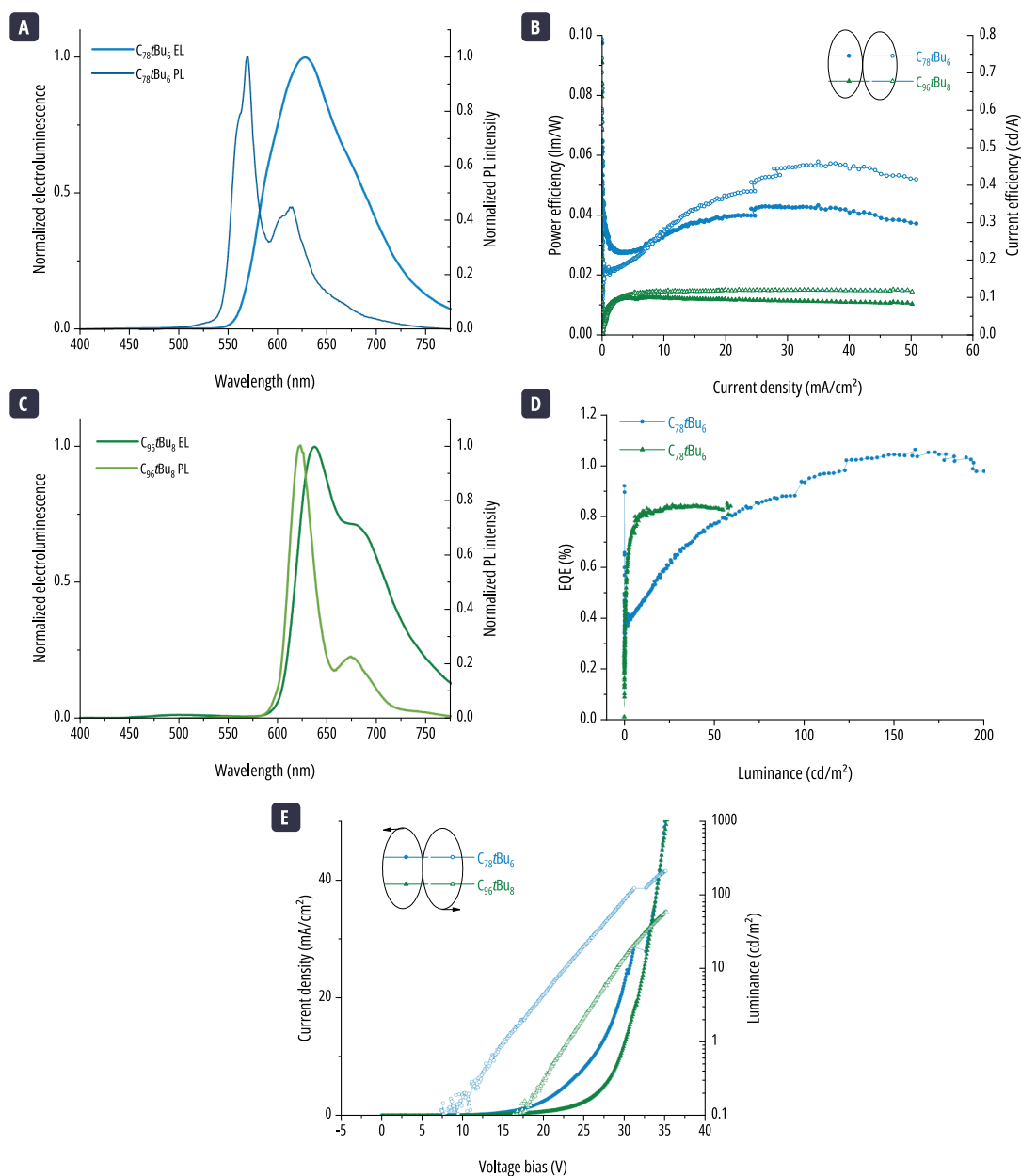


Figure 2.46 | Characteristics of OLEDs based on $C_{78}tBu_6$ and $C_{96}tBu_8$ 10 wt% doped. **(a)** Electroluminescence spectrum and photoluminescence spectrum of $C_{78}tBu_6$. **(b)** Power and current efficiencies as function of the current density. **(c)** Electroluminescence spectrum and photoluminescence spectrum of $C_{96}tBu_8$. **(d)** EQE as function of the luminance. **(e)** Luminance-current-voltage characteristics.

2.6 CONCLUSION

Throughout this chapter, we showed the synthesis, chemical and optical characterizations of a family of rod-shaped GQDs. The four members of this family contain *tert*-butyl groups to help with solubilization which is a challenge in these graphenic materials. The presence of *tert*-butyl groups enhances the oxidation reaction and allows for complete cyclization of the nanoparticle despite the steric hindrance caused by the adjacent groups. The presence of adjacent *tert*-butyl groups along the main axis of the nanoparticle confers an unprecedented solubility. Consequently, we were able to perform purification to get rid of the byproducts of the Scholl reaction and obtained highly pure samples. Additionally, this enhanced solubility allowed us to

perform further characterizations not common for GQDs with such a large size. In this way, we were able to confirm the structure of the GQDs by NMR spectroscopy, which is highly soluble even at high concentrations.

The high solubility and purity of the nanoparticles allowed us to perform advanced optical studies which also suggested that the molecules are well individualized in solution. In collaboration with theoreticians, it was possible to determine the electronic transitions in the absorption spectrum. Additionally, the high resolution of the absorption and emission spectrum enable the identification of vibronic replicas associated to the transitions. These attributions were further confirmed by anisotropy experiments. Studies at the single level confirmed that the observed emission in solution originates from individualized GQDs. Because of the symmetry, the allowed $S_1 \rightarrow S_0$ transition, the rigidity of the nanoparticle, and the high individualisation in solution, extraordinarily high quantum yields up to 94% were obtained. This work was accepted for publication in Nature Communications.²²³

These interesting optical properties observed for the rod-shape family make the GQDs excellent candidates for applications as emitters. First applications in OLED were tested, a first time for such synthesized objects. The performances of the fabricated devices are not as efficient as other examples in the literature, but this constitutes a proof-of-concept.

Finally, calculations showed that the presence of adjacent *tert*-butyl groups are responsible of the good solubility of the GQDs. The smallest member of the family only has a single group along the nanoparticle's main axis. Thus, its solubility is compromised and exhibits differences in the optical properties compared to the rest of the family. However, when adjacent groups are present along the main axis of the nanoparticles, even large nanoparticles containing as much as 132 sp^2 carbon remain well solubilized. To increase their solubility even more, we can try to add additional *tert*-butyl groups all around the GQD. This new family nanoparticles will be the object of the next chapter.

Chapter 3 TOWARDS MORE SOLUBLE QDs

CONTENTS

3.1	Fully <i>tert</i> -butylated rod-shape QDs.....	87
3.1.1	Synthesis.....	88
3.1.2	Characterizations.....	92
3.1.3	Optical properties.....	96
3.2	Twisted nanographenes.....	102
3.2.1	C ₉₆ based triple [6]helicenes.....	103
3.2.2	GQD propeller.....	113
3.3	Conclusion.....	121

CHAPTER 3 TOWARDS MORE SOLUBLE GRAPHENE QUANTUM DOTS

The processability of graphene quantum dots is highly dependent on their solubility. As demonstrated in the previous chapter, the addition bulky functional groups at the edges of the sp^2 domain significantly increases the solubility of GQDs. For the family of nanoparticles previously discussed, the effect is more pronounced when more than one functional group is positioned adjacently along the main axis of the rod-shaped GQD. In an attempt to further increase the solubility of GQDs, we decided to add *tert*-butyl groups around the entire edges of the rod-shaped family. Additionally, to synthesize even more soluble GQDs, their two-dimensional character can be disrupted to diminish the π -stacking interactions.

In this chapter, we will discuss these two distinct approaches to improving the solubility of GQDs. First, we will examine the synthesis of rod-shaped GQDs with additional *tert*-butyl groups along the main axis of the nanoparticle. Then, we will discuss the synthesis of twisted nanographene structures

3.1 FULLY *TERT*-BUTYLATED ROD-SHAPE GQDs

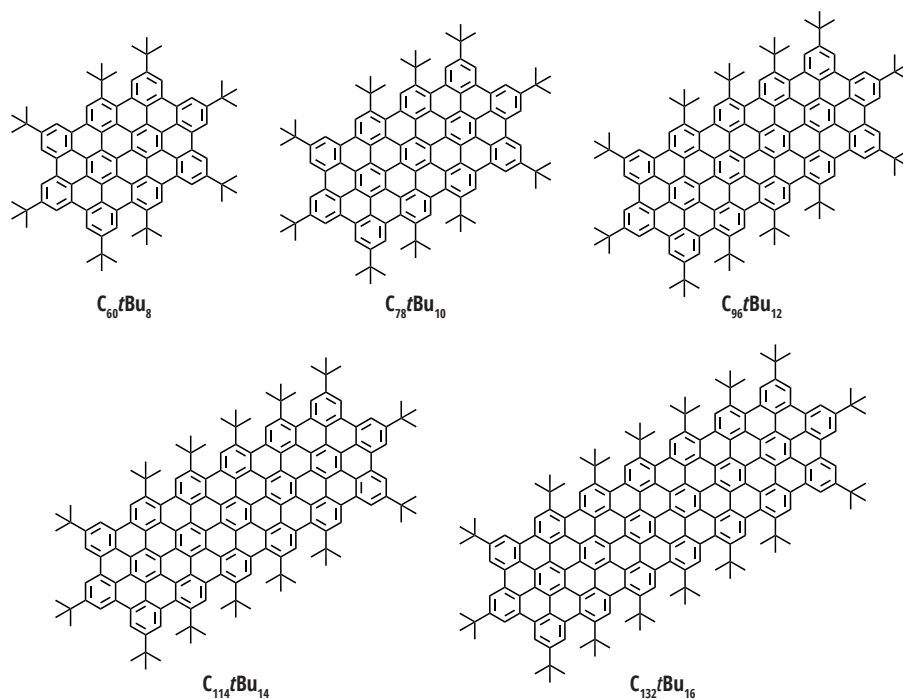


Figure 3.1 | Structure of the five members of the fully *tert*-butylated rod-shaped GQDs family.

In the previous chapter, we presented a family of rod-shaped graphene quantum dots that exhibited high solubility and remained individualized in solution. While the larger members of the GQD family remained highly soluble in common organic solvents, the smallest member, containing 78 sp^2 carbon atoms, showed an aggregation tendency. This was somewhat counterintuitive at first glance since smaller GQDs tend to be more soluble than their larger counterparts. Upon further experimental observations and theoretical descriptions, this lower solubility was attributed to the lack of adjacent bulky *tert*-butyl groups along the main axis of the nanoparticle. To address this problem, we decided to add additional *tert*-butyl groups along

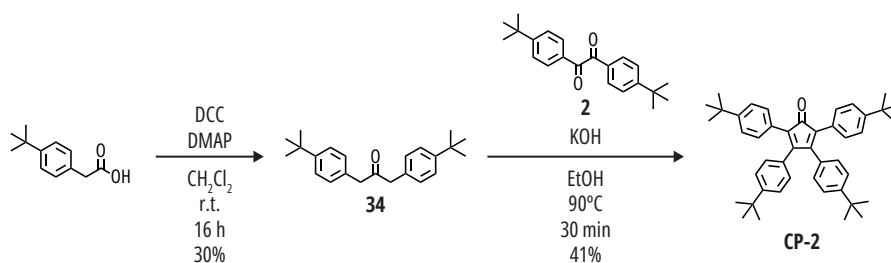
the long axis of the GQDs, given in **Figure 3.1**. In this section, we will discuss the synthesis of five new rod-shaped GQDs, their characterization, and a brief discussion about their optical properties. These five nanoparticles range from 60 sp^2 to 132 sp^2 carbon atoms.

3.1.1 SYNTHESIS

DENDRIMERS SYNTHESIS

The synthesis of the fully *tert*-butylated dendrimers proceeds in a similar fashion as their partially *tert*-butylated homologues (Chapter 2): an alkyne core is reacted with a cyclopentadienone. For **C₇₈tBu₁₀**, **C₉₆tBu₁₂**, **C₁₁₄tBu₁₄**, and **C₁₃₂tBu₁₆**, the alkyne cores are the same as for their homologues, and the extra *tert*-butyl groups are added to the structure through a new cyclopentadienone. The new, smaller member of the family, **C₆₀tBu₈**, has a different synthetic route but also relies on the fully *tert*-butylated cyclopentadienone **CP-2** and a butadiyne derivative.

As highlighted before, the most important new element is the tetra-*tert*-butyl substituted tetraphenylcyclopentadienone **CP-2**, which introduces the new functional groups to the structure. Compared to **CP-1**, the new cyclopentadienone contains two additional *tert*-butyl groups, one on each of the unsubstituted phenyl groups. The synthetic strategy to **CP-2** is summarized in **Scheme 3.1**. 1,3-bis(4-(*tert*-butyl)phenyl)propan-2-one **34** was synthesized according to literature protocols.^{205,224} The commercially available 4-*tert*-butylphenylacetic acid is self-condensed in the presence of 4-(dimethylamino)pyridine (DMAP) and N,N'-Dicyclohexylcarbodiimide (DCC) to give the 1,3-bis(4-(*tert*-butyl)phenyl)propan-2-one **34**. Although the same reaction reported in the literature proceeds with high yields, we observed much more modest yields for this step. Ketone **34** is then reacted through a Knoevenagel condensation to the previously synthesized disubstituted dione **2** to yield the target cyclopentadienone **CP-2**.

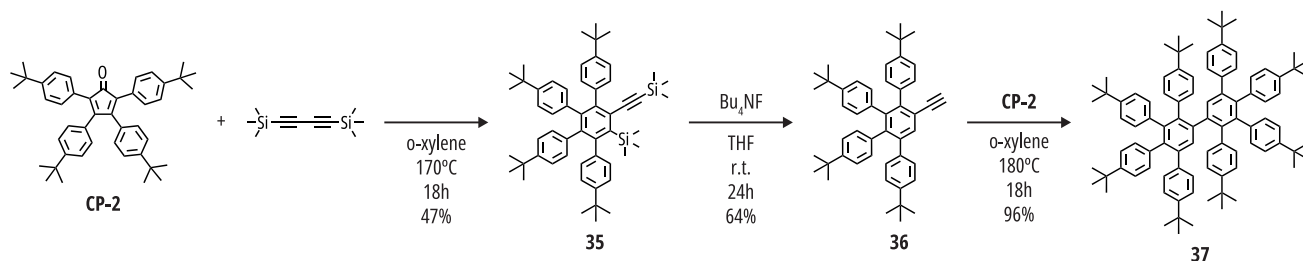


Scheme 3.1 | Synthetic route to the tetra-*tert*-butyl substituted tetraphenylcyclopentadienone **CP-2**.

With this cyclopentadienone, it is now possible to synthesize the new dendrimers. First, let's discuss the synthesis of the dendrimer necessary for **C₆₀tBu₈**, whose synthetic strategy differs slightly from the previously described method involving terphenyl precursors. This synthesis is inspired by the reported synthesis of a similar unsubstituted and alkyl substituted GQD with 60 sp^2 carbon atoms by Iyer *et al.*⁷⁷ The synthetic procedure is summarized in **Scheme 3.2**.

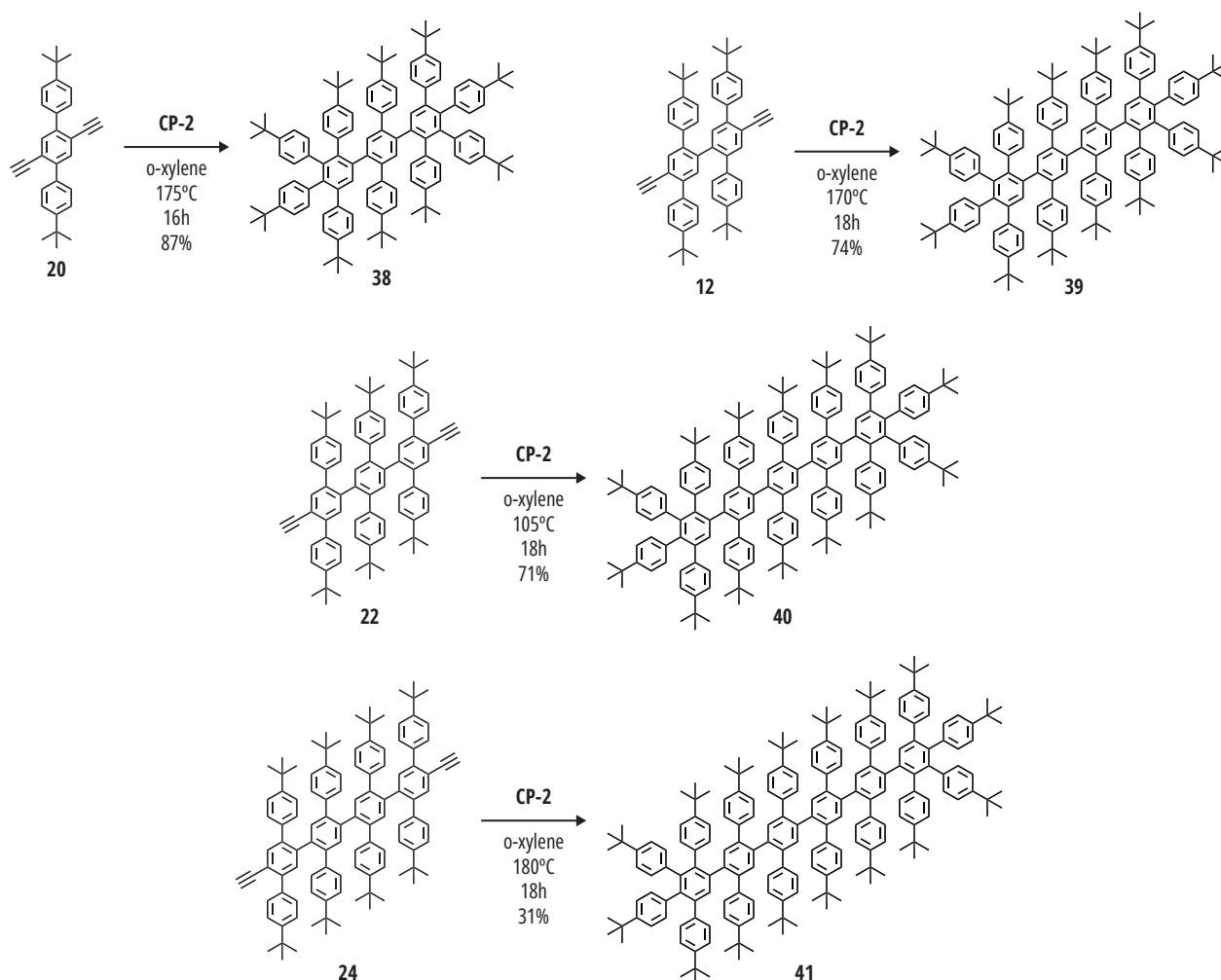
In the first step, the cyclopentadienone **CP-2** is reacted with the commercially available 1,4-bis(trimethylsilyl)butadiyne through a Diels-Alder reaction to obtain the protected alkyne-substituted tetraphenylbenzene **35**. This intermediate is too crowded and does not undergo further reaction with the cyclopentadienone. The trimethylsilyl (TMS) groups in product **35** are removed in the presence of tetrabutylammonium fluoride 1M in THF, to give the deprotected intermediate **36**. Despite the long reaction times at this step, the TMS group attached to the phenyl ring is not easily removed. The target product **36** is formed along

with the mono-deprotected product. Although this mono-deprotected product can undergo the following Diels-Alder reaction, an additional step of deprotection at higher temperatures would be necessary. To avoid this additional step, only the fully deprotected product **36** was used for the following step after purification. Dendrimer **37** was obtained upon exposing intermediate **36** with the cyclopentadienone **CP-2**.



Scheme 3.2 | Synthetic route to dendrimer **37**.

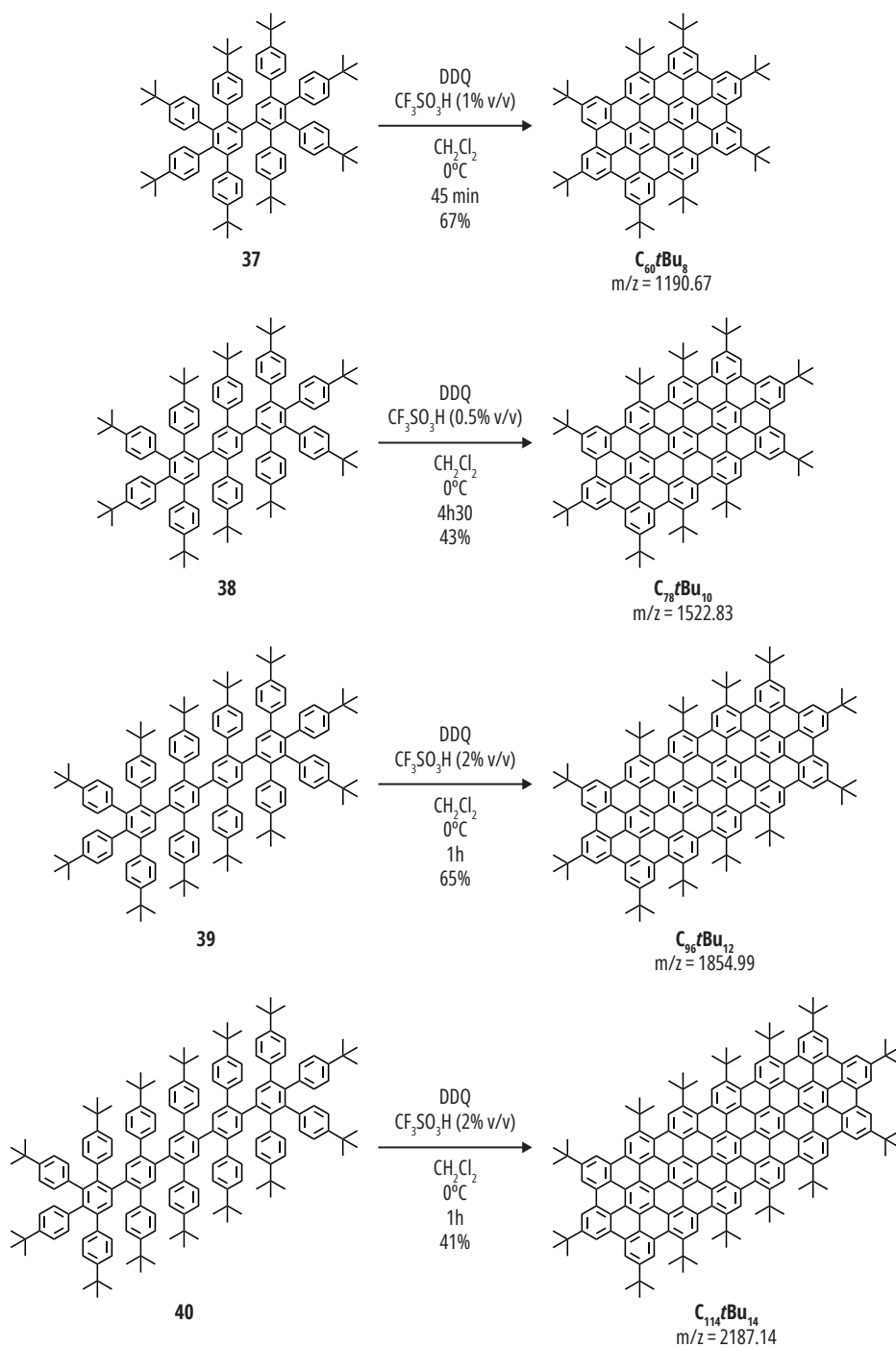
The synthesis of dendrimers **38**, **39**, **40**, and **41**, which correspond to the precursors necessary for the synthesis of $C_{78}tBu_{10}$, $C_{96}tBu_{12}$, $C_{114}tBu_{14}$, and $C_{132}tBu_{16}$ respectively, is conducted using the terphenyl cores described in Chapter 2. The Diels-Alder reaction between the terphenyl cores **20**, **12**, **22**, and **24**, and cyclopentadienone **CP-2** produces dendrimers **38**, **39**, **40**, and **41**, respectively. The specific conditions for the synthesis of each dendrimer are summarized in **Scheme 3.3**.



Scheme 3.3 | Synthesis schemes for the fully *tert*-butylated dendrimers **38**, **39**, **40**, and **41**.

SCHOLL OXIDATION AND PURIFICATION

The Scholl oxidation on dendrimers **37**, **38**, **49**, and **40** into their respective GQD, **C₆₀tBu₈**, **C₇₈tBu₁₀**, **C₉₆tBu₁₂**, and **C₁₁₄tBu₁₄** was performed exclusively with DDQ as the oxidant. The oxidation of dendrimer **41** to produce **C₁₃₂tBu₁₆** is still pending. The specific reaction conditions for each nanoparticle's oxidation are presented in **Scheme 3.4**.



Scheme 3.4 | Synthesis schemes for the Scholl oxidation of **C₆₀tBu₈**, **C₇₈tBu₁₀**, **C₉₆tBu₁₂**, and **C₁₁₄tBu₁₄**.

It is important to underline that the oxidation conditions were not optimized. Although each reaction was monitored by MALDI-ToF mass spectrometry with samples taken every thirty minutes, there were intervals between sampling and analysis during which the reaction continued. The times reported in **Scheme 3.4** reflect the actual reaction durations, but subsequent analysis indicated that the full cyclodehydrogenation of the dendrimers was achieved in less time. For all four nanoparticles, a

clean, complete oxidation was observed after just thirty minutes of reaction. After longer reaction periods, degradation of the nanoparticles began to appear. This degradation was particularly noticeable in the case of **C₉₆tBu₁₂**, where side-products were already observed even at the thirty-minute mark. The oxidation reaction for all four nanoparticles proceeded swiftly under the conditions (DDQ equivalent, temperature, and acid concentration) specified in **Scheme 3.4**. The observations regarding the reaction time should be taken into account when these cyclodehydrogenation reactions are repeated in the future.

C₆₀tBu₈ and **C₇₈tBu₁₀** exhibit a high solubility which allowed them to be easily purified by column chromatography. **C₉₆tBu₁₂** and **C₁₁₄tBu₁₄** are more effectively purified by dispersing them in THF, followed by an ultracentrifugation step at 130 000 g for one hour. **C₁₁₄tBu₁₄** exhibits a lower solubility compared to its partially *tert*-butylated counterpart (**C₁₁₄tBu₁₀** from Chapter 2). During the purification attempts through size exclusion chromatography, a significant portion of the nanoparticle seemed to remain in the column. This phenomenon had not yet been observed for the other rod-shaped nanoparticles.

The MALDI-ToF spectra of the purified nanoparticles are presented in **Figure 3.2**. As it can be seen, the main peak corresponds to the expected mass for each GQD. Furthermore, comparisons between the experimental and simulated isotopic distributions are in excellent agreement for all four nanoparticles. For **C₉₆tBu₁₂**, two additional peaks with a mass difference of -41 and +102 from the product peak can be observed. It was challenging to eliminate these impurities, and no possible structures for these peaks were identified. To minimize the presence of these peaks, a shorter reaction time, as mentioned earlier, should be considered.

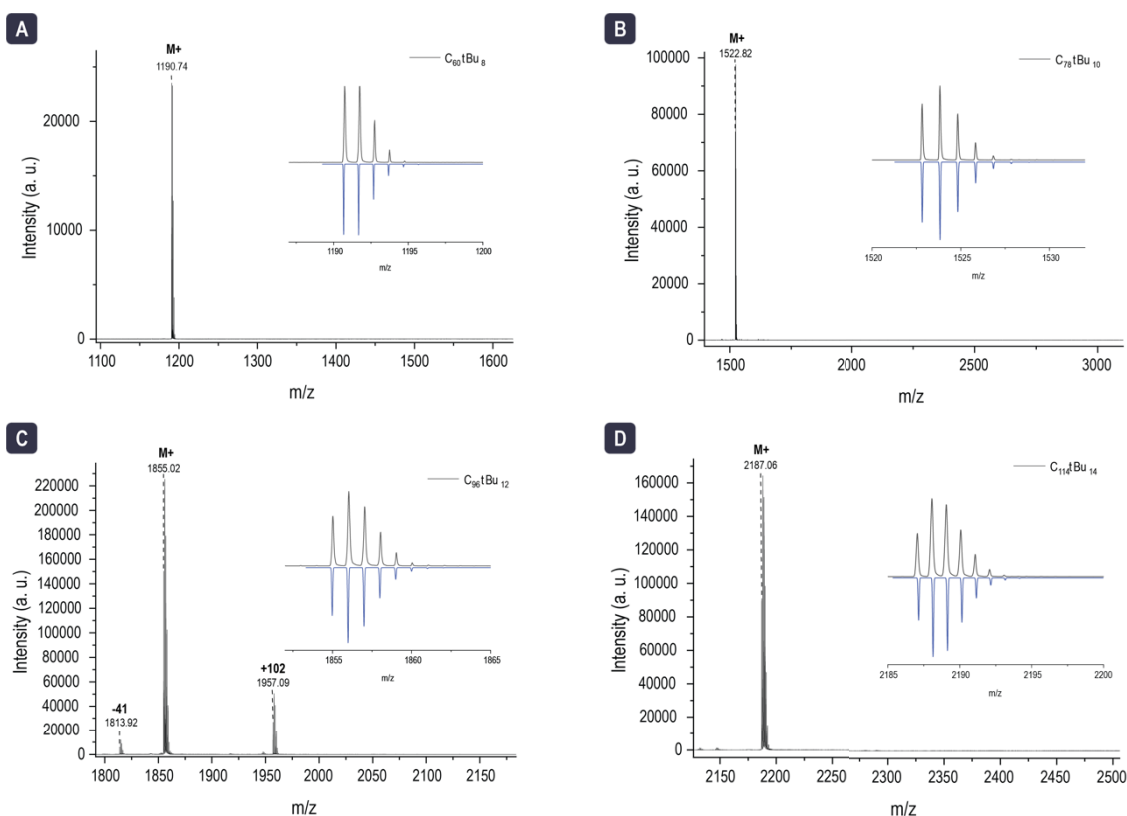


Figure 3.2 | MALDI-ToF mass spectrum of (a) **C₆₀tBu₈**, (b) **C₇₈tBu₁₀**, (c) **C₉₆tBu₁₂**, and (d) **C₁₁₄tBu₁₄** after a purification step. The inserts correspond to the comparison of the experimental (black) and simulated (blue) isotopic distributions of the main peak.

3.1.2 CHARACTERIZATIONS

As for the partially *tert*-butylated family of GQDs (Chapter 2), this fully *tert*-butylated family allows for additional characterization techniques beyond mass spectrometry. In this section, we will discuss the NMR spectroscopy performed on this fully *tert*-butylated family of GQDs, as well as their cyclic voltammetry.

NMR SPECTROSCOPY

NMR spectroscopy was performed in a mixture of tetrahydrofuran- d_8 and carbon disulfide. ^1H , ^1H - ^1H TOCSY, ^1H - ^1H NOESY, ^1H - ^{13}C HSQC, ^1H - ^{13}C HMBC, and, when possible, $^{13}\text{C}\{^1\text{H}\}$ NMR techniques were performed on the nanoparticles to perform the attributions. We will focus on the smallest $\text{C}_{60}\text{tBu}_8$ member on the family for the discussion. Though not approached in detail in this section, the signals in the NMR spectroscopy agree with the expected structures of the $\text{C}_{78}\text{tBu}_{10}$, $\text{C}_{96}\text{tBu}_{12}$, and $\text{C}_{114}\text{tBu}_{14}$.

The ^1H NMR spectrum of $\text{C}_{60}\text{tBu}_8$ is presented in **Figure 3.3a**. In the aromatic region, between 9.07 ppm and 10.03 ppm, it is possible to distinguish seven singlets, corresponding to the seven expected signals at this region. Since every aromatic proton in the structure does not have an adjacent hydrogen, they yield only singlet signals. In the aliphatic region, we can distinguish four peaks corresponding to the four inequivalent *tert*-butyl substituents in the structure. One of these *tert*-butyl signals partially overlaps with the water peak at 2.03 ppm. When calculating the integrals, the fourteen aromatic protons and the seventy-two aliphatic protons are well accounted for.

In this new series of rod-shaped GQDs, there is no vicinal proton-proton coupling, which results in all the detected signals appearing as singlets. Consequently, we can no longer rely on ^1H - ^1H COSY NMR spectroscopy for attributions. Instead, we have to depend on Total Correlation Spectroscopy (TOCSY) NMR spectroscopy. This method reveals the correlation between protons within a spin system, and so the coupling between non-neighboring protons can be observed. For our molecules, each aromatic ring constitutes a spin system. The attributions were performed using ^1H - ^1H NOESY and ^1H - ^1H TOCSY NMR spectroscopy.

The ^1H - ^1H NOESY NMR spectrum is presented in **Figure 3.3b-c**. The most important information we can extract from this spectrum is the peak associated with proton 7. This proton, isolated from other aromatic protons, should not create any spatial correlation, as is the case with the peak at 9.07 ppm. Proton 7 is proximate to two *tert*-butyl groups: C and D. We observe these two couplings with the aliphatic peaks at 2.03 ppm and 1.87 ppm (**Figure 3.3c**). However, using only NOESY NMR spectroscopy, it remains unclear which peak corresponds to D or C. In other words, the peak at 1.87 ppm can correspond either to D or to C. This is where TOCSY NMR spectroscopy becomes useful. Proton 7 shares the same spin system as proton 1. Since we see a cross-peak between the peaks at 9.07 ppm and 9.27 ppm in the TOCSY spectrum (**Figure 3.3d**), we can attribute the 9.27 ppm peak to proton 1. Returning to the NOESY spectrum, we observe that the aliphatic peak at 1.87 ppm correlates with the aromatic peaks at 9.07 ppm and 9.27 ppm. We can therefore conclude that this peak corresponds to the *tert*-butyl group C. From this point, the other attributions follow the correlations observed in the NOESY spectrum: proton 1 correlates with proton 2 who in turn correlates with the *tert*-butyl group B. B correlates with proton 3 who then couples with proton 4. Proton 4 correlates with *tert*-butyl group A. Group A couples with proton 5, who in turn correlates with proton 6. Finally, proton 6 correlates with *tert*-butyl group D.

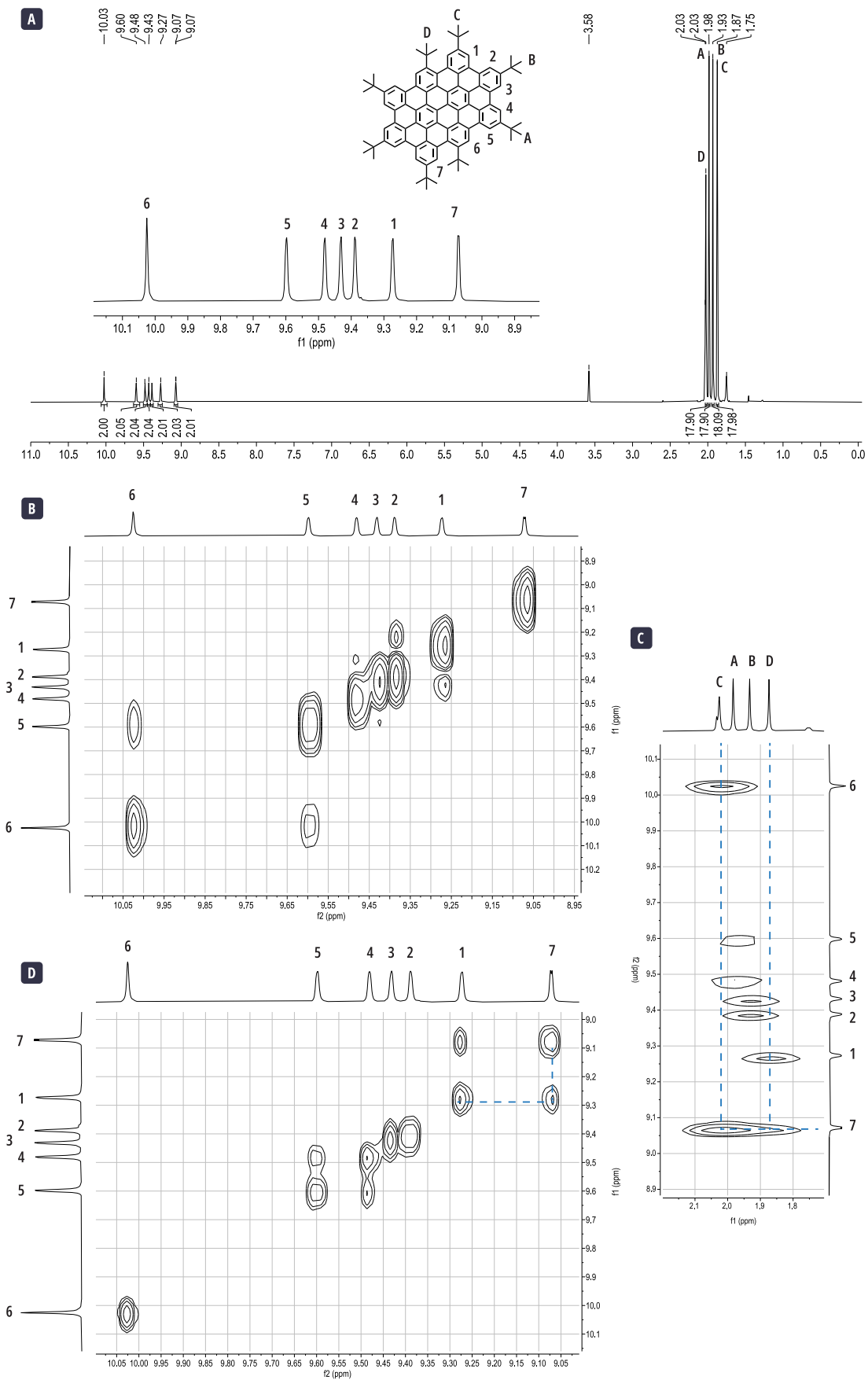


Figure 3.3 | (a) 1H NMR (400 MHz, $THF-d_8+CS_2$, 298 K) spectrum of $C_{60}tBu_8$ along with the peak attributions to the target structure. (b) Aromatic region of the 1H - 1H NOESY spectrum. (c) Couplings between the aromatic and aliphatic regions of the 1H - 1H NOESY spectrum. Dotted lines show the correlations between the 1.87 ppm, 2.03 ppm, and 9.07 ppm peaks. (d) Aromatic region of the 1H - 1H TOCSY spectrum. Dotted lines show the correlation between the 9.07 ppm and 9.27 ppm peaks.

The solubility of this small GQD allowed us to measure the $^{13}\text{C}\{^1\text{H}\}$ NMR spectrum, presented in **Figure 3.4a**. All the observed signals are in the expected aromatic and aliphatic regions. For attributions, we must rely on the ^1H - ^{13}C HSQC and ^1H - ^{13}C HMBC NMR spectra, provided in **Figure 3.4b-c**. We observe the same pattern for **C₉₆tBu₈** (see Section 2.3.2). In the HSQC NMR spectrum, we detect eleven correlations corresponding to the eleven carbons chemically bonded with a proton: seven aromatic and four aliphatic. In the HMBC NMR spectra, we see the long-range correlations between the protons and carbons. The most distinctive feature are the correlations of the aromatic carbons to which the *tert*-butyl groups are attached, which appear at high chemical shifts (145 ppm – 155 ppm).

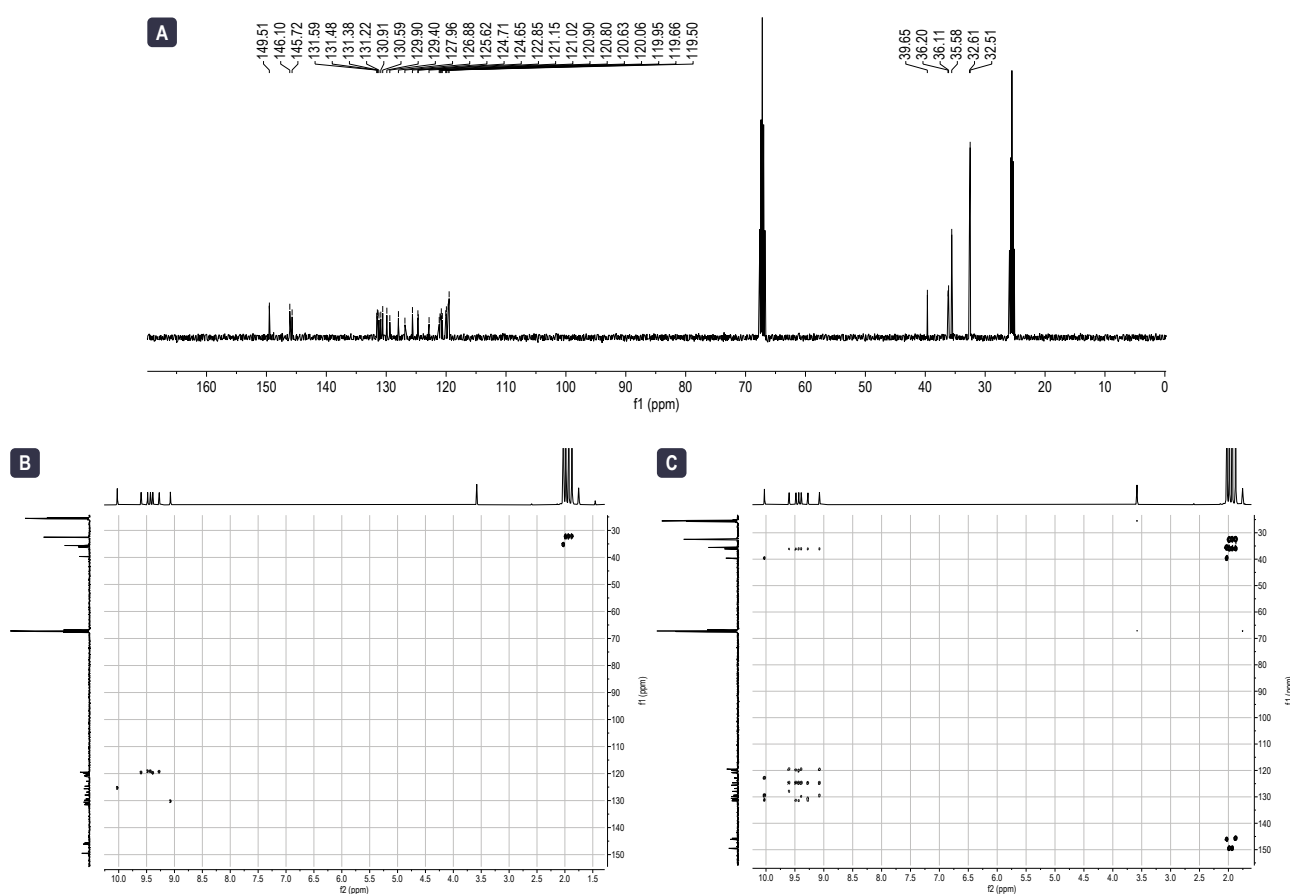


Figure 3.4 | (a) $^{13}\text{C}\{^1\text{H}\}$ NMR spectrum (101 MHz, $\text{THF-d}_8+\text{CS}_2$, 298 K) of **C₆₀tBu₈**. (b) ^1H - ^{13}C HSQC spectrum. (c) ^1H - ^{13}C HMBC spectrum.

Thanks to NMR spectroscopy we were able to validate the expected structure of **C₆₀tBu₈**. Though not presented here, the ^1H NMR spectrum of **C₇₈tBu₁₀**, **C₉₆tBu₁₂**, and **C₁₁₄tBu₁₄** contain the expected signals for the aromatic protons and *tert*-butyl groups. Though their attribution remained more challenging than for **C₆₀tBu₈**, the observed signals in their ^1H NMR are coherent with their expected structure (Appendix 2).

CYCLIC VOLTAMMETRY

The electrochemical properties of **C₆₀tBu₈**, **C₇₈tBu₁₀**, **C₉₆tBu₁₂**, and **C₁₁₄tBu₁₄** were recorded under argon atmosphere at room temperature, using a supporting electrolyte of a 0.1 M solution of tetra-*n*-butylammonium hexafluorophosphate in anhydrous 1,2-dichlorobenzene (*o*-DCB). The three-electrode setup consisted of a platinum working electrode, a platinum counter electrode, and Ag/Ag^+ reference electrode (10 mM AgNO_3). Experiments were conducted at a scan rate of $100 \text{ mV}\cdot\text{s}^{-1}$. The cyclic voltammograms for the fully *tert*-butylated GQDs are presented in **Figure 3.5**. For the four nanoparticles, two reversible

oxidation waves are visible. In the case of **C₆₀tBu₈**, no reduction wave is present, and only the solvent wall can be distinguished at negative potentials. For **C₇₈tBu₁₀**, and **C₉₆tBu₁₂** a reversible reduction wave is observed. In the case of **C₁₁₄tBu₁₄** it is possible to distinguish two reversible reduction waves with an intensity similar to that of the oxidation waves.

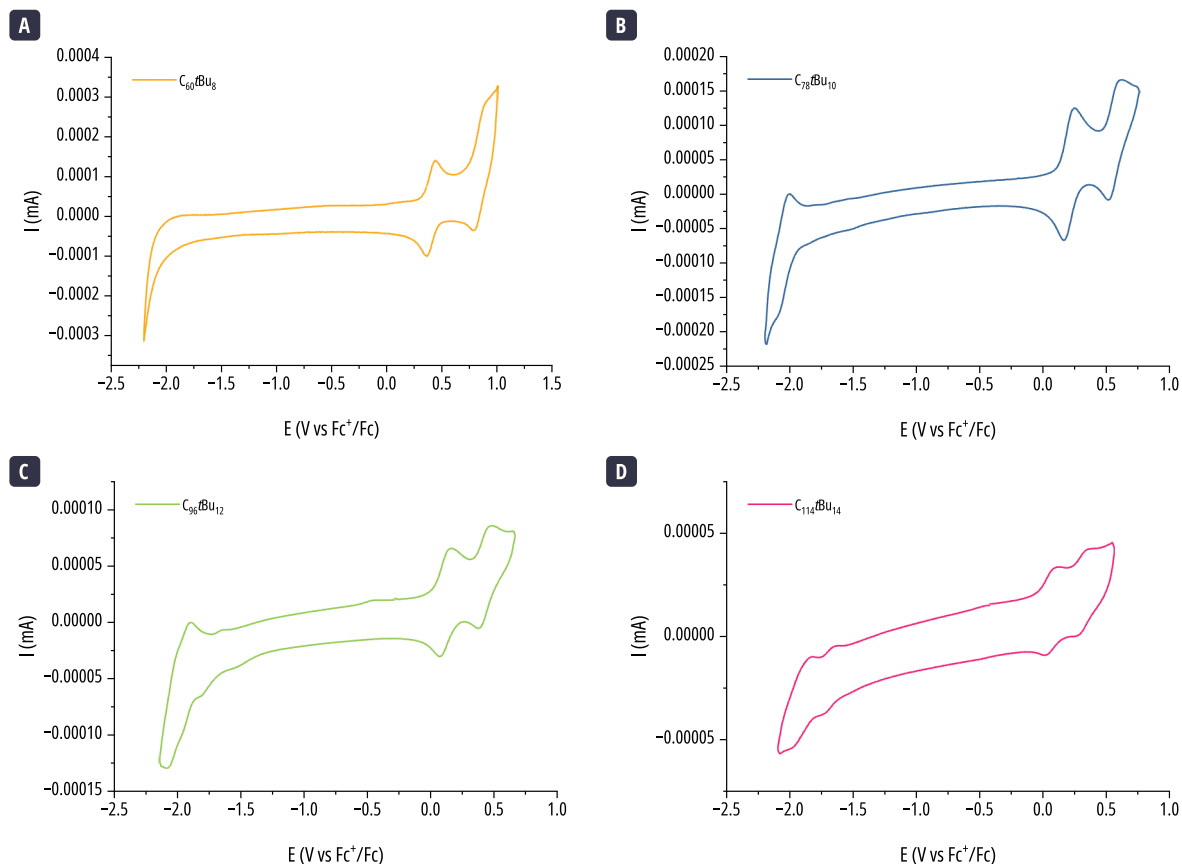


Figure 3.5 | Cyclic voltammograms of (a) **C₆₀tBu₈**, (b) **C₇₈tBu₁₀**, (c) **C₉₆tBu₁₂**, and (d) **C₁₁₄tBu₁₄** in 1,2-dichlorobenzene.

Following the same treatment as described in Section 2.3.2, the values reported in **Table 7** can be obtained. A discernable trend can be observed in the position of the first oxidation and, when present, the first reduction wave. As the size of the nanoparticle increases, the positioning of the oxidation half-wave potentials ($E_{1/2,ox}$) decreases, while those of the reduction waves ($E_{1/2,red}$) increase. This trend also translates in the positioning of the HOMO energy level ($E_{ec,HOMO}$) and in the electrochemical bandgap ($E_{ec,gap}$). As the nanoparticles increase in size, the bandgap diminishes. This contrasts with the observations made for the partially *tert*-butylated GQD family, where aggregation induced a change in the energies observed for **C₇₈tBu₆** (Chapter 2).

Table 7 | Summary of the electrochemical values measured for **C₆₀tBu₈**, **C₇₈tBu₁₀**, **C₉₆tBu₁₂**, and **C₁₁₄tBu₁₄**. Potential values are reported vs. Fc⁺/Fc.

GQD	$E_{1/2,ox1}$ (V)	$E_{1/2,ox2}$ (V)	$E_{1/2,red1}$ (V)	$E_{ox,onset}$ (V)	$E_{red,onset}$ (V)	$E_{ec,HOMO}$ (eV)	$E_{ec,LUMO}$ (eV)	$E_{ec,gap}$ (eV)
C₆₀tBu₈	0.401	0.846	-	0.332	-	-5.132	-	-
C₇₈tBu₁₀	0.206	0.561	-2.045	0.123	-1.951	-4.923	-2.849	2.07
C₉₆tBu₁₂	0.110	0.420	-1.988	0.014	-1.789	-4.841	-3.011	1.83
C₁₁₄tBu₁₄	0.055	0.314	-1.686	-0.051	-1.563	-4.749	-3.237	1.51

3.1.3 OPTICAL PROPERTIES

Let's now discuss the optical properties of this new family of GQDs and compare them to the family presented in the previous chapter. We will first discuss each nanoparticle individually, and compare it, when possible, to its partially *tert*-butylated homologue. We will conclude the discussion of the optical properties with a brief comparison of all the members of this new fully *tert*-butylated GQDs family.

$C_{60}tBu_8$

The absorption and emission spectra of $C_{60}tBu_8$ is presented in **Figure 3.6a**. In the absorption spectrum, we can discern narrow absorption lines, with a maximum absorption at 415 nm. Similarly, the emission spectrum is well-resolved with six narrow emission peaks. The maximum of the emission is located at 538 nm. The Stokes shift of this nanoparticle is 52 nm, considerably larger than that observed for other rod-shaped GQDs described in the previous chapter, whose values are around 10 nm. A large Stokes shift is indicative of a reorganisation of the excited state relative to the ground state. Upon examining the photoluminescence excitation spectra at all emission wavelengths, we can recover the absorption spectrum. This can be appreciated in **Figure 3.6b**. All emission wavelengths originate from the same entity in solution. Finally, we observe a fine detail in the emission, most likely stemming from vibronic coupling. Interestingly, if we compare the emission spectrum to that of $C_{96}tBu_8$, for example, we note a similar progression of three peaks. Because of the smaller size and further steric constraints introduced by the *tert*-butyl groups, the resolution is enhanced, allowing us to better appreciate the vibronic coupling. This warrants further experimental and theoretical investigations.

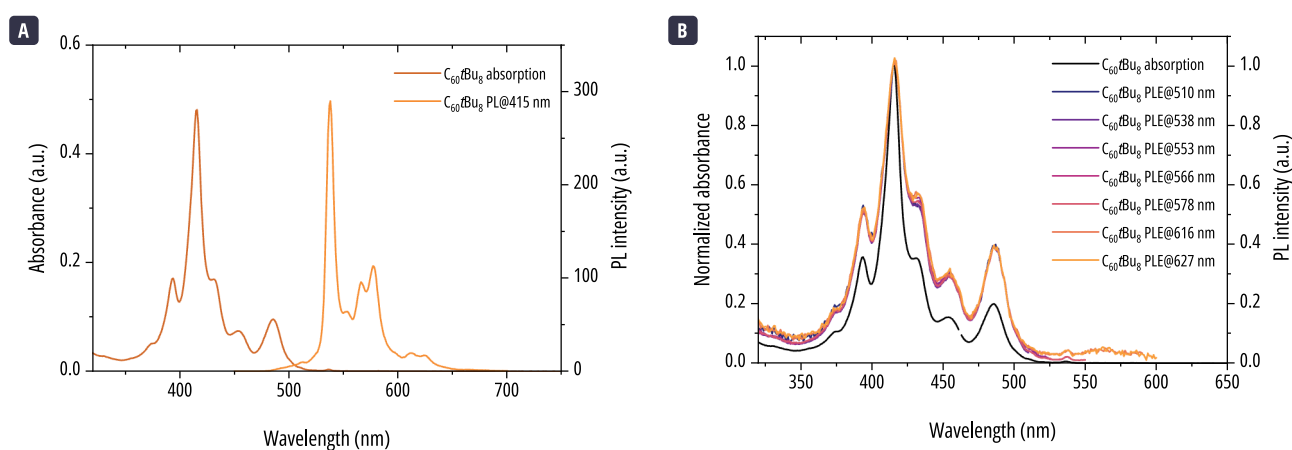


Figure 3.6 | (a) Absorption and emission spectrum of $C_{60}tBu_8$ in 1,2,4-trichlorobenzene. (b) PLE spectra at all the emission peaks of $C_{60}tBu_8$.

$C_{78}tBu_{10}$

The absorption and emission of $C_{78}tBu_{10}$ are presented in **Figure 3.7a**. The absorption spectrum reveals a series of well-defined peaks, with the primary absorption peak at 453 nm. The emission spectrum comprises four easily distinguishable peaks between 550 nm and 650 nm, as well as a small bump at 690 nm. The main emission peak is situated at 584 nm. For the four emission peaks between 550 nm and 650 nm, we can note that two of them (584 nm and 683 nm) are quite sharp, while the other two appear broader (567 nm and 616 nm).

An intriguing feature of the absorption spectrum is the presence of a small, sharp peak at 584 nm. Such feature had not been yet observed for the absorption of the different rod-shaped GQDs presented so far. The photoluminescence excitation

spectra (**Figure 3.7b**) across all emission peaks show similar excitation and absorption spectra, including the presence of the peak at 584 nm. This observation confirms that it is an intrinsic feature of the GQD and excludes the possibility that it originates from an impurity.

We observe a distinct behavior in this GQD compared to the rod-shaped GQDs discussed in the previous chapter. The absorption spectra exhibit a sharp peak at longer wavelengths, while the emission spectrum shows the presence of two sets of peaks, one broad and one sharp. To better understand the origin of these differences, further experiments such as time-resolved photoluminescence and more detailed theoretical calculations are required. These differences could be intrinsic to the nanoparticle itself or potentially due to the presence of conformers induced by the positioning of the *tert*-butyl groups along the main axis of the GQD. Concentration-dependent experiments on **C₇₈tBu₁₀** showed no variation in the linewidth and ratios of the peak intensities in the absorption spectrum (**Figure 3.7c**), ruling out the possibility that these interesting features originate from aggregation.

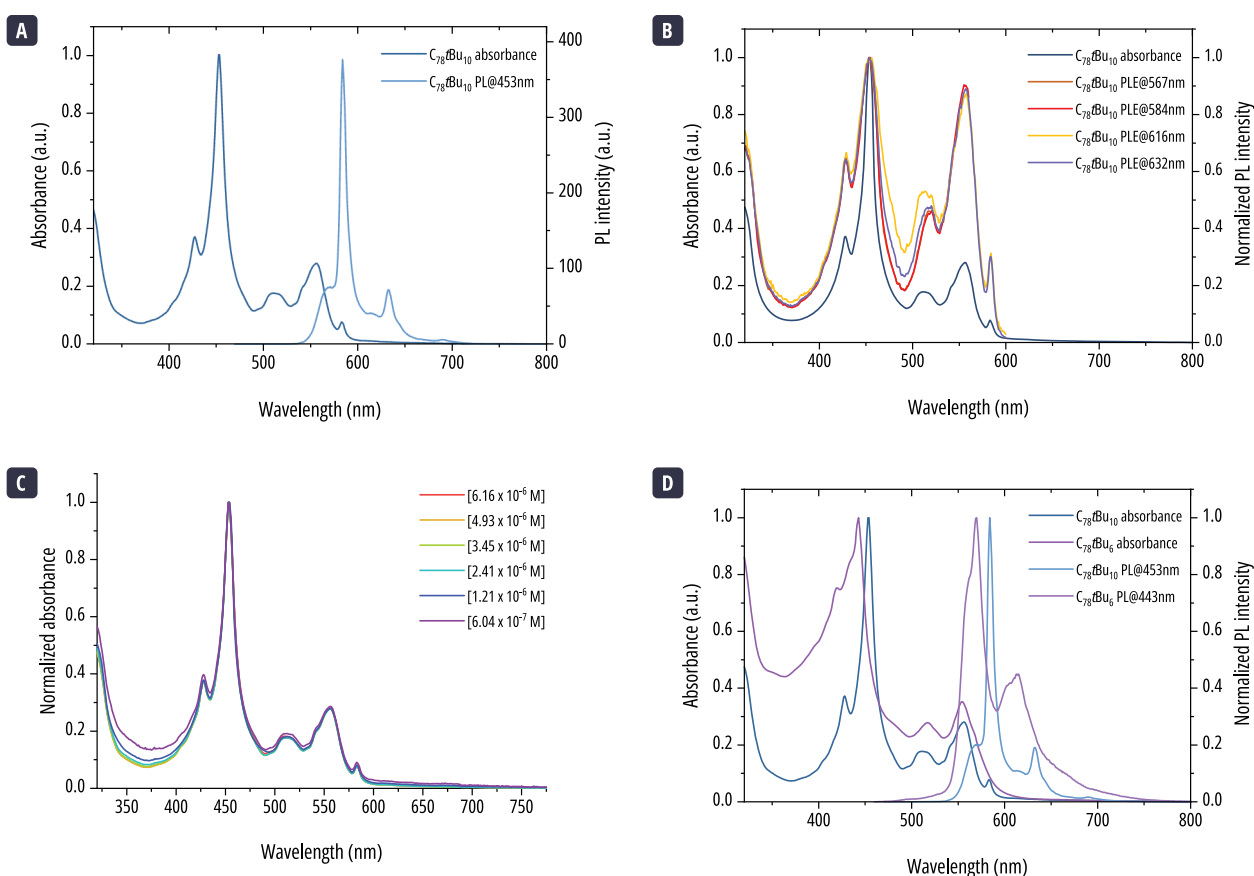


Figure 3.7 | (a) Absorption and emission spectrum of **C₇₈tBu₁₀** in 1,2,4-trichlorobenzene. (b) PLE spectra at all the emission peaks of **C₇₈tBu₁₀**. (c) Concentration dependent absorption spectra of **C₇₈tBu₁₀**. (d) Comparison of the absorption and emission spectrum of **C₇₈tBu₁₀** and **C₇₈tBu₆**.

The comparison of the absorption and emission spectra of the two C₇₈ rod-shaped GQDs: **C₇₈tBu₁₀** and **C₇₈tBu₆** is presented in **Figure 3.7d**. Focusing on the absorption spectra, it's clear that the fully *tert*-butylated nanoparticle, **C₇₈tBu₁₀**, has more well-defined absorption peaks, particularly below 450 nm. The absorption exhibits a red-shift of 10 nm. The emission of **C₇₈tBu₁₀** also experience a red-shift of 14 nm. When observing the emission spectra, the same pattern of peak distribution, characterized by paired broad and narrow peaks, is evident in both GQDs, but can be much clearly appreciated for the fully *tert*-butylated **C₇₈tBu₁₀**. The main difference in the emission spectra is the change of the intensity ratio between the third and fourth

peaks to the main emission, which is smaller for $C_{78}tBu_{10}$. As discussed in the previous chapter, emissions that could be attributed to aggregates, especially in solvents other than 1,2,4-trichlorobenzene, occurred at higher wavelengths than the emission of the monomer. The absence of aggregates in the fully *tert*-butylated $C_{78}tBu_{10}$ could help explain this ratio difference. Based on the observations presented here, it can be concluded that the introduction of additional adjacent *tert*-butyl groups along the main axis of the nanoparticle effectively improves the solubility of the C_{78} GQD.

$C_{96}tBu_{12}$

The fully *tert*-butylated $C_{96}tBu_{12}$ exhibits a well-defined absorption and emission spectra, which are given in **Figure 3.8a**. The absorption of $C_{96}tBu_{12}$ presents features which resemble to $C_{96}tBu_8$ (presented in Chapter 2). A first progression of peaks between 650 nm and 500, and a second progression between 500 nm and 400 nm. The emission peak is composed of three main emission bands at 627 nm, 682 nm, and 754 nm. Additionally, a slight bump can be distinguished at 605 nm. The PLE spectra at all the wavelengths yield the same excitation spectra which recovers all the features of the absorption spectra (**Figure 3.8b**), confirming that the observed emission originates from the same object, which is also responsible for the absorption.

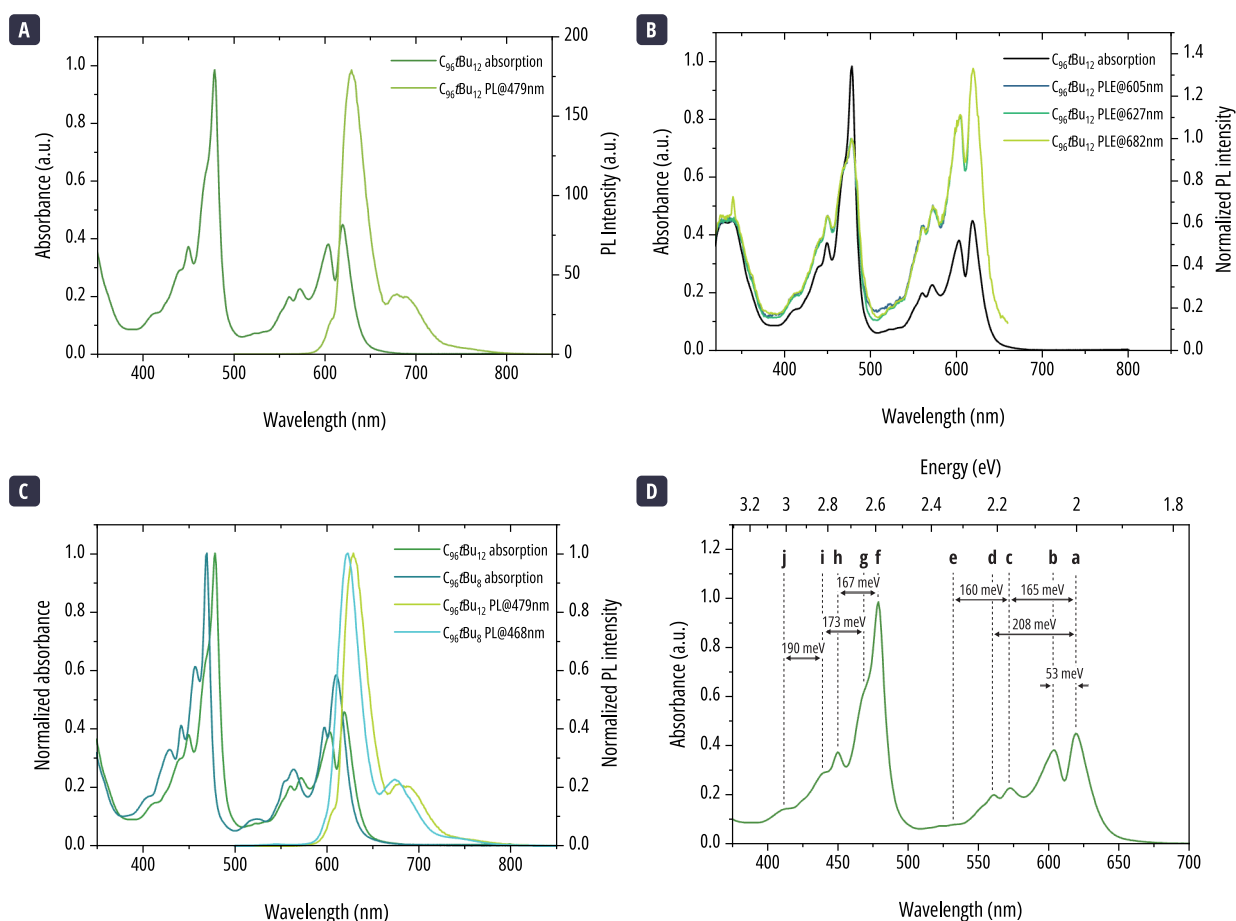


Figure 3.8 | (a) Absorption and emission spectrum of $C_{96}tBu_{12}$ in 1,2,4-trichlorobenzene. (b) PLE spectra at all the emission peaks of $C_{96}tBu_{12}$. (c) Comparison of the absorption and emission spectrum of $C_{96}tBu_{12}$ and $C_{96}tBu_8$. (d) Energy splitting between the absorption peaks of $C_{96}tBu_{12}$.

In figure **Figure 3.8c**, a comparison between the two rod-shaped C_{96} GQDs is given. The first notable difference is a red shift of the absorption and emission of $C_{96}tBu_{12}$ compared to its partially *tert*-butylated homologue. A second difference is the difference in the intensity ratio between the main absorption peak and the first absorption peak. This ratio is smaller for the fully *tert*-butylated $C_{96}tBu_{12}$, suggesting a different electronic distribution of the transitions that would impact the oscillator strength

of the transition. Finally, the energy splitting between the observed peaks of $C_{96}tBu_{12}$ is given in **Figure 3.8d**. Though the values are similar to those presented for $C_{96}tBu_8$, slight differences can be noticed. For instance, the energy splitting between the first and second absorption peaks (a and b) is 53 meV in the case of the fully *tert*-butylated GQD $C_{96}tBu_{12}$, compared to 47 meV in the partially *tert*-butylated $C_{96}tBu_8$ (see **Figure 2.22**). Further theoretical investigations are still needed to explain the changes in behaviour when more *tert*-butyl groups are added to the structure, which would help to elucidate if the differences are originated from vibronic coupling or the presence of conformers.

$C_{114}tBu_{14}$

The absorption and emission spectra of $C_{114}tBu_{14}$ are presented in **Figure 3.9a**. The main absorption band is located at 497 nm. The emission spectrum has a main emission peak at 672 nm and two others at 731 nm and 811 nm. In the emission spectrum a small bump is present at 624 nm. In **Figure 3.9b** is given the comparison of the absorption and emission between $C_{114}tBu_{14}$ and $C_{114}tBu_{10}$ (the C_{114} GQD from Chapter 2). One can notice that the absorption for the fully *tert*-butylated GQD, $C_{114}tBu_{14}$, is red shifted compared to its partially *tert*-butylated analogue. As in the C_{96} series, the ratio between the intensity of the first absorption band and the main absorption peak is different. Finally, the absorption spectra of $C_{114}tBu_{14}$ shows a similar positioning of peaks than $C_{114}tBu_{10}$, however, the spectrum of the first appears to be broader. The same can be observed for the emission spectra; they both exhibit a similar spectrum, but it is broader for $C_{114}tBu_{10}$. It is unclear to what this is due, one possibility is that there are more conformers present due to the increasing of the number of *tert*-butyl groups along the axis of the GQD. Further theoretical description may help elucidate this question.

Similar to the C_{96} series, we observe the same features between the fully and partially substituted C_{114} GQDs. The absorption spectrum of $C_{114}tBu_{14}$ is red shifted in comparison to $C_{114}tBu_{10}$. The red shift is less noticeable for the emission spectrum. The emission spectra for both nanoparticles are quite similar; however, $C_{114}tBu_{14}$ appears to exhibit a slightly broader emission.

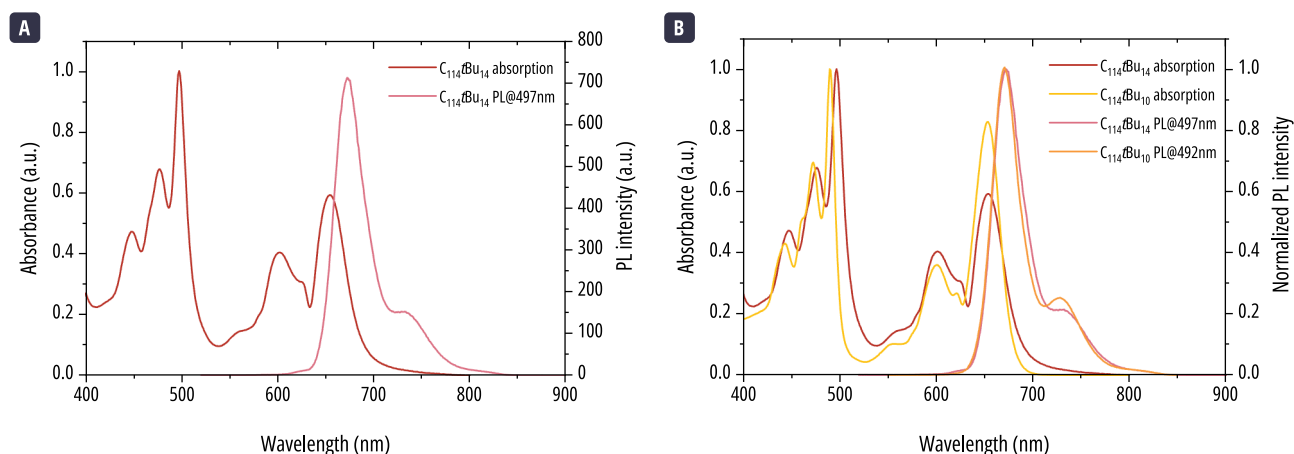


Figure 3.9 | (a) Absorption and emission spectrum of $C_{114}tBu_{14}$ in 1,2,4-trichlorobenzene. (b) Comparison of the absorption and emission spectrum of $C_{114}tBu_{14}$ and $C_{114}tBu_{10}$.

We will pay additional interest to the small shoulder at 625 nm in the emission of $C_{114}tBu_{14}$. Emissions at shorter wavelengths than the main emission peaks of the GQDs are usually associated with impurities (see **Figure 2.11**). Concerning the emission shoulder at 625 nm observed for $C_{114}tBu_{14}$, its excitation spectrum, as well as that of the other emission peaks, are

given in **Figure 3.10a**. The excitation spectrum at 625 nm differs from the absorption spectrum of $\text{C}_{114}\text{tBu}_{14}$, suggesting that indeed this peak originates from an additional object other than the individualized GQD.

So far, for the rod-shaped family of nanoparticles, excepted for $\text{C}_{78}\text{tBu}_6$ (Chapter 2), there has been no observed concentration dependence of the emission of peaks at shorter wavelengths, if present. However, for $\text{C}_{114}\text{tBu}_{14}$, a dependence of the intensity of this peak to the concentration was observed. In **Figure 3.10b**, the photoluminescence intensity as a function of concentration is given. We can notice that as concentration increases, the intensity of the peak at 625 nm increases. This contrasts with the emission of the main peaks attributed to the individualized $\text{C}_{114}\text{tBu}_{14}$, whose intensity increases initially and then diminishes. This can be better visualized in the three-dimensional graphic given in **Figure 3.10c**. These observations differ from what is expected for an impurity, whose emission intensity, in comparison to that of the individualized nanoparticle, should be independent of the concentration. Here, the ratio increases. This can be better evidenced in the normalized photoluminescence spectrum in **Figure 3.10e**.

Assuming the peak at 625 nm originates from impurities, one possible explanation to this behavior is that as the concentration increases, there is a stronger phenomenon of reabsorption of the emitted light, which would explain the decrease in the intensity of recorded photoluminescence for the individualized GQD's emission peak. However, the reabsorption primarily affects high energy photons where the absorption and emission spectra overlap, so the emission at 625 nm should also be impacted by the phenomenon.

Another possibility is that as the concentration increases, the nanoparticle aggregates and this process quenches its photoluminescence. This would explain the decrease in the photoluminescence from the individualized nanoparticle. An alternative hypothesis is that the peaks at 625 nm correspond to small aggregates, which are blue shifted in comparison to the individualized nanoparticle. We reported experimental and theoretical observations that suggested this type of behavior for the triangular $(\text{T})\text{C}_{96}(\text{C}_{12}\text{H}_{25})_6$ GQD.²⁰² This could explain the increase of the PL at 625 nm and the decrease of the PL of individualized $\text{C}_{114}\text{tBu}_{14}$. Additionally, when zooming-in at the emission at different concentrations (**Figure 3.10d**), it is possible to distinguish an isosbestic point for three different concentrations. The observation of an isosbestic point could also support this hypothesis. However, this point does not exist for all the concentration curves and may be just a coincidence. A possible explanation to the disappearance of this point is that the emission of the small aggregates is also impacted by concentration as larger aggregates are formed. Finally, the main limitation to the hypothesis of small aggregates is that they should also impact the absorption spectrum, and this does not occur, as evidenced in **Figure 3.10f**. To better clarify this process, it would be interesting to perform further optical studies with smaller light path cuvettes to be able to work at higher concentrations and prevent any possible reabsorption phenomenon. Another possibility is to do optical experiments in different organic solvents that would give more data to compare.

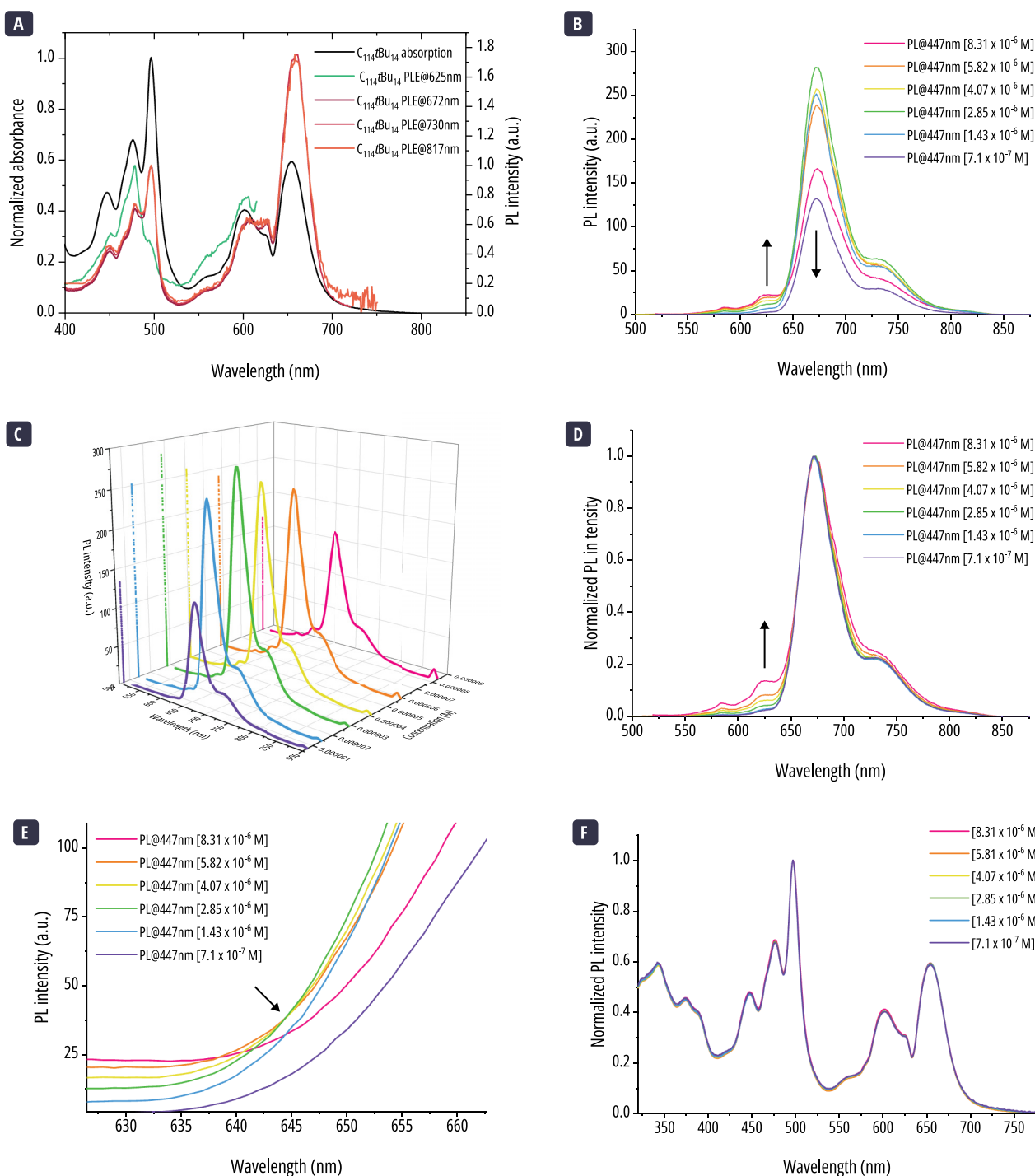


Figure 3.10 | (a) PLE spectra at the emission peaks of $C_{114}tBu_{14}$ in 1,2,4-trichlorobenzene. (b) Concentration dependent PL spectra of $C_{114}tBu_{14}$ excited at 447 nm. (c) Three-dimensional representation of (b). (d) Normalized PL spectra of $C_{114}tBu_{14}$ at different concentrations. (e) Zoom-in on (b). Arrow shows the isosbestic point formed by three curves. (f) Concentration dependent absorption spectra of $C_{114}tBu_{14}$.

So far, the observed trend in the rod-shaped GQD suggests that increasing the number of adjacent *tert*-butyl groups along the main axis of nanoparticle effectively enhances its solubility. The hypothesis of the presence of small aggregates of $C_{114}tBu_{14}$ is not coherent with this observation. Theoretical studies of the aggregation process of $C_{96}tBu_8$ (see Section 2.3.2) demonstrated that its good solubility mainly derives from the absence in solution of certain conformer configurations, which are highly energetic due to the presence of adjacent *tert*-butyl groups. However, in theory, these non-existent conformers could aggregate. A possible explanation for the behavior of $C_{114}tBu_{14}$ may lie in this condition. As the number of adjacent *tert*-butyl

groups increases, so does the number of conformers. Some of these conformers may no longer be energetically disadvantaged and may serve as a starting point for the aggregation process. Theoretical calculations of the energy levels of these conformers, as well as push-pull calculations, might help clarify this hypothesis. In addition, the synthesis of the larger $C_{132}tBu_{16}$ could provide comparative data to better understand the process. It is important to comment that, even if the aggregation hypothesis is verified, $C_{114}tBu_{14}$ remains highly soluble in comparison to other reported planar GQDs of similar size.

COMPARISON OF ALL THE FAMILY

The comparison of the absorption and emission spectra for all the members of the fully *tert*-butylated rod-shaped GQD is given in **Figure 3.11**. As the size of the nanoparticle increases, the absorption and emission spectra are red shifted. For this family we can tune the absorption by 170 nm and the emission by 134 nm.

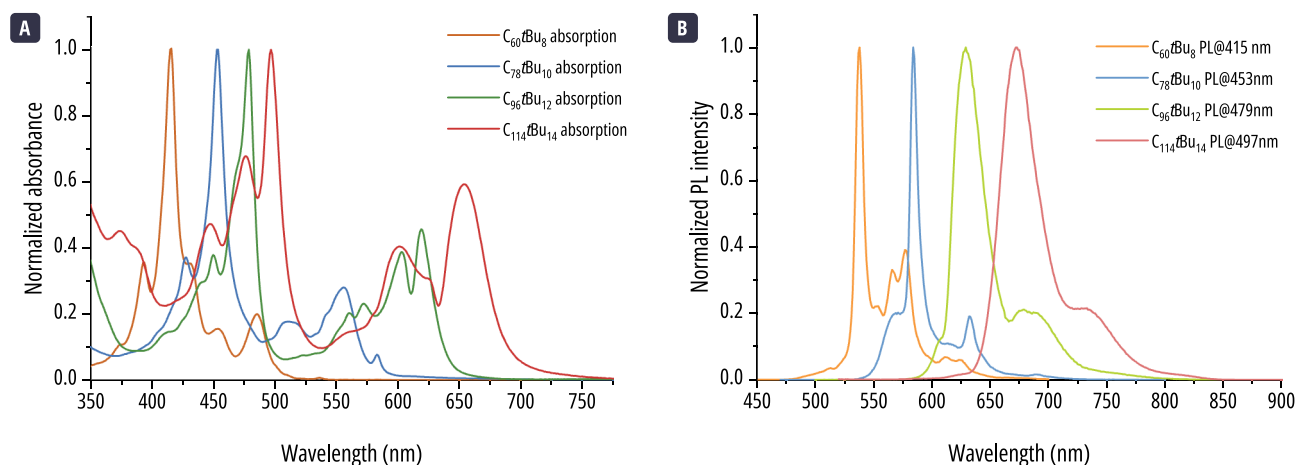


Figure 3.11 | (a) Absorption spectra of $C_{60}tBu_8$, $C_{78}tBu_{10}$, $C_{96}tBu_{12}$, and $C_{114}tBu_{14}$ in 1,2,4-trichlorobenzene. (b) Emission spectra of $C_{60}tBu_8$, $C_{78}tBu_{10}$, $C_{96}tBu_{12}$, and $C_{114}tBu_{14}$ excited at their main absorption peaks.

Though very similar in structure to the family of partially *tert*-butylated rod-shaped nanoparticles presented in the previous chapter, some interesting differences were observed for the optical properties of the GQDs presented in this section. For example, the more complex emission spectrum of the smallest members of the family; or a different intensity of the first electronic transition. These differences warrant further experimental and theoretical investigations and show the importance of understanding the structure and optical properties relationship.

3.2 TWISTED NANOGRAFENES

In this section of the chapter, we will discuss an alternative approach to make more soluble graphene quantum dots. This is achieved by making sterically congested nanoparticles that will force the structure to twist breaking its purely two-dimensional structure. When more than four phenyl rings are fused together in *ortho*-positions, the steric hindrance becomes considerable. To reduce this strain, the molecules twist into a helical structure, forming helicenes. These molecules are named according to the number n of *ortho*-fused rings composing the structure, which is denoted as $[n]$ helicene. The helical structure gives rise to chiral and chiroptic properties. The chirality of the helicene originates from the helix itself, and it will be present regardless of the functional groups attached to the structure.

A helicene will possess an enantiomer, which is a non-superimposable mirror image. These two enantiomers have helices that twist in different directions. When observing the molecule from the top of the helix axis, the turning direction can be

either clockwise or anti-clockwise. The clockwise helicity, for a right-handed helix, is denoted by a P (plus), while the anticlockwise helicity, for a left-handed helix, is denoted by a M (minus). To better illustrate this, **Figure 3.12** shows the two enantiomers of a [6]helicene.

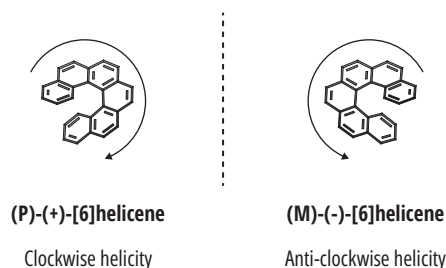


Figure 3.12 | Enantiomer representations of a [6]helicene. The arrows show the direction of the helicity.

Though the first reports of helicenes date back to the beginning of the XXth century, helicenes have been attracting attention in recent years due to their unusual structures, enhanced chiroptical properties, aromaticity, stability, and the advances in the bottom-up synthesis of large PAHs.^{116,225,226} Numerous examples of single-stranded helicenes with different sizes and functional groups can be found in the literature.^{115,116} Although conjugation throughout these structures is present, it is confined to a single row of phenyl rings. Therefore, expanding the π -conjugation laterally has also sparked significant interest.

Itami's research group was pioneering in the synthesis of these π -extended helicene.¹¹⁷ Since, multiple examples of nanographene containing helicenes in their structure has been reported over the years.^{111,227–232} One advantage of this expansion is that, for the same [n]helicene, it allows tuning of the bandgap and optical responses. Additionally, they allow to create multiple helices inside the same nanographene structure. The additional dimension, compared to their planar counterparts, helps to reduce π -stacking and increase solubility. Therefore, in our goal to synthesize more soluble graphene nanoparticles, we have decided to also pursue this strategy.

3.2.1 C₉₆ BASED TRIPLE [6]HELICENES

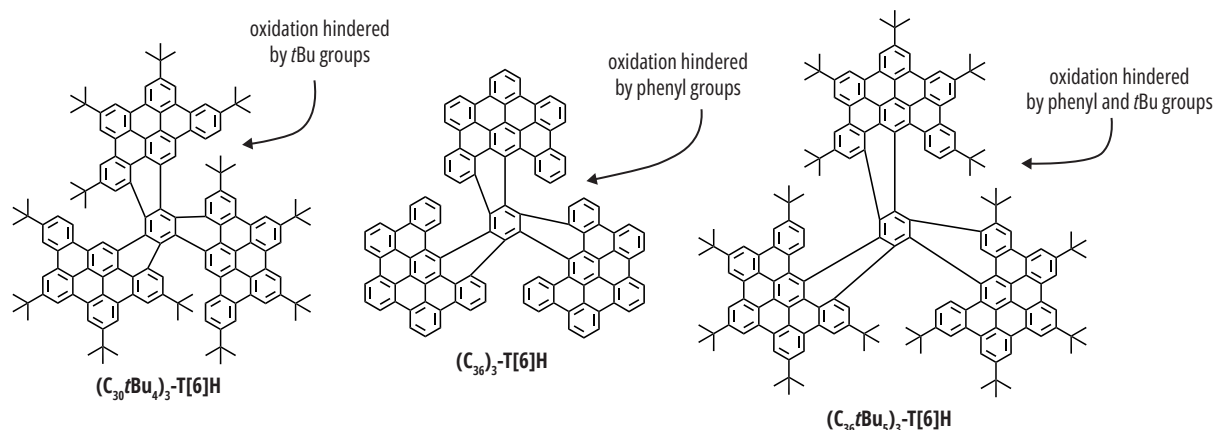


Figure 3.13 | Structures of the three targeted helicenes.

At the beginning of the previous chapter (See Section 2.2.1), we presented the synthesis of a triangular GQD containing 96 sp^2 carbon atoms. Inspired by its synthesis, we designed sterically congested dendrimers whose oxidation would induce twisted structures and create three π -expanded helicenes. The steric hindrance was introduced either by the addition of *tert*-butyl groups, phenyl groups, or both. In this manner, we attempted the synthesis of three helicenes: a small *tert*-butyl substituted helicene (**(C₃₀tBu₄)₃-T[6]H**), a bigger “naked” helicene (**(C₃₆)₃-T[6]H**), and its *tert*-butyl substituted analogue (**(C₃₆tBu₅)₃-T[6]H**). The

common point for these structures is that they contain three [6]helicenes (T[6]H) with a central phenyl unit. The three structures are presented in **Figure 3.13**. In this section, we will discuss their synthesis and associated challenges and some chiroptical studies.

SYNTHESIS

The synthesis of the helicene follows the same strategy adopted so far. A polyphenylene dendrimer is oxidized to create the new C-C bonds and obtain a delocalized structure. As previously mentioned, the dendrimer is designed to exhibit additional steric hindrance that will force the molecule to twist. This steric hindrance is created by adding additional *tert*-butyl groups, additional phenyl groups, or both, which would hinder the oxidation into a planar structure. These congested dendrimers are presented in **Figure 3.14**.

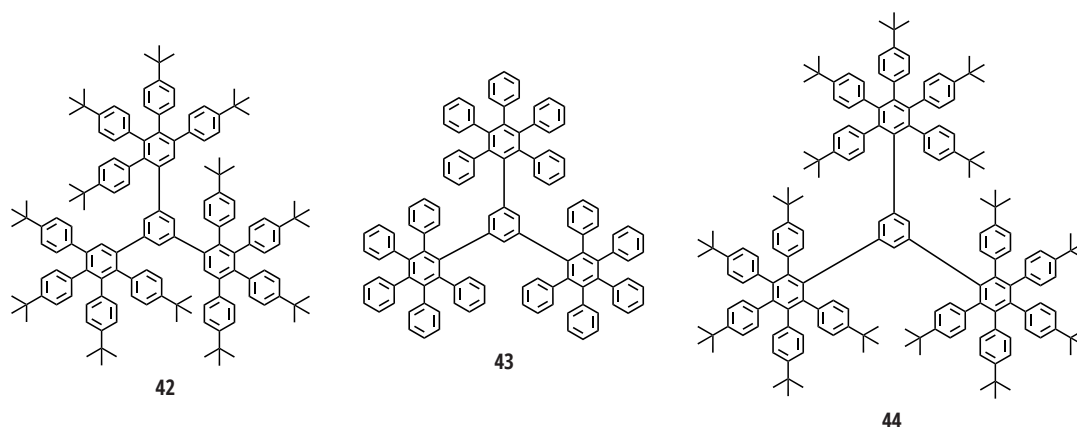
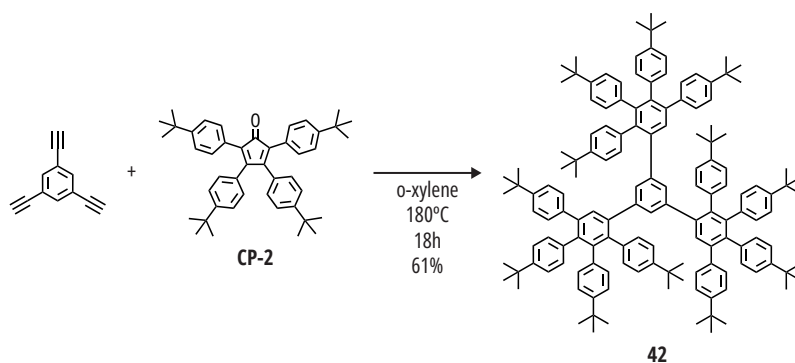


Figure 3.14 | Structures of the dendrimers necessary for the synthesis of the targeted helicenes.

DENDRIMERS SYNTHESIS

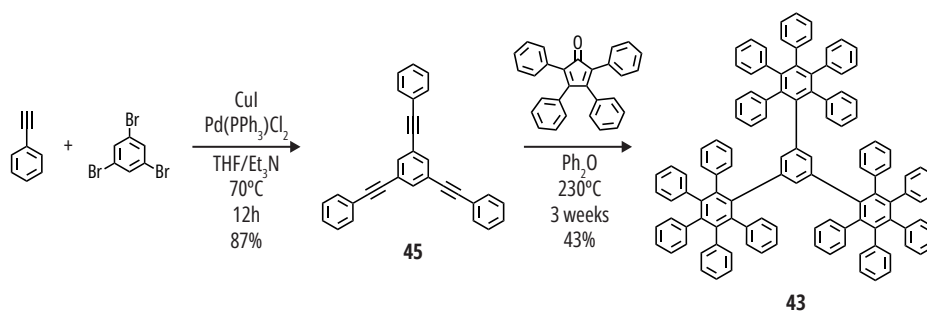
The synthesis of dendrimer **42** is straightforward, with precursors whose synthesis has already been described. 1,3,5-ethynylbenzene is reacted through a Diels-Alder reaction with the tetra-*tert*-butyl substituted cyclopentadienone **CP-2**. The reaction conditions are shown in **Scheme 3.5**.



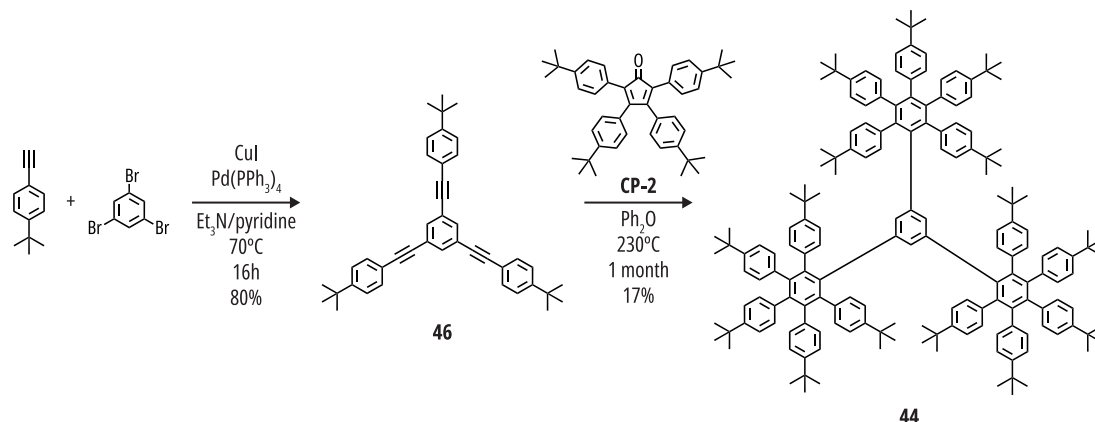
Scheme 3.5 | Synthetic route to **42**.

For the larger dendrimers **43** and **44**, an additional phenyl group must be added to the alkyne functions in 1,3,5-ethynylbenzene before the Diels-Alder reaction can be performed. The strategy to synthesize dendrimer **43** is presented in **Scheme 3.6**, and that for dendrimer **44** in **Scheme 3.7**. The first step for both dendrimers involves a Sonogashira coupling between 1,3,5-tribromobenzene and the corresponding primary alkyne: phenylacetylene for **43** and 4-*tert*-butylphenylacetylene

for **44**. In this way, the "naked" core **45** and the *tert*-butyl substituted core **46** are produced. Subsequently, alkyne core **45** is reacted with the commercially available cyclopentadienone to yield dendrimer **43** through a Diels-Alder reaction. Similarly, **46** is reacted with the tetra-*tert*-butyl substituted cyclopentadienone **CP-2** to create dendrimer **44**. In both cases, the alkyne functions in the cores are internal and no longer terminal. The reaction sites are more hindered and less accessible, so the reaction must be heated to 230°C in diphenyl ether for three weeks to produce **43**. The presence of *tert*-butyl groups in **44** further reduces the accessibility to the reaction sites. Additionally, electronic considerations may also play a role in the diminished kinetics of the reaction. The Diels-Alder reaction involves an electron-rich diene and an electron-poor dienophile or vice versa. The presence of electron donating *tert*-butyl groups in the diene and dienophile makes the two entities electron-rich. Therefore, the reaction needs to be heated to 250°C for a month to produce **44**. Even under these conditions, the yield remains low and a significant quantity of the disubstituted product with an unreacted alkyne function is also obtained.



Scheme 3.6 | Synthetic route to dendrimer **43**.



Scheme 3.7 | Synthetic route to dendrimer **44**.

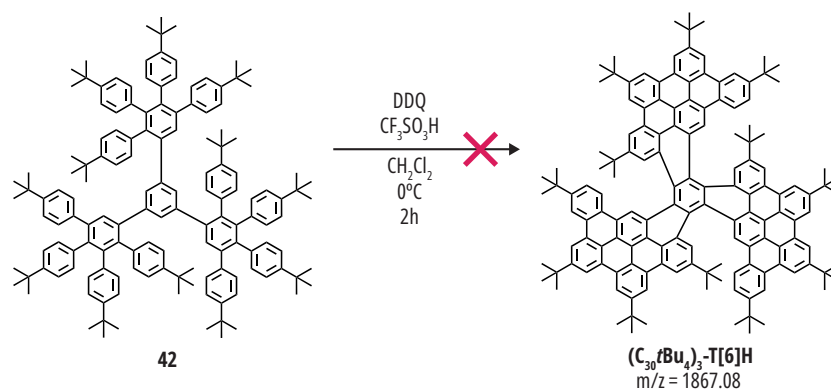
SCHOLL OXIDATIONS

OXIDATION OF (C₃₀tBu₄)₃-T[6]H

Let's first discuss the oxidation of the smallest dendrimer **42**, where only *tert*-butyl groups were added to the structure to induce the twisting. The oxidation was carried out with DDQ as oxidant and the reaction conditions are summarized in **Scheme 3.8**.

Unfortunately, the product was not identified by MALDI-ToF mass spectrometry at different reaction times, despite the use of small quantities of acid. A mass spectrum recorded at one hour thirty minutes into the reaction is presented in **Figure 3.15**. Notably, there are no peaks corresponding to dendrimer **42**, to the target product (C₃₀tBu₄)₃-T[6]H, or at intermediates *m/z* values that would suggest the presence of incomplete oxidations are present. The main peak is located at *m/z* = 3373.43.

Interestingly, it is possible to conceive a structure that would account for this peak: the dimer of the corresponding planarized triangular GQD. This planarized nanoparticle **(T)C₉₆tBu₉**, illustrated in **Figure 3.15**, could be obtained if the *tert*-butyl groups added to impede the planarization are removed during the Scholl oxidation. Such reactivity is not unprecedented, particularly when employing strong oxidants.¹⁹⁴ We observed examples of this while performing the oxidations of the rod-shaped GQDs with FeCl₃, where *tert*-butyl groups were substituted by a chlorine atom. In this case, even though a milder oxidant is employed, the strain introduced by the additional *tert*-butyl groups must significantly increase the reactivity at these sites. Purification and further characterizations of the dimer are still needed to confirm the proposed GQD structure.



Scheme 3.8 | Scholl oxidation of dendrimer **42**.

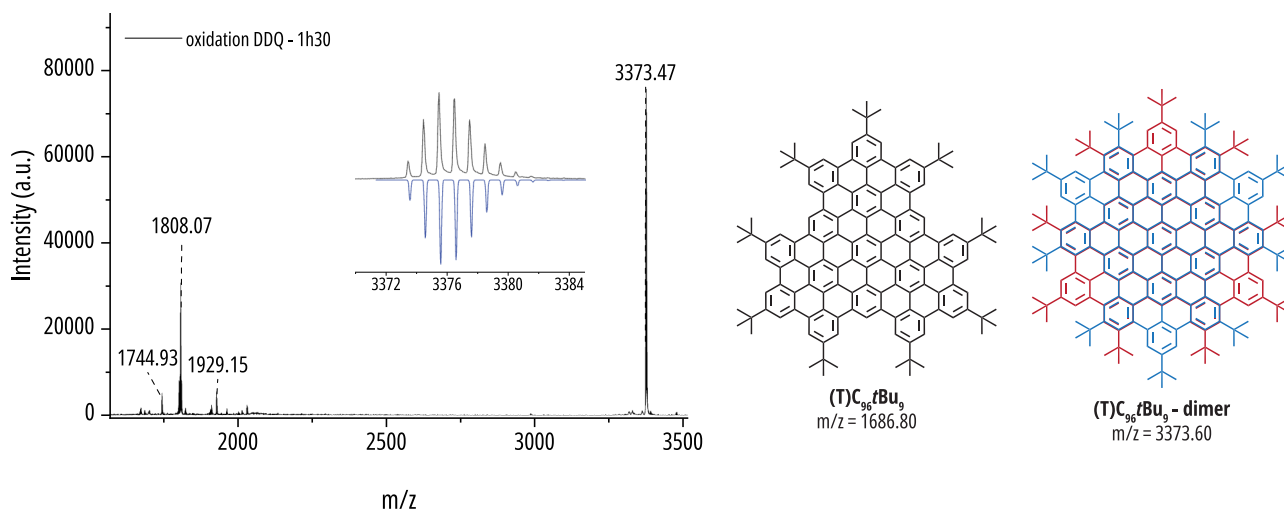
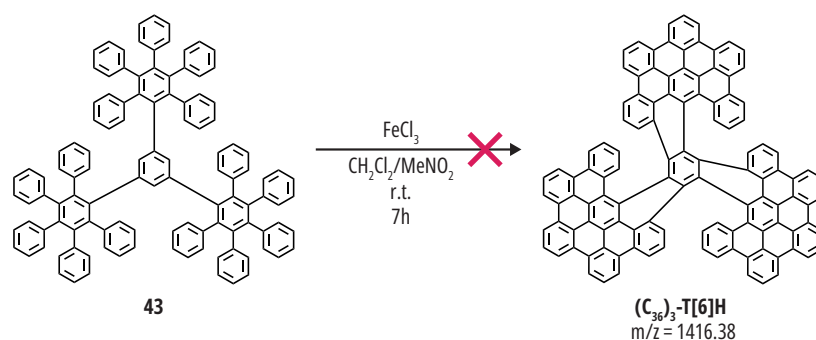


Figure 3.15 | MALDI-ToF mass spectrum of the oxidation of dendrimer **42** after 1h30 of reaction. To the right, the proposed structures to the monomer of the planar GQD **(T)C₉₆tBu₉** and its dimer, the proposed structure for the $m/z = 3373.47$ peak. The insert in mass spectrum correspond to the comparison of the experimental (black) isotopic distribution and the theoretical (blue) isotopic distribution for the **(T)C₉₆tBu₉** dimer.

Soluble dimeric structures of triangular C₉₆ GQD had already been reported by Y.-Z. Than's research group.^{90,233,234} In these reported structures the bilayer GQDs contained mesityl groups instead of *tert*-butyl groups. The **(T)C₉₆tBu₉** structure contains more solubilizing groups than the reported mesityl-substituted dimeric GQDs. Although we had previously conceptualized this **(T)C₉₆tBu₉** architecture, it presented a significant synthetic challenge. This approach to synthesize such type of highly substituted planar structures may be useful in future nanoparticle designs.

OXIDATION OF (C₃₆)₃-T[6]H

Let's now discuss the oxidation of the unfunctionalized dendrimer **43**. It is worth noting that this molecule had previously been synthesized for NMR studies, however, no attempts of oxidation have been reported thus far.^{235,236} Oxidation of **10** was tested with iron(III) chloride using the setup depicted in Section 2.1.1, in the presence of seven equivalents per C-C bond to be formed. This reaction is summarized in **Scheme 3.9**. The reaction was monitored using MALDI-ToF mass spectrometry. After seven hours of reaction, the main peak observed in the mass spectrum, presented in **Figure 3.16**, corresponded to a difference of eight mass units from dendrimer **43**. This peak can be attributed to the structure where only four C-C bonds are created. Despite the long reaction times and the choice of oxidant, the oxidation of dendrimer **43** seems to not proceed to completion. In response we synthesized dendrimer **44**, considering previous observations where *tert*-butyl groups enhance the reactivity towards the cyclodehydrogenation reaction.



Scheme 3.9 | Scholl oxidation of dendrimer **43**.

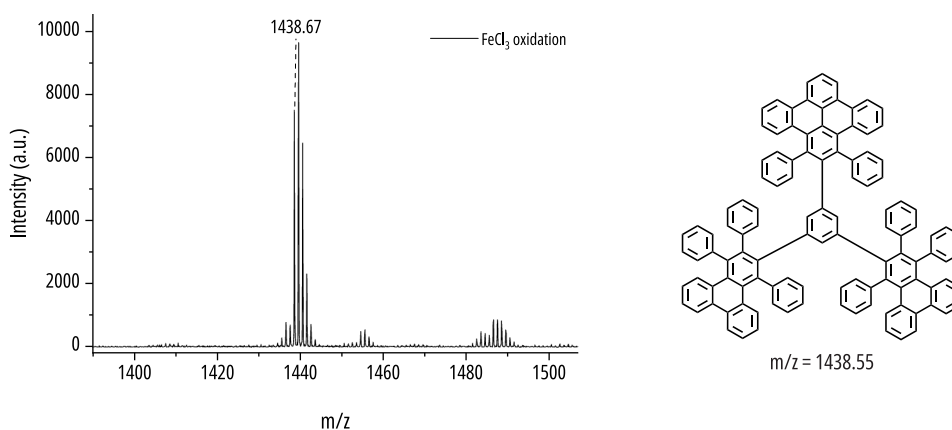
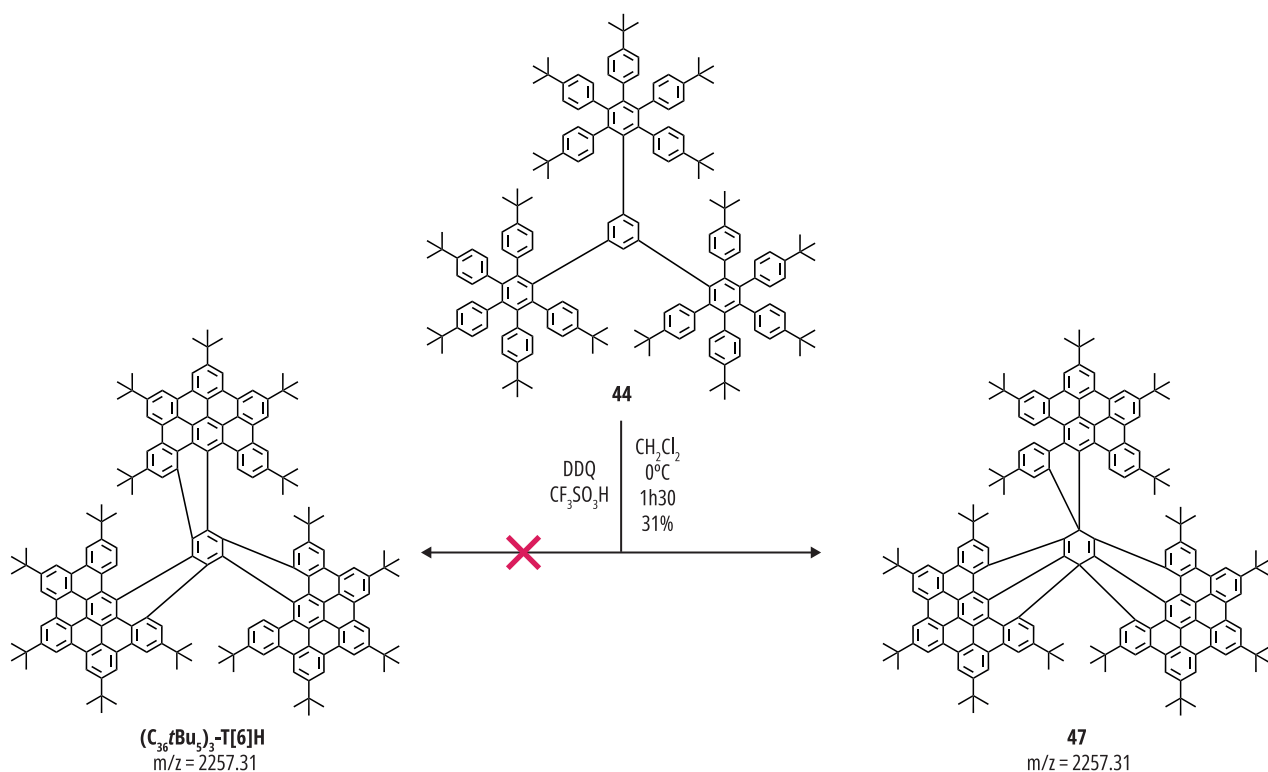


Figure 3.16 | To the left the MALDI-ToF spectrum of the Scholl oxidation of dendrimer **42**. To the right a proposed structure for the main peak.

OXIDATION OF (C₃₆tBU₅)₃-T[6]H

The oxidation of dendrimer **44** was tested using 1.5 equivalent of DDQ per C-C bond to be formed. The reaction conditions are summarized in **Scheme 3.10**. The mass spectrum analysis revealed a peak at the desired M⁺ mass along with other unidentified impurities at higher m/z values. The nanoparticle demonstrated a high solubility, enabling the performance of column chromatography (cyclohexane:toluene 9:1) to obtain a pure product. The MALDI-ToF mass spectrum after purification is given in **Figure 3.17a**. Single crystals were grown by slowly evaporating a solution of the purified product in toluene which allowed the recording of a single crystal X-Ray structure. The X-Ray measurements and structure calculations were done by Dr. Pierre Thuéry at CEA Saclay. The crystal structure showed that the targeted helicene was not formed; instead, a bis-spiro GQD **47** was obtained. In this product the central phenyl ring lost its aromaticity. One lobe of the nanoparticle displays a five-member

ring and a missing C-C bond. The other two lobes have all their C-C bonds formed, as well as an additional C-C bond with the central phenyl. The Single crystal X-Ray structure is presented in **Figure 3.17b**, without the *tert*-butyl groups for clarity purposes.



Scheme 3.10 | Scholl oxidation of dendrimer **44** into **47**.

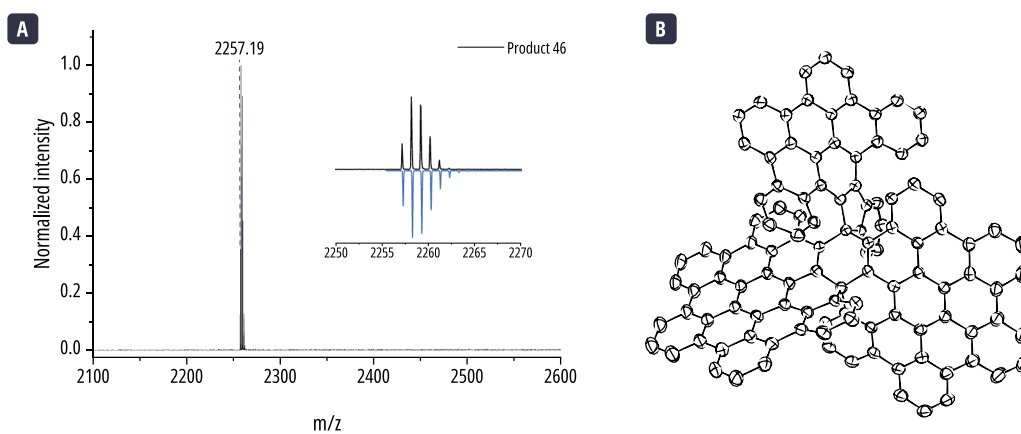


Figure 3.17 | (a) MALDI-ToF mass spectrum of bis-spiro GQD **47**. (b) Single crystal structure of product **47**. *Tert*-butyl groups are omitted for clarity.

The enhanced solubility allowed to perform NMR spectroscopy without the use of CS₂. The ¹H NMR, recorded in dichloromethane-d₂, is presented in **Figure 3.18**. Within the aliphatic region, multiple peaks can be discerned. In total, fifteen aliphatic signals can be identified, corresponding to the fifteen *tert*-butyl groups. Numerous aromatic peaks, ranging between 5.5 ppm and 10 ppm, can also be distinguished. Some shifts are lower than those typically expected for aromatic peaks, which can be explained by the placement of certain protons within the precession cone of other aromatic cycles, thereby increasing the magnetic field they experience.²³⁵ The sum of all the integrals is consistent to the number of expected protons in the structure, 168 protons. Further experiments, such as ¹H-¹H NOESY and ¹H-¹³C HSQC NMR spectroscopies are still necessary to make a full

attribution of the signals. However, it is possible to account for all the observed peaks in the ^1H NMR spectrum to the single crystal structure.

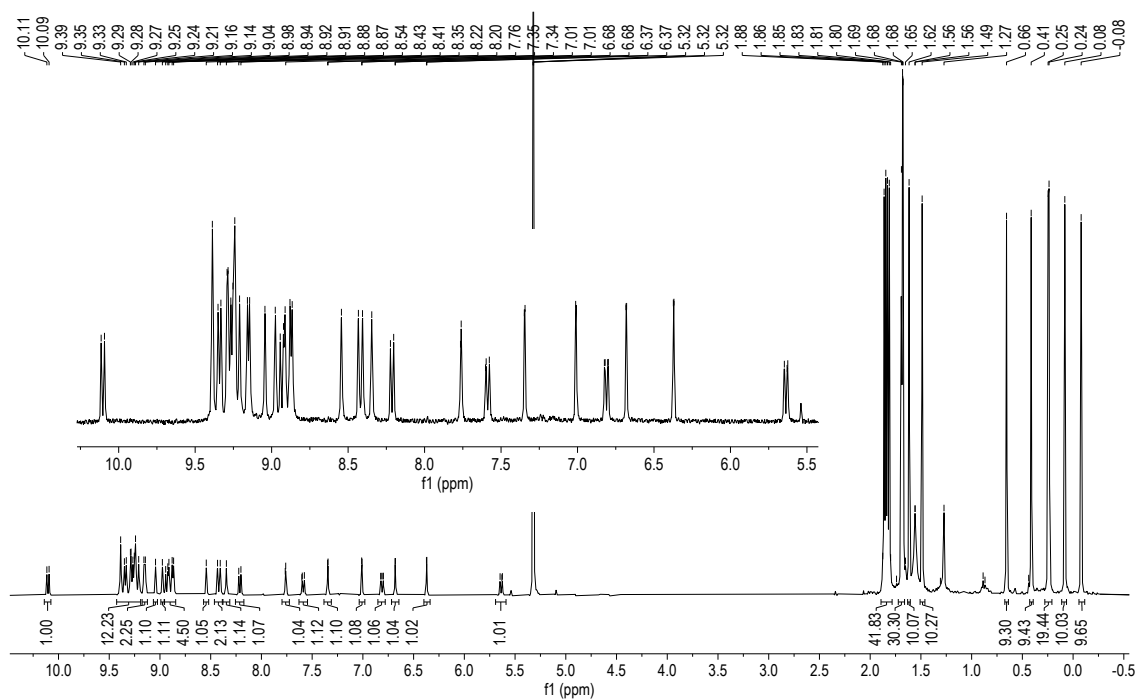


Figure 3.18 | ^1H NMR spectrum of bis-spiro QD **47** (400 MHz, CD_2Cl_2 , 298 K).

A final observation regarding the synthesis and characterization of bis-spiro QD **47**, is that based solely on mass spectrometry, it appears that the desired product was obtained. The purified sample was analyzed by NMR spectroscopy, where multiple peaks could be observed. Initially, it was uncertain whether the surplus of peaks in the NMR spectrum could be attributed to the presence of impurities or from conformers, for which the structure should be greatly altered giving rise to different NMR signals. It was the single crystal structure that allowed us to identify the real structure and account for the recorded ^1H NMR spectrum. It is known that rearrangements can occur during the Scholl reaction for planar and twisted structures, with migrations of phenyl groups and ring closures with five- or seven-members.^{83,194,237} The formation of spiro nanographene has been rarely reported, and in most cases the precursor of the Scholl oxidation is designed to give such compounds.^{238–240} To better comprehend the reactivity at play, we evaluated the oxidation at different reaction times. The preliminary results are presented in the following subsection.

UNDERSTANDING THE OXIDATION OF DENDRIMER 44

To determine whether the synthesis of the targeted helicene is feasible, we need to understand more thoroughly how the oxidation process unfolds. A critical moment is when the fusions with the central phenyl occur, as the major deviations from the target molecule happen here. In the synthesis of a large hexapole [7]helicene, Zhu *et al.* reported that complete oxidation of the lobes occurs in an initial step, and the oxidation to the central unit proceeds in a subsequent oxidative stage.¹¹⁴ In our case, the reaction seems not to follow the same order: the lobes are not completely oxidized before the fusion to the central phenyl. This can be inferred since we know that a C-C bond in a lobe is missing in the final structure. This missing C-C bond is likely the consequence of the previous formation of the adjacent five-member ring that adds additional strain to that part of the molecule.

Since the reaction seems to be complete after 1 hour, we decided to take samples at five-minute intervals to evaluate the reaction progression. The reaction was monitored by thin-layer chromatography (TLC) and MALDI-ToF mass spectrometry.

The reaction monitoring was done using 1.6 equivalents of DDQ per C-C bond to be formed and 1% v/v of triflic acid. The TLC plate is presented in **Figure 3.19**. At five and ten minutes, it is possible to distinguish an orange spot closest to the base on the TLC, labeled as spot "A". After ten minutes spot "A" disappears. The second spot, spot "B", is bright blue and corresponds to product **47**; it is present since the first five-minute aliquot and remains throughout the reaction. An additional bright blue spot, spot "C", which elutes higher than the other two spots, also gradually disappears over time but more slowly than the orange spot.

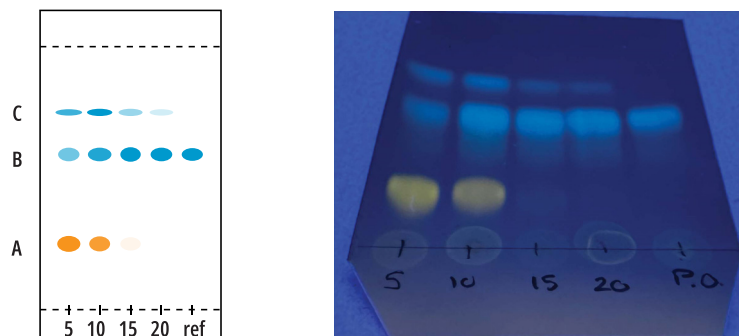


Figure 3.19 | Schematic representation (left) and photography (right) of the TLC plate (cyclohexane:toluene 9:1) of the reaction progression of the oxidation of dendrimer **44**. Lanes from left to right correspond to the sample taken at 5, 10, 15 and 20 minutes. Last lane corresponds to product **47** as reference.

In total, there are 15 C-C bonds that need to be formed. After the purification of a reaction carried out for only five minutes, the mass spectrum of the unknown compound from spots "A" and "C" were recorded. Their mass spectra are presented in **Figure 3.20**. The mass spectrum of compound "A" shows a peak at $m/z = 2267.83$. This is a difference of ten mass units from dendrimer bis-spiro GQD **47**, which would correspond to five missing C-C bonds. Blue intermediate "C" exhibits a mass peak at $m/z = 2259.91$, a difference of two mass units, or only one C-C bond is missing for completion of **47**.

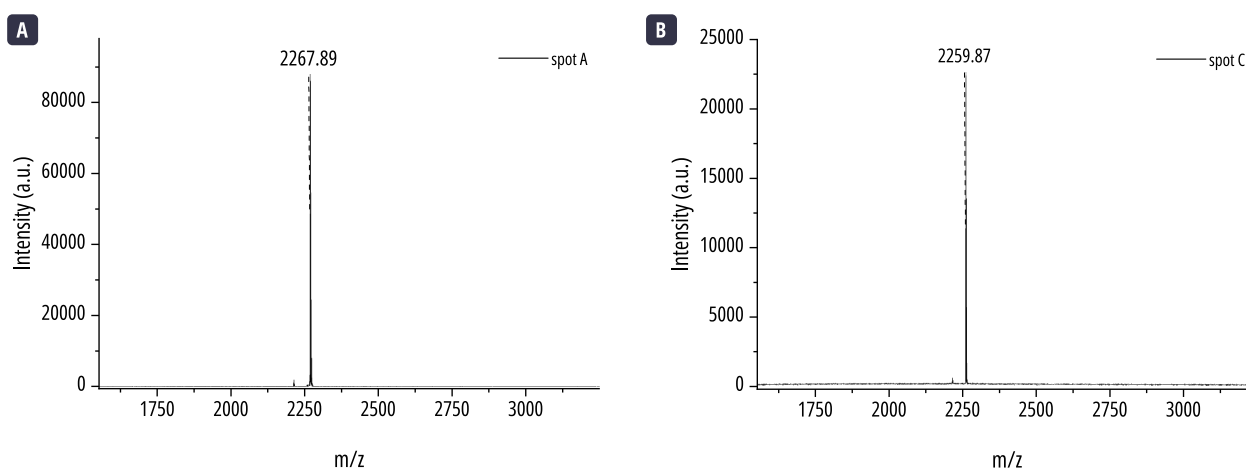


Figure 3.20 | MALDI-ToF mass spectra of the compounds from spot "A" (a) and spot "C" (b).

Interestingly for spot "A", an intermediate for which more C-C bonds are missing, the emission color is at higher wavelengths than the final product **47**. Usually, the opposite is observed in the fusion of nanoparticles, as the formation of C-C bonds increases, so does the conjugation and the shrinking of the bandgap. In this case, when the sp^3 carbons are created at the central phenyl, they break the conjugation, increase the bandgap, and thus shift the emission towards the blue. Therefore, in the intermediate giving spot "A", we can assume that the sp^3 carbon atoms have not yet been formed and can envisage a structure where C-C bonds were formed only in the lobes and not to the central phenyl. However, in intermediate "C", where only one C-C bond is missing to reach the obtained twisted GQD **47**, we return to a blue emission. The conjugation has been broken by the

formation of the sp^3 carbons. The two intermediates described here still need to be isolated in larger quantities to perform further characterizations and better understand which C-C bonds are formed and in which order. This work is ongoing, as well as theoretical calculations on the possible intermediate states to better understand the reactivity of dendrimer **44** towards the Scholl reaction and the formation pathway to **47**.

The reaction seems to proceed quickly, with product **47** formed within the first five minutes of the reaction. An alternative approach to synthesize the initial target ($C_{36}tBu_5$)-T[6]H helicene, might be to test weaker acids, a common alternative being methanesulfonic acid (MSA). A first test in the presence of MSA suggest that the oxidation reaction does not take place in the presence of this acid. Alternatively, other acid/oxidant couples may be tested, for example, using a Lewis acid such as BF_3 , or changing the oxidant to PIFA. Iron(III) chloride may also be considered, but since it is a stronger oxidant than DDQ, similar results may be expected. In an initial approach, milder oxidants will be tested.

CHIROPTICAL PROPERTIES

The obtained bis-spiro GQD **47** is also chiral. The chiral purification and chiroptical properties were done at the Service de Chimie Bioorganique et de Marquage (SCBM) at CEA Saclay with the help of Lilian Estaque and Dr. Gérgory Pieters.

The absorption and PL spectra of the racemic mixture of **47** is given in **Figure 3.21**. Because of the breaking of the conjugation by sp^3 carbon atoms, the absorption and emission of **47** are observed in ultraviolet and beginning of the visible regions of the electromagnetic spectrum. The absorption spectrum is broad between 300 nm and 450 nm with some discernible peaks. The maximum of absorption is situated at 345 nm and exhibits a molar absorption coefficient of $137\,000\text{ M}^{-1}\cdot\text{cm}^{-1}$ at this wavelength. The emission spectrum is composed of three sharp lines at 475 nm, 506 nm, and 544 nm. The colour of the emission lies in the cyan hue. **47** appears to be highly luminescent, however, the measurement of the fluorescence quantum yield is still pending due to a problem with the spectrometer.

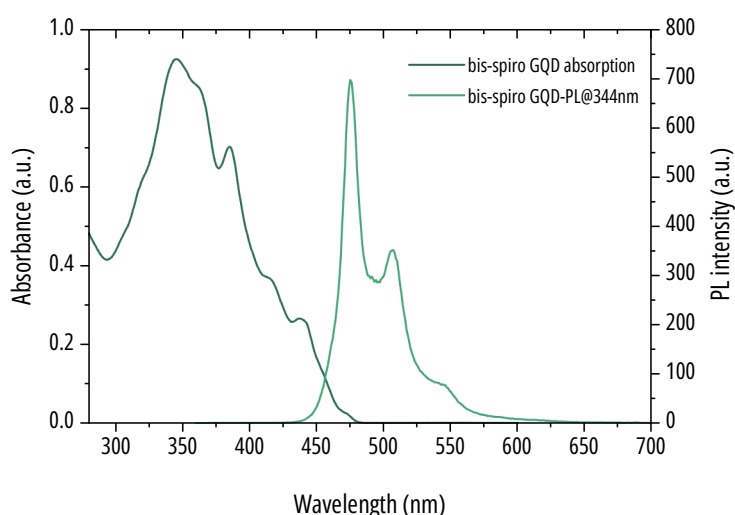


Figure 3.21 | Absorption and emission spectra of the GQD **47** in tetrahydrofuran.

The enantiomers of **47** were separated by chiral HPLC. A first optical characterization to perform with chiral molecules is their absorption response to circularly polarized light. This light can either be polarized to the left or to the right. Circular dichroism (CD) measures the capacity of a molecule to absorb either left- or right circularly polarized light. At each wavelength

the sample is shined with left-handed and right-handed circularly polarized light, and the difference of the absorbance of both, the delta absorbance (ΔA), is measured following the following relationship:

$$\Delta A = A_L - A_R$$

Equation 3.1

As for linearly polarized light the Beer-Lambert law can be applied to calculate the molar circular dichroism ($\Delta\varepsilon(\lambda)$) as follows:

$$\Delta A(\lambda) = \Delta\varepsilon(\lambda)lC = (\varepsilon_L(\lambda) - \varepsilon_R(\lambda))lC$$

Equation 3.2

Where l is the light path length, C the concentration of the sample, and ε_L and ε_R the molar extinction coefficients for left-handed and right-handed CP light respectively. The molar absorption is independent of the concentration and measurement cell length, so it is useful to compare different samples at the same wavelengths. However, to compare the circular dichroism between wavelengths, it is more useful to use the absorptive dissymmetry factor g_{abs} defined in the following relation:

$$g_{abs} = \frac{\Delta\varepsilon(\lambda)}{\varepsilon(\lambda)} = \frac{\varepsilon_L(\lambda) - \varepsilon_R(\lambda)}{1/2(\varepsilon_L(\lambda) + \varepsilon_R(\lambda))}$$

Equation 3.3

Where $\varepsilon(\lambda)$ is the molar absorption coefficient for linearly polarized light, which can also be expressed as the half of the sum of the left-handed and right-handed circularly polarized light molar absorption coefficients. Theoretically, the dissymmetry factor is comprised between 2 and -2. For organic molecules the values typically range between 10^{-4} to 10^{-1} .²⁴¹

The CD spectra of the two enantiomers of product **47** are shown in **Figure 3.22**. The CD spectra are a perfect mirror image of each other, confirming that we are observing enantiomers. It can be observed that the Cotton effect is more important at the longest wavelengths of the absorption, around 450 nm. It is also at this wavelength that the molecule exhibits the maximum g_{abs} of 0.012. This value is in the higher range of g -values usually observed for similar chiral nanographene molecules.¹¹¹

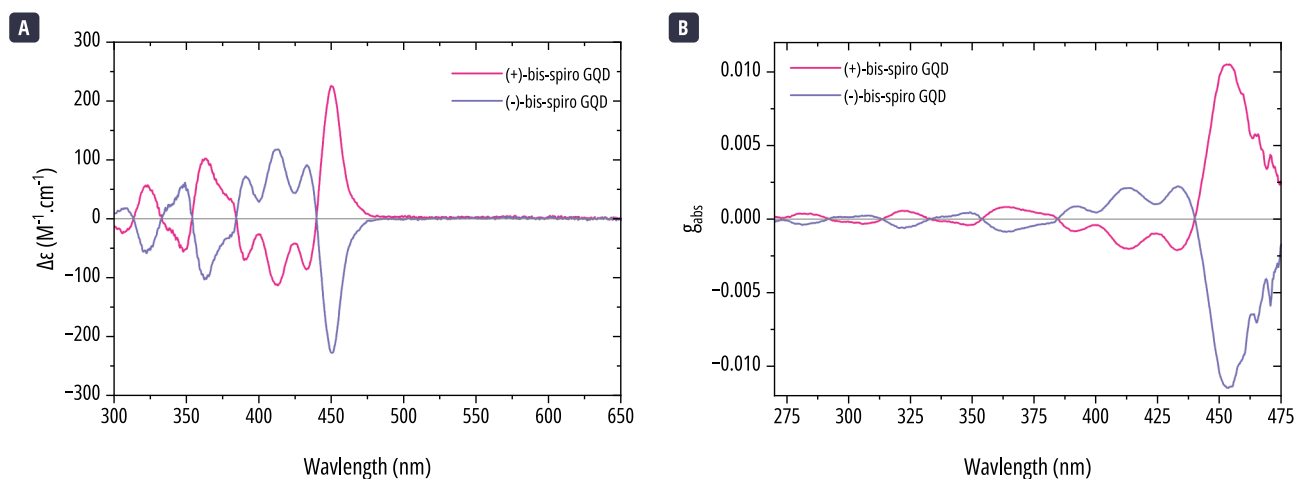


Figure 3.22 | CD spectra of both enantiomers of **47**. (a) Reported as a function of $\Delta\varepsilon$ ($M^{-1}\cdot cm^{-1}$) and (b) of the absorption dissymmetry factor g_{abs} .

Chiral chromophores can spontaneously emit left or right circularly polarized light. This is measured by circularly polarized luminescence (CPL) spectroscopy.²⁴² In an analogous fashion to circular dichroism, the intensity difference ($\Delta I(\lambda)$) between the emitted left ($I_L(\lambda)$) and right ($I_R(\lambda)$) CPL is defined as follows:

$$\Delta I(\lambda) = I_L(\lambda) - I_R(\lambda)$$

Similarly, the luminescence dissymmetry factor g_{lum} is defined as follows:

$$g_{lum} = \frac{2\Delta I(\lambda)}{I(\lambda)}$$

Where ($I(\lambda)$) is the total intensity of the emitted light. As for CD, the limit values for g_{lum} are 2 and -2, where the system would emit pure left or right circularly polarized light, respectively. The typical values for organic chromophores are situated between 10^{-4} and 10^{-2} .

Molecule **47**, being a chiral chromophore also emits circularly polarized light. Its CPL spectrum is given in **Figure 3.23**. As for the CD, the CPL spectra for both enantiomers are mirror images. The maximum of the dissymmetry factor for luminescence (g_{lum}) is 7×10^{-3} . This again is a good value for a chiral organic chromophore.

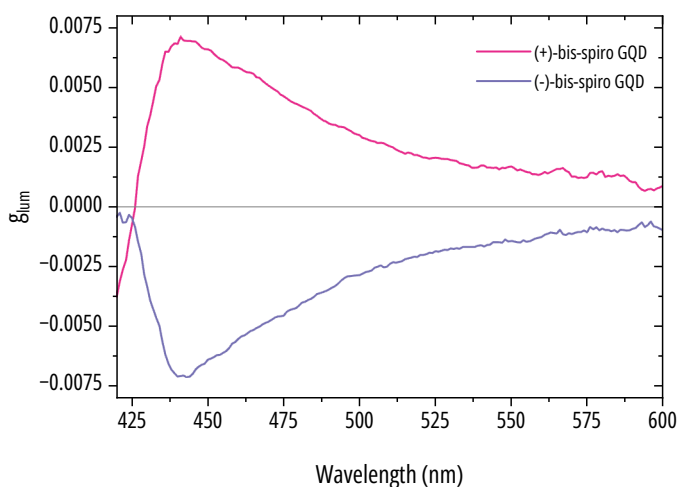


Figure 3.23 | CPL spectra of both enantiomers of **47** reported as function of photoluminescence dissymmetry factor g_{lum} .

Despite the synthesis of a different structure than the one expected, GQD **47** was found extremely interesting, and investigations are still ongoing on its properties and on its mechanism of formation. Upon purification of the enantiomers, we were able to explore its chiroptical properties by CD and CPL. The chiroptical properties of molecule **47** are good and lie in the higher range for similar organic molecules. It would be very interesting to be able to compare these properties to that of the originally planned helicene (**C**₃₆**tBu**₅)₃-**T[6]H**. As previously mentioned, efforts are currently underway to obtain this helicene structure.

3.2.2 GQD PROPELLER

To increase the solubility of the nanoparticles, another possible approach is to interlock two distinct nanoparticles through covalent bonding. These types of structures are known as GQDs propellers.¹¹² We designed a GQD in which two graphene nanoparticles, each containing 72 sp^2 carbon atoms, are held together by a central C-C bond. To further improve the solubility

and the reactivity towards the Scholl oxidation, *tert*-butyl groups were added to the edge of the nanoparticle. This structure is depicted in **Figure 3.24**, along with a relaxed three-dimensional structure. The relaxed structure, attained through an MM2 energy minimization method, suggest that the propeller is likely adopt a twisted conformation.

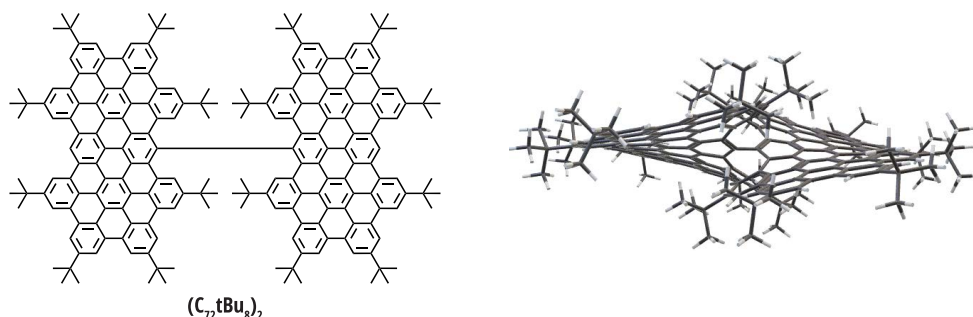
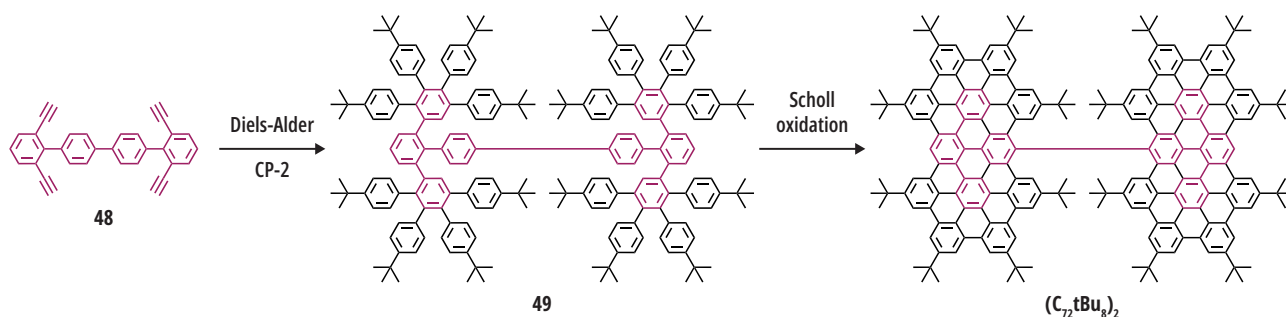


Figure 3.24 | (Left) Schematic structure of $(C_{72}tBu_8)_2$ propeller. (Right) Relaxed three-dimensional structure through MM2 energy minimization.

To synthesize $(C_{72}tBu_8)_2$, the same strategy employed so far for the synthesis of GQDs was used. The main steps are illustrated in **Scheme 3.11**. First, the tetraphenyl alkyne core **48** is synthesized and then reacted with cyclopentadienone **CP-2** to produce the corresponding dendrimer **49**. This dendrimer is subsequently oxidized through the Scholl reaction to yield the desired GQD propeller. Similar to helicenes, steric hindrance is introduced into the structures through *tert*-butyl and phenyl groups at the center of the nanoparticle to prevent the fusion into a larger sp^2 structure.

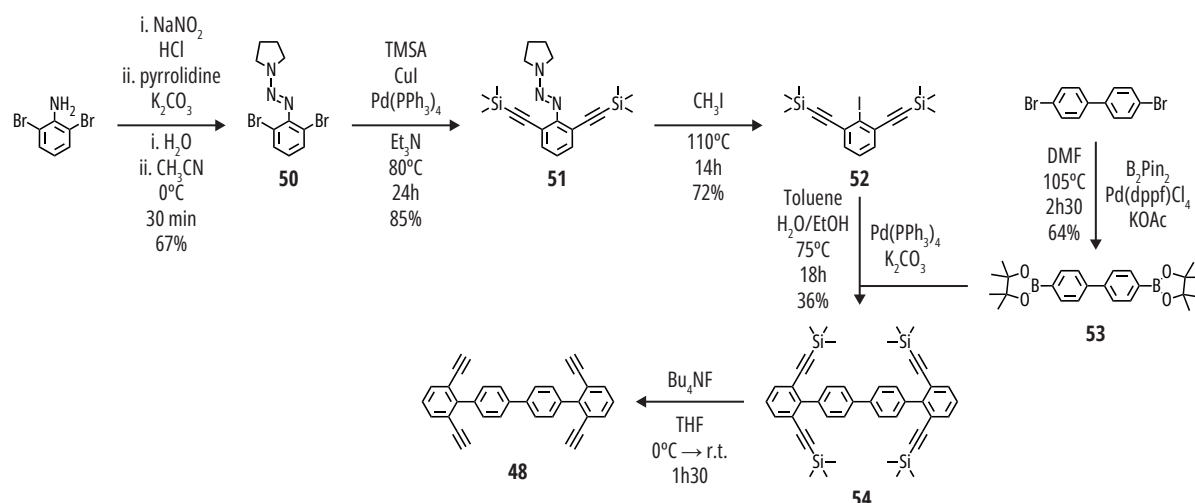


Scheme 3.11 | General synthetic strategy to propeller $(C_{72}tBu_8)_2$.

Throughout this section we will discuss the synthesis of the propeller $(C_{72}tBu_8)_2$ GQD, followed by its characterization and preliminary optical studies.

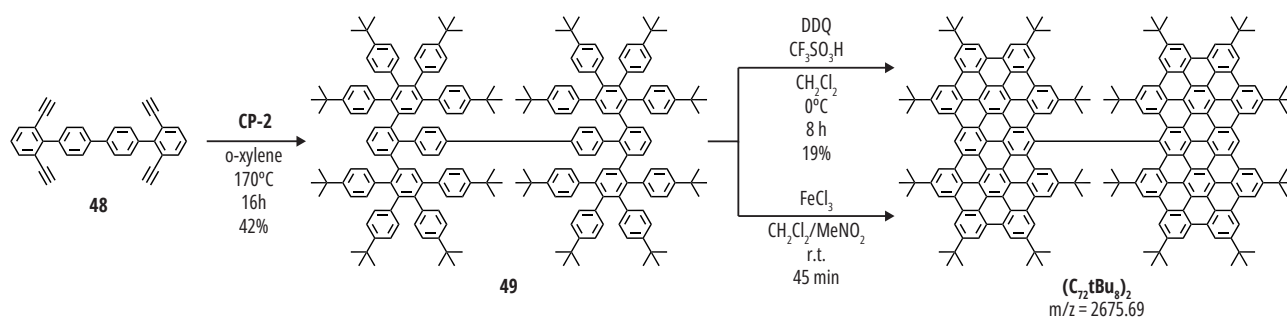
SYNTHESIS

Let's first discuss the synthesis of alkyne core **48**. Its synthetic approach is summarized in **Scheme 3.12**. The synthesis begins with the protection of the amine functions of the commercially available 2,6-bromoaniline, using sodium nitrite and pyrrolidine, to produce the triazene **50**.²⁴³ In this step, a diazonium is formed, which is then trapped by the pyrrolidine to produce the triazene. Triazene **50** is stable and can undergo a Sonogashira coupling with trimethylsilylacetylene (TMSA) to yield compound **51**. The triazene group in **51** is converted into iodine through a reaction with iodomethane, resulting in the iodinated compound **52**. Intermediate **52** is then reacted with biphenyl-diboronic ester **53** through a Suzuki-Miyaura coupling to produce the tetramethylsilane protected tetraphenyl alkyne core **54**. Biphenyl-diboronic ester **53** is synthesized through a Miyaura borylation from the commercially available 4,4'-dibromobiphenyl. Finally, the target alkyne core **48** is obtained after deprotection of **54** in the presence of tetrabutylammonium fluoride. These reactional steps are summarized in **Scheme 3.12**.



Scheme 3.12 | Synthetic route to tetraphenyl alkyne core **48**.

With the desired alkyne core, we proceeded to the dendrimer synthesis and subsequent oxidation into propeller ($\text{C}_{72}\text{tBu}_8$)₂. The reactional steps are presented in **Scheme 3.13**. Dendrimer **49** is synthesized through the Diels-Alder reaction between the alkyne core **48** and the tetra-*tert*-butyl substituted cyclopentadienone **CP-2**. Next, The Scholl reaction was performed with iron(III) chloride and DDQ as oxidant to obtain the ($\text{C}_{72}\text{tBu}_8$)₂ propeller.



Scheme 3.13 | Synthetic route to the synthesis of propeller ($\text{C}_{72}\text{tBu}_8$)₂.

First, eight equivalents of FeCl_3 per C-C to be created were used. The reaction was monitored using MALDI-ToF mass spectrometry. After 45 minutes of reaction time, the targeted mass for the product began to be detectable (**Figure 3.25a**). However, peaks at higher m/z values remained predominant. A possible origin to these peaks could be incomplete fusion or chlorinated byproducts where a *tert*-butyl group has been substituted. To achieve a cleaner reaction, we decided to focus on a milder oxidant.

Initially, the reaction with DDQ as oxidant was attempted in the presence of methanesulfonic acid. However, even after 5 hours of reaction, only 10 C-C bonds were formed. Upon using triflic acid in small quantities, the desired product mass peak began to predominate at 4 hours and seemed to reach completion after 7 hours of reaction. Upon examining the isotopic distribution, a discrepancy at higher mass units was noted between the experimental and simulated mass spectrum for the target product (**Figure 3.25b**). This could be attributed to nanoparticles with one or more missing C-C bond were still present.

The propeller ($\text{C}_{72}\text{tBu}_8$)₂ structure displayed a high solubility, enabling purification via column chromatography. In the mass spectrum, after the purification step, the isotopic distribution appeared more consistent with the simulated one (**Figure 3.25c**). Nonetheless, it is worth mentioning that, despite the good solubility for a GQD, the product tends to drag in the column,

and some fractions of the product remained mixed with other byproducts, thus impacting the calculated reaction yields. Only the best fractions were used for subsequent studies.

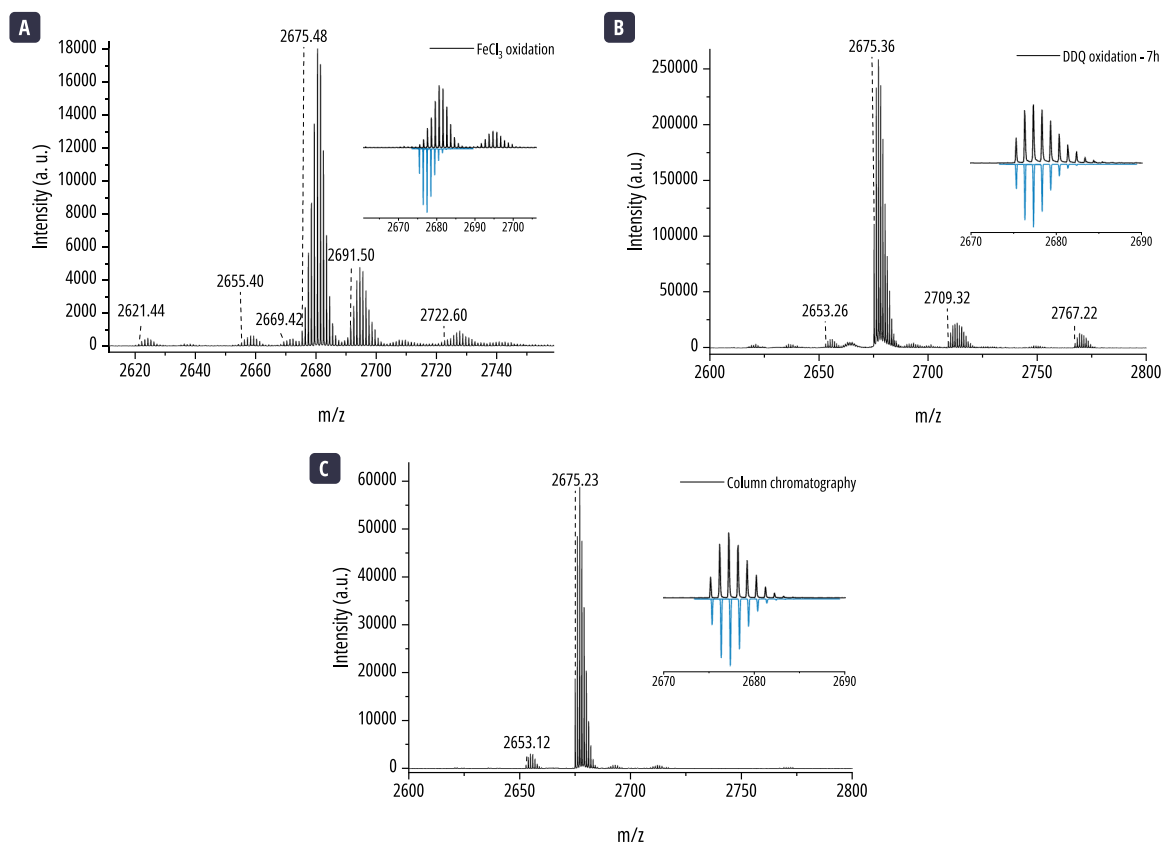


Figure 3.25 | MALDI-ToF spectrum of (a) the oxidation of dendrimer **49** with FeCl_3 after 45 minutes. (b) Mass spectrum of the oxidation of **49** with DDQ after 7 hours. (c) Mass spectrum of (b) after purification through column chromatography. The inserts correspond to the comparison of the experimental (black) and theoretical (blue) isotopic distribution for the target structure of $(\text{C}_{72}\text{tBu}_8)_2$.

NMR CHARACTERIZATION

NMR spectroscopy is in line with the target structure. The ^1H NMR spectrum, recorded in dichloromethane- d_2 , is presented in **Figure 3.26a**. In the aromatic region, we can distinguish nine singlets between 8.3 ppm and 11.8 ppm. All the singlets account for four protons, except for the most low-field signal, which accounts for two protons. This way, we were able to assign proton 1 to the singlet at 11.73 ppm.

Observing the aliphatic region, we can identify four peaks that can be attributed to the *tert*-butyl groups at 2.41 ppm, 1.96 ppm, 1.61 ppm, and -0.24 ppm. The most downfield peak can be assigned to *tert*-butyl A. This *tert*-butyl group experiences a similar effect to that observed for protons in dendrimer **43**. This functional group positions inside the precession cone of the aromatic rings from the sp^2 domain from the adjacent lobe of the molecule, thus decreasing the experienced magnetic field. The remaining protons were assigned using ^1H - ^1H NOESY and ^1H - ^1H TOCSY NMR spectroscopies.

We will focus on the discussion concerning the ^1H - ^1H NOESY NMR spectroscopy, and specifically on the cross-peaks observed between the aromatic and aliphatic regions, which are given in **Figure 3.26b**. It is possible to observe that the *tert*-butyl groups couple through space not only to their adjacent hydrogen but also with the hydrogen atoms located at adjacent rings. For example, protons from the *tert*-butyl group labelled C interacts with protons 3, 4, 5, and 6 with similar intensities instead

of only protons 4 and 5. In the case of the planar rod-shaped structures, where the same environment is present, each *tert*-butyl groups only couples through space to its immediate neighbor. The fact that this propeller shows correlations through space with more distant protons may be a first indication that indeed propeller ($C_{72}tBu_8$)₂ adopts a twisted configuration and that the two lobes are not only two planar GQDs lying perpendicular to each other. However, for finer details of the structure, a single crystal X-Ray analysis would be advantageous, but despite several attempts, no usable crystals were obtained.

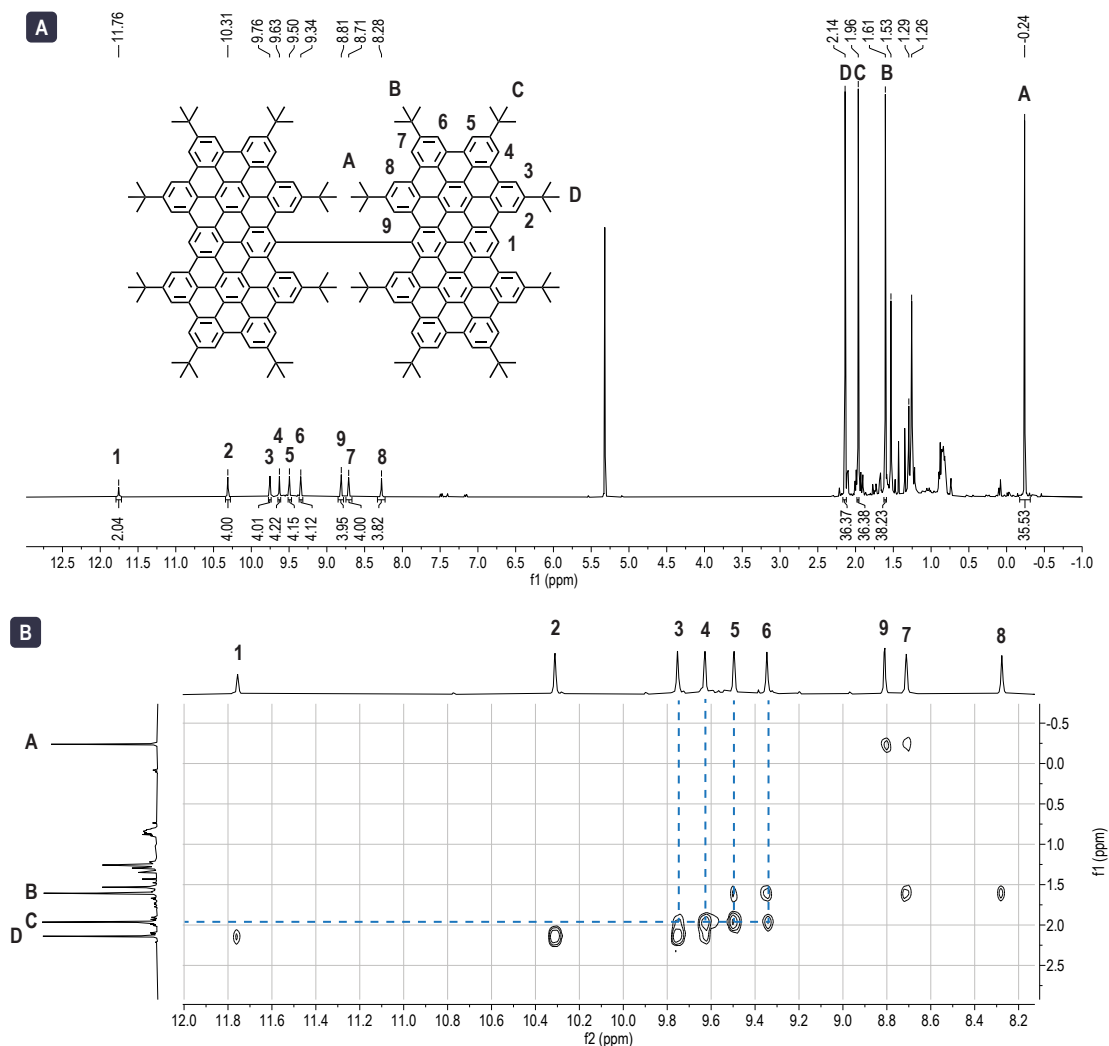


Figure 3.26 | (a) ¹H NMR spectrum of propeller ($C_{72}tBu_8$)₂ (400 MHz, CD₂Cl₂, 298 K) with peak attributions to the structure. (b) ¹H-¹H NOESY NMR spectrum showing the couplings between the aromatic and aliphatic protons. Dotted lines show the correlation between *tert*-butyl protons C and protons 3, 4, 5, and 6.

As a final remark for the NMR analysis, it is possible to detect some impurities in the aliphatic regions as well as in the aromatic region between 7.00 ppm and 7.50 ppm and adjacent to the peaks of the propeller ($C_{72}tBu_8$)₂. These impurities seem to be minimal and will be subject to further discussion in the HPLC analysis section. Nonetheless, NMR spectroscopy confirms the structure of the nanoparticle, which is crucial, since, as we observed in the previous section with helicene ($C_{36}tBu_5$)₃-T[6]H, mass spectrometry alone can have serious limitations to verify the formation of a GQD. This is especially true for twisted structures where the increased strain can give rise to unexpected isomeric structures.

OPTICAL PROPERTIES

Once the propeller ($C_{72}tBu_8$)₂ was purified, its optical properties were examined. The optical spectra were recorded in 1,2,4-trichlorobenzene. The absorption and emission spectra are depicted in **Figure 3.27**. The absorption spectrum displays three main peaks at 416 nm, 441 nm, and 473 nm. Meanwhile, the photoluminescence spectrum exhibits multiple peaks ranging from 500 nm to 650 nm. We can compare the optical properties of a similar C_{72} GQD substituted by 2,6-methylphenyl groups described H. J. Cho *et al.*²⁴⁴ The absorption and emission spectra of this phenyl-substituted GQD is given in **Figure 3.27c**. The maximum of absorption for both nanoparticles are located at similar wavelengths. It is also possible to distinguish a similar pattern of absorption peaks. The emission also takes place at similar wavelengths, but the intensities of the emission pattern differ. The propeller ($C_{72}tBu_8$)₂ behaves similarly as an analogous monomer C_{72} . It could be interesting to better understand if the observed difference, notably for the photoluminescence, originate by the difference of the functional groups or by the proximity of two graphenic domains which has an impact on the electronic distribution. This propeller GQDs merits more extended experimental optical studies and theoretical descriptions.

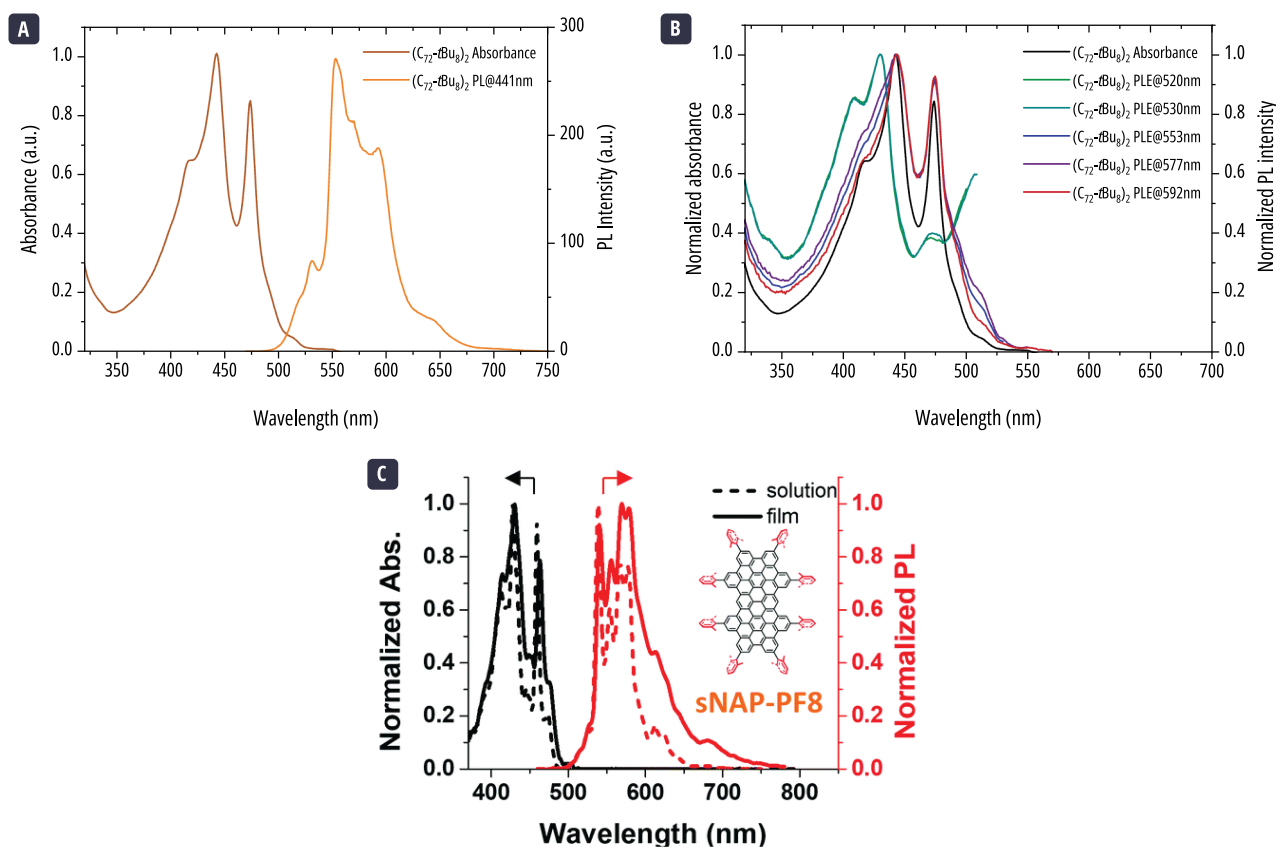


Figure 3.27 | (a) Absorption and emission spectrum of propeller ($C_{72}tBu_8$)₂ in 1,2,4-trichlorobenzene. (b) Excitation spectra at different emission wavelengths. (c) Absorption (black) and emission (red) spectra of a similar C_{72} GQD substituted with phenyl groups.

The spectra are reported in solution (dotted line) and in a film (plain line).²⁴⁴

Comparing the excitation spectra at all the emission wavelengths, two distinct types of spectra can be discerned. The emission peaks below 530 nm display a blue-shifted excitation spectrum at the maximum wavelength, while the emission peaks above 530 nm share an excitation spectrum similar to the absorption spectrum. This suggests the presence of two emitting entities in the solution. A possible hypothesis for the origin of these two entities lies in the presence of different conformers. These conformers could be the helically twisted structure and a meso-structure for which one sp^2 system of the propeller is twisted

towards the same side of the nanoparticle while the other system faces the opposite side. The existence of such meso-compounds has been previously described by Fujikawa *et al.* in the context of a double π -expanded helicene.¹¹⁷

HPLC ANALYSIS

To isolate the objects in solution we performed HPLC on a fraction of the $(C_{72}tBu_8)_2$ propeller from a different batch to the one used for NMR characterization. The chromatogram at 394 nm is presented in **Figure 3.28**. This wavelength, different from the maximum, was chosen to better distinguish the different peaks. It is possible to distinguish three peaks, labeled as peak "A", peak "B", and peak "C".

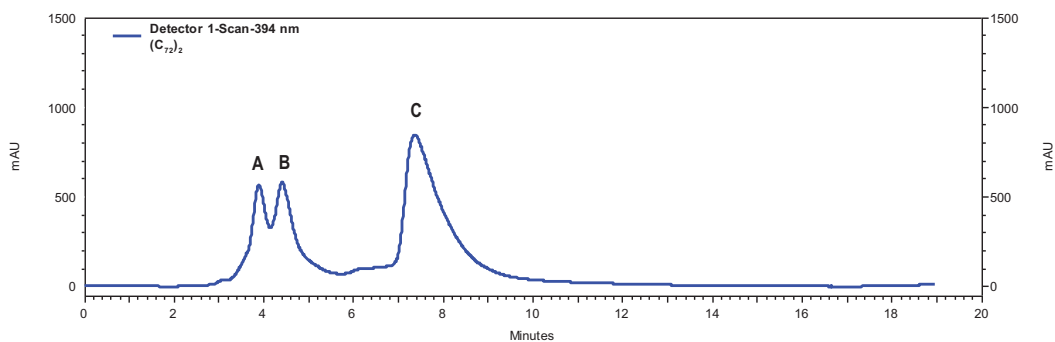


Figure 3.28 | HPLC chromatogram at 394 from a sample of $(C_{72}tBu_8)_2$. Eluent: cyclohexanes/dichloromethane 98/2.

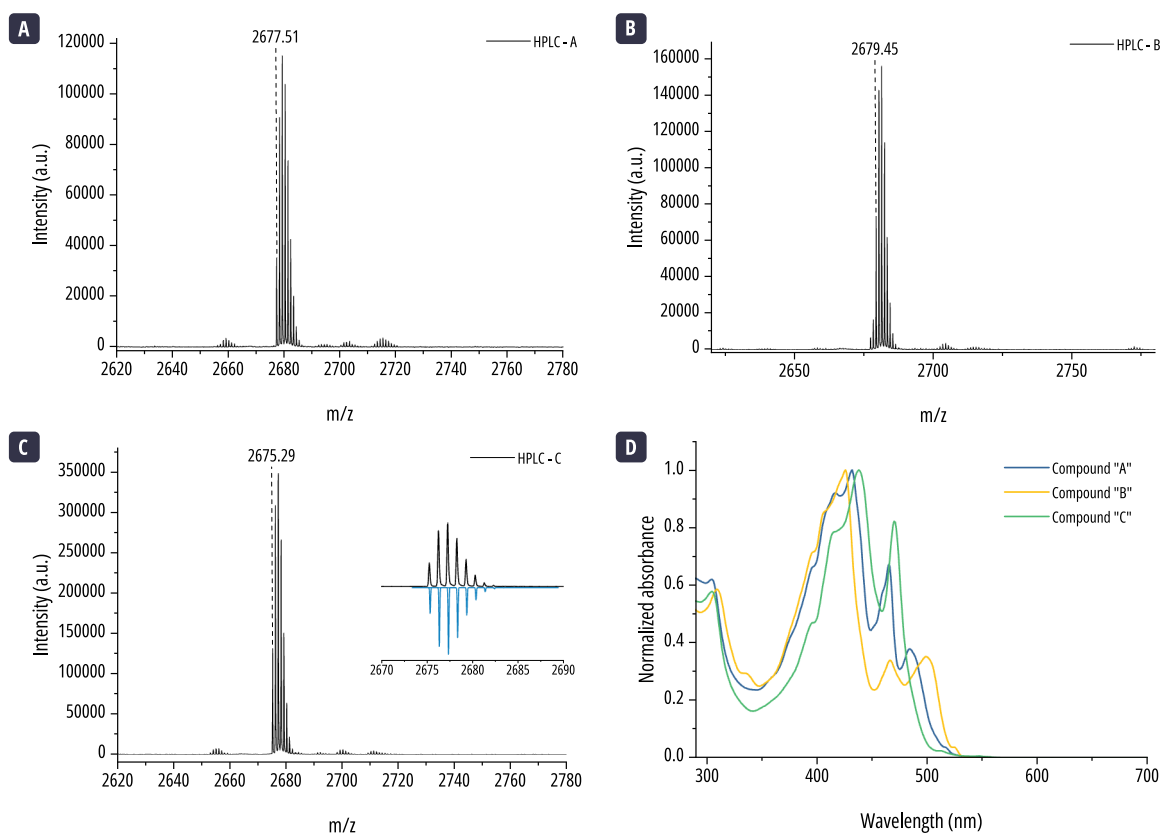


Figure 3.29 | MALDI-ToF mass spectrum of compounds "A" (a), "B" (b), and "C" (c). (d) The absorption spectrum recorded for the three compounds.

The mass spectrometry spectrum of the compound recovered for each peak is presented in **Figure 3.29a-c**. For peak "A", the primary product exhibits a $m/z = 2677.31$, that is a two-mass unit difference from the target mass. The compound from peak "B" has a main peak at $m/z = 2679.45$, a difference of four mass units from the target mass. For the compounds from peak

“A” and “B”, the difference in mass could be due to missing C-C bonds or to an incorrect fusion as for compound **47**. Finally, the compound recovered from peak “C” exhibits main peak at $m/z = 2675.29$, which corresponds to the expected mass for the $(C_{72}tBu_8)_2$ propeller. The comparison of the isotopic distribution at this peak shows an excellent agreement between the experimental results and the simulation. The absorption spectra of the compounds from the three peaks are presented in **Figure 3.29d**. They agree to the two different the excitation spectra observed before.

The HPLC purification showed that the different objects in solution do not correspond to the two twisted and meso isomers of the propeller, but rather to different compounds. These compounds can be separated to yield a pure propeller. The different analysis presented here led us to conclude that we successfully synthesized the $(C_{72}tBu_8)_2$ propeller. Thanks to its functional groups and three-dimensional character this GQD is highly soluble allowing its purification and NMR analysis. The optical investigation of the GQD presented here was just preliminary and more advanced experiments are yet to be performed. Attempts to crystallize $(C_{72}tBu_8)_2$ are still ongoing to see how the propeller evolves in space. This will be useful to confirm whether the different sp^2 domains twist or remain planar. If indeed the sp^2 domains twist, as the computationally relaxed structure suggests, this would be very interesting for the synthesis of interlocked helical structures.

At the beginning of the section, we defined helicenes as *ortho*-fused rings. This type of lateral fusion of cycles generates only one cavity diameter. To obtain larger diameters it is possible to alternate an *ortho*- and *para*-fusion of phenyl rings. These types of structures are known as extended helicenes (**Figure 3.30a**).²⁴⁵ Theoretical calculations, and experimental observations, seem to indicate that expanded helicenes have a higher dissymmetry factor g than helicenes. This is attributed to a larger cavity diameter created by the helix with a more pronounced effect as the helix increases in size.²⁴⁶

The simulated propeller twisted structure (**Figure 3.24**) can be assimilated to two small interlocked extended helicene. Because of the steric hindrance, cause by the proximity of the two small extended helicene fragments, they may adopt a helical formation. This helical configuration would introduce conformational chirality to the structure. This is illustrated in **Figure 3.30b-c**, where only the center of the propeller $(C_{72}tBu_8)_2$ is shown for clarity. However, additional calculations would be required to assess the racemization barrier. This is because the direction of the helical configuration can be changed by the rotation of the central C-C bond thus making the enantiomeric species indistinguishable (**Figure 3.30c**).¹¹⁹ The densely packed nature of the propeller may reduce this effect, potentially giving rise to a chiral structure based on a double expanded helicene. Finally, propeller $(C_{72}tBu_8)_2$ is a first proposition towards this end, we can now imagine new structures where the free C-C rotation is effectively blocked by adding covalent bonding between the sp^2 subunits or coordination bonding through a new structure capable of hosting a metallic atom between the two graphenic subunits.

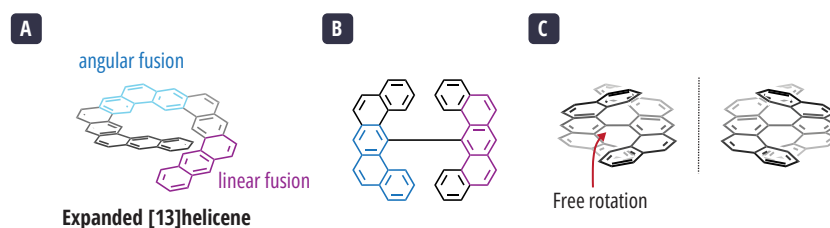


Figure 3.30 | (a) Structure of the extended [13]helicene. (b) Center of the $(C_{72}tBu_8)_2$ showing the alternation between *ortho* and *para* fusion of the aromatic rings. (c) Proposed helically twisted structure of the center of $(C_{72}tBu_8)_2$. The red arrow shows the free C-C bond that can rotate and change the direction of the helicity.

3.3 CONCLUSION

Throughout this chapter we discussed two different approaches to further enhance the solubility of graphene quantum dots. The first one consisted in an extension of the strategy presented in the previous chapter, add adjacent *tert*-butyl groups along the main axis of rod-shaped graphene nanoparticles. The second consisted of adding steric hindrance in the polyphenylene dendrimer to force its oxidation into twisted helical structures.

The first approach was motivated by the limited solubility exhibited by **C₇₈tBu₆** (from Chapter 2), who, despite possessing bulky groups around its edges, experienced an aggregation process not observed for its larger homologues. This effect was attributed to the lack of adjacent of *tert*-butyl groups along its main axis. In response, we decided to add additional functional groups along the axis of the rod-shaped nanoparticles. This originated a new family of fully *tert*-butylated GQDs, whose synthesis and characterizations were presented in the first half of this chapter. The optical studies of the new **C₇₈tBu₁₀** showed that the addition of the *tert*-butyl groups was effective to significantly increase its solubility compared to its partially *tert*-butylated counterpart. Thanks to the new architecture of the GQDs, it was possible to synthesize a smaller **C₆₀tBu₈** nanoparticle who also exhibited a high solubility.

The **C₉₆** and **C₁₁₄** members of this new family remained soluble in organic solvents at optical concentrations and behaved in a similar fashion as their partially *tert*-butylated homologues. However, observations during the manipulation of **C₁₁₄tBu₁₄** in its concentration dependant PL spectra begin to suggest that the increasing of the solubility by positioning multiple adjacent bulky groups along the main axis of the nanoparticle has its limits. Further theoretical calculations of the possible aggregation pathways and conformers energies may help to better elucidate this question. But a possible explanation would be the increasing number of conformers, due to different combinations of the positioning of the *tert*-butyl groups. Some of these conformers may allow the aggregation process to start. Nonetheless, **C₁₁₄tBu₁₄** remains highly soluble compared to other examples of GQDs at optical concentrations. Once the oxidation of the largest member of the family, **C₁₃₂tBu₁₆**, is performed, it will be possible to gain more insight in this matter.

On the second half of this chapter, we discussed the synthesis of two twisted nanographene structures: helicenes and propellers. The synthesis of the presented helicenes remained a challenge because of the unpredictability of the Scholl oxidation with twisted structures that appear to be more reactive. For instance, the least hindered dendrimer tested, dendrimer **42**, gave a planar structure instead of its corresponding helicene. Despite not obtaining the expected product, this result remains very interesting for the design of new planar structures. The most hindered dendrimer, dendrimer **44**, did not yield the expected helicene. Instead, a bis-spiro product was obtained whose structure was determined by single crystal X-Ray diffraction. Interestingly, the unexpected bis-spiro product **47** is a structural isomer of the expected helicene. This shows the important role that solubility plays not only for the purification and study of the optical properties, but also for complete characterizations of the structure. In the case of poorly soluble GQDs, the only method available for characterization is mass spectrometry, but this technique does not allow to identify two different molecules with the same chemical formula as was the case of the helicene and the spiro product. The synthesis of propeller **(C₇₂tBu₈)₂** was successfully achieved, and its structure was validated by NMR experiments. Further optical characterization is still pending. This structure was very soluble thanks to its propeller architecture.

Finally, to fully exploit the solubility of the rod-shaped family of graphene quantum dots in organic solvents, in our research group we are currently developing a series of rod-shaped GQDs containing adjacent *tert*-butyl groups along their main

axis as well as bromine atoms. The halogens groups are a versatile group that will enable the post-functionalization of large nanoparticles with solubilizing groups that would otherwise not withstand the Scholl oxidation conditions. One possible post-functionalization is to incorporate polyethylene glycol chains to make the nanoparticle soluble in water.

Chapter 4 GRAPHENE NANOMESHES

CONTENTS

4.1	Generalities.....	125
4.1.1	Reaction Mechanisms.....	125
4.1.2	Scanning probe microscopies	126
4.1.3	Experimental parameters	127
4.1.4	Preceding work and current objective.....	129
4.2	A GQD strategy for a GNM precursor	131
4.2.1	First approaches to the synthesis of a tetra-halogenated precursor.....	131
4.2.2	An alternative approach to the synthesis of a polyphenylene precursor	134
4.2.3	A GQD as a GNM precursor.....	137
4.3	A GNR strategy to obtain GNM	143
4.3.1	General strategy	144
4.3.2	An iodinated GNR precursor	146
4.3.3	A brominated GNR precursor.....	147
4.3.4	Revising the synthesis of a GNR	149
4.4	Conclusion.....	150

4.1 GENERALITIES

As mentioned in the general introduction, the formation of a regular pattern of holes in a graphene sheet allows opening a bandgap. This graphene-related material is called graphene nanomeshes (GNMs). There are four critical parameters defining the nanomesh structure: the size of the hole, the edges of the hole, the periodicity of the hole, and the neck width. Although all parameters contribute to adjusting and controlling the bandgap in GNMs, the neck width bears the most significant impact, comparable to graphene nanoribbons (GNRs).²⁴⁷ In the general introduction, we have already discussed the differences between the top-down vs. bottom-up approaches to the synthesis of GNMs. In this PhD thesis, our objective was to synthesize nanomeshes via a bottom-up technique leveraging on-surface synthesis. This approach facilitates the control of the parameters defining the nanomesh by meticulously designing the precursor that will be deposited and assembled on the surface. In this chapter, we will focus particularly on the synthesis of different GNMs precursors and their deposition on different surfaces.

4.1.1 REACTION MECHANISMS

Ullmann coupling is the most popular reaction employed in on-surface chemistry. This reaction consists of the coupling between two aromatic halides to create an aryl-aryl bond. The reaction was first reported by Ullmann and Bielecki in 1901 using copper as a catalyst.¹⁵² Since its discovery, the reaction has dramatically benefited molecular chemistry. The on-surface reaction mechanism is not entirely understood since it varies between substrates and precursors.^{149,248,249} Nevertheless, the reaction can be divided into three steps: dehalogenation, diffusion, and coupling (**Figure 4.1a**). The dehalogenation step will depend on the halogen's choice because of the difference in the carbon-halogen bond's dissociation energy. The corresponding haloarene's C-Cl, C-Br, and C-I dissociation energy is 400, 336, and 272 kJ.mol⁻¹, respectively.²⁵⁰ On-surface, the necessary energy is usually given to the system in the form of heat. A phenyl and halogen radicals are formed upon dissociation of the C-X bond, which will remain chemisorbed to the surface. The chemisorption of the radical quenches the unpaired electron; therefore, it is usually referred to as a *surface-stabilized radical*. This radical will diffuse along the surface until it encounters another radical to whom it can couple. The two molecules will be chemisorbed to the same surface atom in this step. The reactants can sometimes be coordinated to a free metallic atom outside the surface plane generated from thermal energy or added on purpose (**Figure 4.1b**).²⁵¹ This metallic atom is called an adatom, the portmanteau of "adsorbed atom". Adatoms can act as catalysts or be incorporated into the structure to form metal-organic frameworks acting as a template for the coupling reaction.^{252–254}

As for the synthesis of GQDs, cyclodehydrogenation is an essential reaction in the on-surface synthesis of nanographene. This reaction is a cyclization between two intramolecular carbons from adjacent phenyls, releasing onto the surface two hydrogen atoms in the process. Depending on the position of the adjacent phenyl rings, different member cycles can be obtained, most commonly five-, six-, and seven-member rings.²⁵⁵ In previous chapters, we already discussed the plausible mechanisms in the solution and the remaining ambiguity around what is happening for different precursors and oxidants. Similarly, the reaction mechanism for on-surface dehydrogenation is not entirely elucidated. Some theoretical studies, combined with experimental observations on the cyclodehydrogenation of anthracene-based graphene nanoribbons, have proposed the mechanisms

depicted in **Figure 4.1c**.^{256–258} The first step is forming a C-C bond between two adjacent phenyl rings. In this process, two delocalized radicals are created in each ring, and the participating carbon atoms see a change in their hybridization from sp^2 to sp^3 . Next, the hydrogen on the substrate side can be eliminated to restore partial conjugation in the molecule. A [1,2]- or [1,3]-sigmatropic shift can then occur, followed by elimination of an additional hydrogen atom to regain complete conjugation. Alternatively, a [1,9]-sigmatropic shift can occur before any hydrogen elimination; hence the rearrangement requires a longer conjugated path. Complete conjugation is regained after eliminating two successive hydrogen atoms on the substrate. This process is repeated several times until the complete cyclodehydrogenation of the precursor is achieved. In contrast to the in-solution mechanism, the proposed on-surface pathway involves the formation of a biradical species that is stabilized by the substrate. Furthermore, on-surface synthesis increases the steric hindrance and confinement effects, so the hydrogen shift can only occur on one side of the molecule.

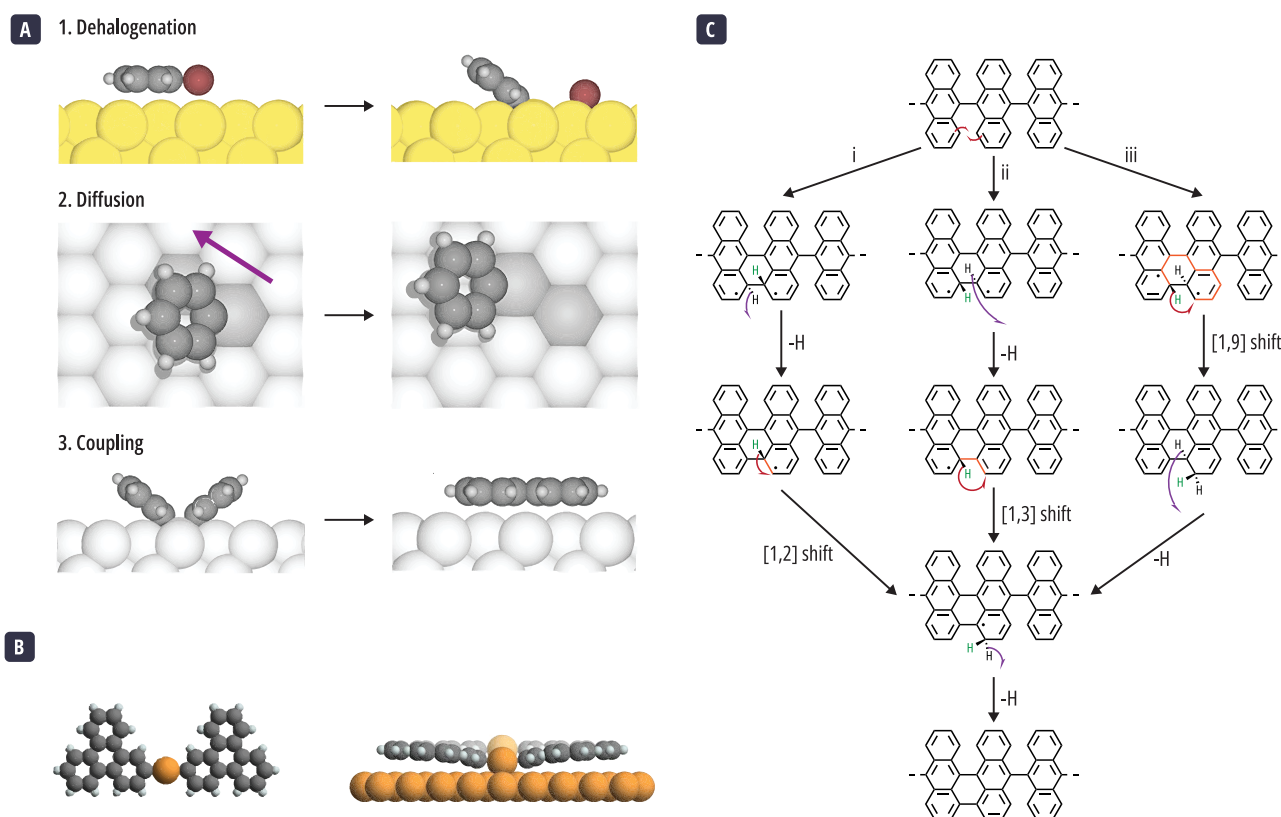


Figure 4.1 | On surface reactions mechanisms. **(a)** Illustration of the on-surface Ullmann coupling mechanism.²⁴⁸ **(b)** Adatom bridged structure.²⁵² **(c)** Scheme of the possible on-surface cyclodehydrogenation mechanisms.

4.1.2 SCANNING PROBE MICROSCOPIES

The characterization of the surface is commonly done using scanning probe microscopy using two methods: scanning tunneling microscopy (STM) and non-contact atomic force microscopy (nc-AFM). In the following paragraphs we will give a quick introduction to the underlying principles of to these two methods.²⁵⁹

Scanning tunneling microscopy relies on tunneling effect. In quantum mechanics, electrons can pass through a potential energy barrier. In an STM setup an atomically sized tip is positioned close to a metallic surface. The current that flows between the surface and the tip is measured when a voltage bias is applied (**Figure 4.2a**). This current depends on the distance between the tip and the surface. A raster scan of the surface is the made. Two types of STM modes can be employed: constant current and

constant height. In the constant height mode, the variation in current is measured, and in the constant current mode the variation of height is measured (**Figure 4.2b**).

In atomic force microscopy a cantilever with an atomically precise tip is placed on top of the sample (**Figure 4.2c**). In non-contact AFM, the cantilever oscillates on top of the surface and probes Van der Waals forces. The variation of the cantilever is measured using the piezoelectric effect with a quartz tuning fork. In nc-AFM, two modes can be employed: amplitude modulation and frequency modulation (**Figure 4.2d**). Additionally, the tip of AFM can be functionalized to probe the short-range forces, such as the Pauli repulsion, which allows to visualize the atomic orbitals or sigma bonds.²⁶⁰ The best resolution is obtained using a carbon monoxide (CO) tip, but other atoms such as oxygen or halogens can be employed.²⁶¹

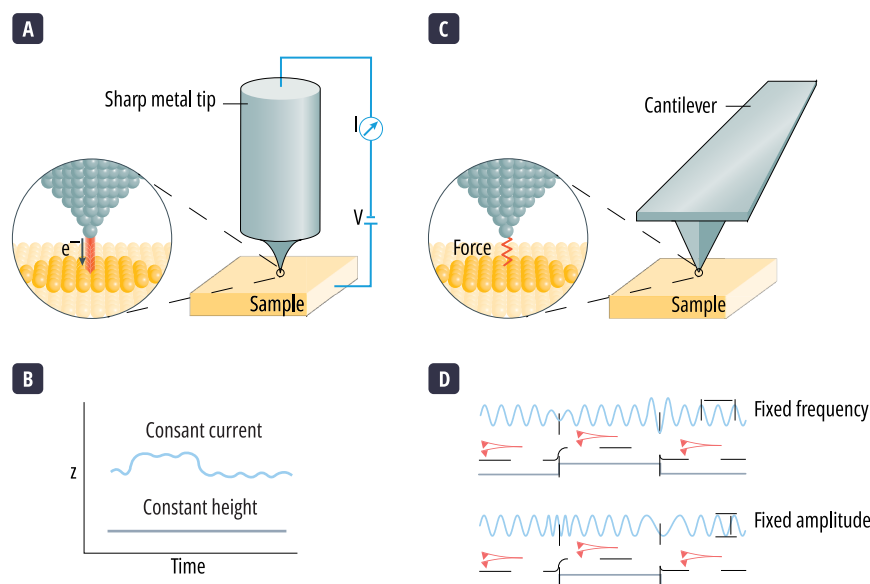


Figure 4.2 | (a) Schematic representation of a STM tip and surface. (b) Profile representations of the constant current and constant height mode. (c) Schematic representation of an AFM tip and surface. (d) Profile representations of the fixed frequency and fixed amplitude modes.²⁵⁹

The measurements presented in this section were done in ultra-high vacuum conditions (10^{-10} mbar) at low temperature (4 K). Low temperature helps to immobilize the observed molecules and prevent vibrations of the setup that could increase the noise. The experimental setup is composed of two chambers in communication: a preparation and an analysis chamber. In the preparation chamber, the surface is cleaned in by Ar^+ bombardment. Afterwards, in a sublimation step, the molecules are deposited on the surface, without the presence of any solvent. Then, subsequent heating of the sample allows the reaction on-surface to take place. After the sample is cooled down, it is transferred to the analysis chamber, where the sample is cooled down and the STM or nc-AFM measurements take place.

4.1.3 EXPERIMENTAL PARAMETERS

What happens on the surface will be closely related to the conditions of the surface: temperature, coverage, precursor structure, and surface nature.¹⁴⁸ The most common metals used for on-surface reactions are the transition metal from group IB of the periodic table; copper (Cu), silver (Ag), and gold (Au). These metals are commonly referred to as coinage metals for their historical importance in the fabrication of coins. For these surfaces, the typical reactivity follows the $\text{Cu} > \text{Ag} > \text{Au}$ order.²⁴⁸ Besides the type of metal employed, the surface reactivity is going to be strongly impacted by the exposed crystallographic plane. This plane is given using the Miller notation (hkl). For a unit cell with lattice vectors \bar{a}_1 , \bar{a}_2 , and \bar{a}_3 , the indices h , k , and l denote a plane

that intercepts the set of three points \bar{a}_1/h , \bar{a}_2/k , and \bar{a}_3/l . For example, in a cubic unit cell where $\bar{a}_1=\bar{a}_2=\bar{a}_3$ and orthogonal to each other, the plane (111) denotes the plane that cuts through the points $1/1\bar{a}_1$, $1/1\bar{a}_2$, and $1/1\bar{a}_3$ (**Figure 4.3d**).

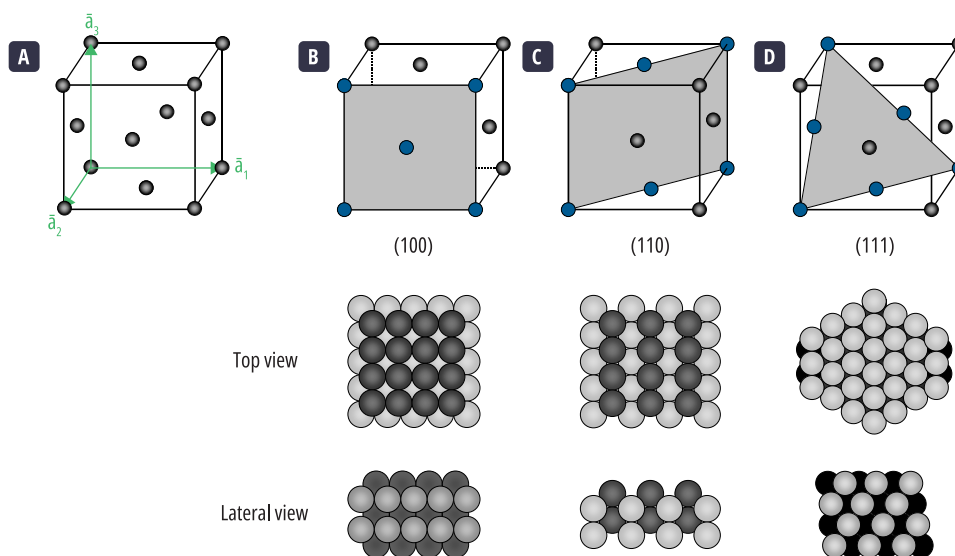


Figure 4.3 | Crystallographic faces in Cu, Ag, and Au. **(a)** Face-centered cubic unit cell structure. **(b)** On top, the illustration of the (100) plane cutting an FCC unit cell. Below, an illustration of the exposed atoms on the surface. **(c)** On top, the illustration of the (110) plane cutting an FCC unit cell. Below, an illustration of the exposed atoms on the surface. **(d)** On top, the illustration of the (111) plane cutting an FCC unit cell. Below, an illustration of the exposed atoms on the surface.²⁶²

The arrangement of the atoms inside the unit cell determines the arrangement of the surface exposed by each plane. In the case of copper, silver, and gold, the unit cell is face-centered cubic (FCC), where atoms are positioned at each corner and in the middle of each face of a cube (**Figure 4.3a**). The exposed surface is going to have a strong impact in the reactivity of the surface. For a FCC cell, the (111) plane exposes a surface with tightly bounded atoms (**Figure 4.3d**), whereas in the (110), the atoms are arranged along alternating lines of metal atoms and empty spaces (**Figure 4.3c**). As a result of these surfaces arrangements, in the tightly bound exposed (111) face the metal atoms have a higher coordination degree than in a (110) face; therefore, the (111) face is going to be less reactive than the (110) face. The (100) (**Figure 4.3b**) face is an intermediate of the two previously depicted surfaces, the atoms are closely packed but not tightly bound, resulting also in an intermediate reactivity.

To better understand the formation of two-dimensional networks, Bieri *et al.* performed a theoretical study of the reactivity of the hexa-iodo substituted cyclohexa-m-phenylene (CHP) on Cu(111) and Au(111) surfaces.²⁶³ They considered that radicals on the surface could either diffuse or couple to another molecule. With that in mind, they defined the parameter P corresponding to the ratio between the coupling rate (v_{coupl}) and the sum of the coupling and diffusion (v_{diff}) rates (**Equation 4.1**).

$$P = \frac{v_{\text{coupl}}}{v_{\text{coupl}} + v_{\text{diff}}}$$

Equation 4.1

This parameter is comprised of between 0 and 1. High coupling rates give P values closer to 1, and the process is described as diffusion limited. Inversely, high diffusion rates give P values closer to 0, and the process is said to be coupling limited. Using a Monte Carlo simulation, they showed that to grow ordered two-dimensional structures, a limited coupling process with small P values is required (**Figure 4.4a-c**). Further density functional theory (DFT) calculations indicated that the

diffusion barrier is reliant on the carbon-metal bond strength, which is higher for Cu(111) than Ag(111), in line with the chemical reactivity of these surfaces. Calculations on the coupling step showed that the C-C bond formation occurs spontaneously on Cu(111) once two radicals encounter each other, whereas on Ag(111), an energetic barrier needs to be overcome. Their theoretical results indicate that Ag(111) surface is coupling-limited and Cu(111) diffusion limited, and so silver is a better surface to obtain two-dimensional polyphenylene networks from CHP. These calculations are in very good agreement with experimental results. Only low-density clusters are obtained on a copper surface, whereas a silver surface allows the formation of large regular two-dimensional domains (Figure 4.4d,f). Growth on an Au(111) surface gives intermediate-quality networks, although this surface was not studied theoretically (Figure 4.4e).

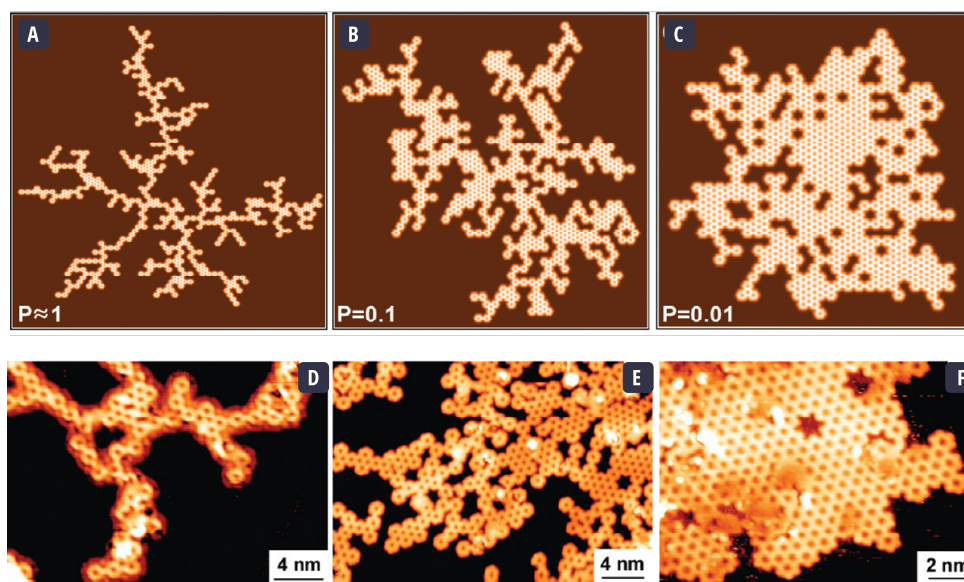


Figure 4.4 | Formation of a two-dimensional network of CHP. (a) Monte Carlo growth simulation with $P=1$. (b) Monte Carlo growth simulation with $P=0.1$. (c) Monte Carlo growth simulation with $P=0.01$. (d) STM image of polyphenylene networks formed on Cu(111). (e) STM image of polyphenylene networks formed on Au(111). (f) STM image of polyphenylene networks formed on Ag(111).²⁶³

4.1.4 PRECEDING WORK AND CURRENT OBJECTIVE

Our research group was previously interested in synthesizing two triangular precursors to yield two-dimensional covalent frameworks with a neck containing more than a single carbon-carbon bond and a continuous hexagonal network (Figure 4.5).²⁰⁷ These precursors exhibit a C_3 symmetry, and upon growth on the surface, they were expected to give two nanomeshes with different pore sizes and neck widths. The smaller 2,2',2''-triiodotriphenylene **55** would give a nanomesh with pore resulting from a missing benzene ring and a neck width equivalent to a naphthalene unit. Theoretical calculations predicted a direct bandgap of 1.28 eV. The larger 1,3,5-tris(4'-iodo-*para*-terphenyl)benzene **56** precursor was expected to yield a nanomesh with a pore corresponding to a missing hexa-*peri*-benzocoronene and a neck width equivalent to a tetracene molecule. The predicted theoretical bandgap was 1.06 eV. Prochirality of the precursors was one limitation expected to be encountered upon surface growth. Depending on the side the molecule would be deposited on the surface, steric hindrance would limit the coupling between sub-units, thus impeding the supramolecular arrangement and growth of the nanomesh and finally this approach was abandoned.

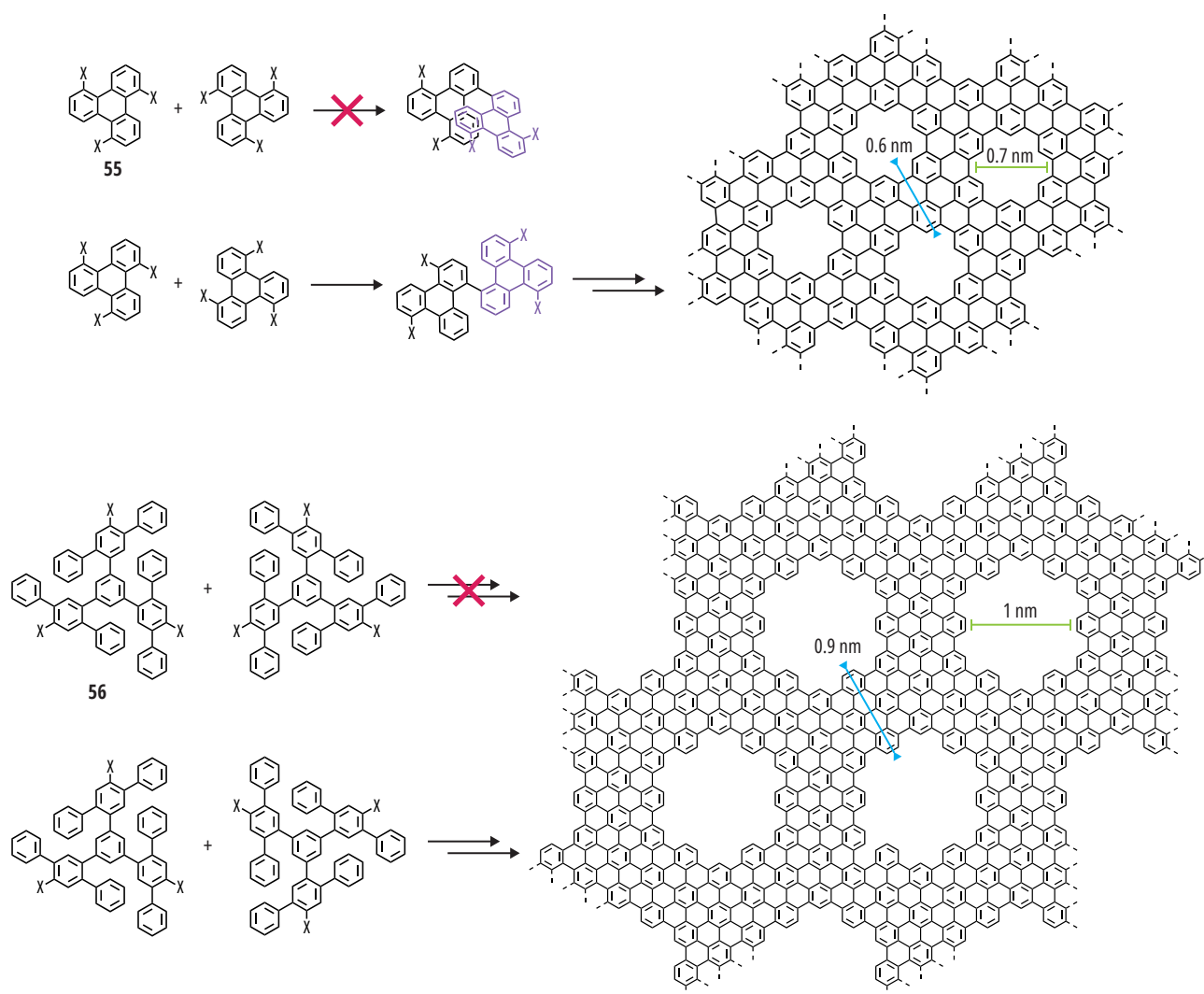


Figure 4.5 | Expected nanomeshes structures from precursors **55** and **56**.

To address the previously depicted problem we designed a non-prochiral precursor derived from a hexaphenylbenzene structure, compound **57**. In the case of **57**, it is expected that the side on which the molecule is deposited will not create any defects during the growth of the nanomesh (**Figure 4.6**). Furthermore, because of steric hindrance caused by the central phenyl group present next to the halogen group, the coupling with another molecule is expected to be shifted, ensuring the nanopore's creation and the formation of the corresponding nanomesh **GNM-1**. In this chapter, we will present the synthesis of this molecule and the growth tests performed so far on-surface.

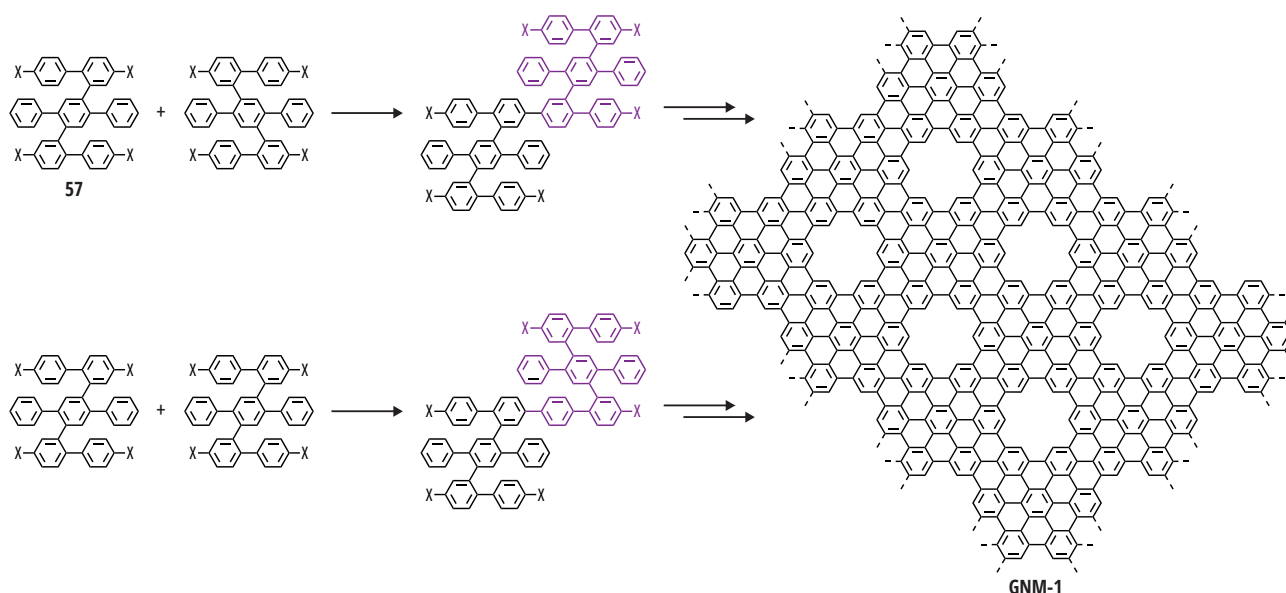


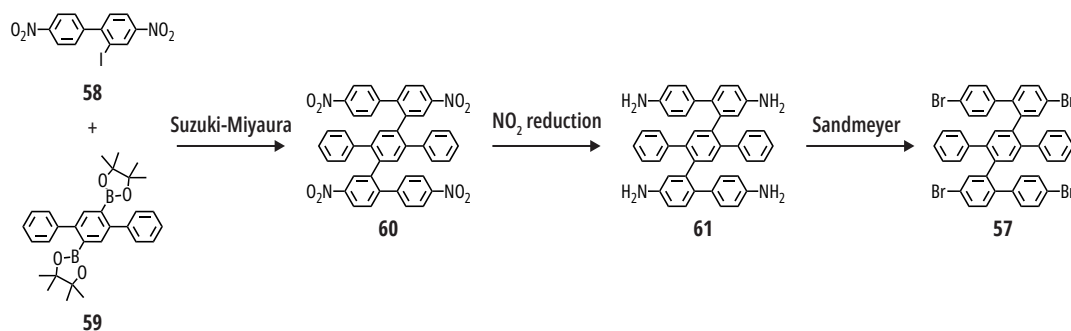
Figure 4.6 | Expected nanomeshes structure GNM-1 from precursor **57**, whose final structure is independent of the side on which the precursor is deposited on the surface.

4.2 A GQD STRATEGY FOR A GNM PRECURSOR

Our first approach to the synthesis of GNM was the synthesis of the halogenated precursor **57**. Throughout its synthesis different challenges were encountered, forcing us to change the approach taken towards its synthesis and perform slight modifications on the targeted structure. Throughout this chapter we will present the different structures synthesized as well as their surface deposition.

4.2.1 FIRST APPROACHES TO THE SYNTHESIS OF A TETRA-HALOGENATED PRECURSOR

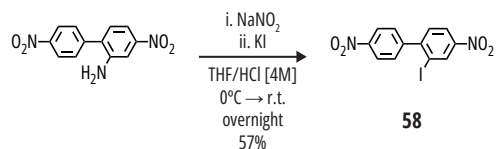
The strategy for the synthesis of the graphene nanomesh precursor **57** is depicted in **Scheme 4.1**. It starts with the carbon-carbon coupling between the 2-iodo-4,4'-dinitro-1,1'-biphenyl **58** and terphenyl diboronic pinacol ester **59**. After the Suzuki-Miyaura coupling, the nitro groups in the resulting compound **60** would be reduced into amine groups and then transformed into the halogen of our choice: bromine or iodine through a Sandmeyer reaction, to give the GNM precursor **57**.



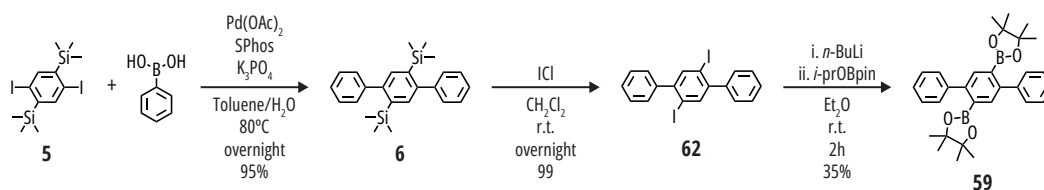
Scheme 4.1 | First strategy for the synthesis of the GNM precursor **57**.

The 2-iodo-4,4'-dinitro-1,1'-biphenyl **58** was obtained after treatment of the commercially available 4,4'-dinitro-[1,1'-biphenyl]-2-amine with sodium nitrite and potassium iodide, in a 57% yield (**Scheme 4.2**). The synthesis of the terphenyl diboronic pinacol ester **59** is described in **Scheme 4.3**. It was synthesized from the borylation of diiodo-*p*-terphenyl **62**, a precursor whose synthesis is already well established in our research group and analogous to the *tert*-butylated terphenyl presented in Chapter 2. The trimethylsilyl di-substituted *p*-terphenyl derivative **6** was synthesized as described in Section 2.2.2.

The trimethylsilyl groups in **6** were iodinated in the presence of iodine monochloride to obtain diiodoterphenyl **62**. The reaction of **62** with *n*-butyllithium, followed by the addition of *iso*-(propoxy)boronpinacol (*i*-prOBpin) gave the terphenyl diboronic pinacol ester **59** in a modest yield of 35%. The borylation reaction is very sensitive; water traces or proton sources in the solvent or precursors can activate the deprotection of boronic ester and its protonolysis, responsible for hydrogenated side products and low reaction yields.

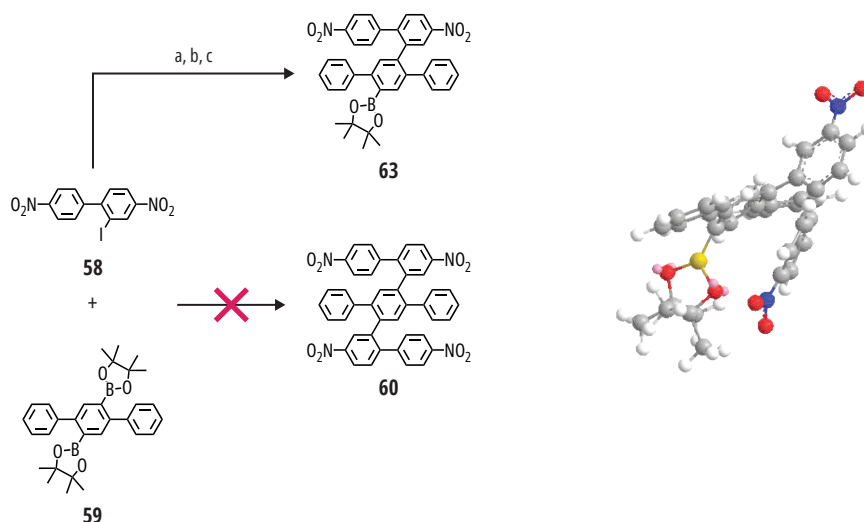


Scheme 4.2 | Synthesis of 2-iodo-4,4'-dinitro-1,1'-biphenyl **58**.



Scheme 4.3 | Reaction scheme for terphenyl diboronic pinacol ester **59**.

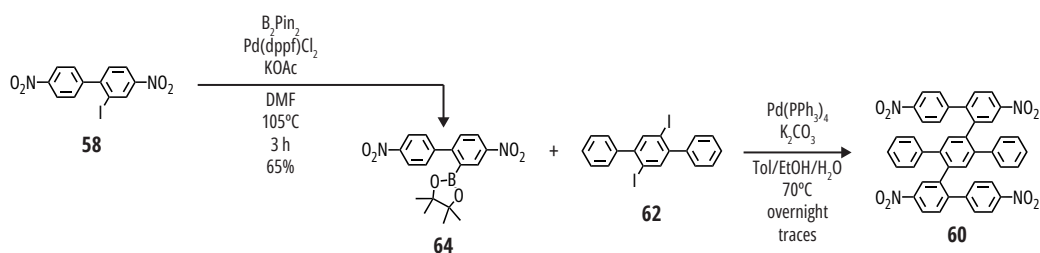
The Suzuki-Miyaura coupling between the biphenyl **58** and the terphenyl boronic ester derivative **59** did not yield the expected disubstituted tetranitro compound **60**, instead only the monosubstituted pinacol ester **63** was obtained. Different reaction conditions were tested to produce product **60**: various palladium catalysts, increased reaction times, and temperatures. Nevertheless, in each case, only the monosubstituted product was observed. A possible explanation of the stability of the monosubstituted intermediate is the interaction of the lone electron pair in the pinacol oxygen with the positively charged nitrogen of a nitro group. The relaxed structure of this intermediate, calculated using an MM2 energy minimization method in Chem3D software, shows the interaction described before. The reaction conditions and the proposed stabilization of intermediate **63** are given in **Scheme 4.4**.



Scheme 4.4 | Scheme of the synthesis of compound **63**. To the right the relaxed tridimensional structure of **63**. (a) Pd₂(dba)₃, SPhos, K₃PO₄, 80°C, toluene/water, 40h. (b) Pd₂(dba)₃, SPhos, K₃PO₄, 100°C, toluene/water, 20h. (c) Pd(PPh₃)₄, K₂CO₃, 90°C, toluene/water, 48h

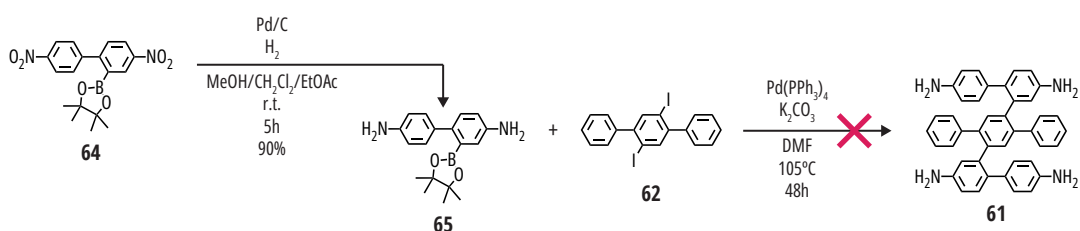
To prevent the formation of the stabilized boronic pinacol ester **63**, a different method for synthesizing tetranitro compound **60** was contemplated. The precursors bearing the functional groups needed for the Suzuki-Miyaura were exchanged.

This alternative strategy is summarized in **Scheme 4.5**. The diiodoterphenyl **62** was already produced. The dinitro-biphenyl boronic pinacol ester **64** was obtained through palladium-catalyzed Miyaura borylation conditions.²⁶⁴ The Suzuki-Miyaura coupling between **62** and **64** did not produce the expected product **60**. However, MALDI-ToF mass spectrometry of the reaction crude showed the presence of **60**, along with the monosubstituted side product and additional non-identified impurities. However, isolating the product through column chromatography or precipitation and subsequent identification through NMR spectroscopy remained a challenge. It is possible that, because of the presence of four nitro groups and the aromatic nature of the molecule, compound **60** is highly insoluble, which could explain the difficulty encountered in its isolation and characterization.



Scheme 4.5 | Alternative reaction scheme for the synthesis of the tetranitro compound **60**.

To circumvent this solubility problem, which could be attributed to the presence of the nitro groups, we tested the direct synthesis of the tetramine compound **61**. This approach is given in **Scheme 4.6**. The nitro groups in the previously synthesized compound **64** were reduced in the presence of palladium on carbon under a three-bar hydrogen atmosphere to yield the boronic ester biphenyl-diamine **65**. The synthesis of **65** proceeded without degradation of the boronic ester and had a good reaction yield of 90%. **65** was then reacted with diiodoterphenyl **62** in the presence of tetrakis(triphenylphosphine)palladium(0) to obtain **61**. Though all the precursor **62** had been consumed after 48 h of reaction, it was impossible to identify the desired compound **61** either by mass spectrometry or NMR spectrometry.



Scheme 4.6 | Reaction scheme for the synthesis of tetramine derivate **61**.

So far, the strategy of coupling a terphenyl sub-unit with two diphenyl sub-units to obtain the precursor for the GNM was unsuccessful. As we saw, we encountered problems in the reactivity and the solubility of the intermediates that prevented the obtention of the different tetrasubstituted derivatives. Besides, it is expected that an additional difficulty would be encountered in the Sandmeyer reaction to transform **61** into **57**. This reaction is very sensitive to temperature, and in the presence of heat, hydroxylated and hydrogenated side products can be formed, dramatically impacting the reaction yields. At this point, it was clear that an alternative synthetic pathway was necessary.

4.2.2 AN ALTERNATIVE APPROACH TO THE SYNTHESIS OF A POLYPHENYLENE PRECURSOR

Taking inspiration from the strategy employed for the synthesis of GQD, *i.e.*, reacting a primary alkyne function with a substituted cyclopentadienone, an alternative route was developed. To ensure a good **GNM-1** precursor, a proper design of the precursors is crucial. To prevent the formation of any isomer on the surface that would lead to defects during the GNM growth, it is important to consider how the halogen atoms are positioned relative to the free rotations of the C_{aryl}-C_{aryl} bonds. For instance, a tetrabromo-hexaphenylbenzene who carries the bromine atoms in the *meta* position relative to the C_{aryl}-C_{aryl} bond can undergo a conformational change following a free rotation of the C_{aryl}-C_{aryl} bond. Upon surface deposition, these differing conformers would lead to multiple defects in the two-dimensional growth (**Figure 4.7a**). Therefore, to ensure the desired templating information is preserved after deposition, the bromine atoms should be in the *para* position relative to any potential C_{aryl}-C_{aryl} bond rotation so that its position in the overall structure remains unchanged. Alternatively, the rotations can be hindered by designing a more rigid precursor (**Figure 4.7b**). Keeping these factors in mind, compound **67** was designed. In this section we will first present the synthesis and characterization of precursor **67**. Afterwards, we will present the first surface deposition attempts.

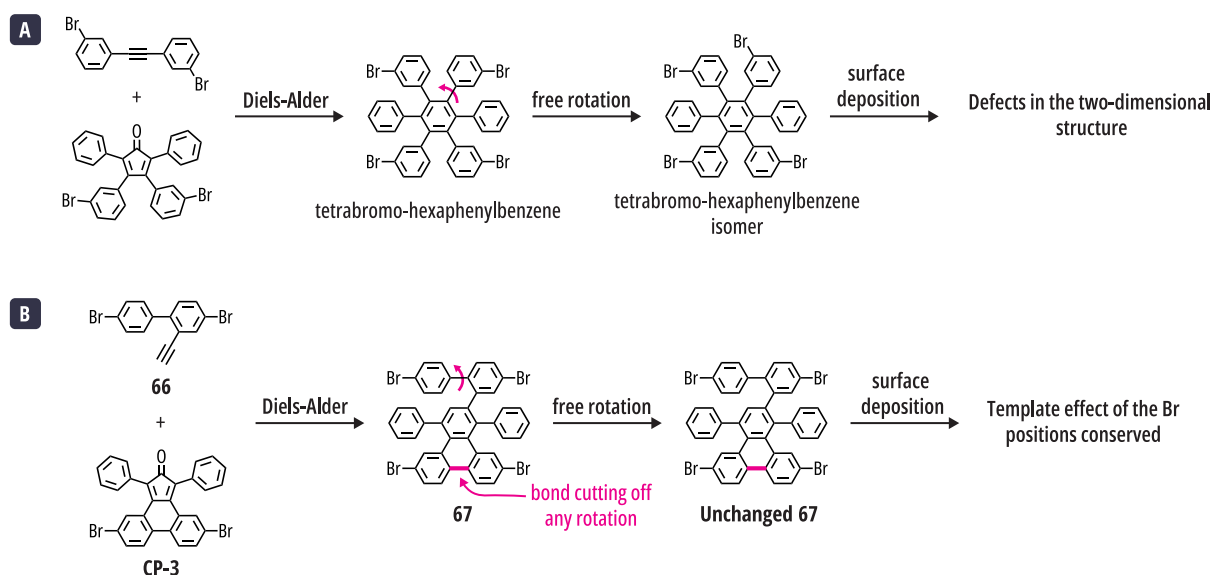
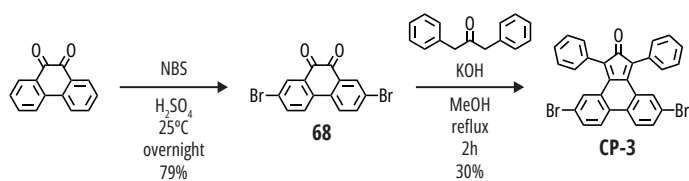


Figure 4.7 | Possible reaction pathways to obtain a tetrabromo polyphenylene derivative through a Diels-Alder reaction, and the effect of the bromo substituents positions on the surface growth.

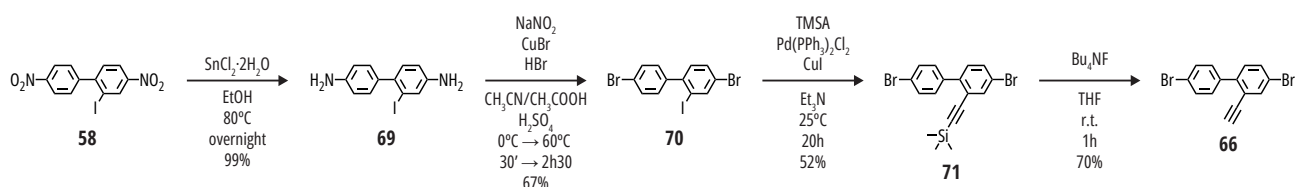
SYNTHESIS

The proposed synthetic pathway to obtain **67** consists in a Diels-Alder reaction between a dibromo-ethynyl-diphenyl **66** and a cyclopentadienone **CP-3** containing a dibromophenanthrene component. The synthesis of the cyclopentadienone **CP-3** has already been described in the literature (**Scheme 4.7**).^{265,266} The commercially available phenanthrenequinone is brominated in the presence of *N*-bromosuccinimide (NBS) to afford 2,7-dibromophenanthrene-9,10-dione **68**. Finally, the desired dibromophenanthrene-substituted cyclopentadienone **CP-3** is obtained through the Knoevenagel condensation reaction between **68** and the commercially available 1,3-diphenylpropan-2-one.



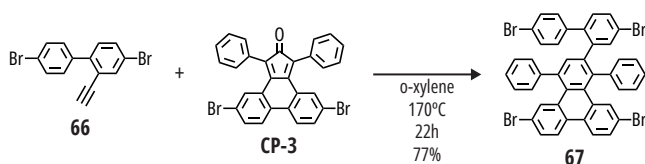
Scheme 4.7 | Synthesis of dibromophenanthrene cyclopentadienone **CP-3**.

The ethynyl function necessary for the Diels-Alder reaction is carried by 4,4'-dibromo-2-ethynyl-1,1'-biphenyl **66**, whose synthesis is presented in **Scheme 4.8**. The nitro groups present in the dinitro-iodobiphenyl **58** are reduced in the presence of tin chloride to give 2-iodo-[1,1'-biphenyl]-4,4'-diamine **69**. 4,4'-dibromo-2-iodo-1,1'-biphenyl **70** is obtained through a Sandmeyer reaction of **69** in the presence of copper(I)bromide, hydrobromic acid, and sodium nitrite. Taking advantage of the difference in bond energies between C-I and C-Br bonds, a selective Sonogashira coupling was carried out in the presence of **70** and trimethylsilylacetylene (TMSA) at 25°C to afford ((4,4'-dibromo-[1,1'-biphenyl]-2-yl)ethynyl) trimethyl silane **71**. Target compound **66** was obtained upon deprotection of **71** in the presence of tetrabutylammonium fluoride.



Scheme 4.8 | Synthesis of dibromo-ethynyl-biphenyl **66**.

The Diels-Alder reaction between **66** and **CP-3** yielded the desired nanomesh precursor **67**, in the conditions summarized in **Scheme 4.9**. The structure of **67** was confirmed by mass spectrometry and NMR spectroscopy. On the ¹H NMR spectrum, various signals are observed, the integration of which totals to the 24 expected proton signals (**Figure 4.8**). The characteristic singlet from the proton in the central phenyl group is present at 7.72 ppm. Although many signals are superimposed, we can discern some of the doublets and doublet of doublets systems from the protons in the phenanthrene section of the molecule and the biphenyl sub-unit. One can notice that the unsubstituted phenyls in the center of the molecule produce broader signals compared to the rest of the molecule, from which a triplet and doublet are distinguishable at 6.83 and 5.91 ppm, respectively. The remaining signals are obscured by other peaks. These broad peaks suggest that the rotation of these phenyl groups is more restricted compared to the rest of the molecule.



Scheme 4.9 | Synthesis of GNM precursor **67**.

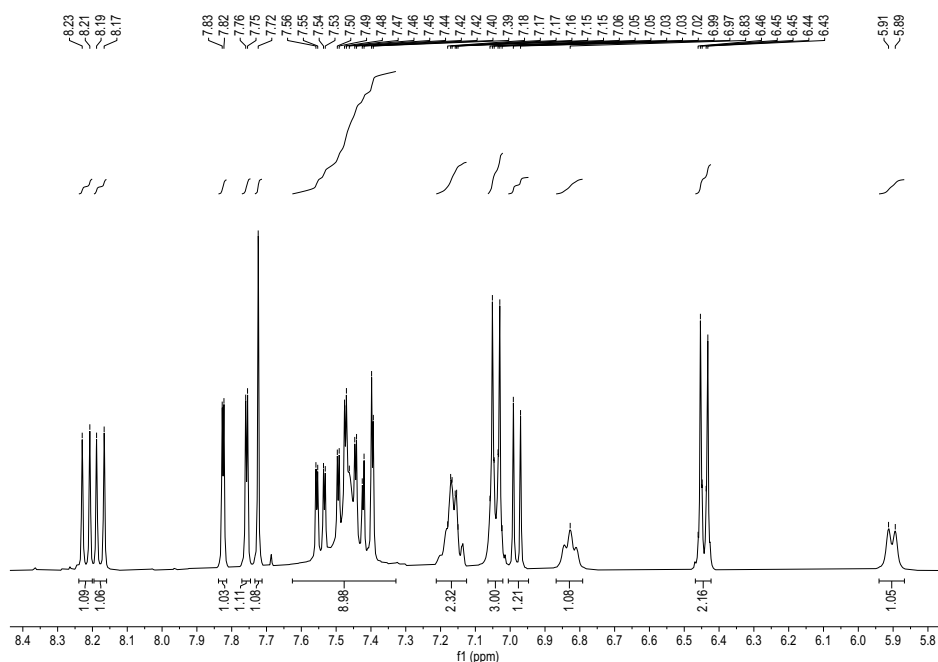


Figure 4.8 | ^1H NMR of compound **67** (400 MHz, CD_2Cl_2 , 298 K).

SURFACE DEPOSITION

With our nanomesh precursor synthesized, it is now possible to grow GNM on the surface. The growth on metallic surfaces and STM characterizations presented here were performed by Dr. Sylvain Clair at the IM2NP institute at Aix-Marseille University on ultrahigh vacuum (UHV) conditions.

In a first attempt, the deposition of molecule **67** was done on a Cu(100) surface with a molecule flow for 10 minutes on a room temperature surface, followed by a 100°C annealing. STM characterization at room temperature showed very little coverage of the precursor, and the presence of a few small linear fragments (**Figure 4.9a**). To favor the formation two-dimensional structures, high surface coverages are needed. To increase the number of molecules on the surface, the deposition time was increased to 30 minutes, followed by a 100°C annealing. Again, only a little coverage was observed with the formation of small linear fragments (**Figure 4.9b**). Annealing at higher temperatures, 150°C, 200°C, and 250°C, yielded only disordered structures. Cyclodehydrogenation started to be observed in a disordered fashion after annealing of 150°C (**Figure 4.9c**).

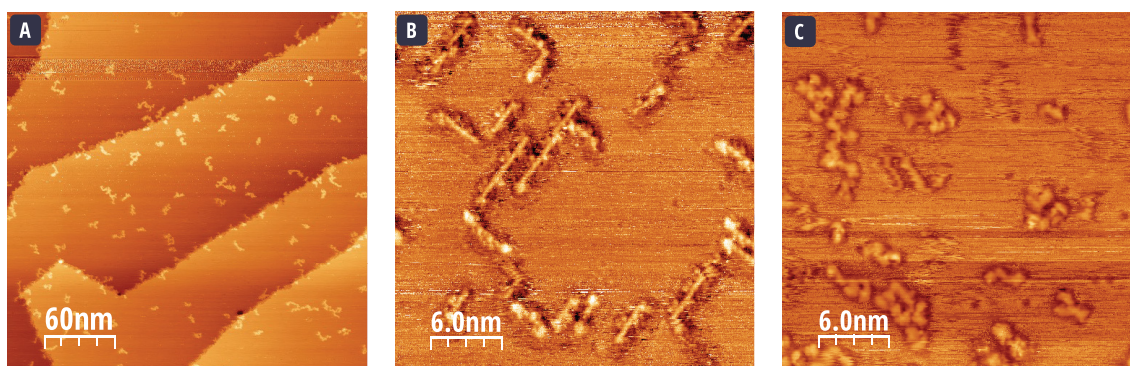


Figure 4.9 | Room temperature STM images of precursor **67** on Cu(100). **(a)** Deposition flow for 10 minutes on a Cu(100) surface at room temperature followed by annealing at 100°C. **(b)** Deposition flow for 30 minutes on a Cu(100) surface at room temperature followed by annealing at 100°C. **(c)** Deposition flow for 20 minutes on a Cu(100) surface at room temperature followed by annealing at 150°C.

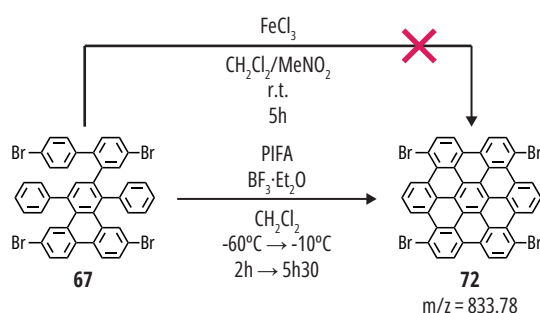
Deposition on less reactive surfaces such as Ag(111) and Au(111) only produced disordered structures with no exploitable results. However, across all three surfaces, precursor **67** was observed to have poor adsorption, resulting in low coverage ratios. This low coverage is accountable for the generation of only small one-dimensional fragments on Cu(100). This behavior can be attributed to the inherent three-dimensional asymmetric nature of precursor **67**, which hinders its adsorption to the surface, leads to asymmetric couplings, and creates multiple configurations on the surface that cannot further link together as anticipated. To address this issue, a new precursor's design needs to be developed. This precursor needs to be symmetric and "less" three-dimensional: it should be planarized.

4.2.3 A GQD AS A GNM PRECURSOR

To design a symmetric precursor exhibiting lower dimensionality, the most straightforward solution was the oxidation of precursor **67** to obtain a rigid flat tetrabromo-hexabenzocoronene derivative **72**. A dibromo-hexabenzocoronene derivative had previously been reported to successfully yield necklace-like structures on an Au(111) surface.²⁶⁷ This report encouraged us to test a similar approach: synthesize the tetrabromo-substituted hexabenzocoronene to evaluate surface deposition and growth into GNMs. Precursor **72** can be assimilated to a graphene quantum dot, which here is also used as a GNM precursor. In this section we will first describe the synthesis of HBC derivate **72**, then we will present its surface deposition.

SYNTHESIS

The synthesis strategy for precursor **72** is illustrated in **Scheme 4.10**. It is noticeable that two different conditions were used for its synthesis. Firstly, let's discuss the cyclodehydrogenation process carried out using iron(III) chloride as an oxidant. The presence of electron-withdrawing bromine groups extended the reaction time compared to the oxidations detailed in Chapter 2 and 3, where more C-C bonds are created in a single step. After five hours of reaction, the targeted structure, along with partially oxidized byproducts with one or two C-C bonds missing, were detected by MALDI-ToF spectrometry. In addition to the incomplete cyclodehydrogenations, peaks corresponding to the replacement of a bromine atom with a chlorine atom, and their corresponding incomplete oxidations, were observed. A peak indicating the addition of a chlorine atom, a common byproduct under the utilized conditions, was also noted. The presence of molecules in which the bromo substituent is replaced by a chlorine atom could pose a problem during GNM growth, due to the reactivity difference between C-Br and C-Cl bonds. While on-surface Ullmann coupling can occur between two C-Cl bonds, its low reactivity necessitates the co-deposition of catalytic metallic atoms and heating to high temperatures.²⁶⁸ This difference in reactivity could lead to asymmetric growth and result in one-dimensional or uncontrolled structures. Both tetrabromo-HBC and the chlorine-substituted byproducts exhibit poor solubility, which hampers their separation through different purification techniques.



Scheme 4.10 | Reaction pathway of tetrabromo-HBC **72**.

An alternative oxidation technique was explored, using (bis(trifluoroacetoxy)iodo)benzene (PIFA) as the oxidant in the presence of boron trifluoride etherate as a Lewis acid. At short reaction time, only a partially fused nanoparticle missing the formation of two or three C-C bonds is produced. Upon increasing reaction times, the fully cyclodehydrogenated nanoparticle is observed, along with some partially fused nanoparticles and unidentified side products. These byproducts and the partially fused intermediates exhibit greater solubility than the desired HB derivative **72**, allowing us to conduct a purification step. The crude powder was dispersed in tetrahydrofuran, sonicated for 1 minute, and the solution was then ultra-centrifugated at 130 000 g. The MALDI-ToF analysis revealed that the recovered black pellet was mainly composed of the desired product **72** (**Figure 4.10**). Due to the low solubility of the compound, no further characterization could be performed. Further analysis of the mass spectrum indicated that the main peak corresponds to the expected product with an isotopic distribution matching the expected theoretical pattern. Some peaks corresponding to impurities and a small fraction of the partially fused nanoparticle were still identifiable, assuming they ionize in a similar manner.

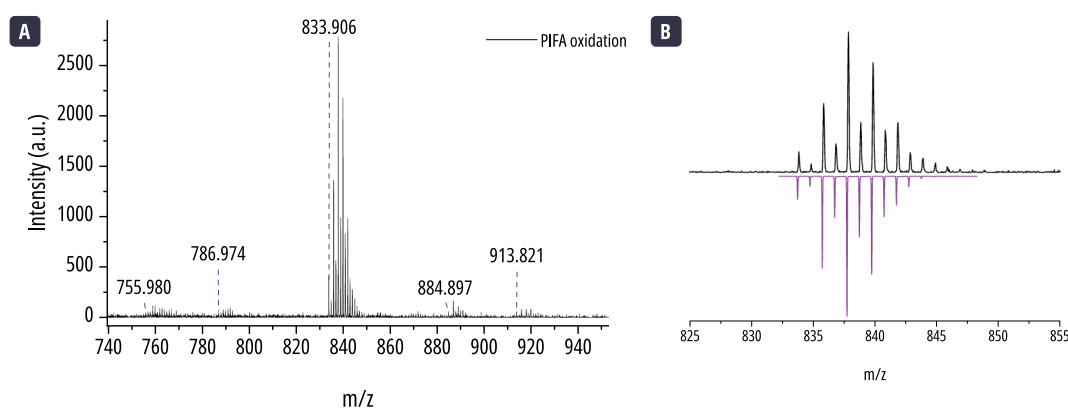


Figure 4.10 | (a) MALDI-ToF mass spectrum of tetrabromo-HBC derivative **72** recorded using a TCNQ matrix. (b) comparison of theoretical (purple) and experimental (black) isotopic distribution pattern.

SURFACE DEPOSITION

Our collaborators at IM2NP institute in Marseille deposited this new precursor on a metallic surface. To sublime compound **72**, it was necessary to heat the evaporation crucible up to 320°C. Four metallic surfaces were tested with this precursor: Au(111), Ag(110), Ag(111), and Cu(111). These varying metallic surfaces encompass different reactivities. As the most interesting results were obtained on gold and silver surfaces, we will now focus exclusively on these two surfaces.

GOLD SURFACE: Au(111)

Upon depositing compound **72** on an Au(111) surface at room temperature (**Figure 4.11a**), we observed the formation of hexagonal phase domains (**Figure 4.11b**), along with more disordered assemblies (**Figure 4.11c**). To obtain the hexagonal domains, it is possible to imagine a precursor lying perfectly flat on the surface, possibly due to the loss of bromine atoms upon adsorption of the precursor. Indeed, the presence of bromine atoms in close interaction with the hydrogen atoms from the adjacent phenyl groups may cause precursor **72** to be slightly distorted, thus, it is not expected to give a hexagonal contrast. On the other hand, the more disordered domains may originate from molecules whose bromine groups remain, at least partially, intact. Another possibility for the origin of these domains is the presence of degraded molecules, a topic that will be further explored later in this section.

To determine whether coupling occurred between the adsorbed precursors, the surface was annealed at 150°C. Following this annealing process, we were able to identify certain areas exhibiting zigzag structures, as depicted in **Figure 4.11d**. These structures begin to resemble our targeted coupling pattern. However, these patterns were limited in size and uncontrolled structures were also observed. To test if further coupling was possible, the annealing step was also performed at 250°C. Unfortunately, after this step, as can be observed in **Figure 4.11e**, we primarily noticed disordered coupling patterns.

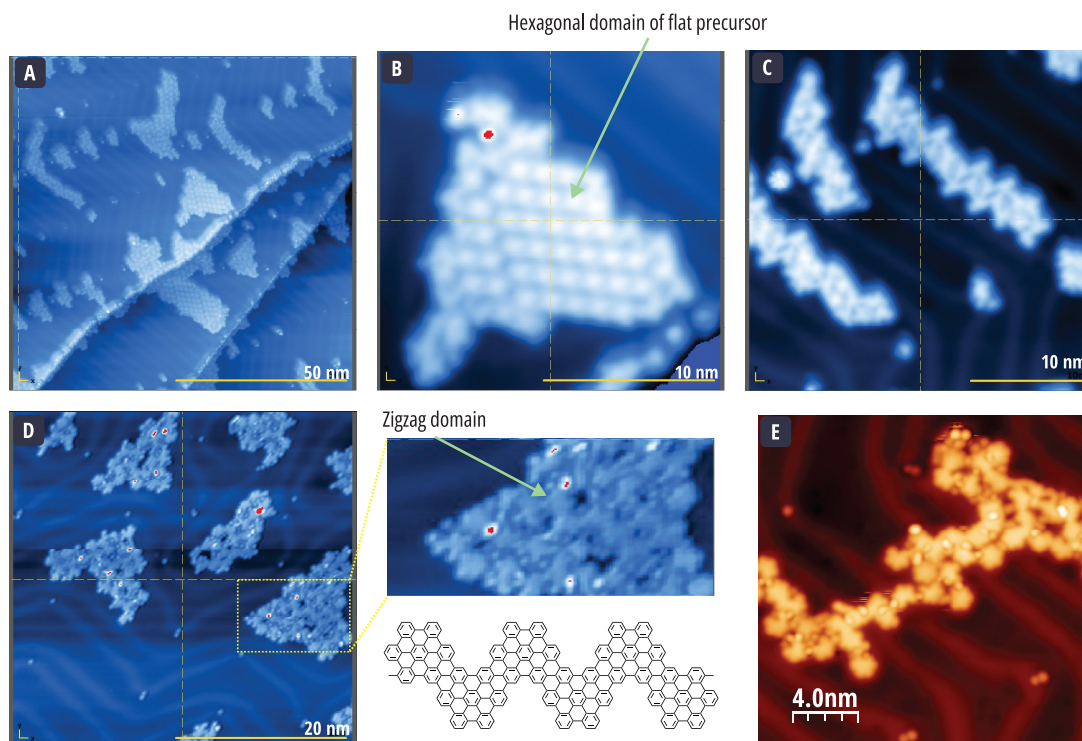


Figure 4.11 | Low temperatures STM images on precursor **72** deposited on an Au(111) surface at room temperature. **(a)** Image obtained after a deposition flow for 30 minutes. **(b)** Zoom-in on a hexagonal domain of **(a)**. **(c)** Zoom-in on a disordered domain of **(a)**. **(d)** Image after annealing the surface at 150°C and zoom in a zigzag domain. **(e)** Image after annealing the surface at 250°C.

In an attempt to stimulate the coupling of the precursors during deposition, **72** was sublimated onto a thermally activated Au(111) surface. We experimented with different surface temperatures for deposition, including 100°C, 150°C, and 200°C, followed by subsequent annealing at 350°C and 400°C. However, in most cases, this process led to uncontrolled reticulations, as depicted in **Figure 4.12a**. The most favorable deposition conditions were achieved at a metal temperature of 100°C, with the corresponding STM image presented in **Figure 4.12b**. Under these conditions, we observed hexagonal domains of intact molecules that self-assembled. Upon closer inspection of the deposited molecules, we noted the presence of both intact hexagonal molecules and degraded molecules that appeared to be missing a phenyl unit. Furthermore, an abundance of free bromine atoms, which spontaneously arrange themselves around the polycyclic aromatic molecules and limit their interaction, were also observed (**Figure 4.12c**).

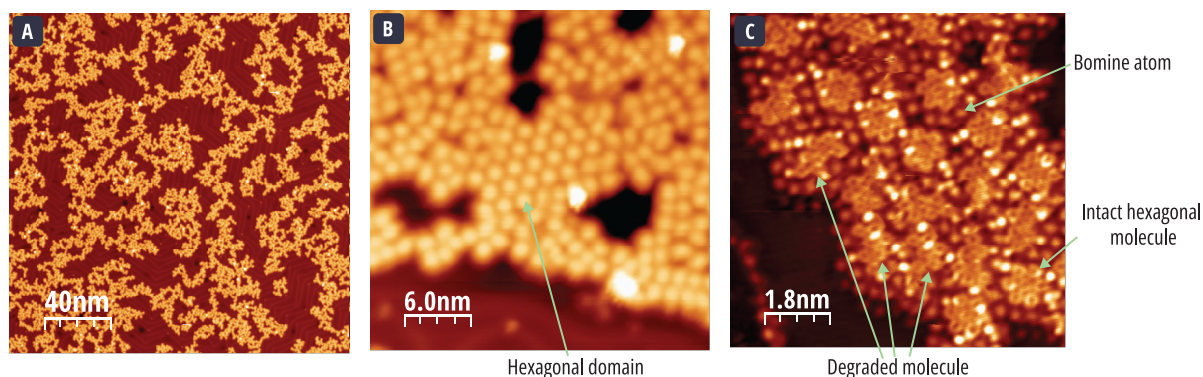


Figure 4.12 | Low temperatures STM images on precursor **72** deposited on a heated Au(111) surface. **(a)** Image obtained after a deposition flow for 20 minutes on an Au(111) surface at 200°C followed by annealing at 400°C. **(b)** Image obtained after a deposition flow for 25 minutes on an Au(111) surface at 100°C. **(c)** Zoom-in on (b).

To further investigate the degraded molecules, both STM and non-contact AFM (with a tip functionalized with CO) measurements were performed on two adjacent molecules: one demonstrating hexagonal symmetry and the other with less symmetry, as shown in **Figure 4.13**. The nc AFM image suggest that the least symmetric structure aligns with the loss of a phenyl unit, which is in line with previous observations from other images. There are several hypotheses to account for the origin of this degraded precursor. One hypothesis suggests that the degradation might have occurred during the deposition step. It is worth noting that the sublimation process entails harsh conditions, as mentioned at the beginning of this section. A second possibility is that the degradation takes place once the molecule is adsorbed to surface. Finally, this molecule could form as a byproduct of the Scholl reaction. Intriguingly, a mass peak matching the molecule missing a phenyl unit was identified at $m/z = 761$ in the mass spectrum of precursor **72**. Though this type of degradations can take place during the oxidation step, they remain very limited.⁸³ Besides, the proportion of this impurity peak remains very small in the mass spectrum. However, this impurity may sublime more easily than the un-fragmented molecule **72** and then be overexpressed on the surface; it is also possible that this impurity is less ionized during MALDI-ToF leading to an underestimation of its presence.

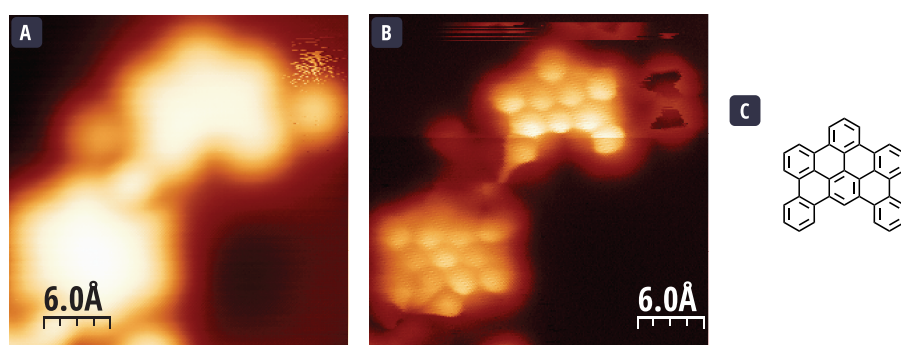


Figure 4.13 | **(a)** Low temperature STM image of a degraded molecule missing a phenyl unit obtained after deposition of **72** on Au(111) at room temperature followed by an annealing step at 250°C. **(b)** Low temperature nc AFM with CO tip image of the same degraded molecule as in (a). **(c)** Proposed structure for the degraded molecule observed.

SILVER SURFACE: Ag(110)

To test a more reactive surface, precursor **72** was deposited on Ag(110). As can be observed on **Figure 4.14a**, high coverage deposition was achieved on this surface. A closer look at the adsorbed molecules indicates that precursor **72** spontaneously organizes in a supramolecular order (**Figure 4.14b**). Upon careful observation, it is possible to notice that the auto-assembly is achieved through the interaction of a flat hexagonal molecule and two free bromine atoms. The hexagonal

molecule aligns linearly face to face in a row. Two molecules are separated by two free bromine atoms. Occasionally, there is a shift in rows by half a molecule length, creating a zigzag pattern. The defective molecules tend to position themselves at the borders of the ordered domains.

To promote the coupling of the nanoparticles, the surface was subsequently annealed at 400°C. Following this annealing step, the long-range supramolecular arrangement was disrupted, with mostly monomers surrounded by bromine atoms being observed. This can be observed in **Figure 4.14c**. Additionally, a few dimers or trimers were also formed. Closer observation of these assemblies (**Figure 4.14d**) suggest that the coupling of the dimers and trimers does not happen at the expected positions where the bromine atoms were previously positioned. The position of the radical is lost, which is not surprising at high temperatures.

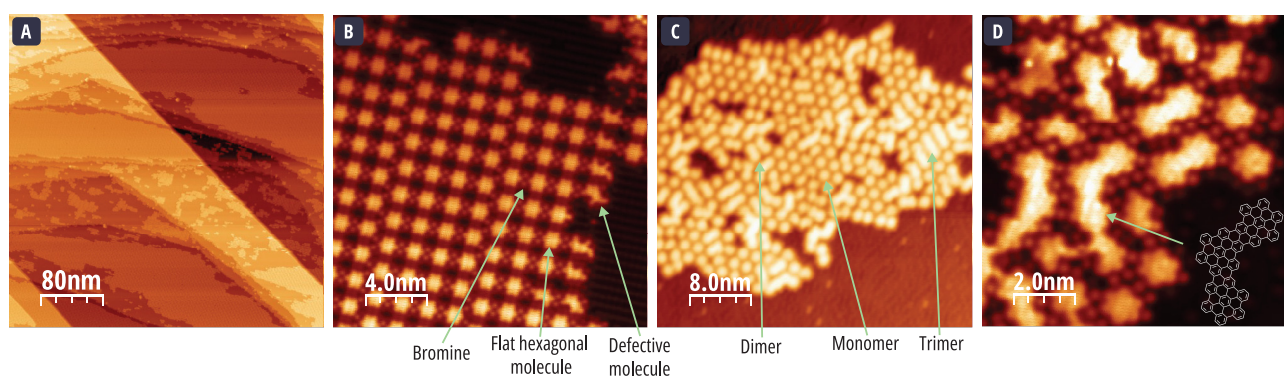


Figure 4.14 | Low temperatures STM images of precursor **72** deposited on an Ag(110) surface. **(a)** Image obtained after a deposition flow for 20 minutes on an Ag(110) surface at room temperature. **(b)** Zoom-in in a region of (a). **(c)** Image obtained after annealing the surface at 400°C. **(d)** Zoom-in in a region of (c).

SILVER SURFACE: AG(111)

An alternative silver surface, Ag(111), was tested. Upon deposition of precursor **72** at room temperature, a supramolecular arrangement was also observed, as shown in **Figure 4.15a**. This time, we observed a spontaneous segregation of domains containing different types of molecules: pristine monomers arranged in a tightly bound hexagonal lattice (**Figure 4.15b**), dimers (**Figure 4.15c-d**), and degraded molecules (**Figure 4.15e**). The dimers, and in some cases trimers, result from the close interaction of two hexagonal molecules without any bromine atoms between them. At this stage, the molecules had not yet covalently bonded. This can be appreciated in the constant current image presented in **Figure 4.15d**. Finally, it was possible to note the presence of bromine superstructures all over the surface (**Figure 4.15f**) and within the ordered domains, encircling the molecules.

The high bromine-to-molecule ratio of six to one indicates that C-Br bond dissociation occurs. This bond breaking could happen in the crucible, as high temperatures are used to sublime the precursor. Another possibility is that the dissociation occurs readily on the surface if the precursor is highly activated. The presence of bromine on the surface makes this latter hypothesis more plausible. Once the precursor has undergone debromination, it might more readily dewet the surface, which could explain the significant excess of bromine atoms. The remaining molecules on the surface are stabilized by H...Br interactions.

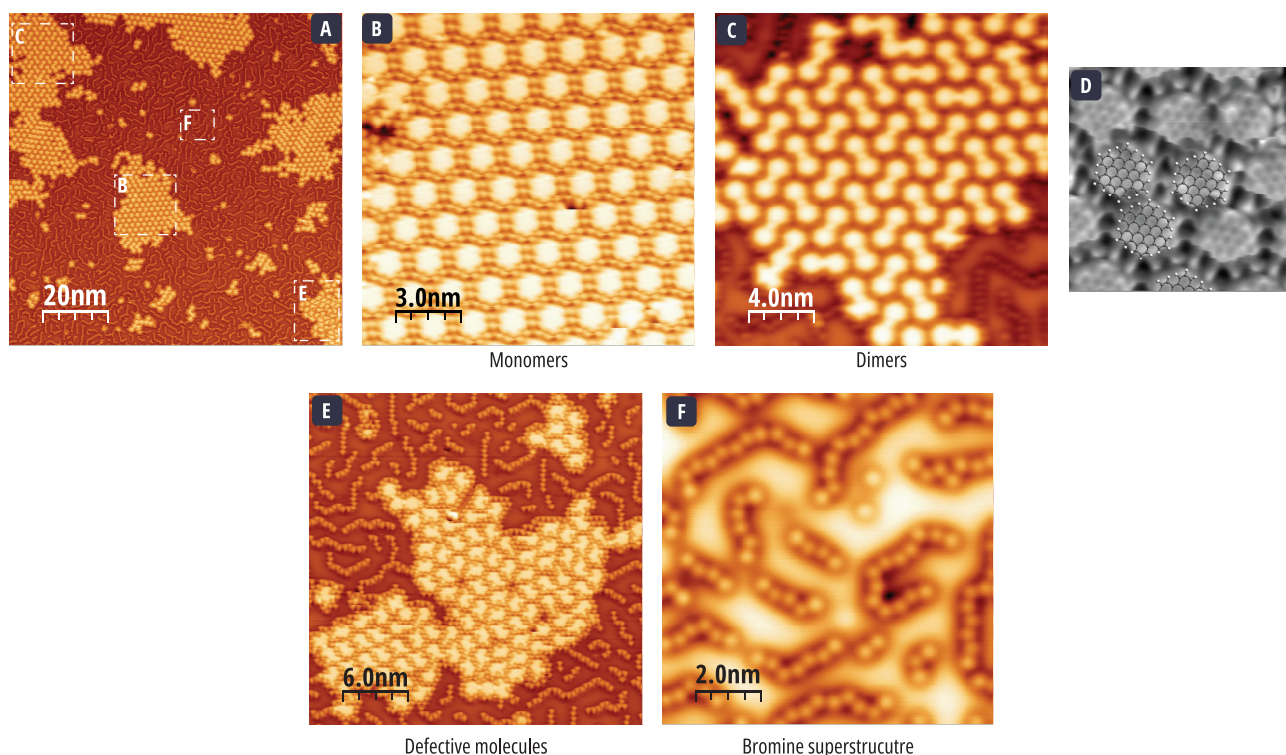


Figure 4.15 | Low temperatures STM images on precursor **72** deposited on an Ag(111) surface. **(a)** Image obtained after a deposition flow for 20 minutes on an Ag(111) surface at room temperature. **(b)** Zoom-in on a monomer assembly. **(c)** Zoom-in on a dimer assembly. **(d)** Constant current image of a trimer assembly and superimposed molecular model of HBC. **(e)** Zoom-in on an assembly of defective molecules. **(f)** Zoom-in on the bromine superstructure present on the surface.

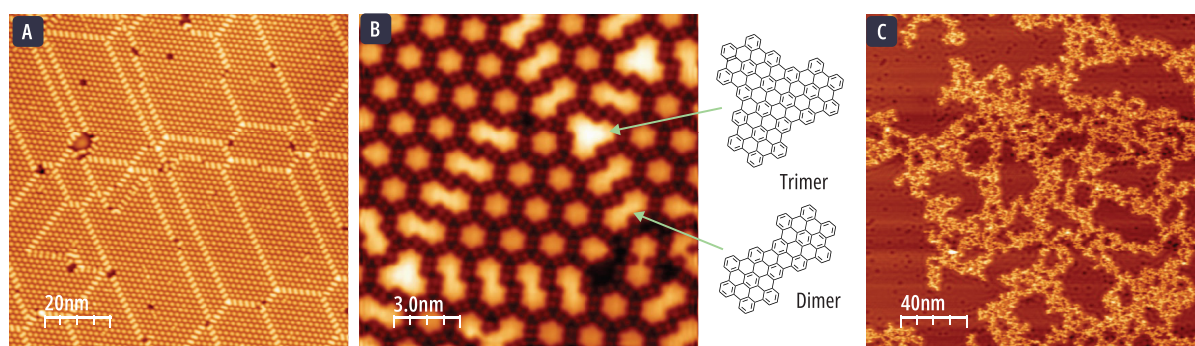


Figure 4.16 | Low temperatures STM images of precursor **72** deposited on an Ag(111) surface. **(a)** Image obtained after a deposition flow for 20 minutes on an Ag(111) surface at room temperature followed by annealing at 400°C. **(b)** Zoom-in on (a). On the right the two proposed structures for the dimers and trimers. **(c)** Image obtained after a deposition flow for 30 minutes on an Ag(111) surface at room temperature followed by annealing at 500°C.

Upon annealing the surface at 400°C, we note that the large supramolecular order is maintained (**Figure 4.16a**). We also observe the formation of fused dimers and triangularly shaped trimers. As with the Ag(110) surface, the position of the radical is lost, leading to unwanted couplings and unexpected structures such as triangular trimers. It is possible to notice that the dimers arrange into continuous lines of side-by-side molecules. Occasionally, a trimer is encountered, which causes a divergence in the dimer lines. It is possible to identify the monomers in the center of these arrangements (**Figure 4.16b**). Furthermore, the polymerization seems to be restricted to dimers and trimers only. One possibility to explain this limitation is that the surrounding bromine atoms stabilize the molecules, limiting their diffusion and interaction with neighboring molecules. To investigate the formation of higher-order fused polymers, the temperature was increased to 420°C and 500°C. However, only uncontrolled polymerization was observed at these temperatures, and the long-range order was completely lost (**Figure 4.16c**).

Precursor **72** did not yield the expected graphene nanomesh. Unlike what was observed with precursor **67**, the HBC derivative displayed a better affinity to the surface, notably on silver where extensive coverage was observed when deposited at room temperature. However, the bromine atoms might not have been optimally positioned. The steric hindrance between the bromine and hydrogen atoms leads to a deformation of the molecule. Furthermore, the steric hindrance from neighboring hydrogens renders the predefined reaction sites poorly accessible. The loss of bromine results in planar structures, which adhere poorly to the surface, causing an excess of bromine atoms on the surface. These bromine atoms engage in strong interactions with the remaining molecules, limiting their mobility and thus inhibiting long-range coupling. As the structure is stabilized, the coupling reaction necessitates high temperatures to occur, during which the position of the radicals is lost, leading to uncontrolled polymerizations. The presence of defective molecules, such as those missing a phenyl group, also contributes to the limitation of on-surface synthesis of graphene nanomeshes as it induces defects during growth. It remains unclear if these impurities are a byproduct of the Scholl reaction used to transform **67** into **72**, if they occur on the surface, or if they are generated during the sublimation step, which requires high temperatures.

4.3 A GNR STRATEGY TO OBTAIN GNM

Inspired by the synthesis of graphene nanomeshes by lateral fusion of graphene nanoribbons (GNRs), we decided to pursue this alternative pathway to produce GNMs. Examples of nanoporous graphene synthesized through this approach were presented in the general introduction and are recalled in **Figure 4.17**.^{167,174} The strategy for their synthesis is first the on-surface formation of a GNR, followed by a dehydrogenative cross coupling between the formed ribbons. The type of precursor used dictates the structure of the GNR and, therefore, the subsequent cross-coupling.

So far, the obtained networks were linked either by single carbon-carbon bonds or rubicene necks. However, as previously mentioned, theoretical calculations suggest that the neck of porous graphene significantly impacts its bandgap. Our main goal is to synthesize GNMs with necks that maintain the hexagonal lattice of graphene and wider than a single C-C bond. To that end, we designed a GNR precursor whose on-surface assembly would yield nanomeshes with necks that align with our primary objective. This section will provide a description of the precursor and the general growth strategy. Subsequently, we will discuss the synthesis of these precursors before describing their surface deposition.

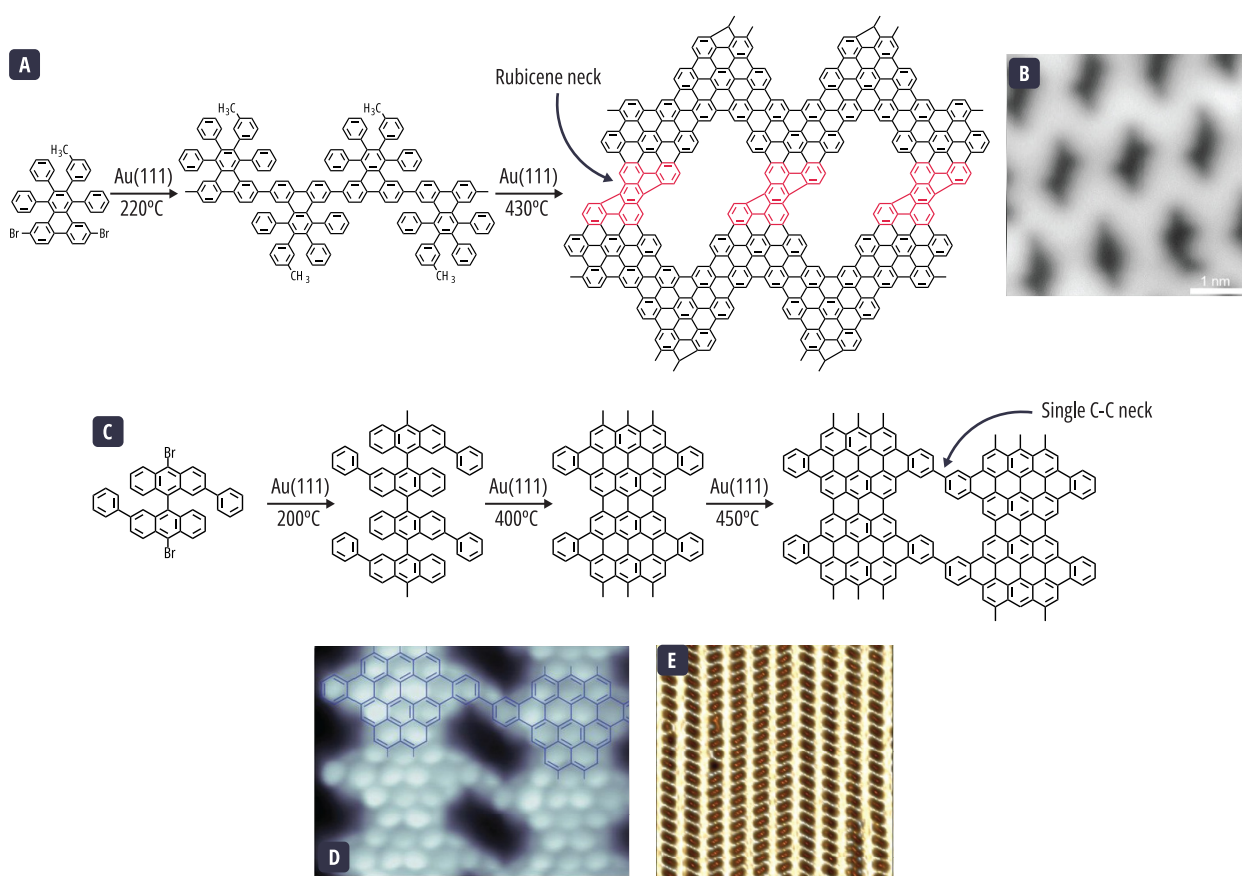
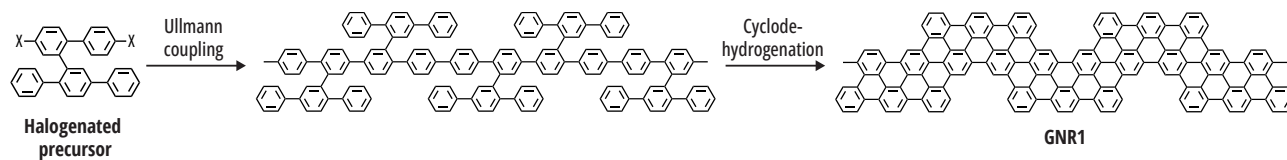


Figure 4.17 | Examples of covalent C-C two dimensional networks synthesized through a formation of GNR. **(a)** Reaction scheme for the synthesis on a gold surface of a GNM with a rubicene neck highlighted in red. **(b)** Topographic STM image of the rubicene necked GNM. (a-b)¹⁷⁴. **(c)** Reaction pathway of DP-DBBA to give nanoporous graphene. **(d)** AFM CO-functionalized tip image of a GNM obtained from annealing DP-DBBA at different temperatures on a gold surface. **(e)** STM laplacian-filtered image topographic close-up image of fused domains of GNM. (c-e)¹⁶⁷

4.3.1 GENERAL STRATEGY

Our planned strategy involves the on-surface synthesis of a chevron-type graphene nanoribbon (GNR), followed by a dehydrogenative cross-coupling between the synthesized GNRs. The precursor we have selected for the synthesis of the GNR has a trapezoid shape, comprising a terphenyl row topped by a biphenyl row to which two halogen atoms are attached. The on-surface Ullmann coupling will occur between two halogens from different precursor molecules. Besides, the steric hindrance generated by the terphenyl part of the molecule necessitates an alternating orientation of the precursors for successful coupling, yielding a chevron-type GNR after the cyclodehydrogenation step. This process is outlined in **Scheme 4.11**.



Scheme 4.11 | Strategy for synthesizing of GNR from the proposed halogenated precursor.

Once the GNR is formed, it may proceed to the lateral fusion to form a GNM. The structure of the GNR suggests that this step could yield a variety of hole sizes and arrangements. Indeed, the expected cross-coupling between two nanoribbons will involve the terphenyl sub-units, which could align either face to face or be offset by a phenyl unit. Moreover, the shift during the

lateral fusion can happen either to the right or to the left, a variation that will account for the resulting differences in pore shapes, sizes, and orientations.

A face-to-face cross-coupling will give an elongated pore, corresponding to two continuous benzene units missing. A shifted cross-coupling will generate two neighboring pores of the size of a single benzene unit, separated by a single carbon-carbon bond. The side to which the nanoribbons shift during the lateral fusion, to the left or right, will affect the nanopores' overall orientation. For instance, if the first coupling occurs face-to-face to the right and the second face-to-face to the left, an alternating pattern of elongated pore orientations is formed (**Figure 4.18a**). In the scenario where both couplings occur on the same side, all pores will share the same orientation (**Figure 4.18b**). The same principle applies to shifted coupling scenarios; if both couplings take place on the same side, so will the pore orientation (**Figure 4.18c**). It is also possible that the first coupling occurs face to face and the second one shifts, or *vice-versa*. In these cases, an alternating pattern of the large single and small double pores is created (**Figure 4.18d**). Again, the orientations will be dictated by the direction to which these cross-couplings take place, which may lead to non-periodic nanostructure in subsequent couplings of GNRs.

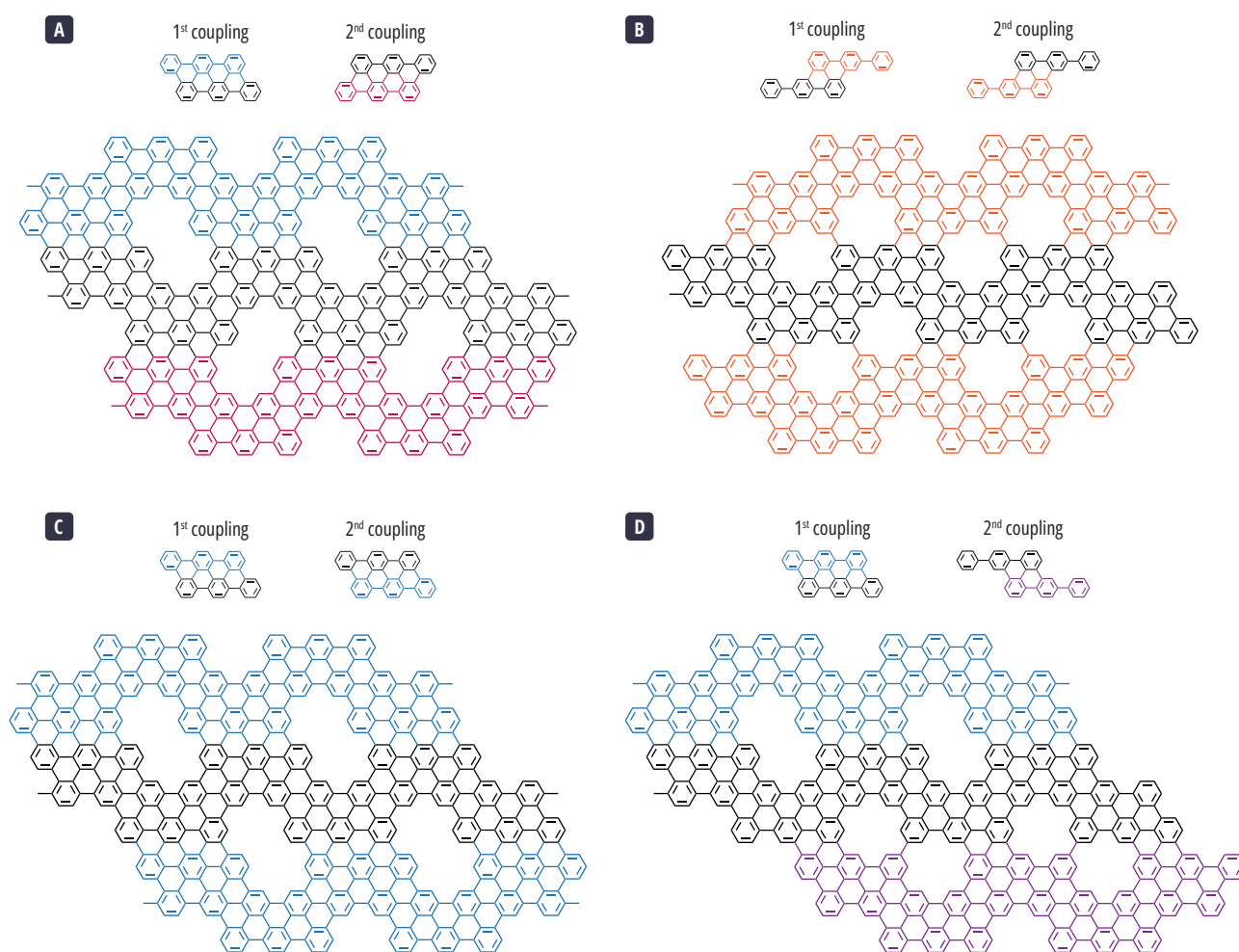


Figure 4.18 | Examples of possible pore configurations obtained after two lateral fusion steps. The direction into which the dehydrogenative cross-couplings take place affects the size, shape, and position of the pores.

As can be seen, with the proposed halogenated precursor, various pore configurations are possible, potentially leading to disordered GNM. However, in all possibilities, a neck containing more than a single carbon-carbon bond is preserved, thereby fulfilling our primary objective. In the scenarios where an offset coupling takes place, adjacent to the double pore separated by a single C-C bond lies a neck containing multiple C-C bonds and so the goal would be also accomplished in these cases. Moreno

et al. reported a two-dimensional network linked by single carbon-carbon bonds and faced a similar issue regarding pore orientation (see **Figure 4.17e**).¹⁶⁷ The directionality in their obtained network is not completely random, suggesting that the first cross-coupling has an influence over the subsequent ones, allowing for preservation of directionality. We hope to observe a similar effect in our synthesis of nanomeshes.

Two nanomesh precursors were synthesized, mainly differing by the choice of halogen atom used: iodine or bromine (**Figure 4.19**). These two precursors were synthesized to test the reactivities involving the C-X bond.²⁶⁹ We will first discuss the results obtained with the iodinated precursor, followed by the discussion on the results from the brominated precursor.

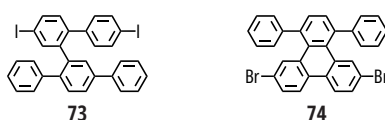


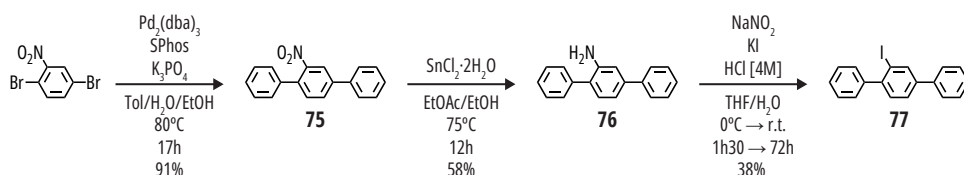
Figure 4.19 | Structure of the two halogenated precursors.

4.3.2 AN IODINATED GNR PRECURSOR

The synthesis of this iodinated precursor was designed to take advantage of the intermediates obtained during the synthesis of GNM precursor **57**, discussed at the beginning of this chapter. The general strategy for the synthesis of the trapezoid shaped iodinated GNR ribbon precursor **73**, consisted in the coupling of the iodoterphenyl **77** and the nitro substituted biphenyl **58**. We will first discuss its synthesis before presenting the firsts results obtained on surface deposition.

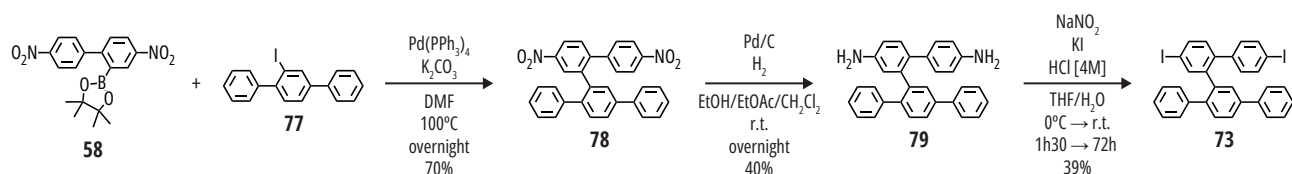
SYNTHESIS

The synthesis of iodoterphenyl **77** is depicted in **Scheme 4.12**. First, the commercially available 1,4-dibromo-2-nitrobenzene was transformed into the nitro-terphenyl **75** through Suzuki-Miyaura coupling with phenyl boronic acid. The nitro group was reduced into an amine to give compound **76** in the presence of tin chloride. **76** was then transformed into **77** using Sandmeyer conditions.



Scheme 4.12 | Synthetic route for the synthesis of iodoterphenyl **77**.

The reaction scheme to the iodinated GNR precursor **73** is described in **Scheme 4.13**. Its synthesis started through the Suzuki-Miyaura coupling of dinitro-biphenyl boronic pinacol ester **58** and iodoterphenyl **77** to give the nitro substituted intermediate **78**. The nitro groups in compound **78** were reduced in the presence of tin chloride to give the diamine **79**. The desired compound **73** was obtained after the Sandmeyer reaction on **79** in the presence of KI as iodine source.



Scheme 4.13 | Synthetic route for synthesizing an iodinated GNR precursor **73**.

SURFACE DEPOSITION

Our collaborators at IM2NP in Marseille deposited compound **73** on a Cu(100) surface to explore its behavior on this reactive surface. The deposition took place on a surface at room temperature, where full coverage was achieved without any supramolecular arrangement of molecules. For a deposition at lower coverage, the C-C coupling reaction was observed even at room temperature. However, it was limited to only a few monomers giving nanoribbons smaller than ten nanometers with a periodicity of 1.1 nm (**Figure 4.20a**). In an attempt to achieve the cyclodehydrogenation, the surface was annealed to 300°C but only disordered planarization was observed.

To further promote the C-C coupling, precursor **24** was deposited on a Cu(100) surface at 200°C. Under these conditions, only small nanoribbons with a length of five to six nanometers and a periodicity of 1.1 nm were observed (**Figure 4.20b**). Additionally, full coverage was impossible, and a lattice of iodine atoms could be observed on the surface (**Figure 4.20c**). The large excess of iodine atoms indicates that molecules largely desorb from the surface, which is not beneficial for the growth of large GNRs. Upon further annealing of the surface at 300°C, planarization is only achieved in a disordered fashion (**Figure 4.20d**).

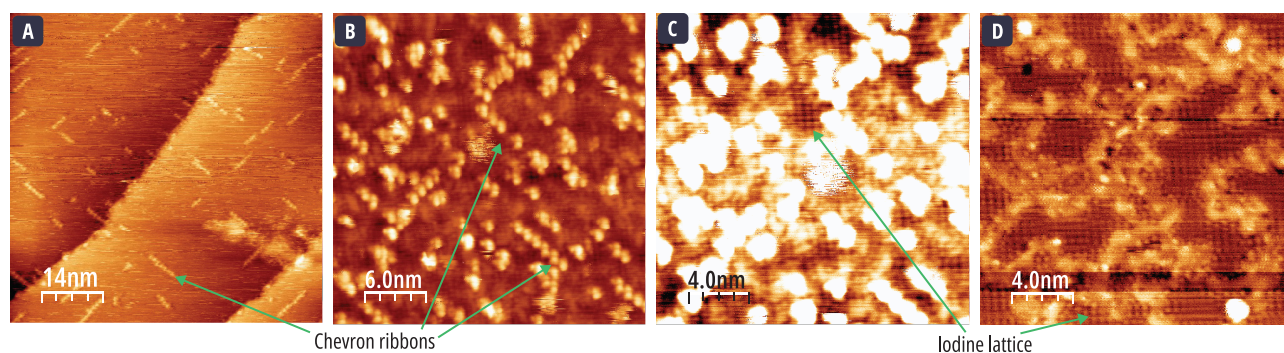


Figure 4.20 | Room temperature STM images of compound **73** on Cu(100). **(a)** Image obtained after deposition on a surface at room temperature. **(b)** Image obtained after deposition on a hot surface at 200°C. **(c)** Zoom in on a section of **(b)** with increased contrast. **(d)** Image after annealing the surface at 300°C.

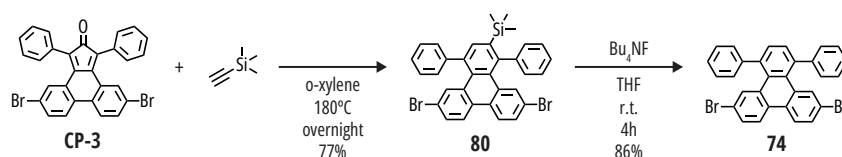
Deposition on this copper surface demonstrated that the formation of structures resembling to the expected chevron nanoribbons is indeed possible. However, the coupling remains limited to a few numbers of monomers. Deposition at higher temperatures promotes the desorption of the precursor, leaving behind its iodine atoms. No additional surfaces were tested for this precursor, as even less reactive surfaces may allow for an additional control of the reaction, the friability of the C-I bond makes similar results possible. At this moment it was decided to pass to the synthesis the brominated precursor, with stronger C-X bonds.

4.3.3 A BROMINATED GNR PRECURSOR

Even though the synthesis of the brominated precursor could be achieved by changing the Sandmeyer conditions from the amino compound **79**, we decided to test a more straightforward route. To synthesize the bromine-substituted precursor **74**, we followed an approach analogous to the synthesis of the hexagonal shaped GNM precursor discussed earlier. Despite the slight difference in the structure of the iodinated and brominated precursor induced by the presence of an additional carbon-carbon bond, the strategy for obtaining GNMs remains the same as previously described. Let's now discuss the synthesis of the brominated precursor and the first results for the deposition on a metallic surface.

SYNTHESIS

The synthesis to the brominated GNR precursor **74** is described in **Scheme 4.14**. First, the dibromophenanthrene cyclopentadienone **CP-3** was heated in the presence of trimethylsilylacetylene (TMSA) to undergo a Diels-Alder reaction and yield the trimethylsilyl-protected compound **80**. Then, the removal of the trimethylsilyl group in the presence of tetramethylammonium fluoride gave the desired dibromo diphenyltriphenylene **74**.



Scheme 4.14 | Synthesis of dibromo-diphenyltriphenylene **74**.

SURFACE DEPOSITION

This time, the deposition was performed on an Au(111) surface to test analogue conditions to previous reports of covalent C-C networks synthesized through a similar approach from the coupling of monomers containing bromine atoms (refer to **Figure 4.17**). First, deposition was performed on a substrate at room temperature, where only low coverage was achieved, and precursors seem to arrange in supramolecular dimers or trimers (**Figure 4.21a**). To promote the C-C coupling, precursor **74** was then deposited on a surface at 200°C. This time higher coverage was achieved and small linear arrangements with a width limited to the size of one stacking phase of the herringbone reconstruction of the gold surface were observed (**Figure 4.21b**). Upon further annealing the surface at 400°C, only disordered planarization occurs (**Figure 4.21c**). Deposition on a slightly hotter surface at 250°C generated domains that underwent uncontrolled polymerizations along with small domains where the expected controlled C-C coupling appeared to have occurred (**Figure 4.21d**). These domains exhibit a chevron-like configuration but are again limited to the size of one stacking phase of the herringbone reconstruction. Further annealing at 400°C does not result in the expected cyclodehydrogenation or lateral fusion, and only disordered planarization occurs (**Figure 4.21e**).

Deposition of **74** on an Au(111) surface showed that the reaction is complicated. Only small domains of GNRs are obtained, co-existing with disordered domains. It is possible that larger nanoribbons could be achieved using a more reactive surface, such as silver. However, our results seem to diverge significantly from previous reports of on-surface GNR synthesis, in which long nanoribbons with high coverage and a small number of defects are obtained.^{135,153,269,270} Consequently, to validate if our deposition conditions are appropriate, we decided to replicate the on-surface synthesis of previously described GNRs.

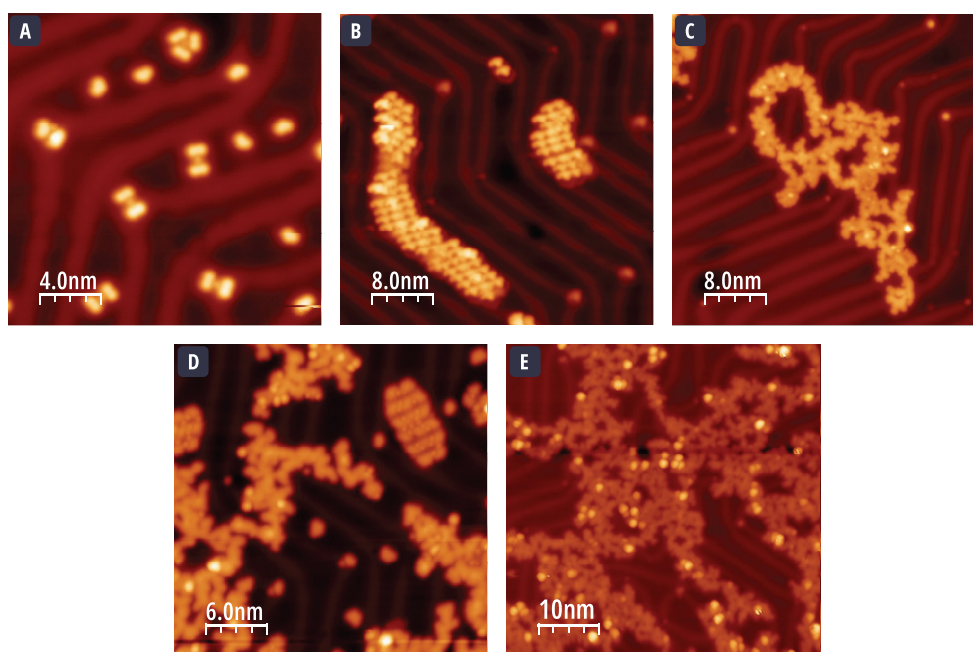
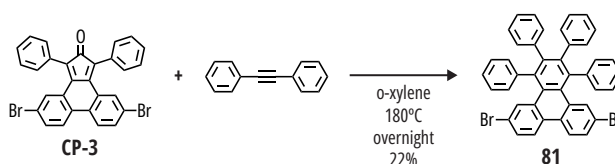


Figure 4.21 | Low-temperature STM images of compound **74** on Au(111). **(a)** Image obtained after a deposition flow for 1 minute on an Au(111) surface at room temperature. **(b)** Image obtained after a deposition flow for 1 minute on an Au(111) surface at 200°C. **(c)** Image obtained after a deposition flow for 1 minute on an Au(111) surface at 200°C and subsequent annealing at 400°C **(d)** Image obtained after a deposition flow for 30 minutes on an Au(111) surface at 250°C. **(e)** Image obtained after a deposition flow for 100 minutes on an Au(111) surface at 150°C and subsequent annealing at 400°C.

4.3.4 REVISING THE SYNTHESIS OF A GNR

So far, the different precursors tested did not yield the expected nanoribbons or nanomeshes. In the mindset to reproduce previously published graphene nanoribbons and better understand if the encountered synthesis limitations come from our deposition protocol or the precursor's design, we decided to synthesize the 6,11-dibromo-1,2,3,4-tetraphenyltriphenylene precursor **81**. This precursor was first deposited on an Au(111) surface by Cai *et al.* to obtain chevron-type graphene nanoribbons varying lengths from a couple of nanometers up to sixty nanometers.¹⁵³ To obtain the GNR, Ullmann coupling of monomers was achieved at a first annealing at 250°C, a second annealing step at 440°C induced intramolecular cyclodehydrogenation. The synthesis of precursor **81** was obtained following the described protocol and it is summarized in **Scheme 4.15**. Cyclopentadienone **CP-3** and the commercially available diphenylacetylene were reacted through Diels-Alder conditions to yield the expected precursor **81**.



Scheme 4.15 | Synthesis of 6,11-dibromo-1,2,3,4-tetraphenyltriphenylene **81**.

Our collaborators at IM2NP in Marseille deposited precursor **81** on Cu(111), Au(111), and Ag(111) surfaces and succeeded in forming the expected GNR in all three surfaces (**Figure 4.22**). After monomer **81** is deposited on the surface, a first annealing step allows the Ullmann coupling, and further annealing enables cyclodehydrogenation. These different steps occur at different temperatures on the three surfaces. On copper, an organometallic polymer is observed at room temperature and further annealing at 200°C forms the covalent C-C polymer. On silver, the organometallic polymer was observed after annealing the

surface at 200°C. On gold, the organometallic polymer was not observed; instead, after annealing at 300°C, a partially fused polymer was observed. Complete cyclodehydrogenation was observed at 300°C on copper, 400°C on silver, and 450°C on gold.

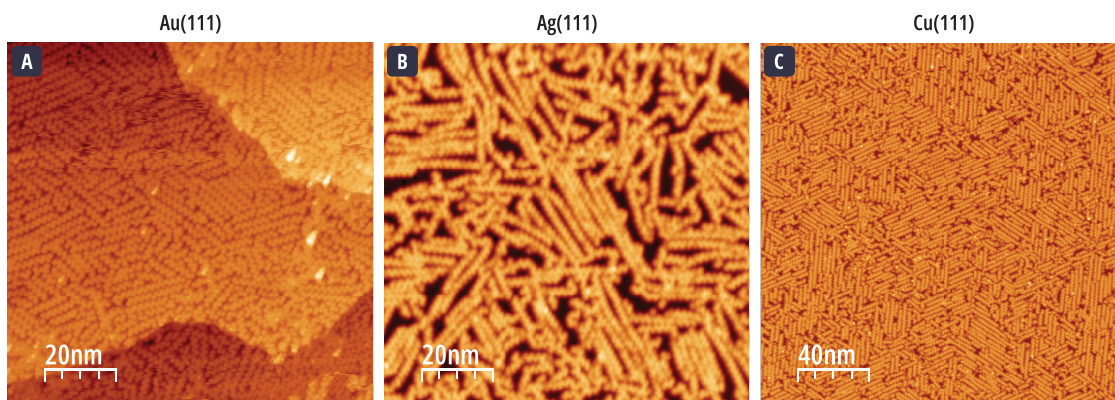


Figure 4.22 | Low-temperature STM images of chevron type GNR obtained from compound **81**. **(a)** Image obtained after a deposition on an Au(111) room temperature surface followed by annealing at 450°C. **(b)** Image obtained after a deposition on an Ag(111) room temperature surface followed by annealing at 450°C. **(c)** Image obtained after a deposition on a Cu(111) room temperature surface followed by annealing at 300°C.

With the obtained GNR, further annealing was tested to see if lateral fusion of the GNR was possible. Though in some cases lateral fusion was observed, it remained very limited. First, no more than two fused nanoribbons were observed. Secondly, the lateral fusion would not occur on the entire length of the nanoribbon but rather on localized zones (**Figure 4.23a**). Heating at large temperatures for long times promoted uncontrolled graphitization rather than further intermolecular cross-coupling (**Figure 4.23b-c**).

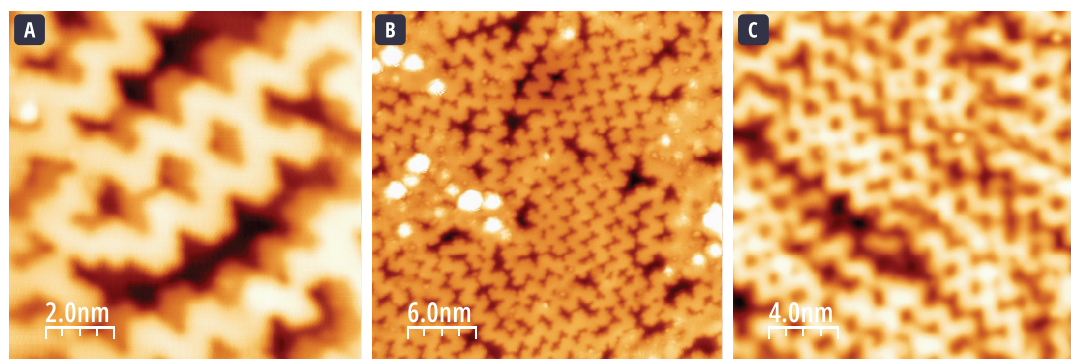


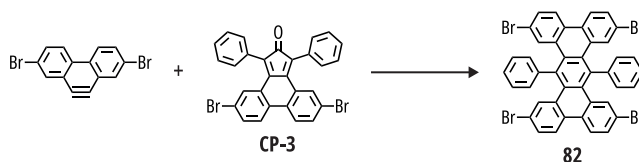
Figure 4.23 | Low-temperature STM images of chevron type GNR lateral fusion obtained from compound **81**. **(a)** Image obtained after a deposition on an Au(111) room temperature surface followed by annealing at 550°C. **(b)** Image obtained after a deposition on an Au(111) room temperature surface followed by a long annealing at 500°C. **(c)** Image obtained after a deposition on a Cu(111) room temperature surface followed by annealing at 400°C.

4.4 CONCLUSION

In this chapter we summarized the synthesis of organic precursors and our attempts to assemble on the surface to obtain graphene nanomeshes. Our main strategy consisted in the synthesis of derivatives from the hexagonal-shaped precursor **57** containing four bromine atoms in specific positions to guide the coupling reaction on the surface. During the synthesis of precursor **57**, we encountered several difficulties regarding the reactivity and solubility of the intermediates. To tackle this problem, we prepared an alternative structure using a strategy analogous to synthesizing GQDs. Unfortunately, the asymmetric and tridimensional nature of the partially fused precursor **67** diminished its adsorption to the metallic substrate, therefore, only

low coupling reaction yields were obtained. To overcome this problem and increase the coverage ratio, we proceeded to the complete fusion of precursor **67**. The hexa-*peri*-benzocoronene derivative **72** was then deposited on metallic surfaces. Deposited at room temperature, the hexagonal precursor yielded delightful supramolecular assemblies where free bromine atoms play an important role. Unfortunately, upon annealing the surface, these assemblies did not give the expected two-dimensional network, rather uncontrolled polymerizations were obtained where the pre-defined radical position was lost. This limitation can be explained by the inaccessibility of the pre-defined coupling sites because of the steric hindrance caused by the neighboring hydrogen atoms. Additionally, the excess of bromine atoms stabilizes the monomers and diminishes their reactivity. Desorption of bromine happens in the form of HBr, where the hydrogen source is the cyclodehydrogenation reaction. In the case of precursor **71**, cyclodehydrogenation is performed before surface deposition which may also disfavor bromine desorption.

In that perspective, a less rigid derivative can be synthesized (**Scheme 4.16**). The symmetric nature may allow for better adsorption and controlled coupling than the ones observed for precursor **67** who differs to the proposed precursor **82** only by a C-C bond. Besides, the absence of bonds locking the central phenyl units may diminish the steric hindrance described before and allow for a better coupling at the predefined sites. The challenge now relies upon synthesizing this alternative precursor, which comes off as complicated. Indeed, we cannot selectively create the missing C-C from molecule **67** using a Scholl reaction. A possible pathway would be synthesizing a cycloalkyne (benzyne) derivative to be used in a further Diels-Alder reaction. Nevertheless, this approach constitutes a synthetic challenge because of the geometric constraint, which also makes mostly of these compounds exist as transient reaction intermediates.²⁷¹



Scheme 4.16 | Proposed synthesis for an alternative GNM precursor with more freedom in the central phenyl groups.

During this chapter, we also presented an alternative strategy to obtain graphene nanomeshes, where first a graphene nanoribbon is formed, and in a further step, the nanomeshes are obtained by lateral fusion of the nanoribbons. Even though the most impressive examples of covalent C-C two-dimensional networks found in the literature were obtained using this approach, our attempts to form nanomeshes through this method were unfruitful. We were first confronted to the synthesize large GNRs from precursors **73** and **74**. Both precursors tend to desorb from the surface, yielding only low coverages. Ullmann coupling in both cases remains limited and upon annealing the surface to induce cyclodehydrogenation only uncontrolled reactions take place. Thus, no nanoribbons were observed from these precursors. To validate the results, we reproduced a chevron-type graphene nanoribbon from the literature. Using monomer **81** we were able to form graphene nanoribbons of great quality on Cu(111), Ag(111), and Au(111). These results seem to suggest that our deposition approach and techniques are good, and rather the difficulties encountered are a result from the monomers we designed. To address this issue, in our research group we are currently developing new GNM precursors with different symmetries as the ones presented in this thesis work. An additional target is the incorporation of heteroatoms into the nanomesh precursor which may increase surface adsorption and have an impact on they reactivity.

Chapter 5 CONCLUSION

CHAPTER 5 CONCLUSION

Throughout this PhD work, we explored the bottom-up synthesis, through organic chemistry methods, of two graphenic materials: graphene quantum dots and graphene nanomeshes. This synthetic approach allowed us to tailor the structures of the GQDs and the GNM precursors. A well-defined structure allowed us to explore the structure-properties relationship, specifically the optical properties. As discussed in the introduction, studies focusing on the intrinsic optical properties of GQDs are scarce. This is because graphene nanoparticles were first synthesized in a top-down approach. These GQDs contained multiple defects and inhomogeneities which were seen to govern their optical properties. Later, with the increasing development of the synthesis of large polycyclic aromatic hydrocarbons new challenges arose because of the poor solubility of these molecules. First, advanced optical studies were limited to the observation of small PAHs, like hexabenzocoronene. Because of more important π -stacking interaction, larger GQDs were only studied by absorption spectroscopy, giving rise to broad spectra that were challenging to analyse. In response to this problem, the approach was to add substituents along the edges of the GQDs (*i.e.*, alkyl chains, *tert*-butyl groups, chlorine atoms, and alkoxy groups). While these substituents did help to slightly improve the solubility of the PAH, for the most part, they remained poorly soluble, thus limiting their processability and, more specifically, their purification. However, having pure samples of the graphene nanoparticles for optical studies is highly important since the presence of impurities may lead to a wrong interpretation of the optical behaviour of the GQDs.

In the first half of this PhD thesis, we focused on further improving the solubility of graphene nanoparticles. We showed that the positioning of the functional groups plays a vital role in their solubilizing efficiency. For that, we synthesized a rod-shaped family of GQDs containing *tert*-butyl groups along their main axis and exhibiting a C_{2h} symmetry. This family comprises four members ranging in size from 1.99 nm to 3.11 nm: **C₇₈tBu₆**, **C₉₆tBu₈**, **C₁₁₄tBu₁₀**, and **C₁₃₂tBu₁₂**. Surprisingly, the preliminary optical studies suggested that the largest GQDs remained highly soluble and individualized in solution despite their large size. At the same time, the smallest member, the **C₇₈tBu₆**, showed a behaviour that could be explained by aggregation in solution. The inverse is usually true: as size increases, the π -stacking interaction becomes more important, thus the aggregation process. Theoretical calculations allowed us to gain a better insight into the aggregation process. They showed two reasons for the suppressing of the aggregation in **C₉₆tBu₈**, both linked to the presence of adjacent *tert*-butyl groups along the main axis of the nanoparticle: the steric hindrance that the solubilizing groups add to the GQD and the existence of stable and unstable conformers. The positioning of the *tert*-butyl groups creates possible conformers for the GQDs, six in the case of **C₉₆tBu₈**. Calculations showed that the energetic barrier generated by the steric hindrance of the *tert*-butyl groups during the aggregation could be overcome if the functional groups are previously disposed in specific configurations. However, for **C₉₆tBu₈** the conformers exhibiting these configurations are highly energetic and are virtually inexistent in solution, thus conferring a high solubility to the GQD. In the case of **C₇₈tBu₆**, all conformers exist in solution, and there is an entry point to the aggregation process.

The high solubility of the partially *tert*-butylated rod-shaped family allowed for efficient purification of the nanoparticles through standard techniques in organic chemistry: precipitations, column chromatography, and size exclusion chromatography. Highly pure samples of GQDs were obtained and their structure was confirmed through mass spectrometry and NMR

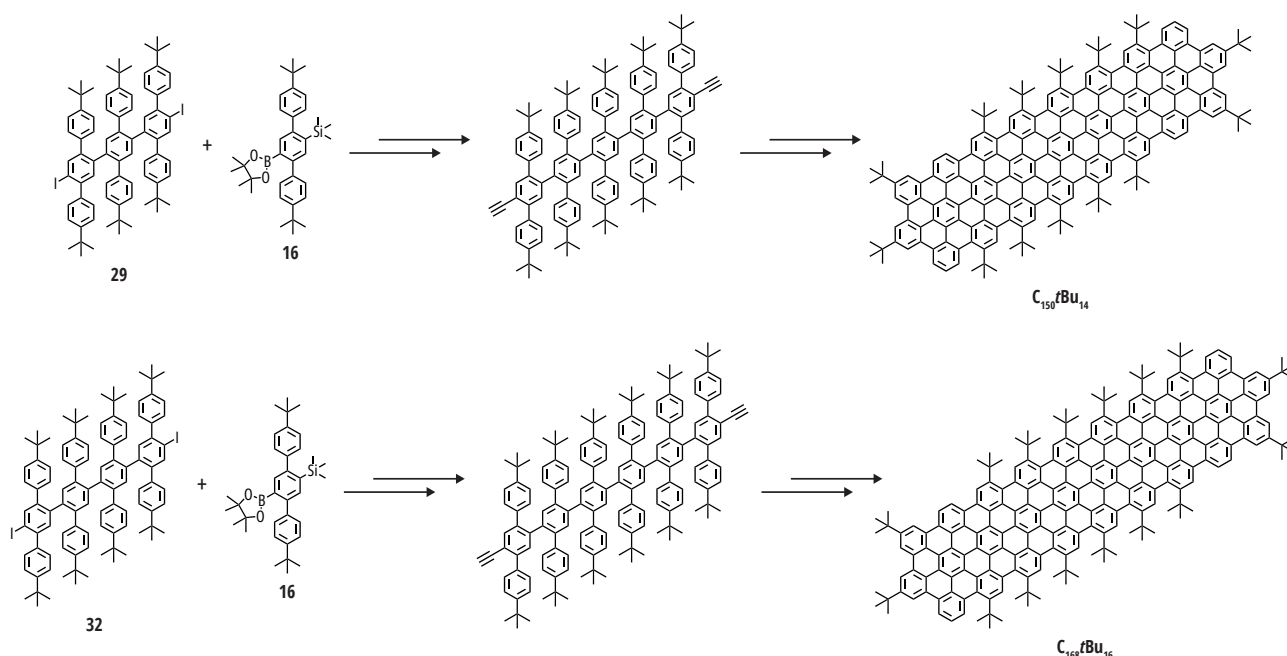
experiments. The pure and soluble samples allowed for more extensive optical experiments. A particular focus was given to **C₉₆tBu₈**. In combination with theoretical descriptions, it was possible to thoroughly attribute the peaks observed in the absorption and emission spectra to the electronic transitions and their associated vibrations, thanks to the spectra exhibiting vibronic resolution. These attributions were confirmed by fluorescence anisotropy, where it was possible to observe the variation of the orientation of the polarization of the different absorption transition moments to the emission transition moment. Finally, single-molecule experiments were performed for **C₉₆tBu₈**. An excellent agreement was found between the optical properties in solution and for a single GQD, confirming that **C₉₆tBu₈** is highly individualized in solution.

With the partially *tert*-butylated family of rod-shaped GQDs, it was possible to tune the absorption and emission by more than 150 nm by changing the size. Emissions up to the near-infrared were obtained for the family's largest member. Additionally, the increasing of size also impacted the size distribution of charges in the electronic transitions, generating differences in their absorption spectra. Finally, this rod-shaped family of GQDs exhibited very high quantum yields, up to 94%. This is one of the highest reported for GQDs. All these exciting behaviours of the GQDs family encouraged us to integrate the **C₇₈tBu₆** and **C₉₆tBu₈** in organic light emitting diodes as emissive materials. Though performances of the devices are not optimal, this served as a proof-of-concept for potential applications of these bottom-up synthesized GQD.

To further enhance the solubility of the rod-shaped GQDs, we added additional *tert*-butyl groups along the axis of the nanoparticles. This generated the fully *tert*-butylated family of nanoparticles composed of four members: **C₆₀tBu₈**, **C₇₈tBu₁₀**, **C₉₆tBu₁₂**, and **C₁₁₄tBu₁₄**. Besides, a fifth member, the **C₁₃₂tBu₁₆**, is on the process of being synthesized. The supplementary functional groups efficiently suppressed the aggregation of the smaller members of the family: **C₆₀tBu₈** and **C₇₈tBu₁₀**. The preliminary optical measurements unveiled new behaviours for these smaller members, compared to the preceding family. The additional *tert*-butyl groups generated a red shift in the absorption and emission and a less pronounced effect in the charge distribution with size as observed for the partially *tert*-butylated family. Further computational studies will help to better understand these changes.

An alternative strategy to increase the solubility of graphene quantum dots is to break their two-dimensional character to perturb the π -stacking. This approach was tested during this PhD thesis by synthesizing helicenes and a nanographene propeller ((**C₇₂tBu₈**)₂). Three triple-[6]helicenes were targeted by introducing steric hindrance to prevent the planarization: (**C₃₀tBu₄**)₃-T[6]H, (**C₃₆**)₃-T[6]H, and (**C₃₆tBu₅**)₃-T[6]H. It was observed that when only *tert*-butyl groups are employed to add steric hindrance, as in (**C₃₀tBu₄**)₃-T[6]H, these groups were removed during the Scholl oxidation to achieve planarization of the nanoparticle. The oxidation of the highly congested dendrimer, **44**, demonstrated the importance of the characterisation with other than mass spectrometry, the method of analysis of choice for large polycyclic aromatic hydrocarbons, to elucidate and verify the structure of the GQDs. This is especially important since the Scholl oxidation mechanism is not always understood, which can lead to unpredicted rearrangements during this oxidative step. The mass spectroscopy of the oxidation of this highly congested dendrimer **44** yielded the expected *m/z* value and isotopic distributions for (**C₃₆tBu₅**)₃-T[6]H, but with an unexpected NMR pattern. However, upon the obtention of single crystals it was possible to identify that the target helicene was not formed. Instead, a bis-spiro GQD **47** was obtained, where some *sp*² domains were broken. This spiro GQD was chiral and exhibited good chiroptic properties for an organic molecule. Further experiments and computational modelling are being done to understand the reactivity of this congested dendrimer better and attempt to obtain the target helicene.

The work presented in this thesis concerning graphene quantum dots paved the way for numerous perspectives to fully exploit the high solubility of the rod-shaped families of GQDs. We will now discuss some of these perspectives, and, when possible, illustrate them with some structures. Since multiple projects (and potential patents) are currently being prepared with these perspectives, only some structures will be described. During this PhD work, we presented an iterative approach for synthesizing large rod-shaped GQDs, where the intermediates of some alkyne cores can be used to synthesize other cores. In this mindset, an alkyne core containing up to four rows of terphenyl groups, *i.e.*, core **24**, was synthesized and used in the synthesis of the C_{132} GQDs: $C_{132}tBu_{12}$ and $C_{132}tBu_{16}$ (whose oxidation is still pending). Nonetheless, the intermediates necessary for the synthesis cores containing five or six terphenyl rows are already described, as illustrated in **Scheme 5.1**. These cores would allow to synthesize bigger soluble GQDs.



Scheme 5.1 | Proposed synthesis of larger GQDs C_{150} and C_{168} employing precursors described in this thesis work.

As we elongate the size of the quantum dots, it is possible to start to describe them as graphene nanoribbons. Theoretically, the bandgap in GNR is limited by the width of the ribbon.^{272,273} The structure of the rod-shaped GQDs presented in this thesis would correspond to $N = 9$ armchair GNRs (**Figure 5.1**) who have a measured bandgap value of 1.35 eV (920 nm).²⁷³ It will be interesting to observe at which number of terphenyl rows the GQDs bandgap converge with the bandgap value of the GNR. To obtain smaller bandgaps, it is necessary to increase the width of the nanoribbon. For instance, the $N = 15$ GNR has a reported bandgap of 1.03 eV (1 200 nm).²⁷³ This can also be translated to the rod-shaped GQDs: for the same length, an increase of the width would exhibit a red shifted emission and may allow us to have a complete emission in the near infrared. In our research group, wider GQDs containing pentaphenyl instead of terphenyl rows with adjacent *tert*-butyl groups to help with solubility are being synthesized using the strategy developed during this PhD work. Additionally, different functional groups can be tested to ensure the good solubility of these GQDs.

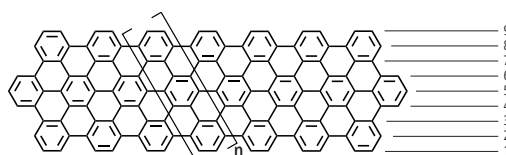


Figure 5.1 | Seeing the rod-shaped GQD as a $N = 9$ armchair GNR.

To fully exploit the high solubility of the rod-shaped families of GQDs. Bromine atoms are being added to the structures alongside the *tert*-butyl groups. The solubility conferred by the adjacent *tert*-butyl groups opens the door to do chemistry in solution to perform the post-functionalization with chemical groups that would otherwise not support the oxidative step. This will enable to add functional groups to render the nanoparticles water soluble, opening a new field of applications in biology. This will be extremely interesting considering the good optical properties of the rod-shaped GQDs presented in this manuscript, notably their excellent quantum yields.

Concerning the helicenes, having a better understanding of the Scholl oxidation of the congested dendrimers will be beneficial to obtain the target helicene (**C₃₆tBu₅**)₃-T[6]H. To achieve this, theoretical DFT mechanistic calculations are being carried out on the reactants, transition states, and intermediates. Additionally, different reaction conditions are also being tested in our research group (oxidant/acid couple and temperature) to achieve the correct oxidation of (**C₃₆tBu₅**)₃-T[6]H.

During this thesis we detailed the use of **C₇₈tBu₆** and **C₉₆tBu₈** as emitting material in OLED devices. The smaller member of the rod-shaped family, **C₆₀tBu₈** is also under investigation as emitting material and preliminary results are encouraging. Its higher solubility and smaller structure may facilitate its integration into the device. Instead of spin-coating this material, it may also be possible to deposit it through sublimation, which generally gives a better-quality deposition and ameliorates the obtained properties. To increase the OLED's external quantum efficiency, it is possible to integrate a thermally activated delayed fluorescent material to recover the triplet excitons, which represent 75 % of the excitons and would otherwise be lost in fluorescent OLEDs.^{220,274} The spiro GQD **47** can also be incorporated into an OLED as a chiral emissive material.^{225,275,276} Furthermore, new helicenes and chiral GQDs can be designed towards this end. It can also be possible to design chiral GQDs capable of hosting metallic atoms to further accentuate their chiral properties.²⁷⁷

Finally, more detailed single molecule spectroscopy of the rod-shaped GQDs is also being performed in collaboration with LUMIN laboratory at ENS Paris-Saclay and with the groups of Michel Orrit in Leiden University in Netherlands and Constanza Tonelli at LENS in Florence, Italy. These additional studies consist of low temperature experiments and the incorporation of the emitters in a host crystal instead of a polymer matrix. This will help to investigate the impact of the environment on the optical properties. Understanding quantum emitters, that are tuneable by chemistry and easily processable, will open the way for using these GQDs for applications in quantum technologies such as in photonic networks or quantum key distributions, where single photons on demand are needed.²⁷⁸

The last part of this PhD thesis work was dedicated to the synthesis of different graphene nanomesh precursors and depositing them on a metallic surface for their assembly. Our first attempts with a hexagonal shaped precursor **67** were unsuccessful, mainly because of its poor adsorption to the surface due to its three-dimensional nature. To improve its adsorption the precursor was cyclodehydrogenated to obtain a hexabenzocoronene derivate **72**. This compound has a better adsorption to the surface and gave very nice supramolecular assemblies. However, it did not couple together to give the expected two-dimensional network, which was attributed to a poor accessibility to the coupling sites due to the steric hindrance from adjacent hydrogen atoms. An alternative strategy to the formation of graphene nanomeshes was also introduced: the synthesis on-surface of a chevron-type graphene nanoribbons followed by their lateral fusion to yield the GNMs. However, obtaining large graphene nanoribbons with our precursors was complicated, and subsequent annealing yielded only disordered structures. Finally, we

validated our deposition techniques by repeating the synthesis of chevron-type graphene nanoribbons previously described in the literature.

New GNM precursors with different symmetries are being developed in our research group. For instance, a less rigid and symmetric precursor **82** can be designed to facilitate the on-surface coupling of the hexagonal precursor. This precursor, being symmetric and less three dimensional than **67** may allow for a better adsorption to the surface. Besides the free rotation of the central phenyl groups may diminish the steric hindrance and allow a better access to the predefined coupling sites carrying the bromine atoms. We are currently investigating synthetic approaches towards this molecule. Alternatively, adding heteroatoms into the GNM precursors may help with their surface adsorption and impact their reactivity. For example, we can imagine the nitrogen-substituted structure **83** (Figure 5.2).

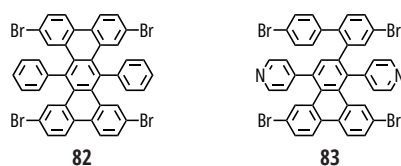


Figure 5.2 | Proposed GNMs precursors.

Chapter 6 EXPERIMENTAL SECTION

6.1 TECHNIQUES

NMR spectra were recorded with a Bruker Avance 400 (400 MHz) instrument or a Bruker Avance II 600 (600 MHz) instrument with solvent used as internal reference. MS MALDI-ToF spectra were recorded on a Bruker Autoflex speed or a Bruker UltrafleXtreme; the samples were analyzed in a trans-2-[3-(4-*tert*-butylphenyl)-2-methyl-2-propenylidene]malononitrile (DCTB) matrix unless otherwise specified. To prepare the samples, 10 μL of a solution (10^{-3} M) of the analyte were mixed with 90 μL of matrix solution (10 mg in 1 mL of tetrahydrofuran). Insoluble samples were deposited in a tetracyanoquinodimethane (TCNQ). To prepare the samples, 15 mg of TCNQ and 1 mg of the analyte were finely crushed together. The resulting powder was dispersed in cyclohexene (200 μL) before deposition on the MALDI-ToF plate. Thin layer chromatography (TLC) was performed on silica gel 60 F254 (Merck) precoated aluminum sheets. Column chromatography was performed on Merck silica gel 60 (0.063-0.200 mm) or on puriFlash[®] Si-HP 60 Å 15 or 30 μm columns with an Interchim puriFlash 430. Size exclusion chromatography (SEC) was performed on Bio-Beads S-X1 or Bio-Beads S-X3 with THF as eluent. HPLC experiments were done using a Thermo Scientific HPLC spectra system P400 with an SN400 Controller. The HPLC column was a Hypersyl GPLD Silica (100 x 4.6 mm) with 5 μm particle size. The microbalance of TA instrument TGA Q50 was used to weight GQDs masses to determine the concentration for dilution experiments.

Absorption spectra were recorded in Perkin Elmer Lambda 900 UV/Vis/NIR spectrometer with 1 cm Hellma Analytics high performance quartz glass cells. Photoluminescence spectrum Photoluminescence experiments were recorded in a Cary Eclipse fluorescence spectrophotometer or a Horiba FluoroMax+ spectrometer with 10x4 mm light path Hellma Analytics high performance quartz glass cuvettes. Time-resolved PL measurements use a solid-state pulsed diode (NanoLED), with excitation at 483 nm (pulse width below below 100 ps, 100 MHz repetition rate) in a Horiba FluoroMax+ spectrometer. Quantum yield measurement are carried on a FS5 spectrofluorometer from Edinburgh Instruments, using the SC-30 integrating sphere. Quartz cuvettes dedicated to the integrating sphere are provided by the manufacturer.

Single-object experiments use a home-built micro-PL setup under ambient conditions. The sample is excited using a 594nm CW diode laser (Cobolt Mambo 100) and focused on the sample using an oil-immersive microscope objective (0.95 NA MPLAPON100X M Plan Apochromat Objective from Evident *Scientific*), mounted on XYZ piezoelectric translational stages (Mad City Labs Inc.) for sample scanning. Luminescence signal is collected using the same objective and focused on a 50 μm pinhole for confocal selection. Spectral selection to remove the excitation beam is performed using a dichroic mirror (zt 594 RDC, Chroma) and a long-pass filter (FELH0600, Thorlabs). After confocal selection, the signal is either directed to silicon-based avalanche photodiodes (SPCM-AQR-13, PerkinElmer) for raster scan measurements, or to a monochromator (SP-2350, Princeton Instruments) coupled to a LN-cooled CCD camera (PyLoN:100BR eXcelon, Princeton Instruments) for spectral measurements.

For STM and AFM experiments the single-crystal surfaces were cleaned by several cycles of Ar⁺ bombardment followed by annealing. Room-temperature STM was performed with an Omicron VT-STM. Low-temperature STM/AFM images were

acquired at $T = 4.8$ K in ultrahigh vacuum ($\approx 10^{-10}$ mbar) using an Omicron microscope. nc-AFM measurements were acquired with a tip mounted to the qPlus sensor. A functionalized tip was created by picking up a single CO molecule from the surface.

Electrochemical experiments were carried out in a three electrodes single-compartment cell using platinum as working and counter electrodes and a silver wire in 10 mM AgNO_3 in acetonitrile as reference electrode under N_2 and at a scan rate of 100 mV/s. The ferrocium/ferrocene couple (Fc^+/Fc) was used as reference potential (+0.42 V vs SCE at 298K). The CV were recorded with a VSP bipotentiostat (Bio-Logic SAS).

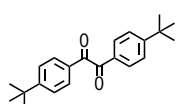
The GQDs studied at the DFT level of theory was done with a HSE functional and 6-31G(d,p) basis set, in gas phase, within the Gaussian16 software. For GQD aggregation, Molecular Dynamics Simulation were performed using LAMMPS software and the classical force-fieldGAFF. The atomic partial charges were assigned with the RESP method, using the Multiwfn package, based on DFT calculations at the B3LYP/6-31g(d,p) using the Gaussian software. All possible conformers were considered during this parameterization.

6.2 SOLVENTS AND REAGENTS

Chemicals were purchased from Aldrich, Fisher Scientific TCI Europe or Interchim and were used as received. dimethylpiperazine-2,3-dione was synthesized according to literature procedures.²⁷⁹ Solvents were purchased from SDS Carlo Erba, Aldrich or Fisher Scientific and were used as received. For optical experiment, spectrometric grade solvents were used. For synthesis, non-stabilized CH_2Cl_2 (CaH_2 , N_2), toluene (K/benzophenone, N_2), THF (K/benzophenone, N_2), Et_3N (CaH_2 , N_2), Et_2O (CaH_2 , N_2) were distilled prior to use.

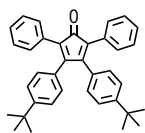
6.3 PROTOCOLS

1,2-bis(4-(*tert*-butyl)phenyl)ethane-1,2-dione **2**²⁰⁵



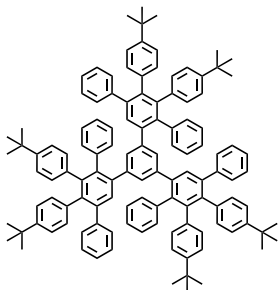
In a round bottom flask, 4-bromo-*tert*-butylbenzene (9 mL, 51.89 mmol) and tetrahydrofuran (90 mL) were added under argon. The mixture was cooled down to -50°C and *n*-butyllithium (2 M in hexanes, 25 mL, 50 mmol) was slowly added. The solution was stirred at -50°C for 1 h under argon. A solution of dimethylpiperazine-2,3-dione (0.3 M in tetrahydrofuran, 2.95 g, 20.75 mmol) was added and the mixture was stirred at ambient temperature for an additional 2 h under argon. Water was added to the mixture to quench the reaction. The organic phase was washed with aqueous hydrochloric acid (0.5 M, 100 mL) and brine. The organic phase was dried with Na_2SO_4 , filtered, and evaporated. The product was purified by column chromatography (SiO_2 , cyclohexane: CH_2Cl_2 4:1, $R_f=0.25$) as a yellowish powder (5.95g, 89% yield). **$^1\text{H NMR}$** (400 MHz, CDCl_3 , 298 K): δ (ppm) 7.91(d, $J=8.6$ Hz, 4H), 7.52(d, $J=8.6$ Hz, 4H), 1.34(s, 18H). **$^{13}\text{C NMR}$** (101 MHz, CDCl_3 , 298 K): δ (ppm) 194.59, 158.94, 130.69, 129.97, 126.08, 35.45, 31.07.

3,4-bis(4-(*tert*-butyl)phenyl)-2,5-diphenylcyclopenta-2,4-dienone **CP-1**^{280,281}



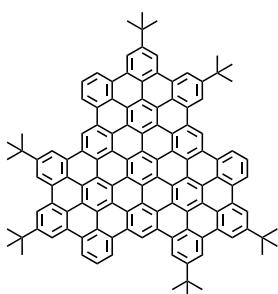
2 (3g, 9.30 mmol) and 1,3-diphenylacetone (1.96 g, 9.25 mmol) were dissolved in ethanol (30 mL). The mixture was heated to reflux and a solution of potassium hydroxide (4 M in ethanol, 541 mg, 9.60 mmol) was added. The mixture was stirred for 25 min. The mixture was then cooled down in an ice bath. The precipitate was filtered and washed with cold ethanol. **CP-1** was recovered as a dark purple powder (2.4 g, 50% yield). **$^1\text{H NMR}$** (400 MHz, CDCl_3 , 298 K): δ (ppm) 7.26-7.21(m, 10H), 7.15(d, $J=8.5$ Hz, 4H), 6.82 (d, $J=8.5$ Hz, 4H), 1.27(s, 18H).

Dendrimer 1



1,3,5-triethynylbenzene (23 mg, 0.15 mmol) and **CP-1** (345 mg, 0.70 mmol) were dissolved in o-xylene (3 mL). In a closed schlenk, the mixture was heated to 180°C for 18 h under argon. The solvent was evaporated, and the product was purified by flash chromatography (SiO₂, cyclohexane:CH₂Cl₂ 3:1, R_f=0.54) as a white powder (147 mg, 52% yield). **¹H NMR** (400 MHz, CDCl₃, 298 K): δ(ppm) 7.15 – 7.10 (m, 14H), 6.86 – 6.76 (m, 27H), 6.73 (s, 3H), 6.65 – 6.62 (m, 10H), 6.55 – 6.51 (m, 6H), 1.12 (s, 27H), 1.08 (s, 27H). **MALDI-ToF** m/z: calc. for C₁₂₀H₁₁₄: 1555.90; found: 1555.16.

(T)C₉₆tBu₆



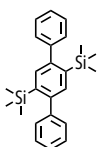
Dendrimer **1** (60 mg, 0.032 mmol) was dissolved in non-stabilized dichloromethane (50 mL). A solution of iron(III) chloride (1 M in nitromethane, 446 mg, 2.75 mmol) was added dropwise to the mixture. The reaction was left at room temperature under a strong flow of extra pure argon for 30 min. The mixture was then added to methanol (150 mL). Hydrazine (5 mL) was added to the mixture to quench the reaction. The precipitate was filtered through a PTFE filter. The powder was washed with aqueous hydrochloric acid (0.5 M) and dried under vacuum. The obtained black powder was dissolved in dichloromethane (5 mL), sonicated for 5 min, and left to precipitate. The precipitate was recovered by centrifugation (100 000 g for 30 min) to give the desired nanoparticle as a black orange solid (19 mg, 40% yield). **MALDI-ToF** m/z: calc. for C₁₂₀H₇₈: 1519.61; found: 1518.56.

1,4-diiodo-3,6-trimethylsilylbenzene **5**²⁸²



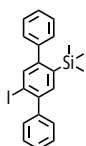
1,3-diiodobenzene (10 g, 30.31 mmol) and trimethylsilyl chloride (8.5 mL, 66.00 mmol) were dissolved in tetrahydrofuran (70 mL). The mixture was cooled down to -50°C and lithium diisopropylamide (33 mL, 66.00 mmol) was slowly added. The reaction was stirred at -20°C for 1 h under argon. A solution of aqueous sulfuric acid (1.5·10⁻² M, 100 mL) was added. The aqueous phase was extracted with diethyl ether. The organic phases were reunited and washed with brine, dried with Na₂SO₄, filtered, and evaporated. The product was recrystallized in a mixture of methanol and water and recovered as a white powder (9.3 g, 19.6 mmol, 67% yield). **¹H NMR** (400 MHz, CDCl₃, 298 K): δ(ppm) 7.76(s,2H), 0.41(s, 18H). **¹³C NMR** (101 MHz, CDCl₃, 298 K): δ(ppm) 149.37, 147.30, 104.54, -0.64. **MALDI-ToF** m/z: calc. for C₁₂H₂₀I₂Si₂: 473.93; found: 473.92.

2',5'-bis(trimethylsilyl)-1,1':4',1''-terphenyl **6**⁸⁰



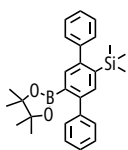
5 (4 g, 8.50 mmol), phenylboronic acid (3 g, 25.50 mmol), palladium(II) acetate (96 mg, 0.43 mmol), 2-dicyclohexylphosphino-2',6'-dimethoxybiphenyl (355 mg, 0.85 mmol) and potassium triphosphate (3.57 g, 18.86 mmol) were inserted in a three necked round-bottom flask. A mixture of toluene (120 mL) and water (12 mL), previously degassed by three freeze-pump-thaw, was added to the mixture. The reaction mixture was stirred at 80°C under argon overnight. The dark solution obtained was extracted with dichloromethane, washed twice with water, brine then dried with Na₂SO₄. The solid was purified by chromatography (SiO₂, cyclohexane:CH₂Cl₂ 90:10). The product was recovered as white powder (3 g, 95%). **¹H NMR** (400 MHz, CDCl₃, 298 K): δ(ppm) 7.47 (s, 2H), 7.44-7.35 (m, 10H), 0.01 (s, 18H). **¹³C NMR** (101 MHz, CDCl₃, 298 K): δ(ppm) 146.89, 144.59, 138.85, 135.58, 129.52, 127.75, 127.03, 0.50. **MALDI-ToF** MS m/z: calc for C₂₄H₃₀Si₂: 374.19; found: 374.20.

2'-iodo-5'-(trimethylsilyl)-1,1':4',1''-terphenyl **7**⁸⁰



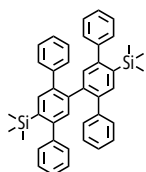
In a round bottom flask, **6** (2 g, 5.30 mmol) was dissolved in tetrahydrofuran (20 mL). A solution of silver tetrafluoroborate (0.5 M in methanol, 936 mg, 4.81 mmol) was transferred flask. The mixture was cooled to 0°C and iodine monochloride (0.5 M in dichloromethane, 9.7 mL, 4.81 mmol) was added dropwise. The mixture was stirred at ambient temperature for 1 h under argon. The mixture was quenched with an aqueous solution of sodium thiosulfate (1 M, 20 mL). The aqueous phase was extracted with dichloromethane. The organic phases were reunited, washed with brine, dried with Na₂SO₄, filtered, and evaporated. The product was recovered as a white solid in a mixture with **6** (950 mg by NMR, 42% yield). **¹H NMR** (400 MHz, CDCl₃, 298 K): δ(ppm) 7.85(s, 1H), 7.49(s, 1H), 7.47-7.37(m, 8H), 7.33-7.31(m, 2H), -0.01(s, 9H). **¹³C NMR** (101 MHz, CDCl₃, 298 K): δ(ppm) 149.51, 144.35, 144.08, 142.47, 140.14, 138.80, 135.86, 129.41, 129.28, 127.98, 127.85, 127.60, 127.53, 99.40, 0.38. **MALDI-ToF** m/z : calc. for C₂₁H₂₁ISi: 428.39; found 428.05.

1,3,2-dioxaborolane, 4,4,5,5-tetramethyl-2-(5-(trimethylsilyl)-1,1':4',1''-terphenyl) **8**⁸⁰



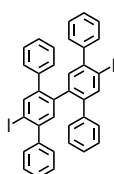
7 (1 g, 2.32 mmol) was dissolved in tetrahydrofuran (60 mL). The solution was cooled down to -45°C and *n*-butyllithium (2 M in hexanes, 1.56 mL, 7.65 mmol) was slowly added. The mixture was stirred for 1 h under argon. 2-Isopropoxy-4,4,5,5-tetramethyl-1,3,2-dioxaborolane (1.4 mmol, 2.95 mmol) was slowly added to the mixture. The mixture was heated up to ambient temperature and stirred for an additional 2 h. Water (50 mL) was added to quench the mixture. The aqueous phase was extracted with dichloromethane. The organic phases were reunited, washed with brine, dried with Na₂SO₄, filtered, and evaporated. The product was purified by flash chromatography (SiO₂, cyclohexane:CH₂Cl₂ 3:1) as a white powder (450 mg, 45 % yield). **¹H NMR** (400 MHz, CDCl₃, 298 K): δ(ppm) 7.61(s, 1H), 7.56(s, 1H), 7.44(m, 2H), 7.42-7.32(m, 8H), 1.18(s, 12H), 0.01(s, 9H). **¹³C NMR** (101 MHz, CDCl₃, 298 K): δ(ppm) 147.03, 145.02, 144.25, 143.29, 140.72, 135.16, 129.58, 129.22, 127.80, 127.61, 126.99, 126.78, 83.75, 24.58, 0.46.

3,3'-di(trimethylsilyl)-2,5,2',5'-tetraphenyl biphenyl **9**⁸⁰



7 (403 mg, 0.94 mmol), **8** (287 mg, 0.67 mmol), palladium(II) acetate (75 mg, 0.33 mmol), 2-dicyclohexylphosphino-2',6'-dimethoxybiphenyl (275 mg, 0.66 mmol) and potassium triphosphate (284 mg, 1.34 mmol) were dissolved in toluene (18 mL) and water (3 mL). The solution was degassed and heated up to 80°C for 18 h under argon. The mixture was filtered through a pad of celite. The organic phase was washed with water, dried with Na₂SO₄, filtered, and evaporated. The product was purified with flash chromatography (SiO₂, cyclohexane:CH₂Cl₂ 95:5, R_f=0.35) as a white powder (291 mg, 71 % yield). **¹H NMR** (400 MHz, CDCl₃, 298 K): δ(ppm) 7.41(s, 2H), 7.34-7.33(m, 4H), 7.23-7.21(m, 6H), 7.16-7.10(m, 8H), 6.80(dd, J=8.2, 1.3 Hz, 4H), 0.01(s, 18H). **¹³C NMR** (101 MHz, CDCl₃, 298 K): δ(ppm) 147.93, 143.98, 141.19, 139.39, 138.65, 137.38, 136.50, 132.84, 129.40, 129.33, 127.61, 127.60, 126.97, 125.89, 0.61.

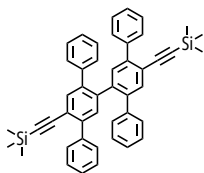
Synthesis of 3,3'-diiodo-2,5,2',5'-tetraphenyl biphenyl **10**⁸⁰



9 (286 mg, 0.47 mmol) was dissolved in non-stabilized dichloromethane (10 mL). The solution was cooled to 0°C and iodine monochloride (0.5 M in dichloromethane, 3.8 mL, 1.88 mmol) was added dropwise. The mixture was stirred for 18 h at ambient temperature under argon. The mixture was quenched with an aqueous solution of sodium thiosulfate (1 M, 30 mL). The aqueous phase was extracted with dichloromethane. The organic phases were washed with brine, dried with Na₂SO₄, filtered, and evaporated. The product was recovered as a white solid without further purification (281 mg, 93% yield). **¹H NMR** (400 MHz, CDCl₃, 298 K): δ(ppm) 7.81(s, 2H), 7.40-7.38(m, 6H), 7.27-7.25(m, 2H), 7.22(s, 2H), 7.24-7.19(m, 4H), 7.15(t, J=7.4 Hz, 4H), 6.81-6.76(m, 4H). **¹³C NMR** (101 MHz, CDCl₃, 298 K): δ(ppm) 145.81, 143.87,

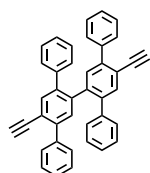
142.14, 141.45, 139.56, 139.21, 133.67, 129.89, 129.73, 128.53, 128.47, 128.27, 127.40, 97.78. **MALDI-ToF** m/z: calc. for C₃₆H₂₄I₂: 710.00; found: 710.01.

3,3'-di(ethynyltrimethylsilane)-2,5,2',5'-tetraphenylnyphenyl **11**⁸⁰



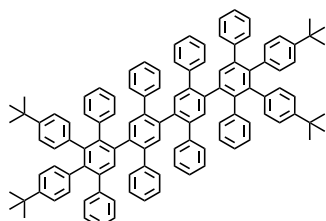
11 (319 mg, 0.45 mmol), copper iodide (42 mg, 0.28 mmol) and bis(triphenylphosphine)palladium(II) dichloride (99.7 mg, 0.14 mmol) were dissolved in toluene (15 mL) and triethylamine (23 mL). The solution was degassed and ethynyltrimethylsilane (150 μ L, 1.60 mmol) was slowly introduced to the mixture. The solution was heated up to 80°C for 18 h under argon. The mixture was filtered through a pad of silica and solvents were evaporated. The product was purified by column chromatography (SiO₂, cyclohexane:CH₂Cl₂ 9:1) as a white solid (60 mg, 8% yield). **¹H NMR** (400 MHz, CDCl₃, 298 K): δ (ppm) 7.53(dd, J=8.0, 1.5 Hz, 4H), 7.46(s, 2H), 7.40-7.33(m, 8H), 7.19-7.07(m, 6H), 6.80-6.76(m, 4H), 0.14(s, 18H). **¹³C NMR** (101 MHz, CDCl₃, 298 K): δ (ppm) 142.60, 139.77, 139.69, 139.52, 139.46, 135.16, 132.76, 129.33, 129.16, 127.86, 127.74, 127.50, 126.47, 120.52, 104.55, 97.94, -0.33. **MALDI-ToF** m/z: calc. for C₂₈H₃₀Si₂: 650.28; found 650.30.

3,3'-diethynyl-2,5,2',5'-tetraphenylnyphenyl **12**⁸⁰



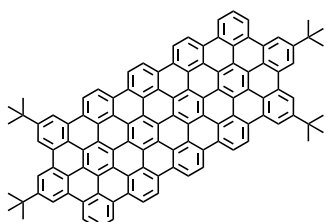
11 (55 mg, 0.085 mmol) was dissolved in tetrahydrofuran (4 mL). Tetrabutylammonium fluoride (200 μ L, 0.20 mmol) was slowly added to the solution. The mixture was stirred at ambient temperature for 3 h. H₂O (20 mL) was added to the mixture. The aqueous phase was extracted with dichloromethane. The organic phases were reunited, washed with brine, dried with Na₂SO₄, filtered, and evaporated. The product was obtained as a pale-yellow powder without further purification. (43 mg, 98% yield). **¹H NMR** (400 MHz, CDCl₃, 298 K): δ (ppm) 7.52-7.50(m, 6H), 7.43-7.37(m, 10H), 7.24-7.12(m, 4H), 6.81-6.76(m, 4H), 3.07(s, 2H).

Dendrimer **4**



12 (43 mg, 0.084 mmol) and **CP-1** (142 mg, 0.255 mmol) were dissolved in o-xylene (4 mL). In a closed schlenk, the mixture was heated to 180°C for 18 h under argon. The solvent was evaporated, and the product was purified by flash chromatography (SiO₂, cyclohexane:CH₂Cl₂ 3:1, R_f=0.59) as a white powder (70 mg, 0.049 mmol, 57% yield). **¹H NMR** (400 MHz, CDCl₃, 298 K): δ (ppm) 7.55 (s, 2H), 7.36 (s, 2H), 7.33 (s, 2H), 7.22 – 6.38 (m, 56H), 1.13 (s, 18H), 1.08 (s, 18H). **¹³C NMR** (101 MHz, CDCl₃, 298 K): δ (ppm) 148.15, 147.78, 141.95, 140.34, 139.73, 139.48, 137.52, 137.24, 134.06, 132.56, 131.23, 130.14, 129.66, 129.20, 127.65, 127.53, 126.13, 125.93, 125.14, 123.55, 123.18, 34.27, 34.17, 31.36, 31.32, 29.85, 27.07, 19.89. **MALDI-ToF** m/z: calc. for C₁₁₂H₉₈: 1442.77; found: 1442.66.

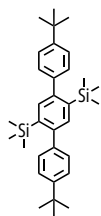
C₉₆tBu₄



Dendrimer **4** (22 mg, 0.015 mmol) was dissolved in non-stabilized dichloromethane (50 mL). A solution of iron(III) chloride (1 M in nitromethane, 236 mg, 1.45 mmol) was added dropwise to the mixture. The reaction was left at room temperature under a strong flow of extra pure argon for 1 h. The mixture was then added to methanol (150 mL). The precipitate was filtered through a PTFE filter. **MALDI-ToF** m/z: calc. for C₁₁₂H₆₂: 1406.49; found: 1413. The main peak

found would correspond to three C-C bonds missing.

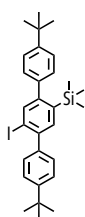
(4,4''-di-*tert*-butyl-[1,1':4',1''-terphenyl]-2',5'-diyl)bis(trimethylsilane) **14**



In a round-bottom-flask, **5** (4 g, 8.50 mmol), 4-*tert*-butylphenylboronic acid (4.54 g, 25.50 mmol), palladium(II) acetate (96 mg, 0.43 mmol), 2-dicyclohexylphosphino-2',6'-dimethoxybiphenyl (355 mg, 0.85 mmol) and potassium triphosphate (3.6 g, 16.86 mmol) were introduced. Toluene (120 mL) and water (12 mL), previously degassed by freeze-pump-thaw, were then added to the reaction mixture. The reaction was stirred at 90°C under argon for 12h.

The mixture was then filtered through celite and washed with dichloromethane. The organic phase was washed with water and brine, dried with Na₂SO₄, filtered, and evaporated. The product was purified by column chromatography (SiO₂, cyclohexane) and recovered as a white powder (3.70 g, 89% Yield). **¹H NMR** (400 MHz, CDCl₃, 298 K): δ(ppm) 7.48 (s, 2H), 7.42 (d, *J* = 8.3 Hz, 4H), 7.29 (d, *J* = 8.3 Hz, 4H), 1.38 (s, 18H), -0.01 (s, 18H). **¹³C NMR** (101 MHz, CDCl₃, 298K): δ(ppm) 150.19, 148.88, 141.80, 139.11, 135.78, 129.29, 124.71, 34.71, 31.62, 0.66. **MALDI-ToF MS**: calc. for C₃₂H₄₆Si₂: 486.31; found: 486.31.

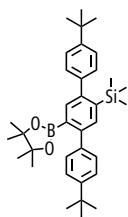
(4,4''-di-*tert*-butyl-5'-iodo-[1,1':4',1''-terphenyl]-2'-yl)trimethylsilane **15**



14 (1.70 g, 3.50 mmol) was dissolved in dry tetrahydrofuran (21 mL). Silver tetrafluoroborate (650 mg, 3.30 mmol) was dissolved in anhydrous methanol (7 mL) and then added to the mixture. The reaction mixture was cooled down in an ice bath and iodine monochloride (1 M in dichloromethane, 3.30 mL, 3.30 mmol) was added dropwise. The mixture was allowed to heat to room temperature and stirred for 1 h 45 min. A saturated aqueous solution of sodium thiosulfate was added to quench the iodine monochloride. The aqueous phase was extracted with dichloromethane.

The organic phase was then washed with brine, dried with Na₂SO₄, filtered, and evaporated. The product was purified by flash chromatography (SiO₂, cyclohexane) and recovered as a white powder (1.17 g, 62 % yield). **¹H NMR** (400 MHz, CDCl₃, 298 K): δ(ppm) 7.85 (s, 1H), 7.48 (s, 1H), 7.46 (d, *J* = 8.4 Hz, 2H), 7.41 (d, *J* = 8.3 Hz, 2H), 7.35 (d, *J* = 8.4 Hz, 2H), 7.24 (d, *J* = 8.4 Hz, 2H), 1.39 (s, 9H), 1.39 (s, 9H), -0.02 (s, 9H). **¹³C NMR** (101 MHz, CDCl₃, 298K): δ(ppm) 150.78, 150.55, 149.51, 144.20, 141.21, 140.44, 139.73, 138.99, 136.21, 129.19, 129.07, 128.97, 125.14, 125.00, 124.81, 99.65, 34.79, 34.75, 31.58, 31.52, 0.56. **MALDI-ToF MS**: calc. for C₃₂H₄₆ISi: 540.17; found: 540.17.

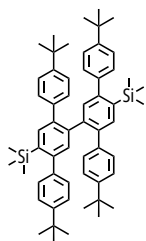
(4,4''-di-*tert*-butyl-5'-(4,4,5,5-tetramethyl-1,3,2-dioxaborolan-2-yl)-[1,1':4',1''-terphenyl]-2'-yl)tri-methylsilane **16**



15 (1.08 g, 2.00 mmol), bis(pinacolato)diboron (1.02 g, 4.00 mmol), [1,1'-bis(diphenylphosphino)ferrocene]dichloropalladium(II) (146 mg, 0.20 mmol), and potassium acetate (588 mg, 6.00 mmol) were dissolved in 1,4-dioxane (30 mL) previously degassed by freeze-pump-thaw. The mixture was heated to 95°C under argon for 48 h. The organic phase was then washed with water and brine, dried with Na₂SO₄, filtered, and evaporated. The product was purified by chromatography (SiO₂, cyclohexane:CH₂Cl₂ 3:2) and

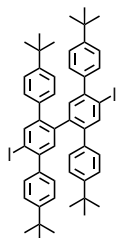
recovered as a white powder (631 mg, 58% yield). **¹H NMR** (400 MHz, CD₂Cl₂, 298 K): δ(ppm) 7.59 (s, 1H), 7.48 (s, 1H), 7.44 – 7.38 (m, 4H), 7.34 (d, *J* = 8.4 Hz, 2H), 7.23 (d, *J* = 8.4 Hz, 2H), 1.35 (s, 18H), 1.18 (s, 12H), -0.01 (s, 9H). **¹³C NMR** (101 MHz, CD₂Cl₂, 298K): δ(ppm) 150.67, 150.40, 147.36, 144.90, 141.69, 141.26, 140.63, 135.71, 135.41, 129.51, 129.14, 125.28, 124.93, 84.16, 34.84, 34.80, 31.59, 31.56, 24.80, 0.57. **MALDI-ToF MS**: calc. for C₃₅H₄₉BO₂Si: 540.36; found: 540.29.

Ditrimethylsilyl diterphenyl derivative **17**



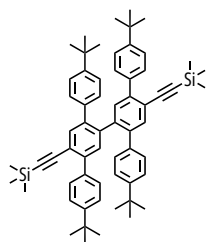
15 (190 mg, 0.36 mmol), **16** (275 mg, 0.51 mmol), palladium(II) acetate (41 mg, 0.18 mmol), 2-dicyclohexylphosphino-2',6'-dimethoxybiphenyl (148 mg, 0.36 mmol), and potassium triphosphate (152 g, 0.72 mmol) were introduced in a round bottom flask. Previously degassed toluene (19 mL) and water (3 mL) were introduced to the reaction mixture. The reaction was stirred at 80°C under argon for 36 h. Dichloromethane was added to the mixture, the organic phase was washed with water then dried with Na₂SO₄, filtered, and evaporated. The product was purified by column chromatography (SiO₂, cyclohexane:CH₂Cl₂ 97:3) and recovered as a white powder (247 mg, 83 % Yield). **¹H NMR** (400 MHz, CDCl₃, 298 K): δ(ppm) 7.42 (s, 2H), 7.32 (d, J=8.2 Hz, 4H), 7.18 (s, 2H), 7.14 - 7.07 (m, 8H), 6.70 (d, J=8.3 Hz, 4H), 1.37 - 1.32 (m, 36H), 0.00 - -0.02 (m, 18H). **¹³C NMR** (101 MHz, CDCl₃, 298K): δ(ppm) 150.02, 148.54, 147.89, 141.28, 139.59, 138.50, 138.35, 137.40, 136.52, 133.23, 129.14, 128.91, 127.44, 126.80, 125.90, 124.68, 124.49, 34.64, 34.52, 31.59, 0.81. **MALDI-ToF MS**: calc. for C₅₈H₇₄Si₂: 826.53; found: 826.53.

Diiodo diterphenyl derivative **18**



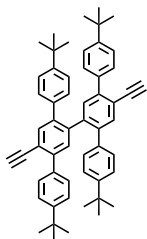
17 (195 mg, 0.24 mmol) was dissolved in non-stabilised dichloromethane (5 mL). The reaction mixture was cooled down in an ice bath and iodine monochloride (1M in dichloromethane, 1 mL, 1.00 mmol) was added dropwise. The mixture was allowed to heat to room temperature and stirred for 15 h under argon. An aqueous solution of saturated sodium thiosulfate was added. The aqueous phase was extracted with dichloromethane. The organic phase was then washed with water and brine, dried with Na₂SO₄, filtered, and evaporated. The product was purified by flash chromatography (SiO₂, cyclohexane:CH₂Cl₂ 97:3) and recovered as a white powder (198 mg, 88 % yield). **¹H NMR** (400 MHz, CDCl₃, 298 K): δ(ppm) 7.81 (s, 2H), 7.38 (d, J= 8.4 Hz, 4H), 7.21 - 7.10 (m, 10H), 6.69 (d, J= 8.3 Hz, 4H), 1.36 (s, 36H). **¹³C NMR** (101 MHz, CDCl₃, 298K): δ(ppm) 150.64, 149.62, 145.04, 141.19, 141.07, 140.39, 138.66, 136.33, 133.63, 129.09, 128.68, 125.09, 124.87, 97.53, 34.75, 34.64, 31.54, 31.52. **MALDI-ToF MS**: calc. for C₅₂H₅₆I₂: 934.25; found: 934.25.

Di-(trimethylsilyl)-ethynyl diterphenyl derivative **19**



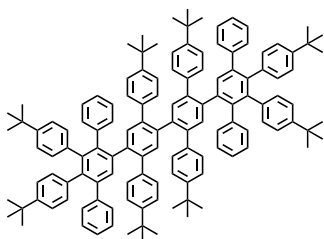
In a round bottom flask, **18** (82mg, 0.09 mmol), bis(triphenylphosphine)palladium(II) dichloride (45 mg, 0.06 mmol) and copper(I) iodide (18 mg, 0.12 mmol) were dissolved in triethylamine (6 mL) and toluene (4 mL) previously degassed by freeze-pump thaw. Ethynyltrimethylsilane (46 μL, 0.32 mmol) was added to the mixture, then stirred under argon at 80°C overnight. Dichloromethane was added to the mixture and filtered through a pad of silica. The filtrate was washed with water and brine, dried with Na₂SO₄, filtered, and evaporated. The product was purified by column chromatography (SiO₂, cyclohexane:CHCl₃ 9:1) to give the desired product as a yellow powder (68 mg, 87% yield). **¹H NMR** (400 MHz, CDCl₃, 298 K): δ(ppm) 7.46 (s, 2H), 7.43 (d, J= 8.4 Hz, 4H), 7.37 (d, J= 8.5 Hz, 4H), 7.33 (s, 2H), 7.10 (d, J= 8.3 Hz, 4H), 6.71 (d, J= 8.3 Hz, 4H), 1.35 (s, 18H), 1.34 (s, 18H), 0.13 (s, 18H). **¹³C NMR** (101 MHz, CDCl₃, 298K): δ(ppm) 150.45, 149.28, 142.57, 139.67, 139.48, 137.09, 136.79, 135.17, 133.10, 132.11, 129.11, 128.75, 128.62, 128.34, 124.95, 124.73, 120.45, 105.19, 97.79, 34.69, 34.58, 31.53, 31.50, -0.15. **MALDI-ToF MS**: calc. for C₆₂H₇₄Si₂: 874.53; found: 874.53.

Diethynyl diterphenyl derivative **12**



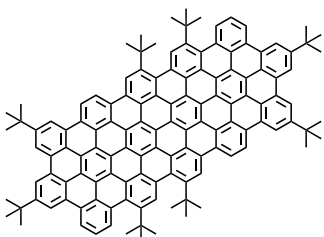
19 (63 mg, 0.07 mmol) was dissolved in dry tetrahydrofuran (5 mL). Tetrabutylammonium fluoride (1M in tetrahydrofuran, 230 μ L, 0.23 mmol) was added dropwise and the brown solution was stirred for 4 h under argon. Dichloromethane and water were then added to the mixture. The organic phase was washed with water and brine, dried with Na₂SO₄, filtered and the solvent evaporated. A yellowish powder was recovered and used in further reactions without further purification.

Dendrimer **13**



12 (20 mg, 0.08 mmol), **CP-1** (114 mg, 0.23 mmol) were dissolved in dry o-xylene (3 mL) in a schlenk. The solution was degassed sparging argon and then heated to 175°C for 16h. The solvent was evaporated and the product purified by flash column chromatography (SiO₂, cyclohexane:CHCl₃ 87:13→4:1) as a yellow powder (55 mg, 43% yield). **¹H NMR** (400 MHz, CDCl₃, 298 K): δ (ppm) 7.57 (s, 2H), 7.40 (s, 2H) 7.34 (s, 2H), 7.18 – 6.41 (m, 52H), 1.36 (s, 18H), 1.29 (s, 18H), 1.13 (s, 18H), 1.09 (s, 18H). **¹³C NMR** (101 MHz, CDCl₃, 298K): δ (ppm) 149.25, 148.43, 148.11, 147.82, 142.07, 141.96, 140.39, 139.97, 139.66, 139.43, 138.95, 138.52, 137.61, 137.31, 133.71, 133.27, 132.79, 131.53, 130.12, 129.30, 128.55, 127.49, 126.08, 125.02, 124.51, 124.37, 123.56, 123.16, 34.51, 34.45, 34.27, 34.18, 31.61, 31.51, 31.36, 31.33. **MALDI-ToF MS**: calc. for C₁₂₈H₁₃₀: 1667.02; found: 1667.03.

C₉₆tBu₈



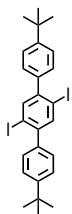
13 (11.5 mg, 6.90 μ mol) was dissolved in non-stabilized dichloromethane (50 mL). A solution of iron(III) chloride (1 M in nitromethane, 185 mg, 1.14 mmol) was added dropwise to the mixture. The reaction was left at room temperature under a strong flow of extra pure argon for 2 h. The mixture was then added to an excess of methanol (150 mL) to precipitate the nanoparticle. The precipitate was filtered through a PTFE filter to recover a greenish powder. The powder was solubilized in a small amount of tetrahydrofuran, sonicated for 1 min followed by ultracentrifugation (130 000 g, 30 min). The precipitate was purified by steric exclusion chromatography (tetrahydrofuran) and obtained as a dark green powder (1 mg, 8% yield).

Alternatively, **C₉₆tBu₈** can also be obtained using 2,3-dichloro-5,6-dicyano-1,4-benzoquinone as oxidant. **13** (30 mg, 0.018 mmol) and 2,3-dichloro-5,6-dicyano-1,4-benzoquinone (132 mg, 0.58 mmol) were dissolved in freshly distilled unstabilized dichloromethane (15 mL). The solution was allowed to cool down to 0°C in an ice bath. Trifluoromethanesulfonic acid (0.9 mL) was slowly added to the mixture. The solution is stirred for 40 min under argon at 0°C. Distilled triethylamine (5 mL) was added to quench the reaction and the mixture was then added to an excess of methanol (100 mL). The precipitate was filtered through a PTFE filter. The obtained powder was dispersed in a small amount of tetrahydrofuran, sonicated for 1 min followed by ultracentrifugation (130 000g, 30 min). The precipitate yielded the product as a dark green powder (11 mg, 26%).

¹H NMR (600 MHz, CS₂+THF-d₈, 298 K): δ (ppm) 11.02 (s, 2H), 10.72 (d, *J* = 8.3 Hz, 2H), 10.50 (d, *J* = 8.3 Hz, 2H), 10.23 (s, 2H), 10.05 (s, 2H), 9.71 (s, 2H), 9.62 (s, 4H), 9.56 (d, *J* = 7.5 Hz, 2H), 9.49 (d, *J* = 7.2 Hz, 2H), 8.47 (t, *J* = 7.3 Hz, 2H), 2.42 (s, 18H), 2.08 (s, 18H), 2.03 (s, 18H), 1.99 (s, 18H). **¹³C NMR** (151 MHz, CS₂+THF-d₈, 298 K, only carbons visible by ¹H-¹³C HSQC and HMBC are reported): δ (ppm) 150.23, 150.03, 146.91, 139.87, 135.97, 133.23, 133.04, 131.86, 131.67, 131.28, 131.08, 130.11, 129.91,

129.52, 129.52, 129.13, 129.13, 126.59, 126.59, 126.00, 125.42, 124.83, 124.64, 124.44, 124.64, 123.07, 122.88, 122.88, 122.68, 120.54, 120.34, 120.15, 120.14, 119.95, 119.75, 40.25, 39.47, 36.54, 36.15, 36.15, 35.18, 32.44, 32.44. **MALDI-ToF HRMS:** calc. for $C_{128}H_{94}$: 1630.7350; found: 1630.7397.

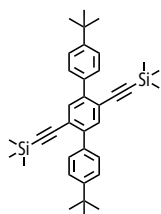
4,4''-di-*tert*-butyl-2',5'-diiodo-1,1':4',1''-terphenyl **26**



26 (650 mg, 1.33 mmol) was introduced into a round bottom flask along with freshly distilled non-stabilized dichloromethane (25 mL). The mixture was cooled down in an ice bath to 0°C then iodine monochloride (1M in dichloromethane, 5.3 mL, 5.30 mmol) added dropwise. The mixture was allowed to come back to room temperature and stirred for 36 h under argon. A saturated aqueous solution of sodium thiosulfate was added to quench the mixture.

The product was extracted with dichloromethane then washed with water and brine. The organic phase was dried with Na_2SO_4 , filtered, and evaporated to give the product as an off-white powder (786 mg, 99% yield). **1H NMR** (400 MHz, $CDCl_3$, 298 K): δ (ppm) 7.87 (s, 2H), 7.46 (d, $J = 8.4$ Hz, 4H), 7.32 (d, $J = 8.4$ Hz, 4H), 1.38 (s, 18H). **^{13}C NMR** (101 MHz, $CDCl_3$, 298K): δ (ppm) 151.17, 146.91, 140.53, 139.47, 128.97, 125.14, 98.30, 34.84, 31.52. **MALDI-ToF MS:** calc. for $C_{26}H_{28}I_2$: 594.03; found: 594.04.

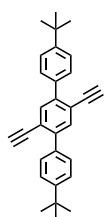
((4,4''-di-*tert*-butyl-[1,1':4',1''-terphenyl]-2',5'-diyl)bis(ethyne-2,1-diyl))bis(trimethylsilane) **27**



27 (1.18 g, 2.00 mmol), bis(triphenylphosphine)palladium(II) dichloride (175 mg, 0.25 mmol) and copper(I) iodide (150 mg, 1.00 mmol) were dissolved in triethylamine (12 mL) and toluene (8 mL) previously degassed by freeze-pump thaw. Ethynyltrimethylsilane (970 μ L, 7.00 mmol) was added to the mixture which was stirred at 80°C for 24 h under argon. The mixture was filtered through a celite pad with dichloromethane. The filtrate was washed with water and brine, dried with Na_2SO_4 , filtered, and evaporated and purified by column

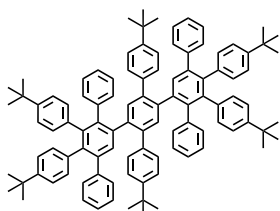
chromatography (SiO_2 , cyclohexane: CH_2Cl_2 9:1) to give the desired product as a white powder (720 mg, 68% yield). **1H NMR** (400 MHz, $CDCl_3$, 298 K): δ (ppm) 7.61 – 7.55 (m, $J = 9.4$ Hz, 6H), 7.43 (d, $J = 8.5$ Hz, 4H), 1.37 (s, 18H), 0.13 (s, 18H). **^{13}C NMR** (101 MHz, $CDCl_3$, 298K): δ (ppm) 150.71, 142.53, 136.34, 134.08, 129.05, 124.86, 121.80, 104.75, 99.38, 34.74, 31.51, 0.22. **MALDI-TOF MS:** calc. for $C_{36}H_{46}Si_2$: 534.31; found: 534.31.

4,4''-di-*tert*-butyl-2',5'-diethynyl-1,1':4',1''-terphenyl **20**



27 (65 mg, 0.12 mmol) was introduced along with freshly distilled tetrahydrofuran (10 mL) in a round bottom flask. Tetrabutylammonium fluoride (1M in tetrahydrofuran, 310 μ L, 0.31 mmol) was added dropwise and the mixture left stirring at room temperature under argon for 2 h. The product was extracted with dichloromethane then washed with water and brine. The organic phase was dried with Na_2SO_4 , filtered, and evaporated to give a yellowish powder which was used without further purification for the next step.

Dendrimer **21**

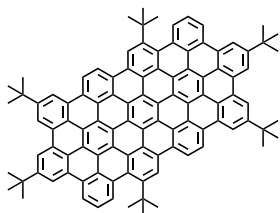


20 (46 mg, 0.12 mmol), and **CP-1** (205 mg, 0.41 mmol) were introduced in a schlenk, followed by the addition of dry *o*-xylene (4 mL). The solution was degassed sparging argon and then heated to 180°C for 16 h. After the mixture cooled down it was added to an excess methanol to precipitate the product as a white powder which was then filtered through a PTFE filter. This process was repeated twice. The product was recovered as a white powder (153 mg, 99% yield). **1H NMR** (400

MHz, $CDCl_3$, 298 K): δ (ppm) 7.53 (s, 1H), 7.33 (s, 1H), 7.21 – 6.28 (m, 45H), 5.69 (s, 1H), 1.29 (s, 18H), 1.13 (s, 18H), 1.08 (s, 18H). **^{13}C NMR** (101 MHz, $CDCl_3$, 298K): δ (ppm) 149.12, 148.07, 147.74, 142.04, 140.21, 139.86, 139.59, 139.36, 138.97, 137.81,

137.65, 137.35, 133.49, 132.86, 131.47, 130.15, 129.36, 127.47, 126.04, 124.87, 124.46, 123.53, 123.08, 77.48, 77.36, 77.16, 76.84, 34.51, 34.26, 34.17, 31.52, 31.36, 31.33. **MALDI-ToF MS:** calc. for $C_{102}H_{102}$: 1326.80; found: 1326.79.

$C_{78}tBu_6$.

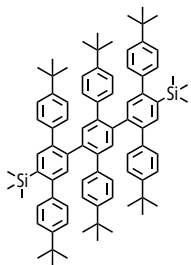


Dendrimer **21** (20 mg, 0.015 mmol) was dissolved in non-stabilized dichloromethane (50 mL). A solution of iron(III) chloride (1 M in nitromethane, 282 mg, 1.74 mmol) was added dropwise to the mixture. The reaction was left at room temperature under a strong flow of extra pure argon for 2 h 30 min. The mixture was then added in one time to methanol (150 mL) and hydrazine (5 mL) to quench the reaction. The precipitate was filtered through a PTFE filter. The powder was washed with aqueous hydrochloric acid (0.5 M) and dried under vacuum. The powder was solubilized in a small amount of tetrahydrofuran, sonicated for 1 min followed by ultracentrifugation. The precipitate was purified in steric exclusion chromatography (tetrahydrofuran) and obtained as a dark orange powder (5 mg, 25% yield).

Alternatively, **$C_{78}tBu_6$** can also be obtained using 2,3-dichloro-5,6-dicyano-1,4-benzoquinone as oxidant. Dendrimer **21** (10 mg, 0.023 mmol) and 2,3-dichloro-5,6-dicyano-1,4-benzoquinone (109 mg, 0.48 mmol) were dissolved in freshly distilled non-stabilized dichloromethane (40 mL). The solution was allowed to cool down to 0°C in an ice bath. Trifluoromethanesulfonic acid (0.4 mL) was slowly added to the mixture. The solution was stirred for 45 min under argon at 0°C. Distilled triethylamine (2 mL) was added to quench the reaction and the mixture then added in one time to methanol (150 mL). The precipitate was filtered through a PTFE filter. The obtained powder was dispersed in a small amount of tetrahydrofuran, sonicated for 1 min followed by ultracentrifugation (130 000 g, 30 min). The precipitate yielded the product as a dark orange powder (8 mg, 27%).

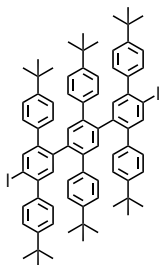
1H NMR (600 MHz, $CS_2+THF-d_8$, 298 K): δ (ppm) 10.00 (d, $J = 7.2$ Hz, 2H), 9.92 (s, 2H), 9.65 (d, $J = 7.0$ Hz, 2H), 9.54 (s, 2H), 9.18 (s, 2H), 8.96 (t, $J = 6.9$ Hz, 2H), 8.92 (s, 2H), 8.41 (s, 2H), 7.96 (d, $J = 8.4$ Hz, 2H), 7.86 (d, $J = 8.1$ Hz, 2H), 2.22 (s, 18H), 1.83 (s, 18H), 1.79 (s, 18H). **^{13}C NMR** (151 MHz, $CS_2+THF-d_8$, 298 K, only carbons visible by $^1H-^{13}C$ HSQC and HMBC are reported): δ (ppm) 149.64, 147.88, 143.98, 133.82, 131.47, 131.08, 130.50, 127.37, 127.18, 126.79, 126.59, 125.42, 125.03, 123.07, 123.07, 122.49, 122.29, 120.93, 119.95, 119.36, 119.17, 118.58, 39.47, 36.54, 35.96, 35.76, 32.64, 32.64. **MALDI-ToF HRMS:** calc. for $C_{102}H_{74}$: 1298.5785; found: 1298.5795.

Ditrimethylsilyl triterphenyl derivative 28



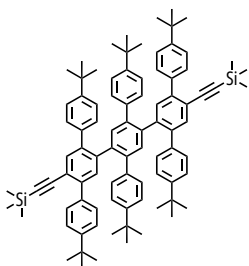
16 (640 mg, 1.18 mmol), **26** (292 mg, 0.49 mmol), tetrakis(triphenylphosphine)palladium(0) (25 mg, 0.02 mmol), and potassium carbonate (691 mg, 5.00 mmol) were introduced along with toluene (20 mL), ethanol (4 mL) and water (4 mL), previously degassed by freeze-pump-thaw. The mixture was stirred under argon at 80°C for 16 h. The mixture was filtered through a celite pad with dichloromethane, then washed with water and brine. The organic phase was dried with Na_2SO_4 , filtered, and evaporated. The product was purified by flash column chromatography (SiO_2 , cyclohexanes: CH_2Cl_2 93:7) and recovered as a white powder (372 mg, 65% yield). **1H NMR** (400 MHz, $CDCl_3$, 298 K): δ (ppm) 7.43 (s, 2H), 7.39 – 7.28 (m, 12H), 7.10 (d, $J = 8.2$ Hz, 4H), 6.96 (d, $J = 8.3$ Hz, 4H), 6.56 (d, $J = 8.3$ Hz, 4H), 6.49 (d, $J = 8.3$ Hz, 4H), 1.36 – 1.32 (m, 54H), 0.03 (s, 18H). **^{13}C NMR** (101 MHz, $CDCl_3$, 298K): δ (ppm) 150.18, 148.60, 148.50, 141.17, 140.15, 139.76, 139.02, 138.17, 137.63, 137.48, 136.20, 133.37, 132.73, 129.14, 128.78, 128.51, 124.64, 124.51, 124.23, 34.65, 34.46, 34.43, 31.58, 31.55, 29.86, 0.89, 0.81. **MALDI-ToF MS:** calc. for $C_{84}H_{102}Si_2$: 1166.75; found: 1166.72.

Diiodo triterphenyl derivative 29



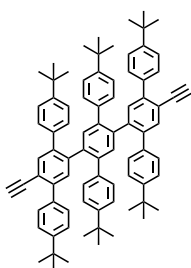
29 (360 mg, 0.31 mmol) was dissolved in freshly distilled non-stabilized dichloromethane (15 mL). The mixture was cooled to 0°C in an ice bath and iodine monochloride (0.5 M in dichloromethane, 2.48 mL, 1.24 mmol) was added dropwise. The mixture was then stirred overnight at room temperature under argon, then quenched with a saturated aqueous solution of sodium thiosulfate, extracted with dichloromethane, washed with water and brine, dried with Na₂SO₄, filtered, and evaporated. The crude product was purified by flash chromatography (SiO₂, petroleum ether 60/80:CHCl₃ 7:1) and recovered as a white powder (320 mg, 85% yield). **¹H NMR** (400 MHz, CDCl₃, 298 K): δ(ppm) 7.75 (s, 2H), 7.46 (s, 2H), 7.42 – 7.38 (m, 7H), 7.31 (s, 2H), 7.12 – 7.06 (m, 6H), 7.03 – 6.97 (m, 4H), 6.53 – 6.44 (m, 7H), 1.34 (s, 54H). **¹³C NMR** (101 MHz, CDCl₃, 298K): δ(ppm) 150.71, 140.99, 139.85, 137.08, 135.64, 133.24, 129.16, 128.51, 128.39, 124.95, 124.82, 124.38, 97.29, 34.75, 34.54, 31.54, 31.50, 27.07. **MALDI-ToF MS**: calc. for C₇₈H₈₄I₂: 1274.47; found: 1274.47.

Di-(trimethylsilyl)-ethynyl triterphenyl derivative 30



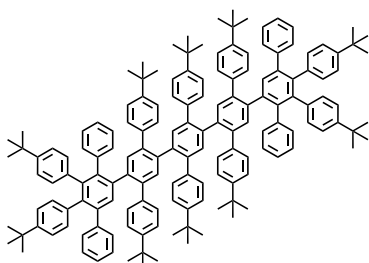
29 (310 mg, 0.24 mmol), bis(triphenylphosphine)palladium(II) dichloride (84 mg, 0.12 mmol) and copper(I) iodide (42 mg, 0.25 mmol) were dissolved in triethylamine (15 mL) and toluene (10 mL), previously degassed by freeze-pump-thaw. Ethynyltrimethylsilane (120 μL, 0.84 mmol) was added to the mixture, which was stirred under argon at 85°C for 21 h. Dichloromethane was added to the mixture and the organic phase was washed with water and brine, dried with Na₂SO₄, filtered, evaporated, and purified by column chromatography (SiO₂, cyclohexane:CH₂Cl₂ 19:1) to give the desired product as a white powder (101 mg, 35% yield). **¹H NMR** (400 MHz, CDCl₃, 298 K): δ(ppm) 7.65 (d, *J* = 8.3 Hz, 4H), 7.60 (s, 2H), 7.42 – 7.32 (m, 8H), 7.08 (d, *J* = 8.3 Hz, 4H), 6.96 (d, *J* = 8.3 Hz, 4H), 6.53 (d, *J* = 8.3 Hz, 4H), 6.48 (d, *J* = 8.2 Hz, 4H), 1.35 – 1.31 (m, 54H), 0.15 (s, 18H). **¹³C NMR** (101 MHz, CDCl₃, 298K): δ(ppm) 150.55, 148.94, 143.10, 140.74, 139.90, 139.20, 137.16, 136.93, 136.73, 134.70, 133.38, 132.48, 129.11, 128.58, 128.44, 124.81, 124.75, 124.27, 120.44, 105.34, 97.65, 34.70, 34.50, 31.52, 31.50, -0.13. **MALDI-ToF MS**: calc. for C₈₈H₁₀₂Si₂: 1214.75; found: 1214.60.

Diethynyl triterphenyl derivative 22



30 (93 mg, 0.08 mmol) and freshly distilled tetrahydrofuran (8 mL) were introduced in a round bottom flask. Tetrabutylammonium fluoride (1M in tetrahydrofuran, 228 μL, 0.23 mmol) was added dropwise and the brown solution was stirred for 2 h under argon. Dichloromethane and water were then added to the mixture. The organic phase was washed with water and brine, dried with Na₂SO₄, filtered, and the solvent evaporated. A yellowish powder was recovered and was used in subsequent reactions without further purification.

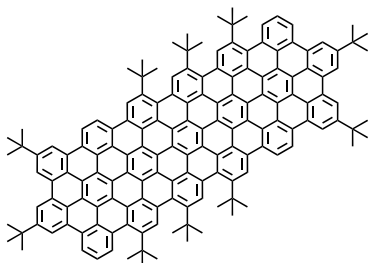
Dendrimer 23



22 (85 mg, 0.08 mmol) and **CP-1** (114 mg, 0.23 mmol) were dissolved in dry *o*-xylene (4 mL) in a schlenk. The solution was degassed sparging argon and then heated to 180°C for 16 h. The solvent was evaporated and the product purified by flash column chromatography (SiO₂, cyclohexane:CH₂Cl₂ 17:3) as a yellow powder (110 mg, 72% yield). **¹H NMR** (400 MHz, CDCl₃, 298 K): δ(ppm) 7.57 (s, 2H), 7.46 (s, 2H), 7.41 (s, 2H), 7.36 (s, 2H), 7.15 – 6.44 (m, 60H), 1.35 (s, 18H), 1.30 (s, 18H), 1.28 (s, 18H), 1.14 (s, 18H),

1.09 (s, 18H). **¹³C NMR** (101 MHz, CDCl₃, 298K): δ(ppm) 149.30, 148.75, 148.61, 148.13, 147.84, 142.12, 141.93, 140.42, 139.94, 139.88, 139.77, 139.73, 139.68, 139.46, 139.27, 138.95, 137.61, 137.55, 137.30, 133.50, 133.34, 132.89, 131.53, 130.82, 130.08, 129.22, 128.63, 128.52, 127.48, 126.07, 125.03, 124.55, 124.36, 124.17, 123.56, 123.17, 34.50, 34.45, 34.39, 34.27, 34.19, 31.60, 31.50, 31.36, 31.33, 29.85. **MALDI-ToF MS**: calc. for C₁₅₄H₁₅₈: 2007.24; found: 2007.13.

C₁₁₄tBu₁₀.

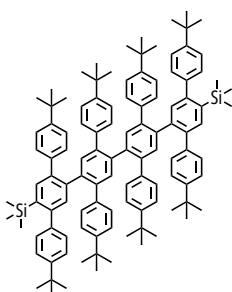


Dendrimer **23** (50 mg, 0.025 mmol) was dissolved in non-stabilized dichloromethane (50 mL). A solution of iron(III) chloride (1 M in nitromethane, 733 mg, 4.50 mmol) was added dropwise to the mixture. The reaction was left at room temperature under a strong flow of extra pure argon for 2 h 15 min. The mixture was then added to an excess of methanol (150 mL) to precipitate the nanoparticle. The precipitate was filtered through a PTFE filter to recover a greenish powder. The powder was solubilized in a small amount of tetrahydrofuran, sonicated for 1 min followed by ultracentrifugation. The precipitate was purified by steric exclusion chromatography (tetrahydrofuran) and obtained as a dark green powder (3 mg, 6% yield).

Alternatively, the C₁₁₄tBu₁₀ can also be obtained using 2,3-dichloro-5,6-dicyano-1,4-benzoquinone as oxidant. Dendrimer **23** (30 mg, 0.015 mmol) and 2,3-dichloro-5,6-dicyano-1,4-benzoquinone (134 mg, 0.59 mmol) were dissolved in freshly distilled non-stabilized dichloromethane (15 mL). The solution was allowed to cool down to 0°C in an ice bath. Trifluoromethanesulfonic acid (0.9 mL) was slowly added to the mixture. The solution is stirred for 40 min under argon at 0°C. Distilled triethylamine (5 mL) was added to quench the reaction and the mixture was then added in one time to methanol (100 mL). The precipitate was filtered through a PTFE filter. The obtained powder was dispersed in a small amount of tetrahydrofuran, sonicated for 1 min followed by ultracentrifugation (130 000 g, 30 min). The precipitate yielded the product as a dark green powder (12 mg, 41%).

¹H NMR (600 MHz, CS₂+THF-d₈, 298 K): δ(ppm) 11.13 (s, 2H), 10.80 (d, *J* = 8.2 Hz, 2H), 10.62 (s, 2H), 10.55 (d, *J* = 8.9 Hz, 2H), 10.43 (s, 2H), 10.08 (s, 2H), 9.73 (s, 2H), 9.65 – 9.60 (m, 4H), 9.55 (d, *J* = 7.3 Hz, 2H), 9.48 (d, *J* = 7.3 Hz, 2H), 8.47 (t, *J* = 7.2 Hz, 2H), 2.56 (s, 18H), 2.31 (s, 18H), 2.13 (s, 18H), 2.10 (s, 18H), 2.00 (s, 18H). **¹³C NMR** (151 MHz, CS₂+THF-d₈, 298 K, only carbons visible by ¹H-¹³C HSQC and HMBC are reported): δ(ppm) 150.42, 150.03, 146.90, 140.65, 140.45, 136.16, 135.77, 133.42, 133.04, 131.86, 131.86, 131.86, 131.47, 130.88, 130.88, 129.91, 129.91, 129.91, 129.71, 129.71, 129.52, 129.52, 128.93, 128.93, 128.34, 126.59, 126.59, 126.40, 126.00, 125.61, 125.02, 124.63, 124.63, 124.44, 123.46, 123.27, 123.07, 122.87, 122.87, 122.68, 122.49, 120.73, 120.53, 120.34, 120.14, 119.94, 119.75, 119.56, 40.44, 39.86, 39.47, 36.34, 36.34, 36.34, 35.56, 35.37, 32.63, 32.44. **MALDI-ToF HRMS**: calc. for C₁₅₄H₁₁₄: 1962.8915; found: 1962.8854.

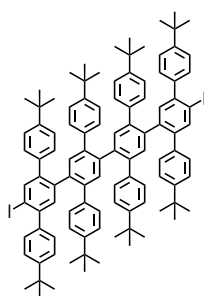
Ditrimethylsilyl tetraterphenyl derivative **31**



16 (222 mg, 0.41 mmol), **18** (163 mg, 0.17 mmol), tetrakis(triphenylphosphine)palladium(0) (39 mg, 0.03 mmol), and potassium carbonate (117 mg, 0.85 mmol) were dissolved in toluene (10 mL), ethanol (2 mL) and water (2 mL), previously degassed by freeze-pump-thaw. The mixture was stirred under argon at 85°C for 20 h. The mixture was filtered through a celite pad with dichloromethane then washed with water and brine. The organic phase was dried with Na₂SO₄, filtered, and evaporated. The product was purified by flash column chromatography (SiO₂, cyclohexane:CH₂Cl₂ 9:1) and recovered as

a white powder (186 mg, 72% yield). **¹H NMR** (400 MHz, CDCl₃, 298 K): δ(ppm) 7.49 (s, 2H), 7.46 (s, 2H), 7.43 – 7.36 (m, 8H), 7.32 (d, *J* = 8.3 Hz, 4H), 7.13 – 7.07 (m, 8H), 6.92 (d, *J* = 8.3 Hz, 4H), 6.63 (d, *J* = 8.3 Hz, 4H), 6.56 (d, *J* = 8.3 Hz, 4H), 6.46 (d, *J* = 8.4 Hz, 4H), 1.37 (s, 18H), 1.36 – 1.32 (m, 36H), 1.30 (s, 18H), 0.05 (s, 18H). **¹³C NMR** (101 MHz, CDCl₃, 298K): δ(ppm) 150.19, 148.99, 148.60, 148.53, 141.19, 140.13, 140.08, 139.59, 139.20, 139.07, 138.18, 138.14, 137.70, 137.43, 137.20, 136.26, 133.28, 133.01, 132.69, 129.12, 128.77, 128.31, 124.67, 124.54, 124.47, 124.25, 34.67, 34.42, 31.68, 31.59, 31.52, 27.06, 0.90. **MALDI-ToF MS**: calc. for C₁₁₀H₁₃₀Si₂: 1506.97; found: 1506.94.

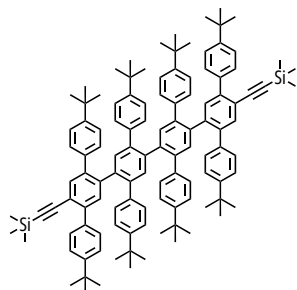
Diiodo tetraterphenyl derivative **32**



31 (166 mg, 0.11 mmol) was dissolved in freshly distilled non-stabilized dichloromethane (8 mL). The mixture was cooled to 0°C in an ice bath and iodine monochloride (1 M in dichloromethane, 0.44 mL, 0.44 mmol) was added dropwise. The mixture was allowed to come back to room temperature and was stirred overnight under argon. The mixture was quenched with a saturated aqueous solution of sodium thiosulfate, extracted with dichloromethane, washed with water and brine, dried with Na₂SO₄, filtered, and evaporated. The crude product was purified by flash chromatography (SiO₂, cyclohexane:CH₂Cl₂ 9:1) and recovered as an off-white powder (164 mg, 93% yield). **¹H NMR** (400 MHz, CDCl₃, 298 K): δ(ppm)

7.75 (s, 2H), 7.50 (s, 2H), 7.43 – 7.36 (m, 12H), 7.11 – 7.06 (m, 8H), 6.93 (d, *J* = 8.4 Hz, 4H), 6.59 (d, *J* = 8.1 Hz, 4H), 6.50 (d, *J* = 8.2 Hz, 4H), 6.43 (d, *J* = 8.2 Hz, 4H), 1.36 (s, 18H), 1.33 (s, 18H), 1.32 (s, 18H), 1.29 (s, 18H). **¹³C NMR** (101 MHz, CDCl₃, 298K): δ(ppm) 150.70, 149.37, 149.22, 148.94, 145.46, 141.06, 140.60, 140.39, 140.31, 140.06, 139.70, 137.24, 136.94, 136.26, 133.18, 131.86, 129.15, 128.70, 128.52, 128.23, 124.95, 124.70, 124.37, 124.32, 97.21, 34.77, 34.47, 31.52, 31.47. **MALDI-ToF MS**: calc. for C₁₀₄H₁₁₂I₂: 1614.69; found: 1614.72.

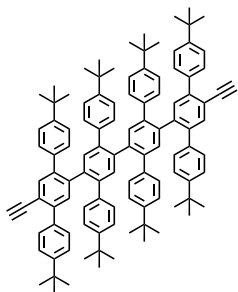
Di-(trimethylsilyl)-ethynyl tetraterphenyl derivative **33**



32 (164 mg, 0.1 mmol), bis(triphenylphosphine)palladium(II) dichloride (35 mg, 0.05 mmol) and copper(I) iodide (15 mg, 0.1 mmol) were dissolved in triethylamine (6 mL) and toluene (4 mL), previously degassed by freeze-pump-thaw along with ethynyltrimethylsilane (55 μL, 0.4 mmol). The mixture was stirred under argon at 80°C for 24 h. Dichloromethane was added to the mixture and then washed with water and brine, dried with Na₂SO₄, filtered, and evaporated and purified by column chromatography (SiO₂, cyclohexane:CH₂Cl₂ 19:1) to give the desired product as a white

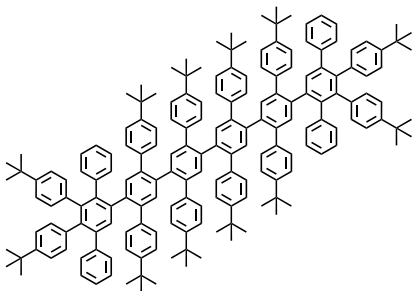
powder (70 mg, 45% yield). **¹H NMR** (400 MHz, CDCl₃, 298 K): δ(ppm) 7.70 – 7.64 (m, 5H), 7.45 – 7.38 (m, 10H), 7.15 – 7.06 (m, 9H), 6.90 (d, *J* = 8.3 Hz, 4H), 6.63 (d, *J* = 8.3 Hz, 4H), 6.53 (d, *J* = 8.3 Hz, 4H), 6.44 (d, *J* = 8.3 Hz, 4H), 1.37 (s, 18H), 1.36 – 1.33 (m, 36H), 1.28 (s, 18H), 0.16 (s, 18H). **¹³C NMR** (101 MHz, CDCl₃, 298K): δ(ppm) 150.55, 149.17, 149.11, 148.86, 143.07, 140.86, 140.19, 139.66, 139.41, 139.28, 138.69, 137.29, 136.98, 136.94, 136.75, 134.75, 133.17, 133.14, 132.37, 129.11, 128.71, 128.61, 128.29, 124.84, 124.77, 124.63, 124.33, 124.26, 120.42, 105.36, 97.65, 34.71, 34.46, 34.43, 31.53, 31.50, 27.06, -0.13. **MALDI-ToF MS**: calc. for C₁₁₄H₁₃₀Si₂: 1554.97; found: 1555.01.

Diethynyl tetraterphenyl derivative **24**



33 (35 mg, 0.02 mmol) and freshly distilled tetrahydrofuran (3 mL) were introduced in a round bottom flask. Tetrabutylammonium fluoride (1M in tetrahydrofuran, 80 μ L, 0.08 mmol) was added to the mixture dropwise and the brown solution was stirred for 2 h under argon. Dichloromethane and water were then added to the mixture. The organic phase was washed with water and brine, dried with Na_2SO_4 , filtered, and evaporated. A yellowish powder was recovered and was used in further reaction without further purification.

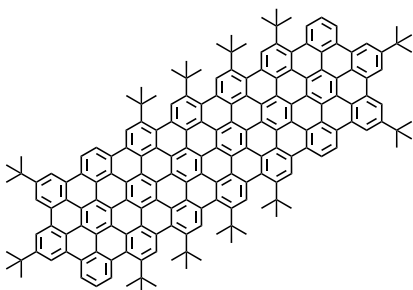
Dendrimer **25**



24 (35 mg, 0.02 mmol), **CP-1** (45 mg, 0.08 mmol) were dissolved in dry o-xylene (4 mL) in a schlenk. The solution was degassed sparging argon and then heated to 180°C for 18 h. The solvent was evaporated, and the product purified by flash column chromatography (SiO_2 , cyclohexane: CH_2Cl_2 87:13) as a yellow powder (29 mg, 59% yield). **$^1\text{H NMR}$** (400 MHz, CDCl_3 , 298 K): δ (ppm) 7.57 (s, 2H), 7.48 (s, 2H), 7.45 (s, 2H), 7.42 (s, 2H), 7.37 (s, 2H), 7.14 – 7.00 (m, 24H), 6.99 – 6.72 (m, 24H), 6.61 – 6.43

(m, 20H), 1.34 (s, 18H), 1.32 – 1.29 (m, 36H), 1.28 (s, 18H), 1.13 (s, 18H), 1.09 (s, 18H). **$^{13}\text{C NMR}$** (101 MHz, CDCl_3 , 298K): δ (ppm) 149.31, 148.99, 148.76, 148.63, 148.13, 147.84, 142.12, 141.93, 140.44, 139.95, 139.74, 139.45, 139.26, 138.98, 137.61, 137.54, 137.29, 133.52, 133.15, 132.99, 132.88, 131.53, 130.82, 130.08, 129.19, 128.66, 128.43, 127.48, 126.08, 125.02, 124.56, 124.35, 124.21, 123.56, 123.18, 34.51, 34.44, 34.40, 34.27, 34.19, 31.58, 31.50, 31.36, 31.33, 27.07. **MALDI-ToF MS**: calc. for $\text{C}_{180}\text{H}_{186}$: 2347.46; found: 2347.50.

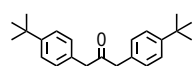
$\text{C}_{132}\text{tBu}_{12}$



25 (10 mg, 0.004 mmol) and 2,3-dichloro-5,6-dicyano-1,4-benzoquinone (43 mg, 0.190 mmol) were dissolved in freshly distilled non-stabilized dichloromethane (15 mL). The solution was allowed to cool down to 0°C in an ice bath. Trifluoromethanesulfonic acid (0.9 mL) was slowly added to the mixture. The solution is stirred for 40 min under argon at 0°C. Distilled triethylamine (5 mL) was added to quench the reaction and the mixture was added in one time to methanol

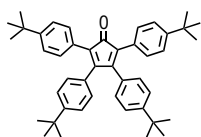
(100 mL). The precipitate was filtered through a PTFE filter. The obtained powder was dispersed in a small amount of tetrahydrofuran followed by ultracentrifugation (130 000 g, 30 min). The precipitate yielded the product as a dark green powder (3 mg, 33%). **$^1\text{H NMR}$** (600 MHz, $\text{CS}_2+\text{THF-d}_8$, 298 K): δ (ppm) 11.17 (s, 2H), 10.89 – 10.81 (m, 4H), 10.77 (s, 2H), 10.58 (d, J = 8.5 Hz, 2H), 10.42 (s, 2H), 10.10 (s, 2H), 9.74 (s, 2H), 9.67 – 9.61 (m, 4H), 9.58 (d, J = 7.2 Hz, 2H), 9.51 (d, J = 7.0 Hz, 2H), 8.49 (t, J = 7.0 Hz, 2H), 2.61 (s, 18H), 2.46 (s, 18H), 2.42 (s, 18H), 2.13 (s, 18H), 2.11 (s, 18H), 2.01 (s, 18H). **$^{13}\text{C NMR}$** (151 MHz, $\text{CS}_2+\text{THF-d}_8$, 298 K, only carbons visible by ^1H - ^{13}C HSQC and HMBC are reported): δ (ppm) 150.42, 150.23, 147.10, 141.24, 140.65, 140.46, 136.16, 135.97, 135.77, 133.62, 133.23, 131.86, 131.86, 131.86, 131.67, 130.89, 130.89, 130.11, 130.11, 129.91, 129.91, 129.72, 129.72, 129.13, 129.13, 126.59, 126.59, 126.40, 126.00, 125.81, 125.03, 124.83, 124.83, 123.86, 123.66, 123.47, 123.27, 123.07, 123.07, 122.88, 122.68, 120.93, 120.54, 120.34, 120.14, 119.75, 119.75, 40.64, 40.06, 40.06, 39.67, 36.54, 36.54, 36.35, 35.96, 35.76, 35.37, 32.64, 32.44. **MALDI-ToF MS HRMS**: calc. for $\text{C}_{180}\text{H}_{134}$: 2295.0480; found: 2295.0502.

1,3-bis(4-(*tert*-butyl)phenyl)propan-2-one **34**²²⁴



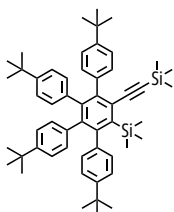
4-dimethylaminopyridine (5.9 g, 28.6 mmol) and *N,N'*-dicyclohexylcarbodiimide (794 mg, 6.5 mmol) were dissolved in non-stabilized dichloromethane (50 mL). 4-*tert*-butylphenylacetic acid (5.0 g, 26.0 mmol) was dissolved in non-stabilized dichloromethane (50 mL) and then added dropwise to the mixture. The reaction was stirred for 16 h under argon at room temperature. The solution was then filtered and evaporated. The product was purified by flash column chromatography (SiO₂, cyclohexane:CH₂Cl₂ 3:2) as a white solid (2.5 g, 30% yield). **¹H NMR** (400 MHz, CDCl₃, 298 K): δ (ppm) 7.32 (d, *J* = 8.4 Hz, 4H), 7.08 (d, *J* = 8.4 Hz, 4H), 3.68 (s, 4H), 1.30 (s, 18H). **¹³C NMR** (101 MHz, CDCl₃, 298 K): δ (ppm) 206.2, 149.8, 131.0, 129.1, 125.6, 48.6, 34.4, 31.3.

2,3,4,5-tetrakis(4-(*tert*-butyl)phenyl)cyclopenta-2,4-dien-1-one **CP-2**²⁸³



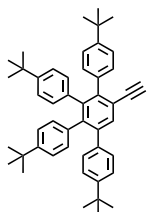
2 (3 g, 9.30 mmol) and **34** (2.98 g, 9.25 mmol) were dissolved in ethanol (30 mL). The mixture was heated to 80°C and potassium hydroxide (540 mg, 9.60 mmol), previously dissolved in ethanol (3 mL), was added to the mixture dropwise. The reaction was heated for 30 min then cooled down in an ice bath. The formed precipitate was filtered and recrystallized in methanol. **CP-2** was recovered as a dark purple powder (2.36 g, 41% yield). **¹H NMR** (400 MHz, CDCl₃, 298 K): δ (ppm) 7.23 (m, 8H), 7.14 (d, *J* = 8.5 Hz, 4H), 6.83 (d, *J* = 8.5 Hz, 4H), 1.29 (s, 18H), 1.27 (s, 18H). **¹³C NMR** (101 MHz, CDCl₃, 298 K): δ (ppm) 201.4, 154.3, 151.3, 150.0, 130.5, 129.6, 129.1, 128.1, 124.9, 124.6, 124.3, 34.6, 34.5, 31.3, 31.2.

Trimethylsilylethynyl -trimethylsilyl- tetraphenylbenzene derivate **35**



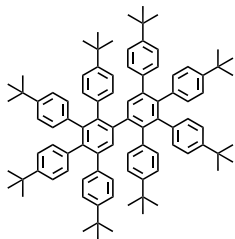
CP-2 (474 mg, 0.78 mmol) and 1,4-bis(trimethylsilyl)butadiyne (186 mg, 0.94 mmol) were dissolved in *o*-xylene (6 mL). The solution was degassed sparging argon and then heated to 170°C for 18 h under argon. The solvent was evaporated, and the product purified by flash column chromatography (SiO₂, cyclohexane:CH₂Cl₂ 23:2) as a yellowish powder (290 mg, 47% yield). **¹H NMR** (400 MHz, CDCl₃, 298 K): δ(ppm) 7.10 (d, *J* = 8.5 Hz, 2H), 7.05 – 7.00 (m, 4H), 6.87 (d, *J* = 8.3 Hz, 2H), 6.78 (d, *J* = 8.4 Hz, 2H), 6.75 (d, *J* = 8.4 Hz, 2H), 6.60 (d, *J* = 8.4 Hz, 2H), 6.50 (d, *J* = 8.3 Hz, 2H), 1.21 (s, 18H), 1.06 (s, 18H), 0.07 (s, 9H), -0.04 (s, 9H). **¹³C NMR** (101 MHz, CDCl₃, 298K): δ(ppm) 149.26, 148.55, 147.79, 147.56, 147.52, 145.10, 141.59, 141.53, 140.44, 140.08, 138.00, 137.40, 137.24, 130.92, 130.82, 130.79, 130.54, 128.12, 123.67, 123.61, 123.22, 123.03, 107.21, 103.60, 34.42, 34.40, 34.18, 34.14, 31.49, 31.46, 31.29, 31.26, 27.07, 1.76, -0.52. **MALDI-ToF MS**: calc. for C₅₄H₇₀Si₂: 774.50; found: .774.54.

Ethynyl-tetraphenylbenzene derivate **36**



35 (73 mg, 0.10 mmol) was dissolved in freshly distilled tetrahydrofuran. Tetrabutylammonium fluoride (1 M in tetrahydrofuran, 4 mL, 4 mmol) was slowly added to the mixture. The reaction was stirred for 24 h under argon. Dichloromethane and water were then added to the mixture. The organic phase was washed with water and brine, dried with Na₂SO₄, filtered, and evaporated. The product was purified by column chromatography (SiO₂, petroleum ether 60/80:CH₂Cl₂ 4:1) as a white powder (41 mg, 64% yield). **¹H NMR** (400 MHz, CDCl₃, 298 K): δ(ppm) 7.71 (s, 1H), 7.18 – 7.09 (m, 4H), 7.03 (d, *J* = 8.3 Hz, 4H), 6.88 (d, *J* = 8.4 Hz, 2H), 6.81 (d, *J* = 8.4 Hz, 2H), 6.66 (d, *J* = 8.3 Hz, 2H), 6.57 (d, *J* = 8.4 Hz, 2H), 2.95 (s, 1H), 1.25 (s, 9H), 1.23 (s, 9H), 1.13 (s, 9H), 1.10 (s, 9H). **¹³C NMR** (101 MHz, CDCl₃, 298K): δ(ppm) 149.19, 149.05, 148.49, 148.08, 143.46, 142.28, 141.37, 140.72, 138.33, 136.91, 136.84, 136.78, 133.74, 131.05, 131.02, 130.26, 129.59, 124.48, 123.93, 123.65, 123.33, 120.89, 83.57, 80.01, 34.48, 34.30, 34.21, 31.42, 31.32.

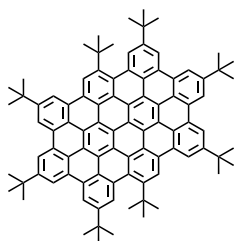
Dendrimer 37



36 (40 mg, 0.06 mmol) and **CP-2** (61 mg, 0.10 mmol) were dissolved in o-xylene (4 mL) in a schlenk. The solution was degassed sparging argon and then heated to 170°C for 18 h under argon. After the mixture cooled down, the solvent was evaporated, and the product purified by flash column chromatography (SiO₂, petroleum ether 60/80:CH₂Cl₂ 4:1) as an off-white powder (71 mg, 96% yield).

¹H NMR (400 MHz, CDCl₃, 298 K): δ(ppm) 7.40 (s, 2H), 7.08 – 7.01 (m, 4H), 6.95 – 6.20 (m, 28H), 1.22 (s, 18H), 1.17 (s, 18H), 1.12 (s, 18H), 1.08 (s, 18H). **¹³C NMR** (101 MHz, CDCl₃, 298K): δ(ppm) 148.43, 147.83, 147.69, 147.48, 141.64, 140.06, 139.72, 139.27, 139.24, 138.92, 138.05, 137.65, 137.09, 132.89, 131.62, 131.30, 129.67, 124.08, 123.36, 123.11, 123.00, 34.38, 34.28, 34.23, 34.15, 31.44, 31.36, 31.33. **MALDI-ToF MS**: calc. for C₉₂H₁₀₆: 1210.83; found: 1210.88.

C₆₀tBu₈

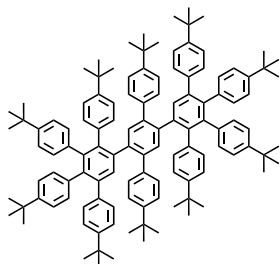


37 (11 mg, 0.008 mmol) and 2,3-dichloro-5,6-dicyano-1,4-benzoquinone (30 mg, 0.130 mmol) were dissolved in freshly distilled non-stabilized dichloromethane (10 mL). The solution was allowed to cool down to 0°C in an ice bath. Trifluoromethanesulfonic acid (0.1 mL) was slowly added to the mixture. The solution is stirred for 2 h 30 min under argon at 0°C. A saturated aqueous solution of sodium bicarbonate (10 mL) was slowly added to the mixture. The organic phase was recovered and washed

with aqueous sodium bicarbonate, water, and brine. The organic phase was then dried with dried with Na₂SO₄, filtered, and evaporated. The product was purified by column chromatography (SiO₂, solid load, cyclohexane:CH₂Cl₂ 6:1) as a white powder (19 mg, 67% yield). **¹H NMR** (400 MHz, THF-d₈+CS₂, 298 K): δ(ppm) 10.03 (s, 2H), 9.60 (s, 2H), 9.48 (s, 2H), 9.43 (s, 2H), 9.39 (s, 2H), 9.27 (s, 2H), 9.07 (s, 2H), 2.03 (s, 18H), 1.98 (s, 18H), 1.93 (s, 18H), 1.87 (s, 18H). **¹³C NMR** (101 MHz, THF-d₈+CS₂, 298K): δ(ppm) 149.51, 146.10, 145.72, 131.59, 131.48, 131.38, 131.22, 130.91, 130.59, 129.90, 129.40, 127.96, 126.88, 125.62, 124.71, 124.65, 122.85, 121.15, 121.02, 120.90, 120.80, 120.63, 120.06, 119.95, 119.66, 119.50, 39.65, 36.20, 36.11, 35.58, 32.61, 32.51.

MALDI-ToF MS: calc. for C₉₂H₈₆: 1190.67; found: 1190.74.

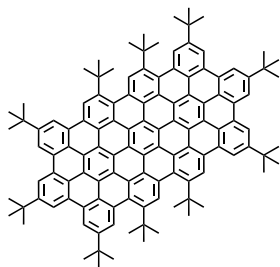
Dendrimer 38



20 (70 mg, 0.18 mmol) and **CP-2** (331 mg, 0.54 mmol) were introduced in a schlenk, followed by the addition of dry o-xylene (5 mL). The solution was degassed sparging argon and then heated to 180°C for 16 h under argon. After the mixture cooled down, the solvent evaporated and the powdered purified by column chromatography (SiO₂, cyclohexane:CH₂Cl₂ 5:1). The product was recovered as a white powder (245 mg, 87% yield). **¹H NMR** (400 MHz, CDCl₃, 298 K): δ(ppm) 7.65 (s, 2H), 7.38 (s, 2H), 7.15 – 6.41 (m, 40H), 1.27 (s, 18H), 1.22 – 1.21 (m, 36H), 1.14 (s, 18H), 1.08

(s, 18H). **¹³C NMR** (101 MHz, CDCl₃, 298K): δ(ppm) 148.84, 148.72, 148.00, 147.62, 146.92, 141.80, 140.46, 140.25, 139.77, 139.49, 139.12, 138.97, 137.92, 137.75, 137.61, 136.13, 133.59, 132.93, 131.69, 131.38, 130.95, 129.74, 129.67, 129.57, 128.87, 125.94, 124.45, 124.34, 123.48, 123.25, 122.94, 34.46, 34.42, 34.28, 34.21, 34.17, 31.54, 31.44, 31.39, 31.36, 27.08. **MALDI-ToF MS**: calc. for C₁₁₈H₁₃₄: 1551.05; found: 1551.02.

C₇₈tBu₁₀

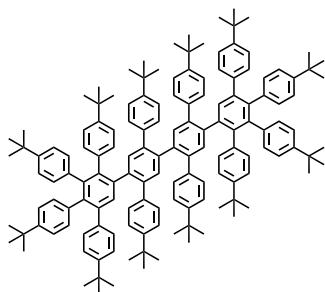


Dendrimer **38** (20 mg, 0.013 mmol) and 2,3-dichloro-5,6-dicyano-1,4-benzoquinone (51 mg, 0.21 mmol) were dissolved in freshly distilled non-stabilized dichloromethane (25 mL). The solution was allowed to cool down to 0°C in an ice bath. Trifluoromethanesulfonic acid (0.13 mL) was slowly added to the mixture. The solution is stirred for 4 h 30 min under argon at 0°C. A saturated aqueous solution of sodium bicarbonate was added to the mixture. The product was extracted with dichloromethane then washed with water and brine. The organic phase was dried with

Na₂SO₄, filtered, and evaporated to give a dark orange powder. The product was purified by column chromatography (SiO₂, CS₂:cyclohexene 7:3) and recovered as a dark orange powder (8 mg, 43% yield). **¹H NMR** (400 MHz, THF-d₈+CS₂, 298 K): δ(ppm) 10.41 (s, 2H), 10.05 (s, 2H), 9.83 (s, 2H), 9.62 (s, 2H), 9.55 (s, 2H), 9.53 (s, 2H), 9.49 (s, 2H), 9.40 (s, 2H), 2.29 (s, 18H), 2.06 (s, 18H), 2.01 – 1.97 (m, 54H). **¹³C NMR** (101 MHz, THF-d₈+CS₂, 298K, only carbons visible by ¹H-¹³C HSQC and HMBC are reported): δ(ppm) 149.72, 146.71, 146.28, 139.83, 135.51, 131.67, 131.45, 131.02, 130.41, 130.38, 129.95, 129.52, 128.45, 125.4, 125.01, 124.79, 123.5, 123.29, 120.5, 120.07, 119.95, 119.86, 119.64, 119.42, 39.92, 39.49, 36.48, 36.27, 35.92, 34.69, 32.31, 32.23.

MALDI-ToF HRMS: calc. for C₁₁₈H₁₀₆: 1522.82890; found: 1522.82669.

Dendrimer 39

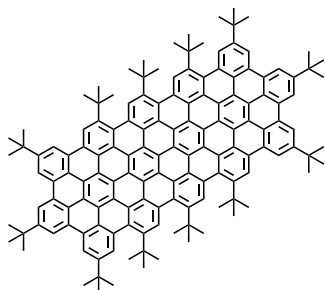


12 (65 mg, 0.09 mmol) and **CP-2** (164 mg, 0.27 mmol) were dissolved in dry o-xylene (5 mL) in a schlenk. The solution was degassed sparging argon and then heated to 170°C for 18 h. The solvent was evaporated and the product purified by flash column chromatography (SiO₂, cyclohexane:CH₂Cl₂ 9:1) as a white powder (127 mg, 74% yield) **¹H NMR** (400 MHz, CDCl₃, 298 K): δ(ppm) 7.69 (s, 2H), 7.46 (s, 2H), 7.38 (s, 2H), 7.11 – 6.43 (m, 48H), 1.37 (s, 18H), 1.26 (s, 18H), 1.22 (s, 18H), 1.16 (s, 18H), 1.14 (s, 18H), 1.08 (s, 18H). **¹³C NMR** (101 MHz, CDCl₃, 298K): δ(ppm) 149.02, 148.75, 148.60, 148.04, 147.68, 147.18, 141.84, 140.47, 140.24,

139.81, 139.53, 139.04, 138.91, 138.79, 137.80, 137.56, 137.52, 137.39, 136.11, 133.54, 132.92, 132.68, 131.61, 130.86, 129.65, 128.91, 128.59, 124.36, 123.51, 123.28, 122.95, 34.46, 34.44, 34.41, 34.27, 34.16, 34.12, 31.63, 31.49, 31.41, 31.37, 31.33.

MALDI-ToF MS: calc. for C₁₄₄H₁₆₂: 1891.27; found: 1891.28.

C₉₆tBu₁₂

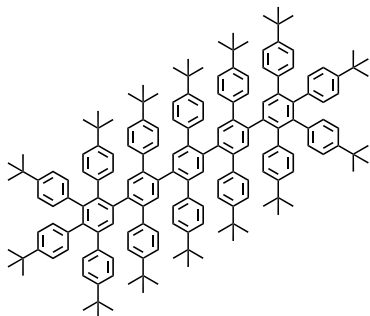


Dendrimer **39** (10 mg, 0.005 mmol) and 2,3-dichloro-5,6-dicyano-1,4-benzoquinone (41 mg, 0.18 mmol) were dissolved in freshly distilled non-stabilized dichloromethane (15 mL). The solution was allowed to cool down to 0°C in an ice bath. Trifluoromethanesulfonic acid (0.3 mL) was slowly added to the mixture. The solution is stirred for 1 h under argon at 0°C. Distilled triethylamine (3 mL) was added to quench the reaction and the mixture is then added in one time to methanol (100 mL). The precipitate was filtered through a PTFE filter. The

obtained powder was dispersed in a small amount of tetrahydrofuran, sonicated for 1 min followed by ultracentrifugation (130 000g, 30 min). The precipitate yielded the product as a dark brown powder (6 mg, 65% yield). **¹H NMR** (400 MHz, THF-d₈+CS₂, 298 K): δ(ppm) 10.50 (s, 2H), 10.42 (s, 2H), 10.35 (s, 2H), 9.89 (s, 2H), 9.64 (s, 2H), 9.57 (s, 2H), 9.55 (s, 2H), 9.50 (s, 2H), 2.40 (s, 18H), 2.27 (s, 18H), 2.13 (s, 18H), 2.09 (s, 18H), 2.01 – 1.99 (m, 36H). **¹³C NMR** (101 MHz, THF-d₈+CS₂, 298K only peaks recorded through HSQC and HMBC NMR are reported): δ(ppm) 149.93, 149.72, 146.71, 146.28, 140.48, 140.26, 135.68, 135.07,

130.58, 125.49, 119.95, 119.86, 119.42, 119.25, 40.14, 39.71, 36.48, 36.27, 35.92, 35.39, 34.86, 32.31, 32.23. **MALDI-ToF HRMS:** calc. for $C_{144}H_{126}$: 1854.98540; found: 1855.98164.

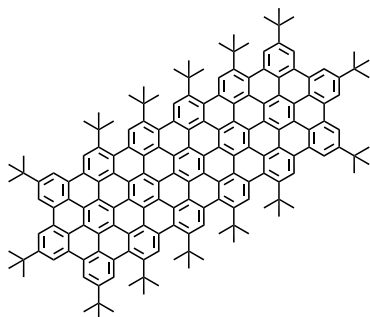
Dendrimer 40



40 (75 mg, 0.07 mmol) and **CP-2** (128 mg, 0.21 mmol) were dissolved in dry o-xylene (5 mL) in a schlenk. The solution was degassed sparging argon and then heated to 170°C for 16 h. The solvent was evaporated, and the product purified by flash column chromatography (SiO_2 , cyclohexane: CH_2Cl_2 9:1) as a yellowish powder (113 mg, 71% yield). **1H NMR** (400 MHz, $CDCl_3$, 298 K): δ (ppm) 7.70 (s, 2H), 7.47 (s, 2H), 7.44 (s, 2H), 7.40 (s, 2H), 7.12 – 6.43 (m, 56H), 1.35 (s, 18H), 1.30 (s, 18H), 1.26 (s, 18H), 1.23 (s, 18H), 1.18 – 1.12 (m, 36H), 1.08 (s, 18H). **^{13}C NMR** (101 MHz, $CDCl_3$, 298K): δ (ppm) 149.03,

148.78, 148.05, 147.68, 147.15, 141.86, 140.50, 140.24, 139.85, 139.57, 139.13, 139.02, 138.91, 138.79, 137.80, 137.55, 137.23, 136.09, 133.54, 133.05, 132.70, 131.61, 130.88, 129.65, 128.85, 128.64, 128.56, 125.93, 124.41, 124.36, 124.21, 123.51, 123.28, 34.44, 34.39, 34.27, 34.16, 34.12, 31.60, 31.50, 31.42, 31.37, 31.33. **MALDI-ToF MS:** calc. for $C_{170}H_{190}$: 2231.49; found: 2231.56.

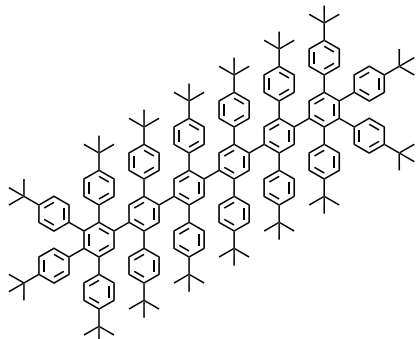
$C_{114}fBU_{14}$.



Dendrimer **39** (20 mg, 0.008 mmol) and 2,3-dichloro-5,6-dicyano-1,4-benzoquinone (88 mg, 0.39 mmol) were dissolved in freshly distilled non-stabilized dichloromethane (20 mL). The solution was allowed to cool down to 0°C in an ice bath. Trifluoromethanesulfonic acid (0.4 mL) was slowly added to the mixture. The solution is stirred for 1 h under argon at 0°C. Distilled triethylamine (3 mL) was added to quench the reaction and the mixture is then added in one time to methanol (100 mL). The precipitate was filtered through a PTFE filter. The obtained powder was solubilized in a small amount

of tetrahydrofuran, sonicated for 1 min followed by ultracentrifugation (130 000g, 30 min). The precipitate yielded the product as a dark green powder (8 mg, 41% yield). **1H NMR** (400 MHz, $THF-d_8+CS_2$, 298 K): δ (ppm) 10.74 (s, 2H), 10.57 (d, $J=2.6$ Hz, 4H), 10.40 (s, 2H), 9.95 (s, 2H), 9.69 (s, 2H), 9.61 (s, 2H), 9.59 (s, 2H), 9.55 (s, 2H), 9.49 (s, 2H), 2.47 (s, 18H), 2.41 (s, 36H), 2.16 (s, 18H), 2.11 (s, 18H), 2.05 (s, 18H), 2.03 (s, 18H). **^{13}C NMR** (101 MHz, $THF-d_8+CS_2$, 298K, only peaks recorded through HSQC and HMBC NMR are reported): δ (ppm) 149.93, 149.93, 146.71, 146.28, 140.69, 140.05, 40.14, 39.92, 39.71, 36.48, 36.27, 36.27, 36.01, 35.48, 34.86, 32.31, 32.31, 32.23. **MALDI-ToF HRMS:** calc. for $C_{170}H_{146}$: 2187.14190; found: 2187.14574.

Dendrimer 41

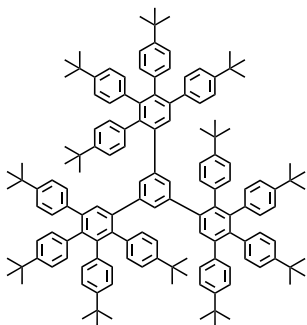


24 (30 mg, 0.02 mmol) and **CP-2** (37 mg, 0.06 mmol) were dissolved in dry o-xylene (4 mL) in a schlenk. The solution was degassed sparging argon and then heated to 180°C for 18 h. The solvent was evaporated, and the product purified by flash column chromatography (SiO_2 , cyclohexane: CH_2Cl_2 9:1) as a yellowish powder (16 mg, 31% yield). **1H NMR** (400 MHz, $CDCl_3$, 298 K): δ (ppm) 7.71 (s, 2H), 7.54 – 7.36 (m, 8H), 7.14 – 6.43 (m, 64H), 1.36 (s, 18H), 1.33 – 1.25 (m, 54H), 1.23 (s, 18H), 1.19 – 1.13 (m, 36H), 1.09 (s, 18H). **^{13}C NMR** (101 MHz, $CDCl_3$, 298K): δ (ppm) 149.08, 148.99, 148.80, 148.07, 147.72, 147.19, 141.88, 140.53, 140.30, 140.23, 139.90, 139.61,

139.16, 139.05, 138.93, 138.80, 137.82, 137.57, 137.23, 136.13, 133.55, 132.71, 131.41, 129.67, 128.89, 128.65, 124.37, 124.22,

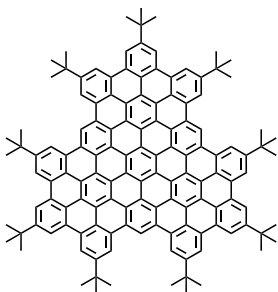
123.52, 77.48, 77.36, 77.16, 76.84, 34.46, 34.42, 34.40, 34.28, 34.17, 34.14, 31.61, 31.50, 31.43, 31.39, 31.34. **MALDI-ToF MS:** calc. for $C_{196}H_{218}$: 2571.71; found: 2571.85.

Dendrimer **42**



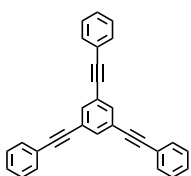
1,3,5-triethynylbenzene (35 mg, 0.23 mmol) and **CP-2** (530 mg, 0.87 mmol) were dissolved in dry *o*-xylene (4 mL) in a schlenk. The solution was degassed sparging argon and then heated to 180°C for 18 h. The solvent was evaporated, and the product purified by flash column chromatography (SiO_2 , cyclohexane: CH_2Cl_2 23:2→4:1) as an off-white powder (264 mg, 61% yield). **1H NMR** (400 MHz, CD_2Cl_2 , 298 K): δ (ppm) 7.17 (s, 3H), 7.15 (d, J = 8.2 Hz, 6H), 7.00 (d, J = 8.2 Hz, 6H), 6.97 – 6.89 (m, 12H), 6.85 (d, J = 8.5 Hz, 6H), 6.70 (t, J = 8.3 Hz, 6H), 6.65 – 6.58 (m, 15H), 1.25 (s, 27H), 1.14 (s, 27H), 1.11 (s, 27H), 1.09 (s, 27H). **^{13}C NMR** (101 MHz, CD_2Cl_2 , 298K): δ (ppm) 149.22, 148.66, 148.30, 142.18, 140.79, 140.56, 140.38, 139.75, 139.44, 139.14, 138.23, 137.90, 137.56, 131.86, 131.51, 131.47, 130.92, 130.21, 129.92, 124.65, 123.90, 123.81, 123.51, 34.60, 34.47, 34.44, 34.38, 31.43, 31.40, 31.34.

(T) $C_{96}tBu_9$



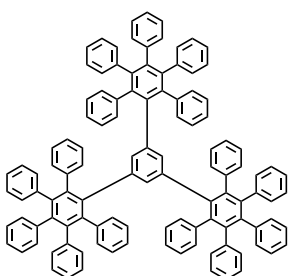
Dendrimer **42** (10 mg, 0.005 mmol) and 2,3-dichloro-5,6-dicyano-1,4-benzoquinone (27 mg, 0.12 mmol) were dissolved in freshly distilled non-stabilized dichloromethane (10 mL). The solution was allowed to cool down to 0°C in an ice bath. Trifluoromethanesulfonic acid (0.1 mL) was slowly added to the mixture. The solution is stirred for 2 h under argon at 0°C. Distilled triethylamine (3 mL) was added to quench the reaction. The solvent was evaporated. No further purification was performed. MALDI-ToF showed the presence of the dimer of (T) $C_{96}tBu_9$. **MALDI-ToF MS:** calc. for $C_{132}H_{102}$ ($2M^+$): 3373.59; found: .3373.47. Further purification is still on-going to confirm the product's formation.

1,3,5-tris(phenylethynyl)benzene **45**^{284,285}



1,3,5-tribromobenzene (210 mg, 0.66 mmol), phenylacetylene (440 μ L, 4.00 mmol), bis(triphenylphosphine)palladium(II) dichloride (11 mg, 0.15 mmol) and copper(I) iodide (38 mg, 0.20 mmol) were dissolved in triethylamine and tetrahydrofuran, previously degassed by freeze-pump-thaw. The mixture was stirred under argon at 70°C for 12 h. Dichloromethane was added to the mixture and then washed with water and brine, dried with Na_2SO_4 , filtered, and evaporated and purified by column chromatography (SiO_2 , cyclohexane: CH_2Cl_2 9:1) to give the desired product as a white powder (214 mg, 87% yield). **1H NMR** (400 MHz, $CDCl_3$, 298 K): δ (ppm) 7.66 (s, 3H), 7.57 – 7.52 (m, 6H), 7.40 – 7.34 (m, 9H). **^{13}C NMR** (101 MHz, $CDCl_3$, 298K): δ (ppm) 134.20, 131.86, 128.77, 128.58, 124.19, 122.96, 90.66, 87.97.

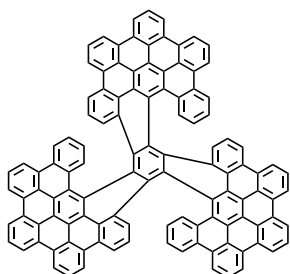
Dendrimer **43**²³⁶



45 (111 mg, 0.3 mmol) and tetraphenylcyclopentadienone (519.1 mg, 1.35 mmol) was dissolved in diphenylether (3 mL). The reaction mixture was stirred at 230°C for 3 weeks in a sealed Schlenk. The mixture was precipitated twice in methanol and evaporated to afford the compound as an off-white solid (188 mg, 43% yield). **1H NMR** (400 MHz, $CDCl_3$, 298 K): δ (ppm) 7.10-7.05 (m, 12H), 6.95-6.90 (t, 6H), 6.80-6.75 (m, 46H), 6.50-6.45 (m, 6H), 6.27 (s, 3H), 5.72 (s, 5H). **^{13}C NMR** (101 MHz, $CDCl_3$, 298K): δ (ppm) 141.16, 140.98, 140.95, 140.75, 140.14, 139.50, 137.71,

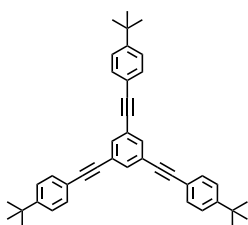
136.82, 134.44, 131.99, 131.70, 131.41, 131.37, 131.32, 127.47, 126.41, 126.39, 126.30, 126.27, 124.98, 124.88, 124.77. **MALDI-ToF MS**: calc. for $C_{114}H_{78}$: 1446.61; found: 1446.63.

(C_{36})₃-T[6]H



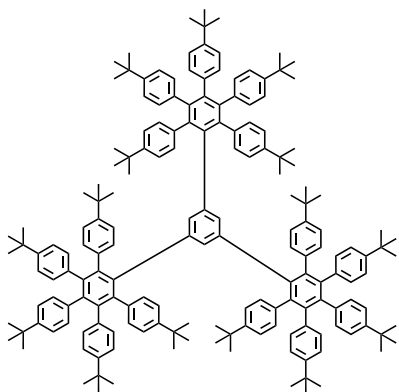
Dendrimer **43** (20 mg, 0.014 mmol) was dissolved in non-stabilized dichloromethane (50 mL). A solution of iron(III) chloride (1 M in nitromethane, 188 mg, 1.16 mmol) was added dropwise to the mixture. The reaction was left at room temperature under a strong flow of extra pure argon for 7 h. The reaction was followed by MALDI-ToF mass spectrometry and showed that the product was not formed. **MALDI-ToF MS**: calc. for $C_{114}H_{48}$: 1416.38; found: 1438.67.

1,3,5-tris((4-(*tert*-butyl)phenyl)ethynyl)benzene **46**²⁸⁴



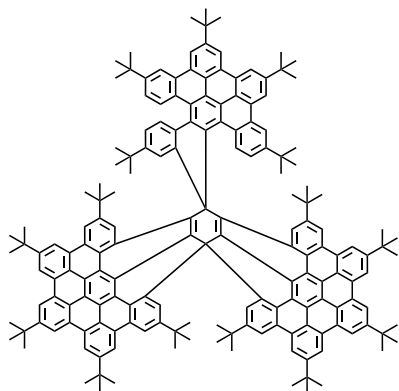
1,3,5-tribromobenzene (314 mg, 1.00 mmol), tetrakis(triphenylphosphine)palladium(0) (96 mg, 0.08 mmol) and copper(I) iodide (16 mg, 0.08 mmol). 4-*tert*-butylphenylacetylene (630 μ L, 3.50 mmol) was dissolved in triethylamine (10 mL) and pyridine (5 mL), then the solution degassed by freeze-pump-thaw. The 4-*tert*-butylphenylacetylene solution was then added dropwise through cannula transfer to the reaction mixture. The mixture was stirred under argon at 70°C for 16 h. The reaction was let to cool down then added into aqueous hydrochloric acid (0.5 M, 200 mL). The precipitate was filtered and purified by flash column chromatography (SiO_2 , 25 g, petroleum ether 60/80) to give the desired product as a white powder (439 mg, 80% yield). **¹H NMR** (400 MHz, $CDCl_3$, 298 K): δ (ppm) 7.63 (s, 3H), 7.47 (d, J = 8.5 Hz, 6H), 7.39 (d, J = 8.5 Hz, 6H), 1.34 (s, 27H). **¹³C NMR** (101 MHz, $CDCl_3$, 298K): δ (ppm) 152.05, 133.98, 131.60, 125.57, 124.32, 119.99, 90.72, 87.48, 34.99, 31.32. **MALDI-ToF MS**: calc. for $C_{42}H_{42}$: 546.33; found: 546.33.

Dendrimer **44**



46 (202 mg, 0.37 mmol) and **CP-2** (1 g, 1.65 mmol) were dissolved in diphenyl ether (6 mL) previously degassed by freeze-pump-thaw. The mixture was heated at 250°C for 1 month in a sealed Schlenk. The solution was precipitated in methanol (150 mL). The precipitate was purified by flash column chromatography (SiO_2 , cyclohexane: CH_2Cl_2 9:1) to yield the product as an off-white powder (144 mg, 17% yield). **¹H NMR** (400 MHz, $CDCl_3$, 298 K): δ (ppm) 7.06 (d, J = 10.3 Hz, 6H), 6.79 (d, J = 8.1 Hz, 6H), 6.77 – 6.69 (m, 19H), 6.48 – 6.40 (m, 24H), 6.32 (d, J = 8.2 Hz, 6H), 5.25 (s, 3H), 1.19 (s, 54H), 1.08 (s, 54H), 1.04 (s, 27H). **¹³C NMR** (101 MHz, $CDCl_3$, 298K): δ (ppm) 147.31, 147.06, 140.22, 139.27, 139.18, 138.95, 138.84, 138.68, 137.44, 136.84, 133.44, 132.62, 131.49, 131.18, 131.05, 130.84, 124.08, 122.98, 122.89, 121.83, 34.33, 34.12, 34.09, 31.40, 31.33, 31.29. **MALDI-ToF MS**: calc. for $C_{174}H_{198}$: 2287.55; found: 2287.58.

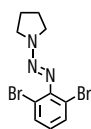
Bis-spiro compound **47**



Dendrimer **44** (30 mg, 0.013 mmol) and 2,3-dichloro-5,6-dicyano-1,4-benzoquinone (54 mg, 0.235 mmol) were dissolved in freshly distilled non-stabilized dichloromethane (40 mL). The solution was allowed to cool down to 0°C in an ice bath. Trifluoromethanesulfonic acid (0.4 mL) was slowly added to the mixture. The solution is stirred for 1 h 20 min under argon at 0°C. A saturated aqueous solution of sodium bicarbonate was added to the mixture. The product was extracted with dichloromethane then washed with water and brine. The organic phase was dried with Na₂SO₄, filtered, and evaporated to give a dark orange powder. The product was

purified by column chromatography (SiO₂, toluene:CH₂Cl₂ 9:1 → 2:1) and recovered as a dark yellow powder (9.5 mg, 32% yield). **¹H NMR** (400 MHz, CD₂Cl₂, 298 K): δ(ppm) 10.10 (d, *J* = 8.7 Hz, 1H), 9.43 – 9.19 (m, 12H), 9.15 (d, *J* = 5.8 Hz, 2H), 9.04 (s, 1H), 8.98 (s, 1H), 8.95 – 8.84 (m, 4H), 8.54 (s, 1H), 8.42 (d, *J* = 10.7 Hz, 2H), 8.35 (s, 1H), 8.21 (d, *J* = 8.5 Hz, 1H), 7.76 (d, *J* = 1.8 Hz, 1H), 7.59 (d, *J* = 8.7 Hz, 1H), 7.35 (d, *J* = 1.9 Hz, 1H), 7.01 (d, *J* = 1.6 Hz, 1H), 6.81 (dd, *J* = 8.5, 1.9 Hz, 1H), 6.68 (d, *J* = 1.6 Hz, 1H), 6.37 (d, *J* = 1.5 Hz, 1H), 5.63 (d, *J* = 9.4 Hz, 1H), 1.89 – 1.78 (m, 36H), 1.72 – 1.66 (m, 27H), 1.62 (s, 9H), 1.49 (s, 9H), 0.66 (s, 9H), 0.41 (s, 9H), 0.28 – 0.21 (m, 18H), 0.08 (s, 9H), -0.08 (s, 9H). **MALDI-ToF HRMS**: calc. for C₁₇₄H₁₆₈: 2257.31461; found: 2257.30720.

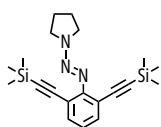
(2,6-dibromophenyl)diazenylpyrrolidine **50**²⁴³



In a round bottom flask, 2,6-dibromoaniline (3 g, 12.0 mmol) was introduced along with concentrated hydrochloric acid (4.7 mL). The mixture was cooled down to 0°C with an ice bath. Sodium nitrite (858 mg, 12.4 mmol) was solubilized in water (2.5 mL), the solution cooled down to 0°C, and added to the main reaction mixture dropwise.

After 30 min of agitation, the mixture was added to a solution of potassium carbonate (8.25 g, 59.0 mmol) and pyrrolidine (2 mL, 1.72 g, 24.2 g) in water (14 mL) and acetonitrile (7 mL) at 0°C. After 30 min, the product was extracted with dichloromethane. The organic phase was washed with water and brine, dried with Na₂SO₄, filtered, and evaporated. The product was purified by chromatography (SiO₂, cyclohexane:CH₂Cl₂ 3:2) as a dark yellow oil (2.67 g, 67% yield). **¹H NMR** (400 MHz, CDCl₃, 298 K): δ(ppm) 7.53 (d, *J* = 8.0 Hz, 2H), 6.84 (t, *J* = 8.0 Hz, 1H), 3.96 (s, 2H), 3.73 (s, 2H), 2.08 (s, 4H). **¹³C NMR** (101 MHz, CDCl₃, 298K): δ(ppm) 148.31, 132.49, 126.73, 118.09, 51.33, 46.72, 24.15, 23.80. **ESI MS** *m/z*: calc for C₁₀H₁₂N₃Br₂(M+H): 331.93; found: 331.94.

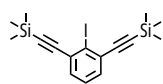
2,6-bis((trimethylsilyl)ethynyl)phenyl diazenylpyrrolidine **51**



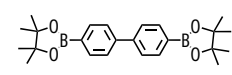
50 (2.65 g, 8.00 mmol), bis(triphenylphosphine)palladium(II) dichloride (156 mg, 0.24 mmol), and copper(I) iodide (356 mg, 0.24 mmol) were dissolved in degassed triethylamine (7 mL). Ethynyltrimethylsilane (1.3 mL, 10.00 mmol) was added to the reaction mixture, which was then stirred under argon at 70°C for 16 h.

Triethylamine was evaporated, and the powder was dissolved in dichloromethane and filtered through a pad of celite. The organic phase was washed with water and brine, dried with Na₂SO₄, filtered, and evaporated. The product was purified by column chromatography (SiO₂, CH₂Cl₂:cyclohexane 3:7 → 4:1) as a pale yellow powder (2.5 g, 85% yield). **¹H NMR** (400 MHz, CDCl₃, 298 K): δ(ppm) 7.40 (d, *J* = 7.7 Hz, 2H), 6.96 (t, *J* = 7.7 Hz, 1H), 3.84 (d, *J* = 84.5 Hz, 4H), 2.05 (s, 4H), 0.20 (s, 18H). **¹³C NMR** (101 MHz, CDCl₃, 298K): δ(ppm) 155.04, 133.96, 124.07, 116.38, 103.28, 97.45, 0.15.

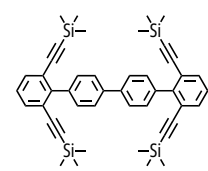
((2-iodo-1,3-phenylene)bis(ethyne-2,1-diyl))bis(trimethylsilane) **52**

 **51** (2.41 g, 6.6 mmol) was added to a Schlenk flask and degassed. Iodomethane (5 mL) was added and the Schlenk sealed. The mixture was heated to 110°C overnight. After 14 h, iodomethane was evaporated. The recovered powder was purified by column chromatography (SiO₂, solid load, cyclohexane:CH₂Cl₂ 3:1) as a yellow powder (1.9 g, 72% yield). **¹H NMR** (400 MHz, CDCl₃, 298 K): δ(ppm) 7.36 (d, *J* = 7.6 Hz, 2H), 7.20 (dd, *J* = 8.1, 7.3 Hz, 1H), 0.28 (s, 18H). **¹³C NMR** (101 MHz, CDCl₃, 298K): δ(ppm) 132.28, 131.03, 127.59, 108.08, 106.89, 99.20, -0.10.

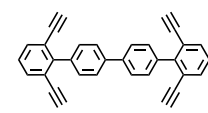
4,4'-bis(4,4,5,5-tetramethyl-1,3,2-dioxaborolan-2-yl)-1,1'-biphenyl **53**²⁸⁶

 4,4'-dibromobiphenyl (2 g, 6.0 mmol), bis(pinacolato)diboron (3.8 g, 15.0 mmol), [1,1'-bis(diphenylphosphino)ferrocene]dichloropalladium(II) (213 mg, 0.3 mmol), and potassium acetate (3.5 g, 36.0 mmol) were dissolved in dimethylformamide (40 mL), previously degassed by freeze-pump-thaw. The reaction mixture was heated at 105°C for 2h30. The mixture was filtered through a celite pad. Water was added to the mixture and then extracted with dichloromethane. The organic phase was washed with water and brine, dried with Na₂SO₄, filtered, and evaporated. The product was purified by recrystallisation in ethyl acetate and recovered as a white powder (2.23 g, 91 % yield). **¹H NMR** (400 MHz, CDCl₃, 298 K): δ(ppm) 7.92 – 7.84 (m, 4H), 7.67 – 7.60 (m, 4H), 1.36 (s, 24H). **¹³C NMR** (101 MHz, CDCl₃, 298K): δ(ppm) 143.67, 135.27, 126.53, 83.86, 24.89.

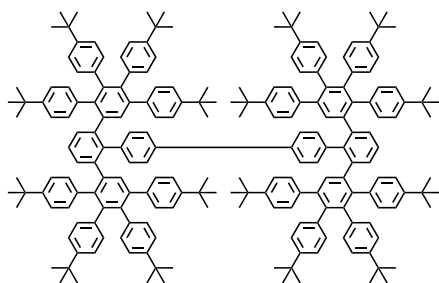
Tetra-(trimethylsilyl)-ethynyl tetraphenyl derivative **54**

 **53** (667 mg, 1.64 mmol), **52** (1.5 g, 3.78 mmol), tetrakis(triphenylphosphine)palladium(0) (92 mg, 0.08 mmol), and potassium carbonate (1.35 g, 9.84 mmol) were dissolved with toluene (35 mL), ethanol (10 mL) and water (10 mL), previously degassed by freeze-pump-thaw. The mixture was stirred under argon at 80°C for 21 h. Water was added to the mixture, then extracted with dichloromethane and washed with water and brine. The organic phase was dried with Na₂SO₄, filtered and evaporated. The product was purified by flash column chromatography (SiO₂, cyclohexane:CH₂Cl₂ 17:3) and recovered as a yellow powder (735 mg, 65% yield). **¹H NMR** (400 MHz, CD₂Cl₂, 298 K): δ(ppm) 7.69 (d, *J* = 8.3 Hz, 4H), 7.58 (d, *J* = 8.3 Hz, 4H), 7.53 (d, *J* = 7.8 Hz, 4H), 7.26 (t, *J* = 7.8 Hz, 2H), 0.05 (s, 36H). **¹³C NMR** (101 MHz, CD₂Cl₂, 298K): δ(ppm) 140.76, 138.02, 132.91, 130.97, 127.43, 126.35, 123.40, 104.30, 98.98, -0.37. **MALDI-ToF MS**: calc. for C₄₄H₅₀Si₄: 690.30; found: 690.29.

Tetraethynyl tetraphenyl derivative **48**

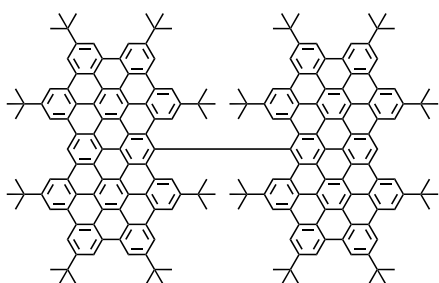
 **54** (83 mg, 0.12 mmol) and freshly distilled tetrahydrofuran (10 mL) were introduced in a round bottom flask. Tetrabutylammonium fluoride (1M in tetrahydrofuran, 960 μL, 0.96 mmol) was added dropwise and the solution was stirred for 1 h 30 min under argon. Dichloromethane and water were then added to the mixture. The organic phase was washed with water and brine, dried with Na₂SO₄, filtered, and the solvent evaporated. A yellowish powder was recovered and was used in further reaction without further purification

Dendrimer **49**



48 (48 mg, 0.12 mmol) and **CP-2** (450 mg, 0.74 mmol) were dissolved in dry o-xylene (4 mL) in a schlenk. The solution was degassed sparging argon and then heated to 170°C for 18 h. After the mixture cooled down it was added to an excess methanol to precipitate the product as a white powder and then filtered through a PTFE filter, this process was repeated twice. The product was recovered as a white powder (153 mg, 99% yield). **¹H NMR** (400 MHz, CDCl₃, 298 K): δ(ppm) 7.39 (t, *J* = 7.3 Hz, 2H), 7.34 – 7.28 (m, 4H), 7.15 – 6.30 (m, 74H), 6.18 – 6.06 (m, 2H), 1.28 – 1.03 (m, 126H), 0.97 – 0.93 (m, 18H). **¹³C NMR** (101 MHz, CDCl₃, 298K): δ(ppm) 148.40, 147.64, 147.24, 147.14, 141.36, 141.24, 141.05, 141.01, 139.30, 139.22, 139.09, 138.96, 137.75, 137.43, 136.41, 136.29, 132.32, 131.11, 129.60, 129.51, 124.91, 124.50, 124.09, 123.89, 123.32, 123.24, 122.87, 34.28, 34.08, 34.05, 33.97, 33.91, 31.45, 31.39, 31.35, 31.24, 31.18. **MALDI-ToF MS**: calc. for C₂₀₈H₂₂₆: 2723.77; found: 2723.86.

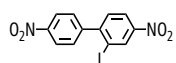
Propeller GQD (C₇₂tBu₈)₂



Dendrimer **49** (52 mg, 0.019 mmol) and 2,3-dichloro-5,6-dicyano-1,4-benzoquinone (114 mg, 0.50 mmol) were dissolved in freshly distilled unstabilized dichloromethane (40 mL). The solution was allowed to cool down to 0°C in an ice bath. Trifluoromethanesulfonic acid (0.4 mL) was slowly added to the mixture. The solution is stirred for 8 h under argon at 0°C. An aqueous saturated solution of sodium bicarbonate (20 mL) was slowly added to quench the reaction.

The organic phase was dried with Na₂SO₄, filtered, and evaporated. The product was purified by flash column chromatography (SiO₂, cyclohexane:toluene 17:3) and recovered as a dark yellow powder (9.5 mg, 19% yield). **¹H NMR** (400 MHz, CD₂Cl₂, 298 K): δ(ppm) 11.76 (s, 2H), 10.31 (s, 4H), 9.76 (s, 4H), 9.63 (s, 4H), 9.50 (s, 4H), 9.34 (s, 4H), 8.81 (s, 4H), 8.71 (s, 4H), 8.28 (s, 4H), 2.14 (s, 36H), 1.96 (s, 36H), 1.61 (s, 36H), -0.24 (s, 36H). **¹³C NMR** (101 MHz, CD₂Cl₂, 298K, only carbons visible by 1H-13C HSQC and HMBC are reported): δ(ppm) 150.29, 146.43, 130.56, 128.85, 125.69, 124.72, 124.65, 123.82, 120.57, 120.28, 119.8, 119.62, 119.45, 119.36, 118.74, 116.28, 36.55, 36.3, 35.98, 34.33, 32.43, 32.34, 32.27, 32.02, 31.54, 30.36, 30.17, 30.1, 29.77, 27.33, 23.1, 14.29. **MALDI-ToF HRMS**: calc. for C₂₀₈H₁₇₈: 2675.39230; found: 2675.38320.

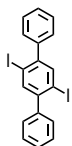
2-iodo-4,4'-dinitro-1,1'-biphenyl **58**²⁸⁷



4,4'-Dinitro-2-biphenylamine (778 mg, 5.0 mmol) was dissolved in tetrahydrofuran (8 mL) and aqueous hydrochloric acid (4 M, 3.8 mL) and the mixture cooled down to 0°C. A cold solution of sodium nitrite (310 mg, 4.5 mmol) in water (1 mL) was added very slowly to the mixture. The mixture was stirred for 1 h at 0°C. A cold solution of potassium iodide (1.2g, 7.2 mmol) in water (1 mL) was then slowly added to the mixture and stirred for 20 min at 0°C. The reaction

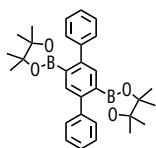
was warmed up to room temperature and stirred overnight. A saturated aqueous solution of sodium thionate was added to quench the reaction. The aqueous phase was extracted with dichloromethane. Then, the organic phase washed with water and brine, dried with Na₂SO₄, filtered, and concentrated in vacuum. The product was purified by chromatography (SiO₂, CH₂Cl₂:cyclohexane 1:1) as a pale yellow powder (616 mg, 57% yield). **¹H NMR** (400 MHz, CDCl₃, 298 K): δ(ppm) 8.83 (d, *J* = 2.2 Hz, 1H), 8.37 – 8.32 (m, 2H), 8.30 (dd, *J* = 8.4, 2.3 Hz, 1H), 7.56 – 7.51 (m, 2H), 7.47 (d, *J* = 8.4 Hz, 1H). **¹³C NMR** (101 MHz, CDCl₃, 298 K): δ(ppm) 150.58, 148.24, 147.92, 147.62, 134.61, 130.00, 123.69, 123.27, 97.02.

2',5'-diiodo-1,1':4',1''-terphenyl **62**⁸⁰



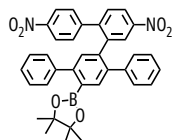
In a round bottom flask, **6** (503 mg, 1.34 mmol) was dissolved in distilled non stabilized dichloromethane (15 mL) and the reaction mixture cooled down to 0°C. Iodine monochloride (0.5 M in dichloromethane, 10.7 mL, 5.36 mmol) was added dropwise and the mixture warmed to room temperature and stirred overnight under argon. An aqueous solution of sodium thiosulfate was added and then extracted with dichloromethane. The organic phases were then washed with water and brine, dried with Na₂SO₄, filtered, and evaporated. The product was recovered as an off-white powder (, 99 % yield). **¹H NMR** (400 MHz, CDCl₃, 298 K): δ(ppm) 7.88 (s, 2H), 7.48-7.41 (m, 6H), 7.40-7.35 (m, 4H). **¹³C NMR** (101 MHz, CDCl₃, 298 K): δ(ppm) 147.06, 142.31, 140.14, 129.16, 128.11, 98.13. No signal was obtained by MALDI-ToF mass spectrometry.

2',5'-bis(4,4,5,5-tetramethyl-1,3,2-dioxaborolan-2-yl)-1,1':4',1''-terphenyl **59**



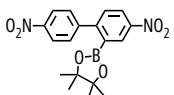
In a round bottom flask, **62** (507 mg, 1.0 mmol) was added along with dry ethyl ether (50 mL). To the stirring suspension, *n*-butyllithium (2 M in hexanes, 1.25 mL, 2.5 mmol) was added dropwise at room temperature and stirred for 45 min under argon. To the yellow solution, 2-Isopropoxy-4,4,5,5-tetramethyl-1,3,2-dioxaborolane (1.35 mL, 6.6 mmol) was added dropwise and stirred for 2 h under argon. Water was then added to the mixture and the product extracted with dichloromethane. The organic phase was washed with water and brine, dried with Na₂SO₄, filtered, and concentrated in vacuum. The product was purified by chromatography (SiO₂, CH₂Cl₂:cyclohexane 1:1→4:1) as a white powder (167 mg, 35% yield). **¹H NMR** (400 MHz, CDCl₃, 298 K): δ(ppm) 7.70 (s, 2H), 7.46 – 7.42 (m, 4H), 7.40 – 7.32 (m, 6H), 1.19 (s, 24H). **¹³C NMR** (101 MHz, CDCl₃, 298 K): δ(ppm) 145.39, 143.19, 134.99, 129.39, 127.85, 126.90, 83.94, 30.47, 24.74. **MALDI-ToF MS** m/z: calc for C₃₀H₃₆B₂O₄: 482.28; found: 481.14.

Monosubstituted product **63**



58 (126 mg, 0.34 mmol), **59** (65 mg, 0.14 mmol), tetrakis(triphenylphosphine)-palladium(0) (68 mg, 0.06 mmol) and potassium carbonate (60 mg, 0.42 mmol) were dissolved in toluene (4 mL), ethanol (1 mL), and water (1 mL), previously degassed by freeze pump thaw. The reaction mixture was heated to 90°C for 48 h. Water and dichloromethane were added to the mixture. The organic phase was recovered, washed with water and brine, dried with Na₂SO₄, filtered, and concentrated in vacuum. The product was purified by chromatography (SiO₂, CH₂Cl₂:cyclohexane 33:17) as a white powder (10 mg, 12% yield). **¹H NMR** (400 MHz, CDCl₃, 298 K): δ(ppm) 8.46 (d, *J* = 2.4 Hz, 1H), 8.24 (dd, *J* = 8.5, 2.4 Hz, 1H), 7.90 (d, *J* = 9.0 Hz, 2H), 7.57 (s, 1H), 7.54 – 7.49 (m, 3H), 7.47 – 7.39 (m, 3H), 7.29 (d, *J* = 8.5 Hz, 1H), 7.13 (t, *J* = 7.4 Hz, 1H), 7.01 (t, *J* = 7.7 Hz, 2H), 6.71 (d, *J* = 8.9 Hz, 2H), 6.52 (d, *J* = 8.2 Hz, 2H), 1.22 (s, 12H). **¹³C NMR** (101 MHz, CDCl₃, 298 K): δ(ppm) 147.98, 147.44, 146.94, 145.40, 145.04, 141.92, 139.60, 138.68, 138.44, 136.91, 134.94, 134.88, 134.82, 131.96, 131.14, 130.95, 130.58, 129.79, 129.30, 129.27, 128.26, 128.23, 128.21, 128.17, 127.66, 126.93, 126.76, 123.21, 123.04, 122.91, 84.30, 24.77. **MALDI-ToF MS** m/z: calc for C₃₆H₃₁BN₂O₆: 598.23; found: 598.18.

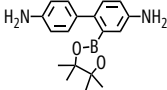
2-(4,4'-dinitro-[1,1'-biphenyl]-2-yl)-4,4,5,5-tetramethyl-1,3,2-dioxaborolane **64**



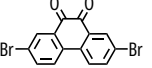
58 (1.3 g, 3.5 mmol), bis(pinacolato)diboron (1.02 g, 4 mmol), [1,1'-bis(diphenylphosphino)ferrocene]palladium(II) dichloride (132 mg, 0.18 mmol), and potassium acetate (1.01 g, 10.5 mmol) were dissolved in degassed dimethylformamide (45 mL). The reaction mixture was heated at 105°C for 1 h. Dichloromethane and water were added to the black mixture, and the aqueous phase was extracted. The organic phase was washed with water, dried with Na₂SO₄, filtered, and evaporated. The dark brown powder was purified by column chromatography (SiO₂, CH₂Cl₂:cyclohexane 4:1) to give the product as a pale yellow powder (851 mg, 65% yield). **¹H NMR**

(400 MHz, CDCl₃, 298 K): δ (ppm) 8.67 (d, J = 2.4 Hz, 1H), 8.34 (dd, J = 8.5, 2.5 Hz, 1H), 8.28 (d, J = 8.8 Hz, 2H), 7.54 (d, J = 8.8 Hz, 2H), 7.51 (d, J = 8.4 Hz, 1H), 1.22 (s, 12H). **¹³C NMR** (101 MHz, CDCl₃, 298 K): δ (ppm) 151.84, 147.87, 147.69, 147.38, 130.44, 130.26, 130.19, 125.47, 123.25, 84.94, 24.76.

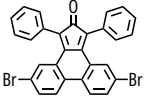
2-(4,4,5,5-tetramethyl-1,3,2-dioxaborolan-2-yl)-[1,1'-biphenyl]-4,4'-diamine **65**

 **65** (365 mg, 1.0 mmol) was dissolved in methanol (110 mL), dichloromethane (60 mL), and ethyl acetate (40 mL). The solution was degassed sparging argon. Afterwards, palladium on carbon (62 mg, 10% Pd) was added to the mixture. The reaction mixture was shaken in a hydrogenator for 5 h at room temperature under a 3-bar hydrogen atmosphere. The reaction was stopped and filtered through a celite pad. The solvents were evaporated, and the product was purified by column chromatography (SiO₂, ethyl acetate:cyclohexane 1:1) to give the product as a bright yellow powder (270 mg, 90% yield). **¹H NMR** (400 MHz, CDCl₃, 298 K): δ (ppm) 7.18 – 7.13 (m, 3H), 7.01 (d, J = 2.6 Hz, 1H), 6.75 (dd, J = 8.2, 2.6 Hz, 1H), 6.70 – 6.65 (m, 2H), 3.62 (s, 4H), 1.23 (s, 12H). **¹³C NMR** (101 MHz, CDCl₃, 298 K): δ (ppm) 144.91, 144.25, 138.24, 134.01, 130.01, 129.98, 121.17, 117.12, 114.81, 83.74, 24.75.

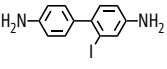
2,7-dibromophenanthrene-9,10-dione **68**¹³⁸

 Phenanthrene-9,10-dione (3.5 g, 16.0 mmol) was dissolved in concentrated sulfuric acid (96 mL). N-bromosuccinimide (6.43 g, 36.0 mmol) was added to the mixture, and the reaction was stirred at room temperature overnight. The solution was added to water (200 mL). The bright orange powder was recovered by Büchner filtration, and then recrystallized in dimethyl sulfoxide to yield the product as an orange powder (4.68 g, 79% yield). **¹H NMR** (400 MHz, DMSO-d₆, 298 K): δ (ppm) 8.26 (s, 2H), 8.17 – 7.86 (m, 4H).

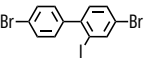
5,10-dibromo-1,3-diphenyl-2H-cyclopenta[*h*]phenanthren-2-one **CP-3**^{138,266}

 **68** (2.4 g, 6.60 mmol) and diphenylacetone (1.8 g, 8.60 mmol) were dissolved in methanol (46 mL). The mixture was heated to 80°C and potassium hydroxide (388 mg, 6.93 mmol), previously dissolved in methanol (20 mL), was added to the mixture dropwise. The reaction was heated for 2 h then cooled down in an ice bath. The formed precipitate was filtered and recrystallized in methanol and chloroform. **CP-3** was recovered as a green powder (1.09 g, 30% yield). **¹H NMR** (400 MHz, CDCl₃, 298 K): δ (ppm) 7.66 (d, J = 2.1 Hz, 2H), 7.61 (d, J = 8.6 Hz, 2H), 7.50 – 7.35 (m, 12H). **MALDI-ToF MS** m/z : calc for C₂₉H₁₆Br₂O: 537.97; found: 537.77.

2-iodo-[1,1'-biphenyl]-4,4'-diamine **69**²⁸⁷

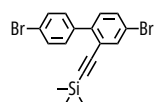
 **69** (555 mg, 1.5 mmol) and tin(II) chloride dihydrate (2.25 g, 10.0 mmol) were dissolved in with previously degassed ethanol (4 mL). The reaction mixture was heated to 80°C under argon overnight. The mixture was then added to crushed ice and a saturated aqueous solution of sodium bicarbonate was slowly added until a pH 8 is reached. The product was extracted with ethyl acetate and then washed with water and brine, dried up with Na₂SO₄, filtered, and evaporated. The product was recovered as a brownish paste (465 mg, 99% yield). **¹H NMR** (400 MHz, CDCl₃, 298 K): δ (ppm) 7.28 (d, J = 2.4 Hz, 1H), 7.12 (d, J = 8.2 Hz, 2H), 7.05 (d, J = 8.1 Hz, 1H), 6.73 – 6.65 (m, 3H), 3.68 (s, 4H). **¹³C NMR** (101 MHz, CDCl₃, 298 K): δ (ppm) 153.37, 152.33, 139.50, 131.56, 131.46, 130.62, 129.14, 123.03, 94.56.

4,4'-dibromo-2-iodo-1,1'-biphenyl **70**

 **69** (465 mg, 1.5 mmol) was dissolved in acetonitrile (3.2 mL), glacial acetic acid (2.2 mL) and 30% sulfuric acid (1.8 mL). The suspension was cooled down in an ice bath and then a cold solution of sodium nitrite in water (1

mL) was added dropwise and stirred for 30 min. Copper(I) bromide was dissolved in concentrated hydrobromic acid (2.5 mL), cooled down, and then slowly added to the reaction mixture. The mixture was heated to 60°C for 2 h 30 min. Dichloromethane was added to the mixture. The organic phase was recovered and washed with water, dried with Na₂SO₄, filtered, and evaporated. The product was purified by column chromatography (SiO₂, cyclohexane) and recovered as a white powder (436 mg, 67% yield). **¹H NMR** (400 MHz, CDCl₃, 298 K): δ(ppm) 8.10 (d, *J* = 2.0 Hz, 1H), 7.56 (d, *J* = 8.4 Hz, 2H), 7.52 (dd, *J* = 8.2, 2.0 Hz, 1H), 7.18 (d, *J* = 8.6 Hz, 2H), 7.13 (d, *J* = 8.2 Hz, 1H). **¹³C NMR** (101 MHz, CDCl₃, 298 K): δ(ppm) 144.39, 141.89, 141.51, 132.03, 131.40, 131.35, 130.90, 130.81, 130.75, 122.32, 121.97, 98.70.

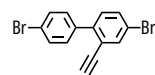
((4,4'-dibromo-[1,1'-biphenyl]-2-yl)ethynyl)trimethylsilane **71**



71 (350 mg, 0.80 mmol), tetrakis(triphenylphosphine)-palladium(0) (56 mg, 0.08 mmol), and copper(I) iodide (24 mg, 0.16 mmol) were dissolved in degassed triethylamine (7 mL). Ethynyltrimethylsilane (118 μL, 0.84 mmol) was added to the mixture which was then stirred under argon at room temperature for 20 h.

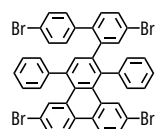
Dichloromethane was added to the mixture and filtered through a pad of celite. The filtrate was evaporated and purified by column chromatography (SiO₂, cyclohexane) to give the desired product as a colorless oil (170 mg, 52% yield). **¹H NMR** (400 MHz, CDCl₃, 298 K): δ(ppm) 7.71 (d, *J* = 2.1 Hz, 1H), 7.53 (d, *J* = 8.6 Hz, 2H), 7.49 (dd, *J* = 8.3, 2.1 Hz, 1H), 7.45 (d, *J* = 8.6 Hz, 2H), 7.20 (d, *J* = 8.3 Hz, 1H), 0.15 (s, 9H). **¹³C NMR** (101 MHz, CDCl₃, 298 K): δ(ppm) 141.83, 138.24, 136.02, 132.07, 131.19, 130.95, 130.67, 123.39, 122.20, 121.13, 102.85, 99.88, -0.28. **APPI MS** *m/z*: calc for C₁₇H₁₆Br₂Si: 405.94; found: 405.94.

4,4'-dibromo-2-ethynyl-1,1'-biphenyl **66**



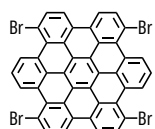
71 (160 mg, 0.40 mmol) was dissolved in tetrahydrofuran (10 mL). Tetrabutylammonium fluoride (1 M in tetrahydrofuran, 480 μL, 0.48 mmol) was added dropwise and stirred under argon at room temperature for 1 h. Water was added to the reaction and then extracted with dichloromethane. The organic phase was washed with water and brine, dried with Na₂SO₄, filtered, and evaporated. The product was used in next steps without further purification.

Nanomesh precursor **67**



66 (234 mg, 0.40 mmol) and **CP-3** (222 mg, 0.41 mmol) were dissolved in *o*-xylene (5 mL) and the solution was degassed sparging argon in a schlenk. The reaction mixture was stirred at 170°C for 20 h. The solution was poured into methanol (200 mL) and the yellowish precipitate was filtered through PTFE filter. The obtained powder was purified by flash column chromatography (SiO₂, cyclohexane) to give the desired product as a white powder (266 mg, 77% yield). **¹H NMR** (400 MHz, CDCl₃, 298 K): δ(ppm) 8.21 (d, *J* = 8.8 Hz, 1H), 8.15 (d, *J* = 8.7 Hz, 1H), 7.83 (d, *J* = 2.0 Hz, 1H), 7.76 (d, *J* = 2.1 Hz, 1H), 7.73 (s, 1H), 7.55 (dd, *J* = 8.7, 2.0 Hz, 2H), 7.51 – 7.46 (m, 4H), 7.43 (dd, *J* = 8.6, 2.0 Hz, 2H), 7.39 (d, *J* = 2.0 Hz, 1H), 7.21 – 7.12 (m, 2H), 7.09 – 7.02 (m, 3H), 6.96 (d, *J* = 8.3 Hz, 1H), 6.83 (s, 1H), 6.45 – 6.38 (m, 2H), 5.89 (d, *J* = 7.8 Hz, 1H). **¹³C NMR** (101 MHz, CDCl₃, 298 K): δ(ppm) 143.61, 141.89, 140.37, 139.34, 139.03, 138.78, 137.39, 134.90, 134.18, 133.24, 132.95, 132.53, 132.26, 131.91, 131.52, 131.46, 131.23, 131.17, 130.88, 130.31, 130.00, 129.95, 129.85, 129.14, 128.37, 128.23, 127.23, 125.10, 124.99, 121.64, 121.20, 120.29, 120.02. **MALDI-ToF MS** *m/z*: calc for C₄₂H₂₄Br₄: 843.86; found: 843.86.

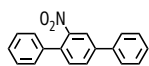
Tetrabromobenzocoronene derivate **72**



66 (100 mg, 0.12 mmol) was dissolved in non-stabilized dichloromethane (40 mL) and the reaction mixture cooled down to -60°C. (bis(trifluoroacetoxy)iodo)benzene (1 g, 2.4 mmol) and boron trifluoride diethyl etherate (295 μL, 2.40 mmol) were dissolved in non-stabilized dichloromethane then added to the reaction

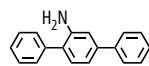
mixture. The reaction was stirred under argon at -60°C for 2 h then at -10°C for 5 h 30 min. The mixture was poured into methanol (200 mL) and the dark precipitate was filtered through PTFE filter. The powder was dispersed in tetrahydrofuran, sonicated for 1 min, followed by ultracentrifugation (130 000g, 30 min). The pellet contained the product (7 mg, 6% yield). $^1\text{H NMR}$ and $^{13}\text{C NMR}$ not recorded because of low solubility. **MALDI-ToF HRMS** m/z : calc for $\text{C}_{42}\text{H}_{14}\text{Br}_4$: 833.78240; found: 833.78001.

2'-nitro-1,1':4',1''-terphenyl **75**²⁸⁸



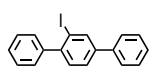
1,4-dibromo-2-nitrobenzene (2.81 g, 10.0 mmol), phenylboronic acid (3.66 g, 30.0 mmol), tris(dibenzylideneacetone)dipalladium(0) (458 mg, 0.5 mmol), 2-dicyclohexylphosphino-2',6'-dimethoxybiphenyl (616 mg, 1.5 mmol), and tripotassium phosphate (4.67 g, 22 mol) were dissolved in toluene (80 mL), ethanol (10 mL), and water (10 mL), previously degassed by freeze-pump-thaw. The reaction was stirred for 17 h at 80°C under argon. The mixture was filtered through a celite pad with dichloromethane. The organic phase was washed with water and brine, dried with Na_2SO_4 , filtered, and evaporated. The product was purified by column chromatography (SiO_2 , cyclohexane: CH_2Cl_2 1:1) and recovered as a yellow powder (2.5 mg, 91% yield). $^1\text{H NMR}$ (400 MHz, CDCl_3 , 298 K): δ (ppm) 8.07 (d, J = 1.9 Hz, 1H), 7.84 (dd, J = 8.0, 1.9 Hz, 1H), 7.68 – 7.63 (m, 2H), 7.55 – 7.48 (m, 3H), 7.48 – 7.41 (m, 4H), 7.40 – 7.34 (m, 2H). $^{13}\text{C NMR}$ (101 MHz, CDCl_3 , 298 K): δ (ppm). 149.71, 141.60, 138.33, 137.15, 134.91, 132.43, 130.61, 129.24, 128.79, 128.60, 128.33, 127.97, 127.10, 122.53. **APPI MS** m/z : calc for $\text{C}_{18}\text{H}_{13}\text{NO}_2$: 275.09; found: 275.09.

[1,1':4',1''-terphenyl]-2'-amine **76**²⁸⁸



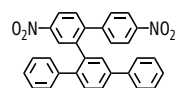
75 (825 mg, 3.0 mmol) and tin(II) chloride dihydrate (2.24 g, 9.9 mmol) were dissolved in ethanol (5 mL) and ethyl acetate (5 mL) previously degassed sparging argon. The reaction mixture was heated to 75°C under argon for 12 h. The mixture was then added to crushed ice and a saturated aqueous solution of sodium bicarbonate was slowly added until a pH 8 is reached. The product was extracted with ethyl acetate and then washed with water and brine, dried up with Na_2SO_4 , filtered, and evaporated. The product was recovered as a pale-yellow powder (425 mg, 58% yield). $^1\text{H NMR}$ (400 MHz, CD_2Cl_2 , 298 K): δ (ppm) 7.65 – 7.60 (m, 2H), 7.53 – 7.41 (m, 6H), 7.39 – 7.31 (m, 2H), 7.19 (d, J = 7.8 Hz, 1H), 7.05 (dd, J = 7.8, 1.8 Hz, 1H), 7.01 (d, J = 1.8 Hz, 1H), 3.93 (s, 2H). $^{13}\text{C NMR}$ (101 MHz, CD_2Cl_2 , 298 K): δ (ppm) 144.49, 141.77, 141.40, 139.69, 131.24, 129.38, 129.26, 129.11, 127.68, 127.59, 127.29, 127.00, 117.69, 114.38. **ESI MS** m/z : calc for $\text{C}_{18}\text{H}_{16}\text{N}$ (M+H): 246.12; found: 246.13.

2'-iodo-1,1':4',1''-terphenyl **77**^{288,289}



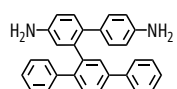
76 (735 mg, 3.0 mmol) was dissolved in tetrahydrofuran (7 mL), water (7 mL), and hydrochloric acid (4 M, 4 mL), and the mixture cooled down to 0°C . A cold solution of sodium nitrite (310 mg, 4.5 mmol) in water (1 mL) was added very slowly to the mixture. The mixture was stirred for 1 h at 0°C . A cold solution of potassium iodide (1.2g, 7.2 mmol) in water (1 mL) was then slowly added to the mixture and stirred for 1 h 30 min at 0°C . The reaction was warmed up to room temperature and stirred for 72 h. A saturated aqueous solution of sodium thionate was added to quench the reaction. The aqueous phase was extracted with dichloromethane. Then, the organic phase washed with water and brine, dried with Na_2SO_4 , filtered, and concentrated in vacuum. The product was purified by chromatography (SiO_2 , cyclohexane: CH_2Cl_2 3:1) as a white powder (409 mg, 38% yield). $^1\text{H NMR}$ (400 MHz, CD_2Cl_2 , 298 K): δ (ppm) 6.22 (d, J = 1.9 Hz, 1H), 5.68 – 5.60 (m, 3H), 5.51 – 5.36 (m, 10H). $^{13}\text{C NMR}$ (101 MHz, CD_2Cl_2 , 298 K): δ (ppm) 145.77, 144.22, 142.21, 139.41, 138.37, 130.68, 129.72, 129.33, 128.39, 128.29, 128.10, 127.41, 127.29, 99.17. **APPI MS** m/z : calc for $\text{C}_{18}\text{H}_{13}\text{NO}_2$: 356.01; found: 356.01.

Nitro-disubstituted pentaphenyl compound **78**



77 (400 mg, 1.12 mmol), **64** (622 mg, 1.68 mmol), tetrakis(triphenylphosphine)-palladium(0) (127 mg, 0.11 mmol) and potassium carbonate (464 mg, 3.36 mmol) were dissolved in dimethylformamide (30 mL) previously degassed by freeze pump thaw. The reaction mixture was heated at 100°C overnight. Water and dichloromethane were added to the mixture. The organic phase was recovered, washed with water and brine, dried with Na₂SO₄, filtered, and concentrated in vacuum. The product was purified by chromatography (SiO₂, CH₂Cl₂:cyclohexane 7:3) as a pale-yellow powder (371 mg, 70% yield). **¹H NMR** (400 MHz, CDCl₃, 298 K): δ(ppm) 8.53 (d, *J* = 2.4 Hz, 1H), 8.26 (dd, *J* = 8.4, 2.4 Hz, 1H), 7.88 (d, *J* = 8.6 Hz, 2H), 7.78 (d, *J* = 1.9 Hz, 1H), 7.74 – 7.68 (m, 3H), 7.52 (t, *J* = 7.2 Hz, 2H), 7.43 (d, *J* = 7.4 Hz, 1H), 7.31 (d, *J* = 8.5 Hz, 1H), 7.27 (d, *J* = 8.0 Hz, 1H), 7.14 (d, *J* = 7.4 Hz, 1H), 7.02 (t, *J* = 7.7 Hz, 2H), 6.70 (d, *J* = 8.9 Hz, 2H), 6.51 (d, *J* = 7.4 Hz, 2H). **MALDI-ToF MS** *m/z*: calc for C₃₀H₂₀N₂O₄: 427.14; found: 427.17.

Amine-disubstituted pentaphenyl compound **79**



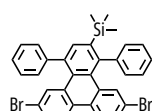
78 (360 mg, 0.76 mmol) was dissolved in methanol (75 mL), dichloromethane (100 mL), and ethyl acetate (25 mL), previously degassed sparging with argon for 5 min. Afterwards, palladium on carbon (51 mg, 10% Pd) was added to the mixture. The reaction mixture was shaken in a hydrogenator overnight at room temperature under a 3 bar hydrogen atmosphere. The reaction was stopped and filtered through a celite pad. The solvents were evaporated, and the product was purified by column chromatography (SiO₂, CH₂Cl₂:ethyl acetate 49:1) to give the product as an orange powder (123 mg, 40% yield). **¹H NMR** (400 MHz, CDCl₃, 298 K): δ(ppm) 7.68 – 7.63 (m, 3H), 7.56 (dd, *J* = 8.0, 2.1 Hz, 1H), 7.45 (t, *J* = 7.6 Hz, 2H), 7.35 (t, *J* = 7.5 Hz, 1H), 7.26 – 7.23 (m, 1H), 7.11 – 7.02 (m, 3H), 6.94 (d, *J* = 8.2 Hz, 1H), 6.81 – 6.75 (m, 3H), 6.66 (dd, *J* = 8.2, 2.5 Hz, 1H), 6.38 (d, *J* = 8.6 Hz, 2H), 6.32 (d, *J* = 8.6 Hz, 2H), 3.57 (d, *J* = 71.2 Hz, 4H). **MALDI-ToF MS** *m/z*: calc for C₃₀H₂₄N₂: 412.19; found: 412.20.

Nanomesh precursor **73**



79 (120 mg, 0.3 mmol) was dissolved in tetrahydrofuran (3 mL), water (73 mL), and aqueous hydrochloric acid (4 M, 2 mL), and the mixture cooled down to 0°C. A cold solution of sodium nitrite (50 mg, 0.72 mmol) in water (0.5 mL) was added very slowly to the mixture. The mixture was stirred for 30 min at 0°C. A cold solution of potassium iodide (250 g, 1.5 mmol) in water (0.5 mL) was then slowly added to the mixture. The reaction was warmed up to room temperature and stirred for 72 h. A saturated aqueous solution of sodium thionate was added to quench the reaction. The aqueous phase was extracted with dichloromethane. Then, the organic phase washed with water and brine, dried with Na₂SO₄, filtered, and concentrated in vacuum. The product was purified by chromatography (SiO₂, cyclohexane:CS₂ 1:1) as a white powder (75 mg, 39% yield). **¹H NMR** (400 MHz, CDCl₃, 298 K): δ(ppm) 7.92 (d, *J* = 1.9 Hz, 1H), 7.70 – 7.65 (m, 4H), 7.62 (dd, *J* = 8.0, 2.0 Hz, 1H), 7.49 (t, *J* = 7.4 Hz, 2H), 7.41 (t, *J* = 7.2 Hz, 1H), 7.30 (d, *J* = 8.6 Hz, 2H), 7.24 (d, *J* = 8.0 Hz, 1H), 7.10 (t, *J* = 7.1 Hz, 1H), 7.04 (t, *J* = 7.9 Hz, 2H), 6.83 (d, *J* = 8.1 Hz, 1H), 6.59 (d, *J* = 6.7 Hz, 2H), 6.25 (d, *J* = 8.4 Hz, 2H). **¹³C NMR** (101 MHz, CDCl₃, 298 K): δ(ppm) 142.18, 140.37, 140.33, 140.25, 140.11, 139.95, 139.65, 139.51, 138.53, 136.95, 136.84, 131.39, 130.87, 130.81, 130.12, 129.21, 129.06, 127.86, 127.76, 127.18, 126.90, 126.41, 93.27, 92.31. **MALDI-ToF MS** *m/z*: calc for C₃₀H₂₀I₂: 633.97; found: 633.97.

Trimethylsilyl protected dibromo nanomesh precursor **80**



CP-3 (450 mg, 0.74 mmol) were added to a schlenk, then dissolved in dry o-xylene (4 mL), previously degassed sparging argon. Ethynyltrimethylsilane (70 μL, 0.5 mmol) was added to the reaction mixture and then heated to 180°C overnight. The solvent was evaporated, and the product purified by flash column chromatography

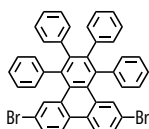
(SiO₂, cyclohexane:CH₂Cl₂ 9:1). The product was recovered as a white powder (136 mg, 77% yield). **¹H NMR** (400 MHz, CDCl₃, 298 K): δ(ppm) 8.21 – 8.16 (m, 2H), 7.85 (s, 1H), 7.79 (d, *J* = 2.0 Hz, 1H), 7.70 (d, *J* = 2.0 Hz, 1H), 7.53 – 7.43 (m, 10H), 7.40 – 7.35 (m, 2H), 0.07 (s, 9H). **¹³C NMR** (101 MHz, CDCl₃, 298 K): δ(ppm) 145.74, 144.49, 144.09, 140.40, 137.68, 137.15, 132.89, 132.38, 131.83, 131.25, 130.34, 130.07, 130.03, 129.73, 129.67, 129.64, 129.51, 129.17, 128.16, 127.71, 125.93, 124.66, 124.62, 120.19, 120.09, 1.09. **MALDI-ToF MS** *m/z*: calc for C₃₃H₂₆Br₂Si: 608.02; found: 608.01.

Dibromo-substituted nanomesh precursor **74**



80 (140 mg, 0.23 mmol) was dissolved in tetrahydrofuran (5 mL). Tetrabutylammonium fluoride (1 M in tetrahydrofuran, 280 μL, 0.28 mmol) was added dropwise and stirred under argon for 4 h at room temperature. Water was added to the reaction and then extracted with dichloromethane. The organic phase was washed with water and brine, dried with Na₂SO₄, filtered, and evaporated. The product was purified by a flash column chromatography (SiO₂, cyclohexane:CH₂Cl₂ 9:1) as a white powder (106 mg, 86% yield). **¹H NMR** (400 MHz, CDCl₃, 298 K): δ(ppm) 8.22 (d, *J* = 8.7 Hz, 2H), 7.77 (d, *J* = 2.0 Hz, 2H), 7.58 (s, 2H), 7.53 (dd, *J* = 8.7, 2.0 Hz, 2H), 7.49 – 7.41 (m, 10H). **¹³C NMR** (101 MHz, CDCl₃, 298 K): δ(ppm) 143.75, 139.53, 132.97, 131.93, 130.68, 130.23, 129.93, 129.59, 129.46, 129.40, 127.78, 124.72, 120.10. **MALDI-ToF MS** *m/z*: calc for C₃₃H₁₈Br₂: 535.98; found: 535.96.

GNR-precursor **81**^{153,266}



CP-3 (336 mg, 0.62 mmol) and diphenyl acetylene (100 mg, 0.33 mmol) were dissolved in *o*-xylene (5 mL) in a schlenk. The solution was degassed sparging argon and then heated to 180°C for overnight. After the mixture cooled down it was added to an excess methanol to precipitate the product as a white powder and then filtered through a PTFE. The powder was purified by column chromatography (SiO₂, cyclohexane:CH₂Cl₂ 9:1) to yield the product as a yellowish powder (80 mg, 22% yield). **¹H NMR** (400 MHz, CDCl₃, 298 K): δ(ppm) 8.20 (d, *J* = 8.6 Hz, 2H), 7.67 (d, *J* = 2.0 Hz, 2H), 7.48 (dd, *J* = 8.7, 2.1 Hz, 2H), 7.19 – 7.12 (m, 6H), 7.07 – 7.02 (m, 4H), 6.95 – 6.86 (m, 6H), 6.76 – 6.66 (m, 4H). **¹³C NMR** (101 MHz, CDCl₃, 298K): δ(ppm) 142.00, 141.39, 140.00, 137.72, 133.01, 132.44, 131.98, 131.53, 130.44, 129.67, 128.44, 126.91, 126.87, 125.63, 124.63, 120.26. **MALDI-ToF MS**: calc. for C₄₂H₂₆Br₂: 688.04; found: 688.03.

REFERENCES

- (1) Wallace, P. R. The Band Theory of Graphite. *Phys. Rev.* **1947**, *71* (9), 622–634. <https://doi.org/10.1103/PhysRev.71.622>.
- (2) McClure, J. W. Diamagnetism of Graphite. *Phys. Rev.* **1956**, *104* (3), 666–671. <https://doi.org/10.1103/PhysRev.104.666>.
- (3) Slonczewski, J. C.; Weiss, P. R. Band Structure of Graphite. *Phys. Rev.* **1958**, *109* (2), 272–279. <https://doi.org/10.1103/PhysRev.109.272>.
- (4) Novoselov, K. S.; Geim, A. K.; Morozov, S. V.; Jiang, D.; Zhang, Y.; Dubonos, S. V.; Grigorieva, I. V.; Firsov, A. A. Electric Field Effect in Atomically Thin Carbon Films. *Science* **2004**, *306* (5696), 666–669. <https://doi.org/10.1126/science.1102896>.
- (5) Novoselov, K. S.; Jiang, D.; Schedin, F.; Booth, T. J.; Khotkevich, V. V.; Morozov, S. V.; Geim, A. K. Two-Dimensional Atomic Crystals. *Proc. Natl. Acad. Sci.* **2005**, *102* (30), 10451–10453. <https://doi.org/10.1073/pnas.0502848102>.
- (6) *The Nobel Prize in Physics 2010*. NobelPrize.org. <https://www.nobelprize.org/prizes/physics/2010/summary/> (accessed 2020-03-18).
- (7) Woodward, P. M.; Karen, P.; Evans, J. S. O.; Vogt, T. *Solid State Materials Chemistry*, 1st ed.; Cambridge University Press, 2021. <https://doi.org/10.1017/9781139025348>.
- (8) Novoselov, K. S.; Geim, A. K.; Morozov, S. V.; Jiang, D.; Katsnelson, M. I.; Grigorieva, I. V.; Dubonos, S. V.; Firsov, A. A. Two-Dimensional Gas of Massless Dirac Fermions in Graphene. *Nature* **2005**, *438* (7065), 197–200. <https://doi.org/10.1038/nature04233>.
- (9) Nair, R. R.; Blake, P.; Grigorenko, A. N.; Novoselov, K. S.; Booth, T. J.; Stauber, T.; Peres, N. M. R.; Geim, A. K. Fine Structure Constant Defines Visual Transparency of Graphene. *Science* **2008**, *320* (5881), 1308–1308. <https://doi.org/10.1126/science.1156965>.
- (10) Chen, Y.; Yue, Y.; Wang, S.; Zhang, N.; Feng, J.; Sun, H. Graphene as a Transparent and Conductive Electrode for Organic Optoelectronic Devices. *Adv. Electron. Mater.* **2019**, *5* (10), 1900247. <https://doi.org/10.1002/aelm.201900247>.
- (11) Wang, X.; Zhi, L.; Müllen, K. Transparent, Conductive Graphene Electrodes for Dye-Sensitized Solar Cells. *Nano Lett.* **2008**, *8* (1), 323–327. <https://doi.org/10.1021/nl072838r>.
- (12) Chen, S.; Moore, A. L.; Cai, W.; Suk, J. W.; An, J.; Mishra, C.; Amos, C.; Magnuson, C. W.; Kang, J.; Shi, L.; Ruoff, R. S. Raman Measurements of Thermal Transport in Suspended Monolayer Graphene of Variable Sizes in Vacuum and Gaseous Environments. *ACS Nano* **2011**, *5* (1), 321–328. <https://doi.org/10.1021/nn102915x>.
- (13) Sang, M.; Shin, J.; Kim, K.; Yu, K. Electronic and Thermal Properties of Graphene and Recent Advances in Graphene Based Electronics Applications. *Nanomaterials* **2019**, *9* (3), 374. <https://doi.org/10.3390/nano9030374>.
- (14) Ho, D. H.; Sun, Q.; Kim, S. Y.; Han, J. T.; Kim, D. H.; Cho, J. H. Stretchable and Multimodal All Graphene Electronic Skin. *Adv. Mater.* **2016**, *28* (13), 2601–2608. <https://doi.org/10.1002/adma.201505739>.
- (15) Kumar, P.; Shahzad, F.; Yu, S.; Hong, S. M.; Kim, Y.-H.; Koo, C. M. Large-Area Reduced Graphene Oxide Thin Film with Excellent Thermal Conductivity and Electromagnetic Interference Shielding Effectiveness. *Carbon* **2015**, *94*, 494–500. <https://doi.org/10.1016/j.carbon.2015.07.032>.
- (16) Han, H.; Zhang, Y.; Wang, N.; Samani, M. K.; Ni, Y.; Mijbil, Z. Y.; Edwards, M.; Xiong, S.; Säskilahti, K.; Murugesan, M.; Fu, Y.; Ye, L.; Sadeghi, H.; Bailey, S.; Kosevich, Y. A.; Lambert, C. J.; Liu, J.; Volz, S. Functionalization Mediates Heat Transport in Graphene Nanoflakes. *Nat. Commun.* **2016**, *7* (1), 11281. <https://doi.org/10.1038/ncomms11281>.
- (17) Lee, C.; Wei, X.; Kysar, J. W.; Hone, J. Measurement of the Elastic Properties and Intrinsic Strength of Monolayer Graphene. *Science* **2008**, *321* (5887), 385–388. <https://doi.org/10.1126/science.1157996>.
- (18) Luecke, W. E.; McColskey, J. D.; McCowan, C. N.; Banovic, S. W.; Fields, R. J.; Foecke, T.; Siewert, T. A.; Gayle, F. W. *Mechanical Properties of Structural Steel*, 0 ed.; NIST NCSTAR 1-3d; National Institute of Standards and Technology: Gaithersburg, MD, 2005; p NIST NCSTAR 1-3d. <https://doi.org/10.6028/NIST.NCSTAR.1-3d>.
- (19) Lee, J.-H.; Loya, P. E.; Lou, J.; Thomas, E. L. Dynamic Mechanical Behavior of Multilayer Graphene via Supersonic Projectile Penetration. *Science* **2014**, *346* (6213), 1092–1096. <https://doi.org/10.1126/science.1258544>.
- (20) Al Faruque, M. A.; Syduzzaman, M.; Sarkar, J.; Bilisik, K.; Naebe, M. A Review on the Production Methods and Applications of Graphene-Based Materials. *Nanomaterials* **2021**, *11* (9), 2414. <https://doi.org/10.3390/nano11092414>.

- (21) Fu, B.; Gao, J. Study on the Application of Graphene Polymer Material in Sports Equipment. *J. Phys. Conf. Ser.* **2020**, *1676* (1), 012044. <https://doi.org/10.1088/1742-6596/1676/1/012044>.
- (22) Othman, N. H.; Che Ismail, M.; Mustapha, M.; Sallih, N.; Kee, K. E.; Ahmad Jaal, R. Graphene-Based Polymer Nanocomposites as Barrier Coatings for Corrosion Protection. *Prog. Org. Coat.* **2019**, *135*, 82–99. <https://doi.org/10.1016/j.porgcoat.2019.05.030>.
- (23) Bolotin, K. I.; Sikes, K. J.; Jiang, Z.; Klima, M.; Fudenberg, G.; Hone, J.; Kim, P.; Stormer, H. L. Ultrahigh Electron Mobility in Suspended Graphene. *Solid State Commun.* **2008**, *146* (9), 351–355. <https://doi.org/10.1016/j.ssc.2008.02.024>.
- (24) Kedzierski, J.; Hsu, P.-L.; Healey, P.; Wyatt, P.; Keast, C. Epitaxial Graphene Transistors on SiC Substrates. In *2008 Device Research Conference*; IEEE: Santa Barbara, CA, USA, 2008; pp 25–26. <https://doi.org/10.1109/DRC.2008.4800720>.
- (25) Ohta, T.; Bostwick, A.; Seyller, T.; Horn, K.; Rotenberg, E. Controlling the Electronic Structure of Bilayer Graphene. *Science* **2006**, *313* (5789), 951–954. <https://doi.org/10.1126/science.1130681>.
- (26) Zhou, S. Y.; Gweon, G.-H.; Fedorov, A. V.; First, P. N.; de Heer, W. A.; Lee, D.-H.; Guinea, F.; Castro Neto, A. H.; Lanzara, A. Substrate-Induced Bandgap Opening in Epitaxial Graphene. *Nat. Mater.* **2007**, *6* (10), 770–775. <https://doi.org/10.1038/nmat2003>.
- (27) Wang, E.; Lu, X.; Ding, S.; Yao, W.; Yan, M.; Wan, G.; Deng, K.; Wang, S.; Chen, G.; Ma, L.; Jung, J.; Fedorov, A. V.; Zhang, Y.; Zhang, G.; Zhou, S. Gaps Induced by Inversion Symmetry Breaking and Second-Generation Dirac Cones in Graphene/Hexagonal Boron Nitride. *Nat. Phys.* **2016**, *12* (12), 1111–1115. <https://doi.org/10.1038/nphys3856>.
- (28) Elias, D. C.; Nair, R. R.; Mohiuddin, T. M. G.; Morozov, S. V.; Blake, P.; Halsall, M. P.; Ferrari, A. C.; Boukhvalov, D. W.; Katsnelson, M. I.; Geim, A. K.; Novoselov, K. S. Control of Graphene's Properties by Reversible Hydrogenation: Evidence for Graphane. *Science* **2009**, *323* (5914), 610–613. <https://doi.org/10.1126/science.1167130>.
- (29) Robinson, J. T.; Burgess, J. S.; Junkermeier, C. E.; Badescu, S. C.; Reinecke, T. L.; Perkins, F. K.; Zalalutdniov, M. K.; Baldwin, J. W.; Culbertson, J. C.; Sheehan, P. E.; Snow, E. S. Properties of Fluorinated Graphene Films. *Nano Lett.* **2010**, *10* (8), 3001–3005. <https://doi.org/10.1021/nl101437p>.
- (30) Nair, R. R.; Ren, W.; Jalil, R.; Riaz, I.; Kravets, V. G.; Britnell, L.; Blake, P.; Schedin, F.; Mayorov, A. S.; Yuan, S.; Katsnelson, M. I.; Cheng, H.-M.; Strupinski, W.; Bulusheva, L. G.; Okotrub, A. V.; Grigorieva, I. V.; Grigorenko, A. N.; Novoselov, K. S.; Geim, A. K. Fluorographene: A Two-Dimensional Counterpart of Teflon. *Small* **2010**, *6* (24), 2877–2884. <https://doi.org/10.1002/sml.201001555>.
- (31) Cheng, S.-H.; Zou, K.; Okino, F.; Gutierrez, H. R.; Gupta, A.; Shen, N.; Eklund, P. C.; Sofu, J. O.; Zhu, J. Reversible Fluorination of Graphene: Evidence of a Two-Dimensional Wide Bandgap Semiconductor. *Phys. Rev. B* **2010**, *81* (20), 205435. <https://doi.org/10.1103/PhysRevB.81.205435>.
- (32) Kovtyukhova, N. I.; Ollivier, P. J.; Martin, B. R.; Mallouk, T. E.; Chizhik, S. A.; Buzaneva, E. V.; Gorchinskiy, A. D. Layer-by-Layer Assembly of Ultrathin Composite Films from Micron-Sized Graphite Oxide Sheets and Polycations. *Chem. Mater.* **1999**, *11* (3), 771–778. <https://doi.org/10.1021/cm981085u>.
- (33) Pei, S.; Cheng, H.-M. The Reduction of Graphene Oxide. *Carbon* **2012**, *50* (9), 3210–3228. <https://doi.org/10.1016/j.carbon.2011.11.010>.
- (34) Jin, Y.; Zheng, Y.; Podkolzin, S. G.; Lee, W. Band Gap of Reduced Graphene Oxide Tuned by Controlling Functional Groups. *J. Mater. Chem. C* **2020**, *8* (14), 4885–4894. <https://doi.org/10.1039/C9TC07063J>.
- (35) Nourbakhsh, A.; Cantoro, M.; Vosch, T.; Pourtois, G.; Clemente, F.; van der Veen, M. H.; Hofkens, J.; Heyns, M. M.; De Gendt, S.; Sels, B. F. Bandgap Opening in Oxygen Plasma-Treated Graphene. *Nanotechnology* **2010**, *21* (43), 435203. <https://doi.org/10.1088/0957-4484/21/43/435203>.
- (36) Huang, H.; Li, Z.; She, J.; Wang, W. Oxygen Density Dependent Band Gap of Reduced Graphene Oxide. *J. Appl. Phys.* **2012**, *111* (5), 054317. <https://doi.org/10.1063/1.3694665>.
- (37) Usachov, D.; Vilkov, O.; Grüneis, A.; Haberer, D.; Fedorov, A.; Adamchuk, V. K.; Preobrajenski, A. B.; Dudin, P.; Barinov, A.; Oehzelt, M.; Laubschat, C.; Vyalikh, D. V. Nitrogen-Doped Graphene: Efficient Growth, Structure, and Electronic Properties. *Nano Lett.* **2011**, *11* (12), 5401–5407. <https://doi.org/10.1021/nl2031037>.
- (38) Chang, C.-K.; Kataria, S.; Kuo, C.-C.; Ganguly, A.; Wang, B.-Y.; Hwang, J.-Y.; Huang, K.-J.; Yang, W.-H.; Wang, S.-B.; Chuang, C.-H.; Chen, M.; Huang, C.-I.; Pong, W.-F.; Song, K.-J.; Chang, S.-J.; Guo, J.-H.; Tai, Y.; Tsujimoto, M.; Isoda, S.; Chen, C.-W.;

- Chen, L.-C.; Chen, K.-H. Band Gap Engineering of Chemical Vapor Deposited Graphene by *in Situ* BN Doping. *ACS Nano* **2013**, *7* (2), 1333–1341. <https://doi.org/10.1021/nn3049158>.
- (39) Susi, T.; Hardcastle, T. P.; Hofsäss, H.; Mittelberger, A.; Pennycook, T. J.; Mangler, C.; Drummond-Brydson, R.; Scott, A. J.; Meyer, J. C.; Kotakoski, J. Single-Atom Spectroscopy of Phosphorus Dopants Implanted into Graphene. *2D Mater.* **2017**, *4* (2), 021013. <https://doi.org/10.1088/2053-1583/aa5e78>.
- (40) Ramasse, Q. M.; Seabourne, C. R.; Kepaptsoglou, D.-M.; Zan, R.; Bangert, U.; Scott, A. J. Probing the Bonding and Electronic Structure of Single Atom Dopants in Graphene with Electron Energy Loss Spectroscopy. *Nano Lett.* **2013**, *13* (10), 4989–4995. <https://doi.org/10.1021/nl304187e>.
- (41) Susi, T.; Meyer, J. C.; Kotakoski, J. Manipulating Low-Dimensional Materials down to the Level of Single Atoms with Electron Irradiation. *Ultramicroscopy* **2017**, *180*, 163–172. <https://doi.org/10.1016/j.ultramic.2017.03.005>.
- (42) Robertson, A. W.; Montanari, B.; He, K.; Kim, J.; Allen, C. S.; Wu, Y. A.; Olivier, J.; Neethling, J.; Harrison, N.; Kirkland, A. I.; Warner, J. H. Dynamics of Single Fe Atoms in Graphene Vacancies. *Nano Lett.* **2013**, *13* (4), 1468–1475. <https://doi.org/10.1021/nl304495v>.
- (43) Lin, P.-C.; Villarreal, R.; Achilli, S.; Bana, H.; Nair, M. N.; Tejada, A.; Verguts, K.; De Gendt, S.; Auge, M.; Hofsäss, H.; De Feyter, S.; Di Santo, G.; Petaccia, L.; Brems, S.; Fratesi, G.; Pereira, L. M. C. Doping Graphene with Substitutional Mn. *ACS Nano* **2021**, *15* (3), 5449–5458. <https://doi.org/10.1021/acsnano.1c00139>.
- (44) Wang, H.; Wang, Q.; Cheng, Y.; Li, K.; Yao, Y.; Zhang, Q.; Dong, C.; Wang, P.; Schwingenschlögl, U.; Yang, W.; Zhang, X. X. Doping Monolayer Graphene with Single Atom Substitutions. *Nano Lett.* **2012**, *12* (1), 141–144. <https://doi.org/10.1021/nl2031629>.
- (45) Mousavi, H.; Moradian, R. Nitrogen and Boron Doping Effects on the Electrical Conductivity of Graphene and Nanotube. *Solid State Sci.* **2011**, *13* (8), 1459–1464. <https://doi.org/10.1016/j.solidstatesciences.2011.03.008>.
- (46) Eda, G.; Fanchini, G.; Chhowalla, M. Large-Area Ultrathin Films of Reduced Graphene Oxide as a Transparent and Flexible Electronic Material. *Nat. Nanotechnol.* **2008**, *3* (5), 270–274. <https://doi.org/10.1038/nnano.2008.83>.
- (47) Ohta, T.; Bostwick, A.; Seyller, T.; Horn, K.; Rotenberg, E. Controlling the Electronic Structure of Bilayer Graphene. *Science* **2006**, *313* (5789), 951–954. <https://doi.org/10.1126/science.1130681>.
- (48) Liang, Y.; Yang, L. Electronic Structure and Optical Absorption of Fluorographene. *MRS Proc.* **2011**, *1370*, mrss11-1370-yy04-02. <https://doi.org/10.1557/opl.2011.894>.
- (49) Pedersen, T. G.; Flindt, C.; Pedersen, J.; Mortensen, N. A.; Jauho, A.-P.; Pedersen, K. Graphene Antidot Lattices: Designed Defects and Spin Qubits. *Phys. Rev. Lett.* **2008**, *100* (13), 136804. <https://doi.org/10.1103/PhysRevLett.100.136804>.
- (50) He, S.; Turnbull, M. J.; Nie, Y.; Sun, X.; Ding, Z. Band Structures of Blue Luminescent Nitrogen-Doped Graphene Quantum Dots by Synchrotron-Based XPS. *Surf. Sci.* **2018**, *676*, 51–55. <https://doi.org/10.1016/j.susc.2018.01.013>.
- (51) Li, X.; Cai, W.; An, J.; Kim, S.; Nah, J.; Yang, D.; Piner, R.; Velamakanni, A.; Jung, I.; Tutuc, E.; Banerjee, S. K.; Colombo, L.; Ruoff, R. S. Large-Area Synthesis of High-Quality and Uniform Graphene Films on Copper Foils. *Science* **2009**, *324* (5932), 1312–1314. <https://doi.org/10.1126/science.1171245>.
- (52) Hummers, W. S.; Offeman, R. E. Preparation of Graphitic Oxide. *J. Am. Chem. Soc.* **1958**, *80* (6), 1339–1339. <https://doi.org/10.1021/ja01539a017>.
- (53) Shen, J.; Zhu, Y.; Chen, C.; Yang, X.; Li, C. Facile Preparation and Upconversion Luminescence of Graphene Quantum Dots. *Chem Commun* **2011**, *47* (9), 2580–2582. <https://doi.org/10.1039/C0CC04812G>.
- (54) Pan, D.; Zhang, J.; Li, Z.; Wu, M. Hydrothermal Route for Cutting Graphene Sheets into Blue-Luminescent Graphene Quantum Dots. *Adv. Mater.* **2010**, *22* (6), 734–738. <https://doi.org/10.1002/adma.200902825>.
- (55) Shen, J.; Zhu, Y.; Yang, X.; Li, C. Graphene Quantum Dots: Emergent Nanolights for Bioimaging, Sensors, Catalysis and Photovoltaic Devices. *Chem. Commun.* **2012**, *48* (31), 3686. <https://doi.org/10.1039/c2cc00110a>.
- (56) Ahirwar, S.; Mallick, S.; Bahadur, D. Electrochemical Method To Prepare Graphene Quantum Dots and Graphene Oxide Quantum Dots. *ACS Omega* **2017**, *2* (11), 8343–8353. <https://doi.org/10.1021/acsomega.7b01539>.
- (57) Kang, H.; Kim, D. Y.; Cho, J. Top-Down Fabrication of Luminescent Graphene Quantum Dots Using Self-Assembled Au Nanoparticles. *ACS Omega* **2023**, *8* (6), 5885–5892. <https://doi.org/10.1021/acsomega.2c07683>.

- (58) Haque, E.; Kim, J.; Malgras, V.; Reddy, K. R.; Ward, A. C.; You, J.; Bando, Y.; Hossain, Md. S. A.; Yamauchi, Y. Recent Advances in Graphene Quantum Dots: Synthesis, Properties, and Applications. *Small Methods* **2018**, *2* (10), 1800050. <https://doi.org/10.1002/smt.201800050>.
- (59) Ghaffarkhah, A.; Hosseini, E.; Kamkar, M.; Sehat, A. A.; Dordanihaghighi, S.; Allahbakhsh, A.; Kuur, C.; Arjmand, M. Synthesis, Applications, and Prospects of Graphene Quantum Dots: A Comprehensive Review. *Small* **2022**, *18* (2), 2102683. <https://doi.org/10.1002/sml.202102683>.
- (60) Ravindra, K.; Sokhi, R.; Van Grieken, R. Atmospheric Polycyclic Aromatic Hydrocarbons: Source Attribution, Emission Factors and Regulation. *Atmos. Environ.* **2008**, *42* (13), 2895–2921. <https://doi.org/10.1016/j.atmosenv.2007.12.010>.
- (61) Scholl, R. Pyranthron, Ein Stickstoffreies Methinanalogen Des Flavanthrens, Und Dimethylpyranthron. *Berichte Dtsch. Chem. Ges.* **1910**, *43* (1), 346–356. <https://doi.org/10.1002/cber.19100430155>.
- (62) Scholl, R.; Meyer, K. Synthese Des *Anti-diperi* -Dibenz-coronens Und Dessen Abbau Zum Coronen (Hexabenzobenzol). (Mitbearbeitet von Horst v. Hoeßle Und Solon Brissimdj). *Berichte Dtsch. Chem. Ges. B Ser.* **1932**, *65* (5), 902–915. <https://doi.org/10.1002/cber.19320650546>.
- (63) Bally, O.; Scholl, R. Einwirkung von Glycerin Und Schwefelsäure Auf Amidierte Und Auf Stickstofffreie Verbindungen Der Anthracen-Reihe: Benzanthron Und Seine Reduktionsprodukte, Nebst Bemerkungen Über Namenbildung Und Ortsbezeichnung Hochgegliederter Ringsysteme Der Anthracen-Reihe. *Berichte Dtsch. Chem. Ges.* **1911**, *44* (2), 1656–1670. <https://doi.org/10.1002/cber.19110440264>.
- (64) Clar, E.; Zander, M. Syntheses of Coronene and 1 : 2-7 : 8-Dibenzocoronene. *J. Chem. Soc. Resumed* **1957**, 4616. <https://doi.org/10.1039/jr9570004616>.
- (65) Clar, E.; Schoental, R. *Polycyclic Hydrocarbons: Volume 1*; Springer Berlin / Heidelberg: Berlin, Heidelberg, 2013.
- (66) Clar, E.; Ironside, C. T.; Zander, M. The Electronic Interaction between Benzenoid Rings in Condensed Aromatic Hydrocarbons. 1 : 12-2 : 3-4 : 5-6 : 7-8 : 9-10 : 11-Hexabenzocoronene, 1 : 2-3 : 4-5 : 6-10 : 11-Tetrabenzoanthanthrene, and 4 : 5-6 : 7-11 : 12-13 : 14-Tetrabenzoperopyrene. *J. Chem. Soc. Resumed* **1959**, 142. <https://doi.org/10.1039/jr9590000142>.
- (67) Halleux, A.; Martin, R. H.; King, G. S. D. Synthèses Dans La Série Des Dérivés Polycycliques Aromatiques Hautement Condensés. L'hexabenzobenzol, 1,2; 2,3; 4,5; 6,7; 8,9; 10,11-Coronène, Le tétrabenzobenzol, 4,5; 6,7; 11,12; 13,14-Péropyrène et Le tétrabenzobenzol, 1,2; 3,4; 8,9; 10,11-Bisanthène. *Helv. Chim. Acta* **1958**, *41* (5), 1177–1183. <https://doi.org/10.1002/hlca.19580410502>.
- (68) Stabel, A.; Herwig, P.; Müllen, K.; Rabe, J. P. Diodelike Current–Voltage Curves for a Single Molecule–Tunneling Spectroscopy with Submolecular Resolution of an Alkylated, Peri-Condensed Hexabenzocoronene. *Angew. Chem. Int. Ed. Engl.* **1995**, *34* (15), 1609–1611. <https://doi.org/10.1002/anie.199516091>.
- (69) Iyer, V. S.; Wehmeier, M.; Brand, J. D.; Keegstra, M. A.; Müllen, K. From Hexa-Peri-Hexabenzocoronene to “Superacenes.” *Angew. Chem. Int. Ed. Engl.* **1997**, *36* (15), 1604–1607. <https://doi.org/10.1002/anie.199716041>.
- (70) Diltthey, W.; Schommer, W.; Höschen, W.; Die-richs, H. Hocharylierte Aromatische Verbindungen (V. Mitteil.). *Berichte Dtsch. Chem. Ges. B Ser.* **1935**, *68* (6), 1159–1162. <https://doi.org/10.1002/cber.19350680634>.
- (71) Ried, W.; Bönnighausen, K. H. Diensynthesen Mit Diinen. *Chem. Ber.* **1960**, *93* (8), 1769–1773. <https://doi.org/10.1002/cber.19600930812>.
- (72) Ogliaruso, M. A.; Shadoff, L. A.; Becker, E. I. “Bistetracyclones” and “Bishexaphenylbenzenes.” *J. Org. Chem.* **1963**, *28* (10), 2725–2728. <https://doi.org/10.1021/jo01045a055>.
- (73) Roglans, A.; Pla-Quintana, A.; Solà, M. Mechanistic Studies of Transition-Metal-Catalyzed [2 + 2 + 2] Cycloaddition Reactions. *Chem. Rev.* **2021**, *121* (3), 1894–1979. <https://doi.org/10.1021/acs.chemrev.0c00062>.
- (74) Dyan, O. T.; Borodkin, G. I.; Zaikin, P. A. The Diels-Alder Reaction for the Synthesis of Polycyclic Aromatic Compounds: The Diels-Alder Reaction for the Synthesis of Polycyclic Aromatic Compounds. *Eur. J. Org. Chem.* **2019**, *2019* (44), 7271–7306. <https://doi.org/10.1002/ejoc.201901254>.
- (75) Johansson Seechurn, C. C. C.; Kitching, M. O.; Colacot, T. J.; Snieckus, V. Palladium-Catalyzed Cross-Coupling: A Historical Contextual Perspective to the 2010 Nobel Prize. *Angew. Chem. Int. Ed.* **2012**, *51* (21), 5062–5085. <https://doi.org/10.1002/anie.201107017>.

- (76) Wu, J.; Pisula, W.; Müllen, K. Graphenes as Potential Material for Electronics. *Chem. Rev.* **2007**, *107* (3), 718–747. <https://doi.org/10.1021/cr068010r>.
- (77) Iyer, V. S.; Yoshimura, K.; Enkelmann, V.; Epsch, R.; Rabe, J. P.; Müllen, K. A Soluble C60 Graphite Segment. *Angew. Chem. Int. Ed.* **1998**, *37* (19), 2696–2699. [https://doi.org/10.1002/\(SICI\)1521-3773\(19981016\)37:19<2696::AID-ANIE2696>3.0.CO;2-E](https://doi.org/10.1002/(SICI)1521-3773(19981016)37:19<2696::AID-ANIE2696>3.0.CO;2-E).
- (78) Müller, M.; Kübel, C.; Müllen, K. Giant Polycyclic Aromatic Hydrocarbons. *Chem. – Eur. J.* **1998**, *4* (11), 2099–2109. [https://doi.org/10.1002/\(SICI\)1521-3765\(19981102\)4:11<2099::AID-CHEM2099>3.0.CO;2-T](https://doi.org/10.1002/(SICI)1521-3765(19981102)4:11<2099::AID-CHEM2099>3.0.CO;2-T).
- (79) Dötz, F.; Brand, J. D.; Ito, S.; Gherghel, L.; Müllen, K. Synthesis of Large Polycyclic Aromatic Hydrocarbons: Variation of Size and Periphery. *J. Am. Chem. Soc.* **2000**, *122* (32), 7707–7717. <https://doi.org/10.1021/ja000832x>.
- (80) Lavie, J.; Vu, V. B.; Medina-Lopez, D.; Dappe, Y.; Liu, T.; Rondin, L.; Lauret, J.-S.; Latil, S.; Campidelli, S. Bottom-up Synthesis, Dispersion and Properties of Rectangular-shaped Graphene Quantum Dots. *Helv. Chim. Acta* **2023**, e202300034. <https://doi.org/10.1002/hlca.202300034>.
- (81) Simpson, C. D.; Brand, J. D.; Berresheim, A. J.; Przybilla, L.; Räder, H. J.; Müllen, K. Synthesis of a Giant 222 Carbon Graphite Sheet. *Chem. – Eur. J.* **2002**, *8* (6), 1424–1429. [https://doi.org/10.1002/1521-3765\(20020315\)8:6<1424::AID-CHEM1424>3.0.CO;2-Z](https://doi.org/10.1002/1521-3765(20020315)8:6<1424::AID-CHEM1424>3.0.CO;2-Z).
- (82) Yan, X.; Cui, X.; Li, L. Synthesis of Large, Stable Colloidal Graphene Quantum Dots with Tunable Size. *J. Am. Chem. Soc.* **2010**, *132* (17), 5944–5945. <https://doi.org/10.1021/ja1009376>.
- (83) Ponugoti, N.; Parthasarathy, V. Rearrangements in Scholl Reaction. *Chem. – Eur. J.* **2022**, *28* (17). <https://doi.org/10.1002/chem.202103530>.
- (84) Weiss, K.; Beernink, G.; Dötz, F.; Birkner, A.; Müllen, K.; Wöll, C. H. Template-Mediated Synthesis of Polycyclic Aromatic Hydrocarbons: Cyclodehydrogenation and Planarization of a Hexaphenylbenzene Derivative at a Copper Surface. *Angew. Chem. Int. Ed.* **1999**, *38* (24), 3748–3752. [https://doi.org/10.1002/\(SICI\)1521-3773\(19991216\)38:24<3748::AID-ANIE3748>3.0.CO;2-0](https://doi.org/10.1002/(SICI)1521-3773(19991216)38:24<3748::AID-ANIE3748>3.0.CO;2-0).
- (85) Zhai, L.; Shukla, R.; Rathore, R. Oxidative C–C Bond Formation (Scholl Reaction) with DDQ as an Efficient and Easily Recyclable Oxidant. *Org. Lett.* **2009**, *11* (15), 3474–3477. <https://doi.org/10.1021/ol901331p>.
- (86) King, B. T.; Kroulík, J.; Robertson, C. R.; Rempala, P.; Hilton, C. L.; Korinek, J. D.; Gortari, L. M. Controlling the Scholl Reaction. *J. Org. Chem.* **2007**, *72* (7), 2279–2288. <https://doi.org/10.1021/jo061515x>.
- (87) Wasserfallen, D.; Kastler, M.; Pisula, W.; Hofer, W. A.; Fogel, Y.; Wang, Z.; Müllen, K. Suppressing Aggregation in a Large Polycyclic Aromatic Hydrocarbon. *J. Am. Chem. Soc.* **2006**, *128* (4), 1334–1339. <https://doi.org/10.1021/ja056782j>.
- (88) Müller, M.; Iyer, V. S.; Kübel, C.; Enkelmann, V.; Müllen, K. Polycyclic Aromatic Hydrocarbons by Cyclodehydrogenation and Skeletal Rearrangement of Oligophenylenes. *Angew. Chem. Int. Ed. Engl.* **1997**, *36* (15), 1607–1610. <https://doi.org/10.1002/anie.199716071>.
- (89) Tomović, Ž.; Watson, M. D.; Müllen, K. Superphenalene-Based Columnar Liquid Crystals. *Angew. Chem. Int. Ed.* **2004**, *43* (6), 755–758. <https://doi.org/10.1002/anie.200352855>.
- (90) Zhao, X.-J.; Hou, H.; Fan, X.-T.; Wang, Y.; Liu, Y.-M.; Tang, C.; Liu, S.-H.; Ding, P.-P.; Cheng, J.; Lin, D.-H.; Wang, C.; Yang, Y.; Tan, Y.-Z. Molecular Bilayer Graphene. *Nat. Commun.* **2019**, *10* (1), 1–7. <https://doi.org/10.1038/s41467-019-11098-9>.
- (91) Morgenroth, F.; Reuther, E.; Müllen, K. Polyphenylene Dendrimers: From Three-Dimensional to Two-Dimensional Structures. *Angew. Chem. Int. Ed. Engl.* **1997**, *36* (6), 631–634. <https://doi.org/10.1002/anie.199706311>.
- (92) Wu, J.; Tomović, Ž.; Enkelmann, V.; Müllen, K. From Branched Hydrocarbon Propellers to C₃-Symmetric Graphite Disks. *J. Org. Chem.* **2004**, *69* (16), 5179–5186. <https://doi.org/10.1021/jo049452a>.
- (93) Clar, E. *Aromatic Sextet*; New York, Wiley, 1972.
- (94) Solà, M. Forty Years of Clar's Aromatic π -Sextet Rule. *Front. Chem.* **2013**, *1*. <https://doi.org/10.3389/fchem.2013.00022>.
- (95) Sun, Z.; Lee, S.; Park, K. H.; Zhu, X.; Zhang, W.; Zheng, B.; Hu, P.; Zeng, Z.; Das, S.; Li, Y.; Chi, C.; Li, R.-W.; Huang, K.-W.; Ding, J.; Kim, D.; Wu, J. Dibenzoheptazethrene Isomers with Different Biradical Characters: An Exercise of Clar's Aromatic Sextet Rule in Singlet Biradicaloids. *J. Am. Chem. Soc.* **2013**, *135* (48), 18229–18236. <https://doi.org/10.1021/ja410279j>.
- (96) Stein, S. E.; Brown, R. L. π -Electron Properties of Large Condensed Polyaromatic Hydrocarbons. *J. Am. Chem. Soc.* **1987**, *109* (12), 3721–3729. <https://doi.org/10.1021/ja00246a033>.

- (97) Schuler, B.; Collazos, S.; Gross, L.; Meyer, G.; Pérez, D.; Guitián, E.; Peña, D. From Perylene to a 22-Ring Aromatic Hydrocarbon in One-Pot. *Angew. Chem. Int. Ed.* **2014**, *53* (34), 9004–9006. <https://doi.org/10.1002/anie.201403707>.
- (98) Rüdiger, E. C.; Porz, M.; Schaffroth, M.; Rominger, F.; Bunz, U. H. F. Synthesis of Soluble, Alkyne-Substituted Trideca- and Hexadeca-Starphenes. *Chem. - Eur. J.* **2014**, *20* (40), 12725–12728. <https://doi.org/10.1002/chem.201403697>.
- (99) Iuliano, A.; Piccioli, P.; Fabbri, D. Ring-Closing Olefin Metathesis of 2,2'-Divinylbiphenyls: A Novel and General Approach to Phenanthrenes. *Org. Lett.* **2004**, *6* (21), 3711–3714. <https://doi.org/10.1021/ol048668w>.
- (100) Bonifacio, M. C.; Robertson, C. R.; Jung, J.-Y.; King, B. T. Polycyclic Aromatic Hydrocarbons by Ring-Closing Metathesis. *J. Org. Chem.* **2005**, *70* (21), 8522–8526. <https://doi.org/10.1021/jo051418o>.
- (101) Yao, T.; Campo, M. A.; Larock, R. C. Synthesis of Polycyclic Aromatic Iodides via ICl-Induced Intramolecular Cyclization. *Org. Lett.* **2004**, *6* (16), 2677–2680. <https://doi.org/10.1021/ol049161o>.
- (102) Shen, H.-C.; Tang, J.-M.; Chang, H.-K.; Yang, C.-W.; Liu, R.-S. Short and Efficient Synthesis of Coronene Derivatives via Ruthenium-Catalyzed Benzannulation Protocol. *J. Org. Chem.* **2005**, *70* (24), 10113–10116. <https://doi.org/10.1021/jo0512599>.
- (103) Wang, X.-Y.; Yao, X.; Müllen, K. Polycyclic Aromatic Hydrocarbons in the Graphene Era. *Sci. China Chem.* **2019**, *62* (9), 1099–1144. <https://doi.org/10.1007/s11426-019-9491-2>.
- (104) Ito, H.; Segawa, Y.; Murakami, K.; Itami, K. Polycyclic Arene Synthesis by Annulative π -Extension. *J. Am. Chem. Soc.* **2019**, *141* (1), 3–10. <https://doi.org/10.1021/jacs.8b09232>.
- (105) Fort, E. H.; Scott, L. T. One-Step Conversion of Aromatic Hydrocarbon Bay Regions into Unsubstituted Benzene Rings: A Reagent for the Low-Temperature, Metal-Free Growth of Single-Chirality Carbon Nanotubes. *Angew. Chem. Int. Ed.* **2010**, *49* (37), 6626–6628. <https://doi.org/10.1002/anie.201002859>.
- (106) Chen, Q.; Schollmeyer, D.; Müllen, K.; Narita, A. Synthesis of Circumphyrene by Alkyne Benzannulation of Brominated Dibenzo[*Hi*, *St*]Ovalene. *J. Am. Chem. Soc.* **2019**, *141* (51), 19994–19999. <https://doi.org/10.1021/jacs.9b10957>.
- (107) Przybilla, L.; Brand, J.-D.; Yoshimura, K.; Räder, H. J.; Müllen, K. MALDI-TOF Mass Spectrometry of Insoluble Giant Polycyclic Aromatic Hydrocarbons by a New Method of Sample Preparation. *Anal. Chem.* **2000**, *72* (19), 4591–4597. <https://doi.org/10.1021/ac000372q>.
- (108) Kawasumi, K.; Zhang, Q.; Segawa, Y.; Scott, L. T.; Itami, K. A Grossly Warped Nanographene and the Consequences of Multiple Odd-Membered-Ring Defects. *Nat. Chem.* **2013**, *5* (9), 739–744. <https://doi.org/10.1038/nchem.1704>.
- (109) Li, Y.; Jia, Z.; Xiao, S.; Liu, H.; Li, Y. A Method for Controlling the Synthesis of Stable Twisted Two-Dimensional Conjugated Molecules. *Nat. Commun.* **2016**, *7* (1), 11637. <https://doi.org/10.1038/ncomms11637>.
- (110) Márquez, I. R.; Castro-Fernández, S.; Millán, A.; Campaña, A. G. Synthesis of Distorted Nanographenes Containing Seven- and Eight-Membered Carbocycles. *Chem. Commun.* **2018**, *54* (50), 6705–6718. <https://doi.org/10.1039/C8CC02325E>.
- (111) Zhu, Y.; Wang, J. Helical Synthetic Nanographenes with Atomic Precision. *Acc. Chem. Res.* **2023**, *56* (3), 363–373. <https://doi.org/10.1021/acs.accounts.2c00767>.
- (112) Simpson, C. D.; Mattersteig, G.; Martin, K.; Gherghel, L.; Bauer, R. E.; Räder, H. J.; Müllen, K. Nanosized Molecular Propellers by Cyclodehydrogenation of Polyphenylene Dendrimers. *J. Am. Chem. Soc.* **2004**, *126* (10), 3139–3147. <https://doi.org/10.1021/ja036732j>.
- (113) Tan, J.; Xu, X.; Liu, J.; Vasylevskiy, S.; Lin, Z.; Kabe, R.; Zou, Y.; Müllen, K.; Narita, A.; Hu, Y. Synthesis of a π -Extended Double [9]Helicene. *Angew. Chem. Int. Ed.* **2023**, *62* (18), e202218494. <https://doi.org/10.1002/anie.202218494>.
- (114) Zhu, Y.; Guo, X.; Li, Y.; Wang, J. Fusing of Seven HBCs toward a Green Nanographene Propeller. *J. Am. Chem. Soc.* **2019**, *141* (13), 5511–5517. <https://doi.org/10.1021/jacs.9b01266>.
- (115) Shen, Y.; Chen, C.-F. Helicenes: Synthesis and Applications. *Chem. Rev.* **2012**, *112* (3), 1463–1535. <https://doi.org/10.1021/cr200087r>.
- (116) Jakubec, M.; Storch, J. Recent Advances in Functionalizations of Helicene Backbone. *J. Org. Chem.* **2020**, *acs.joc.0c01837*. <https://doi.org/10.1021/acs.joc.0c01837>.
- (117) Fujikawa, T.; Segawa, Y.; Itami, K. Synthesis, Structures, and Properties of π -Extended Double Helicene: A Combination of Planar and Nonplanar π -Systems. *J. Am. Chem. Soc.* **2015**, *137* (24), 7763–7768. <https://doi.org/10.1021/jacs.5b03118>.
- (118) Bedi, A.; Gidron, O. The Consequences of Twisting Nanocarbons: Lessons from Tethered Twisted Acenes. *Acc. Chem. Res.* **2019**, *52* (9), 2482–2490. <https://doi.org/10.1021/acs.accounts.9b00271>.

- (119) Fernández-García, J. M.; Izquierdo-García, P.; Buendía, M.; Filippone, S.; Martín, N. Synthetic Chiral Molecular Nanographenes: The Key Figure of the Racemization Barrier. *Chem. Commun.* **2022**, *58* (16), 2634–2645. <https://doi.org/10.1039/D1CC06561K>.
- (120) Ma, L.; Wang, J.; Ding, F. Recent Progress and Challenges in Graphene Nanoribbon Synthesis. *ChemPhysChem* **2013**, *14* (1), 47–54. <https://doi.org/10.1002/cphc.201200253>.
- (121) Han, M. Y.; Özyilmaz, B.; Zhang, Y.; Kim, P. Energy Band-Gap Engineering of Graphene Nanoribbons. *Phys. Rev. Lett.* **2007**, *98* (20), 206805. <https://doi.org/10.1103/PhysRevLett.98.206805>.
- (122) Li, X.; Wang, X.; Zhang, L.; Lee, S.; Dai, H. Chemically Derived, Ultrasoft Graphene Nanoribbon Semiconductors. *Science* **2008**, *319* (5867), 1229–1232. <https://doi.org/10.1126/science.1150878>.
- (123) Jiao, L.; Zhang, L.; Wang, X.; Diankov, G.; Dai, H. Narrow Graphene Nanoribbons from Carbon Nanotubes. *Nature* **2009**, *458* (7240), 877–880. <https://doi.org/10.1038/nature07919>.
- (124) Stille, J. K.; Noren, G. K.; Green, L. Hydrocarbon Ladder Aromatics from a Diels-Alder Reaction. *J. Polym. Sci. [A1]* **1970**, *8* (8), 2245–2254. <https://doi.org/10.1002/pol.1970.150080830>.
- (125) Schlüter, A.-D.; Löffler, M.; Enkelmann, V. Synthesis of a Fully Unsaturated All-Carbon Ladder Polymer. *Nature* **1994**, *368* (6474), 831–834. <https://doi.org/10.1038/368831a0>.
- (126) Scherf, U. Ladder-Type Materials. *J. Mater. Chem.* **1999**, *9* (9), 1853–1864. <https://doi.org/10.1039/a900447e>.
- (127) Shifrina, Z. B.; Averina, M. S.; Rusanov, A. L.; Wagner, M.; Müllen, K. Branched Polyphenylenes by Repetitive Diels-Alder Cycloaddition. *Macromolecules* **2000**, *33* (10), 3525–3529. <https://doi.org/10.1021/ma991369f>.
- (128) Wu, J.; Gherghel, L.; Watson, M. D.; Li, J.; Wang, Z.; Simpson, C. D.; Kolb, U.; Müllen, K. From Branched Polyphenylenes to Graphite Ribbons. *Macromolecules* **2003**, *36* (19), 7082–7089. <https://doi.org/10.1021/ma0257752>.
- (129) Yang, X.; Dou, X.; Rouhanipour, A.; Zhi, L.; Räder, H. J.; Müllen, K. Two-Dimensional Graphene Nanoribbons. *J. Am. Chem. Soc.* **2008**, *130* (13), 4216–4217. <https://doi.org/10.1021/ja710234t>.
- (130) Narita, A.; Wang, X.-Y.; Feng, X.; Müllen, K. New Advances in Nanographene Chemistry. *Chem. Soc. Rev.* **2015**, *44* (18), 6616–6643. <https://doi.org/10.1039/C5CS00183H>.
- (131) Yoon, K.-Y.; Dong, G. Liquid-Phase Bottom-up Synthesis of Graphene Nanoribbons. *Mater. Chem. Front.* **2020**, *4* (1), 29–45. <https://doi.org/10.1039/C9QM00519F>.
- (132) Kim, K. T.; Jung, J. W.; Jo, W. H. Synthesis of Graphene Nanoribbons with Various Widths and Its Application to Thin-Film Transistor. *Carbon* **2013**, *63*, 202–209. <https://doi.org/10.1016/j.carbon.2013.06.074>.
- (133) Schwab, M. G.; Narita, A.; Osella, S.; Hu, Y.; Maghsoumi, A.; Mavrinsky, A.; Pisula, W.; Castiglioni, C.; Tommasini, M.; Beljonne, D.; Feng, X.; Müllen, K. Bottom-Up Synthesis of Necklace-Like Graphene Nanoribbons. *Chem. - Asian J.* **2015**, *10* (10), 2134–2138. <https://doi.org/10.1002/asia.201500450>.
- (134) Niu, W.; Fu, Y.; Serra, G.; Liu, K.; Droste, J.; Lee, Y.; Ling, Z.; Xu, F.; Cojal González, J. D.; Lucotti, A.; Rabe, J. P.; Ryan Hansen, M.; Pisula, W.; Blom, P. W. M.; Palma, C.; Tommasini, M.; Mai, Y.; Ma, J.; Feng, X. Bottom-up Solution Synthesis of Graphene Nanoribbons with Precisely Engineered Nanopores. *Angew. Chem. Int. Ed.* **2023**, e202305737. <https://doi.org/10.1002/anie.202305737>.
- (135) Schwab, M. G.; Narita, A.; Hernandez, Y.; Balandina, T.; Mali, K. S.; De Feyter, S.; Feng, X.; Müllen, K. Structurally Defined Graphene Nanoribbons with High Lateral Extension. *J. Am. Chem. Soc.* **2012**, *134* (44), 18169–18172. <https://doi.org/10.1021/ja307697j>.
- (136) El Gemayel, M.; Narita, A.; Dössel, L. F.; Sundaram, R. S.; Kiersnowski, A.; Pisula, W.; Hansen, M. R.; Ferrari, A. C.; Orgiu, E.; Feng, X.; Müllen, K.; Samorì, P. Graphene Nanoribbon Blends with P3HT for Organic Electronics. *Nanoscale* **2014**, *6* (12), 6301–6314. <https://doi.org/10.1039/C4NR00256C>.
- (137) Huang, Y.; Mai, Y.; Yang, X.; Beser, U.; Liu, J.; Zhang, F.; Yan, D.; Müllen, K.; Feng, X. Temperature-Dependent Multidimensional Self-Assembly of Polyphenylene-Based “Rod-Coil” Graft Polymers. *J. Am. Chem. Soc.* **2015**, *137* (36), 11602–11605. <https://doi.org/10.1021/jacs.5b07487>.
- (138) Vo, T. H.; Shekhirev, M.; Kunkel, D. A.; Orange, F.; Guinel, M. J.-F.; Enders, A.; Sinitskii, A. Bottom-up Solution Synthesis of Narrow Nitrogen-Doped Graphene Nanoribbons. *Chem Commun* **2014**, *50* (32), 4172–4174. <https://doi.org/10.1039/C4CC00885E>.

- (139) Narita, A.; Feng, X.; Hernandez, Y.; Jensen, S. A.; Bonn, M.; Yang, H.; Verzhbitskiy, I. A.; Casiraghi, C.; Hansen, M. R.; Koch, A. H. R.; Fytas, G.; Ivasenko, O.; Li, B.; Mali, K. S.; Balandina, T.; Mahesh, S.; De Feyter, S.; Müllen, K. Synthesis of Structurally Well-Defined and Liquid-Phase-Processable Graphene Nanoribbons. *Nat. Chem.* **2014**, *6* (2), 126–132. <https://doi.org/10.1038/nchem.1819>.
- (140) Narita, A.; Verzhbitskiy, I. A.; Frederickx, W.; Mali, K. S.; Jensen, S. A.; Hansen, M. R.; Bonn, M.; De Feyter, S.; Casiraghi, C.; Feng, X.; Müllen, K. Bottom-Up Synthesis of Liquid-Phase-Processable Graphene Nanoribbons with Near-Infrared Absorption. *ACS Nano* **2014**, *8* (11), 11622–11630. <https://doi.org/10.1021/nn5049014>.
- (141) Slota, M.; Keerthi, A.; Myers, W. K.; Tretyakov, E.; Baumgarten, M.; Ardavan, A.; Sadeghi, H.; Lambert, C. J.; Narita, A.; Müllen, K.; Bogani, L. Magnetic Edge States and Coherent Manipulation of Graphene Nanoribbons. *Nature* **2018**, *557* (7707), 691–695. <https://doi.org/10.1038/s41586-018-0154-7>.
- (142) Jordan, R. S.; Li, Y. L.; Lin, C.-W.; McCurdy, R. D.; Lin, J. B.; Brosmer, J. L.; Marsh, K. L.; Khan, S. I.; Houk, K. N.; Kaner, R. B.; Rubin, Y. Synthesis of $N = 8$ Armchair Graphene Nanoribbons from Four Distinct Polydiacetylenes. *J. Am. Chem. Soc.* **2017**, *139* (44), 15878–15890. <https://doi.org/10.1021/jacs.7b08800>.
- (143) Richter, A.; Floris, A.; Bechstein, R.; Kantorovich, L.; Kühnle, A. On-Surface Synthesis on a Bulk Insulator Surface. *J. Phys. Condens. Matter* **2018**, *30* (13), 133001. <https://doi.org/10.1088/1361-648X/aab0b9>.
- (144) Para, F.; Bocquet, F.; Nony, L.; Loppacher, C.; Féron, M.; Cherioux, F.; Gao, D. Z.; Federici Canova, F.; Watkins, M. B. Micrometre-Long Covalent Organic Fibres by Photoinitiated Chain-Growth Radical Polymerization on an Alkali-Halide Surface. *Nat. Chem.* **2018**, *10* (11), 1112–1117. <https://doi.org/10.1038/s41557-018-0120-x>.
- (145) Abel, M.; Clair, S.; Ourdjini, O.; Mossoyan, M.; Porte, L. Single Layer of Polymeric Fe-Phthalocyanine: An Organometallic Sheet on Metal and Thin Insulating Film. *J. Am. Chem. Soc.* **2011**, *133* (5), 1203–1205. <https://doi.org/10.1021/ja108628r>.
- (146) Dong, L.; Liu, P. N.; Lin, N. Surface-Activated Coupling Reactions Confined on a Surface. *Acc. Chem. Res.* **2015**, *48* (10), 2765–2774. <https://doi.org/10.1021/acs.accounts.5b00160>.
- (147) Lackinger, M. Surface-Assisted Ullmann Coupling. *Chem. Commun.* **2017**, *53* (56), 7872–7885. <https://doi.org/10.1039/C7CC03402D>.
- (148) Clair, S.; de Oteyza, D. G. Controlling a Chemical Coupling Reaction on a Surface: Tools and Strategies for On-Surface Synthesis. *Chem. Rev.* **2019**, *119* (7), 4717–4776. <https://doi.org/10.1021/acs.chemrev.8b00601>.
- (149) Xi, M.; Bent, B. E. Mechanisms of the Ullmann Coupling Reaction in Adsorbed Monolayers. *J. Am. Chem. Soc.* **1993**, *115* (16), 7426–7433. <https://doi.org/10.1021/ja00069a048>.
- (150) Hla, S.-W.; Bartels, L.; Meyer, G.; Rieder, K.-H. Inducing All Steps of a Chemical Reaction with the Scanning Tunneling Microscope Tip: Towards Single Molecule Engineering. *Phys. Rev. Lett.* **2000**, *85* (13), 2777–2780. <https://doi.org/10.1103/PhysRevLett.85.2777>.
- (151) Grill, L.; Dyer, M.; Lafferentz, L.; Persson, M.; Peters, M. V.; Hecht, S. Nano-Architectures by Covalent Assembly of Molecular Building Blocks. *Nat. Nanotechnol.* **2007**, *2* (11), 687–691. <https://doi.org/10.1038/nnano.2007.346>.
- (152) Ullmann, F.; Bielecki, J. Ueber Synthesen in Der Biphenylreihe. *Berichte Dtsch. Chem. Ges.* **1901**, *34* (2), 2174–2185. <https://doi.org/10.1002/cber.190103402141>.
- (153) Cai, J.; Ruffieux, P.; Jaafar, R.; Bieri, M.; Braun, T.; Blankenburg, S.; Muoth, M.; Seitsonen, A. P.; Saleh, M.; Feng, X.; Müllen, K.; Fasel, R. Atomically Precise Bottom-up Fabrication of Graphene Nanoribbons. *Nature* **2010**, *466* (7305), 470–473. <https://doi.org/10.1038/nature09211>.
- (154) Talirz, L.; Ruffieux, P.; Fasel, R. On-Surface Synthesis of Atomically Precise Graphene Nanoribbons. *Adv. Mater.* **2016**, *28* (29), 6222–6231. <https://doi.org/10.1002/adma.201505738>.
- (155) Houtsma, R. S. K.; De La Rie, J.; Stöhr, M. Atomically Precise Graphene Nanoribbons: Interplay of Structural and Electronic Properties. *Chem. Soc. Rev.* **2021**, *50* (11), 6541–6568. <https://doi.org/10.1039/D0CS01541E>.
- (156) Ruffieux, P.; Wang, S.; Yang, B.; Sánchez-Sánchez, C.; Liu, J.; Dienel, T.; Talirz, L.; Shinde, P.; Pignedoli, C. A.; Passerone, D.; Dumslaff, T.; Feng, X.; Müllen, K.; Fasel, R. On-Surface Synthesis of Graphene Nanoribbons with Zigzag Edge Topology. *Nature* **2016**, *531* (7595), 489–492. <https://doi.org/10.1038/nature17151>.
- (157) Bai, J.; Zhong, X.; Jiang, S.; Huang, Y.; Duan, X. Graphene Nanomesh. *Nat. Nanotechnol.* **2010**, *5* (3), 190–194. <https://doi.org/10.1038/nnano.2010.8>.

- (158) Zeng, Z.; Huang, X.; Yin, Z.; Li, H.; Chen, Y.; Li, H.; Zhang, Q.; Ma, J.; Boey, F.; Zhang, H. Fabrication of Graphene Nanomesh by Using an Anodic Aluminum Oxide Membrane as a Template. *Adv. Mater.* **2012**, *24* (30), 4138–4142. <https://doi.org/10.1002/adma.201104281>.
- (159) Akhavan, O. Graphene Nanomesh by ZnO Nanorod Photocatalysts. *ACS Nano* **2010**, *4* (7), 4174–4180. <https://doi.org/10.1021/nn1007429>.
- (160) Safron, N. S.; Kim, M.; Gopalan, P.; Arnold, M. S. Barrier-Guided Growth of Micro- and Nano-Structured Graphene. *Adv. Mater.* **2012**, *24* (8), 1041–1045. <https://doi.org/10.1002/adma.201104195>.
- (161) Jung, I.; Young Jang, H.; Park, S. Direct Growth of Graphene Nanomesh Using a Au Nano-Network as a Metal Catalyst via Chemical Vapor Deposition. *Appl. Phys. Lett.* **2013**, *103* (2), 023105. <https://doi.org/10.1063/1.4813318>.
- (162) Zhou, Q.; Ma, Y.; Ma, X.; Luo, X.; Zheng, S.; Nan, Y.; Ou, E.; Wang, K.; Xu, W. Synthesis of Nanoporous Graphenes via Decarboxylation Reaction. *Chem. Commun.* **2020**, *56* (47), 6336–6339. <https://doi.org/10.1039/D0CC01913E>.
- (163) Nath, S.; Puthukkudi, A.; Mohapatra, J.; Bommakanti, S.; Chandrasekhar, N.; Biswal, B. P. Carbon–Carbon Linked Organic Frameworks: An Explicit Summary and Analysis. *Macromol. Rapid Commun.* **2023**, 2200950. <https://doi.org/10.1002/marc.202200950>.
- (164) Bieri, M.; Treier, M.; Cai, J.; Ait-Mansour, K.; Ruffieux, P.; Gröning, O.; Gröning, P.; Kastler, M.; Rieger, R.; Feng, X.; Müllen, K.; Fasel, R. Porous Graphenes: Two-Dimensional Polymer Synthesis with Atomic Precision. *Chem. Commun.* **2009**, No. 45, 6919. <https://doi.org/10.1039/b915190g>.
- (165) Gutzler, R.; Walch, H.; Eder, G.; Kloft, S.; Heckl, W. M.; Lackinger, M. Surface Mediated Synthesis of 2D Covalent Organic Frameworks: 1,3,5-Tris(4-Bromophenyl)Benzene on Graphite(001), Cu(111), and Ag(110). *Chem. Commun.* **2009**, No. 29, 4456. <https://doi.org/10.1039/b906836h>.
- (166) Blunt, M. O.; Russell, J. C.; Champness, N. R.; Beton, P. H. Templating Molecular Adsorption Using a Covalent Organic Framework. *Chem. Commun.* **2010**, *46* (38), 7157. <https://doi.org/10.1039/c0cc01810d>.
- (167) Moreno, C.; Vilas-Varela, M.; Kretz, B.; Garcia-Lekue, A.; Costache, M. V.; Paradinas, M.; Panighel, M.; Ceballos, G.; Valenzuela, S. O.; Peña, D.; Mugarza, A. Bottom-up Synthesis of Multifunctional Nanoporous Graphene. *Science* **2018**, *360* (6385), 199–203. <https://doi.org/10.1126/science.aar2009>.
- (168) Bieri, M.; Blankenburg, S.; Kivala, M.; Pignedoli, C. A.; Ruffieux, P.; Müllen, K.; Fasel, R. Surface-Supported 2D Heterotriangulene Polymers. *Chem. Commun.* **2011**, *47* (37), 10239. <https://doi.org/10.1039/c1cc12490k>.
- (169) Fan, Q.; Gottfried, J. M.; Zhu, J. Surface-Catalyzed C–C Covalent Coupling Strategies toward the Synthesis of Low-Dimensional Carbon-Based Nanostructures. *Acc. Chem. Res.* **2015**, *48* (8), 2484–2494. <https://doi.org/10.1021/acs.accounts.5b00168>.
- (170) Steiner, C.; Gebhardt, J.; Ammon, M.; Yang, Z.; Heidenreich, A.; Hammer, N.; Görling, A.; Kivala, M.; Maier, S. Hierarchical On-Surface Synthesis and Electronic Structure of Carbonyl-Functionalized One- and Two-Dimensional Covalent Nanoarchitectures. *Nat. Commun.* **2017**, *8* (1), 14765. <https://doi.org/10.1038/ncomms14765>.
- (171) Lafferentz, L.; Eberhardt, V.; Dri, C.; Africh, C.; Comelli, G.; Esch, F.; Hecht, S.; Grill, L. Controlling On-Surface Polymerization by Hierarchical and Substrate-Directed Growth. *Nat. Chem.* **2012**, *4* (3), 215–220. <https://doi.org/10.1038/nchem.1242>.
- (172) Yang, B.; Björk, J.; Lin, H.; Zhang, X.; Zhang, H.; Li, Y.; Fan, J.; Li, Q.; Chi, L. Synthesis of Surface Covalent Organic Frameworks via Dimerization and Cyclotrimerization of Acetyls. *J. Am. Chem. Soc.* **2015**, *137* (15), 4904–4907. <https://doi.org/10.1021/jacs.5b00774>.
- (173) Liu, J.; Ruffieux, P.; Feng, X.; Müllen, K.; Fasel, R. Cyclotrimerization of Arylalkynes on Au(111). *Chem Commun* **2014**, *50* (76), 11200–11203. <https://doi.org/10.1039/C4CC02859G>.
- (174) Mutlu, Z.; Jacobse, P. H.; McCurdy, R. D.; Llinas, J. P.; Lin, Y.; Veber, G. C.; Fischer, F. R.; Crommie, M. F.; Bokor, J. Bottom-Up Synthesized Nanoporous Graphene Transistors. *Adv. Funct. Mater.* **2021**, 2103798. <https://doi.org/10.1002/adfm.202103798>.
- (175) Valeur, B.; Berberan-Santos, M. N. *Molecular Fluorescence: Principles and Applications*, Second edition.; Wiley-VCH ; Wiley-VCH Verlag GmbH & Co. KGaA: Weinheim, Germany : [Chichester, England], 2012.
- (176) Niehues, I.; Marauhn, P.; Deilmann, T.; Wigger, D.; Schmidt, R.; Arora, A.; Michaelis De Vasconcellos, S.; Rohlfing, M.; Bratschitsch, R. Strain Tuning of the Stokes Shift in Atomically Thin Semiconductors. *Nanoscale* **2020**, *12* (40), 20786–20796. <https://doi.org/10.1039/D0NR04557H>.

- (177) Xu, Q.; Zhou, Q.; Hua, Z.; Xue, Q.; Zhang, C.; Wang, X.; Pan, D.; Xiao, M. Single-Particle Spectroscopic Measurements of Fluorescent Graphene Quantum Dots. *ACS Nano* **2013**, *7* (12), 10654–10661. <https://doi.org/10.1021/nn4053342>.
- (178) Zhu, S.; Zhang, J.; Tang, S.; Qiao, C.; Wang, L.; Wang, H.; Liu, X.; Li, B.; Li, Y.; Yu, W.; Wang, X.; Sun, H.; Yang, B. Surface Chemistry Routes to Modulate the Photoluminescence of Graphene Quantum Dots: From Fluorescence Mechanism to Up-Conversion Bioimaging Applications. *Adv. Funct. Mater.* **2012**, *22* (22), 4732–4740. <https://doi.org/10.1002/adfm.201201499>.
- (179) Lingam, K.; Podila, R.; Qian, H.; Serkiz, S.; Rao, A. M. Evidence for Edge-State Photoluminescence in Graphene Quantum Dots. *Adv. Funct. Mater.* **2013**, *23* (40), 5062–5065. <https://doi.org/10.1002/adfm.201203441>.
- (180) Hughes, J. M.; Hernandez, Y.; Aherne, D.; Doessel, L.; Müllen, K.; Moreton, B.; White, T. W.; Partridge, C.; Costantini, G.; Shmeliov, A.; Shannon, M.; Nicolosi, V.; Coleman, J. N. High Quality Dispersions of Hexabenzocoronene in Organic Solvents. *J. Am. Chem. Soc.* **2012**, *134* (29), 12168–12179. <https://doi.org/10.1021/ja303683v>.
- (181) Englert, J. M.; Hauke, F.; Feng, X.; Müllen, K.; Hirsch, A. Exfoliation of Hexa-Peri-Hexabenzocoronene in Water. *Chem. Commun.* **2010**, *46* (48), 9194–9196. <https://doi.org/10.1039/C0CC03849K>.
- (182) Haines, P.; Reger, D.; Träg, J.; Strauss, V.; Lungerich, D.; Zahn, D.; Jux, N.; Guldi, D. M. On the Photophysics of Nanographenes – Investigation of Functionalized Hexa-Peri-Hexabenzocoronenes as Model Systems. *Nanoscale* **2021**, *13* (2), 801–809. <https://doi.org/10.1039/D0NR06802K>.
- (183) Debije, M. G.; Piris, J.; de Haas, M. P.; Warman, J. M.; Tomović, Ž.; Simpson, C. D.; Watson, M. D.; Müllen, K. The Optical and Charge Transport Properties of Discotic Materials with Large Aromatic Hydrocarbon Cores. *J. Am. Chem. Soc.* **2004**, *126* (14), 4641–4645. <https://doi.org/10.1021/ja0395994>.
- (184) Tan, Y.-Z.; Yang, B.; Parvez, K.; Narita, A.; Osella, S.; Beljonne, D.; Feng, X.; Müllen, K. Atomically Precise Edge Chlorination of Nanographenes and Its Application in Graphene Nanoribbons. *Nat. Commun.* **2013**, *4* (1), 2646. <https://doi.org/10.1038/ncomms3646>.
- (185) Mueller, M. L.; Yan, X.; McGuire, J. A.; Li, L. Triplet States and Electronic Relaxation in Photoexcited Graphene Quantum Dots. *Nano Lett.* **2010**, *10* (7), 2679–2682. <https://doi.org/10.1021/nl101474d>.
- (186) Riesen, H.; Wiebeler, C.; Schumacher, S. Optical Spectroscopy of Graphene Quantum Dots: The Case of C132. *J. Phys. Chem. A* **2014**, *118* (28), 5189–5195. <https://doi.org/10.1021/jp502753a>.
- (187) Zhao, S.; Lavie, J.; Rondin, L.; Orcin-Chaix, L.; Diederichs, C.; Roussignol, P.; Chassagneux, Y.; Voisin, C.; Müllen, K.; Narita, A.; Campidelli, S.; Lauret, J.-S. Single Photon Emission from Graphene Quantum Dots at Room Temperature. *Nat. Commun.* **2018**, *9* (1), 1–5. <https://doi.org/10.1038/s41467-018-05888-w>.
- (188) Basché, Th.; Moerner, W. E.; Orrit, M.; Talon, H. Photon Antibunching in the Fluorescence of a Single Dye Molecule Trapped in a Solid. *Phys. Rev. Lett.* **1992**, *69* (10), 1516–1519. <https://doi.org/10.1103/PhysRevLett.69.1516>.
- (189) Lounis, B.; Moerner, W. E. Single Photons on Demand from a Single Molecule at Room Temperature. *Nature* **2000**, *407* (6803), 491–493. <https://doi.org/10.1038/35035032>.
- (190) Nicolet, A. A. L.; Hofmann, C.; Kol'chenko, M. A.; Kozankiewicz, B.; Orrit, M. Single Dibenzoterrylene Molecules in an Anthracene Crystal: Spectroscopy and Photophysics. *ChemPhysChem* **2007**, *8* (8), 1215–1220. <https://doi.org/10.1002/cphc.200700091>.
- (191) Toninelli, C.; Gerhardt, I.; Clark, A. S.; Reserbat-Plantey, A.; Götzinger, S.; Ristanović, Z.; Colautti, M.; Lombardi, P.; Major, K. D.; Deperasińska, I.; Pernice, W. H.; Koppens, F. H. L.; Kozankiewicz, B.; Gourdon, A.; Sandoghdar, V.; Orrit, M. Single Organic Molecules for Photonic Quantum Technologies. *Nat. Mater.* **2021**. <https://doi.org/10.1038/s41563-021-00987-4>.
- (192) Aharonovich, I.; Englund, D.; Toth, M. Solid-State Single-Photon Emitters. *Nat. Photonics* **2016**, *10* (10), 631–641. <https://doi.org/10.1038/nphoton.2016.186>.
- (193) Scholl, R.; Mansfeld, J. (*Meso*)-Benzdianthron (Helianthron), (*Meso*)-Naphthodianthron, Und Ein Neuer Weg Zum Flavanthren. *Berichte Dtsch. Chem. Ges.* **1910**, *43* (2), 1734–1746. <https://doi.org/10.1002/cber.19100430288>.
- (194) Zhang, Y.; Pun, S. H.; Miao, Q. The Scholl Reaction as a Powerful Tool for Synthesis of Curved Polycyclic Aromatics. *Chem. Rev.* **2022**, *122* (18), 14554–14593. <https://doi.org/10.1021/acs.chemrev.2c00186>.
- (195) Jassas, R. S.; Mughal, E. U.; Sadiq, A.; Alsantali, R. I.; Al-Rooqi, M. M.; Naeem, N.; Moussa, Z.; Ahmed, S. A. Scholl Reaction as a Powerful Tool for the Synthesis of Nanographenes: A Systematic Review. *RSC Adv.* **2021**, *11* (51), 32158–32202. <https://doi.org/10.1039/D1RA05910F>.

- (196) Grzybowski, M.; Skonieczny, K.; Butenschön, H.; Gryko, D. T. Comparison of Oxidative Aromatic Coupling and the Scholl Reaction. *Angew. Chem. Int. Ed.* **2013**, *52* (38), 9900–9930. <https://doi.org/10.1002/anie.201210238>.
- (197) Sarhan, A. A. O.; Bolm, C. Iron(III) Chloride in Oxidative C–C Coupling Reactions. *Chem. Soc. Rev.* **2009**, *38* (9), 2730–2744. <https://doi.org/10.1039/B906026j>.
- (198) Moreno, I.; Tellitu, I.; Domínguez, E.; SanMartín, R. A Simple Route to New Phenanthro- and Phenanthroid-Fused Thiazoles by a PIFA-Mediated (Hetero)Biaryl Coupling Reaction. *Eur. J. Org. Chem.* **2002**, *2002* (13), 2126. [https://doi.org/10.1002/1099-0690\(200207\)2002:13<2126::AID-EJOC2126>3.0.CO;2-A](https://doi.org/10.1002/1099-0690(200207)2002:13<2126::AID-EJOC2126>3.0.CO;2-A).
- (199) Di Stefano, M.; Negri, F.; Carbone, P.; Müllen, K. Oxidative Cyclodehydrogenation Reaction for the Design of Extended 2D and 3D Carbon Nanostructures: A Theoretical Study. *Chem. Phys.* **2005**, *314* (1), 85–99. <https://doi.org/10.1016/j.chemphys.2005.02.002>.
- (200) Zhai, L.; Shukla, R.; Wadumethrige, S. H.; Rathore, R. Probing the Arenium-Ion (Proton Transfer) versus the Cation-Radical (Electron Transfer) Mechanism of Scholl Reaction Using DDQ as Oxidant. *J. Org. Chem.* **2010**, *75* (14), 4748–4760. <https://doi.org/10.1021/jo100611k>.
- (201) Danz, M.; Tonner, R.; Hilt, G. Understanding the Regioselectivity in Scholl Reactions for the Synthesis of Oligoarenes. *Chem Commun* **2012**, *48* (3), 377–379. <https://doi.org/10.1039/C1CC15980A>.
- (202) Liu, T.; Tonnelé, C.; Zhao, S.; Rondin, L.; Elias, C.; Medina-Lopez, D.; Okuno, H.; Narita, A.; Chassagneux, Y.; Voisin, C.; Campidelli, S.; Beljonne, D.; Lauret, J.-S. Vibronic Effect and Influence of Aggregation on the Photophysics of Graphene Quantum Dots. *Nanoscale* **2022**, *14* (10), 3826–3833. <https://doi.org/10.1039/D1NR08279E>.
- (203) Liu, T.; Carles, B.; Elias, C.; Tonnelé, C.; Medina-Lopez, D.; Narita, A.; Chassagneux, Y.; Voisin, C.; Beljonne, D.; Campidelli, S.; Rondin, L.; Lauret, J.-S. Vibronic Fingerprints in the Luminescence of Graphene Quantum Dots at Cryogenic Temperature. *J. Chem. Phys.* **2022**, *156* (10), 104302. <https://doi.org/10.1063/5.0083282>.
- (204) Mueller-Westerhoff, U. T.; Zhou, M. Synthesis of Symmetrically and Unsymmetrically Substituted .Alpha.-Diones from Organometallic Reagents and 1,4-Dialkylpiperazine-2,3-Diones. *J. Org. Chem.* **1994**, *59* (17), 4988–4992. <https://doi.org/10.1021/jo00096a049>.
- (205) Lungerich, D.; Hitzenberger, J. F.; Marcia, M.; Hampel, F.; Drewello, T.; Jux, N. Superbenzene-Porphyrin Conjugates. *Angew. Chem. Int. Ed.* **2014**, *53* (45), 12231–12235. <https://doi.org/10.1002/anie.201407053>.
- (206) Martin, M. M.; Lungerich, D.; Haines, P.; Hampel, F.; Jux, N. Electronic Communication across Porphyrin Hexabenzocoronene Isomers. *Angew. Chem. Int. Ed.* **2019**, *58* (26), 8932–8937. <https://doi.org/10.1002/anie.201903654>.
- (207) Lavie, J. Synthesis and Properties of Graphene Quantum Dots and Nanomeshes, Université Paris-Saclay, Saint-Aubin, 2018.
- (208) Wilson, S. R.; Jacob, L. A. Iodination of Aryltrimethylsilanes. A Mild Approach to (Iodophenyl)Alanine. *J. Org. Chem.* **1986**, *51* (25), 4833–4836. <https://doi.org/10.1021/jo00375a015>.
- (209) Arslan, H.; Uribe-Romo, F. J.; Smith, B. J.; Dichtel, W. R. Accessing Extended and Partially Fused Hexabenzocoronenes Using a Benzannulation–Cyclodehydrogenation Approach. *Chem. Sci.* **2013**, *4* (10), 3973. <https://doi.org/10.1039/c3sc51212f>.
- (210) Alsharif, M. A.; Raja, Q. A.; Majeed, N. A.; Jassas, Rabab. S.; Alsimaree, A. A.; Sadiq, A.; Naeem, N.; Mughal, E. U.; Alsantali, R. I.; Moussa, Z.; Ahmed, S. A. DDQ as a Versatile and Easily Recyclable Oxidant: A Systematic Review. *RSC Adv.* **2021**, *11* (47), 29826–29858. <https://doi.org/10.1039/D1RA04575J>.
- (211) Adeniyi, A. A.; Ngake, T. L.; Conradie, J. Cyclic Voltammetric Study of 2-Hydroxybenzophenone (HBP) Derivatives and the Correspondent Change in the Orbital Energy Levels in Different Solvents. *Electroanalysis* **2020**, *32* (12), 2659–2668. <https://doi.org/10.1002/elan.202060163>.
- (212) Lu, M.; Wang, W.; Liang, L.; Yan, S.; Ling, Q. Synthesis of D–A Low-Bandgap Polymer-Based Thieno[3,4-b]Pyrazine and Benzo[1,2-b:4,5-b']Dithiophene for Polymer Solar Cells. *Polym. Bull.* **2017**, *74* (2), 603–614. <https://doi.org/10.1007/s00289-016-1732-1>.
- (213) Pommerehne, J.; Vestweber, H.; Guss, W.; Mahrt, R. F.; Bäessler, H.; Porsch, M.; Daub, J. Efficient Two Layer LedS on a Polymer Blend Basis. *Adv. Mater.* **1995**, *7* (6), 551–554. <https://doi.org/10.1002/adma.19950070608>.
- (214) Chen, Q.; Thoms, S.; Stöttinger, S.; Schollmeyer, D.; Müllen, K.; Narita, A.; Basché, T. Dibenzo[Hi, St]Ovalene as Highly Luminescent Nanographene: Efficient Synthesis via Photochemical Cyclodehydroiodination, Optoelectronic Properties, and Single-Molecule Spectroscopy. *J. Am. Chem. Soc.* **2019**, *141* (41), 16439–16449. <https://doi.org/10.1021/jacs.9b08320>.
- (215) Lakowicz, J. R. *Principles of Fluorescence Spectroscopy*, 3rd ed.; Springer: New York, 2006.

- (216) Cocchi, C.; Prezzi, D.; Ruini, A.; Caldas, M. J.; Molinari, E. Anisotropy and Size Effects on the Optical Spectra of Polycyclic Aromatic Hydrocarbons. *J. Phys. Chem. A* **2014**, *118* (33), 6507–6513. <https://doi.org/10.1021/jp503054j>.
- (217) Liu, Thomas. Optical Spectroscopy of Graphene Quantum Dots, Université Paris-Saclay, 2023.
- (218) Moerner, W. E.; Kador, L. Optical Detection and Spectroscopy of Single Molecules in a Solid. *Phys. Rev. Lett.* **1989**, *62* (21), 2535–2538. <https://doi.org/10.1103/PhysRevLett.62.2535>.
- (219) Parenti, F.; Tassinari, F.; Libertini, E.; Lanzi, M.; Mucci, A. π -Stacking Signature in NMR Solution Spectra of Thiophene-Based Conjugated Polymers. *ACS Omega* **2017**, *2* (9), 5775–5784. <https://doi.org/10.1021/acsomega.7b00943>.
- (220) Geffroy, B.; Le Roy, P.; Prat, C. Organic Light-Emitting Diode (OLED) Technology: Materials, Devices and Display Technologies. *Polym. Int.* **2006**, *55* (6), 572–582. <https://doi.org/10.1002/pi.1974>.
- (221) Yuan, F.; Yuan, T.; Sui, L.; Wang, Z.; Xi, Z.; Li, Y.; Li, X.; Fan, L.; Tan, Z.; Chen, A.; Jin, M.; Yang, S. Engineering Triangular Carbon Quantum Dots with Unprecedented Narrow Bandwidth Emission for Multicolored LEDs. *Nat. Commun.* **2018**, *9* (1), 2249. <https://doi.org/10.1038/s41467-018-04635-5>.
- (222) Wallwork, N. R.; Mamada, M.; Shukla, A.; McGregor, S. K. M.; Adachi, C.; Namdas, E. B.; Lo, S.-C. High-Performance Solution-Processed Red Hyperfluorescent OLEDs Based on Cibalackrot. *J. Mater. Chem. C* **2022**, *10* (12), 4767–4774. <https://doi.org/10.1039/D1TC04937B>.
- (223) Medina-Lopez, D.; Liu, T.; Osella, S.; Levy-Falk, H.; Rolland, N.; Elias, C.; Huber, G.; Ticku, P.; Rondin, L.; Joussetme, B.; Beljonne, D.; Lauret, J.-S.; Campidelli, S. Interplay of Structure and Photophysics of Individualized Rod-Shaped Graphene Quantum Dots with up to 132 Sp² Carbon Atoms. *Nat. Commun.* **2023**, *14* (1), 4728. <https://doi.org/10.1038/s41467-023-40376-w>.
- (224) Geng, X.; Mague, J. T.; Donahue, J. P.; Pascal, R. A. Hairpin Furans and Giant Biaryls. *J. Org. Chem.* **2016**, *81* (9), 3838–3847. <https://doi.org/10.1021/acs.joc.6b00492>.
- (225) Crassous, J.; Fuchter, M. J.; Freedman, D. E.; Kotov, N. A.; Moon, J.; Beard, M. C.; Feldmann, S. Materials for Chiral Light Control. *Nat. Rev. Mater.* **2023**, *8* (6), 365–371. <https://doi.org/10.1038/s41578-023-00543-3>.
- (226) *Helicenes: Synthesis, Properties and Applications*, 1st ed.; Crassous, J., Stará, I. G., Starý, I., Eds.; Wiley, 2022. <https://doi.org/10.1002/9783527829415>.
- (227) Nakakuki, Y.; Hirose, T.; Sotome, H.; Miyasaka, H.; Matsuda, K. Hexa-Peri-Hexabenz[7]Helicene: Homogeneously π -Extended Helicene as a Primary Substructure of Helically Twisted Chiral Graphenes. *J. Am. Chem. Soc.* **2018**, *140* (12), 4317–4326. <https://doi.org/10.1021/jacs.7b13412>.
- (228) Hu, Y.; Wang, X.-Y.; Peng, P.-X.; Wang, X.-C.; Cao, X.-Y.; Feng, X.; Müllen, K.; Narita, A. Benzo-Fused Double [7]Carbohelicene: Synthesis, Structures, and Physicochemical Properties. *Angew. Chem. Int. Ed.* **2017**, *56* (12), 3374–3378. <https://doi.org/10.1002/anie.201610434>.
- (229) Wang, Y.; Yin, Z.; Zhu, Y.; Gu, J.; Li, Y.; Wang, J. Hexapole [9]Helicene. *Angew. Chem. Int. Ed.* **2019**, *58* (2), 587–591. <https://doi.org/10.1002/anie.201811706>.
- (230) Evans, P. J.; Ouyang, J.; Favereau, L.; Crassous, J.; Fernández, I.; Perles, J.; Martín, N. Synthesis of a Helical Bilayer Nanographene. *Angew. Chem. Int. Ed.* **2018**, *57* (23), 6774–6779. <https://doi.org/10.1002/anie.201800798>.
- (231) Ma, S.; Gu, J.; Lin, C.; Luo, Z.; Zhu, Y.; Wang, J. Supertwistacene: A Helical Graphene Nanoribbon. *J. Am. Chem. Soc.* **2020**, *142* (39), 16887–16893. <https://doi.org/10.1021/jacs.0c08555>.
- (232) Wu, Y.-F.; Ying, S.-W.; Su, L.-Y.; Du, J.-J.; Zhang, L.; Chen, B.-W.; Tian, H.-R.; Xu, H.; Zhang, M.-L.; Yan, X.; Zhang, Q.; Xie, S.-Y.; Zheng, L.-S. Nitrogen-Embedded Quintuple [7]Helicene: A Helicene–Azacorannulene Hybrid with Strong Near-Infrared Fluorescence. *J. Am. Chem. Soc.* **2022**, *144* (24), 10736–10742. <https://doi.org/10.1021/jacs.2c00794>.
- (233) Zhao, X.-J.; Hou, H.; Ding, P.-P.; Deng, Z.-Y.; Ju, Y.-Y.; Liu, S.-H.; Liu, Y.-M.; Tang, C.; Feng, L.-B.; Tan, Y.-Z. Molecular Defect-Containing Bilayer Graphene Exhibiting Brightened Luminescence. *Sci. Adv.* **2020**, *6* (9), eaay8541. <https://doi.org/10.1126/sciadv.aay8541>.
- (234) Ju, Y.; Shi, X.; Xu, S.; Ma, X.; Wei, R.; Hou, H.; Chu, C.; Sun, D.; Liu, G.; Tan, Y. Atomically Precise Water-Soluble Graphene Quantum Dot for Cancer Sonodynamic Therapy. *Adv. Sci.* **2022**, *9* (19), 2105034. <https://doi.org/10.1002/adv.202105034>.
- (235) Tong, L.; Ho, D. M.; Vogelaar, N. J.; Schutt, C. E.; Pascal, R. A. The Albatrossenes: Large, Cleft-Containing, Polyphenyl Polycyclic Aromatic Hydrocarbons. *J. Am. Chem. Soc.* **1997**, *119* (31), 7291–7302. <https://doi.org/10.1021/ja971261k>.

- (236) Komber, H.; Stumpe, K.; Voit, B. The Rotation of Pentaphenylphenyl Groups and Their Terminal Phenyl Groups: A Variable-Temperature ¹H NMR Study on an Albatrossene and a Three-Bladed Molecular Propeller. *Tetrahedron Lett.* **2007**, *48* (15), 2655–2659. <https://doi.org/10.1016/j.tetlet.2007.02.079>.
- (237) Shen, C.; Zhang, G.; Ding, Y.; Yang, N.; Gan, F.; Crassous, J.; Qiu, H. Oxidative Cyclo-Rearrangement of Helicenes into Chiral Nanographenes. *Nat. Commun.* **2021**, *12* (1), 2786. <https://doi.org/10.1038/s41467-021-22992-6>.
- (238) Izquierdo-García, P.; Fernández-García, J. M.; Perles, J.; Fernández, I.; Martín, N. Electronic Control of the Scholl Reaction: Selective Synthesis of Spiro vs Helical Nanographenes. *Angew. Chem. Int. Ed.* **2023**, *62* (7). <https://doi.org/10.1002/anie.202215655>.
- (239) Zhang, X.; Xu, Z.; Si, W.; Oniwa, K.; Bao, M.; Yamamoto, Y.; Jin, T. Synthesis of Extended Polycyclic Aromatic Hydrocarbons by Oxidative Tandem Spirocyclization and 1,2-Aryl Migration. *Nat. Commun.* **2017**, *8* (1), 15073. <https://doi.org/10.1038/ncomms15073>.
- (240) Liu, S.; Xia, D.; Baumgarten, M. Rigidly Fused Spiro-Conjugated π -Systems. *ChemPlusChem* **2021**, *86* (1), 36–48. <https://doi.org/10.1002/cplu.202000467>.
- (241) Tanaka, H.; Inoue, Y.; Mori, T. Circularly Polarized Luminescence and Circular Dichroisms in Small Organic Molecules: Correlation between Excitation and Emission Dissymmetry Factors. *ChemPhotoChem* **2018**, *2* (5), 386–402. <https://doi.org/10.1002/cptc.201800015>.
- (242) Riehl, J. P.; Richardson, F. S. Circularly Polarized Luminescence Spectroscopy. *Chem. Rev.* **1986**, *86* (1), 1–16. <https://doi.org/10.1021/cr00071a001>.
- (243) Liu, C.-Y.; Knochel, P. Preparation of Polyfunctional Arylmagnesium Reagents Bearing a Triazene Moiety. A New Carbazole Synthesis. *Org. Lett.* **2005**, *7* (13), 2543–2546. <https://doi.org/10.1021/ol0505454>.
- (244) Cho, H. J.; Kim, S. W.; Kim, S.; Lee, S.; Lee, J.; Cho, Y.; Lee, Y.; Lee, T.-W.; Shin, H.-J.; Song, C. Suppressing π - π Stacking Interactions for Enhanced Solid-State Emission of Flat Aromatic Molecules *via* Edge Functionalization with Picket-Fence-Type Groups. *J. Mater. Chem. C* **2020**, *8* (48), 17289–17296. <https://doi.org/10.1039/D0TC04376A>.
- (245) Kiel, G. R.; Patel, S. C.; Smith, P. W.; Levine, D. S.; Tilley, T. D. Expanded Helicenes: A General Synthetic Strategy and Remarkable Supramolecular and Solid-State Behavior. *J. Am. Chem. Soc.* **2017**, *139* (51), 18456–18459. <https://doi.org/10.1021/jacs.7b10902>.
- (246) Kiel, G. R.; Bergman, H. M.; Samkian, A. E.; Schuster, N. J.; Handford, R. C.; Rothenberger, A. J.; Gomez-Bombarelli, R.; Nuckolls, C.; Tilley, T. D. Expanded [23]-Helicene with Exceptional Chiroptical Properties *via* an Iterative Ring-Fusion Strategy. *J. Am. Chem. Soc.* **2022**, *144* (51), 23421–23427. <https://doi.org/10.1021/jacs.2c09555>.
- (247) Oswald, W.; Wu, Z. Energy Gaps in Graphene Nanomeshes. *Phys. Rev. B* **2012**, *85* (11), 115431. <https://doi.org/10.1103/PhysRevB.85.115431>.
- (248) Björk, J.; Hanke, F.; Stafström, S. Mechanisms of Halogen-Based Covalent Self-Assembly on Metal Surfaces. *J. Am. Chem. Soc.* **2013**, *135* (15), 5768–5775. <https://doi.org/10.1021/ja400304b>.
- (249) Nguyen, M.-T.; Pignedoli, C. A.; Passerone, D. An Ab Initio Insight into the Cu(111)-Mediated Ullmann Reaction. *Phys Chem Chem Phys* **2011**, *13* (1), 154–160. <https://doi.org/10.1039/C0CP00759E>.
- (250) Luo, Y.-R. *Comprehensive Handbook of Chemical Bond Energies*, 1st ed.; CRC Press, 2007. <https://doi.org/10.1201/9781420007282>.
- (251) Lewis, E. A.; Murphy, C. J.; Liriano, M. L.; Sykes, E. C. H. Atomic-Scale Insight into the Formation, Mobility and Reaction of Ullmann Coupling Intermediates. *Chem Commun* **2014**, *50* (8), 1006–1008. <https://doi.org/10.1039/C3CC47002D>.
- (252) Zint, S.; Ebeling, D.; Schlöder, T.; Ahles, S.; Mollenhauer, D.; Wegner, H. A.; Schirmeisen, A. Imaging Successive Intermediate States of the On-Surface Ullmann Reaction on Cu(111): Role of the Metal Coordination. *ACS Nano* **2017**, *11* (4), 4183–4190. <https://doi.org/10.1021/acsnano.7b01109>.
- (253) Fan, Q.; Wang, C.; Han, Y.; Zhu, J.; Kuttner, J.; Hilt, G.; Gottfried, J. M. Surface-Assisted Formation, Assembly, and Dynamics of Planar Organometallic Macrocycles and Zigzag Shaped Polymer Chains with C–Cu–C Bonds. *ACS Nano* **2014**, *8* (1), 709–718. <https://doi.org/10.1021/nn405370s>.
- (254) Adisojoso, J.; Lin, T.; Shang, X. S.; Shi, K. J.; Gupta, A.; Liu, P. N.; Lin, N. A Single-Molecule-Level Mechanistic Study of Pd-Catalyzed and Cu-Catalyzed Homocoupling of Aryl Bromide on an Au(111) Surface. *Chem. - Eur. J.* **2014**, *20* (14), 4111–4116. <https://doi.org/10.1002/chem.201304443>.

- (255) Björk, J.; Sánchez-Sánchez, C.; Chen, Q.; Pignedoli, C. A.; Rosen, J.; Ruffieux, P.; Feng, X.; Narita, A.; Müllen, K.; Fasel, R. The Role of Metal Adatoms in a Surface-Assisted Cyclodehydrogenation Reaction on a Gold Surface. *Angew. Chem. Int. Ed.* **2022**, *61* (49). <https://doi.org/10.1002/anie.202212354>.
- (256) Björk, J. Reaction Mechanisms for On-Surface Synthesis of Covalent Nanostructures. *J. Phys. Condens. Matter* **2016**, *28* (8), 083002. <https://doi.org/10.1088/0953-8984/28/8/083002>.
- (257) Blankenburg, S.; Cai, J.; Ruffieux, P.; Jaafar, R.; Passerone, D.; Feng, X.; Müllen, K.; Fasel, R.; Pignedoli, C. A. Intraribbon Heterojunction Formation in Ultranarrow Graphene Nanoribbons. *ACS Nano* **2012**, *6* (3), 2020–2025. <https://doi.org/10.1021/nn203129a>.
- (258) Ma, C.; Xiao, Z.; Bonnesen, P. V.; Liang, L.; Poretzky, A. A.; Huang, J.; Kolmer, M.; Sumpter, B. G.; Lu, W.; Hong, K.; Bernholc, J.; Li, A.-P. On-Surface Cyclodehydrogenation Reaction Pathway Determined by Selective Molecular Deuterations. *Chem. Sci.* **2021**, *12* (47), 15637–15644. <https://doi.org/10.1039/D1SC04908A>.
- (259) Bian, K.; Gerber, C.; Heinrich, A. J.; Müller, D. J.; Scheuring, S.; Jiang, Y. Scanning Probe Microscopy. *Nat. Rev. Methods Primer* **2021**, *1* (1), 36. <https://doi.org/10.1038/s43586-021-00033-2>.
- (260) Gross, L.; Moll, N.; Mohn, F.; Curioni, A.; Meyer, G.; Hanke, F.; Persson, M. High-Resolution Molecular Orbital Imaging Using a p-Wave STM Tip. *Phys. Rev. Lett.* **2011**, *107* (8), 086101. <https://doi.org/10.1103/PhysRevLett.107.086101>.
- (261) Zhong, Q.; Li, X.; Zhang, H.; Chi, L. Noncontact Atomic Force Microscopy: Bond Imaging and Beyond. *Surf. Sci. Rep.* **2020**, *75* (4), 100509. <https://doi.org/10.1016/j.surfrep.2020.100509>.
- (262) Mayrhofer, K. J. J. Oxygen Reduction and Carbon Monoxide Oxidation on Pt - from Model to Real Systems for Fuel Cell Electrocatalysis, Technische Universität Wien, 2005.
- (263) Bieri, M.; Nguyen, M.-T.; Gröning, O.; Cai, J.; Treier, M.; Ait-Mansour, K.; Ruffieux, P.; Pignedoli, C. A.; Passerone, D.; Kastler, M.; Müllen, K.; Fasel, R. Two-Dimensional Polymer Formation on Surfaces: Insight into the Roles of Precursor Mobility and Reactivity. *J. Am. Chem. Soc.* **2010**, *132* (46), 16669–16676. <https://doi.org/10.1021/ja107947z>.
- (264) Ishiyama, T.; Murata, M.; Miyaura, N. Palladium(0)-Catalyzed Cross-Coupling Reaction of Alkoxydiboron with Haloarenes: A Direct Procedure for Arylboronic Esters. *J. Org. Chem.* **1995**, *60* (23), 7508–7510. <https://doi.org/10.1021/jo00128a024>.
- (265) Hanif, M.; Lu, P.; Li, M.; Zheng, Y.; Xie, Z.; Ma, Y.; Li, D.; Li, J. Synthesis, Characterization, Electrochemistry and Optical Properties of a Novel Phenanthrenequinone-Alt-Dialkylfluorene Conjugated Copolymer. *Polym. Int.* **2007**, *56* (12), 1507–1513. <https://doi.org/10.1002/pi.2286>.
- (266) Saleh, M.; Baumgarten, M.; Mavrinskiy, A.; Schäfer, T.; Müllen, K. Triphenylene-Based Polymers for Blue Polymeric Light Emitting Diodes. *Macromolecules* **2010**, *43* (1), 137–143. <https://doi.org/10.1021/ma901912t>.
- (267) Koch, M.; Gille, M.; Viertel, A.; Hecht, S.; Grill, L. Substrate-Controlled Linking of Molecular Building Blocks: Au(111) vs. Cu(111). *Surf. Sci.* **2014**, *627*, 70–74. <https://doi.org/10.1016/j.susc.2014.04.011>.
- (268) Shi, K. J.; Zhang, X.; Shu, C. H.; Li, D. Y.; Wu, X. Y.; Liu, P. N. Ullmann Coupling Reaction of Aryl Chlorides on Au(111) Using Dosed Cu as a Catalyst and the Programmed Growth of 2D Covalent Organic Frameworks. *Chem. Commun.* **2016**, *52* (56), 8726–8729. <https://doi.org/10.1039/C6CC03137D>.
- (269) Di Giovannantonio, M.; Deniz, O.; Urgel, J. I.; Widmer, R.; Dienel, T.; Stolz, S.; Sánchez-Sánchez, C.; Muntwiler, M.; Dumsclaff, T.; Berger, R.; Narita, A.; Feng, X.; Müllen, K.; Ruffieux, P.; Fasel, R. On-Surface Growth Dynamics of Graphene Nanoribbons: The Role of Halogen Functionalization. *ACS Nano* **2018**, *12* (1), 74–81. <https://doi.org/10.1021/acsnano.7b07077>.
- (270) Kimouche, A.; Ervasti, M. M.; Drost, R.; Halonen, S.; Harju, A.; Joensuu, P. M.; Sainio, J.; Liljeroth, P. Ultra-Narrow Metallic Armchair Graphene Nanoribbons. *Nat. Commun.* **2015**, *6* (1), 10177. <https://doi.org/10.1038/ncomms10177>.
- (271) Gampe, C. M.; Carreira, E. M. Arynes and Cyclohexyne in Natural Product Synthesis. *Angew. Chem. Int. Ed.* **2012**, *51* (16), 3766–3778. <https://doi.org/10.1002/anie.201107485>.
- (272) Son, Y.-W.; Cohen, M. L.; Louie, S. G. Energy Gaps in Graphene Nanoribbons. *Phys. Rev. Lett.* **2006**, *97* (21), 216803. <https://doi.org/10.1103/PhysRevLett.97.216803>.
- (273) Merino-Díez, N.; García-Lekue, A.; Carbonell-Sanromà, E.; Li, J.; Corso, M.; Colazzo, L.; Sedona, F.; Sánchez-Portal, D.; Pascual, J. I.; de Oteyza, D. G. Width-Dependent Band Gap in Armchair Graphene Nanoribbons Reveals Fermi Level Pinning on Au(111). *ACS Nano* **2017**, *11* (11), 11661–11668. <https://doi.org/10.1021/acsnano.7b06765>.
- (274) Rault-Berthelot, J.; Poriol, C. Diodes électroluminescentes organiques : quatre technologies différentes. *Opt. Photonique* **2021**. <https://doi.org/10.51257/a-v1-e6507>.

- (275) Dhbaibi, K.; Abella, L.; Meunier-Della-Gatta, S.; Roisnel, T.; Vanthuyne, N.; Jamoussi, B.; Pieters, G.; Racine, B.; Quesnel, E.; Autschbach, J.; Crassous, J.; Favereau, L. Achieving High Circularly Polarized Luminescence with Push–Pull Helicenic Systems: From Rationalized Design to Top-Emission CP-OLED Applications. *Chem. Sci.* **2021**, *12* (15), 5522–5533. <https://doi.org/10.1039/D0SC06895K>.
- (276) Zhang, D.-W.; Li, M.; Chen, C.-F. Recent Advances in Circularly Polarized Electroluminescence Based on Organic Light-Emitting Diodes. *Chem. Soc. Rev.* **2020**, *49* (5), 1331–1343. <https://doi.org/10.1039/C9CS00680J>.
- (277) Gauthier, E. S.; Abella, L.; Hellou, N.; Darquié, B.; Caytan, E.; Roisnel, T.; Vanthuyne, N.; Favereau, L.; Srebro-Hooper, M.; Williams, J. A. G.; Autschbach, J.; Crassous, J. Long-Lived Circularly Polarized Phosphorescence in Helicene-NHC Rhenium(I) Complexes: The Influence of Helicene, Halogen, and Stereochemistry on Emission Properties. *Angew. Chem. Int. Ed.* **2020**, *59* (22), 8394–8400. <https://doi.org/10.1002/anie.202002387>.
- (278) Murtaza, G.; Colautti, M.; Hilke, M.; Lombardi, P.; Cataliotti, F. S.; Zavatta, A.; Bacco, D.; Toninelli, C. Efficient Room-Temperature Molecular Single-Photon Sources for Quantum Key Distribution. *Opt. Express* **2023**, *31* (6), 9437. <https://doi.org/10.1364/OE.476440>.
- (279) Mohr, B.; Enkelmann, V.; Wegner, G. Synthesis of Alkyl- and Alkoxy-Substituted Benzils and Oxidative Coupling to Tetraalkoxyphenanthrene-9,10-Diones. *J. Org. Chem.* **1994**, *59* (3), 635–638. <https://doi.org/10.1021/jo00082a022>.
- (280) Thomas, K. R. J.; Velusamy, M.; Lin, J. T.; Chuen, C. H.; Tao, Y.-T. Hexaphenylphenylene Dendronised Pyrenylamines for Efficient Organic Light-Emitting Diodes. *J. Mater. Chem.* **2005**, *15* (41), 4453. <https://doi.org/10.1039/b509325b>.
- (281) Basu, C.; Barthes, C.; Sadhukhan, S. K.; Girdhar, N. K.; Gourdon, A. Synthesis of a 2D Lander. *Eur. J. Org. Chem.* **2007**, *2007* (1), 136–140. <https://doi.org/10.1002/ejoc.200600675>.
- (282) Luliński, S.; Serwatowski, J. Bromine as the Ortho-Directing Group in the Aromatic Metalation/Silylation of Substituted Bromobenzenes. *J. Org. Chem.* **2003**, *68* (24), 9384–9388. <https://doi.org/10.1021/jo034790h>.
- (283) Meitinger, N.; Mengele, A. K.; Witas, K.; Kupfer, S.; Rau, S.; Nauroozi, D. Tetraaryl Cyclopentadienones: Experimental and Theoretical Insights into Negative Solvatochromism and Electrochemistry. *Eur. J. Org. Chem.* **2020**, *2020* (42), 6555–6562. <https://doi.org/10.1002/ejoc.202001091>.
- (284) Jandke, M.; Stroehriegel, P.; Berleb, S.; Werner, E.; Brütting, W. Phenylquinoxaline Polymers and Low Molar Mass Glasses as Electron-Transport Materials in Organic Light-Emitting Diodes. *Macromolecules* **1998**, *31* (19), 6434–6443. <https://doi.org/10.1021/ma9806054>.
- (285) Yamaguchi, Y.; Ochi, T.; Miyamura, S.; Tanaka, T.; Kobayashi, S.; Wakamiya, T.; Matsubara, Y.; Yoshida, Z. Rigid Molecular Architectures That Comprise a 1,3,5-Trisubstituted Benzene Core and Three Oligoaryleneethynylene Arms: Light-Emitting Characteristics and π Conjugation between the Arms. *J. Am. Chem. Soc.* **2006**, *128* (14), 4504–4505. <https://doi.org/10.1021/ja057751r>.
- (286) Wang, D.; Talipov, M. R.; Ivanov, M. V.; Rathore, R. Energy Gap between the Poly-*p*-Phenylene Bridge and Donor Groups Controls the Hole Delocalization in Donor–Bridge–Donor Wires. *J. Am. Chem. Soc.* **2016**, *138* (50), 16337–16344. <https://doi.org/10.1021/jacs.6b09209>.
- (287) Zhu, C.; Zhao, Y.; Wang, D.; Sun, W.-Y.; Shi, Z. Palladium-Catalyzed Direct Arylation and Cyclization of *o*-Iodobiphenyls to a Library of Tetraphenylenes. *Sci. Rep.* **2016**, *6* (1), 33131. <https://doi.org/10.1038/srep33131>.
- (288) Wee, K.-R.; Han, W.-S.; Kim, J.-E.; Kim, A.-L.; Kwon, S.; Kang, S. O. Asymmetric Anthracene-Based Blue Host Materials: Synthesis and Electroluminescence Properties of 9-(2-Naphthyl)-10-Arylanthracenes. *J. Mater. Chem.* **2011**, *21* (4), 1115–1123. <https://doi.org/10.1039/C0JM02877K>.
- (289) Ibuki, E.; Ozasa, S.; Fujioka, Y.; Kitamura, H. Syntheses and Physical Properties of Several Symmetrical Sexiphenyls. *Chem. Pharm. Bull. (Tokyo)* **1980**, *28* (5), 1468–1476. <https://doi.org/10.1248/cpb.28.1468>.

APPENDIX 1

SUPPLEMENTARY NMR EXPERIMENTS OF THE PARTIALLY *TERT*-BUTYLATED GQDS.

C₇₈tBu₆

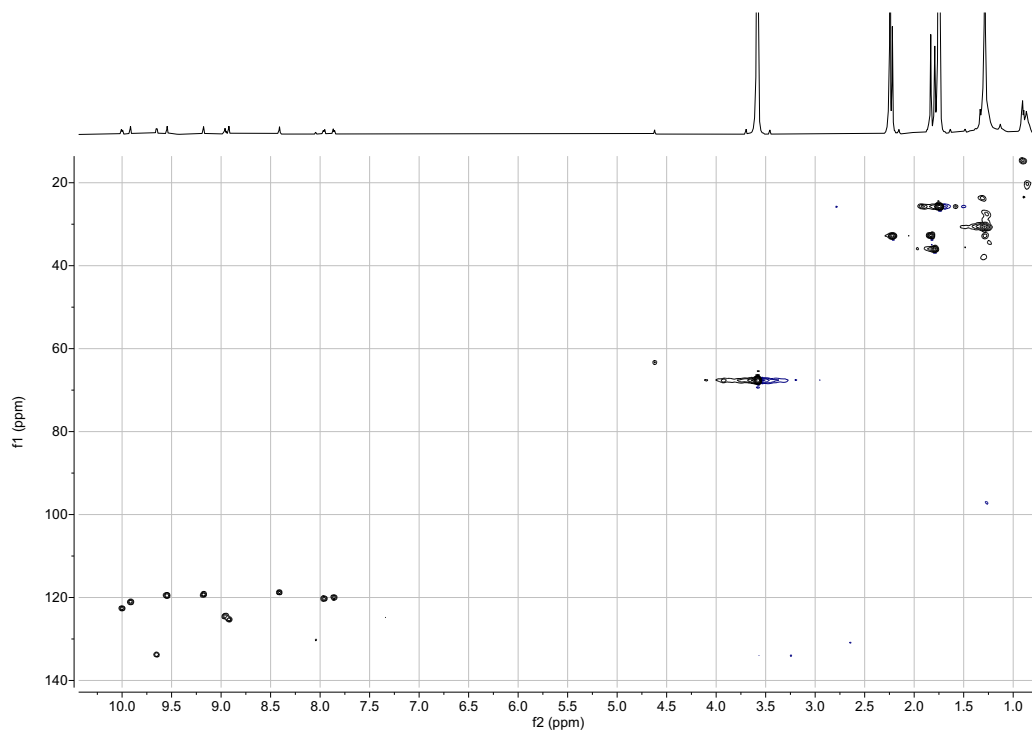


Figure A1.1 | ¹H - ¹³C HSQC NMR spectrum of **C₇₈tBu₆**. 600 MHz, CS₂ + THF-d₈ (250 μL + 350 μL), 298 K, [5.39·10⁻⁴ M].

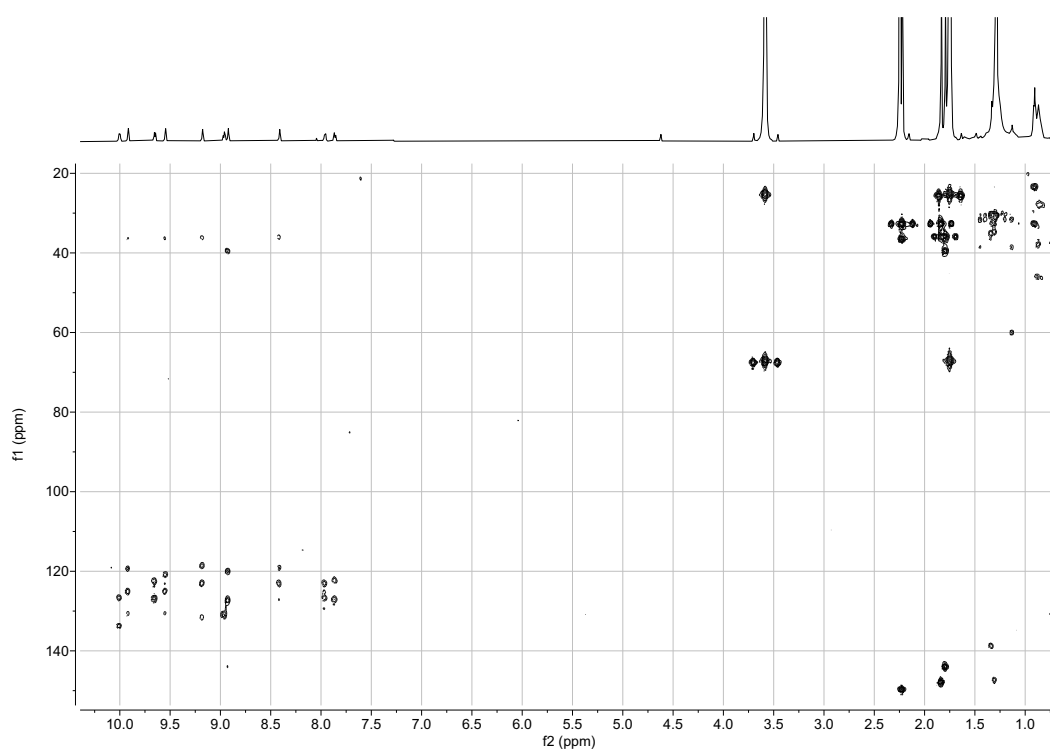


Figure A1.2 | ¹H - ¹³C HMBC NMR spectrum of **C₇₈tBu₆**. 600 MHz, CS₂ + THF-d₈ (250 μL + 350 μL), 298 K, [5.39·10⁻⁴ M].

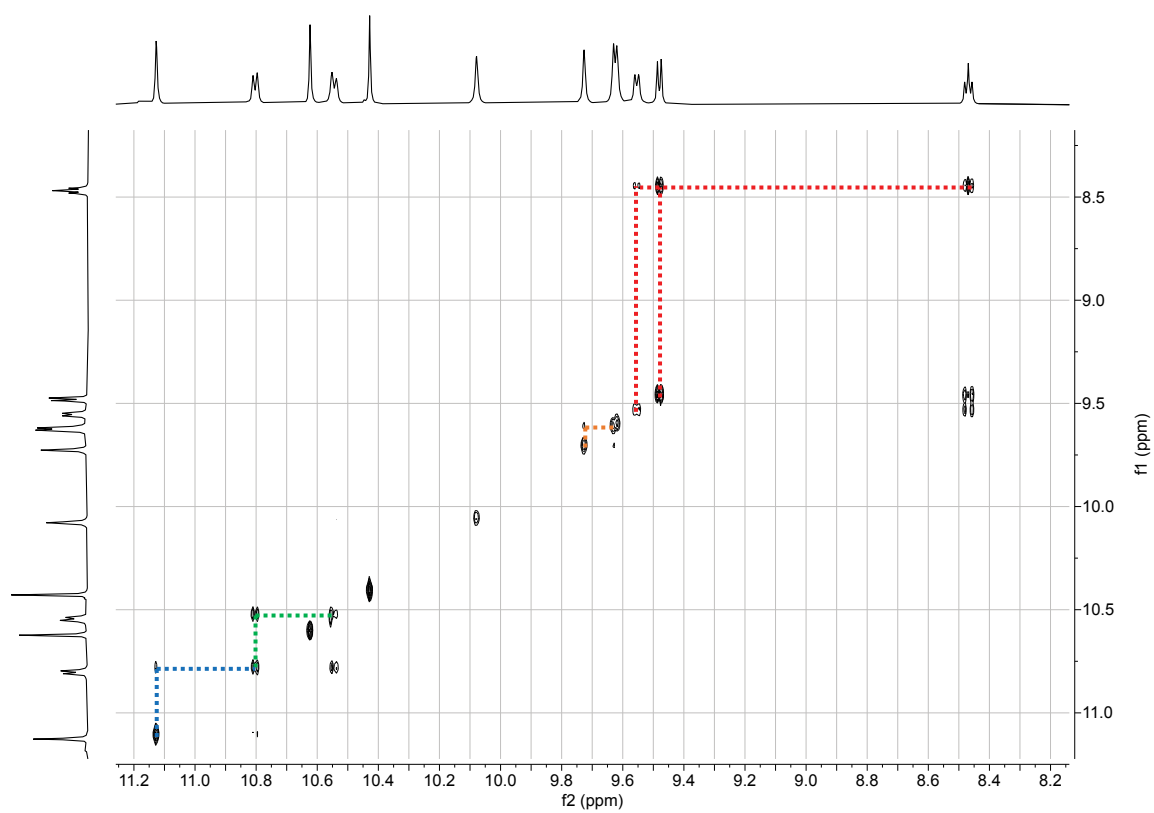


Figure A1.3 | ¹H-¹H COSY NMR spectrum of C₁₁₄tBU₁₀. 600 MHz, CS₂ + THF-d₈ (250 μL + 350 μL), 298 K, [5.86·10⁻⁴ M]. Lines show the correlations between peaks.

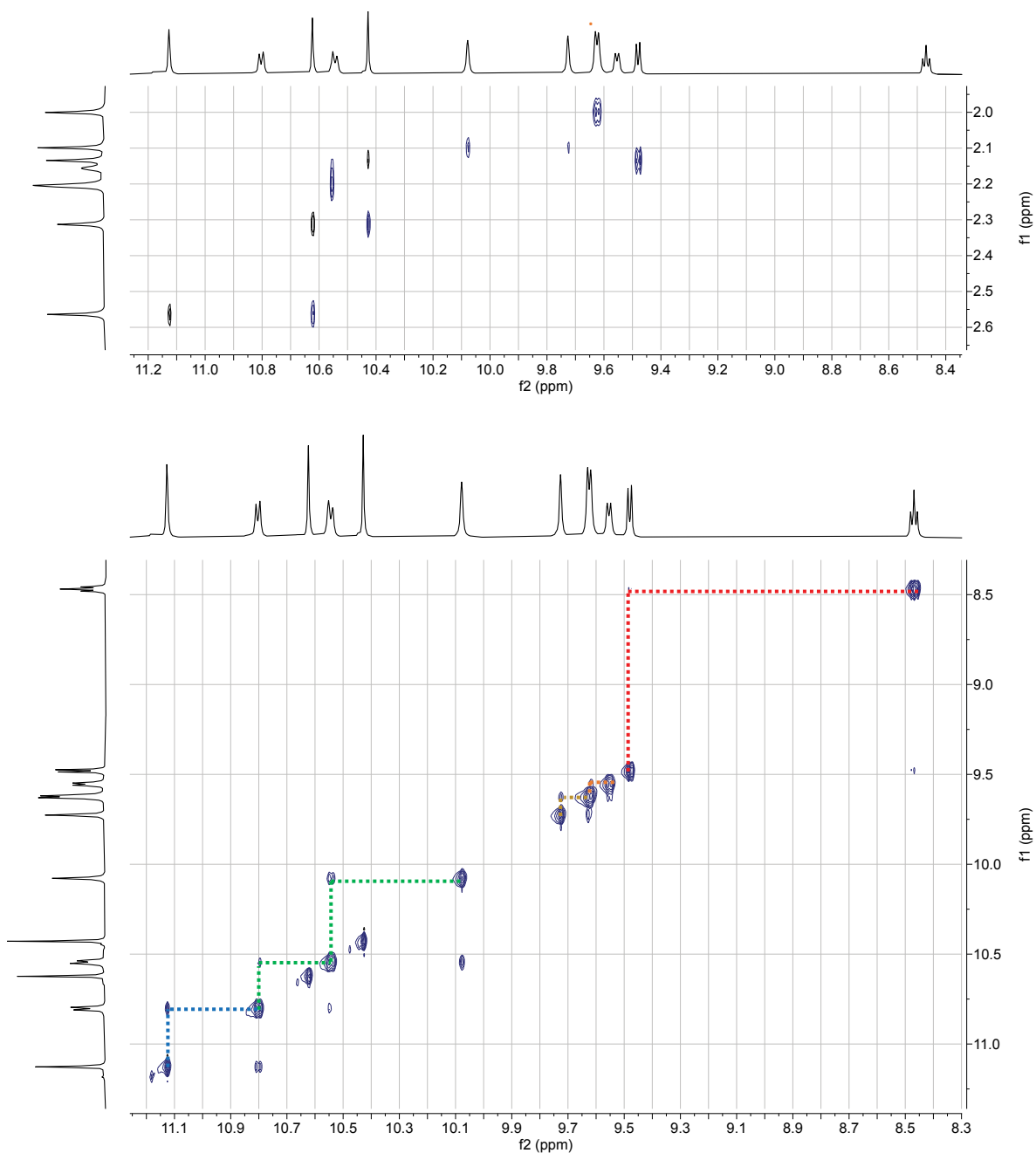


Figure A1.4 | ¹H-¹H NOESY NMR spectrum of **C₁₁₄tBu₁₀**. 600 MHz, CS₂ + THF-d₈ (250 μL + 350 μL), 298 K, [5.86·10⁻⁴ M]. Top, zoom to the coupling between the aromatic and aliphatic regions. Bottom, zoom-in the aromatic region. Lines show the correlations between peaks.

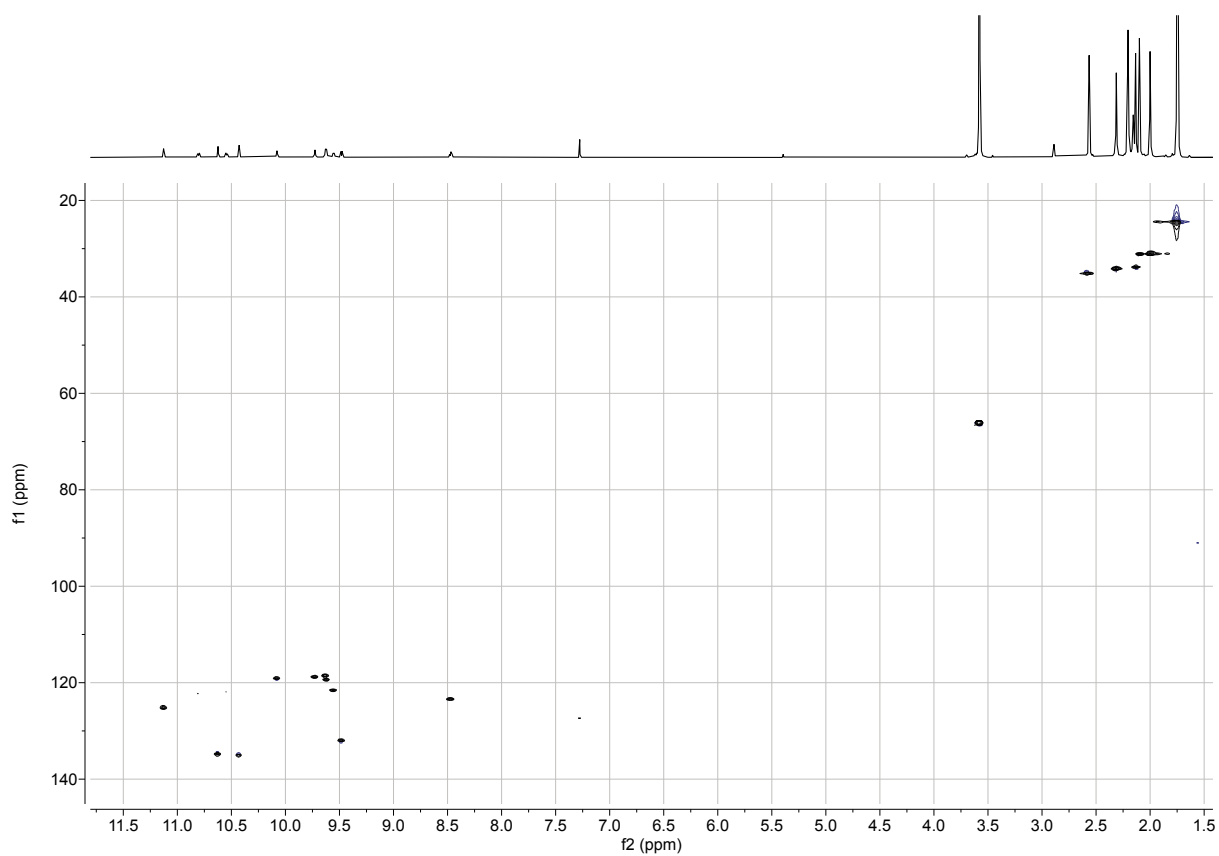


Figure A1.5 | ^1H - ^{13}C HSQC NMR spectrum of $\text{C}_{114}\text{tBu}_{10}$. 600 MHz, $\text{CS}_2 + \text{THF-d}_8$ 250 $\mu\text{L} + 350 \mu\text{L}$, 298 K, $[5.86 \cdot 10^{-4} \text{ M}]$.

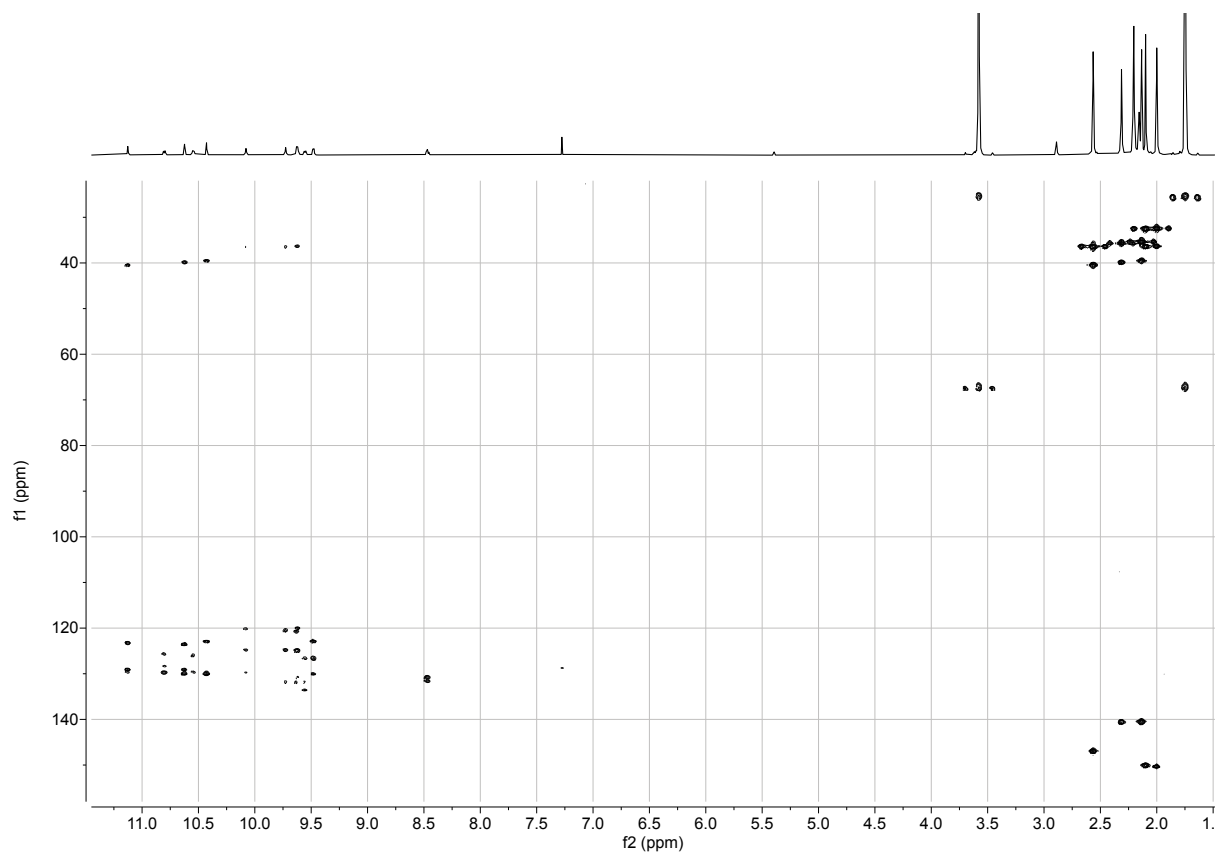


Figure A1.6 | ^1H - ^{13}C HMBC NMR spectrum of $\text{C}_{114}\text{tBu}_{10}$. 600 MHz, $\text{CS}_2 + \text{THF-d}_8$ 250 $\mu\text{L} + 350 \mu\text{L}$, 298 K, $[5.86 \cdot 10^{-4} \text{ M}]$.

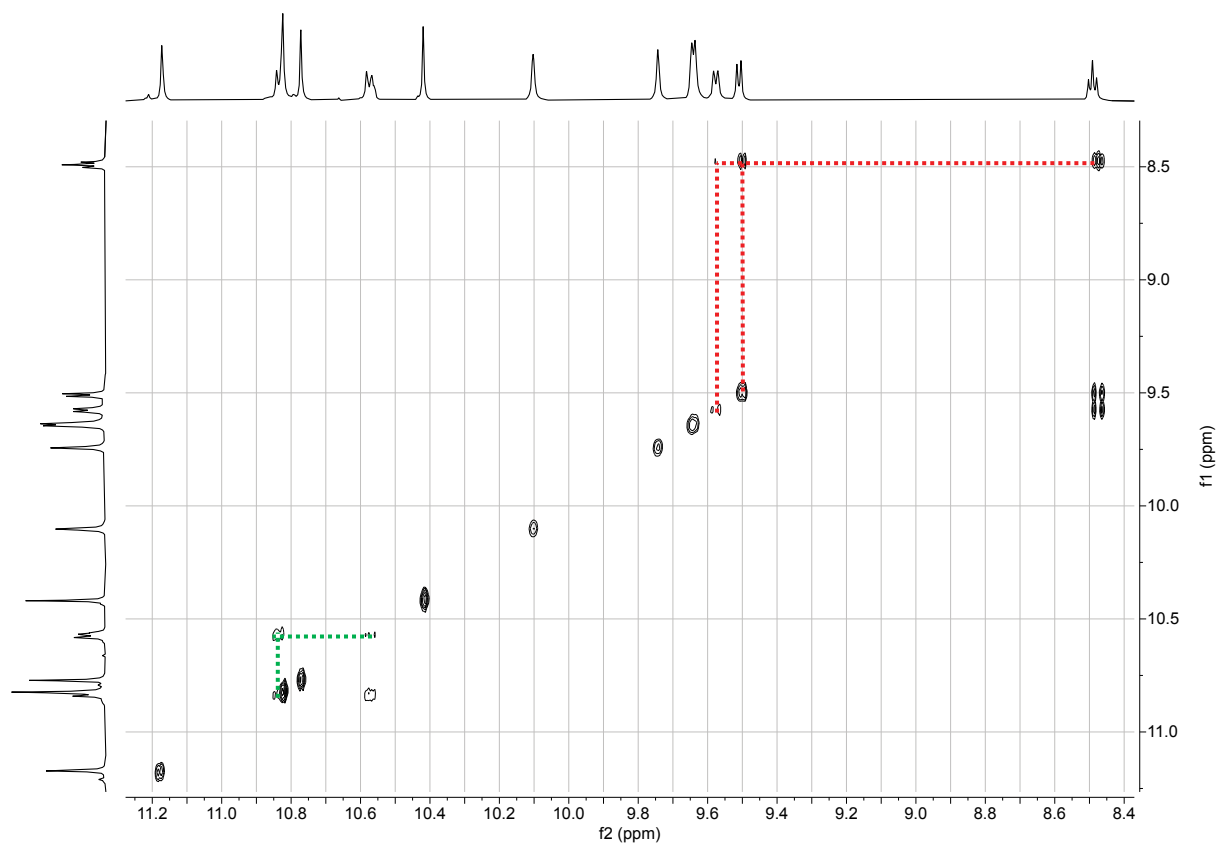


Figure A1.7 | ¹H-¹H COSY NMR spectrum of **C₁₃₂tBU₁₂**. 600 MHz, CS₂ + THF-d₈ (250 μL + 350 μL), 298 K, [5.54·10⁻⁴ M]. Lines show the correlations between peaks.

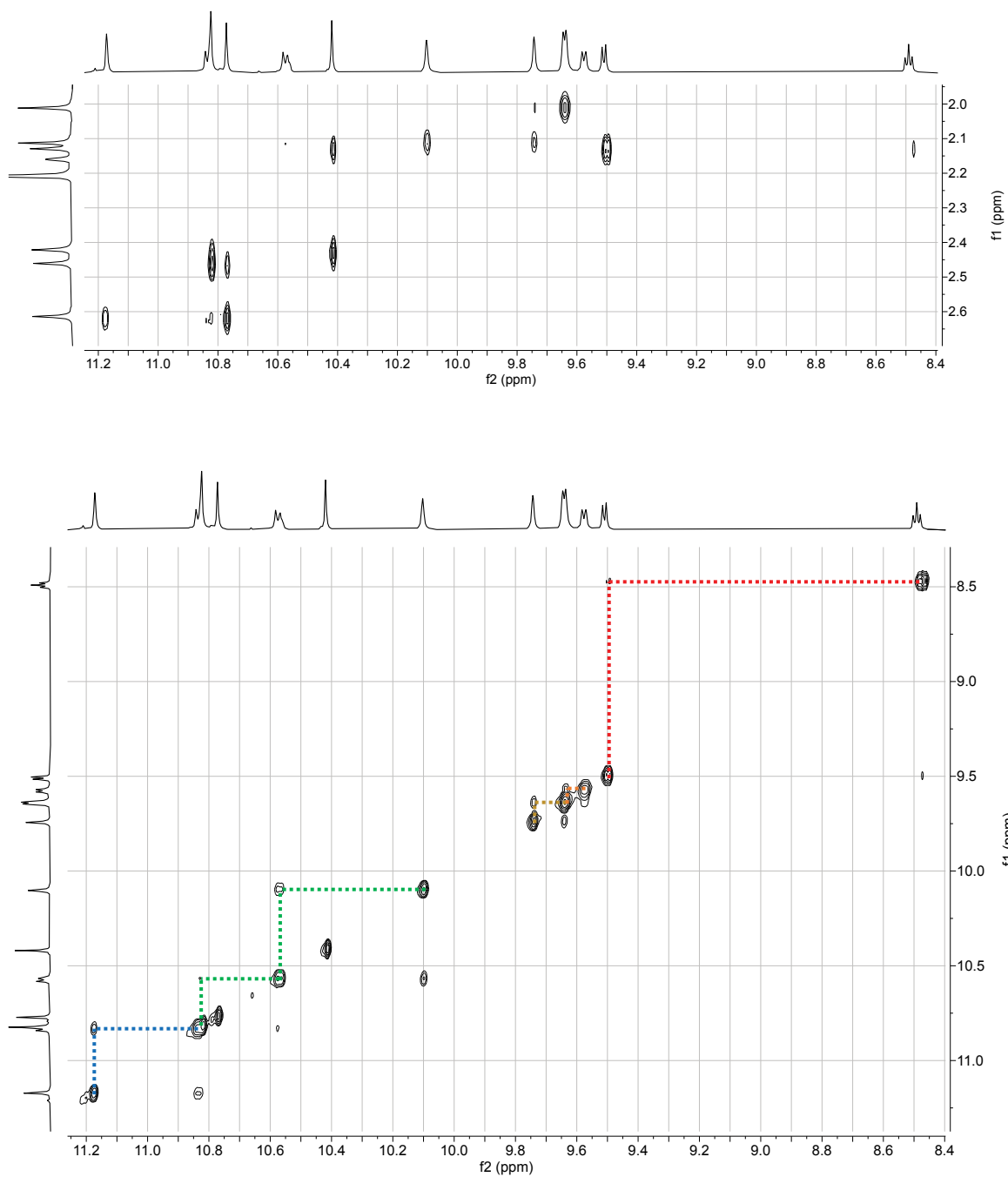


Figure A1.8 | ^1H - ^1H NOESY NMR spectrum of $\text{C}_{132}\text{tBu}_{12}$. 600 MHz, $\text{CS}_2 + \text{THF-d}_8$ (250 $\mu\text{L} + 350 \mu\text{L}$), 298 K, $[5.54 \cdot 10^{-4} \text{ M}]$. Top, zoom to the coupling between the aromatic and aliphatic regions. Bottom, zoom-in the aromatic region. Lines show the correlations between peaks.

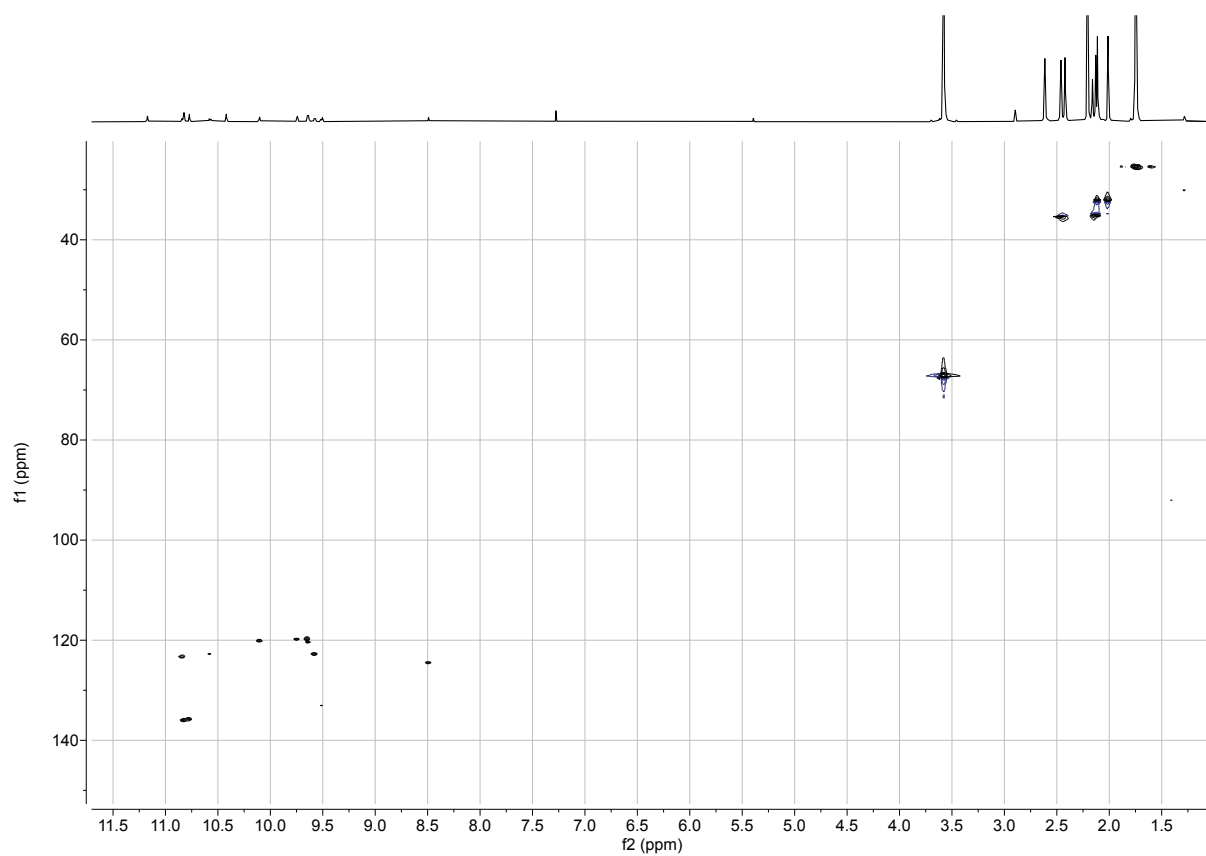


Figure A1.9 | ^1H - ^{13}C HSQC NMR spectrum of $\text{C}_{132}\text{tBu}_{12}$. 600 MHz, $\text{CS}_2 + \text{THF-d}_8$ (250 $\mu\text{L} + 350 \mu\text{L}$), 298 K, $[5.54 \cdot 10^{-4} \text{ M}]$.

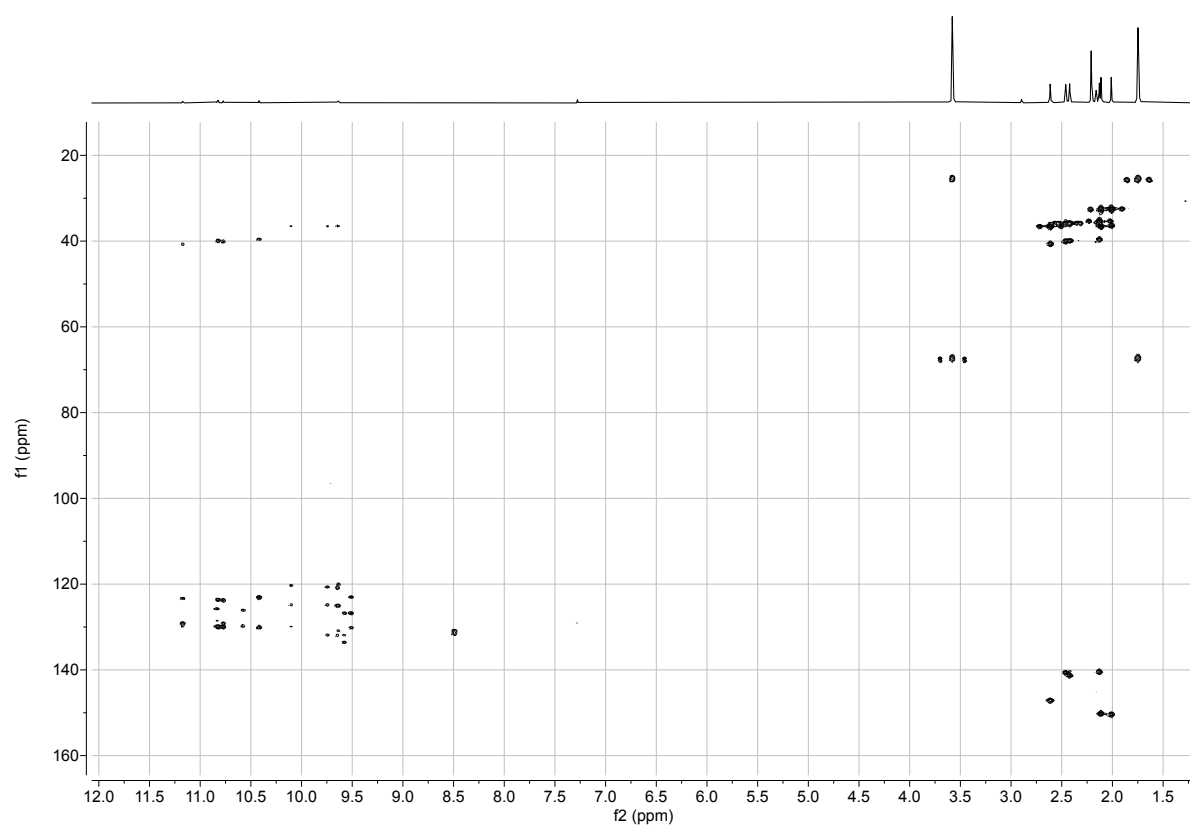


Figure A1.10 | ^1H - ^{13}C HMBC NMR spectrum of $\text{C}_{132}\text{tBu}_{12}$. 600 MHz, $\text{CS}_2 + \text{THF-d}_8$ (250 $\mu\text{L} + 350 \mu\text{L}$), 298 K, $[5.54 \cdot 10^{-4} \text{ M}]$.

APPENDIX 2

^1H NMR EXPERIMENTS OF $\text{C}_{78}\text{tBU}_{10}$, $\text{C}_{96}\text{tBU}_{12}$, AND $\text{C}_{114}\text{tBU}_{14}$

Attribution of the peaks to the structures of $\text{C}_{78}\text{tBU}_{10}$, $\text{C}_{96}\text{tBU}_{12}$, and $\text{C}_{114}\text{tBU}_{14}$ using ^1H - ^1H NOESY and TOCSY NMR spectroscopy remained a challenge. Some peaks are close together and the resolution did not allow to fully distinguish the correlations. Further experiments are needed to help with attribution. To help with resolution, it is possible to try to increase the number of scans, perform experiments on a spectrometer with a higher magnetic field or changing the solvent. However, ^1H - ^{13}C HSQC and HMBC NMR experiments showed the expected cross peaks for the *tert*-butyl groups of the GQD (marked with a pink star) from those of water, solvent, and impurities, for which no carbon signal was present, or the carbon signal did not match the pattern observed so far in the rod-shaped GQDs. The integration of the peaks in the aromatic regions and the *tert*-butyl peaks yielded the expected number of protons for the three structures. The ^1H spectrum of each GQD is showed in the following figures.

$\text{C}_{78}\text{tBU}_{10}$ ^1H NMR

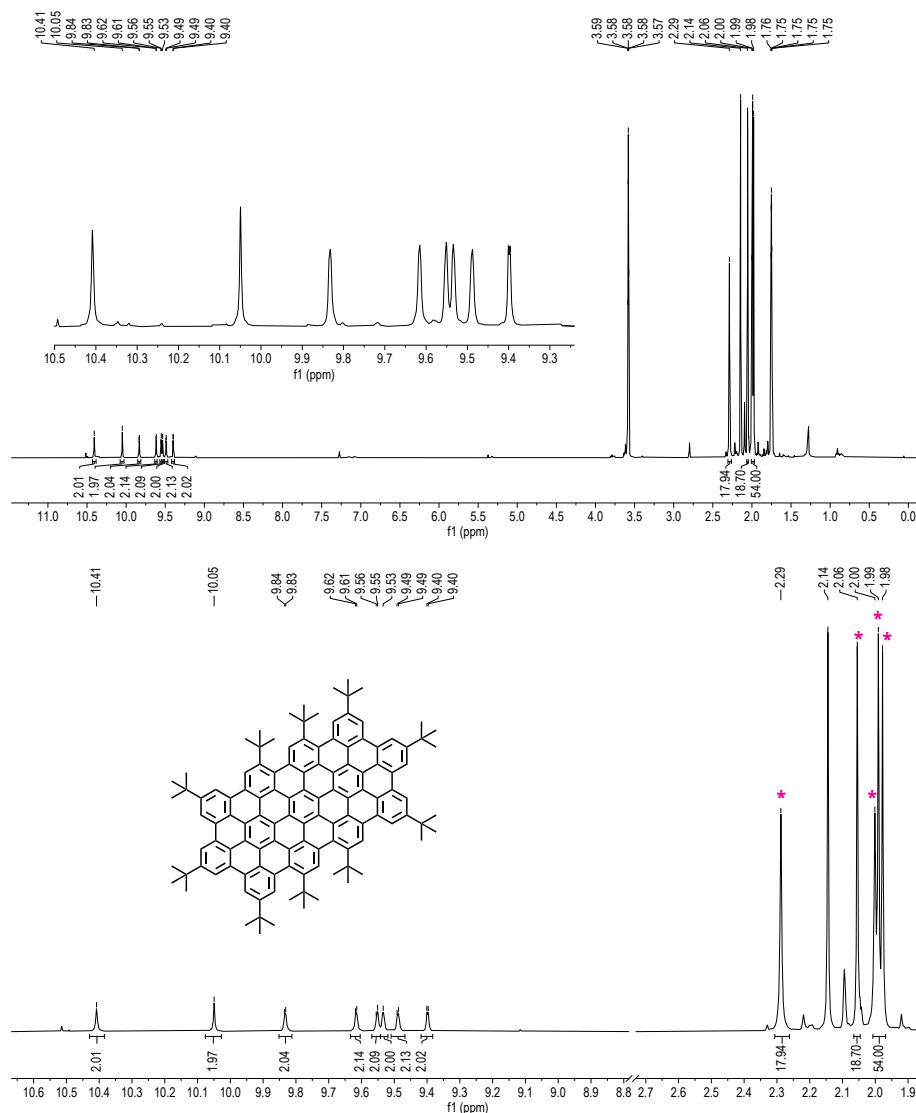


Figure A2.1 | Top, ^1H NMR (400 MHz, $\text{THF-d}_8 + \text{CS}_2$, 298 K) spectrum of $\text{C}_{78}\text{tBU}_{10}$ with zoom on the aromatic region. Below, zoom on the aromatic and aliphatic regions. Pink stars showed the signals corresponding to the *tert*-butyl groups of the GQD.

C₉₆tBu₁₂ ¹H NMR

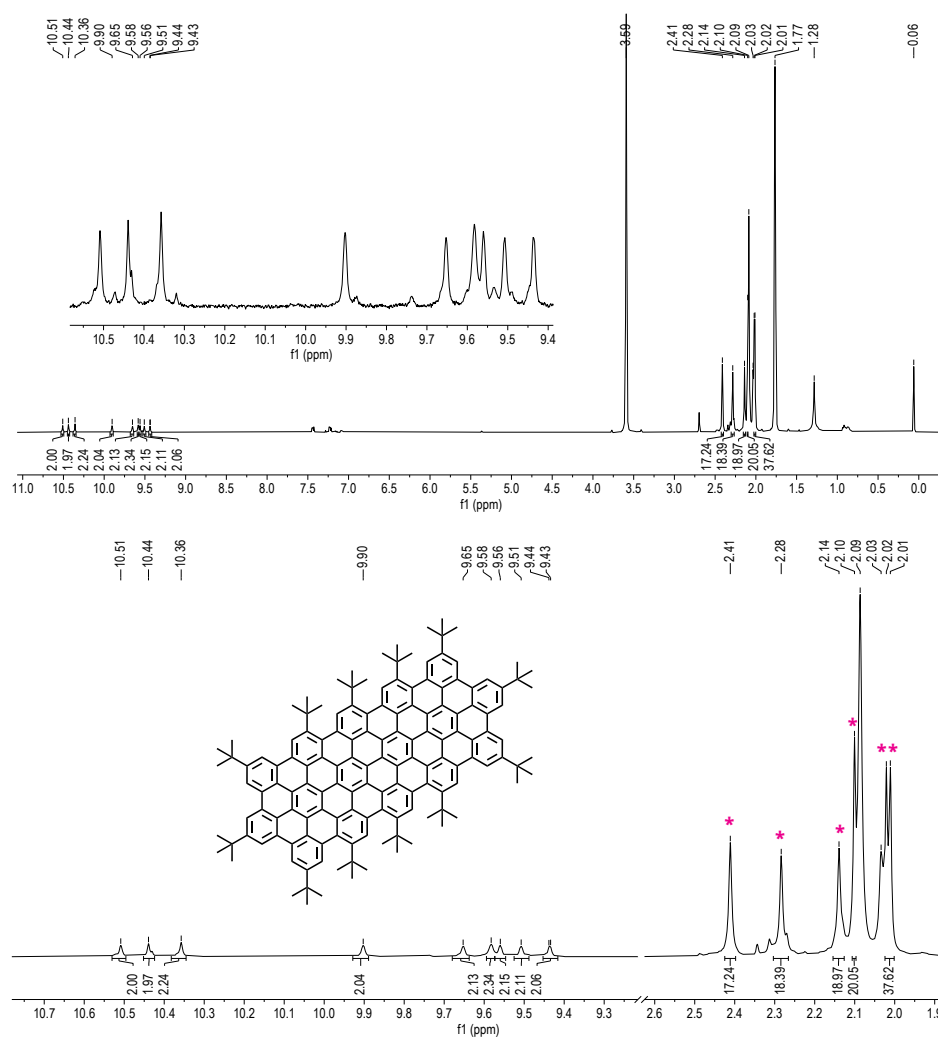


Figure A2.2 | Top, ¹H NMR (400 MHz, THF-d₈+CS₂, 298 K) spectrum of C₉₆tBu₁₂ with zoom on the aromatic region. Below, zoom on the aromatic and aliphatic regions. Pink stars showed the signals corresponding to the *tert*-butyl groups of the GQD.

C₁₁₄tBu₁₄ ¹H NMR

Two *tert*-butyl groups could not be integrated because they superimpose with the water peak, but the presence of the peaks was confirmed by ¹H-¹³C HSQC and HMBC NMR. The signals around 7.5 ppm did not correlate with any proton in the 2D experiments, suggesting they may arise from impurities. However, its identification was not possible. Besides in the MALDI-ToF spectrum no impurity was detected. After a few days, a precipitate formed at the bottom of the NMR tube.

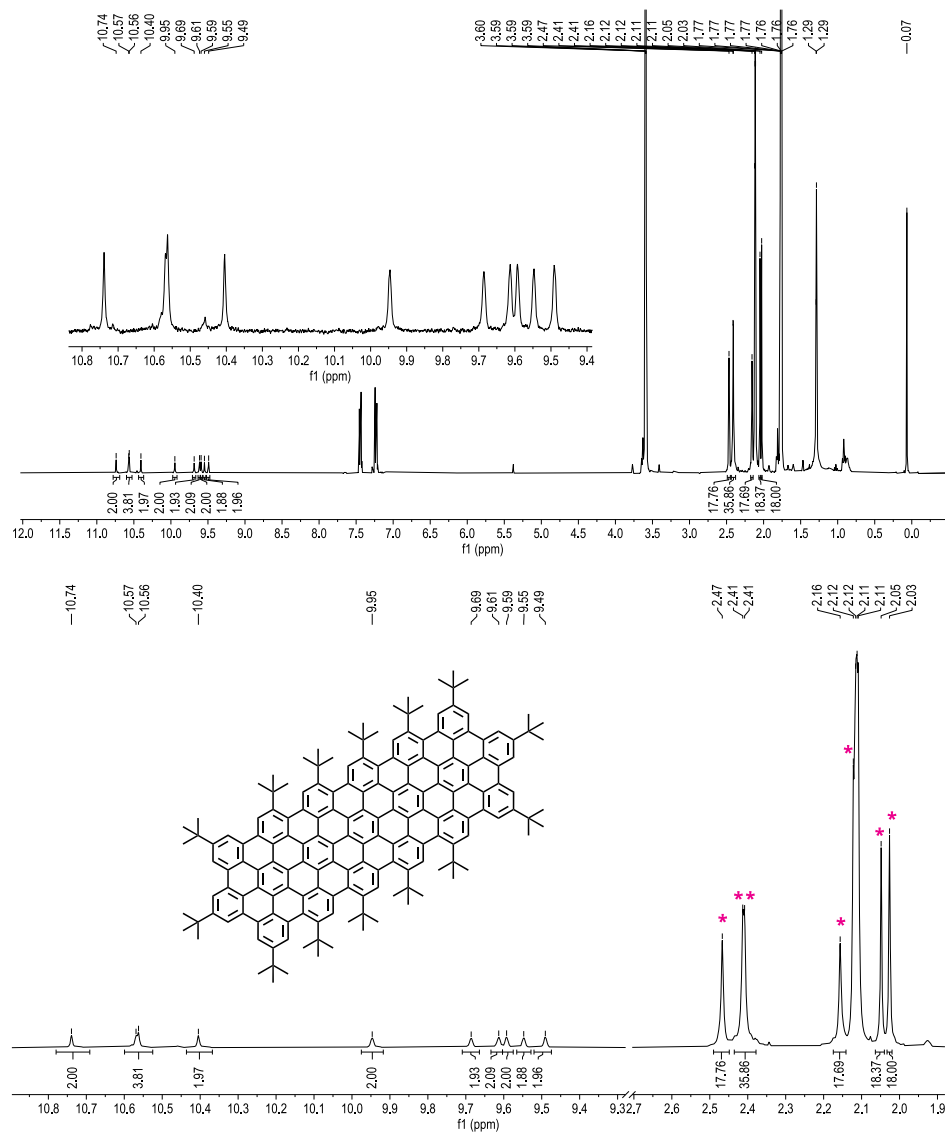
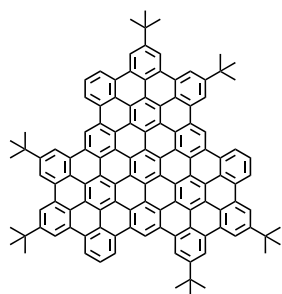


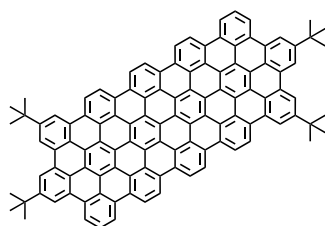
Figure A2.3 | Top, ¹H NMR (400 MHz, THF-d₈+CS₂, 298 K) spectrum of C₁₁₄tBu₁₄ with zoom on the aromatic region. Below, zoom on the aromatic and aliphatic regions. Pink stars showed the signals corresponding to the *tert*-butyl groups of the QGD.

Molecule Glossary

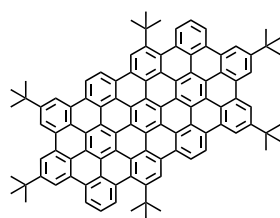
Graphene quantum dots



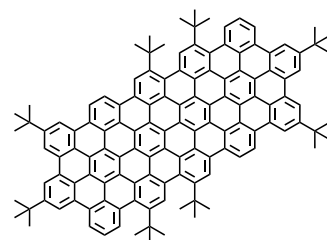
(T)C₉₆tBu₈



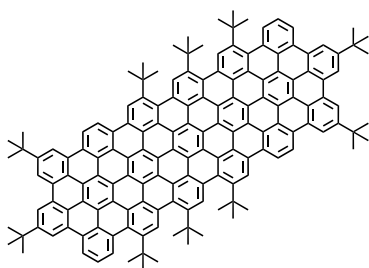
C₉₆tBu₄



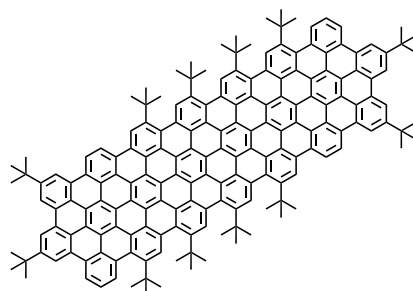
C₇₈tBu₆



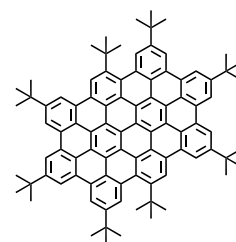
C₉₆tBu₈



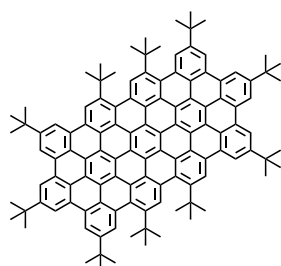
C₁₁₄tBu₁₀



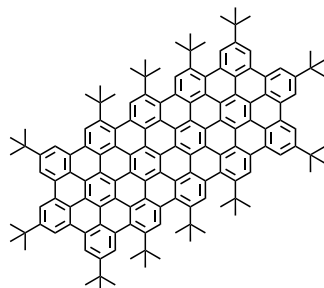
C₁₃₂tBu₁₂



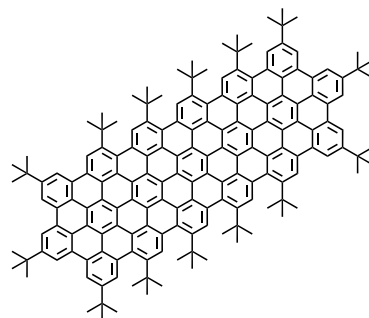
C₇₂tBu₈



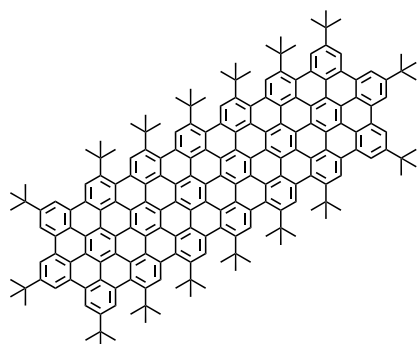
C₇₈tBu₁₀



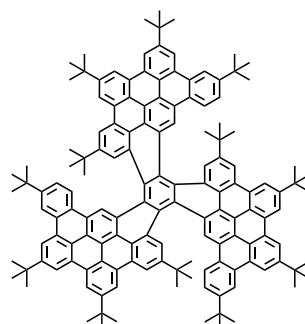
C₉₆tBu₁₂



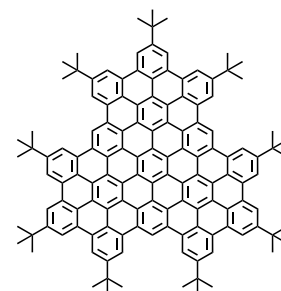
C₁₁₄tBu₁₄



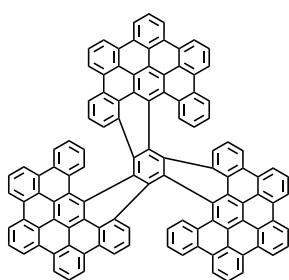
C₁₃₂tBu₁₆



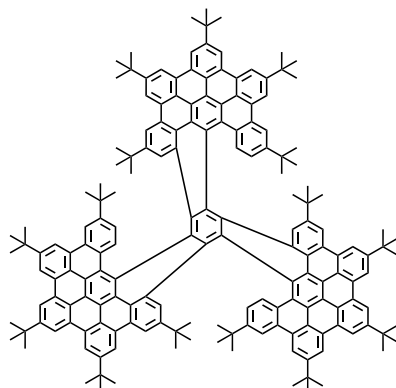
(C₃₀tBu₄)₃-T[6]H



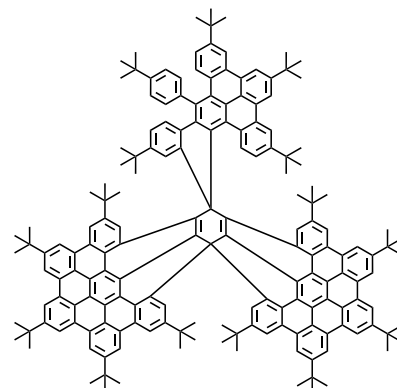
(T)C₉₆tBu₉



(C₃₆)₃-T[6]H

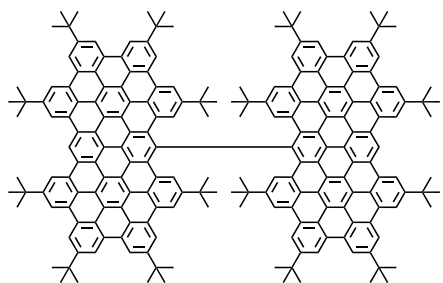


(C₃₆tBu₅)₃-T[6]H

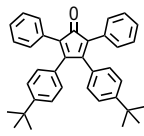


bis-spiro 47

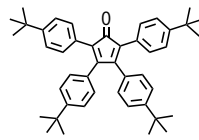
Cyclopentadienones



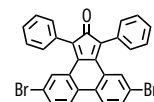
$(C_{72}tBu_8)_2$



CP-1

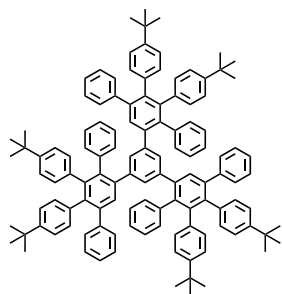


CP-2

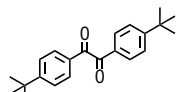


CP-3

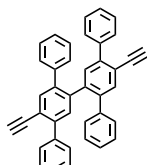
Chapter 2



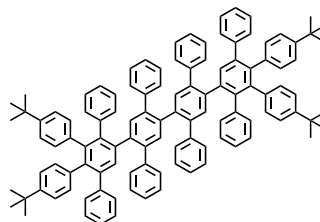
1



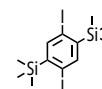
2



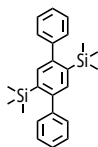
3



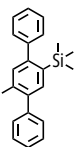
4



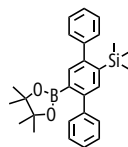
5



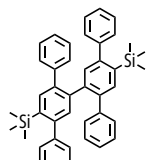
6



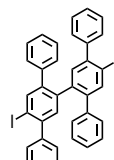
7



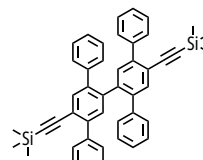
8



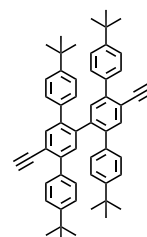
9



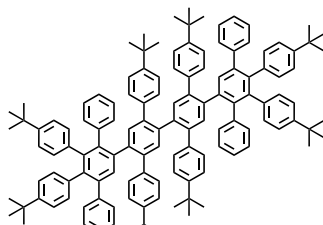
10



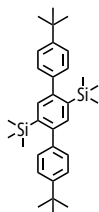
11



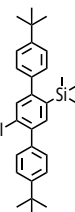
12



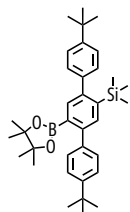
13



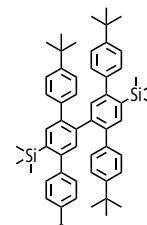
14



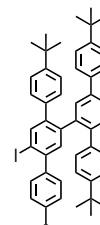
15



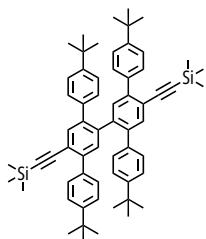
16



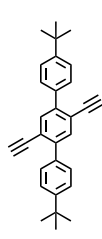
17



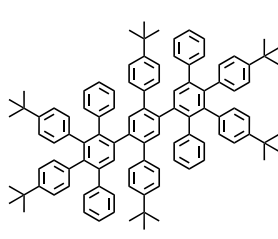
18



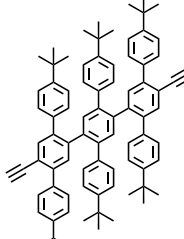
19



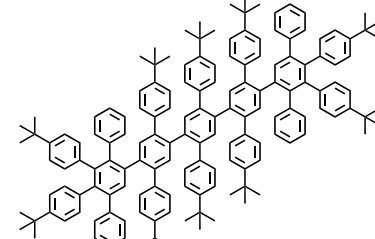
20



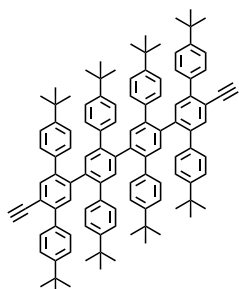
21



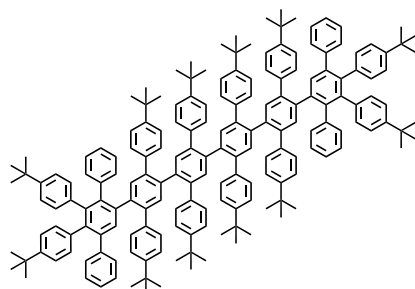
22



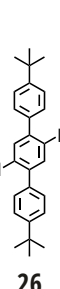
23



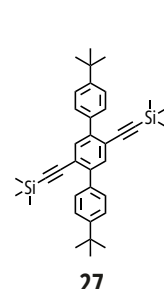
24



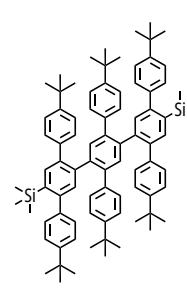
25



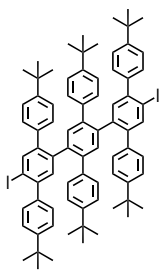
26



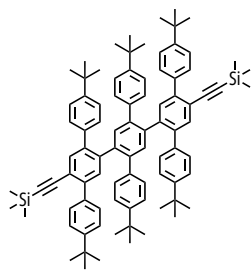
27



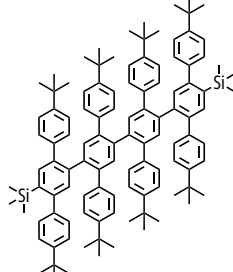
28



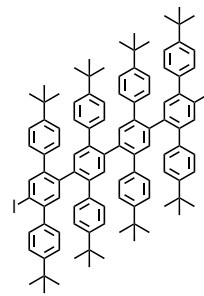
29



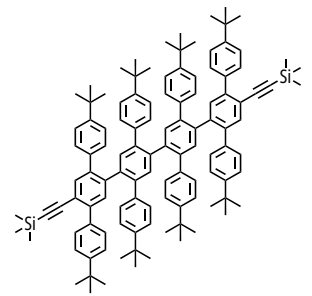
30



31

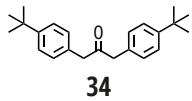


32

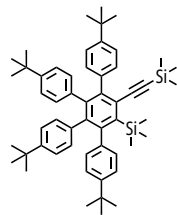


33

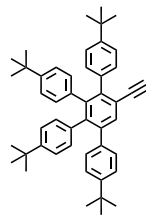
Chapter 3



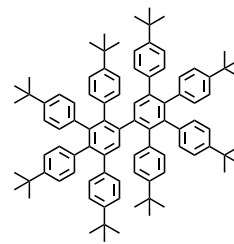
34



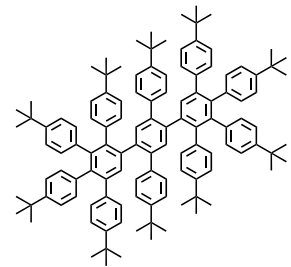
35



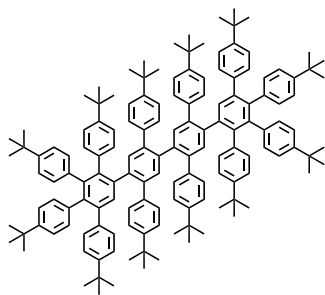
36



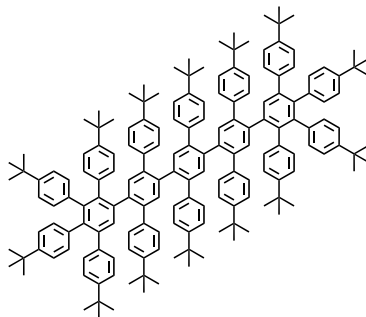
37



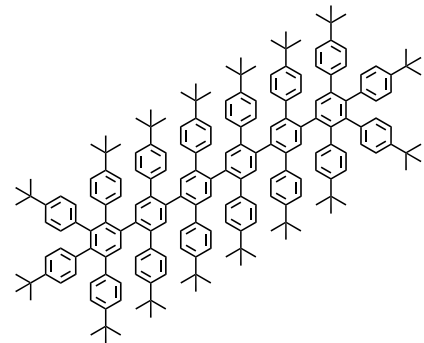
18



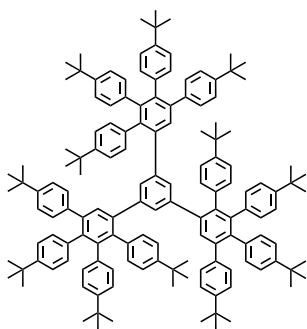
39



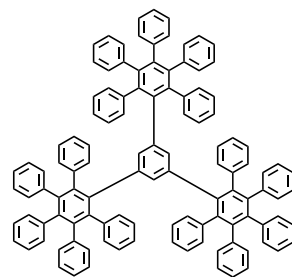
40



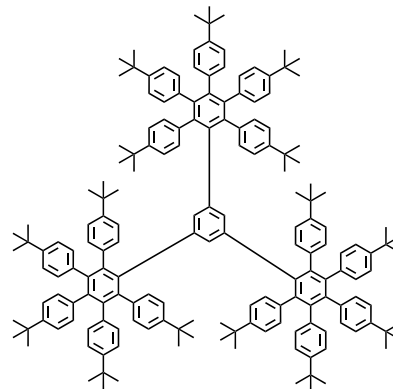
41



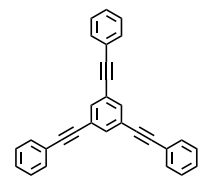
42



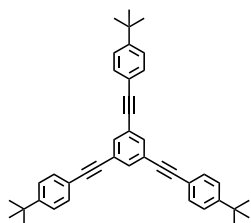
43



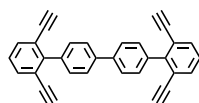
44



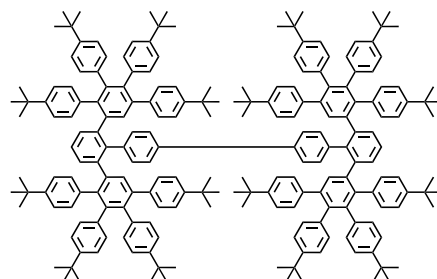
45



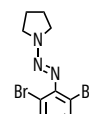
46



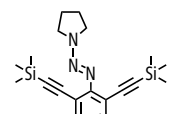
48



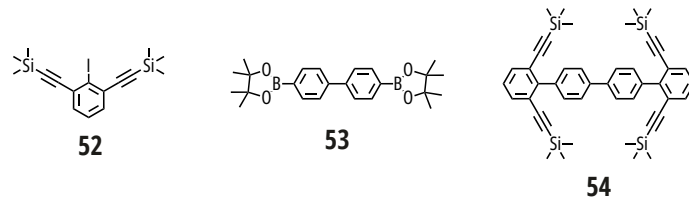
49



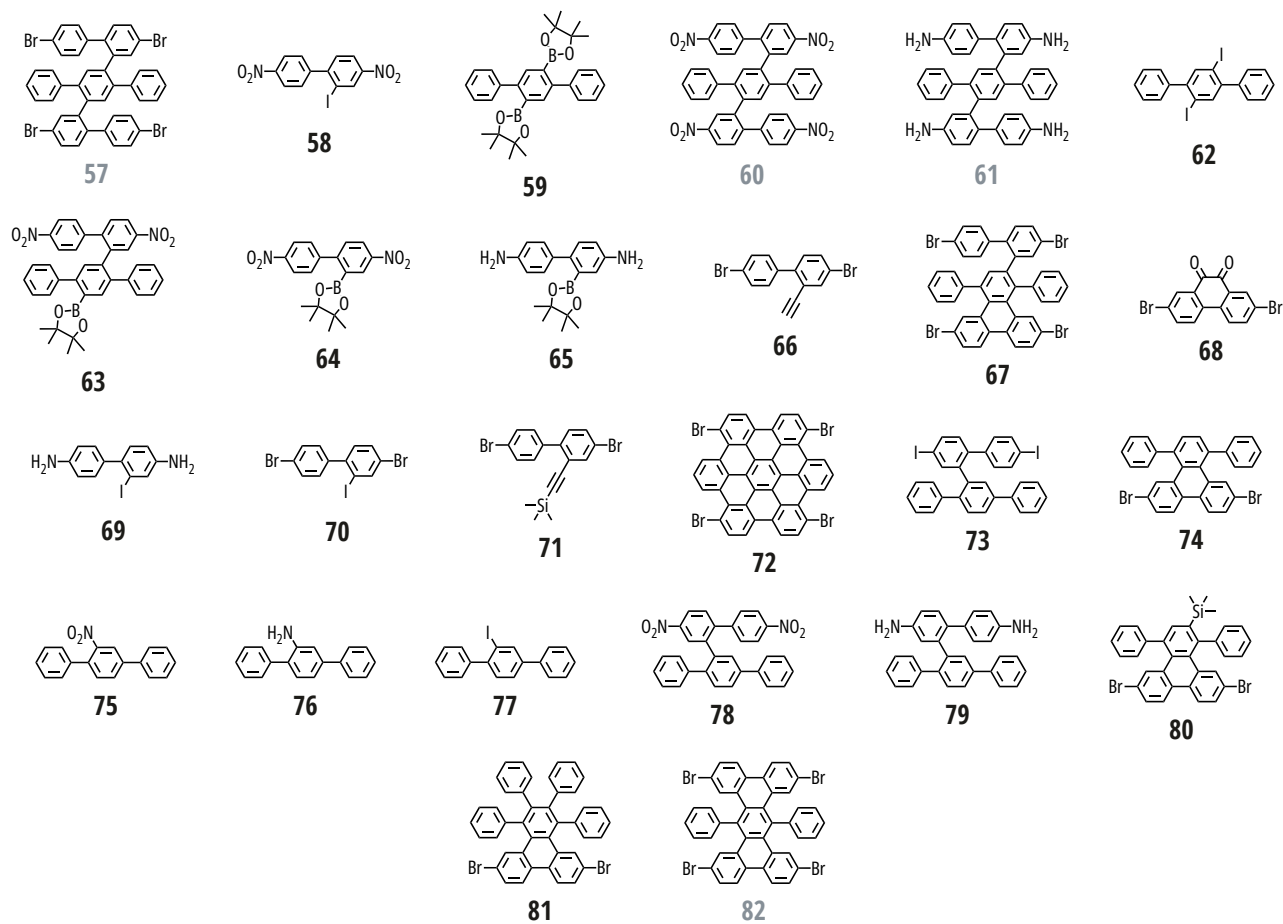
50



51



Chapter 4



* Molecules indicated with a grey name correspond to compounds that have not yet been synthesized, but were discussed in the main manuscript.